NUREG/CR–6167
SAND93–3931

Late-Phase Melt Progression Experiment: MP–2

Results and Analysis

Prepared by
R. D. Gasser, R. O. Gauntt, S. C. Bourcier, R. C. Schmidt, L. L. Humphries, K. O. Reil

Sandia National Laboratories
Operated by
Sandia Corporation

Prepared for
U.S. Nuclear Regulatory Commission

AVAILABILITY NOTICE

Availability of Reference Materials Cited in NRC Publications

Most documents cited in NRC publications will be available from one of the following sources:

1. The NRC Public Document Room, 2120 L Street, NW., Lower Level, Washington, DC 20555-0001

2. The Superintendent of Documents, U.S. Government Printing Office, P. O. Box 37082, Washington, DC 20402-9328

3. The National Technical Information Service, Springfield, VA 22161-0002

Although the listing that follows represents the majority of documents cited in NRC publications, it is not intended to be exhaustive.

Referenced documents available for inspection and copying for a fee from the NRC Public Document Room include NRC correspondence and internal NRC memoranda; NRC bulletins, circulars, information notices, inspection and investigation notices; licensee event reports; vendor reports and correspondence; Commission papers; and applicant and licensee documents and correspondence.

The following documents in the NUREG series are available for purchase from the Government Printing Office: formal NRC staff and contractor reports, NRC-sponsored conference proceedings, international agreement reports, grantee reports, and NRC booklets and brochures. Also available are regulatory guides, NRC regulations in the *Code of Federal Regulations*, and *Nuclear Regulatory Commission Issuances*.

Documents available from the National Technical Information Service include NUREG-series reports and technical reports prepared by other Federal agencies and reports prepared by the Atomic Energy Commission, forerunner agency to the Nuclear Regulatory Commission.

Documents available from public and special technical libraries include all open literature items, such as books, journal articles, and transactions. *Federal Register* notices, Federal and State legislation, and congressional reports can usually be obtained from these libraries.

Documents such as theses, dissertations, foreign reports and translations, and non-NRC conference proceedings are available for purchase from the organization sponsoring the publication cited.

Single copies of NRC draft reports are available free, to the extent of supply, upon written request to the Office of Administration, Distribution and Mail Services Section, U.S. Nuclear Regulatory Commission, Washington, DC 20555-0001.

Copies of industry codes and standards used in a substantive manner in the NRC regulatory process are maintained at the NRC Library, Two White Flint North, 11545 Rockville Pike, Rockville, MD 20852-2738, for use by the public. Codes and standards are usually copyrighted and may be purchased from the originating organization or, if they are American National Standards, from the American National Standards Institute, 1430 Broadway, New York, NY 10018-3308.

DISCLAIMER NOTICE

NUREG/CR-6167
SAND93-3931

Late-Phase Melt Progression Experiment: MP-2

Results and Analysis

Manuscript Completed: December 1996
Date Published: May 1997

Prepared by
R. D. Gasser, R. O. Gauntt, S. C. Bourcier, R. C. Schmidt, L. L. Humphries*, K. O. Reil

Sandia National Laboratories
Albuquerque, NM 87185

A. Malliakos, NRC Project Manager

Prepared for
Division of Systems Technology
Office of Nuclear Regulatory Research
U.S. Nuclear Regulatory Commission
Washington, DC 20555-0001
NRC Job Code A1335, L2452

*SAIC, Albuquerque, NM 87106

For sale by the U.S. Government Printing Office
Superintendent of Documents, Mail Stop: SSOP, Washington, DC 20402-9328
ISBN 0-16-049095-2

Abstract

A series of in-pile experiments that addresses the phenomenology associated with Late-Phase processes in Light Water Reactors (LWRs) has been performed in the Annular Core Research Reactor (ACRR) at Sandia National Laboratories. The Melt Progression (MP) experiments were designed to provide information as part of the effort to develop and verify computer models for the analysis of LWR core damage during severe accidents. The MP-2 experiment is the second experiment in the series. The MP experiments examine the formation and movement of ceramic molten pools that form in the disrupted regions of a reactor core and migrate through the disrupted and intact regions of the core toward the core boundaries. The late phase of a reactor accident evolves as a consequence of early phase core degradation processes that include cladding oxidation, melting, core blockage formation, and general loss of fuel rod geometry. The MP-2 experiment assembly consisted of three regions: (1) a rubble bed composed of enriched UO_2 and ZrO_2 that simulated the severely disrupted regions of the reactor core, (2) a composite ceramic/metallic crust which represented the blockage formed by the early phase melting, relocation, and refreezing of mostly metallic core components, and (3) an intact rod stub region that remained in place below the blockage region. The test assembly was fission heated in the central cavity of the ACRR at an average rate of ~0.2 K/s ultimately achieving a peak temperature in the molten pool of ~3400 K. Melting of the debris bed ceramic components was initiated near the center of the bed. The molten material relocated downward under the influence of gravity, refreezing to form a ceramic crust near the bottom of the rubble bed. As ACRR power levels were increased over time, the crust gradually remelted and reformed at progressively lower positions in the bed until late in the experiment when it penetrated into and attacked the ceramic/metallic blockage. The metallic components of the blockage region melted and relocated downward to the bottom of the intact rod stub region prior to the time at which the ceramic melt penetrated the blockage region from above. The ceramic pool had penetrated halfway into the blockage region at the end of the experiment. The measurements of thermal response and material relocation are discussed and compared to the results of the computer simulations. Postexperiment examination of the assembly with the associated material interactions and metallurgy are also discussed in detail together with the analyses and interpretation of the results.

Contents

Page

1.0 EXECUTIVE SUMMARY 1.1

1.1 Introduction 1.1
1.2 The MP Late-Phase Experiments 1.1
1.3 Conduct of the MP-2 Test 1.1
1.4 Posttest Examination 1.2
1.5 Posttest Analysis 1.2

2.0 EXPERIMENT DESCRIPTION 2.1

2.1 Debris Bed 2.1
2.2 Prefabricated Crust 2.1
2.3 Fuel Rod Stub Region 2.2
2.4 Melt and Thermal Barriers 2.2
2.5 Containment Structures 2.3
2.6 Heat Removal System 2.3
2.7 Instrumentation System 2.4
2.8 Conduct of the MP-2 Test 2.4
2.8.1 Method of Test Control 2.4
2.8.2 Chronology of MP-2 Progression 2.5

3.0 MP-2 POST-IRRADIATION EXAMINATION 3.1

3.1 Post-Irradiation Examination Procedure 3.1
3.1.1 Stabilization of the Experiment Package 3.1
3.1.2 X-Ray Analysis 3.1
3.1.3 Sectioning of the Experiment Capsule 3.1
3.1.4 Metallography 3.2
3.1.4.1 Remote Metallography 3.2
3.1.4.2 Glove Box Metallography and Optical Macroscopy 3.2
3.1.5 Scanning Electron Microscopy and X-Ray Analysis 3.2
3.2 Post-Irradiation Examination Results 3.3
3.2.1 X-Ray Analysis 3.3
3.2.1.1 Radiography of Pretest and Posttest Experiment Capsule 3.3
3.2.1.2 Implications From the Radiographs 3.3
3.2.2 Optical Macroscopy 3.3
3.2.3 Scanning Electron Microscopy and X-Ray Analysis 3.4
3.2.3.1 Regions of Interest 3.4
3.2.3.2 Physical Description of Phases Present 3.5
3.2.3.3 Elemental Analysis Results 3.8
3.3 Interpretation of Elemental Analyses 3.10
3.4 Conclusions 3.11
3.4.1 Debris Bed 3.11
3.4.2 Melt Pool 3.12
3.4.3 Metallic Crust Remnant 3.12
3.4.4 Relocated Material 3.12

4.0 RESULTS AND ANALYSES 4.1

4.1 Measured Data 4.1
4.1.1 Measurement Uncertainties 4.1
4.1.2 Summary of Temperature Measurements 4.2
4.2 MP-2 Analyses 4.3

Contents (Concluded)

Page

4.2.1 Analysis Uncertainties 4.3
4.2.2 DEBRIS Code Analysis of MP-2 ..... 4.4
4.2.2.1 DEBRIS Code Description 4.4
4.2.2.2 Comparison of DEBRIS Thermal Analysis With Measurements 4.5
4.2.2.3 Overview of DEBRIS Thermal Analysis 4.8
4.2.2.4 Overall Energy Balance 4.9
4.2.2.5 DEBRIS Analysis of Material Motion 4.10
4.2.3 Implication of MP-2 Analysis for DEBRIS Code Modeling 4.15

5.0 CONCLUSIONS 5.1

5.1 Experimental Results 5.1
5.1.1 Conclusions from Temperature Measurements and Analysis 5.1
5.1.2 Conclusions from Post-Irradiation Examination 5.2
5.2 DEBRIS Code Performance 5.4
5.3 Conclusions Regarding Generic Late-Phase Processes 5.5

REFERENCES R.1

Appendix A. DEBRIS Model Description A.1

Appendix B. Heat Transfer in the MP-2 Cooling Jacket B.1

Appendix C-1. Preexperiment Analysis of the Preformed Crust C-1.1

Appendix C-2. Discussion of Scanning Electron Microscopy of Selected Areas C-2.1

Appendix D. MP-2 Measured Data D-1

List of Tables

Page

2.1 MP-2 Material Inventory 2.7
3.1 Longitudinal Section Designation 3.14
3.2 Standards Data for Scanning Electron Microscopy With X-Ray Analysis 3.14
3.3 Sample Identification, Location and Microstructure as Determined by Scanning Electron Microscopy 3.15
3.4 Uranium and Oxygen Content at Various Locations Within a Fuel Rod Within the Ceramic Melt (sample 4-2-2) 3.16
3.5 Radial locations of Measurements Made of Sample 4-2-2 and Atomic Percent Average at Each of Nine Locations 3.17
3.6 Chemical Analysis of the Upper Debris Bed 3.18
3.7 Chemical Analysis of the Melt Pool - Top 3.19
3.8 Chemical Analysis of the Melt Pool - Middle 3.20
3.9 Chemical Analysis of the Melt Pool - Bottom 3.21
3.10 Chemical Analysis of the Metallic Crust Remnant 3.22
3.11 Chemical Analysis of the Metallic Crust Remnant 3.23
3.12 Chemical Analysis of the Metallic Crust Remnant 3.24
3.13 Normalized Elemental Atomic Fraction for Areas of Interest 3.26
4.1 MP-2 End-of-Test Heat Transfer Rates 4.17
4.2 Molten Pool Composition (Zr/(Zr+U)) 4.17
A.1 Calculated MP-2 Coupling Factors A.10
A.2 Gamma Heating Coupling Factors for Nonfueled Regions A.10
A.3 Comparison of Coupling Factors Predicted by Heatup Rate and Neutronic Code Estimates A.11
C-2.1 Relocated Material - Top (RM-1) C-2.6
C-2.2 Relocated Material - Middle (RM-2) C-2.7
C-2.3 Chemical Analysis of the Relocated Material (RM-2*) C-2.8
C-2.4 Chemical Analysis of the Relocated Material (RM-2.5*) C-2.9
C-2.5 Chemical Analysis of the Relocated Material (RM 3.0*) C-2.10
C-2.6 Relocated Material - Bottom (RM-3) C-2.11

List of Figures

Page

1.1 Schematic of MP-2 Test Package 1.4
1.2 Radiograph of MP-1 and MP-2 Tests 1.5
2.1 Cutaway View of The Annular Core Research Reactorand Peripheral Systems 2.8
2.2 Schematic of the MP-2 Test Section 2.9
2.3 Schematic of the MP-2 Test Package Showing the Primary Containments and Key Components 2.10
2.4 Cross-Sectional View of the MP-2 Preformed Metallic/Ceramic Crust 2.11
2.5 MP-2 Primary System Thermocouple Location Map 2.12
2.6 ACRR Power History Used to Fission Heat the MP-2 Experiment. 2.13
2.7 Measured Thermal Responses of the MP-2 Test Section 2.13
3.1 Primary Containment Vessel with the Locations of Section Cuts 3.27
3.2 Three-Dimensional View of Test Capsule Indicating the -45° Longitudinal Extracted Slab 3.28
3.3 Preirradiation and Postirradiation Radiograph of the MP-1 Test Capsule and Postirradiation Radiograph of the MP-2 Capsule. 3.29
3.4 Postirradiation Radiograph with the Cutting Diagram of the Test Capsule 3.30
3.5 Optical Macrograph of Section 1-2 ..... 3.31
3.6 Optical Macrograph of Section 2-2 ..... 3.32
3.7 Optical Macrograph of Section 3-2 ..... 3.33
3.8 Optical Macrograph of Section 4-2 ..... 3.34
3.9 Optical Macrograph of Section 5-2 ..... 3.35
3.10 Optical Macrograph of Section 6-2 ..... 3.36
3.11 Montage of All Sections Indicating Areas in Which Scanning Electron Microscopy With Chemical Analysis Was Performed 3.37
3.12a Scanning Electron Micrographs and Corresponding Elemental Maps for the Retained Structure at the Top of the Debris Bed 3.38
3.12b Scanning Electron Micrographs and Corresponding Elemental Maps for the Retained Structure at the Top of the Debris Bed 3.39
3.13a Scanning Electron Micrographs and Corresponding Elemental Maps for the Top of the Ceramic Melt Pool 3.40
3.13b Scanning Electron Micrographs and Corresponding Elemental Maps for the Top of the Ceramic Melt Pool 3.41
3.13c Scanning Electron Micrographs and Corresponding Elemental Maps for the Top of the Ceramic Melt Pool 3.42
3.13d Scanning Electron Micrographs and Corresponding Elemental Maps for the Top of the Ceramic Melt Pool 3.43
3.14a Scanning Electron Micrographs and Corresponding Elemental Maps for the Middle of the Ceramic Melt Pool 3.44
3.14b Scanning Electron Micrographs and Corresponding Elemental Maps for the Middle of the Ceramic Melt Pool 3.45
3.14c Scanning Electron Micrographs and Corresponding Elemental Maps for the Middle of the Ceramic Melt Pool 3.46
3.15a Scanning Electron Micrographs and Corresponding Elemental Maps for the Bottom of the Ceramic Melt Pool 3.47
3.15b Scanning Electron Micrographs and Corresponding Elemental Maps for the Bottom of the Ceramic Melt Pool 3.48
3.16 Location of the Nine Measuring Points on Sample 4-2-2 ..... 3.49
3.17 Atomic Percent Average at Nine Locations of Sample 4-2-2 ..... 3.50
3.18 The Dark Band of Material at the Edge of the Ceramic Melt Pool 3.51
3.19a Scanning Electron Micrographs and Corresponding Elemental Maps for the Dark Band in the Ceramic Melt Pool 3.52

List of Figures (Cont.)

Page

3.19b Scanning Electron Micrographs and Corresponding Elemental Maps for the Dark Band in the Ceramic Melt Pool 3.53
3.19c Scanning Electron Micrographs and Corresponding Elemental Maps for the Dark Band in the Ceramic Melt Pool 3.54
3.20a Scanning Electron Micrographs and Corresponding Elemental Maps for the Metallic Crust Remnant 3.55
3.20b Scanning Electron Micrographs and Corresponding Elemental Maps for the Metallic Crust Remnant 3.56
3.20c Scanning Electron Micrographs and Corresponding Elemental Maps for the Metallic Crust Remnant 3.57
3.20d Scanning Electron Micrographs and Corresponding Elemental Maps for the Metallic Crust Remnant 3.58
3.21 Pie Charts Representing the Bulk Elemental Chemistry for Regions in the Upper Portion of the Test Capsule 3.59
3.22 Pie Charts Representing the Bulk Elemental Chemistry for Regions in the Crust Remnant of the Test Capsule 3.60
3.23 Pie Charts Representing the Bulk Elemental Chemistry for Regions in the Lower Portion of the Test Capsule 3.61
3.24 Pie Charts Representing the Bulk Elemental Chemistry for Regions in the Bottom Portion of the Test Capsule 3.62
3.25 Elemental Bar Graphs Representing the Bulk Chemistry for Regions in the Upper Portion of the Test Capsule 3.63
3.26 Elemental Bar Graphs Representing the Bulk Chemistry for Regions in the Crust Portion of the Test Capsule 3.64
3.27 Elemental Bar Graphs Representing the Bulk Chemistry for Regions in the Lower Portion of the Test Capsule 3.65
3.28 Mole Fractions of Four Simplified Material Classes Used to Approximate the Relocated Materials RM-1, RM-2, and RM-3 ..... 3.66
3.29 Relative Error in Elemental Compositions of the "Simplified" Material Representations of RM-1, RM-2,and RM-3 Shown in Figure 3.28 ..... 3.67
4.1 MP-2 Reactor Power Duty Cycle 4.18
4.2 Measured Temperatures in the Lower Regions of the Debris Bed 4.18
4.3 Measured Temperatures Near the Middle of the Debris Bed 4.19
4.4 Measured Temperatures in the Upper Regions of the Debris Bed 4.19
4.5 Measured Temperatures in the Preformed Crust 4.20
4.6 Measured Temperatures in the Rod Stub Region 4.20
4.7 Measured Lower Tantalum Liner Temperatures 4.21
4.8 Measured Middle Tantalum Liner Temperatures 4.21
4.9 Measured Upper Tantalum Liner Temperatures 4.22
4.10 Measured Temperatures in the Radial Insulation 4.22
4.11 Measured Temperatures in the Upper Insulation 4.23
4.12 Measured Temperatures on the Aluminum Spacer 4.23
4.13 Measured Temperatures on the Radial Primary Containment 4.24
4.14 Measured Temperatures on the Upper and Lower Test Section Boundaries 4.24
4.15 DEBRIS Code Results Compared With Debris Bed Thermocouple DBC1400 ..... 4.25
4.16 DEBRIS Code Results Compared With Debris Bed Thermocouple DBC1401 ..... 4.25
4.17 DEBRIS Code Results Compared With Debris Bed Thermocouple DBC1601 ..... 4.26
4.18 DEBRIS Code Results Compared With Debris Bed Thermocouple DBC1801 ..... 4.26
4.19 DEBRIS Code Results Compared With Debris Bed Thermocouple DBC2100 ..... 4.27
4.20 DEBRIS Code Results Compared With Debris Bed Thermocouple DBC2102 ..... 4.27
4.21 DEBRIS Code Results Compared With Debris Bed Thermocouple DBC2103 ..... 4.28
4.22 DEBRIS Code Results Compared With Debris Bed Thermocouple DBC2501 ..... 4.28
4.23 DEBRIS Code Results Compared With Debris Bed Thermocouple DBC3000 ..... 4.29

List of Figures (Cont.)

Page

4.24 DEBRIS Code Results Compared With Crust Thermocouple CRC11-2 ..... 4.29
4.25 DEBRIS Code Results Compared With Crust Thermocouple CRC11-4 ..... 4.30
4.26 DEBRIS Code Results Compared With Crust Thermocouple CRC12-0 ..... 4.30
4.27 DEBRIS Code Results Compared With Crust Thermocouple CRC13-1 ..... 4.31
4.28 DEBRIS Code Results Compared With Rod Region Thermocouple FRK0514 ..... 4.31
4.29 DEBRIS Code Results Compared With Rod Region Thermocouple FRK0531 ..... 4.32
4.30 DEBRIS Code Results Compared With Rod Region Thermocouple FRK1044 ..... 4.32
4.31 DEBRIS Code Results Compared With Rod Region Thermocouple FRS1000 ..... 4.33
4.32 DEBRIS Code Results Compared With Rod Region Thermocouple GSK0013 ..... 4.33
4.33 DEBRIS Code Results Compared With Rod Region Thermocouple GSK0018 ..... 4.34
4.34 DEBRIS Code Results Compared With Tantalum Liner Thermocouple ZRK0058 ..... 4.34
4.35 DEBRIS Code Results Compared With Tantalum Liner Thermocouple ZRK0558 ..... 4.35
4.36 DEBRIS Code Results Compared With Tantalum Liner Thermocouple ZRC1158 ..... 4.35
4.37 DEBRIS Code Results Compared With Tantalum Liner Thermocouple ZRC1258 ..... 4.36
4.38 DEBRIS Code Results Compared With Tantalum Liner Thermocouple ZRC1458 ..... 4.36
4.39 DEBRIS Code Results Compared With Tantalum Liner Thermocouple ZRC1658 ..... 4.37
4.40 DEBRIS Code Results Compared With Tantalum Liner Thermocouple ZRC1858 ..... 4.37
4.41 DEBRIS Code Results Compared With Tantalum Liner Thermocouple ZRC2158 ..... 4.38
4.42 DEBRIS Code Results Compared With Tantalum Liner Thermocouple ZRC3058 ..... 4.38
4.43 Calculated and Measured Axial Temperature Profiles at 6600 Seconds 4.39
4.44 Calculated and Measured Axial Temperature Profiles at 7900 Seconds 4.39
4.45 Calculated and Measured Axial Temperature Profiles at 9500 Seconds 4.40
4.46 Calculated and Measured Axial Temperature Profiles at 12,000 Seconds 4.40
4.47 Calculated and Measured Axial Temperature Profiles at 13,500 Seconds 4.41
4.48 Calculated and Measured Axial Temperature Profiles at 15,600 Seconds 4.41
4.49 Calculated and Measured Axial Temperature Profiles at 16,500 Seconds 4.42
4.50 Calculated and Measured Axial Temperature Profiles at 19,000 Seconds 4.42
4.51 Calculated and Measured Axial Temperature Profiles at 19,600 Seconds 4.43
4.52 Calculated and Measured Axial Temperature Profiles at 19,870 Seconds 4.43
4.53 Calculated and Measured Radial Temperature Profiles at 6600 Seconds 4.44
4.54 Calculated and Measured Radial Temperature Profiles at 7900 Seconds 4.44
4.55 Calculated and Measured Radial Temperature Profiles at 9500 Seconds 4.45
4.56 Calculated and Measured Radial Temperature Profiles at 12,000 Seconds 4.45
4.57 Calculated and Measured Radial Temperature Profiles at 13,500 Seconds 4.46
4.58 Calculated and Measured Radial Temperature Profiles at 15,600 Seconds 4.46
4.59 Calculated and Measured Radial Temperature Profiles at 16,500 Seconds 4.47
4.60 Calculated and Measured Radial Temperature Profiles at 19,000 Seconds 4.47
4.61 Calculated and Measured Radial Temperature Profiles at 19,600 Seconds 4.48
4.62 Calculated and Measured Radial Temperature Profiles at 19,870 Seconds 4.48
4.63 MP-2 Calculated Temperature Profile at 6600 Seconds in Heatup Phase 4.49
4.64 MP-2 Calculated Temperature Profile at 7900 Seconds in Heatup Phase 4.49
4.65 MP-2 Calculated Temperature Profile at 9500 Seconds in Heatup Phase 4.50
4.66 MP-2 Calculated Temperature Profile at 12,000 Seconds in Heatup Phase 4.50
4.67 MP-2 Calculated Temperature Profile at 13,500 Seconds in Heatup Phase 4.51
4.68 MP-2 Calculated Temperature Profile at 15,600 Seconds in Melt Phase 4.51
4.69 MP-2 Calculated Temperature Profile at 16,500 Seconds in Melt Phase 4.52
4.70 MP-2 Calculated Temperature Profile at 19,000 Seconds in Melt Phase 4.52
4.71 MP-2 Calculated Temperature Profile at 19,600 Seconds in Melt Phase 4.53
4.72 MP-2 Calculated Temperature Profile at 19,870 Seconds at End of Test 4.53
4.73 Comparison of Cases "A" and "B" End-of-Test Axial Temperature Profiles 4.54
4.74 MP-2 Calculated Versus Measured Coolant Heat Rejection Rate 4.54
4.75 MP-2 Calculated Versus Measured Total Heat Losses 4.55
4.76 MP-2 DEBRIS Code Calculated Energy Balance 4.55

List of Figures (Cont.)

Page

4.77 "Case-A" Gross Material Disposition Along Axial Centerline at 13,500 Seconds 4.56
4.78 "Case-A" Gross Material Disposition Along Axial Centerline at 15,600 Seconds 4.56
4.79 "Case-A" Gross Material Disposition Along Axial Centerline at 16,500 Seconds 4.57
4.80 "Case-A" Gross Material Disposition Along Axial Centerline at 19,000 Seconds 4.57
4.81 "Case-A" Gross Material Disposition Along Axial Centerline at 19,600 Seconds 4.58
4.82 "Case-A" Gross Material Disposition Along Axial Centerline at 19,870 Seconds (End of Test) 4.58
4.83 "Case-A" Gross Material Disposition at Radius = 2.09 cm at 19,870 Seconds (End of Test)....4.59
4.84 "Case-A" Gross Material Disposition at Radius = 3.27 cm at 19,870 Seconds (End of Test)....4.59
4.85 "Case-A" Gross Material Disposition at Radius = 4.28 cm at 19,870 Seconds (End of Test)....4.60
4.86 "Case-B" Gross Material Disposition Along Axial Centerline at 15,600 Seconds....4.60
4.87 "Case-B" Gross Material Disposition Along Axial Centerline at 16,500 Seconds....4.61
4.88 "Case-B" Gross Material Disposition Along Axial Centerline at 19,000 Seconds....4.61
4.89 "Case-B" Gross Material Disposition Along Axial Centerline at 19,600 Seconds....4.62
4.90 "Case-B" Gross Material Disposition Along Axial Centerline at 19,870 Seconds (End of Test)....4.62
4.91 "Case-B" Gross Material Disposition at Radius = 2.09 cm at 19,870 Seconds (End of Test)....4.63
4.92 "Case-B" Gross Material Disposition at Radius = 3.27 cm at 19,870 Seconds (End of Test)....4.63
4.93 "Case-B" Gross Material Disposition at Radius = 4.28 cm at 19,870 Seconds (End of Test)....4.64
4.94 Comparison of Cases "A" and "B" UO_2 Disposition Along Axial Centerline at End of Test....4.65
4.95 Comparison of Cases "A" and "B" ZrO_2 Disposition Along Axial Centerline at End of Test....4.65
4.96 Comparison of Cases "A" and "B" Zr Disposition Along Axial Centerline at End of Test 4.66
4.97 Comparison of Cases "A" and "B" Steel Disposition Along Axial Centerline at End of Test 4.66
4.98 Comparison of Cases "A" and "B" Silver Disposition Along Axial Centerline at End of Test....4.67
4.99 Comparison of Estimated Actual End Condition Gross Material Disposition with DEBRIS Code Estimates....4.67
A.1 Simplified Phase Diagram for Hyper-Stoichiometric UO_2-ZrO_2 Pseudo-Binary System A.12
A.2 MP-2 Radial Power Shape Factors in the Fission Zones A.12
A.3 MP-2 Axial Power Shape Factors in the Fission Zones....A.13
A.4 MP-2 Radial Gamma-Heating Shape Factors in Axial Zones 1 to 4 ....A.13
A.5 MP-2 Radial Gamma-Heating Shape Factors in Axial Zones 5 to 8 ....A.14
A.6 MP-2 DEBRIS Code Nodalization Scheme Showing System Dimensions....A.15
A.7 Coupling Factor Estimates from Thermocouple DBC1601 Responses A.16
A.8 Coupling Factor Estimates from Thermocouple DBC1801 Responses A.16
A.9 Coupling Factor Estimates from Thermocouple DBC2100 Responses A.17
A.10 Coupling Factor Estimates from Thermocouple DBC2501 Responses A.17
B.1 Diagram of the MP-2 Cooling Jacket Showing the Coordinate System Used in the Cooling Jacket Heat Transfer Analysis....B.14
B.2 Nusselt Number for Constant Inner Wall Temperature with Annular Flow and an Adiabatic Outer Wall. B.15
B.3 Coolant Temperature Response to a Constant Wall Temperature (u_m = 2.5 cm/s) Using Dimensions of MP-2 Cooling Jacket B.15
B.4 Coolant Temperature Response to a Linear Wall Temperature (u_m = 2.5 cm/s) Using Dimensions of MP-2 Cooling Jacket B.16
B.5 Coolant Temperature Response to a Parabolic Wall Temperature (u_m = 2.5 cm/s) Using Dimensions of MP-2 Cooling Jacket B.16
B.6 Boundary Layer Thickness for Constant Wall Temperature (u_m = 2.5 cm/s) Using Dimensions of MP-2 Cooling Jacket B.17
B.7 Nusselt Number Correlations for Three Wall Temperature Profiles (u_m = 2.5 cm/s) Using Dimensions of MP-2 Cooling Jacket B.17
C-1.1 Depleted Uranium C-1.3
C-1.2 Depleted Uranium C-1.4
C-1.3 Depleted Uranium C-1.5
C-2.1a Scanning Electron Micrographs and Corresponding Elemental Maps for the Metallic Crust Element....C-2.12

List of Figures (Cont.)

Page

C-2.1b Scanning Electron Micrographs and Corresponding Elemental Maps for the Metallic Crust Element C-2.13
C-2.1c Scanning Electron Micrographs and Corresponding Elemental Maps for the Metallic Crust Element C-2.14
C-2.1d Scanning Electron Micrographs and Corresponding Elemental Maps for the Metallic Crust Element C-2.15
C-2.2a Scanning Electron Micrographs and Corresponding Elemental Maps for the Metallic Crust Remnant C-2.16
C-2.2b Scanning Electron Micrographs and Corresponding Elemental Maps for the Metallic Crust Remnant C-2.17
C-2.2c Scanning Electron Micrographs and Corresponding Elemental Maps for the Metallic Crust Remnant C-2.18
C-2.2d Scanning Electron Micrographs and Corresponding Elemental Maps for the Metallic Crust Remnant C-2.19
C-2.2e Scanning Electron Micrographs and Corresponding Elemental Maps for the Metallic Crust Remnant C-2.20
C-2.3a Scanning Electron Micrographs and Corresponding Elemental Maps for the As-Fabricated Metallic Crust C-2.21
C-2.3b Scanning Electron Micrographs and Corresponding Elemental Maps for the As-Fabricated Metallic Crust C-2.22
C-2.3c Scanning Electron Micrographs and Corresponding Elemental Maps for the As-Fabricated Metallic Crust C-2.23
C-2.3d Scanning Electron Micrographs and Corresponding Elemental Maps for the As-Fabricated Metallic Crust C-2.24
C-2.4a Scanning Electron Micrographs and Corresponding Elemental Maps for the Relocated Material Just Under the Metallic Crust Remnant (RM-1) C-2.25
C-2.4b Scanning Electron Micrographs and Corresponding Elemental Maps for the Relocated Material Just Under the Metallic Crust Remnant (RM-1) C-2.26
C-2.4c Scanning Electron Micrographs and Corresponding Elemental Maps for the Relocated Material Just Under the Metallic Crust Remnant (RM-1) C-2.27
C-2.4d Scanning Electron Micrographs and Corresponding Elemental Maps for the Relocated Material Just Under the Metallic Crust Remnant (RM-1) C-2.28
C-2.5a Scanning Electron Micrographs and Corresponding Elemental Maps for the Relocated Material in the Mid-Section of the Fuel Array (RM-2) C-2.29
C-3.5b Scanning Electron Micrographs and Corresponding Elemental Maps for the Relocated Material in the Mid-Section of the Fuel Array (RM-2) C-2.30
C-2.5c Scanning Electron Micrographs and Corresponding Elemental Maps for the Relocated Material in the Mid-Section of the Fuel Array (RM-2) C-2.31
C-2.5d Scanning Electron Micrographs and Corresponding Elemental Maps for the Relocated Material in the Mid-Section of the Fuel Array (RM-2) C-2.32
C-2.6a Scanning Electron Micrographs and Corresponding Elemental Maps for the Relocated Material in the Mid-Section of the Fuel Array (RM-2*) C-2.33
C-2.6b Scanning Electron Micrographs and Corresponding Elemental Maps for the Relocated Material in the Mid-Section of the Fuel Array (RM-2*) C-2.34
C-2.6c Scanning Electron Micrographs and Corresponding Elemental Maps for the Relocated Material in the Mid-Section of the Fuel Array (RM-2*) C-2.35
C-2.6d Scanning Electron Micrographs and Corresponding Elemental Maps for the Relocated Material in the Mid-Section of the Fuel Array (RM-2*) C-2.36
C-2.7a Scanning Electron Micrographs and Corresponding Elemental Maps for the Relocated Material in the Bottom of the Test Capsule (RM-2.5*) C-2.37
C-2.7b Scanning Electron Micrographs and Corresponding Elemental Maps for the Relocated Material in the Bottom of the Test Capsule (RM-2.5*) C-2.38

List of Figures (Concluded)

Page

C-2.7c Scanning Electron Micrographs and Corresponding Elemental Maps for the Relocated Material in the Bottom of the Test Capsule (RM-2.5*) C-2.39
C-2.7d Scanning Electron Micrographs and Corresponding Elemental Maps for the Relocated Material in the Bottom of the Test Capsule (RM-2.5*) C-2.40
C-2.8a Scanning Electron Micrographs and Corresponding Elemental Maps for the Relocated Material in the Bottom of the Test Capsule (RM-3*) C-2.41
C-2.8b Scanning Electron Micrographs and Corresponding Elemental Maps for the Relocated Material in the Bottom of the Test Capsule (RM-3*) C-2.42
C-2.8c Scanning Electron Micrographs and Corresponding Elemental Maps for the Relocated Material in the Bottom of the Test Capsule (RM-3*) C-2.43
C-2.8d Scanning Electron Micrographs and Corresponding Elemental Maps for the Relocated Material in the Bottom of the Test Capsule (RM-3*) C-2.44
C-2.9a Scanning Electron Micrographs and Corresponding Elemental Maps for the Relocated Material in the Bottom of the Test Capsule (RM-3) C-2.45
C-2.9b Scanning Electron Micrographs and Corresponding Elemental Maps for the Relocated Material in the Bottom of the Test Capsule (RM-3) C-2.46
C-2.9c Scanning Electron Micrographs and Corresponding Elemental Maps for the Relocated Material in the Bottom of the Test Capsule (RM-3) C-2.47
C-2.9d Scanning Electron Micrographs and Corresponding Elemental Maps for the Relocated Material in the Bottom of the Test Capsule (RM-3) C-2.48

Acknowledgments

The design, fabrication, and implementation of an experiment having the magnitude and complexity of the MP-2 experiment necessarily requires the talents of a large number of individuals. It is probably not possible to list the contributions of all the people who were involved with the MP-2 experiment. The list that follows, however, attempts to acknowledge those individuals who made significant contributions to the MP-2 experiment effort.

Ken O. Reil	Program Director
Randy O. Gauntt	Chief Experimentalist
Paul S. Pickard	Assistant in Conduct
Jim W. Bryson and Staff	ACRR Operating Staff
John Garcia	Experiment Assembly
John H. Bentz	Data Aquisition
Susan C. Bourcier and Hot Cell Staff	PIE
Larry Humphries	Safety Analysis
Jim W. Fisk	Instrumentation
W. R. Chambers	Drafting

1. Executive Summary

1.1 Introduction

A severe accident in a nuclear reactor can lead to release of radionuclides to the environment, and the phenomenological pathways followed by such a release can be complex. (In this context, pathways refers to the phenomenological sequence of physical processes, and not a physical conduit for radionuclide transport.) Characterizing this pathway to radionuclide release is a principal goal of severe accident research. This pathway is characterized in terms of quantity and rate of release of radionuclides, beginning with accident initiation, proceeding through core melt progression, core material relocation within the reactor vessel, core material release from the vessel to the containment building, and ending with release from the containment system to the environment. Of course, an accident may terminated at any point along this pathway with correspondingly lesser consequences.

Because of the complexity and interdependencies of the phenomena governing the progression of a severe accident, systems modeling approaches, using computers, are generally required to analyze a severe accident. It is important to realize that the system model (computer code) describing the accident phenomena is a mathematical synthesis of many separate, and often, coupled phenomena. One key reason for this is that models are very often formed on the basis of experimental information, and generally, experiments must be practically limited in scope to something far less than a full-scale reactor meltdown.

Research in the area of in-vessel ***core melt progression*** is focused on the loss of core geometry and movement of core materials within the reactor vessel. Events occurring during this time determine the mass, temperature, composition, and rate of relocation of core material to the reactor vessel boundaries. These events, in turn, influence whether or not vessel failure occurs, and, if vessel failure does occur, they determine the composition and release rate of materials from the vessel.

In the taxonomy of severe accident research, ***early phase*** core melt progression refers to the initial heatup, oxidation and melting of the fuel cladding, where the core geometry is still very rod-like in nature. ***Late phase*** core melt progression refers to the later stages of core degradation, where molten ceramic fuel material is migrating toward a boundary of the core region. Over the past decade, a great deal of experimental research in the area of early phase core melt progression has been performed at Sandia National Laboratories (SNL)[1-7] and at other research facilities[8,9]; however, the area of late phase core melt progression has received far less attention.[10-14] This report describes the results of the MP-2 experiment that investigated late phase-melt progression processes using prototypical materials, realistic geometry, and internal fission heating to approximate the in-core conditions associated with a core-melt accident.

1.2 The MP Late Phase Experiments

The two experiments in the MP series, entitled MP-1 and MP-2, for **m**elt **p**rogression, were designed to examine the formation of ceramic fuel melts and the movement of such melts through intact core geometry towards a boundary of the core. The MP tests made use of prototypical materials and fission heating in order to accurately reflect the dominant melt progression phenomena. The MP test design, shown in Figure 1.1, was intended to reflect degraded core conditions after the early phase events of fuel cladding oxidation and melting, metallic blockage formation, and loss of fuel rod geometry had already occurred. The design included a rubblized fuel debris region, composed of UO_2 fuel fragments and oxidized cladding shards. The debris region overlies an intact fuel rod stub region around which is formed a metallic blockage. The metallic blockage is composed of zircaloy, PWR control materials, stainless steel, and some "dissolved" UO_2. In many ways, the initial state of the MP-2 test resembles the end state typical of early phase experiments such as were conducted in the ACRR-DF and PBF-SFD series of tests. The MP tests were intended to "pick up where the early phase fuel bundle tests left off." That is to say, the MP tests are designed to proceed beyond the end state of the early phase experiments and advance the melt progression into the ceramic melt formation and pool growth/melt front migration regime characterizing "late phase."

The MP-1 and MP-2 experiments were fission heated in the Annular Core Research Reactor (ACRR) at an average rate of a ~0.2 K/s to simulate the decay heating of degraded reactor fuel. Because of gradation in the U^{235} enrichment in the fueled regions of the experiment (highest in the debris bed), and because of the cold lower fuel rod base, an axial thermal gradient was present over the length of the test section. The experiments were designed to direct the heat flux downward into the preformed metallic crust and fuel rod regions, and to minimize radial heat losses.

1.3 Conduct of the MP-2 Test

Figure 1.2 shows the end state of the MP-1 and MP-2 experiments, as reflected from radiological examination. The MP tests 1 and 2 were very similar in nature and may be considered as two points along the melt progression time path,

with MP-2 experiencing a greater degree of melt progression than MP-1. In the MP-1 test, melting was limited to the fuel debris region where, as seen in Figure 1.1, a molten ceramic fuel region formed within the debris bed, advancing to within ~2 cm of the underlying metallic crust and fuel rod region. In MP-2, the ceramic melt pool progressed beyond that of MP-1, advancing into the fuel stub array about halfway down through the region occupied by the metallic crust. About half of the metallic crust melted under the thermal load of the advancing ceramic melt and relocated to the bottom of the fuel stub array.

The first region to melt in the experiment was the center of the debris bed, where a molten zone accumulated within a bowl-shaped lower crust formed by freezing of the ceramic fuel melt in the porosity of the adjacent debris bed. In time, the molten pool grew in size, incorporating larger amounts of the ceramic fuel debris as it advanced downward. Measurements and posttest analyses indicate that temperatures as high as 3400 K were attained in the melt pool region during the last melt relocation stages of the experiment. Temperatures in excess of 3000 K were maintained for approximately one hour. Before the migrating ceramic crust/melt interface reached the metallic crust region, the upper surface of the metallic crust reached the melting temperature. This point in the melt progression is typified by the end-state of the MP-1 test, as seen in the radiograph of Figure 1.2. Beyond this point, the molten ceramic pool continued to enlarge until almost all of the fuel debris was molten. Simultaneously, the molten metallic crust layer, held in place by the lower unmelted surface of the crust, was growing in size. At the end of the test, the ceramic crust/melt interface met with the underlying metallic crust. At this time, the ceramic melt front advanced quickly about halfway down through the region previously occupied by the molten metallic crust material where it froze in place. Coincident with this event, portions of the metallic crust were released and flowed down the rod array forming accumulations at the base of the bundle. Portions of the lower half of the metallic crust remained in place as a porous structure, and was later found to have a significantly increased oxygen content due to depletion of metallic components. The crust material that relocated to the base of the bundle was later determined to be largely metallic in character with much lower oxygen concentrations. The conduct of the MP-2 test and the overall behavior of the experiment are described in Chapter 2 together with specific details on the test package.

1.4 Posttest Examination

Following completion of the MP-2 test, the experiment package was filled with epoxy to stabilize the configuration and was subsequently dissected in the Sandia Hot Cell Facility. The stabilized test section was first sectioned into five cylindrical pieces that were in turn sectioned axially to reveal a longitudinal face through the axial centerline of the experiment. Each face was polished and prepared for optical and scanning electron microscope examination. Optical examination revealed the major physical changes and the various material phases that resulted from the melt progression processes. The major findings from the destructive examination were;

1.) Initial melting in the UO_2/ZrO_2 fuel debris appeared to initiate with melting of the ZrO_2 phase followed rapidly by dissolution of the wetted UO_2 particles.

2.) The molten debris formed a pool that was contained inside a bowl-shaped crucible formed by the freezing of fuel melt within the porosity of the surrounding cooler (unmelted) fuel debris (*this is actually an observation from the MP-1 experiment, which was practically identical to MP-2 except that it was terminated at an earlier point in the melt process*).

3.) At the end of the MP-2 test almost all the ceramic fuel debris was melted and the lower extent of the ceramic melt front had penetrated about halfway down through the initial preformed metallic crust region.

4.) Most of the metallic components of the preformed crust relocated to the base of the fuel rod lower array at about the time that the ceramic melt front moved into the former metallic crust region. Some evidence suggests that the metallic crust relocation event preceded the migration of ceramic melt into the fuel rod/metallic crust region, and could have acted as a trigger for the ceramic relocation event.

5.) The displaced metallic crust material at the base of the fuel rod array was very metallic in nature (~5 atomic percent oxygen).

6.) The residual metallic crust material lying just below the ceramic melt lower surface was found to be considerably more oxidic in nature (~40 atomic percent oxygen), primarily due to loss of metallic Zr and other metals from the crust, leaving a residual porous material with a higher melting temperature than the original composite crust material.

Details on the destructive post irradiation examination (PIE) are described in Chapter 3.

1.5 Posttest Analysis

The thermal response and melt progression behavior observed from the MP-2 test thermocouple data and the PIE results were compared to analyses of the test progression made using the DEBRIS porous media melt progression models in Chapter 4. In addition to heat generation and heat

transfer processes, the modeling in DEBRIS treats material melting in multicomponent systems latent heat, the flow of melt through porous media, (rubblized debris and fuel rod arrays) including the effects of viscous flow, and molten pool formation, growth, and migration through degraded core geometry. The analysis of the MP-2 test using DEBRIS was very favorable. The timing of the major melt relocation events (ceramic and metallic), and the ultimate reconfiguration of materials following melt relocation was in good agreement with the post test observations. The overall heat balance from the analysis matched experimentally measured values within 5%.

In the late phase regime, material interactions would not appear to play as important a role as has been seen in numerous early phase experiments. The underlying metallic crust appeared to interact very little with the overlying ceramic region, since its metallic components melted and ran away from the ceramic region, and, for the most part, only the residual oxides remained and became incorporated into the ceramic phase. It is important to emphasize that the molten ceramic fuel region is not "contained by the metallic crust. Rather, the ceramic melt is contained within a ceramic "crucible" formed by the refreezing of melt flowing into the adjacent cooler unmelted ceramic debris at the margins of the molten ceramic pool. The melt pool migrated by gradually melting the boundaries of the "crucible" whereupon, the molten perimeter advanced into the adjacent unmelted porous region where it refroze and "healed" the crucible.

The following chapters describe in greater detail the conduct, posttest examinations, and analysis of the MP-2 test.

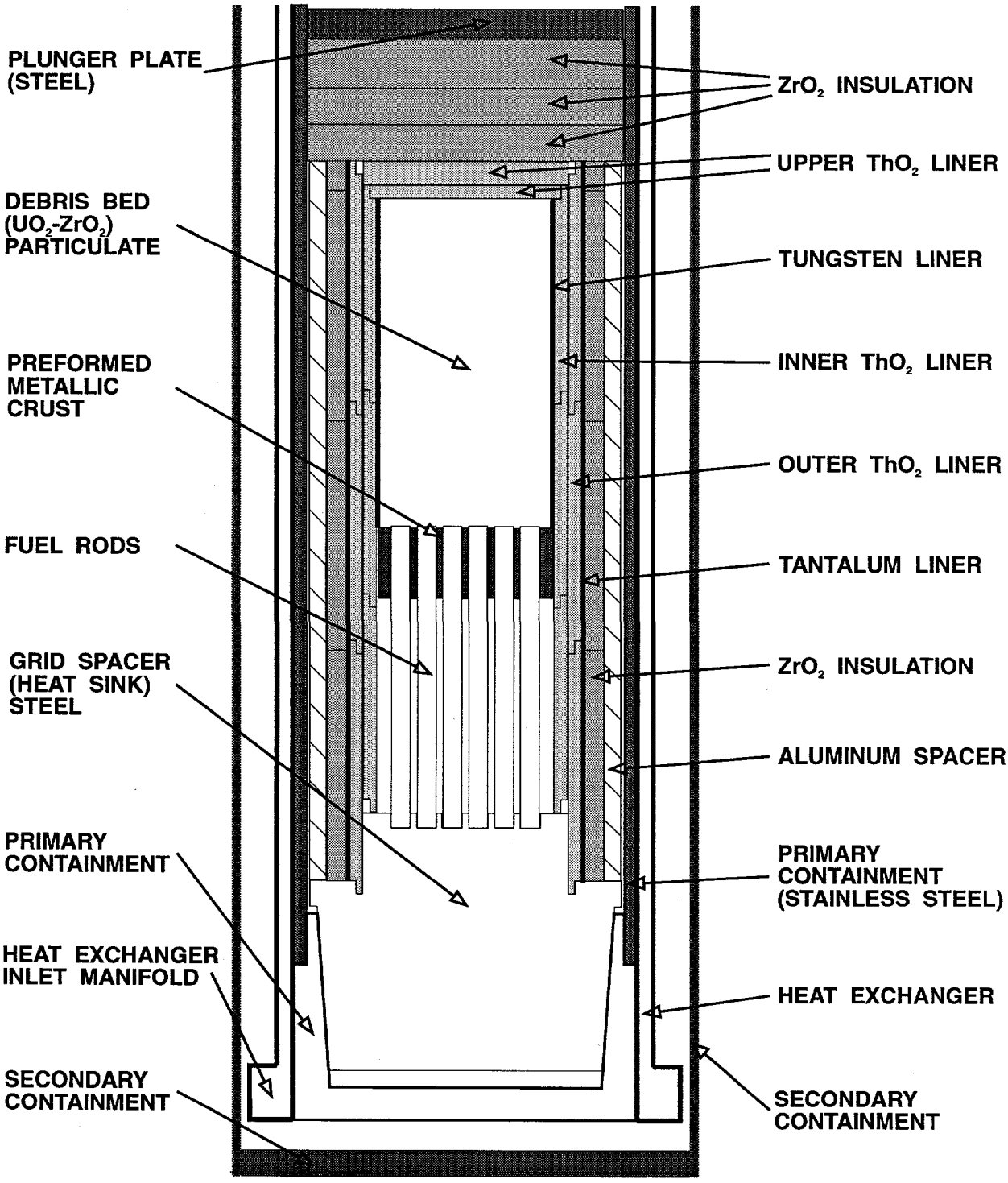

Figure 1.1 Schematic of the MP-2 Test Section

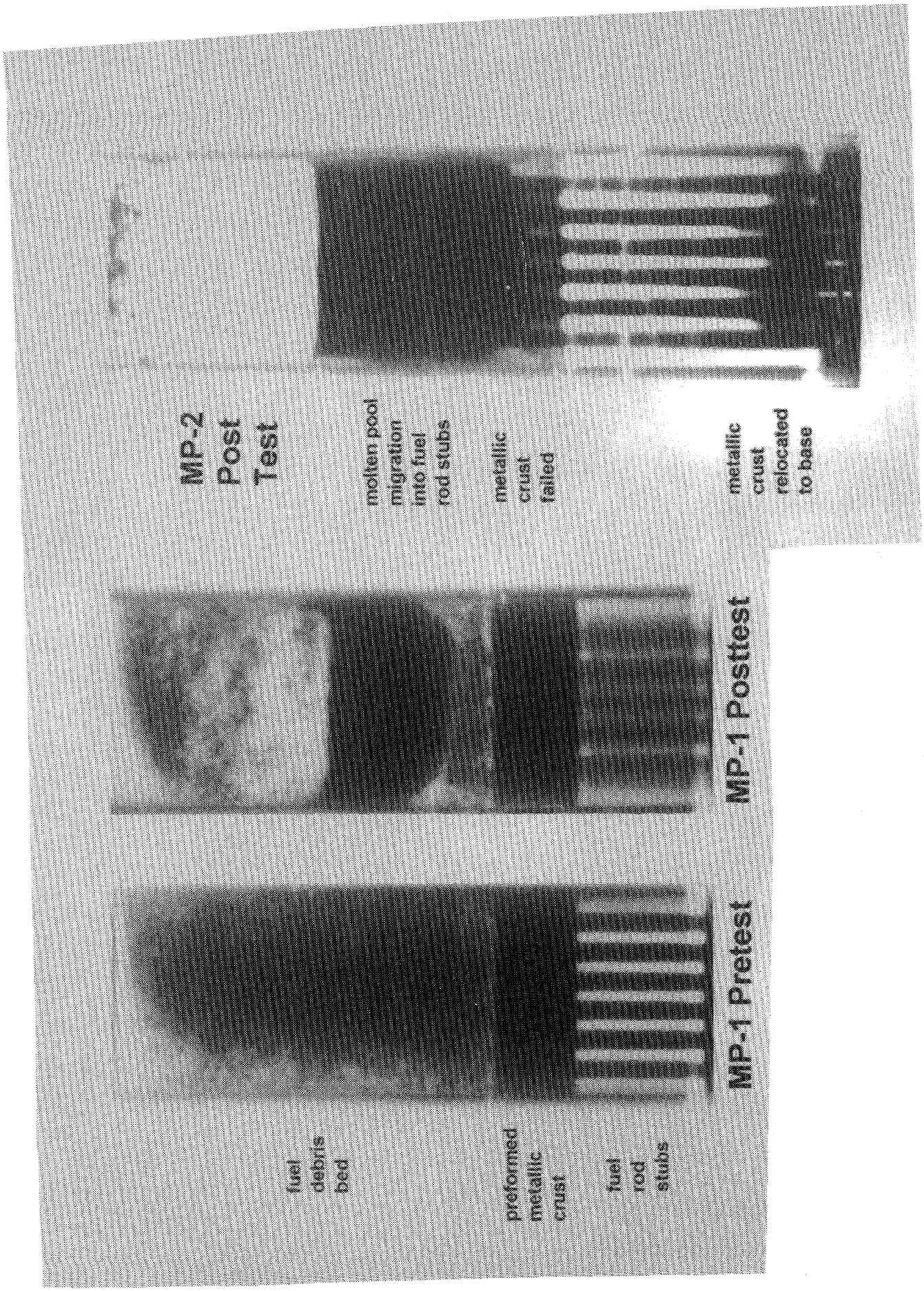

Figure 1.2 Radiograph of MP-1 and MP-2 Tests

2. Experiment Description

The MP-2 experiment was conducted in the Annual Core Research Reactor (ACRR) at Sandia Laboratories. The ACRR is a pool-type reactor capable of operating in either pulsed or steady-state mode. In the steady-state mode, which is the mode of operation employed in the MP series, the reactor can sustain power levels of 2 MW continuous and 4 MW intermittent. The core contains 236 fuel elements arranged in an hexagonal, annular configuration with an hexagonal central cavity designed for the insertion of experimental assemblies. The fuel elements are composed of 21.5% UO_2 (35% enriched) and 78.5% BeO by weight. The central cavity measures 23.5 cm across the flats of the hex and the height of the core is 52.2 cm. These two dimension are the limiting parameters that determine the axial and radial dimensions of all experimental packages irradiated in the central cavity region of the reactor. The core is light water cooled (by natural convection) and moderated.

The active regions of the MP-2 experiment package consisted of a particulate debris bed resting on the top of a prefabricated crust, which was supported by an assembly of 32 fuel rod stubs. In addition to these three active (heated) regions, the experiment package included several other components. The most important additional components were the melt and thermal barriers, the radial cooling system, the supporting structures, the containment structures, and the instrumentation system. These are described in this section.

Figure 2.1 is a cutaway view of the ACRR showing the core and central experiment cavity in relation to the overall reactor systems and components.

Figure 2.2 shows a general schematic of the experiment package detailing the components within the active region of the primary system. A view of the main features of the primary and secondary systems including the fueled zones, the primary and secondary system bulkheads, the thermocouple mounting block, and the principle containment penetrations is seen schematically in Figure 2.3.

2.1 Debris Bed

The debris bed was contained within a cylindrical region (8.72 cm in diameter by 16.5 cm in height) bounded on the top and sides by thermal barriers and on the bottom by the preformed crust. The debris consisted of a mixture of UO_2 and ZrO_2 in a ratio consistent with that observed in the upper debris bed of the TMI-2 core.

The actual bed loading involved 3859 gm of UO_2 93% enriched in U_{235} and 802 gm of ZrO_2 (see Table 2.1 for inventories). These quantities of UO_2 and ZrO_2 particulate filled the cylindrical volume described above, forming a debris bed with a porosity of about 50%. No attempt was made to either shake the bed or apply a compressive load to the bed to increase the loading. Shaking would tend to stratify the bed both by composition and particle size while application of a compressive force would tend to crush particles and change the particle size distribution. The particle size distribution was based on the range observed in the TMI-2 investigation[15] except that the range was limited to sizes varying between 1 and 5 mm in diameter. The mass mean particle size was about 2 mm.

The UO_2 was obtained from fired fuel pellet fragments, and the ZrO_2 was obtained by crushing preoxidized fuel rod cladding. In a solid solution of this composition the mixture would be expected to begin melting at approximately 2900 K, which corresponds to the solidus temperature on the binary-isomorphous phase diagram for the MP-2 bed composition (see Chapter 3 or Appendix A for Phase Diagrams). Note that the initial configuration of the debris bed, although a well mixed combination of UO_2 and ZrO_2 particulate, did not consist of a "solid solution", but rather a mixture of particles of these two constituents with each particle composed of one or the other of the two components.

2.2 Prefabricated Crust

The preformed crust was designed to simulate a blockage region that is formed when primarily metallic molten materials flow into cooler regions of the core and solidify around a basically intact, standing rod configuration. The crust used in the MP-1 experiment represented the low melting temperature regime for a metallic/oxidic mixture (the eutectic composition, melting at ~2200 K) and consisted of UO_2, ZrO_2, and Zr in weight fractions of 32%, 18%, and 50%, respectively. Further study of the TMI-2 lower blockage has suggested that the fraction of uranium in the blockage was perhaps closer to 10%, which would yield a lower melting temperature for the crust material. An assessment of core inventory and assays of the TMI-2 lower core blockage were used to fix the composition of the MP-2 crust. Unlike the MP-1 crust, which was somewhat simplified in composition, structural and control material were employed in the composition of the MP-2 crust with the primary components being Zr(44.8%), Fe(15.2%), ZrO_2(12.2%), Ni(9.0%) and Ag(7.7%) atomic fractions. The complete inventory of materials contained in the crust are summarized in Table-2.1 The bulk concentrations of Zr and ZrO_2 give these components an overall composition of $Zr_{0.7}O_{0.3}$, and the concen-

tration of UO_2 in the bulk sample puts the composition at 11.6% $U_{0.33}O_{0.67}$ on the α Zr(O)-UO_2 pseudo-binary phase diagram. This composition is "undersaturated" in UO_2 and was selected to assure that incorporation of UO_2 from the fuel pellets would not significantly raise the crust melting temperature thereby inhibit the penetration of molten ceramic into the crust region.

Samples of the crust taken from drill cores were subjected to two sets of tests designed to determine the physical characteristics of this material under high-temperature conditions. The first set of tests involved differential thermal analysis (DTA). In these tests milligram samples were placed in the DTA equipment and heated to temperatures in excess of 1850 K. The results showed isotherms at several temperatures indicating melting of the lower melting temperature metals, particularly silver, but at the peak temperature there was no indication of structural deformation of the samples. In the DTA tests, no mechanical load was placed on the sample, and these tests were not conclusive in terms of mechanical stability of the crust at high temperatures.

A second set of tests was performed using a Gleeble high-temperature testing apparatus, which measures mechanical deformation of the sample under compressive load at high temperature. These tests showed that, although a liquid phase existed within the refractory metal and ceramic structure at temperatures above the indium and tin melting points, under no-load conditions there was no breakdown of the rigid structure until temperatures greater than 1925 K. Under negligible load conditions (the compressive load due to the debris bed is about ~1.1 psi) the critical temperature for breakdown of the structure (deformation) appeared to be in the range from 1925 to 2075 K. Thus it was expected that temperatures in this range at the bottom surface of the crust would lead to slumping and relocation of this material into the free standing rod stub region below the crust.

The UO_2 in the preformed crust was depleted in U_{235} while the segment of fuel rods that extended into the crust was enriched to 19%. Figure 2.4 shows a diagram of the crust and provides some key dimensions.

The crust was fabricated using techniques employed in powder metallurgy that involve pressing mixtures of component powders under high pressure and heat sintering to obtain a high density homogeneous composite solid. The crust measured 8.65 cm in diameter and 3.5 cm in height and, like the debris bed, was bounded in the radial direction by the thoria melt barrier (see Figure 2.2). The crust region supported the overburden of debris bed material and was itself suspended and held in place from below by zircaloy tube spacers that were installed on 4 of the 32 fuel rod stubs.

The crust contained 32 penetrations that were each one centimeter in diameter. These penetrations were drilled in a square pattern that matched a similar pattern of holes in the lower grid structure. The fuel rods extended completely through the preformed crust with the topmost fuel pellet in each rod approximately level with the top surface of the crust. The rods were thus held in place radially at the top by the crust and at the bottom by the steel grid spacer.

2.3 Fuel Rod Stub Region

This region was included to simulate a region of basically intact fuel rod geometry below the metallic blockage zone. In this region there is postulated to be little if any ingress of relocated molten material or other debris until such time as the overlaying blockage remelts or fails structurally.

In the MP-2 experiment, this zone was composed of a 32-rod square 6x6 lattice with a 1.27-cm pitch and the four corner positions deleted so as to conform to the cylindrical geometry of the package. Each of the rods measured 14.81 cm in length with the upper 3.5 cm penetrating into the overlaying crust and ~1 cm extending into the bottom grid spacer so that the free standing rod zone was 10.03 cm in height. Each fuel rod included 15 fuel pellets. The upper five fuel pellets (at the end extending into the crust) were enriched to 19% while the lower ten pellets (at the bottom of the fuel rod) were enriched to 10%. The rod cladding tubes were fabricated from zircaloy-4 with an outside diameter of 0.963 cm and an inside diameter of 0.851 cm. The fuel pellets had a mean diameter of 0.826 cm, which left a 0.06 mm fuel-to-clad gap.

Zircaloy spacer tubes were placed on four of the fuel rods at the radial periphery of the rod bundle to vertically position and provide support for the crust. These tubes were 10.03 cm in length with a 1.092-cm OD and a 0.980-cm ID.

2.4 Melt and Thermal Barriers

To assure confinement of high-temperature molten materials within the experimental assembly, several barriers were incorporated in the design. The first line of barriers consisted of the melt and thermal barriers. The melt barrier was intended to inhibit the movement of molten material out of the active regions of the experiment. The melt barrier consisted of five components, an inner tungsten metal barrier, two radial thoria barriers, an upper thoria barrier, and a radial tantalum liner. The exact dimensions and relative locations of these structures can be determined from the test section nodalization map given in Appendix A.

The first component of the radial barrier consisted of two layers of 5 mil (0.13 mm) tungsten metal sheet extending axially from the top of the crust to the top of the debris bed. This barrier was included because temperatures in the region of 3400 K in the molten pool were anticipated, and at this temperature interaction between UO_2/ZrO_2 and ThO_2 may begin to occur. The tungsten barrier was designed to

provide separation between the molten pool and the thoria wall.

The second and third radial barrier components consisted of two concentric cylinders of high density ceramic thoria. The two concentric thoria cylinders were fabricated in the form of three interlocking tubes fitted together with deep lap joints (see the drawings in Figure 2.2) and stacked vertically to form the radial boundary of the test section. The inner thoria barrier had an ID of 8.70 cm and an OD of 9.97 cm while the outer thoria liner had a 10.12 cm ID and 11.39-cm OD.

The fourth component of the melt barrier was formed using a 2.5-cm thick thoria disk that was mated with the uppermost thoria tube using a lap joint. This structure served as the upper surface of the debris bed. The radial components of the melt barrier extended from the bottom of the fuel rod stub region to the top of the debris bed with the thoria disk capping the debris bed at the top. Estimates of the thoria melting temperature range from 3273 to 3542 K with the higher number as a best estimate for pure ThO_2.

A metallic tube that fit around the outer thoria liner served as the final melt barrier. This barrier consisted of a 0.9-mm-thick (11.68-cm OD) tantalum metal tube (melting temperature ~3300 K). The tantalum sleeve, in addition to acting as a melt barrier, also served to add mechanical stability to the ceramic thoria liner.

In addition to the obvious requirement that sufficient heat be confined in the active region of the experiment to obtain temperatures at least as high as the debris melting point, it was necessary to prevent the overheating of sensitive structures and instrumentation within the test assembly. These constraints were satisfied by insulating the test section with a low thermal conductivity ceramic fiber insulation. For the MP-2 experiment, a high porosity (70%), low density (1400 kg/m^3), yttria stabilized ZrO_2 insulating material (ZIRCAR Corp. Type FDB) was employed for the radial thermal barrier as shown in Figure 2.2. The same material was also employed as an insulator in the region above the debris bed to inhibit heat losses to the upper structures. The radial fiber insulator extended from the tantalum liner outward to the aluminum spacer that served to stabilize the insulator. This insulating material, although highly porous is fabricated in the form of a solid tube. These tubes were constructed from several sections that were stacked and joined with lap joints similar to the thoria liners. The insulator tubes had an 11.68-cm ID and a 13.56-cm OD. The ZrO_2 fiber insulation used above the upper thoria liner consisted of three disks with a total thickness of 6.35 cm.

2.5 Containment Structures

Figure 2.3 shows a schematic representation of the MP-2 test section as it is situated with respect to the two containment structures. Exact dimensions of containment structures are given in Appendix A. The primary containment was designed to isolate and contain all fission products, nuclear components, or otherwise hazardous materials within its boundaries.

The primary containment structure comprised three separate pieces, a steel tube, a bottom piece, and the primary steel bulkhead (plunger plate assembly). These three pieces formed a sealed vessel that enclosed the entire experiment assembly except for the heat removal system. The steel tube was 104 cm in length and had a 16.8-cm (6.625 inches) OD with a wall thickness of 0.635 cm (0.25 inch) and was composed of type 316 stainless steel (SS).

The bottom piece, also composed of type 316 SS, had a "cup-shape" with the inside vertical wall tapered slightly (4^o) to receive the lower grid spacer of the test section and to form a good thermal contact for efficient heat transfer from the grid spacer to the primary containment. The lower piece had a 1.57-cm (0.63 inch) wall thickness at the bottom surface.

The primary containment was enclosed at the top by the primary closure bulkhead. The bulkhead was fabricated from a 1.27-cm-thick (0.5 inch) "disk- shaped" type 316 SS plate. All penetrations through the primary containment were located in the containment closure bulkhead, including the thermocouple PAVE or LJT leak tight connectors and the plumbing for introducing the "potting" material necessary for stabilizing the test section in the post-irradiation-examination procedures. Figure 2.3 shows some of the principle components of the wiring and plumbing systems.

A secondary containment (see Figure 2.3), also composed of a steel vessel, enclosed the primary containment as well as the heat removal system. This structure consisted of a 22.2-cm-(8.75 inch) diameter stainless steel tube 164.5 cm in length and sealed at the bottom with a 1.27-cm-(0.5 inch) steel plate and at the top by a 2.54-cm (1.0 inch) secondary bulkhead. The boundary of this structure also included the water lines and associated fittings for the cooling jacket.

Bounding calculations for the MP-2 test predicted maximum primary system pressures in the range of 165 kPa (24 psia). To assure containment integrity, the primary system was designed to 345 kPa (50 psia) and the secondary containment to 240 kPa (35 psia). Helium at 69 kPa (10 psia) was employed as the cover gas in both the primary and secondary containments.

2.6 Heat Removal System

The entire length of the primary containment was cooled by an annular single-pass cooling jacket. The cooling jacket

consisted of two half-annular sections of co-axial steel tubing sealed at the top and bottom. Water from the source was directed downward in eight tubes, four tubes per half-annulus, into a plenum at the bottom. Water was then directed from the lower plenum through a series of 11 orifices in each half of the cooling jacket into an annular section that had its inside surface in thermal contact with the primary containment wall.

Flow in the cooling jacket proceeded from bottom to top emerging at the top into an upper plenum in each half-annulus and subsequently discharging through a single outlet tube in each half of the cooling jacket. The two halves of the cooling jacket were mounted tightly to the outside of the primary containment in order to achieve good thermal contact.

Cooling water was supplied to the jacket by means of gravity flow from a 100-gallon tank situated above the level of the ACRR pool. The flow was regulated by a flow control valve and monitored by a turbine flowmeter, both of which were located in the line from the tank to the experiment package. Flow rates were adjusted during the experiment according to the power level in the test section. The maximum flow rate with the inlet valve full open was 1.4 gal/min. At this flow rate and assuming an outlet temperature at the boiling point, the heat removal capacity of the system was approximately 47 kW.

The temperatures at the inlet and outlet of the cooling jacket were measured and monitored during the experiment and the heat ejection rate was calculated by the data acquisition system (DACS) and also monitored. The maximum heat rejection rate during the experiment was approximately 13 kW. Measurement of the coolant flow rate and the coolant inlet/outlet temperatures provided a check on the overall energy balance for the system.

2.7 Instrumentation System

The instrumentation system was composed of two primary components, the sensing equipment, primarily thermocouples, and the DACS. The DACS computer acquired and recorded data and performed real-time calculations to obtain critical information regarding the condition of the test section.

Figure 2.3 provides an overall view of the test package showing both the primary and secondary containment systems together with a schematic representation of the basic thermocouple and plumbing penetrations.

Type C thermocouples (W/Re) were used in the debris bed, crust region, and on the tantalum liner where high temperatures were expected. These thermocouples were obtained from HEDL (Hanford Engineering Development Laboratories). The thermocouples that were located in the debris bed and crust consisted of tungsten/rhenium thermocouple wires encased in a rhenium metal sheath and electrically insulated with high purity HfO_2. There is considerable confidence in the reliability of these thermocouples to supply reasonably accurate characterization of the debris bed temperatures up to temperatures (2600 K) ~300 K below that required to melt the debris (~2900 K). The Type C thermocouples on the tantalum liner were not sheathed. Figure 2.5 is a scale drawing of the test section showing the locations of all the thermocouples sited within the primary containment boundary. Other thermocouples were located outside the primary boundary and are not shown. Note that the thermocouple type (C,S,or K) for a given thermocouple can usually be determined from the third character in the thermocouple identifier. For example, thermocouple DBC1601 located in the debris bed (thus DB) was a type C thermocouple.

Type S (Pt/Rh) and type K (chromel/alumel) thermocouples were also employed in regions where lower temperature ranges were anticipated such as in the outer layers of the ZrO_2 insulation and in the lower sections of the rod stub region.

Other instrumentation included pressure transducers that measured the primary system pressure and turbine flowmeters that measured coolant flow rates.

Data from all the instrumentation channels were fed to the DAC system, which sampled and recorded the types of data referred to above as well as additional parameters coming from devices outside the experiment such as ACRR power level, power supply monitor, the main time signal and others.

2.8 Conduct of the MP-2 Test

The following two sections describe the techniques used to perform the MP-2 experiment and a chronology of major melt progression events that occurred.

2.8.1 Method of Test Control

In conducting the MP-2 experiment, the test assembly was loaded into the ACRR central irradiation cavity such that the fueled portion of the experiment was axially centered in the core. Neutrons from the ACRR driver core induce fission heating in the fueled components of the experiment, thereby simulating internal fission product decay heat. The cooling jacket provided a relatively constant boundary temperature for the insulated test section radial boundary as the internal fueled regions were fission heated at a rate of about 0.5 K/s. Figure 2.6 shows the ACRR reactor power history that was used to fission heat the MP-2 experiment and Fig-

ure 2.7 shows the thermal response of the thermocouples situated within the debris bed regions.

As seen in the figures, the debris region heatup was accomplished in a "stair-stepped" fashion using a "square-wave" reactor power history. During each "step-up" in temperature, the ACRR power level was adjusted to give a ~1 K/s rise rate in the debris bed. This provided a measure of the net internal heat generation (heat deposition minus heat loss) in the debris bed as a function of the applied ACRR power level. This trend was charted as a function of debris bed temperature throughout the heatup of the experiment. As the target temperature for the step was approached, the ACRR power level was decreased so as to maintain the debris bed at the target temperature. This provided a measure of the heat loss rate from the test section at points in time when heat losses were essentially balanced by the fission heat generation. These trends were also charted as the debris bed was stepwise heated, providing a "forecasting ability" relative to subsequent step increases in temperature. Nonlinearities in the charted trends due to increasing heat loss rates with increasing temperature were observed and considered in determining each successive ACRR power boost.

These charted trends were very useful in estimating the power boosts required to heat the debris through the melt range, since the thermocouple measurements in this regime were not considered necessarily reliable. Additionally, a correlation plot of debris region temperatures versus Ta liner temperatures was also charted during the heatup. This information was used to establish an indirect measure of debris region temperatures by inference from the Ta liner thermocouples, which remained several hundred degrees cooler than the debris thermocouples. By these means, the temperature history shown in Figure 2.7 was obtained. Also shown in Figure 2.7 are temperatures measured internal to the preformed metallic crust and temperatures at the base of the fuel rod array.

2.8.2 Chronology of MP-2 Progression

The following melt progression scenario for the MP-2 test is based upon an evaluation of the thermal responses measured in the experiment, the posttest examination, posttest analytical studies, and the known results from the MP-1 test, which was terminated at an earlier melt progression state than MP-2. As can be seen in Figure 2.7, the first region to undergo melting was the central portion of the fuel debris bed, beginning at about 14,000 seconds. Temperatures at the lower regions of the debris bed at this time were 500 to 1000 K lower, but increasing rapidly. Over the next 1600 seconds (~25 minutes), a molten pool of ceramic fuel material formed in the center of the debris bed, and increased in size both radially and axially downward. At 15,600 seconds, the top surface of the pre-formed metallic crust is estimated to be liquefied when the melting temperature of Zr was attained. It is important to point out that the molten ceramic debris region at this time was confined within a densified ceramic crust formed from the flow of ceramic melt into the porosity of cooler ceramic debris, and that a region of relatively undisturbed solid ceramic fuel debris existed between the molten ceramic pool region above and the "just-beginning-to-melt" metallic crust below. **The foregoing is actually an observation from the end state of the MP-1 experiment, which was terminated at about this time in the melt progression process.**

Between 15,600 and 16,500 seconds (15 minutes), several "splashes" of molten material were detected to have arrived at the lower base of the fuel rod array, as seen by the transient thermocouple responses in Figure 2.7. These splashes are not considered to reflect the relocation of a large amount of melt because the thermocouple indications quickly returned to the base line values. Larger amounts of relocated melt would have resulted in a shift in the base line thermocouple temperature as the heat released from freezing would have heated up the surrounding region. The drops reaching the fuel rod base during this time are known to be Zr-rich, and are presumed to be largely fuel rod cladding originating from within the preformed crust region.

Several incremental power boosts were applied between the time of 14,600 and 19,500 seconds, resulting in a steady growth of the ceramic molten pool region and in the molten interface region in the preformed metallic crust. Aside from the droplets of molten metal observed to splash on the lower grid structure, the molten ceramic crust material was largely contained in place by the still-solid lower metallic crust periphery. Toward the end of this period, at around 19,000 seconds, the ceramic melt region is thought to have migrated down to the metallic crust interface. At this time, a sudden temperature transient was observed on the Ta-liner thermocouples adjacent to the metallic crust region and on the thermocouples situated at the base of the fuel rod array. The transient response, shown in Figure 2.7, resulted in a rise rate above the base line much in excess of that attributable to the fission power increases, and for this reason is presumed to reflect a relatively major melt relocation event.

There are two viable interpretations that have been postulated to explain this event. In the first interpretation it is postulated that the relocation of the molten ceramic pool into the preformed crust region occurred first and ultimately led to the failure of the crust and relocation of the its metallic components. The second interpretation reverses the causality so that the relocation of the metallic crust constituents led to the slumping of the ceramic pool into the pre-formed crust zone. The first interpretation postulates that the ceramic melt front reached the metallic crust interface, a sudden slumping of the ceramic crust into the rod region occurred, which subsequently caused the molten metallic crust material to be ejected from the crust region by physi-

cal displacement. The other interpretation involves first the melting or slumping of the bottom of the preformed crust, which allowed the molten crust material above to suddenly "drain" downward out of the region leaving behind a partially voided porous structure. Loss of the high-thermal-conductivity metals from the preformed crust rapidly raised the thermal gradient in the remnant crust leading to melting of the overlying ceramic crucible and release of the ceramic pool to slump into the freshly voided pore space in the preformed crust region.

In either of these scenarios, the ceramic melt, encountering a relatively more permeable rod geometry, moved quickly about halfway down into the former metallic crust region, freezing in place, and causing the thermal transients in the adjacent Ta-liner thermocouples. The metallic melt rapidly relocated to the base of the fuel rod array, causing the transient thermocouple responses in this region.

Based upon the overall perception of a significant melt relocation event having occurred at 19,500 seconds, the MP-2 test was subsequently terminated, whereupon a slow cooldown period followed.

Table 2.1 MP-2 Material Inventory

Region	Material	Mass (kg)	Mass Fraction
Debris Bed	UO_2	3.8589	0.8279
	ZrO_2	0.8023	0.1721
Crust	UO_2*	0.0649	0.0425
	UO_2**	0.6129	0.4014
	UO_2+	0.6778	0.4439
	Zr*	0.2958	0.1937
	Zr**	0.1220	0.0799
	Zr+	0.4178	0.2736
	ZrO_2	0.1090	0.0714
	Sn	0.0328	0.0215
	Ag	0.0919	0.0602
	In	0.0232	0.0152
	Fe	0.0941	0.0616
	Cr	0.0172	0.0113
	Ni	0.0585	0.0383
	Mo	0.0045	0.0029
Rods	UO_2	1.9117	0.8217
	Zr	0.4149	0.1783

* Component of Crust Matrix
** Component of Embedded Fuel Rods
+ Sum of Embedded and Matrix Component

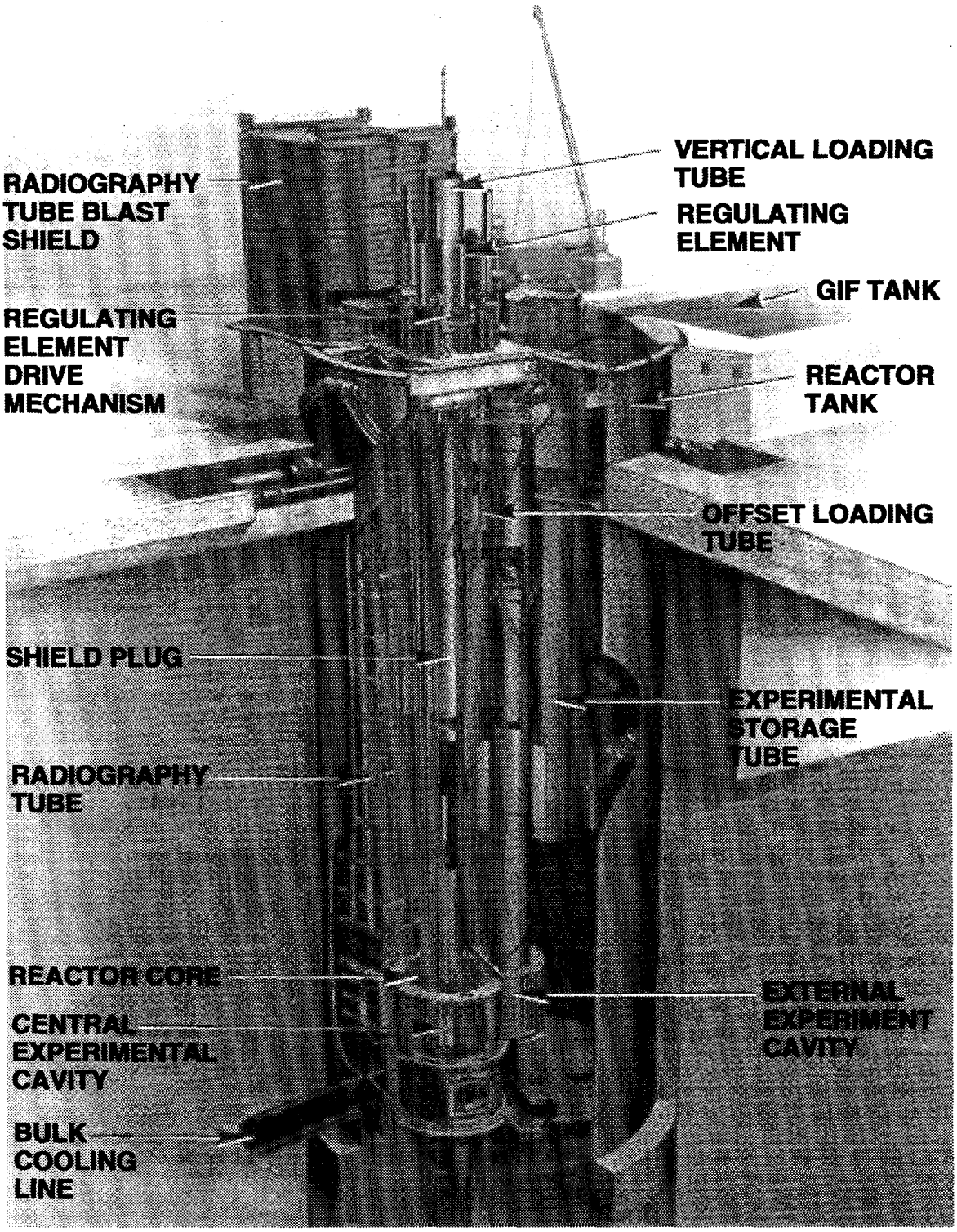

Figure 2.1 Cutaway View of The Annular Core Research Reactor and Peripheral Systems

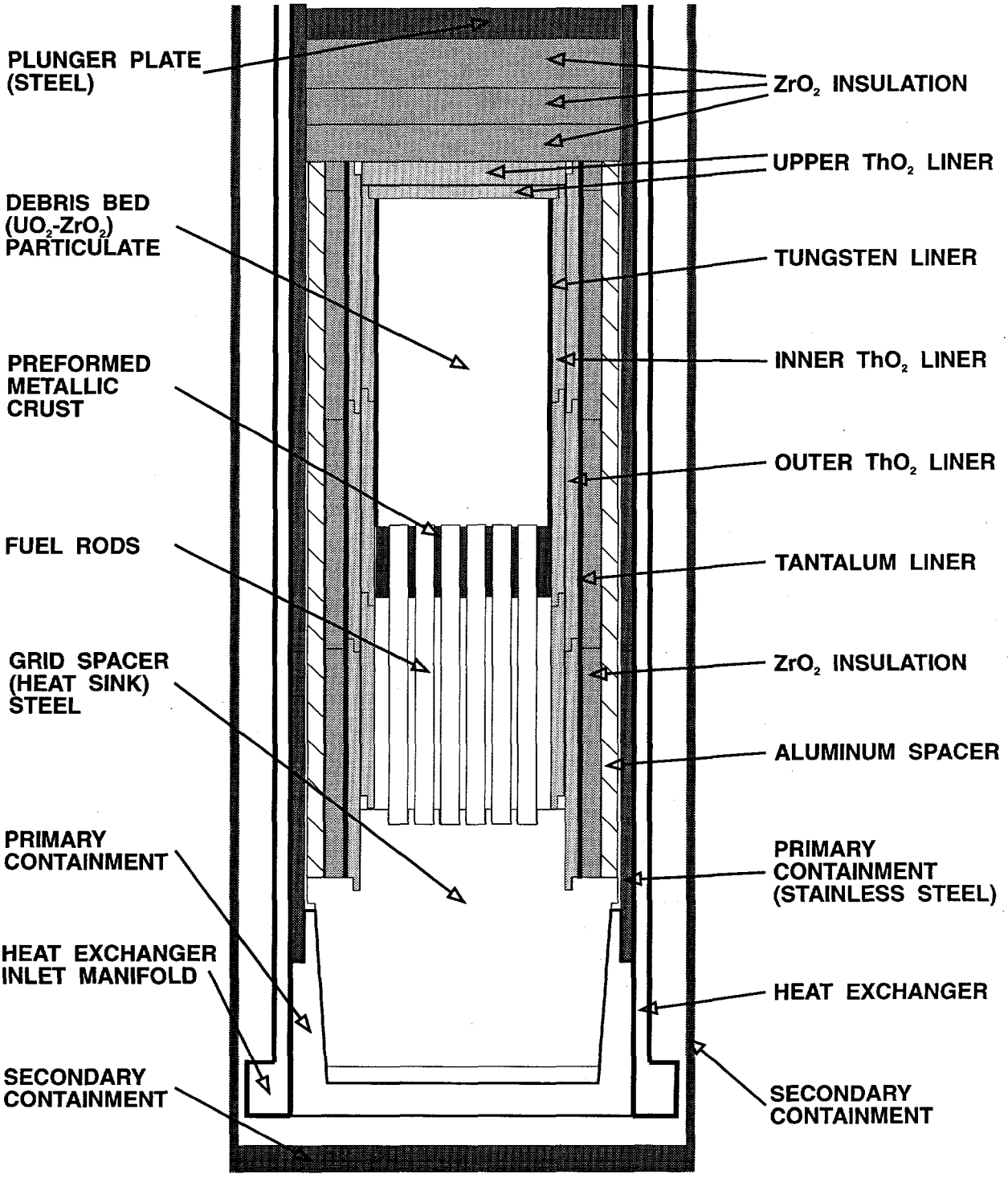

Figure 2.2 Schematic of the MP-2 Test Section

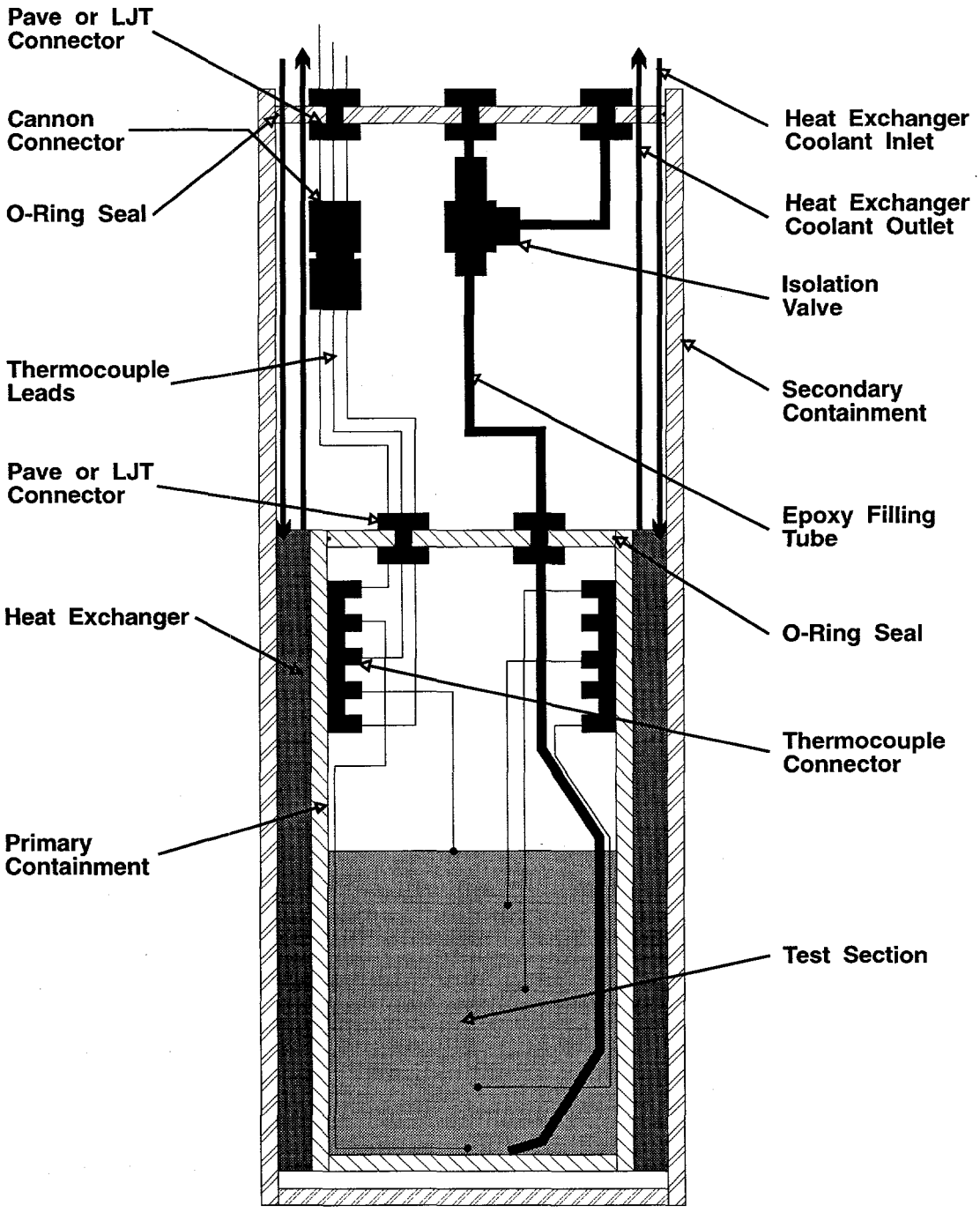

Figure 2.3 Schematic of the MP-2 Test Package Showing the Primary and Secondary Containments and Key Components

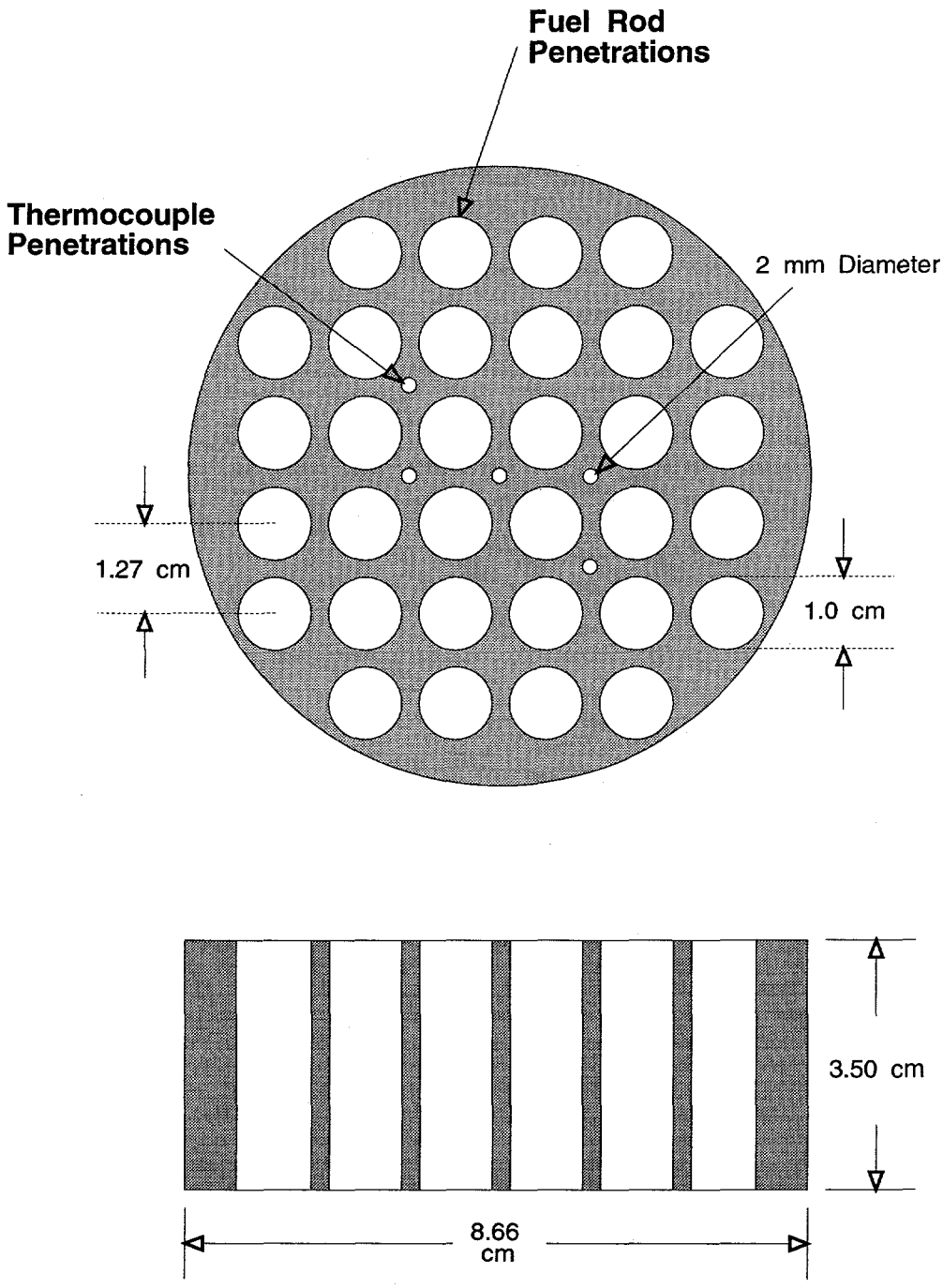

Figure 2.4 Cross-Sectional Views of the MP-2 Preformed Metallic/Ceramic Crust

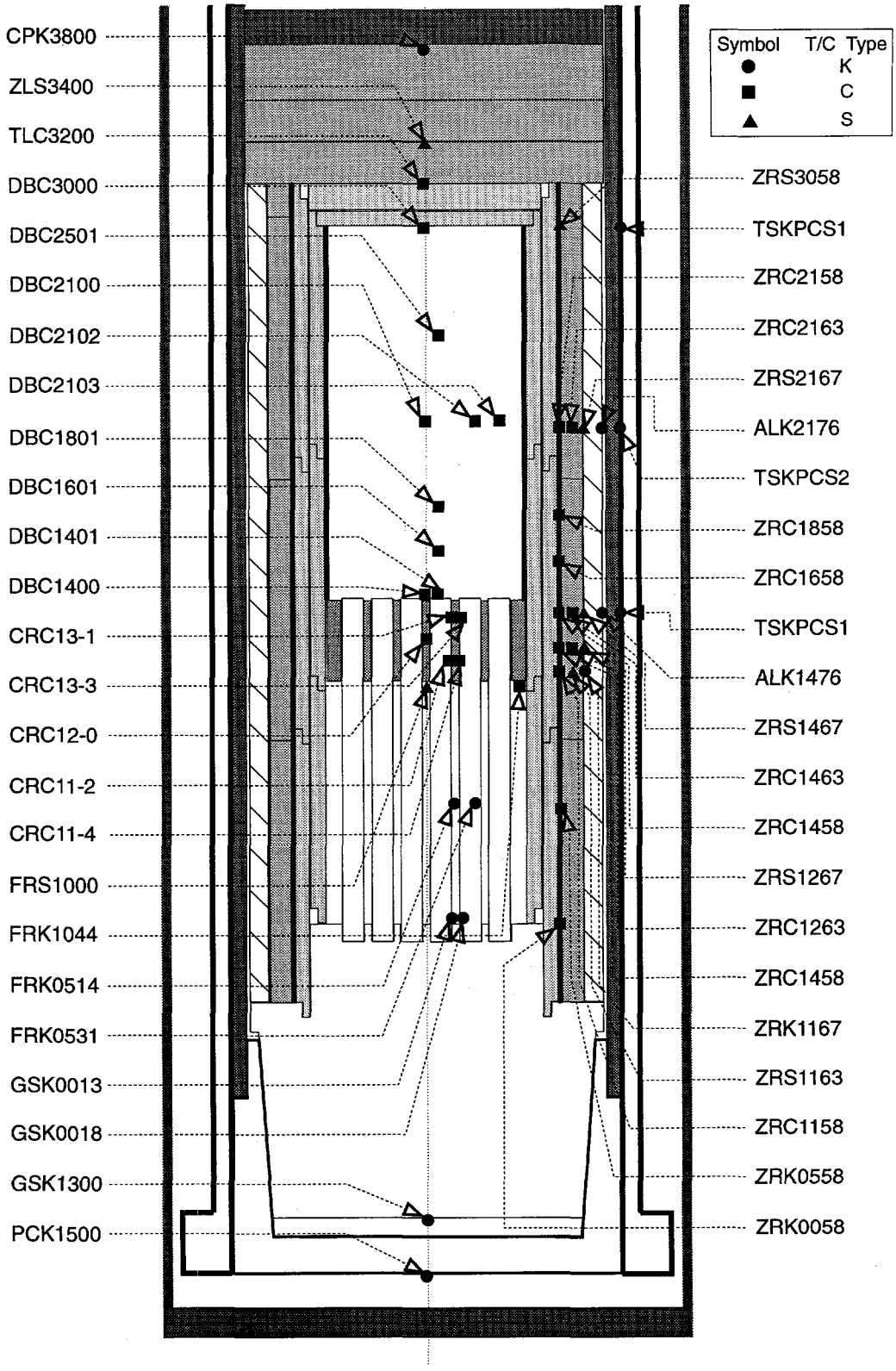

Figure 2.5 MP-2 Primary System Thermocouple Location Map

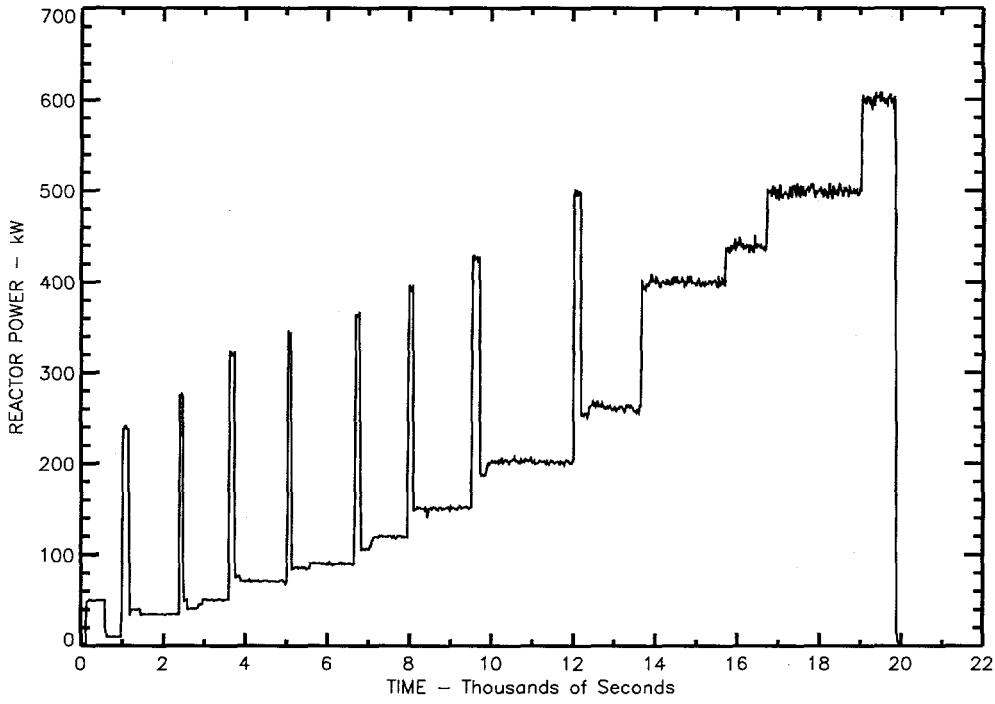

Figure 2.6 ACRR Power History Used to Fission Heat the MP-2 Experiment

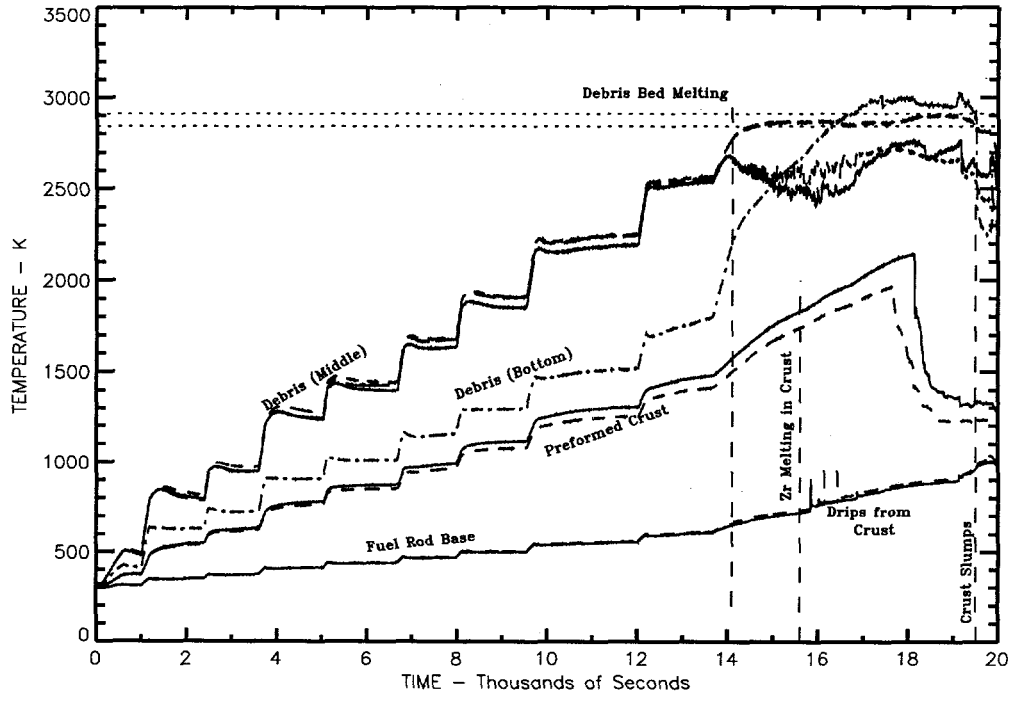

Figure 2.7 Measured Thermal Responses of the MP-2 Test Section

3.0 MP-2 Post-Irradiation Examination

3.1 Post-Irradiation Examination Procedure

Following the conduct and cool down of the MP-2 experiment in the ACRR, a detailed examination of the end-state was made in the Sandia National Laboratories Hot Cell Facility (HCF). The purpose of this post-irradiation examination (PIE) was to quantify the material behavior and interaction in the melt relocation process. The techniques used permitted the determination of the physical and chemical end-state of the test section materials. The results and analyses of a preexperiment thermal test on the preformed crust are given in Appendix C-1.

In Section 3.1, detailed descriptions of the procedures used in conducting the PIE are given. The experimental procedure consisted of the following six key tasks: package stabilization, x-ray analysis, sectioning, metallography, optical macroscopy, and electron microscopy. In Section 3.2 the results of each element of the PIE are presented together with interpretive commentary. Section 3.3 presents an interpretation of the data associated with relocated melt. Finally, a summary of the key conclusions, which can be drawn from this analysis, is given in Section 3.4.

3.1.1 Stabilization of the Experiment Package

The experiment package was allowed to radiologically decay for a period of approximately five weeks in order to reduce the radiological emission rate to acceptable levels. At the end of this period, the test section fuel components were stabilized with epoxy to preserve the test section in the physical configuration it had attained at the end of the test. The experiment capsule was flooded with epoxy without the removal of the containment bulkheads. A filtered purge pump was used to evacuate the primary containment gas of helium into the ACRR cavity purge system. Following the purging of the background gases, the secondary containment was opened. The valves to the primary containment epoxy fill tubes were accessed through a small port in the secondary containment. The experiment capsule was then backfilled with epoxy and subsequently stabilized. Prior to sectioning an x-ray analysis was performed on the test package using a gamma source. This procedure was carried out in the ACRR high-bay.

3.1.2 X-Ray Analysis

Pre- and posttest x-ray imaging were performed on the test package. The procedure involved using a portable point gamma source, which was aligned with the test package, and a photographic film pack to obtain a projection x-ray image. The major features and components of the test package are easily discernible in these images (see Section 3.2.1.1). The x-ray images were useful in determining relative locations of the key components in advance of the test and to show the relative displacement of components at the end of the test. The posttest x-rays were also useful in the selection of the sectioning cuts for the post-irradiation examination.

3.1.3 Sectioning of the Experiment Capsule

The experiment capsule was introduced into the HCF to a remote, manipulator-controlled box called a steel containment box (SCB). The sectioning operation was achieved by the completion of three major tasks: 1. extraction of the primary containment vessel from the secondary containment vessel, 2. radial cross sectioning of the primary containment vessel to achieve six circular sections, and 3. longitudinal cross sectioning of the circular sections to obtain a longitudinal profile of the experimental capsule.

First the secondary bulkhead was removed as were the associated connectors and valves. Then the primary containment canister was removed from the secondary containment canister. A band saw was then used to score the primary stainless steel containment vessel to prepare for the first series of horizontal cuts. The first series of cuts into the primary containment vessel was made perpendicular to the longitudinal axis, as illustrated in Figure 3.1. The first cut was made approximately 48.5 cm from the base of the test capsule, which served to separate the test section from the rest of the primary containment vessel. The second cut was made approximately 14 cm from the bottom of the test capsule. This cut served to separate the stainless steel base / heat sink from the test section. As a result of these preliminary cuts, a 34.5-cm in length section of the capsule remained. Five horizontal cuts were then made at various intervals from 4 - 8 cm, so that the test section would be separated into six circular log sections, as indicated in Figure 3.1.

The stainless steel containment vessel material was removed from the outer edge of each section. The remaining cross sectioning was performed on these sections in a longitudinal manner. A longitudinal slab approximately 1.3 cm in thickness was extracted from the diameter of each log section at the +135° (-45°) azimuthal location as shown in Figure 3.2. These -45° slabs were approximately 4 - 8 cm in the longitudinal direction and extended across the outer diameter of the thoria liner. The final operation of cross sectioning was to remove the zirconia insulation from each of the slabs. As a result each slab was bordered by the thoria liner. Table 3.1 summarizes the slab location, orientation, contents, and designation that will be utilized for the remainder of this report. Section 6-2 was cut out of a plane such that it was difficult to prepare metallographic. Therefore, another

longitudinal slab, 6-4, which is not shown in Figure 3.2, was extracted. This is the Section 6-4 identified in Table 3.1 and throughout the balance of the text, tables, and figures.

3.1.4 Metallography

The following metallographic procedures were used for the preparation of the longitudinal sections for this experiment.

3.1.4.1 Remote Metallography

The following procedures were performed in the remote, manipulator-controlled SCB in the HCF. All longitudinal sections were mounted to plywood using a standard wood glue to provide additional support and structure. The sections were then stabilized by the addition of epoxy. The sections were ground on a rotating grinding wheel using metallographic papers of 100, 200, 400, and 600 grit in succession with Freon as a lubricant. A light polish was achieved on a rotating wheel with 6-μm diamond paste with Freon as a lubricant.

3.1.4.2 Glove Box Metallography and Optical Macroscopy

The following procedures were performed in an un-shielded glove box in the HCF. Each longitudinal slab was approximately 100 mR/h on contact. The longitudinal sections (1-2 through 6-4) were photographed using a Wild-Leitz macroscope with a controlled x-y stage at a magnification of approximately 7X. The montages were produced for characterizing regions of material behavior.

After the optical macroscopy was complete, the longitudinal sections (1-2 through 6-4) were further sectioned for subsequent scanning electron microscopy. The samples were cut using a diamond saw with Freon as a coolant. Each square was then lightly polished on a rotating wheel using 6- and then 1-μm diamond paste with Freon as the lubricant. The plywood backing material was removed. Each specimen was then sputter coated, using a Au-Pd target, for examination in the scanning electron microscope.

3.1.5 Scanning Electron Microscopy and X-Ray Analysis

Scanning electron microscopy was performed to determine the elemental species of the microstructural phases that were present. A Hitachi 520 scanning electron microscope (SEM) with a remote column specifically designed for radioactive materials located in the HCF was used for this study. Three analytical techniques were employed. First, secondary electron images were obtained, which provided microstructural information such as phase morphology. Secondary electron images were used for phase identification where optical macroscopy did not provided the needed resolution for phase identification.

Second, the elemental species were determined using a back scattered electron detector. The number of back scattered electrons, which are emitted from a specimen, increases as the atomic number of the specimen increases. In fact, if the atomic numbers of two elements differ by more than three, those phases may be distinguished in a back scattered electron image. The element of higher atomic number will show stronger emission resulting in lighter areas in the image. Back scattered electron images provide chemical species maps of specific elements. The SEM was operated at 20 kV with take off angle normal to the sample plane for back scattered images.

Third, the chemical composition of selected areas was determined using x-ray analysis with a Microspec® wavelength spectrometer. The SEM was operated at 20kV, a beam current of 40 nanoamps, and 65° take-off angle for the x-ray analysis. Table 3.2 lists the details of the standards that were used for the determination of the wt % of the elements present. The correction actors that were applied to the wavelength measurements included those for atomic number, adsorption, fluorescence (ZAF), and compound factor (i.e., bound with oxygen). Wavelength analysis was performed at one of two magnifications, either 20,000 X or 1000 X. The choice of analysis magnification was determined by the number of phases that were present in the sample. If the sample was composed of several elements in a homogeneous solid solution (i.e., one phase), the wavelength analysis was performed at 20,000 X. In this case, the sample area, in which characteristic x-rays are being collected from, is $(5\ \mu m)^2$. However, if the elements present result in the formation of a heterogeneous mixture (i.e., several phases), the wavelength analysis was performed at a magnification of 1000 X. The sample area in a 1000 X analysis is much larger and is $(100\ \mu m)^2$. A larger area must be sampled when several different phases are present, to assure the collection of x-rays from all phases. Since several phases were found to be present in several locations, no attempt was made to determine the chemical compositions of all these phases. Instead the bulk elemental chemistry of a particular location was determined. The depth of x-ray penetration for all samples was nominally 2 μm. For each region of interest, several areas within a region were analyzed and the statistical average was calculated to represent the best measure of the bulk chemistry for the region. Based upon the SEM calibration, spectrometer calibration, and the correction factors applied the level of accuracy with this technique is within 2.0 atomic percent.

3.2 Post-Irradiation Examination Results

3.2.1 X-Ray Analysis

3.2.1.1 Radiography of Pretest and Posttest Experiment Capsule

The x-ray images of the pre-irradiation and post-irradiation MP-1 and post-irradiation MP-2 experimental capsules are shown in Figure 3.3. The difference between the two experimental configurations that is evident in the radiographs is the shorter fuel rod array of MP-1. The pretest x-ray image clearly shows the three zones of the test capsule: The ZrO2 and UO2 ceramic debris bed in the upper test region, separated by the prefabricated metallic crust with the embedded zircaloy clad/UO2 fuel stubs and the continuation of the fuel rod stubs in the lower region. Note the sharp interface of the prefabricated metallic crust to the ceramic debris bed.

The experimental histories for the two tests can be compared by the post-irradiation radiographs. Taken together, the MP-1 and MP-2 tests provide information on two points along a common melt progression pathway, where MP-2 represents a point further down the time-line. The MP-1 test was terminated after the development of a molten ceramic pool region but before the ceramic crust/pool interface had migrated to the rod region of the experiment, as shown in Figure 3.3. In MP-2, the melt progression continued through this stage such that the ceramic crust/pool interface migrated into the fuel rod region formerly occupied by the preformed metallic crust, and displaced about half of the metallic crust blockage. Additionally, a greater fraction of the debris became molten and incorporated into the melt pool. Remnants of the metallic blockage and the lower boundary of the ceramic crust/pool interface are clearly visible in the MP-2 posttest x-ray image (Figure 3.3). The displaced metallic crust material was visible as an accumulation/blockage region situated at the base of the fuel rod array.

The following observations can be made in examining the posttest radiograph adjacent to the log section cutting diagram as shown in Figure 3.4. The upper debris bed (Section 1-2), exhibited a low density, almost skeletal region of material which was located near the thoria cap and extended a short distance along the thoria wall. Further into the debris bed (Section 2-2), the region was completely void of material. The next section (3-2) contained a large mass of material which appears to be the melted and relocated debris material. The upper boundary of this primarily densified region appeared very distinct and extended across the entire diameter of the test capsule bound by the thoria liner. A slight meniscus was formed on the upper interface at the liner wall. Some internal void regions and cracks were evident in the upper portion of the material mass. The relocated debris bed extended into the prefabricated crust/fuel rod assembly and appeared to be more densified. The lower boundary of the relocated material (Section 4-2) was flat in the central region of the prefabricated crust and exhibited a sharp curvature as it extended to the thoria liner wall. Portions of the prefabricated crust appeared to be present as shown by the presence of its lower boundary. The fuel rod assembly (Section 5-2) appeared to be intact. However, the fuel pellet stack showed large separations that did not correspond to the initial fuel pellet interfaces. Finally, the lower portion of the test capsule (Section 6-4) showed relocated material present between the fuel rod stacks. A majority of the relocated material was present in the central portion of the capsule, with a lower density of relocated material present near the thoria walls.

3.2.1.2 Implications From the Radiographs

At this point in the PIE, it was clear that most of the analysis would concentrate on the behavior in the relocated debris bed (Section 3-2), the prefabricated crust region (Section 4-2), and the relocated material mass at the bottom of the test capsule (Section 6-4). The posttest radiograph clearly showed that the debris bed did, in fact, melt and relocation did occur. The relocating debris material did interact with the prefabricated crust and the extent of that interaction was of interest. Also of interest, with regard to the crust, was the remnant crust. Of final interest was the source and relative amount of relocated material at the bottom of the test capsule.

The assumption of an axisymmetric thermal profile for the test capsule was verified. There was strong evidence of an axisymmetric thermal profile in the densified debris region or melt region as indicated by the contours of the upper and lower boundaries. Axisymmetric behavior also appeared to be prevalent in the lower region (6-4).

3.2.2 Optical Macroscopy

The optical macrographs Sections of 1-2 through 6-4 are shown in Figures 3.5 through 3.10, at magnification of 1.5 X. These sections were examined to allow a more detailed understanding of the key physical changes that occurred and to provide a qualitative measure of the behavior. Key phenomena and regions of interest for further chemical analysis were identified.

The upper debris bed, Section 1-2, is shown in Figure 3.5. The uppermost section of the debris bed contained particle agglomerations that were determined to be a network of retained urania particles held together by a phase that wet the surface of the urania. In this region there are no retained zirconia shards nor any unreacted urania particles present. The interparticle phase, which held the retained urania particle network in place was determined to be primarily produced by the melting of zirconia. The remainder of the upper debris bed consisted of porosity. Significant levels of porosity are visible in the lower half of this section, as both open holes and areas that have been backfilled with epoxy. The material behavior in this section was found to be consistent to the

behavior observed in the MP-1 experiment upper debris bed.

Section 2-2 is shown in Figure 3.6. This section was found to be completely void of material as shown by the presence of a thermocouple remnant embedded in epoxy material.

The relocated ceramic melt from the debris bed (Section 3-2) is shown in Figure 3.7. Most of the upper surface was fairly flat with the exceptions of a slight central bump and the meniscus forming at both sides near the thoria wall. The ceramic melt pool appeared to be fairly dense with the exception of regions of internal porosity. The area fraction of porosity in the melt pool was determined to be 9.0%. Some of the large voids appeared to be the result of coalescing of smaller voids. This was especially true near the top of the ceramic melt pool. The large internal porosity may be the result of the downward relocation of the ceramic pool, late in the experiment. The voids were in the process of coalescing and escaping at the upper interface when they were entrapped during solidification. The fine porosity near the bottom of the melt pool was shrinkage from solidification. Radial cracks emanate from porosity and occurred upon cool down. The grain size of the melt pool was found to be very fine at the thoria walls and the lower edge of the melt pool region. The grain size in the central melt pool was found to be larger in comparison. The difference in grain size was due to a difference in cooling rate upon termination of the experiment. The fine grain resolidified melt occurred due to a faster cooling rate. Whereas, the large grain, centrally located, resolidified melt experienced a slower cooling rate.

The lower interface of the ceramic melt pool and the metallic crust remnant (Section 4-2) are shown in Figure 3.8. The metallic crust had been penetrated by the relocating melt pool and approximately one-half of the original crust height remained. However, the metallic crust remnant morphology was found to be very different than that of the original crust features. What remained of the crust was a very porous structure, which indicated that the crust had not been fully molten (scanning electron examination revealed unreacted phases, Section 3.2.3.2). There was no evidence of a solid resolidification structure. There were large, ellipsoidal intrusions in the metallic crust remnant near the fuel rods. Some of these intrusions were found to be filled with relocated ceramic melt material, as seen in Figure 3.8 on extreme sides of the section. Some of the intrusions were completely void of material, as shown in the central location of the test section. These post-test intrusions into the crust were the primary paths for relocation of the crust material to the bottom of the test capsule. Fuel rods were found extending into the ceramic melt pool, and erosion of the top two fuel pellets was evident . The centrally located fuel rods were eroded and displaced from their original position. There was an absence of all zircaloy cladding on the fuel rods in the melt pool location, the crust remnant region, and in regions below the crust remnant. Material of metallic crust origin was found between the fuel pellets within a stack at locations below the melt pool. The zircaloy cladding, within the metallic crust, appeared to have melted prior to the gross movement of the metallic crust or the dissolution of the fuel pellet stacks. This event apparently influenced the subsequent relocation of metallic crust material by providing an easy path for relocation.

Relocated metallic material was also observed in the next lower section (Section 5-2) as shown in Figure 3.9. A majority of the relocated material was along the central axis of the test section. Metallic material invaded the gap between fuel pellets, to varying degrees, and fused the fuel pellet stack together. Upon cool down, the fused stack was subjected to large tensile forces that were sufficient to fracture the fuel pellets preferentially to the metallic joints. A majority of the fuel pellet stacks were deficient in the zircaloy cladding.

The bottom of the test capsule (Section 6-4) contained the bulk of the relocated metallic crust as shown in Figure 3.10. Individual droplets of material were revealed between fuel pins near the lower stainless steel plate. Sharp, rounded interfaces were observed between individual droplets. This indicated that the relocation process of metallic crust material was composed of separated and distinct events. Furthermore, these droplets were the first material to move in the relocation process. The bulk of the relocated metallic material was located above these initial droplets. This material showed no interfaces or striations within its mass, which indicated that this material corresponded to a single and continuous relocation event. Zircaloy cladding was observed on a majority of the fuel pellets in this region. However, metallic material was found between fuel pellets even where zircaloy clad appeared to be intact. This indicated that the metallic material could invade the zircaloy clad by one of two methods. First, the relocating metallic material could dissolve the zircaloy on the cladding outside as the metallic material moved down the test capsule. Second, the relocating materials could breach the cladding at higher elevations and continue to move down the capsule in the gap between the inside cladding/fuel pellet interface. As a result, zircaloy cladding need not be absent for the metallic material to fill the fuel pellet gap.

3.2.3 Scanning Electron Microscopy and X-Ray Analysis

3.2.3.1 Regions of Interest

There were four general regions of material behavior in which scanning electron microscopy with chemical analysis was performed, in addition to the optical observations, and these are shown in Figure 3.11. The four regions were grouped as follows: upper debris bed, ceramic melt pool, metallic crust remnant, and relocated metallic material. The first region was at the top of the debris bed to chemically characterize the retained structure. The second region was the ceramic melt pool characterization. Chemical analyses were performed at the top, middle and bottom of the ceramic melt pool.

Chemical analyses were performed on the crust remnant along the center line of the capsule. Finally, the fourth region of relocated metallic material was analyzed just below the crust, and for the two distinct relocation events, namely, the larger material mass and the small droplets at the very bottom of the test capsule. Table 3.3 lists the sample identification, corresponding location and resulting microstructure determined by the scanning electron analysis.

3.2.3.2 Physical Description of Phases Present

Upper Debris Bed

Scanning electron micrographs and the corresponding elemental maps are given in Figure 3.12 for the retained structure at the top of the ceramic debris bed. The secondary and backscattered electron images revealed a two-phase mixture. The elemental dot maps revealed a mixture of retained urania particles that have been wet by a resolidified melt of (U, Zr)O2. The morphology of the urania particles was a very fine grain size and a fine dispersion of porosity, both which are characteristic of a pressed and sintered ceramic material. In contrast, the resolidified melt exhibited a very large grain structure with little evidence of internal porosity. Cracking, which followed the grain boundaries of the resolidified structure and the urania particle interface, occurred during cool down due to differential expansion of the two phases. The material behavior, which occurred at the top of the ceramic debris bed, was found to be consistent with the material behavior in the MP-1 experiment.

Ceramic Melt Pool

Scanning electron micrographs and the corresponding elemental maps are shown in Figure 3.13 for the material located at the top of the ceramic melt pool. The secondary and backscattered electron images revealed a (U, Zr) O2 single phase, ceramic, homogeneous microstructure. Small ($\approx$ 3 μm) pockets of trace elements, whose origin was the metallic crust, were found segregated at the grain boundaries of the single phase, resolidified microstructure. The trace elements, which were segregated from the single phase and tied primarily with Zr, were determined to be Fe, Ni, and Cr, whereas, Ag was found to be distributed throughout the single-phase microstructure.

Material near the center of the ceramic melt pool was examined and the results are shown in Figure 3.14. The resulting microstructure was very similar to that at the top of the melt pool: a (U, Zr)O2 single-phase microstructure with small pockets of metallic element segregation. As with the top, Fe, Ni, and Cr were found to be segregated with Zr, and separate from the single phase matrix. Again the Ag was evenly mixed distributed throughout the single-phase matrix.

Scanning electron micrographs and the corresponding elemental maps are shown in Figure 3.15 for material located at the bottom of the ceramic melt pool: a single-phase (U, Zr)O2 solid solution. Unlike the top and middle of the ceramic melt pool, there were no trace elements detected in this location.

Measurements of the uranium and oxygen content of Sample 4-2-2 were made at nine different locations on the surface of the sample. Each location on the sample, which was the fuel rod located within the ceramic melt pool, had two readings made as indicated in Table 3.4. Each location is shown in Figure 3.16 and the sketch immediately below Figure 3.16. As indicated in both the sketch and Table 3.5, samples 1 and 2 were taken at the center of the fuel rod, samples 3, 4, and 5 at 0.25 r, 6 and 7 at 0.75 r, and 8 and 9 at 0.9 r. The plotted averages are shown in Figure 3.17.

Figure 3.17 shows an apparent decrease in the amount of oxygen from the center of the fuel rod to the surface. This condition can be explained in either one of two ways: It is an artifact of the manufacturing process or the melt pool served as a sink for the oxygen content of the fuel rod. The issue can be resolved by performing scanning electron microscopy in conjunction with wave length dispersive analysis of an as-received fuel rod. These two actions will provide an oxygen profile of the as-received fuel rod material before any experiments are made. If the microscopy/dispersive analysis oxygen profile is the same as the experimental results, the radial decrease in oxygen is an artifact of manufacturing; if different, then the melt pool served as a sink for the oxygen content. However, neither the microscopy nor the dispersive analysis was performed on the as-received fuel rod.

A thin, dark band of material located at the outermost edge of the ceramic melt pool served as the interface between the ceramic melt pool and the metallic crust remnant. The band is shown in Figure 3.18. The band of material had an optically dark appearance. Scanning electron microscopic examination showed that the band was approximately 1500 μm in thickness.

Scanning electron micrographs and the corresponding elemental maps are shown in Figure 3.19. These maps revealed a primary phase of large grains— 150 μm in diameter—that yielded 10 grams through thickness, and a secondary phase that showed up in the crust remnant in two forms: solid massive chunks and a fine structure on the grain boundaries. A third phase/characteristic of the melt if the large porosity shown in Figure 3.19a.

The conclusion is that the liquid melt pool fell onto the crust. This action resulted in (1) some solid chunks of crust material breaking off as shown by the solid massive chunks seen in Figure 3.19 and (2) some of the crust liquefying and when it solidified, it precipitated on the grain boundaries of the ceramic melt as shown by the fine structure.

We also have concluded that the porosity is the result of the vaporization of the tin and indium when the liquid ceramic fell on the crust.

Metallic Crust Remnant (Wall)

Scanning electron micrographs and the corresponding elemental maps are given in Figure 3.20 for the metallic crust remnant at the thoria liner wall near the upper portion of the crust. The secondary and backscattered electron images revealed a multiple phase mixture. Large spherical porosity varying between 60 - 100 μm in size was present. The elemental dot maps revealed the microstructure present consisted of six distinct phases.

The following trends are observed for the phases present in the crust remnant at the location near the thoria liner wall. The numbers in parentheses are the standard deviation.

Element	Center/Top		Center/Bottom		Wall		Original
	wt %		wt %		wt %		wt %
U	8.61	(.04)	13.0	(.1)	10.66	(.45)	7.05
O	8.26	(.03)	8.9	(.1)	6.83	(.93)	4.53
Zr	57.34	(.01)	50.5	(.5)	50.78	(1.93)	47.53
Fe	8.25	(.08)	8.4	(.2)	8.92	(1.59)	11.88
Ni	5.82	(.01)	6.0	(.2)	6.91	(.96)	7.39
Cr	1.67	(.02)	1.3	(.03)	1.44	(.65)	2.17
Mo	0.33	(0)	.2	(.01)	.23	(.14)	0.57
Ag	6.16	(.01)	4.8	(.04)	9.2	(3.16)	11.61
Sn	2.81	(.07)	5.5	(.1)	3.31	(.05)	4.14
In	.77	(.01)	1.6	(.03)	1.83	(.64)	2.93

Scanning electron micromaps and a detailed discussion of selected areas in the metallic crust remnant, as-fabricated crust, and relocated materials are given in their entirety in Appendix C-2. The following is an abbreviated discussion of those selected areas.

Metallic Crust Remnant (Center Top)

The metallic crust remnant at the center line near the upper portion of the crust had large spherical porosity varying between 60 and 100 μm in size. The following trends are observed for the phases present in the crust remnant at the top, center line location:

Fe/Ni/Ag/Zr/In/Sn/U are associated

Fe/Ni/Cr/Mo/Zr are associated

Ni/In/Fe/Sn/Zr are associated

U/Zr/O are associated

U/O are associated

Sn/In/Ni/Zr/Ag are associated

Metallic Crust Remnant (Middle)

The metallic crust remnant revealed a multiple phase mixture which had large spherical porosity varying between 60 and 90 μm in size. The microstructure present consisted of six distinct phases.

The following trends are observed for the phases present in the crust remnant:

Fe/Ni/Ag/Zr are associated

Fe/Cr/Zr are associated

Ni/In/Fe/Sn/U/Zr/Ag are associated

U/Zr/O are associated

U/O are associated

Sn/In/Ni/Zr are associated

As-Fabricated Crust

The as-fabricated metallic crust revealed a multiple phase mixture and large spherical porosity varying between 40 and 70 μm in size. The microstructure present consisted of eight distinct phases. The following

trends are observed for the phases present in the as-fabricated crust:

Fe/Ni/Ag/Zr are associated

Cr was distinct

In/Sn/Zr/Ni are associated

ZrO_2 was distinct

UO_2 was distinct

Fe was distinct

Ni/Zr are associated

In comparing the evolved microstructure of the crust remnant to that of the as-fabricated condition, the following observations can be made. First and foremost, urania particles that remained were retained in the crust remnant, which indicated that the crust was not at a temperature high enough or at temperature long enough to dissolve the initial amount of urania in the crust. Second, Fe/Ni/Zr/Ag and In/Sn/Zr/Ni still maintained their association despite liquefaction and solidification. Finally, the ZrO_2 that was present initially, had dissolved and upon solidification was associated with every phase that had once been liquid (i.e., every phase except undissolved UO2).

Relocated Metallic Material

Six regions of relocated material were examined using scanning electron microscopy in conjunction with wave length dispersive analysis. The name, location, and sample number of the six regions are (1) Relocated Material/Top (RM-1), 5.2.3; (2) Relocated Material/Middle (RM-2), 6.4.3A; (3) Relocated Material/Middle (RM-2*), 6.4.3; (4) Relocated Material/Bottom (RM-2.5*), 6.4.7; (5) Relocated Material/Bottom (RM-3*), 6.4.12; and (6) Relocated Material/Bottom (RM-3), 6.4.10. The RM is relocated material -1, -2, etc.

A description of the morphology of the RM-1, RM-2, and RM-3 phases are given in the following paragraphs.

The relocated material that was just below the crust remnant (RM-1) consisted of six distinct phases. The following trends are observed for those six phases:

Ag/Zr are associated

Fe/Cr/Zr are associated

Ni/In/Fe/Sn/U/Sr/Ag are associated

Fe/Ni/Cr/Zr are associated

U/Zr/Ni/Fe are associated

Sn/In/Zr are associated

The **bold** items indicate similarity to the crust remnant.

The relocated material that was located in the middle section of the fuel rod array (RM-2) consisted of six distinct phases. The following trends are observed for those six phases:

Fe/Ni/U/Ag/Zr are associated

Fe/Cr/Zr are associated

In/Fe/Ni/Sn/Zr are associated

Fe/Ni/U/Zr are associated

Fe/Ni/Cr/U/Zr are associated

Sn/Zr are associated

The **bold** items indicate similarities to RM-1.

The relocated material that was located at the bottom of the test capsule (RM-3) consisted of three distinct phases. The following trends are observed for those three phases:

In/Sn/Zr are associated

Fe/Ni/Cr/U/Ag/Zr are associated

Ag/Fe/Ni/Cr/U/Zr/In/Mo/Sn are associated

The **bold** items indicate similarities to RM-1.

Crust and Relocated Material Phase Summary

There were several different phases located in the experiment package, especially in the lower section (crust remnant to capsule bottom). There was no attempt made to identify the chemical compositions of each phase, rather a general elemental association was made. The following listing summarizes the phases that were observed and their relative locations.

Phase	As-Fabricated Crust	Crust Remnant	RM-1	RM-2	RM-3
Zr/O	x				
Fe	x				
Zr/Ni	x				
Cr	x				
U/O	x	x			
Zr/U/O		x			
Zr/Ni/Fe/Ag	x	x			
Zr/Fe/Cr		x	x	x	
Zr/U/Sn/Ni/In/Fe/Ag		x	x		
Zr/Sn/Ni/In	x	x			
Zr/Ag			x		
Zr/Ni/Fe/Cr			x		
Zr/U/Ni/Fe			x	x	
Zr/Sn/In			x		x
Zr/U/Ni/Fe/Ag				x	
Zr/Sn/Ni/In/Fe					
Zr/U/Ni/Fe/Cr				x	
Zr/Sn				x	
Zr/U/Ni/Fe/Cr/Ag					x
Zr/U/Sn/Ni/Mo/In/Fe/Cr/Ag					x

3.2.3.3 Elemental Analysis Results

Scanning electron microscopy with x-ray analysis was utilized for the determination of the elemental chemistry of each region. Since several phases were found to be present in several locations, no attempt was made to determine the chemical compositions of all these phases. Instead the bulk elemental chemistry of a particular location was determined. As stated in the experimental procedure, several areas were measured for a particular region and the statistical average was used to represent the elemental composition of the region. The following chart lists the table number that contains the x-ray analysis raw data and elemental average for the regions.

A summary of these results are given in Figures 3.21 through 3.27. The pie charts (Figures 3.21 through 3.24) represent the elemental composition (in terms of wt %) for each region analyzed. The bar graphs (Figures 3.25 through 3.27) show a particular element and indicate how the wt % of the element varied as a function of location in the test capsule. It is important to note that these elemental compositions can not be used in terms of a mass balance from one location to another. These compositions were taken for a relative measure of material behavior down the center line of the test capsule and over very small areas when compared to the total amount of material present. In order to attain a mass balance of all the elements with minimal error, a large number of samples would need to be analyzed.

The elemental variation in the upper portion of the capsule is given in Figure 3.25. This region, extending from the solid solution in the upper debris bed to the lower portion of the melt pool, showed fairly constant elemental behavior when compared to the initial ceramic debris bed composition. There were slight increases in uranium concentration, at the expense of zirconium, in two locations. First, at the top of the debris bed, in the solid solution which wet the urania debris, was uranium rich. This was expected, since the zirconia shards had melted and a source of uranium (i.e., the urania particle) was still present to enrich the solid solution. The second location in which uranium was slightly elevated was at the bottom of the ceramic melt pool. The optical micrograph (Figure 3.8) of Section 4-2 showed that the bottom of the ceramic melt pool had encroached the metallic crust and fuel rod assembly. The upper fuel pellets in the stack had been dissolved and thus provided a source and supply for uranium in this location.

Location	Sample	Table
Upper Debris Bed - Solid Solution	1.2.3	3.6
Melt Pool - Top	3.2.3	3.7
Melt Pool - Middle	3.2.8	3.8
Melt Pool - Bottom	4.2.11	3.9
Fuel Rod - Inside Melt Pool	4.2.2	3.4
Crust Remnant - Wall	4.2.9	3.10
Crust Remnant - Center - Top	4.2.12	3.11
Crust Remnant - Below Melt Pool	4.2.13	3.12
Crust Remnant - Inside	4.2.6B	No table
Solid Core - Below Melt Pool	4.2.6C	No table
Relocated Material - Top (RM-1)	5.2.3	C-2.1*
Relocated Material - Middle (RM-2)	6.4.3A	C-2.2*
Relocated Material - Middle (RM-2*)	6.4.3	C-2.3*
Relocated Material - Bottom (RM-2.5*)	6.4.7	C-2.4*
Relocated Material - Bottom (RM-3*)	6.4.12	C-2.5*
Relocated Material - Bottom (RM-3)	6.4.10	C-2.6*

* In Appendix C-2

The elemental variation in the lower portion of the capsule is given in Figure 3.27. This region was located from the metallic crust remnant to the bottom of the experiment capsule and was compared to the initial metallic crust composition. The crust remnant was largely ceramic with a oxygen content nearly double the initial oxygen content (i.e., 4.5 wt% to 8.9 wt%). There was an increase in uranium content because the urania particles did not fully dissolve and relocate, as uranium was mainly tied with oxide phases (U/Zr/O and U/O). The metallic crust remnant was depleted of a majority of the metallic elements (Fe, Ni, Cr, Mo, Ag, and In). Only two metallic elements were enriched in the crust remnant, Zr and Sn. The additional source of zirconium and tin in the metallic crust was the zircaloy clad on the embedded fuel rod stubs. The zircaloy cladding was absent, posttest, in the crust/fuel rod assembly. The cladding melted at lower temperatures than the bulk of the crust and preferentially dissolved the crust material adjacent to the cladding.

The relocated materials (RM-1 through RM-3) all follow the same trend. They all are zirconium enriched and oxygen deficient when compared to the initial crust composition. The deficiency in oxygen occurred because the oxide materials (22% by weight in the initial crust) did not participate in the relocation process and remain, in some form, in the crust remnant. The enrichment in zirconium increased from RM-1 to RM-3. In other words, the first material to reach the bottom of the capsule (RM-3) had the highest concentration of zirconium by weight (69 wt%). The increase in zirconium was due to the additional source of zirconium in the metallic crust/fuel rod assembly, namely the zircaloy clad on the fuel rod stubs. This material was the first material to relocate to the bottom of the capsule (RM-3). As material continued to relocate from the crust down the capsule, there was an additional source of zircaloy provided by the fuel rod assembly, to enrich the relocated materials in zirconium.

All the metallic elements that were present in the initial crust participated in the relocation process. The only metallic element that was enriched above its initial metallic crust composition was Sn. The source for the additional amounts of Sn in the relocated material was the zircaloy cladding of the fuel rod assembly.

The atomic compositions of selected regions of interest were determined from the information given in Tables 3.6 - 3.12 and are given in Table 3.13. The oxygen to metal ratio was also determined at each location. It was computed by comparing the oxygen concentration to the sum of all metals. In comparing the oxygen to metal ratio of the initial debris bed which was 2.0, to the behavior at the top of the test capsule (upper bed to melt

pool - bottom), the oxygen was found to be fairly constant, ranging in value from 1.86 to 1.7.

The oxygen to metal ratio was found to vary considerably for the lower one-half of the test capsule. The initial metallic crust had the stoichiometry of 0.25, whereas the crust remnant had an oxygen to metal ratio of 0.56. This increase in oxygen content in the crust remnant was primarily due to the loss of metallic elements in the posttest crust. It is important to note that the compositional change in metals was primarily due to the preferential loss of all metals with the exception of zirconium. The initial crust composition contained an atomic fraction of zirconium of 0.37, with a posttest value of 0.358, accounting for a 3% change in zirconium. In contrast, the sum atomic fraction of the other metallic elements changed from 0.43 to 0.28, accounting for a 35% decrease in metallic components in the crust.

The relocated materials (RM-1 through RM-3), were all oxygen deficient when compared to the initial metallic crust, and therefore, it would be expected that their melt temperature to be lower than that of the bulk crust remnant. The lower oxygen to metal ratio of the relocated materials further emphasizes the importance that the presence of the zircaloy cladding had on the melt process. The relocated materials were oxygen deficient and zirconium rich and therefore melted at a much lower temperature than the bulk crust. As the metallic elements drained from the crust and relocated, the crust remnant became more oxygen enriched and stabilized.

3.3 Interpretation of Elemental Analyses

The following section provides some interpretation of the relocated melts observed in the MP-2 PIE and of the metallic crust remnant material residing below the ceramic crust region. As described previously, four regions below the ceramic crust were examined in detail using scanning electron microscopy. The regions include the crust remnant region (Figure 3.8, sample 4-2-13) which lies just below the ceramic crust, and metallic relocated material regions identified as RM-1, RM-2, and RM-3, where RM-3 is situated at the very bottom of the fuel rod array (Figure 3.10, sample 6-4-10), RM-2 is located at the upper part of the lowermost metallic accumulation at the base of the rod array (sample 6-4-3), and RM-1 is situated about midway between the base of the rod array and the upper metallic crust remnant (sample 5-2-3). The following list restates the measured material compositions of these regions in terms of atomic fractions. Notice that the crust remnant region has a significantly elevated oxygen content relative to the original crust composition and the relocated material compositions, RM-1, -2, and -3 are significantly depleted in oxygen.

Distribution of Elements Measured in MP-2 Samples by Atomic Fraction
(Crust Liquid is normalized difference between original crust and crust remnant materials)

Region	O	U	Zr	Fe	Ni	Cr	Mo	Ag	Sn	In	Total
Original Crust	.2	.022	.37	.015	.09	.03	.004	.08	.025	.019	.99
Crust Remnant	.36	.035	.358	.095	.066	.016	.001	.029	.03	.009	.999
Crust Liquid	.00	.006	.393	.219	.132	.044	.007	.146	.018	.035	1.00
RM-1	.079	.029	.451	.167	.132	.031	.005	.054	.035	.018	1.001
RM-2	.05	.031	.596	.119	.062	.035	.002	.032	.063	.011	1.001
RM-3	.069	.025	.646	.096	.059	.019	.002	.046	.028	.01	1.000

The distribution of elements found in the relocated material (RM) regions and in the crust remnant region may be understood in terms of the behavior of a reduced set of material compositions, where each separate material class is assumed to behave similarly. While the model offered here may not be strictly unique (other material classes might be identified which might provide similar consistency with the measured data), the model does provide a physically based consistent interpretation of the material behavior. Two of the material classes chosen for this interpretation, ZR and UO2, were selected because of their marked difference in melting temperature relative to other of the crust components and because of the potential sources of these materials in the fuel rod cladding and the fuel pellets. Two other material classes were identified: (1) the crust remnant composition, chosen because this material was found separate from the other relocated material compositions, and (2) the material that relocated from the original crust material leaving the crust remnant, namely the liquefied crust composition; it was determined by subtracting the crust remnant material from the original metallic crust composition. This last material class is described quantitatively in the preceding table.

The crust remnant material can be understood in terms of the common behavior of distinct classes of materials. The observed crust remnant material composition can be well expressed as the original metallic crust composition *minus* ~12% of the original U, ~46% of the original Zr, ~41% of the original Fe, Ni, and Cr (i.e., stainless steel), ~80% of the Ag, In, and Mo (i.e., control materials), and 32% of the original Sn. Note that the Sn behaves similarly to the Zr and could have been classed with the Zr as "zircaloy" without significantly perturbing these interpretations.

The three metallic relocated material regions (RM-1, -2, and -3) can be expressed in terms of mole fractions of the four material classes: UO2, Zr, crust remnant material and crust liquid. The mole fractions required to approximate the measured material distributions are summarized in the following chart. The goodness of fit is a least squares indicator of the multivariate fit algorithm used to assess the optimum fit.

Mole Fractions of Four Material Classes Approximating RM-1, -2, and -3

RM-Region	Crust Remnant	Crust Liquid	Added UO2	Added Zr	Goodness of fit
RM-1	.238	.638	.005	.001	.010
RM-1	0	.716	.110	.173	.011
RM-2	.164	.448	.015	.375	.011
RM-3	.164	.356	.023	.456	.003
RM-3	0	.411	.096	.493	.004

The lowermost relocated materials, RM-2 and RM-3, are well approximated by comparatively equal mole fractions of the crust melt material and additional Zr from the fuel rod cladding. Slight adjustments in the U content improve the fit. The relocated material that froze out highest in the fuel rod array, RM-1, is composed of a relative large proportion of the "crust liquid" class with lesser proportions of "crust remnant" material. Notice that a similar fit can be obtained for the RM-1 and RM-3 regions without using any of the crust remnant material, requiring only slight adjustments in the remaining materials. These results are shown graphically in Figures 3.28 and 3.29. Figure 3.28 shows the mole fractions of the four classes of materials used to approximate the RM-1, -2, and -3 compositions, and Figure 3.29 shows the relative error for each element for each mixture. Note that he largest relative errors are generally associated with the elements found in lowest concentration. Silver proved more difficult to describe with this model.

These interpretations, while perhaps not unique, do provide a means of understanding the general behavior of the metallic materials in terms of a reduced set of material classes. The classes used in this analysis are consistent with the overall material relocation scenario presented from the PIE characterizations.

3.4 Conclusions

The following conclusions can be made as a result of the post-irradiation examination of the test capsule:

3.4.1 Debris Bed

1. A majority of the debris bed inventory of urania and zirconia particulate had melted during the experiment forming the ceramic melt pool.

2. A retained debris bed structure remained at the upper surface of the test capsule near the thoria lid. This structure was composed of urania particles held together by a resolidified (U, Zr)Ox single phase, where x was determined to be 1.8. There was no evidence of retained zirconia shards in this region of the test capsule.

3. The behavior of the ceramic debris bed in the MP-2 experiment was found to be consistent with the material behavior in the MP-1 experiment. The debris bed melt behavior was initiated by the melting of zirconia. The molten zirconia then wet the urania particles and continued to dissolve the urania. The molten material relocated when a critical saturation was achieved.

4. A large region approximately one-half of the original debris bed volume was void of material and was located in the upper region of the original debris bed.

3.4.2 Melt Pool

1. A large region approximately one-half of the original debris bed volume was associated with the ceramic melt pool. The ceramic pool was located in the lower region of the initial debris bed and extended into the original prefabricated metallic crust.

2. The ceramic melt pool appeared to be fairly dense with the exception of internal porosity. The large internal porosity was due to the relocation of the ceramic melt into the region originally occupied by the preformed crust. This event resulted in the entrapment of porosity into the melt. Radial cracks emanate from porosity and occurred upon cool down. A variation in grain size was observed radially, due to the difference in cooling rates between the outer edge (finer grain size, faster cooling rate) and the material located near the central portion of the pool (larger grain size, slower cooling rate).

3. The composition of the ceramic melt pool was found to be fairly constant, with a slight increase in uranium content near the bottom of the melt pool. This was to be expected since the bottom of the melt pool invaded the prefabricated crust/fuel rod assembly and there was evidence of erosion of the uppermost fuel pellets in the stack. Trace amounts of the metallic elements of the prefabricated crust were found in the ceramic melt pool.

3.4.3 Metallic Crust Remnant

1. The metallic crust had been penetrated by the relocating melt pool and approximately half of the original crust height remained. The remnant morphology was found to be a very porous structure. The crust was depleted of the metallic elements and enriched in uranium, zirconium, and oxygen. The presence of undissolved urania particles posttest confirmed that the crust remnant had not been fully molten. The oxide phases that were present posttest were the urania and a $(U, Zr)O_x$ phase. There were no zirconia particles present in the crust remnant, in contrast to the as fabricated crust. As the zircaloy clad and the zirconia that were present in the crust melted, they dissolved some amount of the crust's urania . Therefore, upon solidification the Zr was tied to the U and O. The enrichment of U and Zr was primarily due to their preferential retention of oxides, when compared to the metallic elements, which melted at lower temperatures and relocated.

2. There were large, ellipsoidal intrusions in the metallic crust remnant near the fuel rods. There was an absence of all zircaloy cladding on the fuel rods in the crust remnant region and in regions below the crust remnant.

3. The zircaloy cladding, within the metallic crust, appeared to melt prior to the gross movement of the metallic crust or the dissolution of the fuel pellet stacks. This event apparently influenced the subsequent relocation of metallic crust material by providing an easy path for relocation.

4. The crust remnant had a high oxygen content (oxygen / metal = 0.56) that resulted in the formation of the $(U, Zr)O_x$ phase. This final microstructure had a higher melt temperature, than the original phases of ZrO2 (from the crust) or Zr (from the clad embedded in the crust).

3.4.4 Relocated Material

1. Material of metallic crust origin was found between the fuel pellets within a stack at locations below the melt pool. Metallic material invaded the gap between fuel pellets, to varying degrees, and fused the fuel pellet stack together. Upon cool down, the fused stack was subjected to large tensile forces that fractured the fuel pellets preferentially with respect to the metallic joints.

2. A majority of the relocated material was seen along the central axis of the test section. Individual droplets of material were found between fuel pins near the lower stainless steel plate. Sharp, rounded interfaces were observed between individual droplets. This indicated that the relocation process of metallic crust material was composed of separated and distinct events.

3. The relocated materials (RM-1 through RM-3) all follow the same trend. They all are zirconium enriched and oxygen deficient when compared to the initial crust composition. The deficiency in oxygen occurred because the oxide materials (22 % by weight in the initial crust) did not participate in the relocation process and remain, in some form, in the crust remnant.

4. The first droplets of relocated material, those located near the bottom of the capsule, were found to be significantly enriched in zirconium. The zirconium enrichment was due to the early melting of the zircaloy cladding on the fuel rods that were embedded in the crust. The cladding melted at lower temperatures than the bulk of the crust and preferentially dissolved the adjacent crust material and then relocated to the bottom of the capsule.

5. The bulk of the relocated metallic material was located above these initial droplets and corresponded to a single and continuous relocation event, which occurred later. This relocated material was enriched in zirconium when compared to the initial crust remnant, but not as enriched as the material corresponding to the first relocation event.

Table 3.1 Longitudinal Section Designation

Longitudinal Section	Axial Location (cm from bottom of test capsule)	Contents
1-2	42 - 48.5	Upper Debris Bed
2-2	38 - 42	Void
3-2	30 - 38	Ceramic Melt Pool
4-2	25 - 30	Ceramic Melt Pool and Prefabricated Metallic Crust
5-2	20 - 25	Fuel Rod Array
6-4	14 - 20	Fuel Rod Array/Stainless Steel Base

Table 3.2 Standards Data for Scanning Electron Microscopy With X-Ray Analysis

Element	Atomic Number	Line	Standard	Lambda (Angle)	Crystal
Uranium	92	Ma	Uranium	3.91	PET
Zirconium	40	La1	Zirconium	6.071	PET
Oxygen	8	Ka	Thoria	23.62	TAP
Iron	26	KA	Iron	1.937	LiF
Nickel	28	Ka	Nickel	1.6586	LiF
Chromium	24	Ka	Chromium	2.291	LiF
Molybdenum	42	La	Molybdenum	5.4054	PET
Silver	47	La	Silver	4.1527	PET
Tin	50	La	Tin	3.5986	LiF
Indium	49	La	48.54 w% In/Sb	3.7713	PET

Table 3.3 Sample Identification, Location and Microstructure as Determined by Scanning Electron Microscopy

Sample Identification	Location	Resulting Microstructure
1.2.3	Upper debris bed	Two-phase mixture
3.2.3	Ceramic Melt Pool - Top	One homogeneous phase
3.2.8	Ceramic Melt Pool - Middle	One homogeneous phase
4.2.11	Ceramic Melt Pool - Bottom	One homogeneous phase
4.2.2	Inside the Melt Pool (fuel rod/O_2?)	
4.2.9	Crust Remnant (Wall)	
4.2.12	Crust Remnant (Center-Top)	Six-phase mixture
4.2.13	Crust Remnant (Middle)	Six-phase mixture
4.2.6B	Inside Crust Remnant (Zr clad)	
4.2.6C	Below Melt Pool (composition of solid core)	
5.2.3	Relocated Material - Top (RM-1)	Six-phase mixture
6.4.3A	Relocated Material - Middle (RM-2)	Six-phase mixture
6.4.3	Relocated Material - Middle (RM-2*)	
6.4.7	Relocated Material - Bottom (RM-2.5*)	
6.4.12	Relocated Material - Bottom (RM-3*)	
6.4.10	Relocated Material - Bottom (RM-3)	Three-phase mixture

Table 3.4 Uranium and Oxygen Content at Various Locations Within a Fuel Rod Within the Ceramic Melt (Sample 4-2-2)

UO_2 is 88.15 wt% U and 11.85 wt% 0

Sample	Element	Normalized Wt %	Normalized at %	Count Err (s wt %)
1.1	U	88.59	34.3	0.1272
	O	11.41	65.7	0.0678
1.2	U	88.53	34.15	0.127
	O	11.47	65.85	0.0681
2.1	U	89.53	36.5	0.1247
	O	10.47	63.5	0.0633
2.2	U	89.45	36.3	0.1253
	O	10.55	63.7	0.0648
3.1	U	89.52	36.46	0.1246
	O	10.49	63.54	0.0641
3.2	U	89.12	35.51	0.1246
	O	10.88	64.49	0.0654
4.1	U	89.24	35.8	0.1243
	O	10.76	64.2	0.065
4.2	U	89.47	36.35	0.1238
	O	10.53	63.65	0.0642
5.1	U	89.15	35.59	0.1263
	O	10.85	64.41	0.0658
5.2	U	88.93	35.07	0.1261
	O	11.07	64.93	0.0663
6.1	U	89.16	35.6	0.1258
	O	10.84	64.4	0.0657
6.2	U	89.23	35.78	0.1254
	O	10.77	64.22	0.0654
7.1	U	89.47	36.34	0.1246
	O	10.53	63.66	0.0636
7.2	U	89.79	37.15	0.1225
	O	10.21	62.85	0.0618
8.1	U	90.12	37.99	0.1229
	O	9.88	62	0.0616
8.2	U	90.67	39.5	0.1231
	O	9.33	60.5	0.0587
9.1	U	89.8	37.17	0.123
	O	10.2	62.83	0.0617
9.2	U	90.54	39.14	0.1218
	O	9.46	60.86	0.0586

Conclusion: Apparent oxygen variation as a function of location. Slight depletion of oxygen from center to surface.

Table 3.5 Radial Locations of Measurements Made of Sample 4-2-2 and Atomic Percent Average at Each of Nine Locations

	Location	Radial Location	Weight %	Atomic %	Count Error	Atomic % (Average)
1						
2						
3					0.1272	
4	center.1.1	0.0000	11.410	65.700	0.0678	65.780
5					0.127	
6	center.1.2	0.0000	11.470	65.850	0.0681	
7					0.1247	
8	center.2.1	0.0000	10.470	63.500	0.0633	63.600
9					0.1253	
10	center.2.2	0.0000	10.550	63.700	0.0648	
11					0.1246	
12	near.3.1	0.25000	10.490	63.540	0.0641	64.020
13					0.1246	
14	near.3.2	0.25000	10.880	64.490	0.0654	
15					0.1243	
16	near.4.1	0.25000	10.760	64.200	0.065	63.930
17					0.1238	
18	near.4.2	0.25000	10.530	63.650	0.0642	
19					0.1263	
20	near.5.1	0.25000	10.850	64.410	0.0658	64.470
21					0.1261	
22	near.5.2	0.25000	11.070	64.930	0.0663	
23					0.1258	
24	mid.6.1	0.75000	10.840	64.400	0.0657	64.310
25					0.1254	
26	mid.6.2	0.75000	10.770	64.220	0.0654	
27					0.1246	
28	mid.7.1	0.75000	10.530	63.660	0.0636	63.260
29					0.1225	
30	mid.7.2	0.75000	10.210	62.850	0.0618	
31					0.1229	
32	edge.8.1	0.90000	9.8800	62.000	0.0616	61.250
33					0.1231	
34	edge.8.2	0.90000	9.3300	60.500	0.0587	
35					0.123	
36	edge.9.1	0.90000	10.200	62.830	0.0617	61.850
37					0.1218	
38	edge.9.2	0.90000	9.4600	60.860	0.0586	

Table 3.6 Chemical Analysis of the Upper Debris Bed

LOCATION: 1-2-3
Debris Bed Undissolved UO2 particles and (U, Zr)O2 solid solution

ANALYSIS:

1-2-3a (20,000x)	UO2 particle
1-2-3aa (20,000x)	UO2 particle
1-2-3d (20,000x)	UO2 particle
1-2-3dd (20,000x)	UO2 particle
1-2-3b (20,000x)	(U, Zr)O2 solid solution
1-2-3bb (20,000x)	(U, Zr)O2 solid solution
1-2-3c (20,000x)	(U, Zr)O2 solid solution
1-2-3cc (20,000x)	(U, Zr)O2 solid solution

Sample	Element	Normalized Wt %	Normalized at %	Count Err (s wt %)
1-2-3b	U	79.16	27.93	0.1064
	O	12.22	64.13	0.0641
	Zr	8.62	7.94	0.0207
1-2-3bb	U	79.29	28.25	0.1074
	O	12.01	63.66	0.0636
	Zr	8.69	8.09	0.021
1-2-3c	U	79.28	27.97	0.1072
	O	12.24	64.22	0.0644
	Zr	8.49	7.82	0.0207
1-2-3CC	U	78.16	26.54	0.1075
	O	12.99	65.61	0.0676
	Zr	8.86	7.85	0.0216
average	**U**	**79.0 (.5)**	**27.7 (.7)**	
(SD)	**O**	**12.4 (.4)**	**64.4 (.7)**	
	Zr	**8.7 (.1)**	**7.9 (.1)**	

Table 3.7 Chemical Analysis of the Melt Pool - Top

LOCATION: 3-2-3

ANALYSIS: 3-2-3 (1000x) Primarily (U, Zr)O2 solid solution with trace amounts of crust elements

3-2-3a (1000x) Primarily (U, Zr)O2 solid solution with trace amounts of crust elements

Sample	Element	Normalized Wt %	Normalized at %	Count Err (s wt %)
3-2-3	U	74.27	23.38	0.1035
	O	14.35	67.21	0.0761
	Zr	11	9	0.0236
	Fe	0.1115	0.1496	0.0066
	Ni	0.0345	0.044	0.0082
	Cr	0.0252	0.0364	0.0057
	Mo	0	0	0
	Ag	0.2095	0.1455	0.0103
	Sn	0	0	0
	In	0	0	0
3-2-3	U	76.59	26.97	0.1078
	O	11.92	62.44	0.0663
	Zr	10.89	10	0.0238
	Fe	0.1046	0.157	0.0068
	Ni	0.0346	0.0494	0.0085
	Cr	0.0293	0.0472	0.0058
	Mo	0	0	0
	Ag	0.4421	0.3435	0.0111
	Sn	0	0	0
	In	0	0	0
average	**U**	**75.4 (1.2)**	**25.2 (1.80)**	
(SD)	**O**	**13.1 (1.2)**	**64.8 (2.4)**	
	Zr	**11 (.1)**	**9.5 (.5)**	
	Fe	**.1 (.004)**	**.2 (.004)**	
	Ni	**.04 (.00005)**	**.5 (.003)**	
	Cr	**.03 (.002)**	**.04 (.005)**	
	Mo	**0**	**0**	
	Ag	**.3 (.1)**	**.3 (.1)**	
	Sn	**0**	**0**	
	In	**0**	**0**	

Table 3.8 Chemical Analysis of Melt Pool - Middle

ANALYSIS: 3-2-8 (1000x)

Sample	Element	Normalized Wt %	Normalized At %	Count Err (s wt %)
3-2-8	U	73.63	23.86	0.1059
	O	13.53	65.25	0.0742
	Zr	12.58	10.63	0.0262
	Fe	0.056	0.077	0.0065
	Ni	0.026	0.034	0.0081
	Cr	0.021	0.031	0.0056
	Mo	0	0	0
	Ag	0.16	0.1144	0.0103
	Sn	0	0	0
	In	0	0	0
3-2-8a	U	74.09	24.46	0.1066
	O	13.13	64.5	0.0719
	Zr	12.52	10.78	0.0262
	Fe	0.067	0.0945	0.0065
	Ni	0.026	0.035	0.0081
	Cr	0.016	0.024	0.0057
	Mo	0	0	0
	Ag	0.148	0.108	0.0104
	Sn	0	0	0
	In	0	0	0
average	**U**	**73.9 (.2)**	**24.2 (1.80)**	
(SD)	**O**	**13.3 (.2)**	**64.9 (.4)**	
	Zr	**12.6 (.03**	**1.7 (.08)**	
	Fe	**.06 (.006)**	**.09 (.009)**	
	Ni	**.03 (0)**	**.04 (.005)**	
	Cr	**.02 (.003)**	**.03 (.004)**	
	Mo	**0**	**0**	
	Ag	**.2 (.006)**	**.1 (.03)**	
	Sn	**0**	**0**	
	In	**0**	**0**	

Table 3.9 Chemical Analysis of Melt Pool - Bottom

ANALYSIS: 4-2-11 (20,000x) Melt pool - center line directly above crust

Sample	Element	Normalized Wt %	Normalized at %	Count Err (s wt %)
4-2-11a	U	80.05	29.31	0.1123
	O	11.49	62.61	0.0633
	Zr	8.46	8.08	0.0216
4-2-11b	U	79.02	28.33	0.113
	O	11.83	63.1	0.0654
	Zr	9.16	8.57	0.0229
4-2-11aa	U	79.1	28.57	0.1117
	O	11.93	63.62	0.0649
	Zr	8.36	7.81	0.021
average	**U**	**79.4 (.5)**	**28.7 (.4)**	
(SD)	**O**	**11.7 (.2)**	**63.1 (.4)**	
	Zr	**8.7 (.4)**	**8.4 (.4)**	

Table 3.10 Chemical Analysis of the Metallic Crust Remnant

LOCATION: 4.2.9

ANALYSIS: 4.2.9 (1000x) Crust Remnant (Wall)

Sample	Element	Normalized Wt %	Normalized at %	Count Err (s wt %)
4.2.9.a	U	11.1	3.34	0.0363
	O	5.9	26.43	0.0325
	Zr	48.85	38.39	0.0502
	Fe	7.24	9.29	0.0128
	Ni	7.87	9.61	0.0143
	Cr	0.79	1.09	0.0061
	Mo	0.098	0.073	0.0062
	Ag	12.35	8.21	0.024
	Sn	3.35	2.02	0.0141
	In	2.47	1.54	0.0101
4.2.9.d	U	10.21	2.8	0.0344
	O	7.76	31.68	0.039
	Zr	52.71	37.72	0.0519
	Fe	10.42	12.19	0.0146
	Ni	5.95	6.62	0.0125
	Cr	2.09	2.62	0.0076
	Mo	0.37	0.25	0.0064
	Ag	6.04	3.66	0.0172
	Sn	3.26	1.79	0.0138
	In	1.19	0.67	0.008
average	**U**	**10.66 (.45)**	**3.07 (.27)**	
(SD)	**O**	**6.83 (.93)**	**29.06 (2.63)**	
	Zr	**50.78 (1.93)**	**35.04 (.34)**	
	Fe	**8.92 (1.59)**	**10.74 (1.45)**	
	Ni	**6.91 (.96)**	**8.12 (1.5)**	
	Cr	**1.44 (.65)**	**1.86 (.77)**	
	Mo	**.23 (.14)**	**.16 (.09)**	
	Ag	**9.2 (3.16)**	**5.94 (2.28)**	
	Sn	**3.31 (.05)**	**1.91 (.12)**	
	In	**1.83 (.64)**	**1.11 (.44)**	

Table 3.11 Chemical Analysis of the Metallic Crust Remnant

LOCATION: 4.2.12

ANALYSIS: 4.2.12 (1000x) Crust Remnant (Center Line - Top)

Sample	Element	Normalized Wt %	Normalized at %	Count Err (s wt %)
4.2.12.1	U	8.64	2.34	0.032
	O	8.29	33.39	0.0379
	Zr	57.33	40.52	0.0538
	Fe	8.17	9.43	0.0126
	Ni	5.81	6.39	0.012
	Cr	1.65	2.05	0.0069
	Mo	0.33	0.22	0.0062
	Ag	6.15	3.67	0.0168
	Sn	2.87	1.56	0.0126
	In	0.76	0.43	0.073
4.2.12.2	U	8.57	2.32	0.0319
	O	8.23	33.17	0.0381
	Zr	57.35	40.57	0.0539
	Fe	8.32	9.61	0.0127
	Ni	5.83	6.41	0.012
	Cr	1.68	2.08	0.0069
	Mo	0.33	0.22	0.0064
	Ag	6.17	3.69	0.0168
	Sn	2.74	1.49	0.0126
	In	0.78	0.44	0.0074
average	**U**	**8.61 (.04)**	**2.33 (.01)**	
(SD)	**O**	**8.26 (.03)**	**33.28 (.11)**	
	Zr	**57.34 (.01)**	**40.55 (.03)**	
	Fe	**8.25 (.08)**	**9.52 (.09)**	
	Ni	**5.82 (.01)**	**6.40 (.01)**	
	Cr	**1.67 (.02)**	**2.07 (.02)**	
	Mo	**0.33 (0)**	**.22 (0)**	
	Ag	**6.16 (.01)**	**3.68 (.01)**	
	Sn	**2.81 (.07)**	**1.53 (.04)**	
	In	**.77 (.01)**	**.44 (.005)**	

Table 3.12 Chemical Analysis of Metallic Crust Remnant

ANALYSIS: 4-2-13 (1000x) Crust region - directly below the melt pool

Sample	Element	Normalized Wt %	Normalized at %	Count Err (s wt %)
4-2-13a	U	13.21	3.58	0.0365
	O	9	36.23	0.0423
	Zr	49.87	35.23	0.0521
	Fe	8.41	9.71	0.0129
	Ni	6.16	6.76	0.0122
	Cr	1.34	1.66	0.0067
	Mo	0.178	0.119	0.0057
	Ag	4.83	2.89	0.0143
	Sn	5.36	2.91	0.0179
	In	1.66	0.93	0.0084
4-2-13b	U	12.97	3.5	0.0368
	O	9.2	36.87	0.0429
	Zr	50.85	35.76	0.0536
	Fe	8.04	9.24	0.0129
	Ni	5.79	6.33	0.0122
	Cr	1.28	1.58	0.0067
	Mo	0.173	0.115	0.0058
	Ag	4.71	2.8	0.0143
	Sn	5.4	2.92	0.0182
	In	1.58	0.885	0.0084
4-2-13c	U	12.88	3.53	0.0367
	O	8.7	35.44	0.0422
	Zr	51.09	36.5	0.0542
	Fe	8.7	9.42	0.013
	Ni	5.9	6.55	0.0124
	Cr	1.29	1.62	0.0068
	Mo	0.186	0.127	0.0057
	Ag	4.8	2.9	0.0145
	Sn	5.5	3.02	0.0186
	In	1.58	0.897	0.0085

Table 3.12 (concluded)

Sample	Element	Normalized Wt %	Normalized at %	Count Err (s wt %)
4-2-13d	U	12.98	0.354	0.0368
	O	8.78	35.63	0.0417
	Zr	50.2	35.73	0.0531
	Fe	8.25	9.6	0.0131
	Ni	6.12	6.77	0.0124
	Cr	1.35	1.68	0.0069
	Mo	0.203	0.137	0.0059
	Ag	4.79	2.89	0.0145
	Sn	5.68	3.11	0.0187
	In	1.63	0.922	0.0084
average	**U**	**13.0 (.1)**	**3.5 (.03)**	
(SD)	**O**	**8.9 (.1)**	**36.0 (.6)**	
	Zr	**50.5 (.5)**	**35.8 (.5)**	
	Fe	**8.4 (.2)**	**9.5 (.2)**	
	Ni	**6.0 (.2)**	**6.6 (.2)**	
	Cr	**1.3 (.03)**	**1.6 (.04)**	
	Mo	**.2 (.01)**	**.1 (.008)**	
	Ag	**4.8 (.04)**	**2.9 (.04)**	
	Sn	**5.5 (.1)**	**3.0 (.08)**	
	In	**1.6 (.03)**	**.9 (.02)**	

Table 3.13 Normalized Elemental Atomic Fraction for Areas of Interest

Location	O	U	Zr	Fe	Ni	Cr	Mo	Ag	Sn	In	Metal	O/M
Upper Debris (Solid Solution)	.644	.277	.079									1.8
*MP-1	.648	.252	.095	.002	.0005	.0004	--	.003	--	--	.3529	1.84
MP-2	.649	.242	.107	.0009	.0004	.0003	--	.001	--	--	.3516	1.86
MP-3	.631	.287	.084	--	--	--	--	--	--	--	.371	1.7
Crust Remnant	.36	.035	.358	.095	.066	.016	.001	.029	.03	.009	.639	0.56
**RM-1	.079	.029	.451	.167	.132	.031	.005	.054	.035	.018	.921	.086
RM-2	.05	.031	.596	.119	.062	.035	.002	.032	.063	.011	.95	.053
RM-3	.069	.025	.646	.096	.059	.019	.002	.046	.028	.01	.931	.074
Upper Debris-Initial Bed	.667	.2289	.1042	--	--	--	--	--	--	--	--	2.0
Original Crust	.20	.022	.37	.15	.09	.03	.004	.08	.025	.019	.8	0.25

*MP = Melt Pool
**RM = Relocated Material

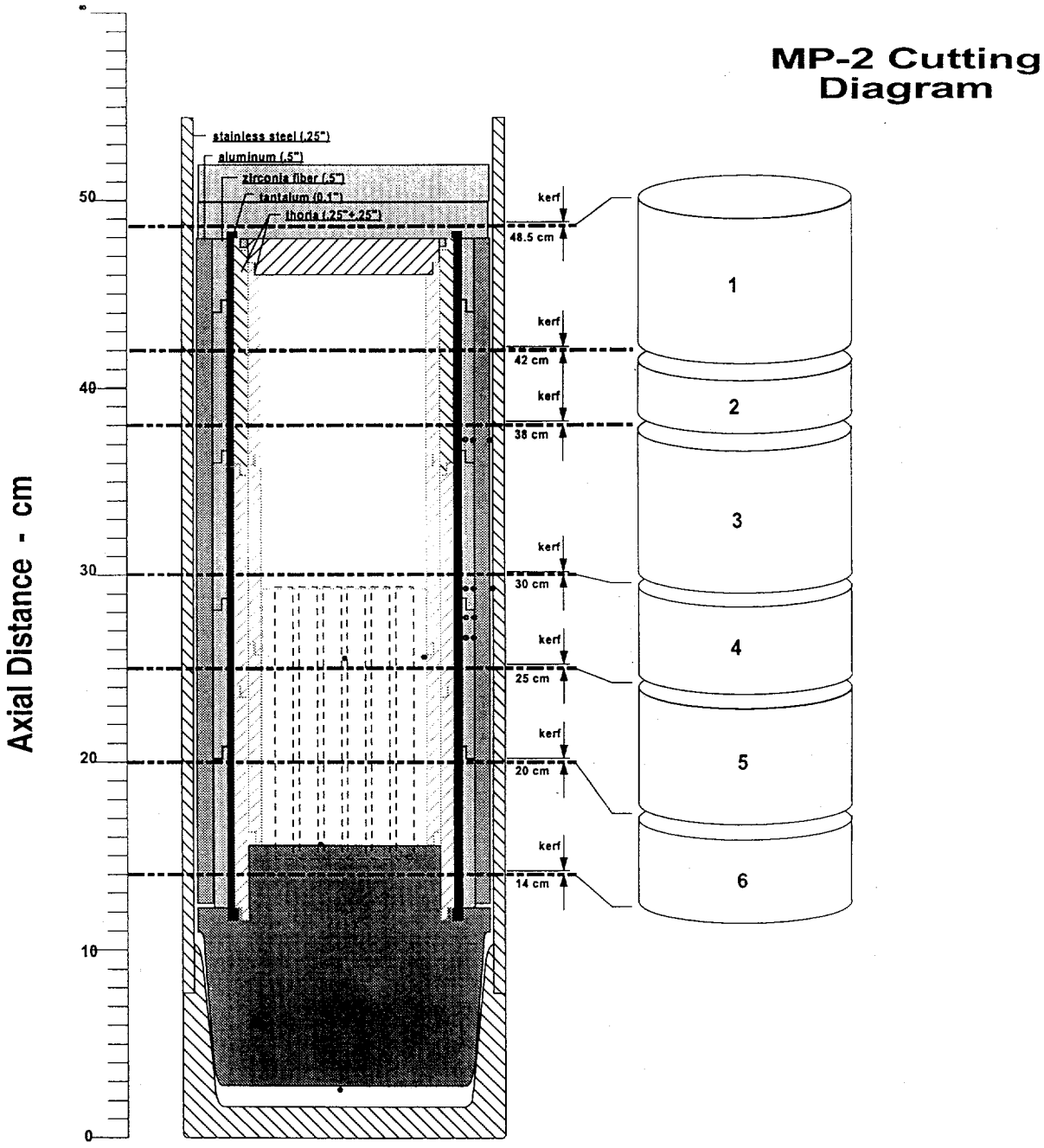

Figure 3.1 Primary Containment Vessel with the Locations of Section Cuts

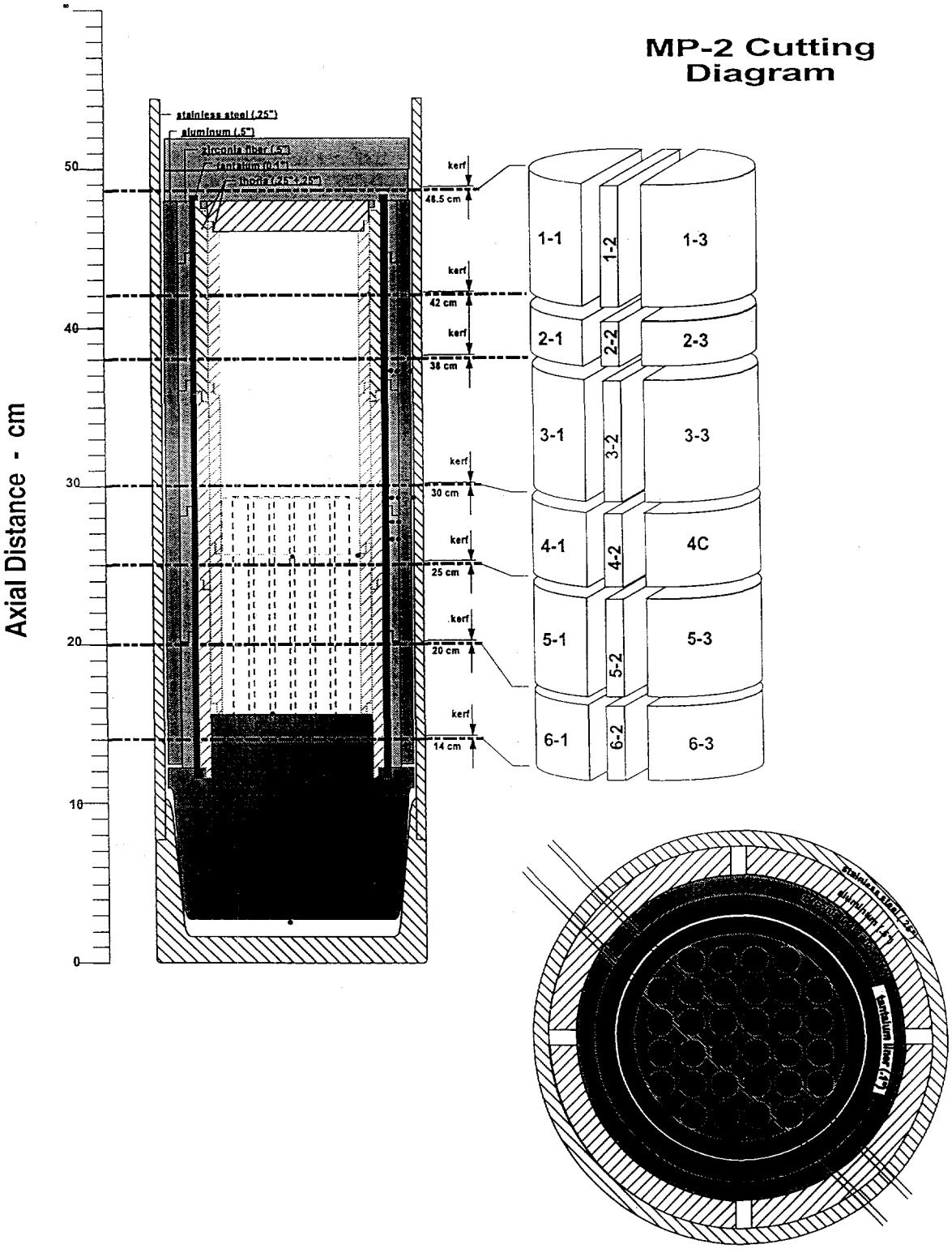

Figure 3.2 Three-Dimensional View of Test Capsule Indicating the -45° Longitudinal Extracted Slab

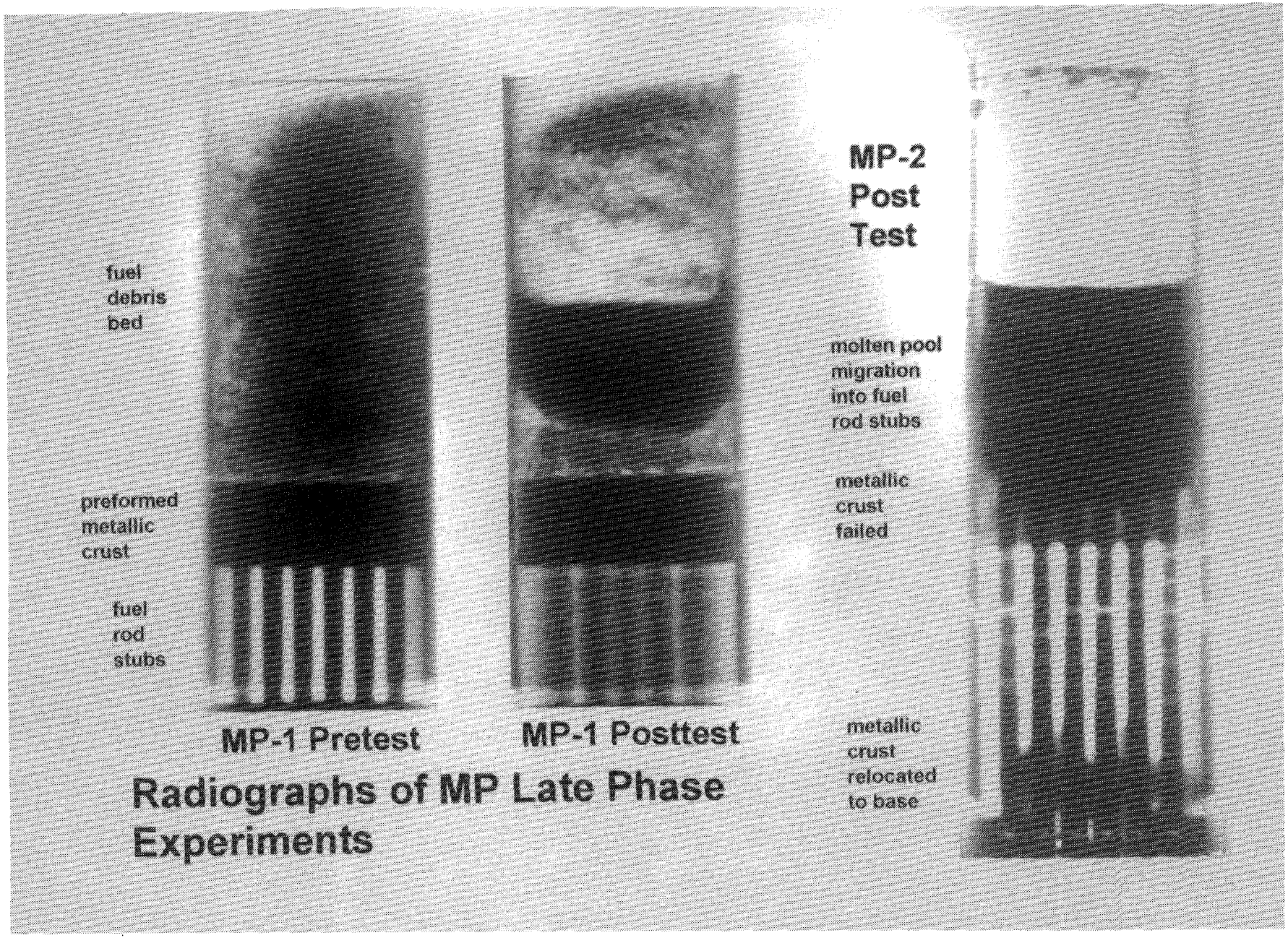

Figure 3.3 Preirradiation and Postirradiation Radiograph of the MP-1 Test Capsule and Postirradiation Radiograph of the MP-2 Test Capsule

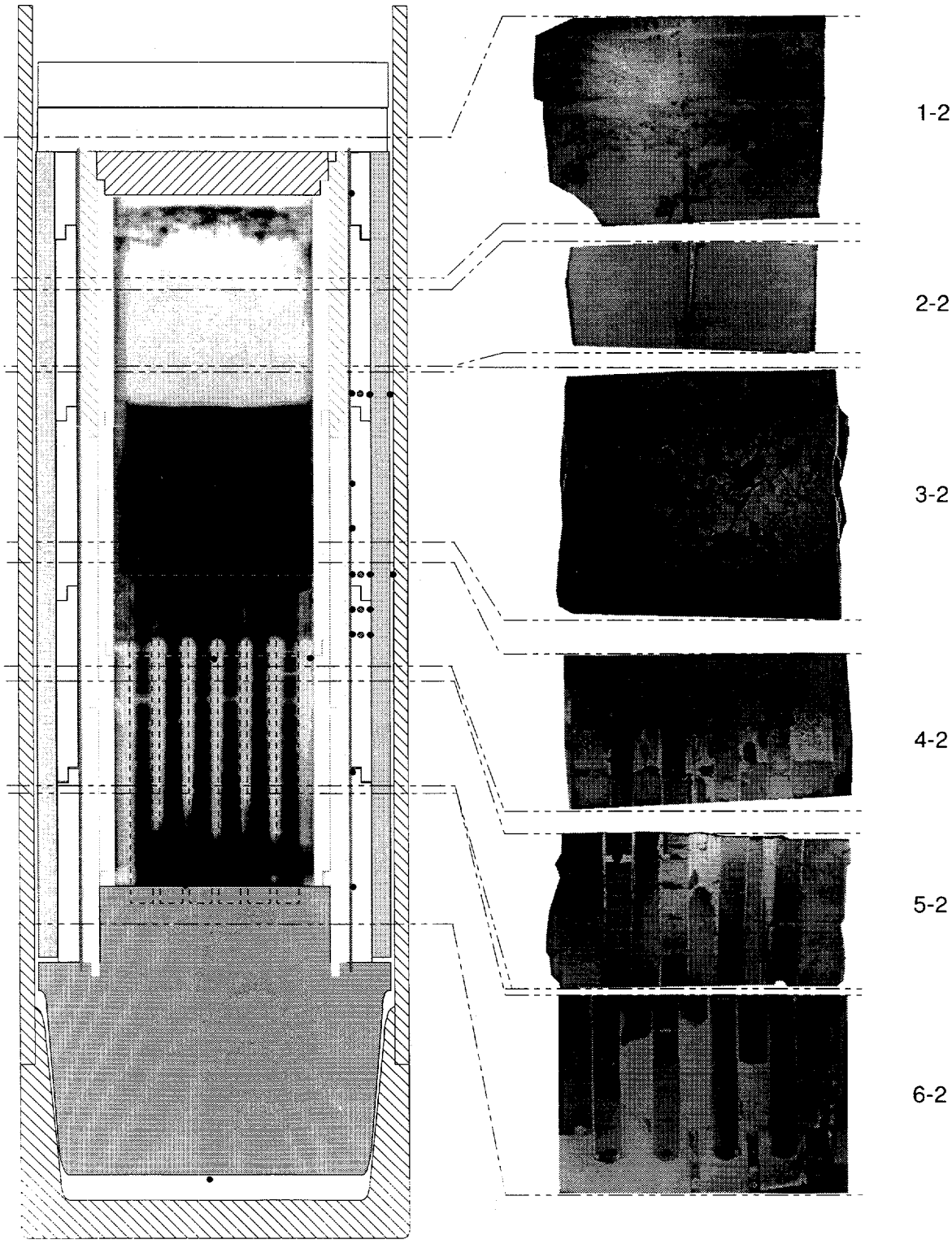

Figure 3.4 Postirradiation Radiograph with the Cutting Diagram of the Test Capsule

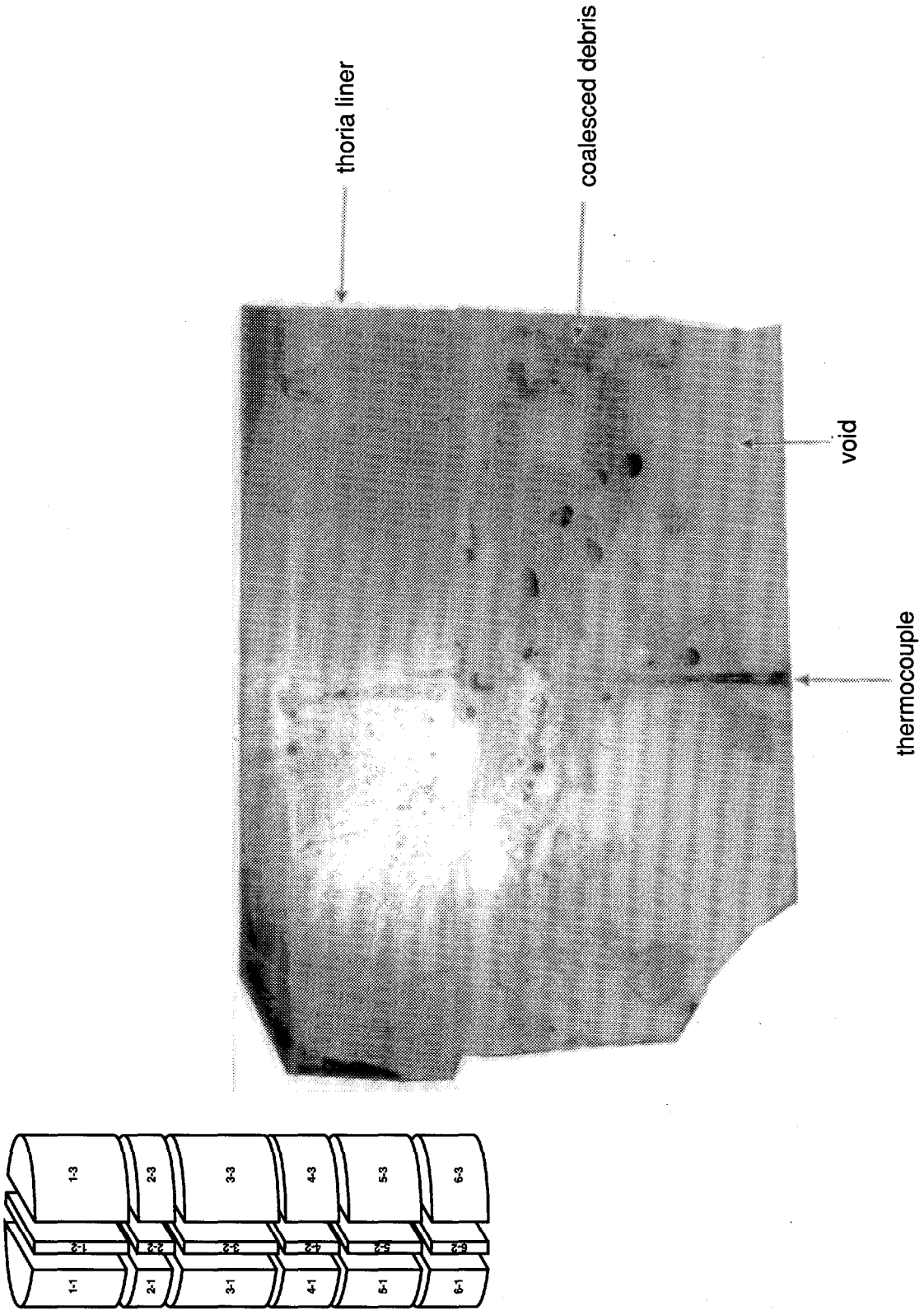

Figure 3.5. Optical macrograph of Section 1-2

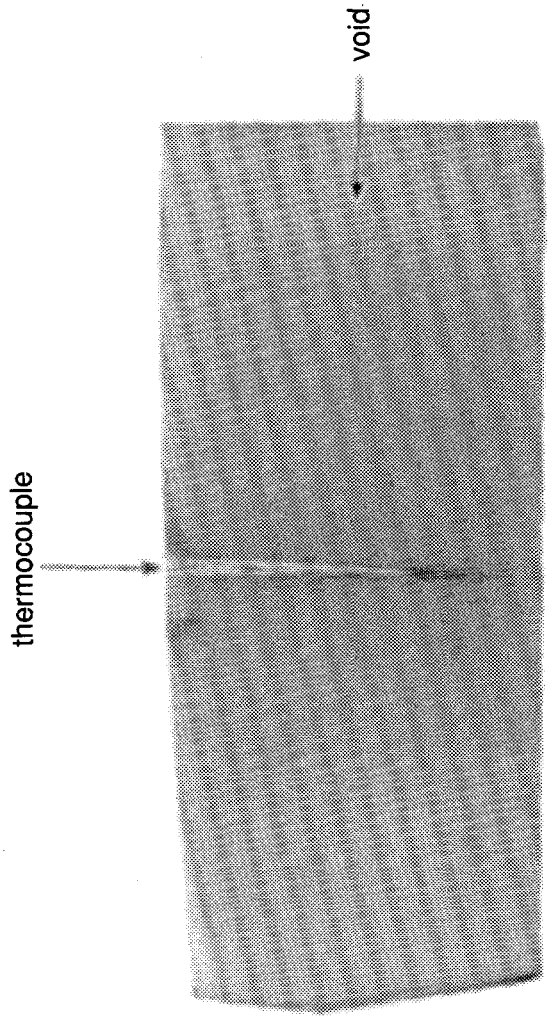

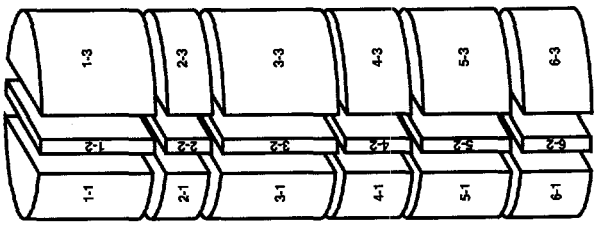

Figure 3.6. Optical macrograph of Section 2-2

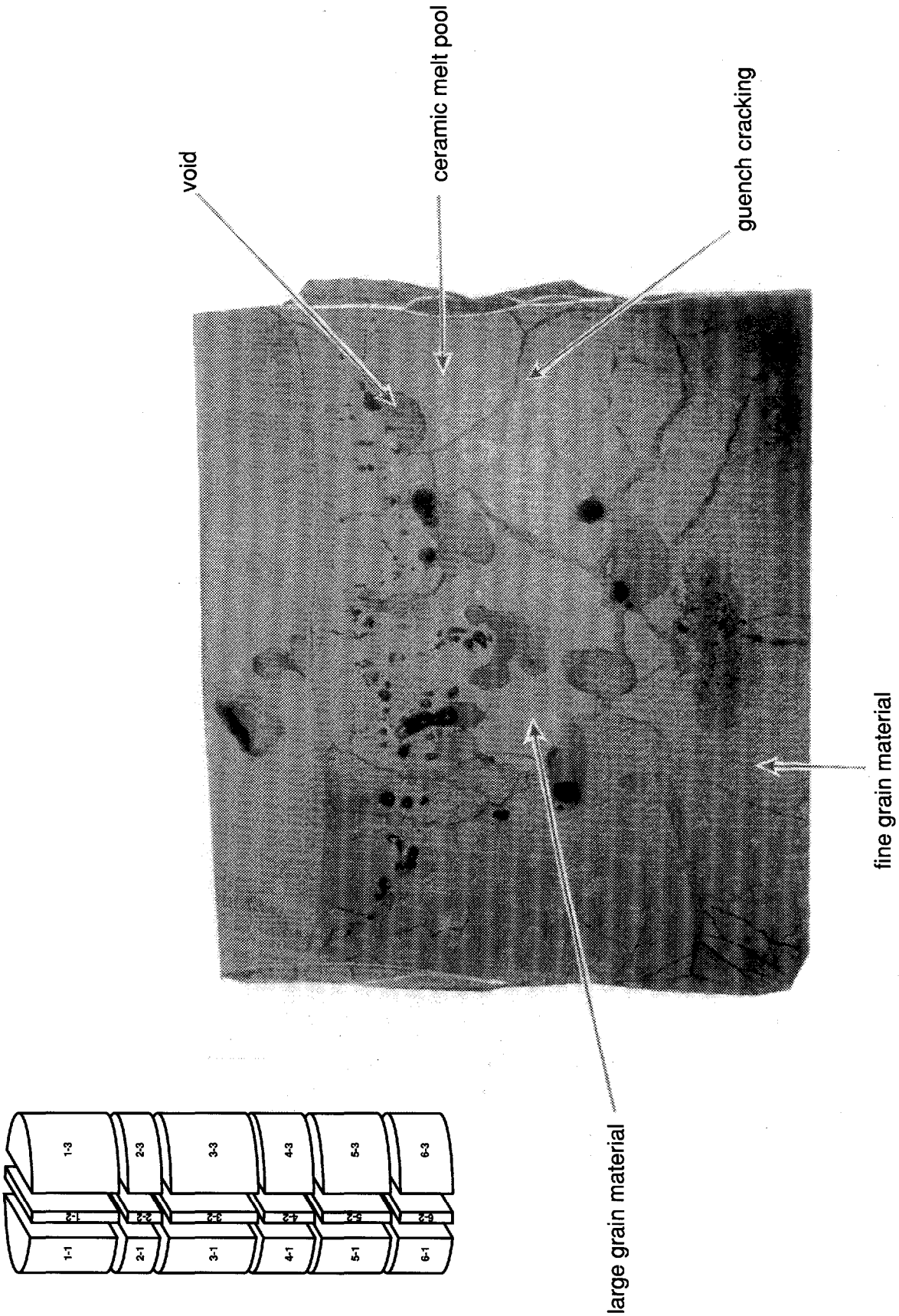

Figure 3.7. Optical macrograph of Section 3-2

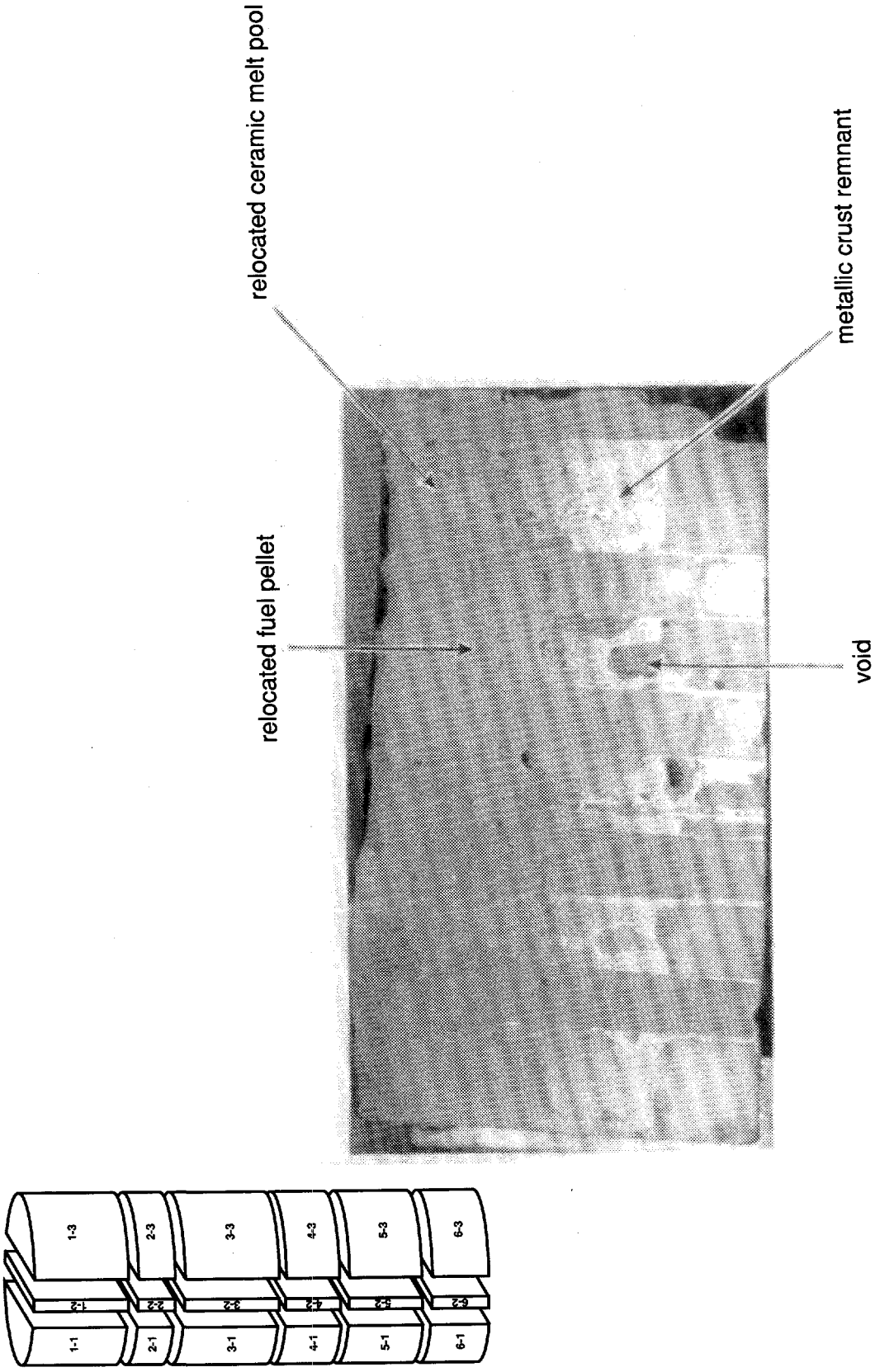

Figure 3.8. Optical macrograph of Section 4-2

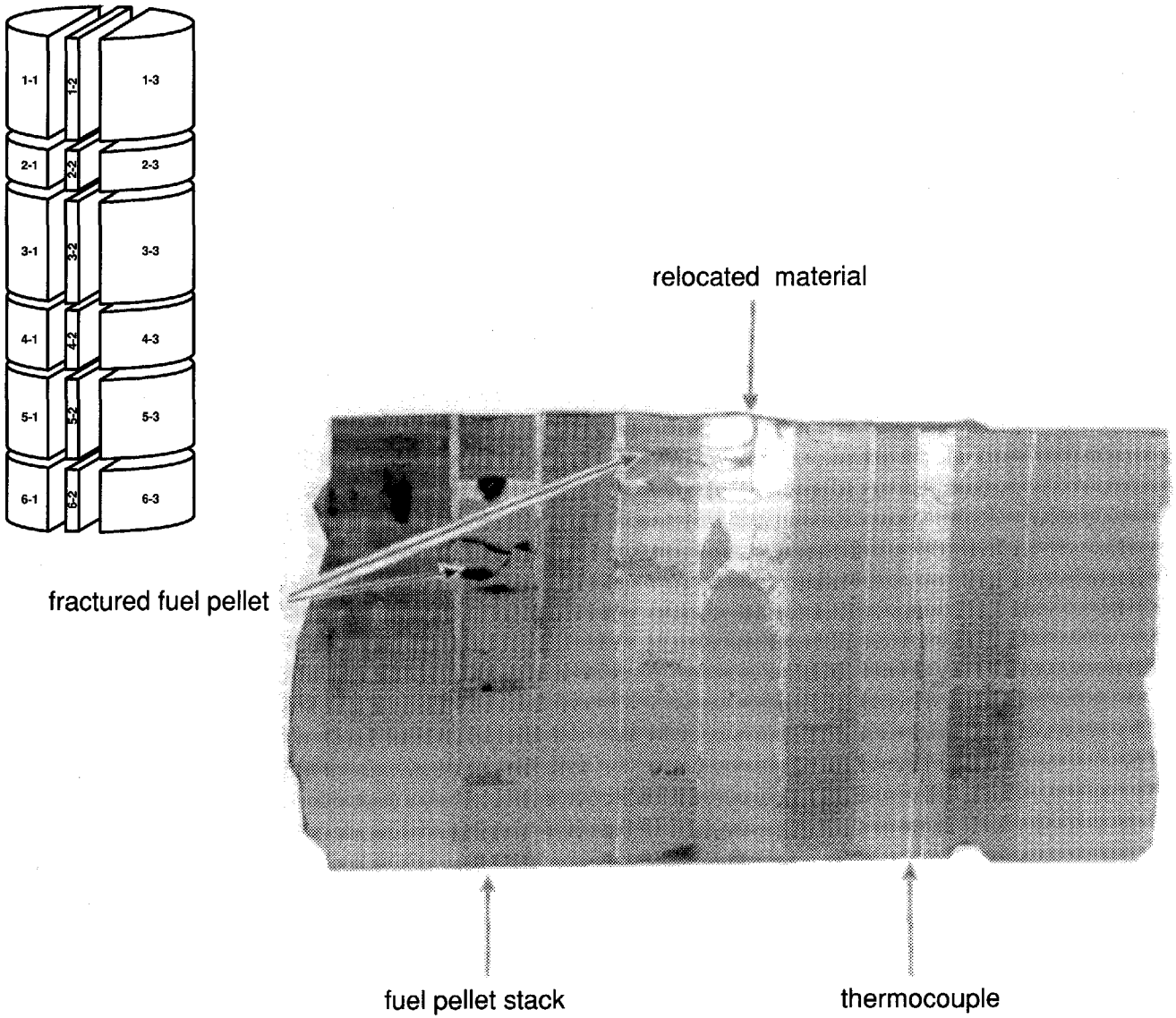

Figure 3.9. Optical macrograph of Section 5-2

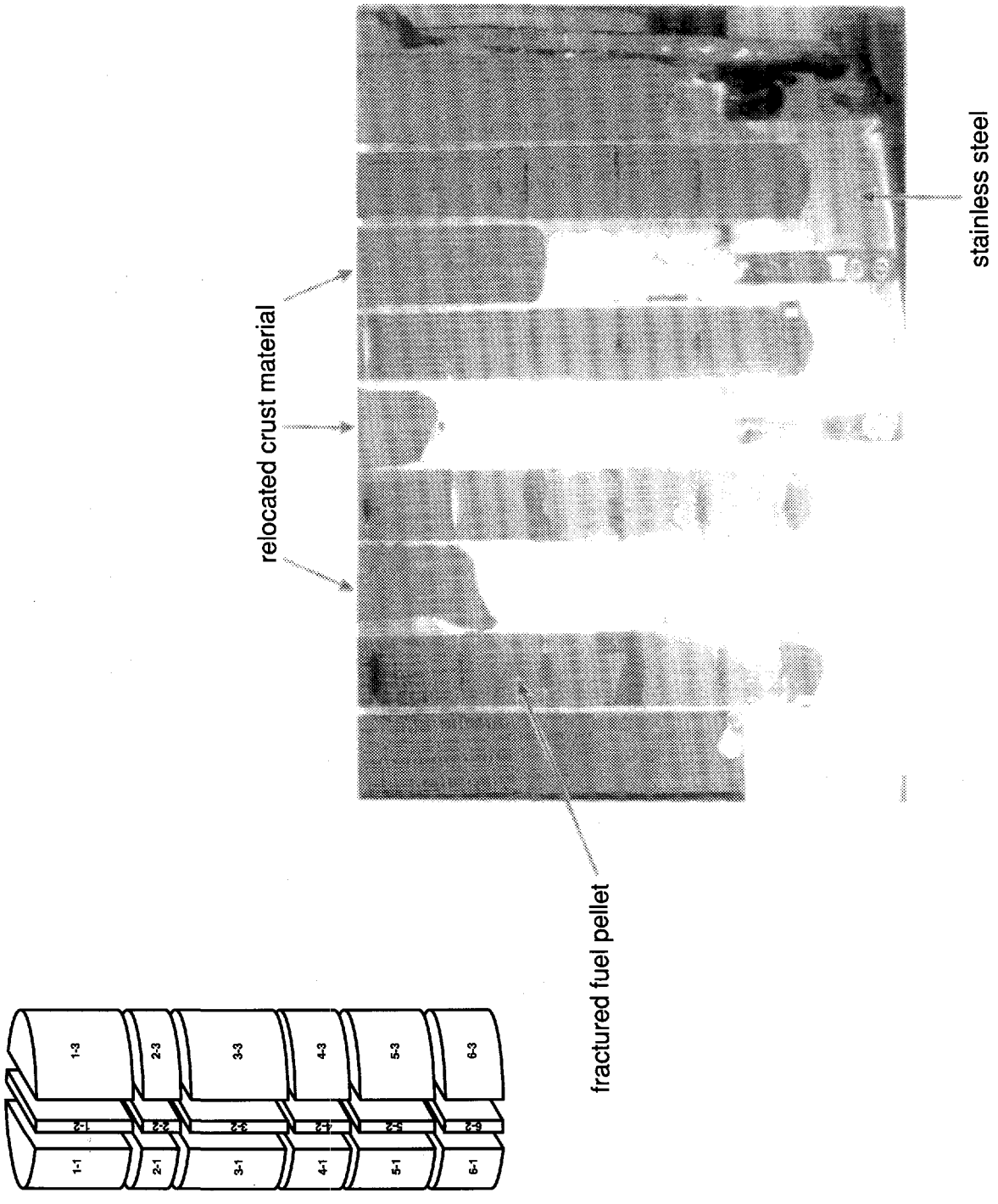

Figure 3.10. Optical macrograph of Section 6-4

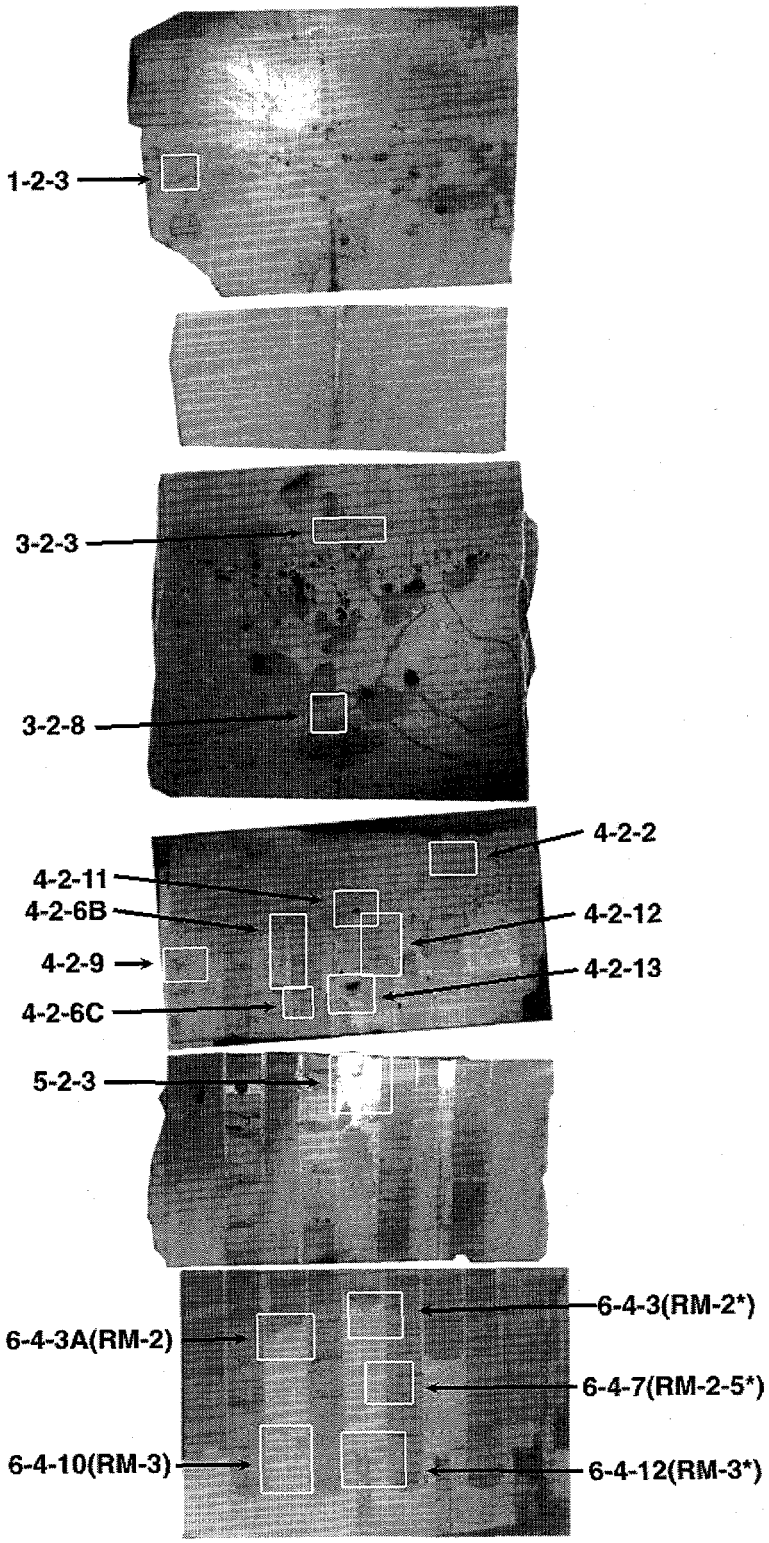

Figure 3.11 Montage of All Sections Indicating Areas in Which Scanning Electron Microscopy With Chemical Analysis Was Performed

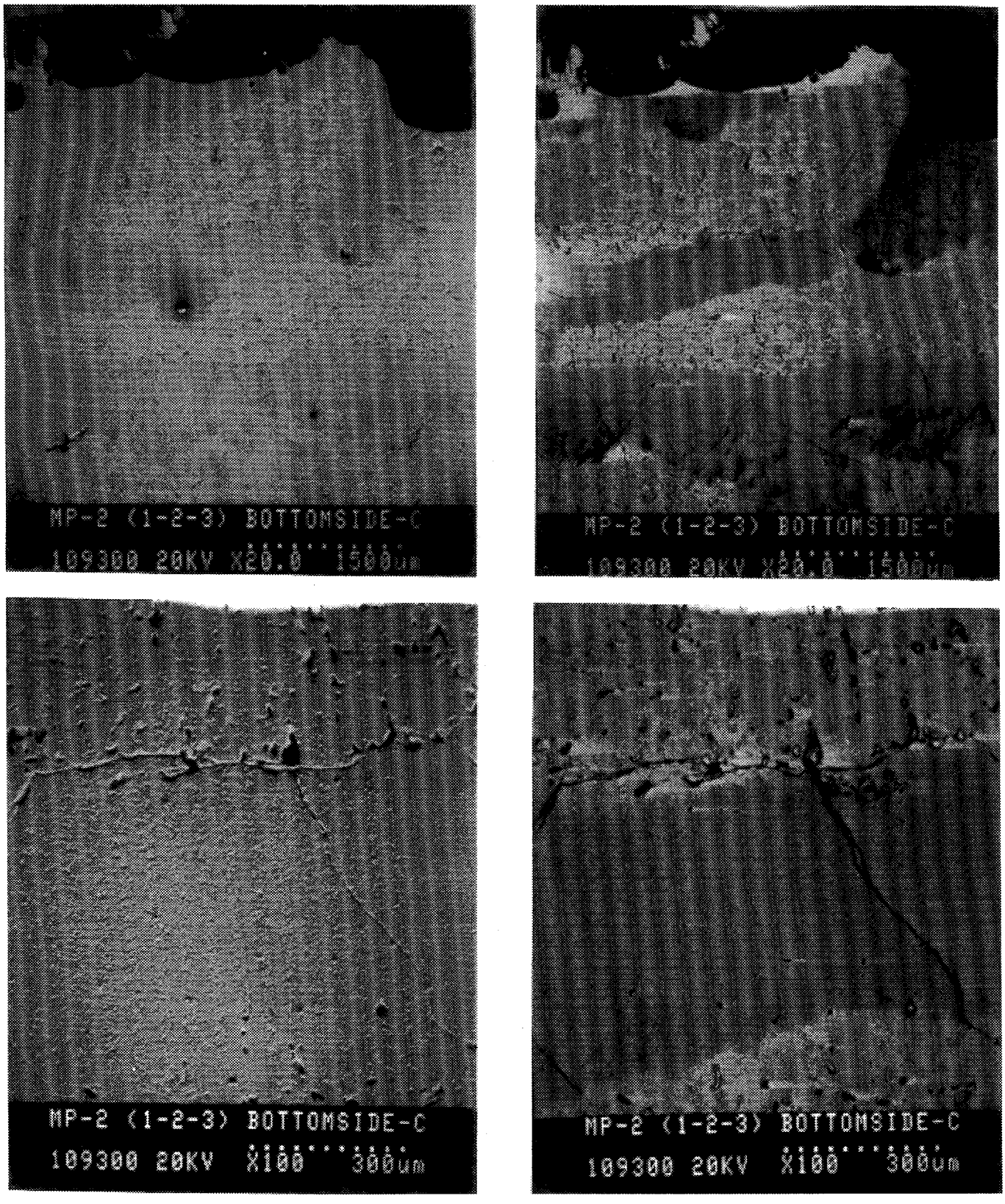

Figure 3.12a Scanning Electron Micrographs and Corresponding Elemental Maps for the Retained Structure at the Top of the Debris Bed

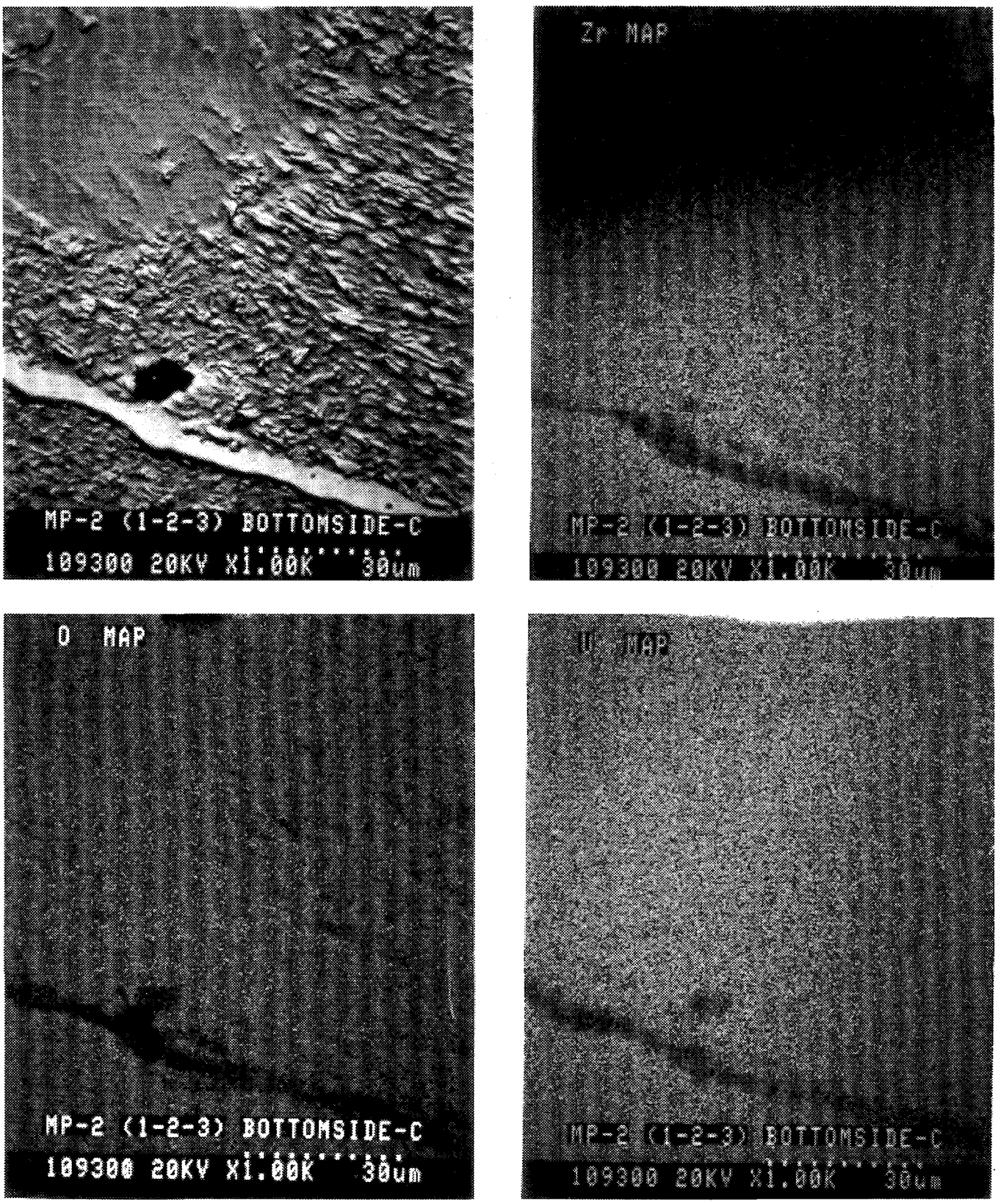

Figure 3.12b Scanning Electron Micrographs and Corresponding Elemental Maps for the Retained Structure at the Top of the Debris Bed

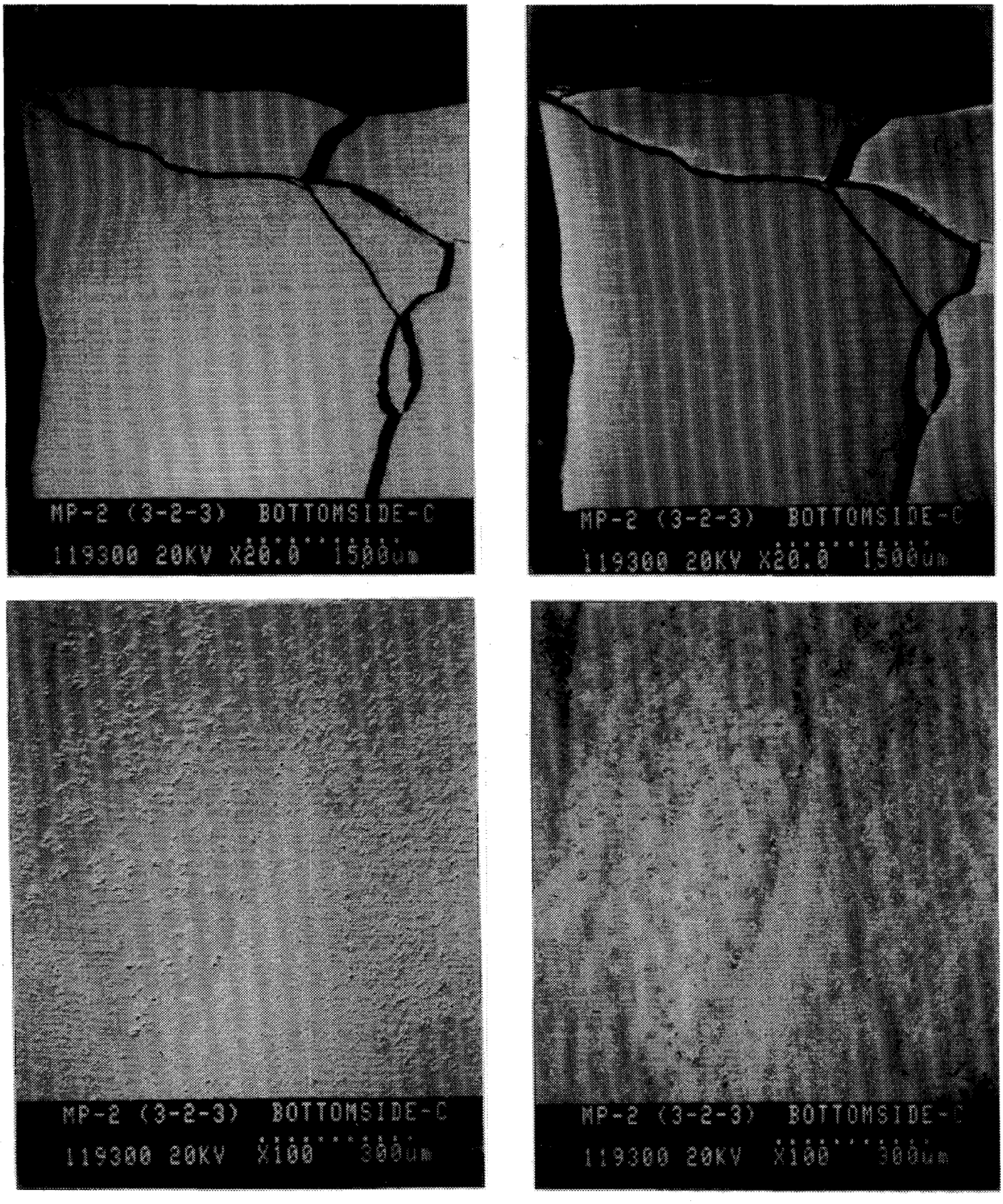

Figure 3.13a Scanning Electron Micrographs and Corresponding Elemental Maps for the Ceramic Melt Pool

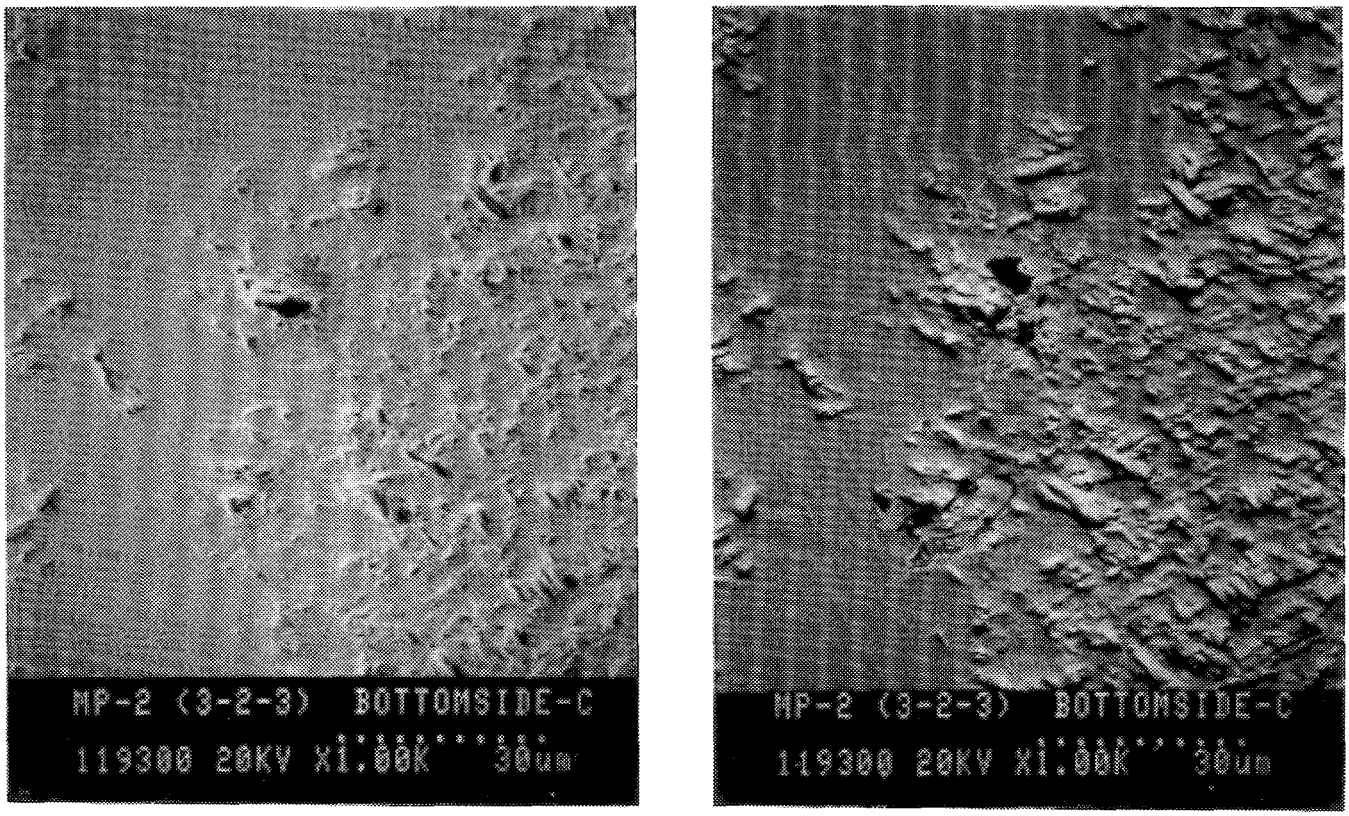

Figure 3.13b Scanning Electron Micrographs and Corresponding Elemental Maps for the Ceramic Melt Pool

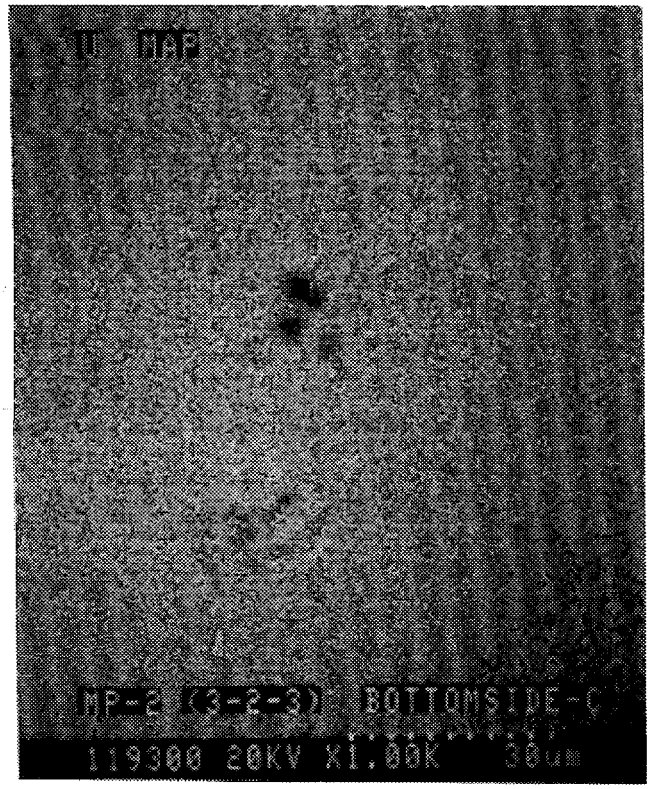

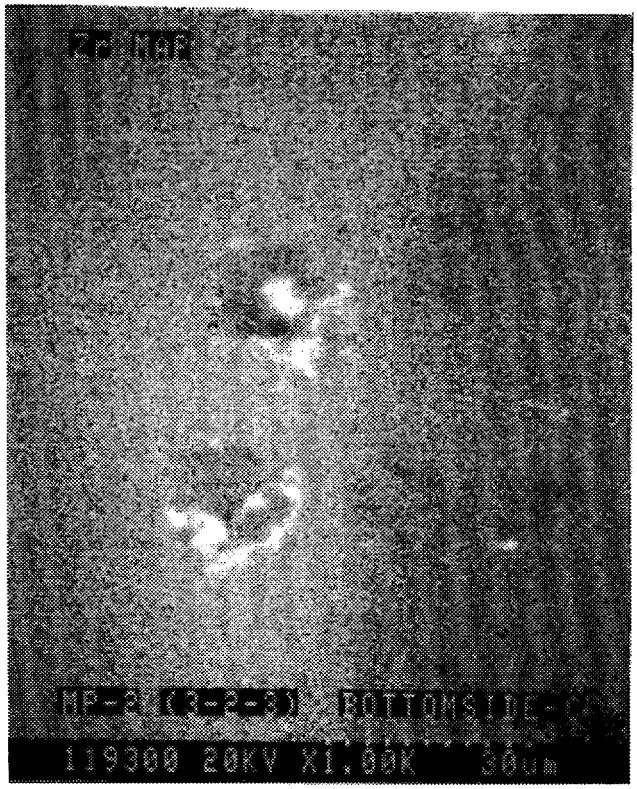

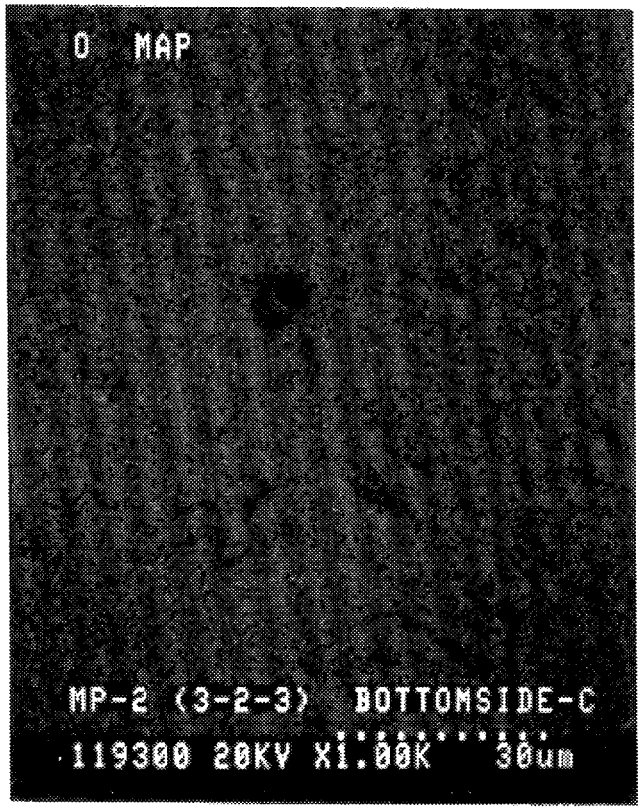

Figure 3.13c Scanning Electron Micrographs and Corresponding Elemental Maps for the Ceramic Melt Pool

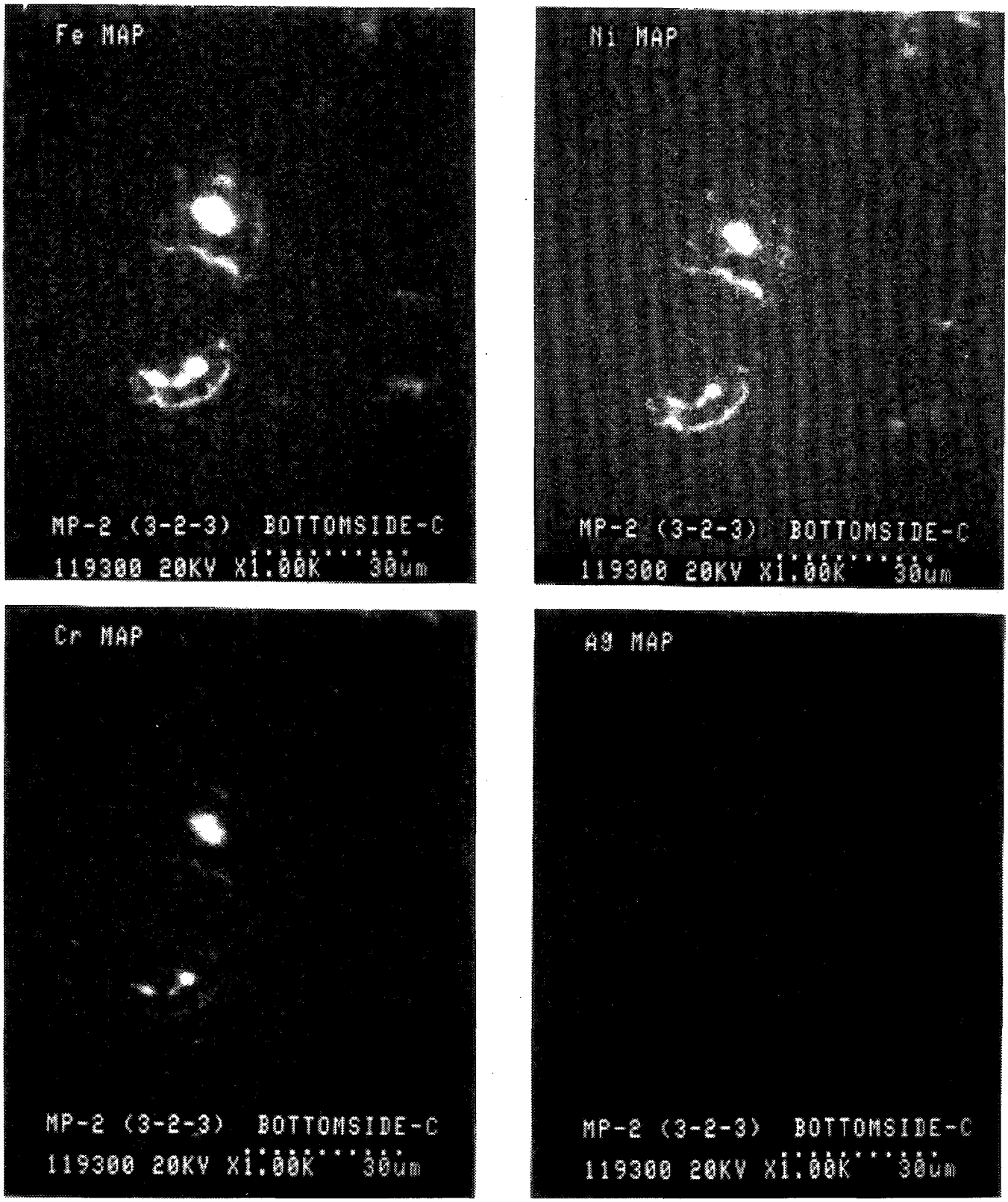

Figure 3.13d Scanning Electron Micrographs and Corresponding Elemental Maps for the Top of the Ceramic Melt Pool

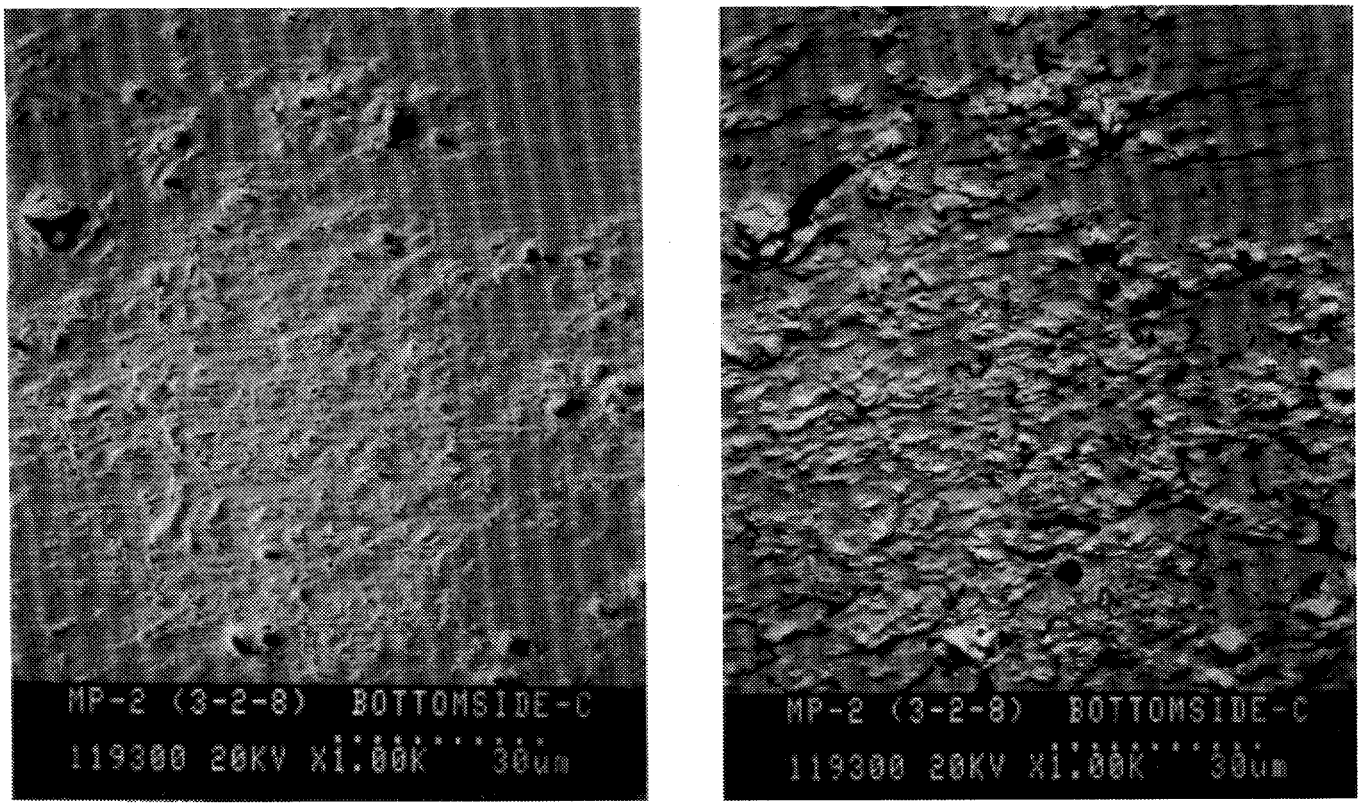

Figure 3.14a Scanning Electron Micrographs and Corresponding Elemental Maps for the Middle of the Ceramic Melt Pool

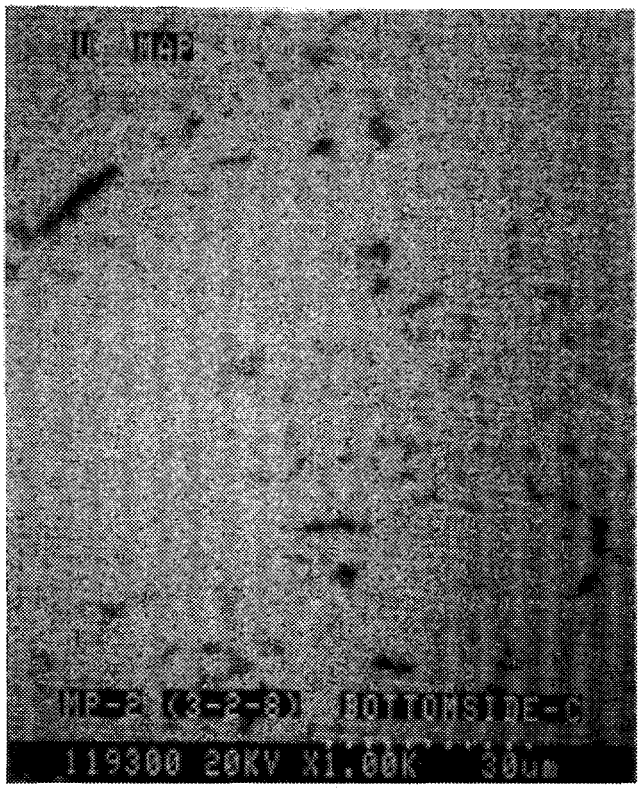

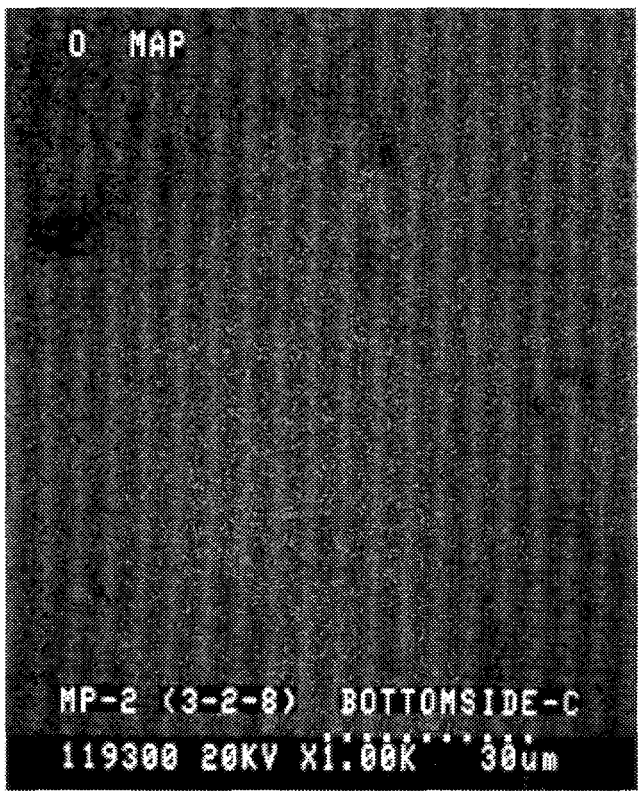

Figure 3.14b Scanning Electron Micrographs and Corresponding Elemental Maps for the Middle of the Ceramic Melt Pool

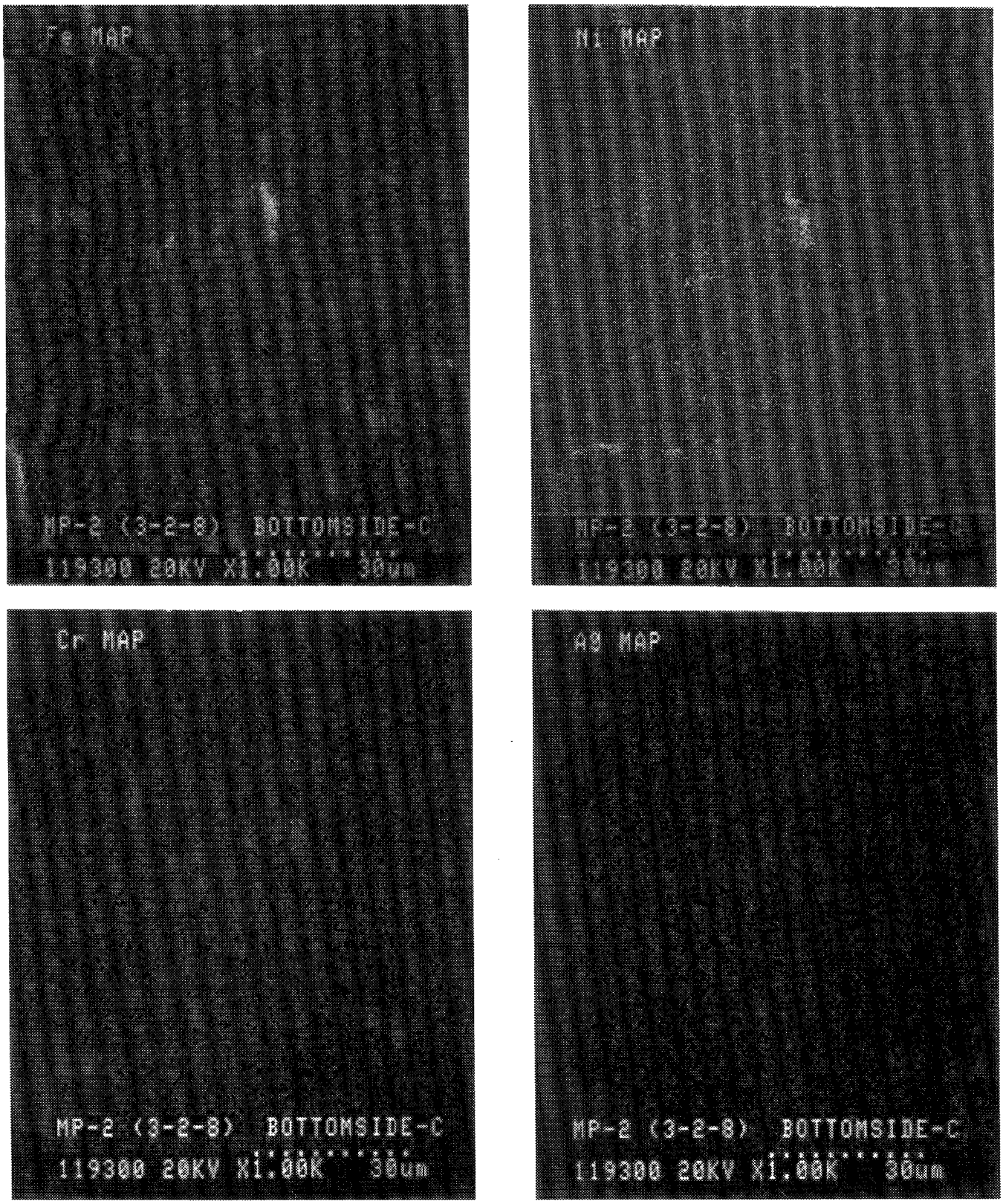

Figure 3.14c Scanning Electron Micrographs and Corresponding Elemental Maps for the Middle of the Ceramic Melt Pool

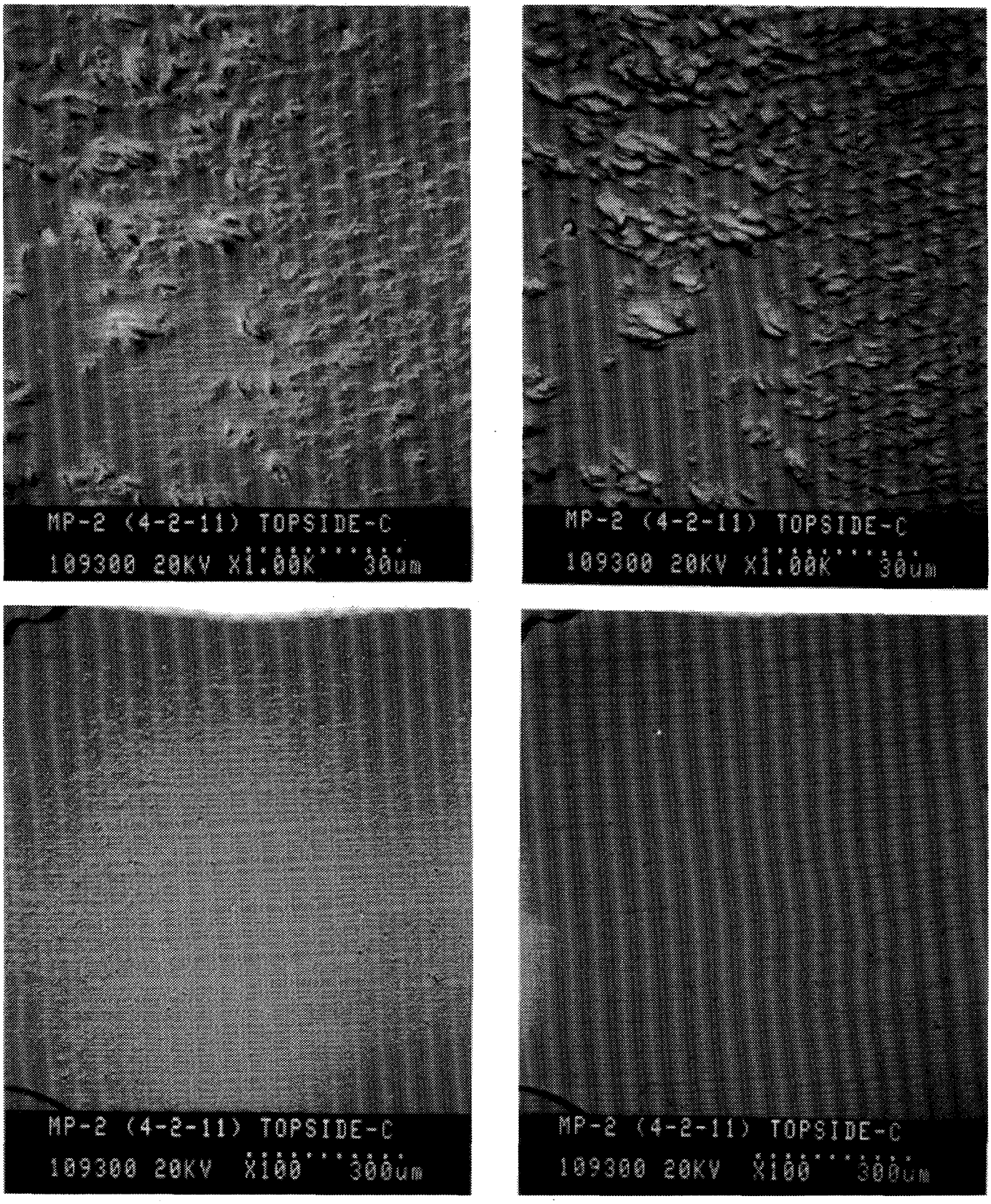

Figure 3.15a Scanning Electron Micrographs and Corresponding Elemental Maps for the Bottom of the Ceramic Melt Pool

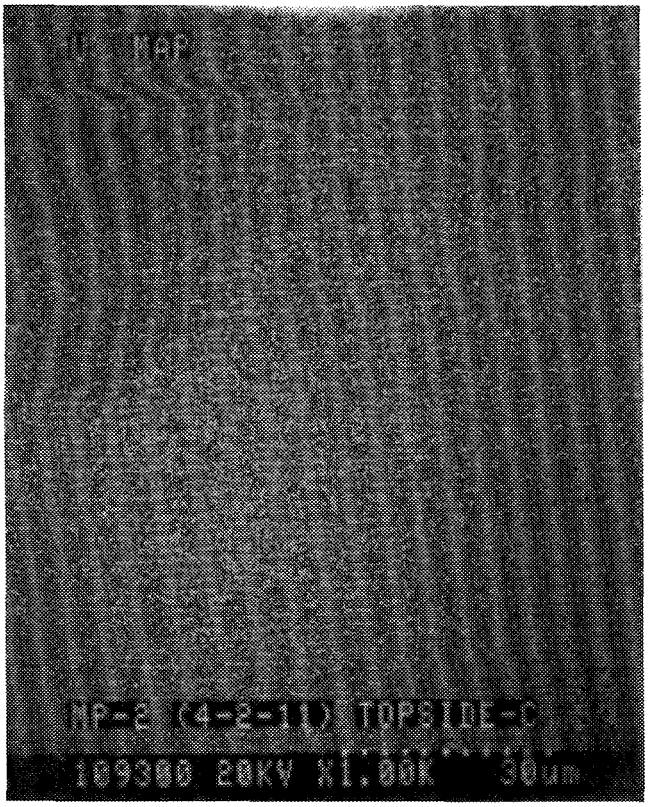

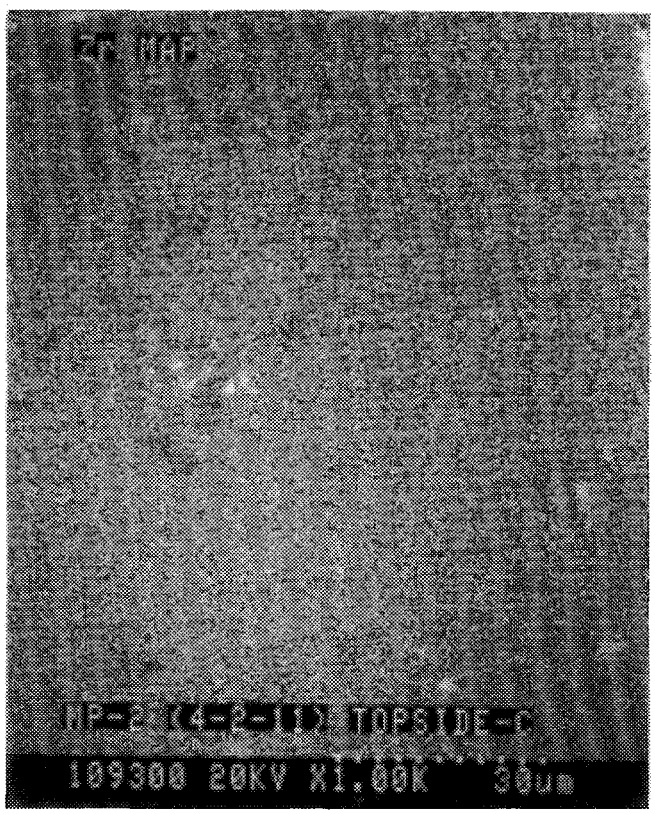

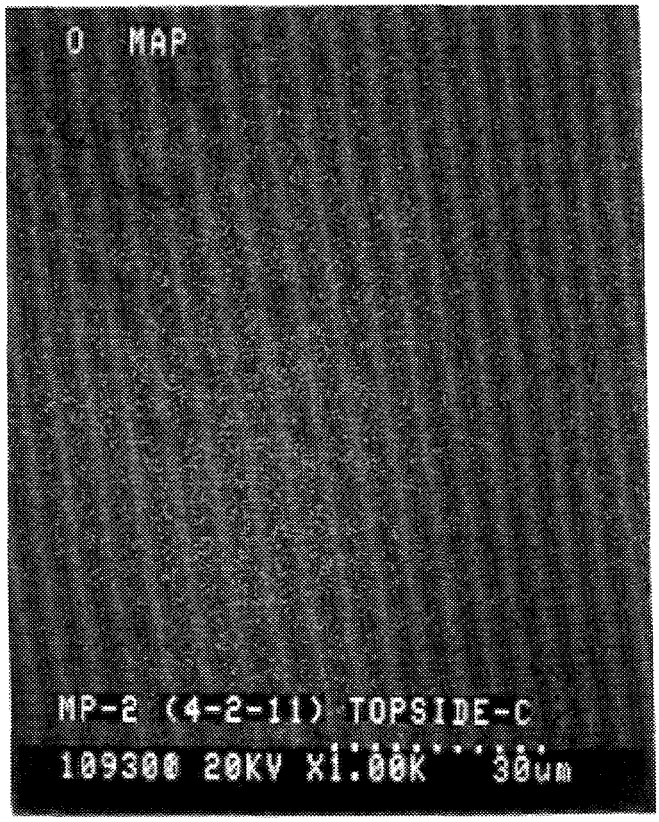

Figure 3.15b Scanning Electron Micrographs and Corresponding Elemental Maps for the Bottom of the Ceramic Melt Pool

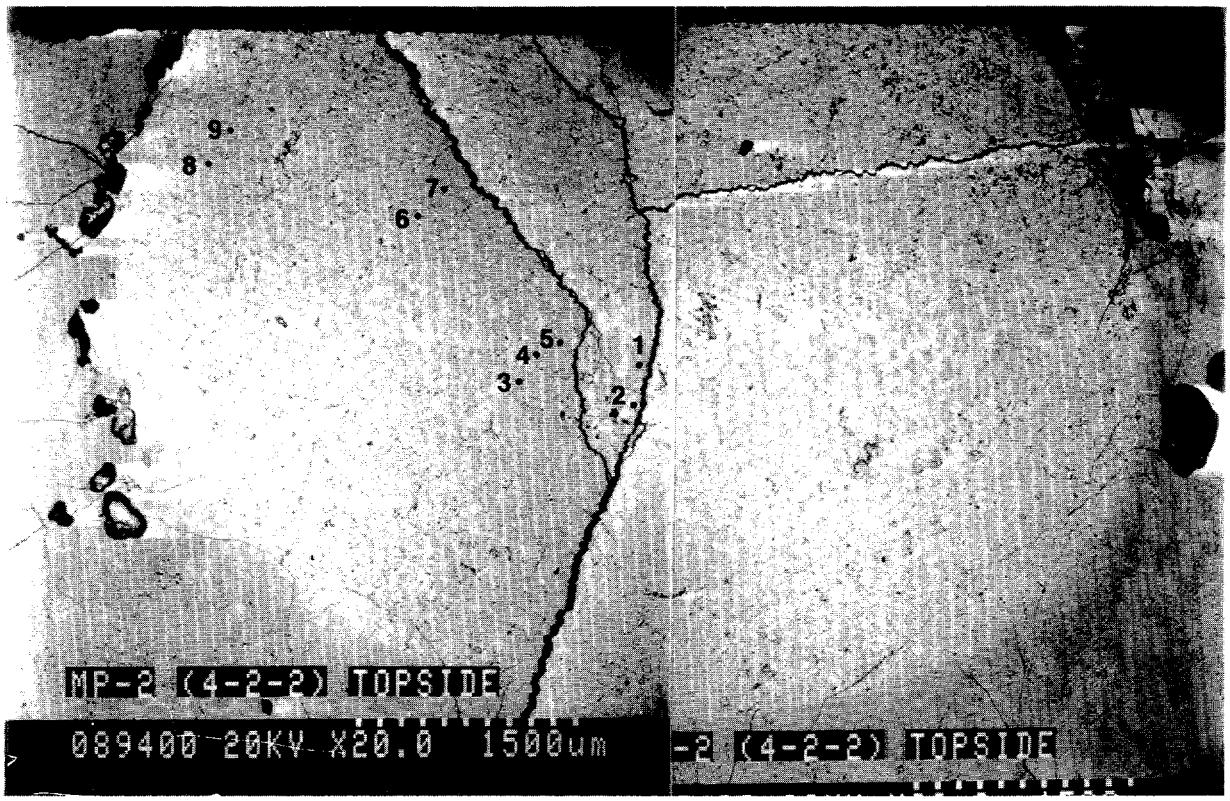

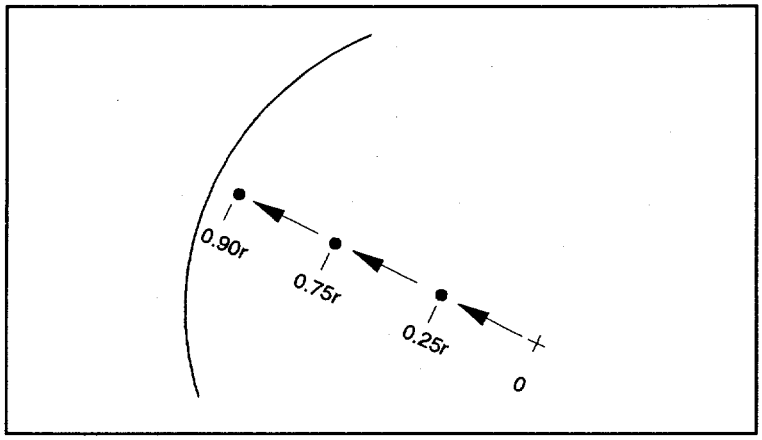

Figure 3.16 Location of the Nine Measuring Points on Sample 4-2-2

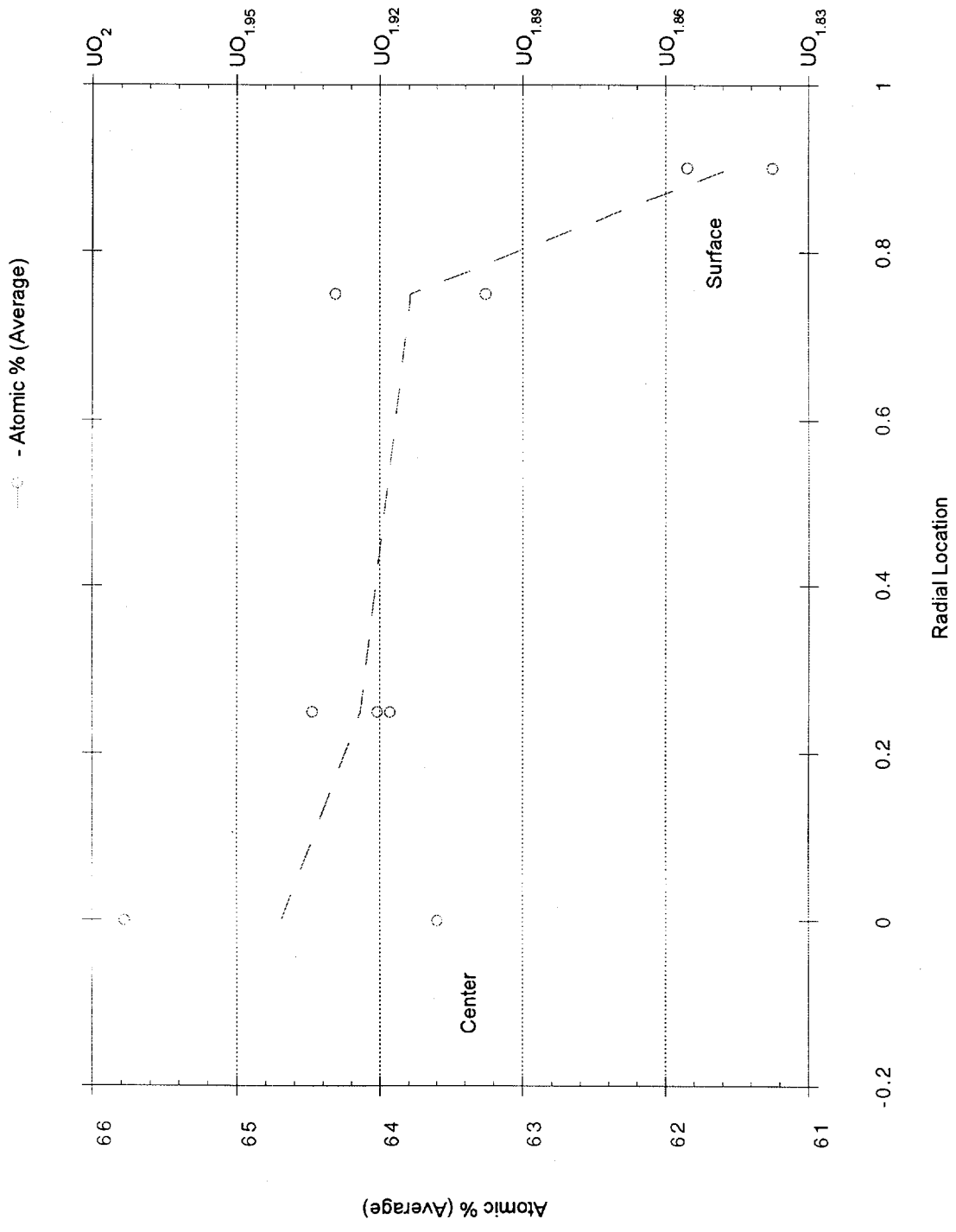

Figure 3.17 Atomic Percent Average at Nine Locations of Sample 4-2-2

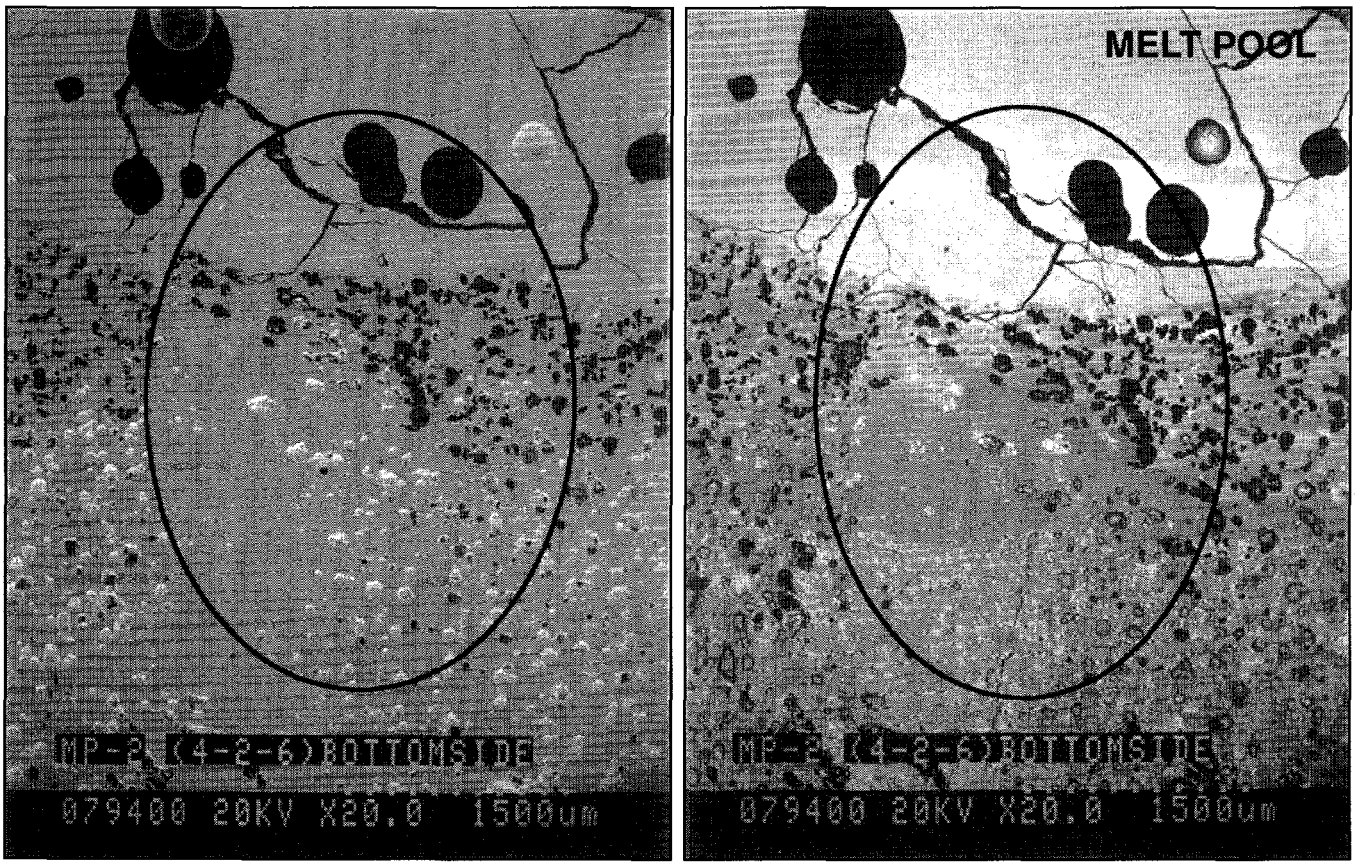

Figure 3.18 The Dark Band of Material at the Edge of the Ceramic Melt Pool

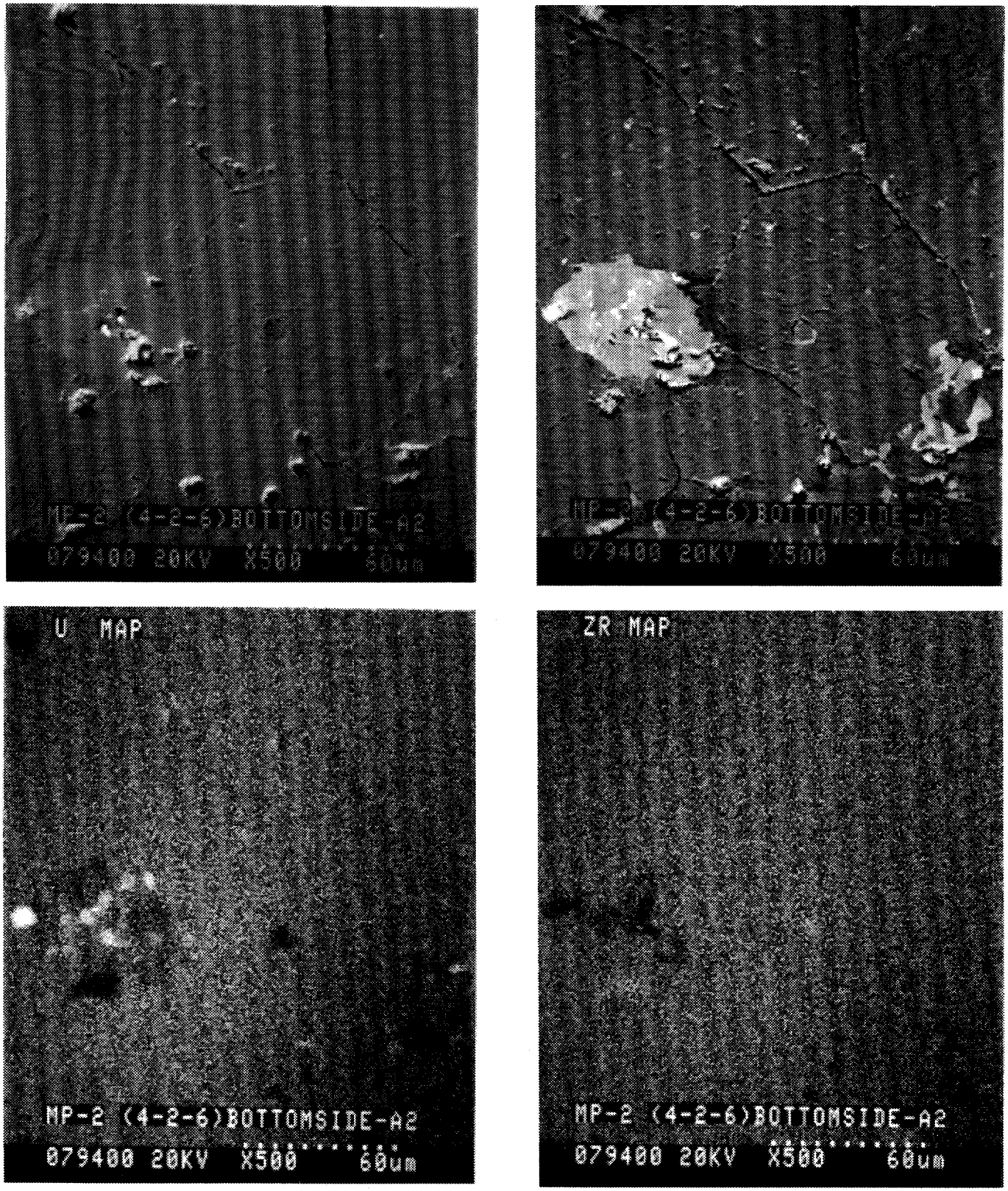

Figure 3.19a Scanning Electron Micrographs and Corresponding Elemental Maps for the Dark Band in the Ceramic Melt Pool

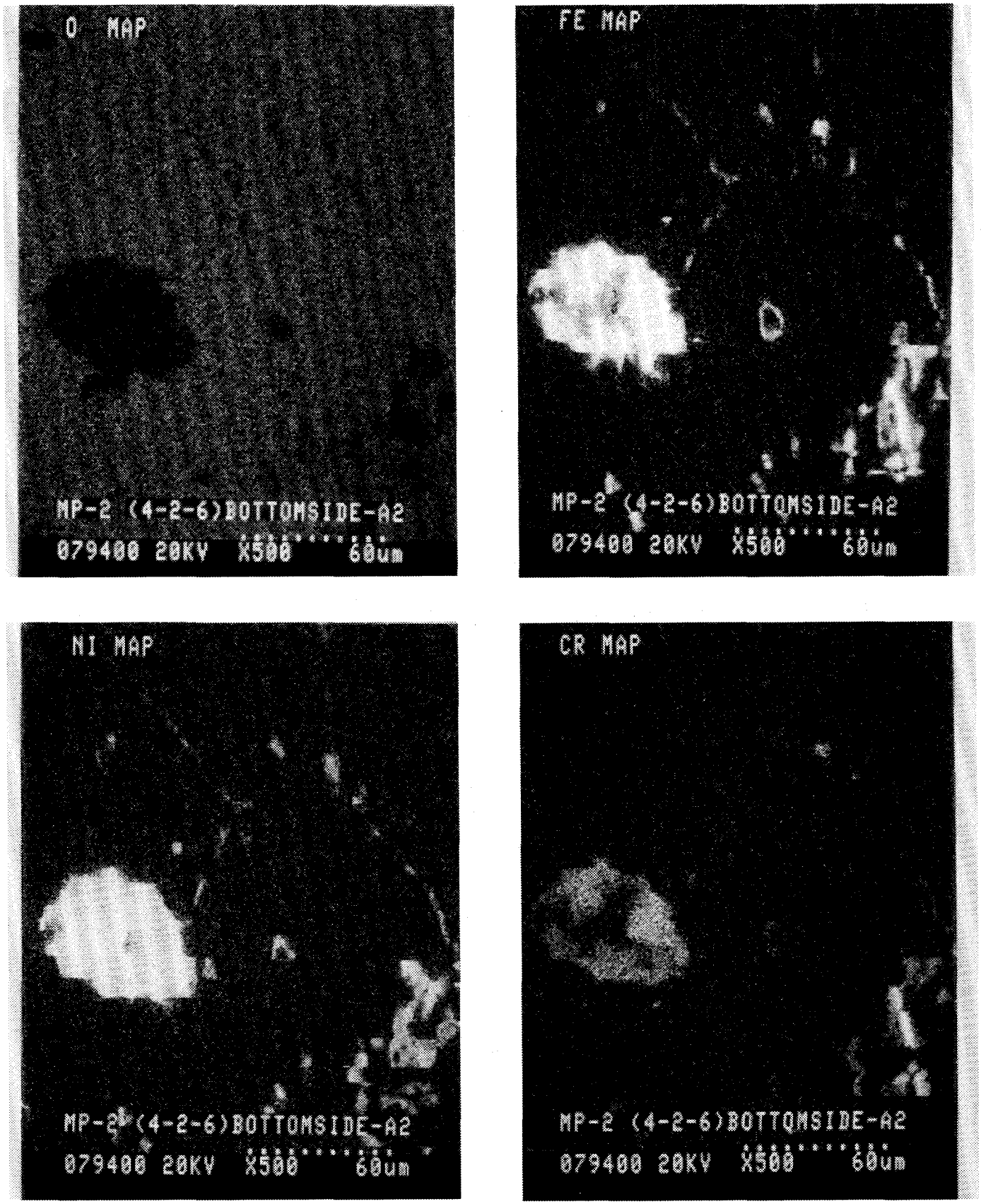

Figure 3.19b Scanning Electron Micrographs and Corresponding Elemental Maps for the Dark Band in the Ceramic Melt Pool

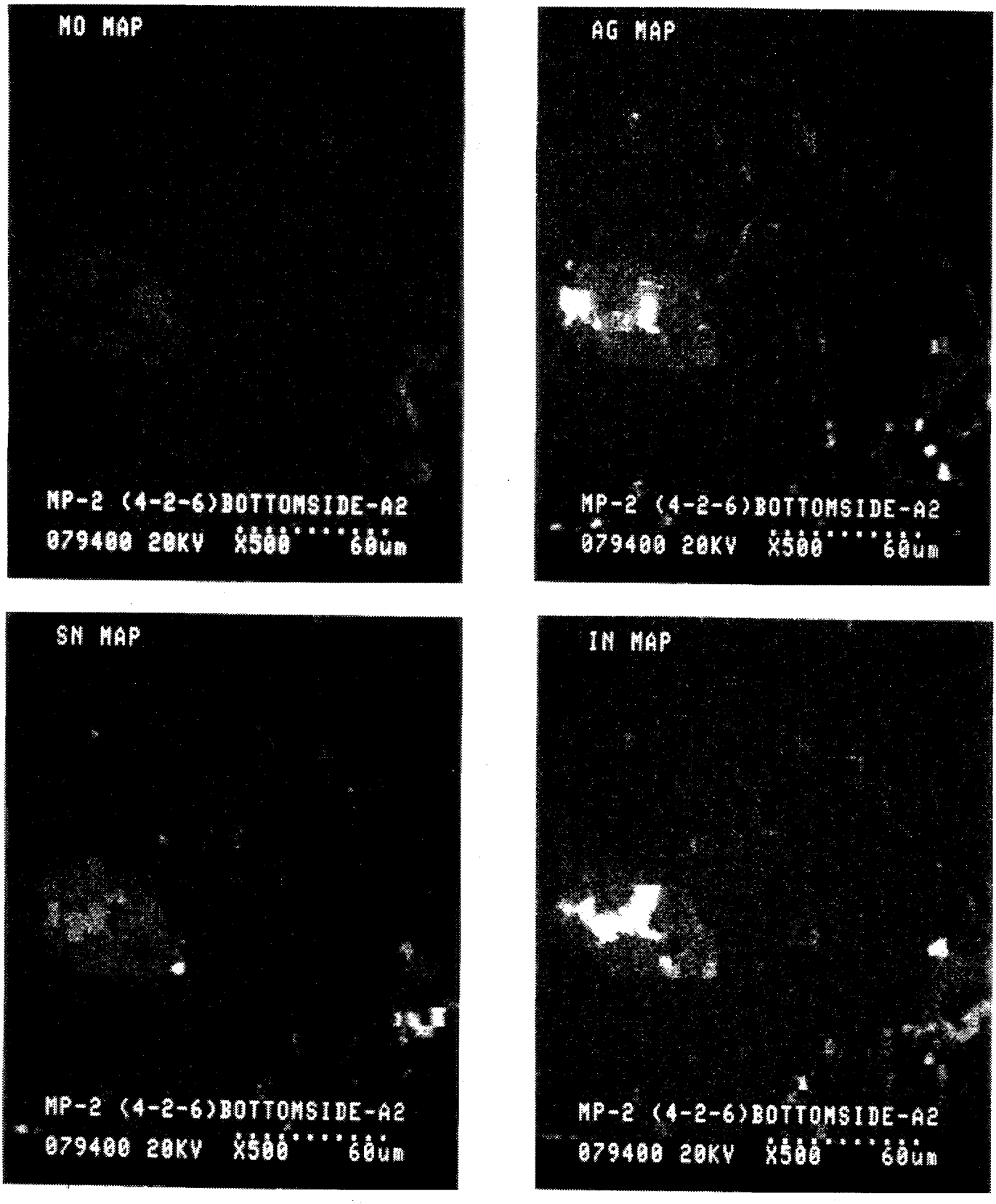

Figure 3.19c Scanning Electron Micrographs and Corresponding Elemental Maps for the Dark Band in the Ceramic Melt Pool

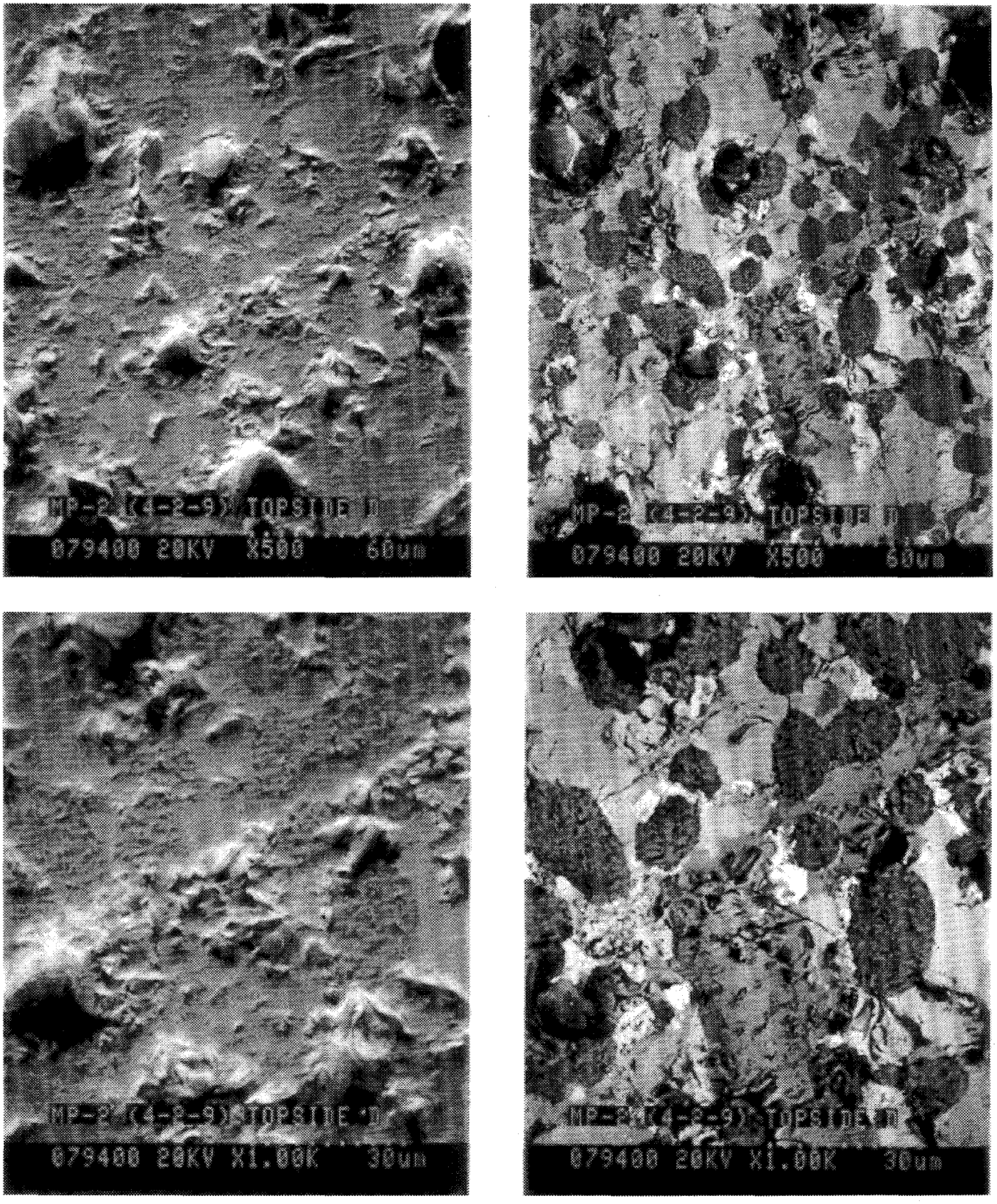

Figure 3.20a Scanning Electron Micrographs and Corresponding Elemental Maps for the Metallic Crust Remnant

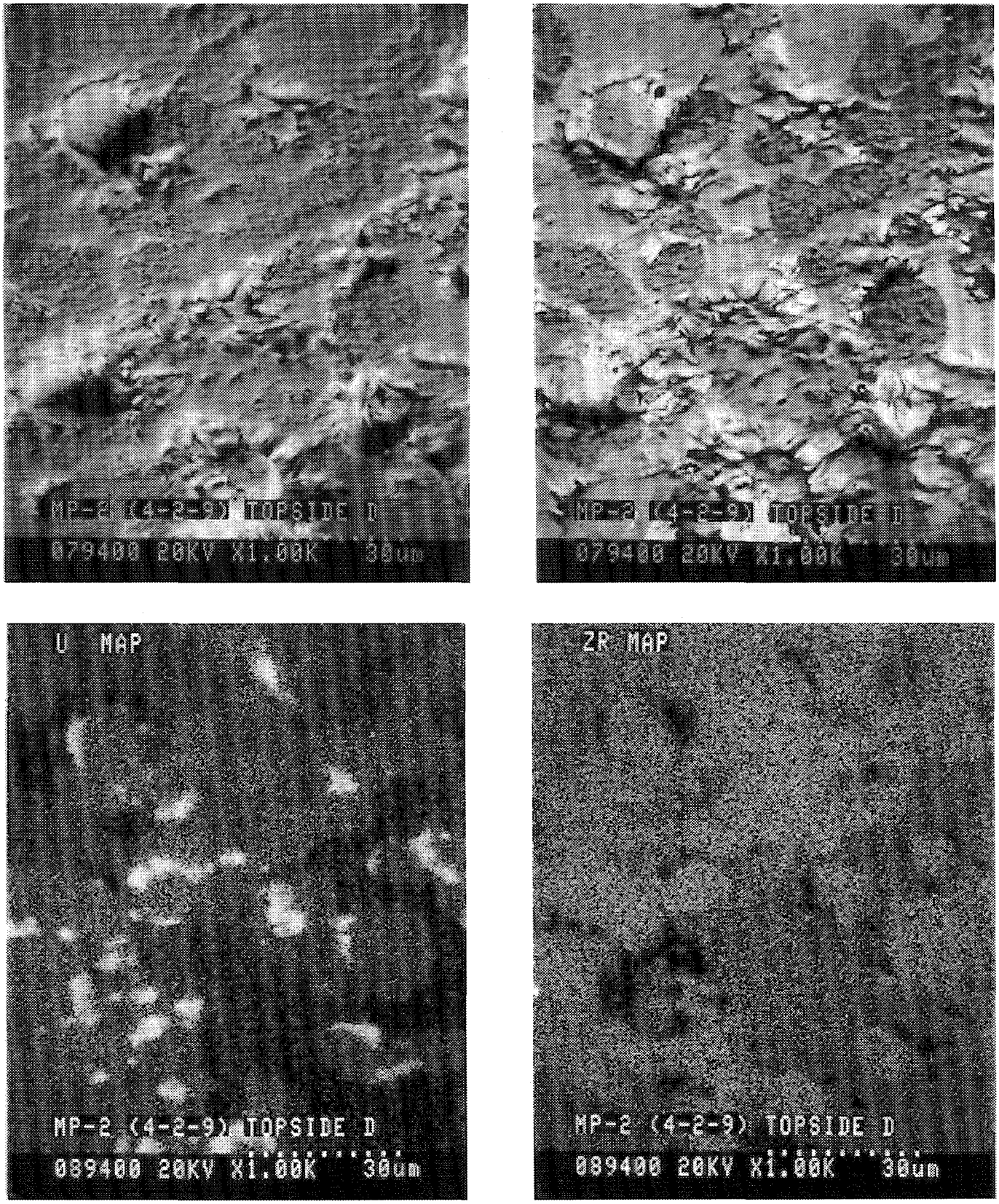

Figure 3.20b Scanning Electron Micrographs and Corresponding Elemental Maps for the Metallic Crust Remnant

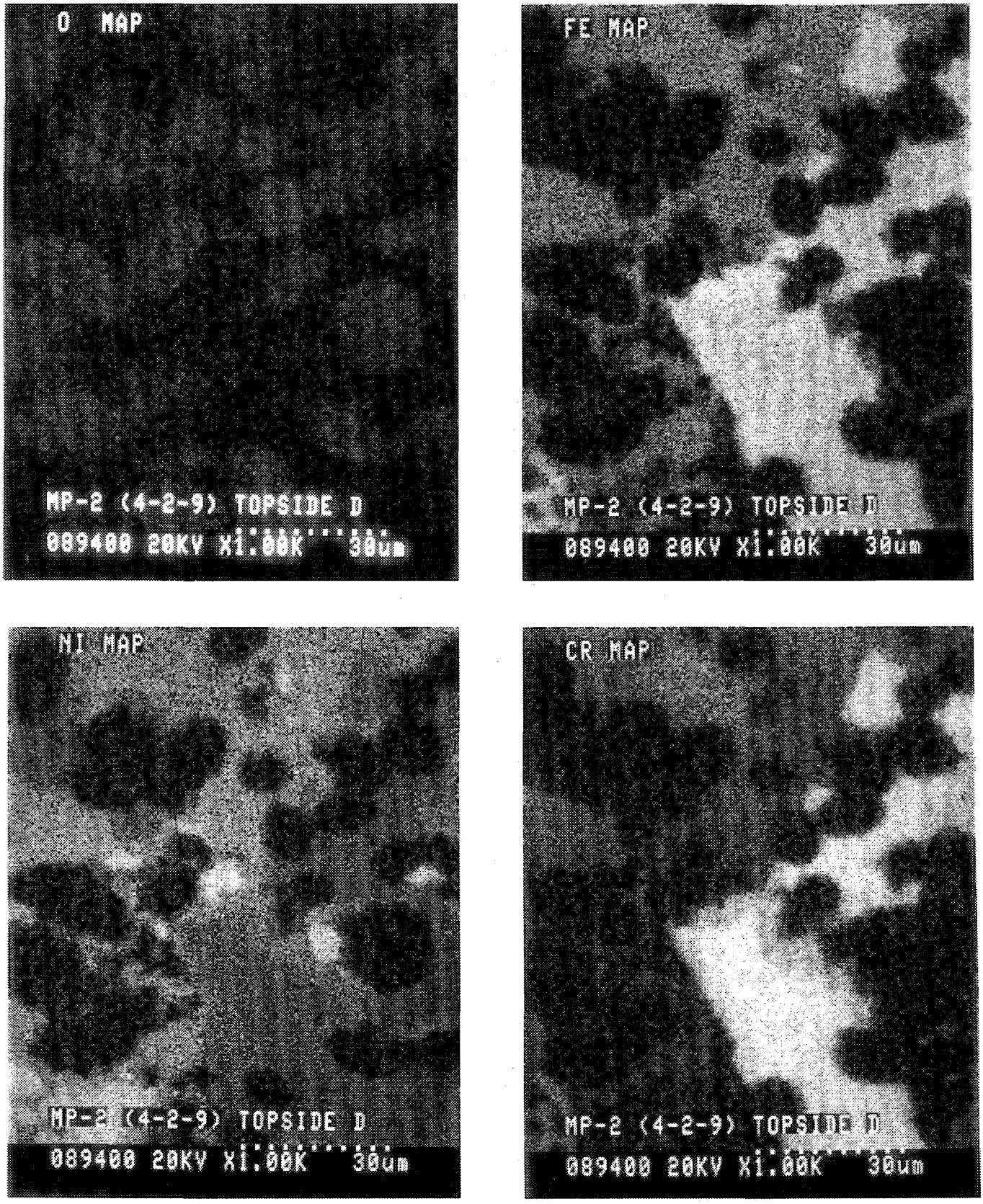

Figure 3.20c Scanning Electron Micrographs and Corresponding Elemental Maps for the Metallic Crust Remnant

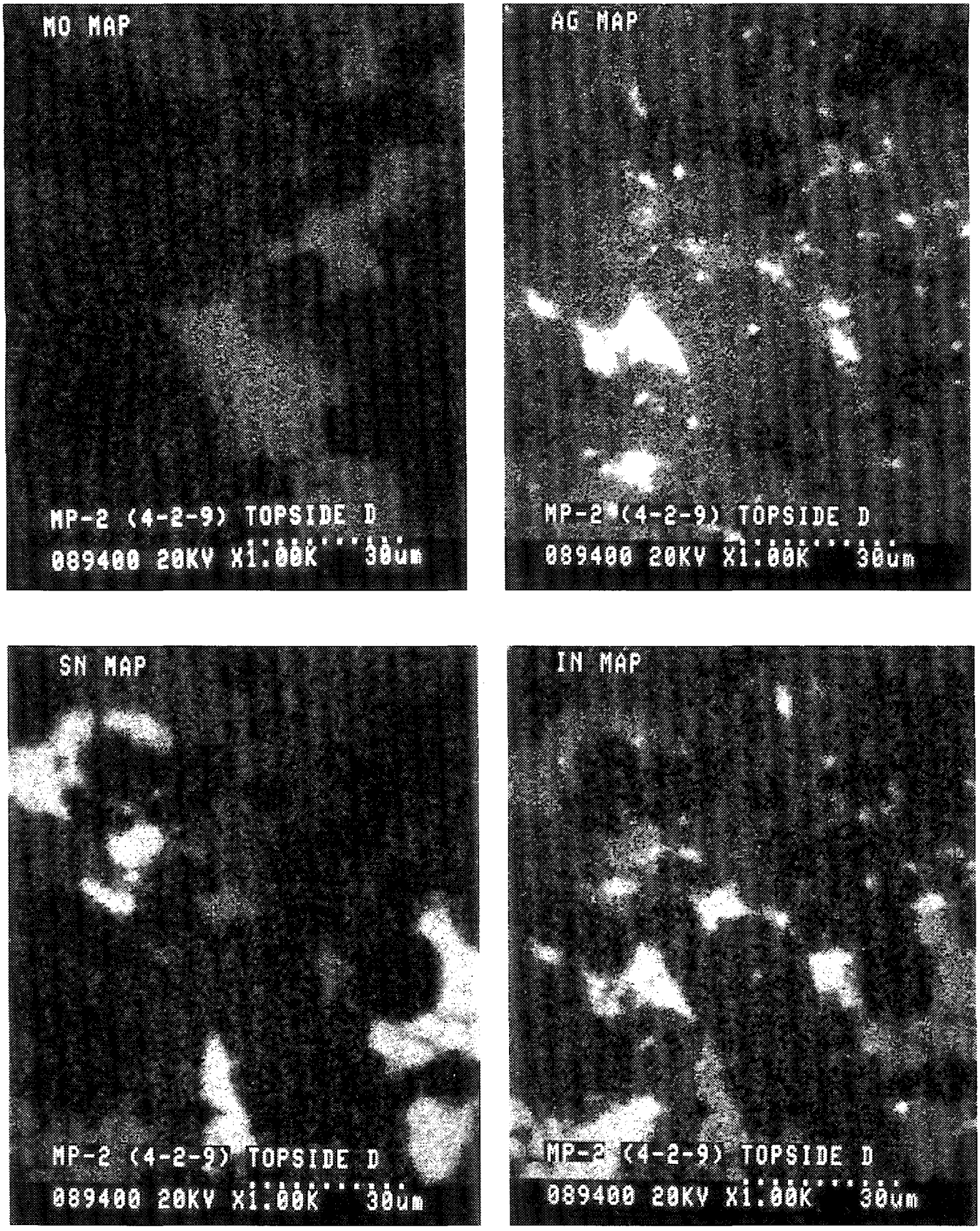

Figure 3.20d Scanning Electron Micrographs and Corresponding Elemental Maps for the Metallic Crust Remnant

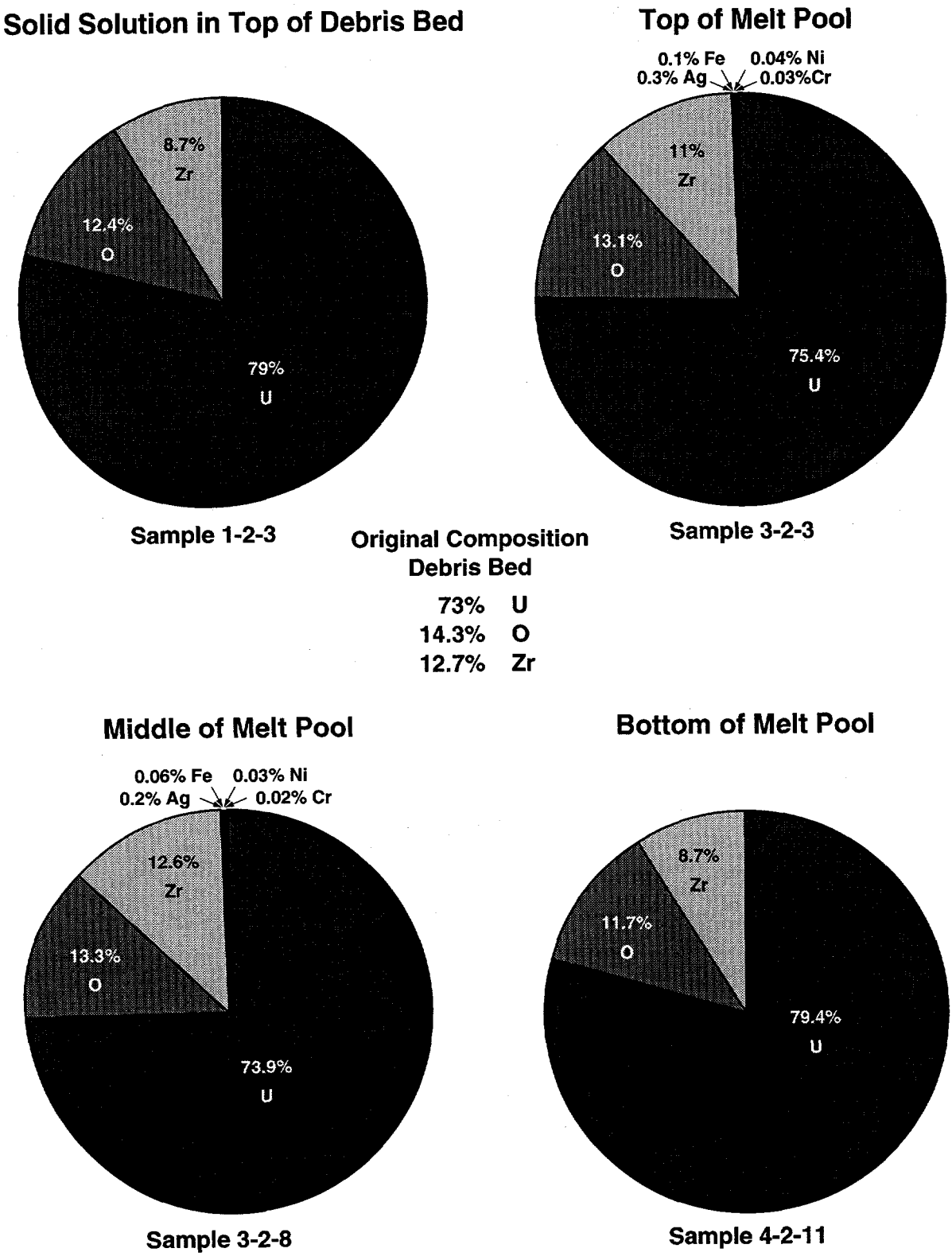

Figure 3.21 Pie Charts Representing the Bulk Elemental Chemistry for Regions in the Upper Portion of the Test Capsule

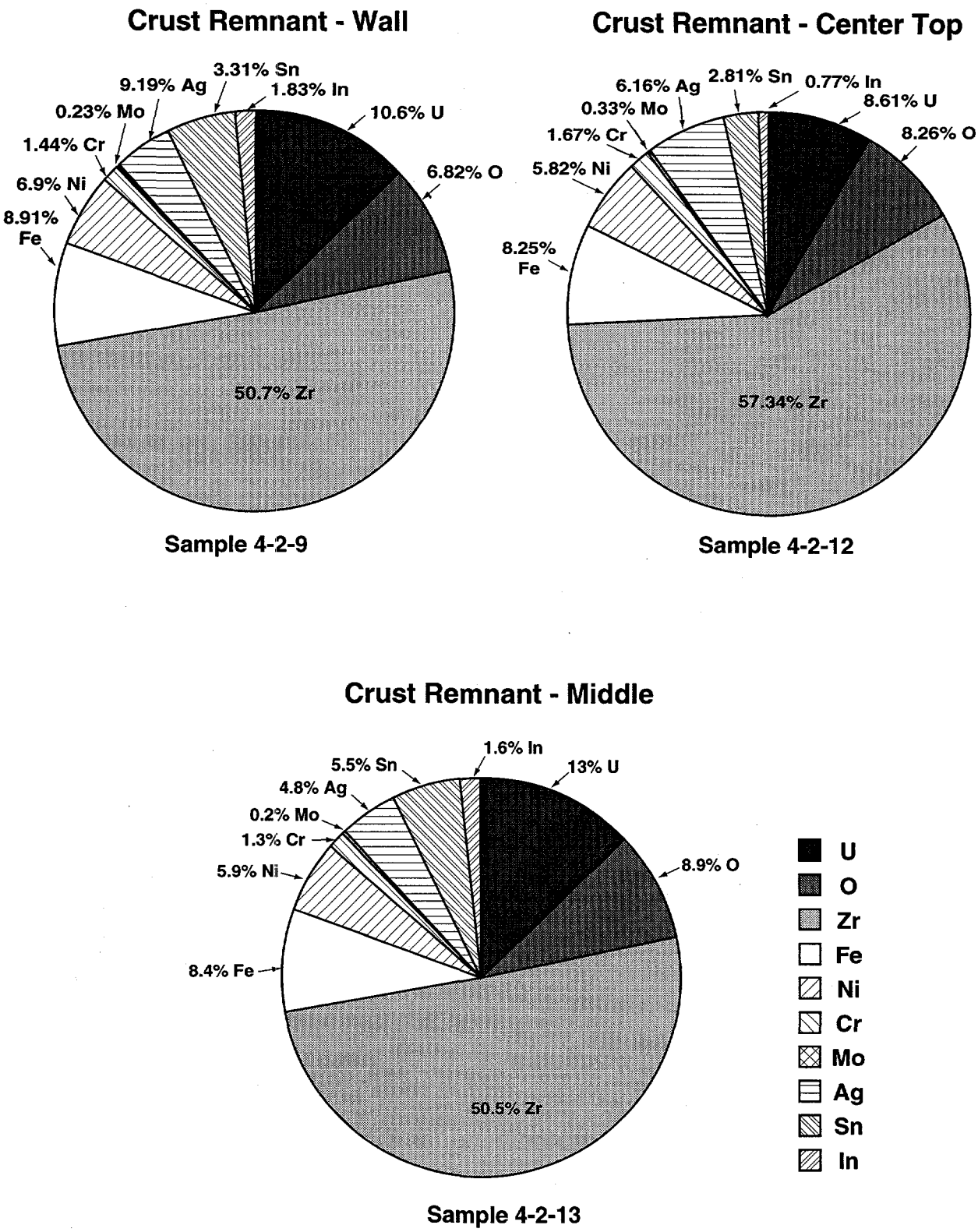

Figure 3.22 Pie Charts Representing the Bulk Elemental Chemistry for Regions in the Crust Remnant of the Test Capsule

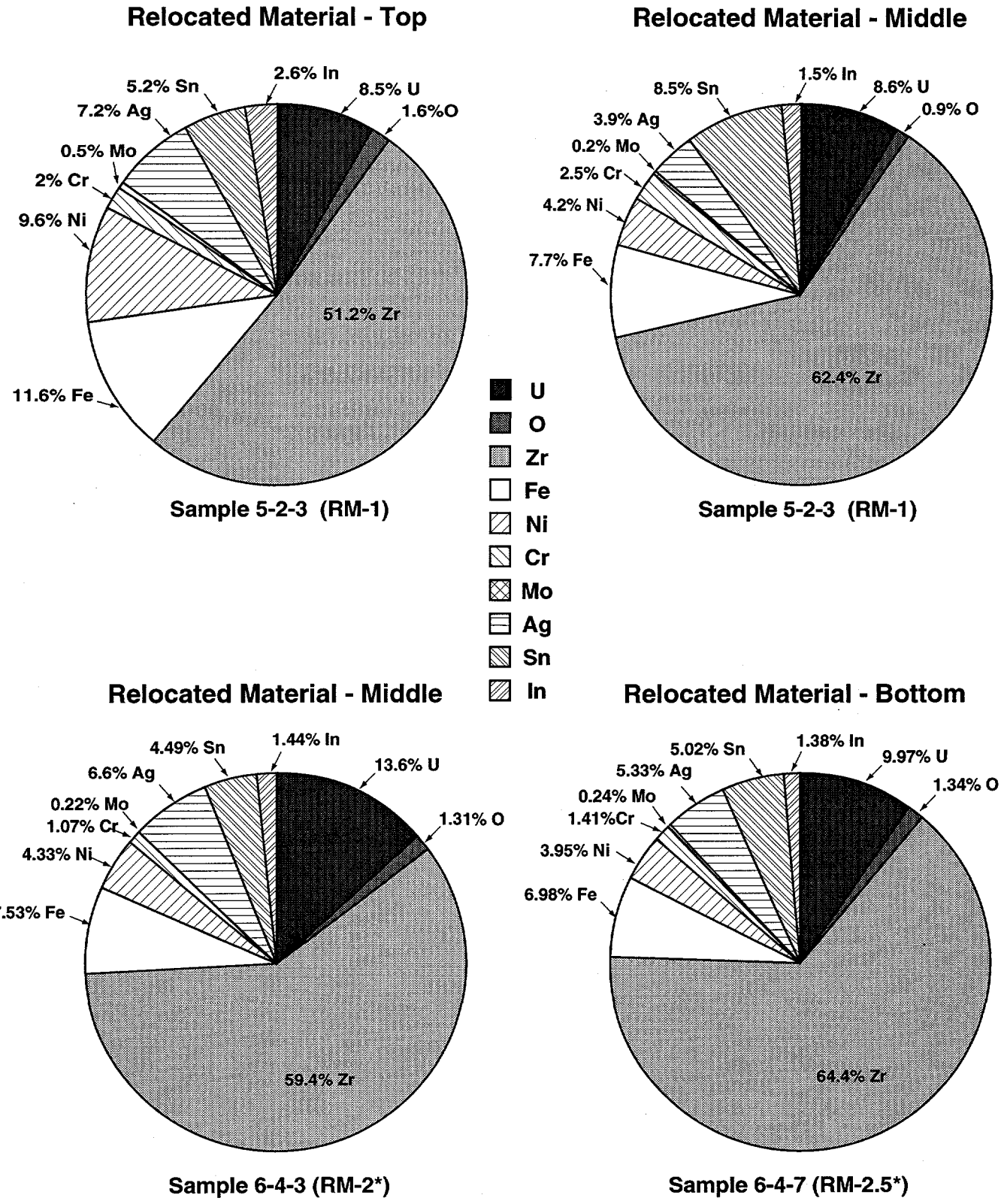

Figure 3.23 Pie Charts Representing the Bulk Elemental Chemistry for Regions in the Lower Portion of the Test Capsule

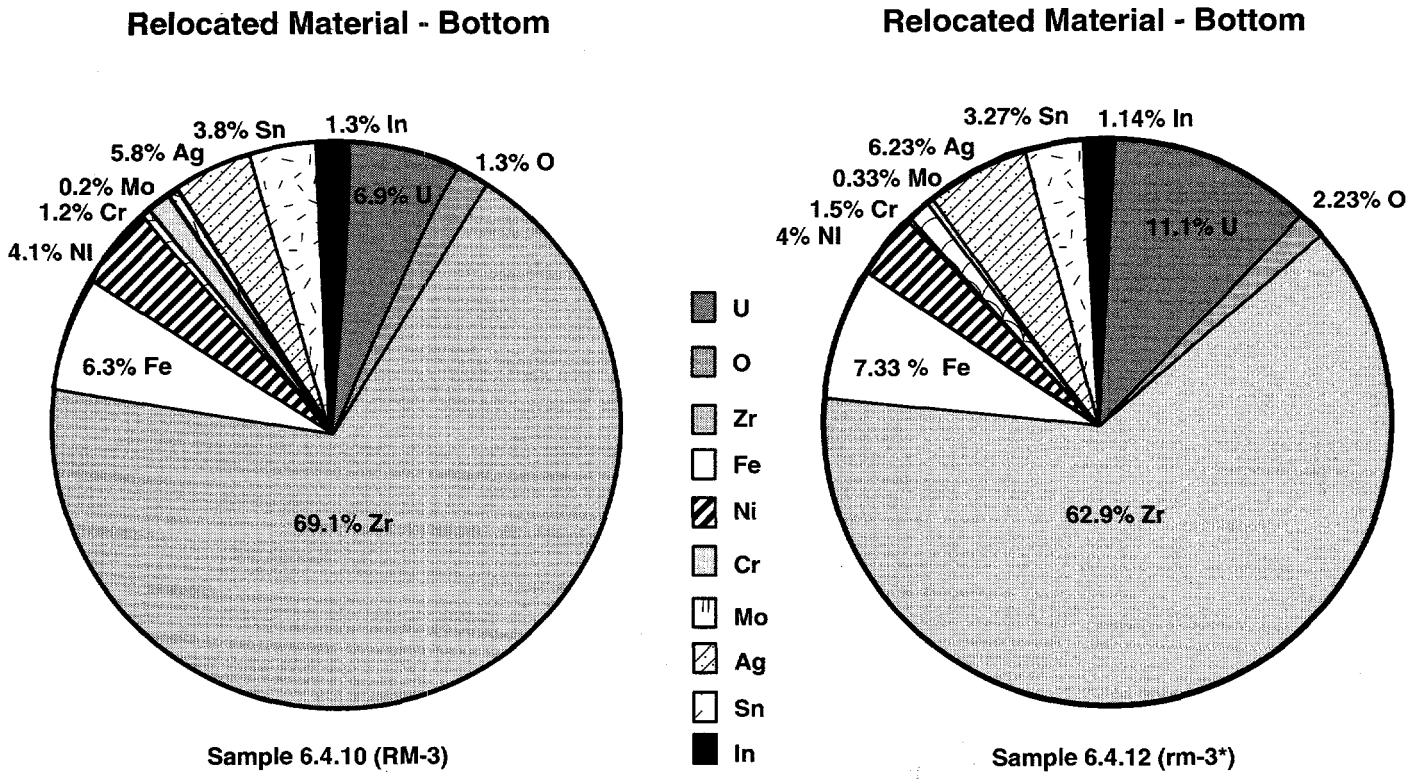

Figure 3.24 Pie Charts Representing the Bulk Elemental Chemistry for Regions in the Bottom Portion of the Test Capsule

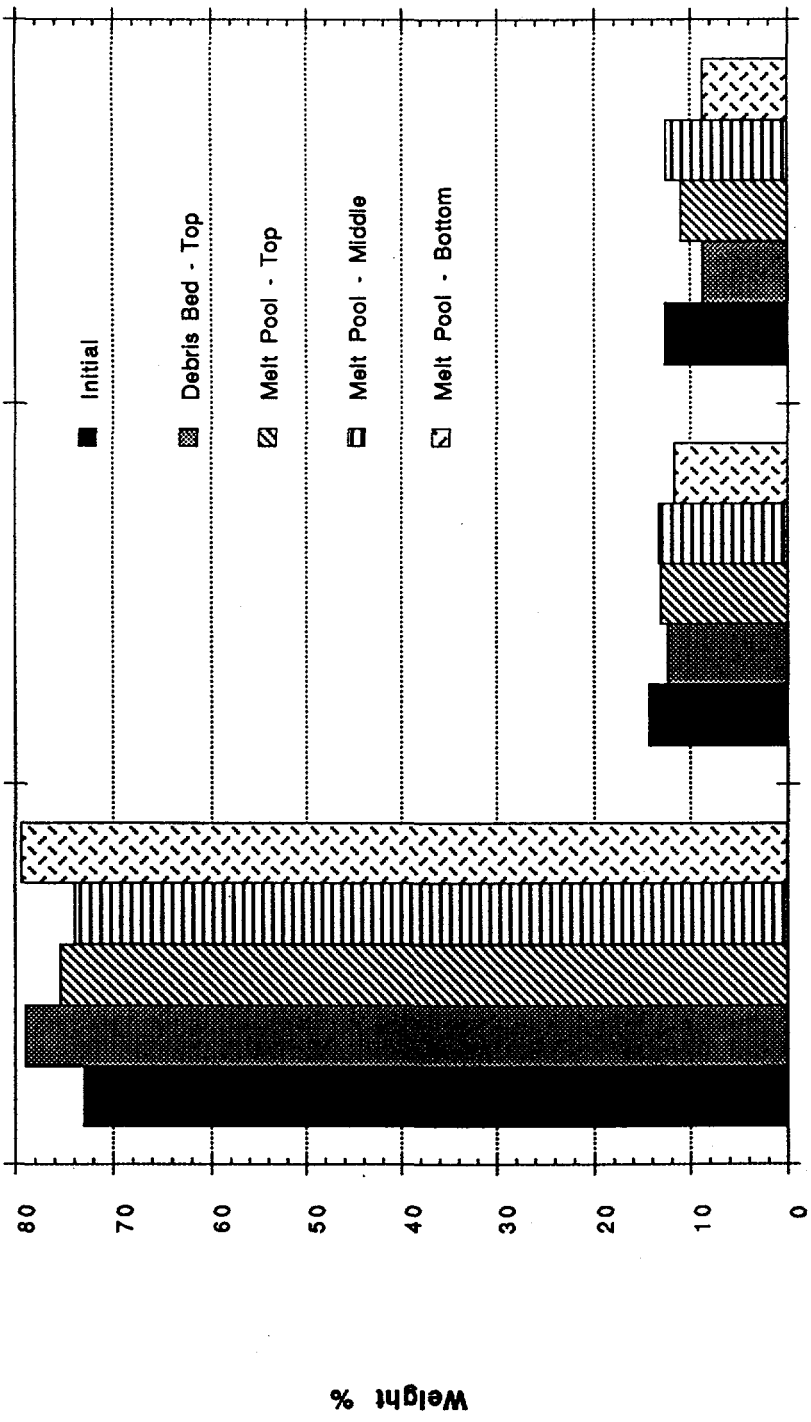

Figure 3.25 Elemental Bar Graphs Representing the Bulk Chemistry for Regions in the Upper Portion of the Test Capsule

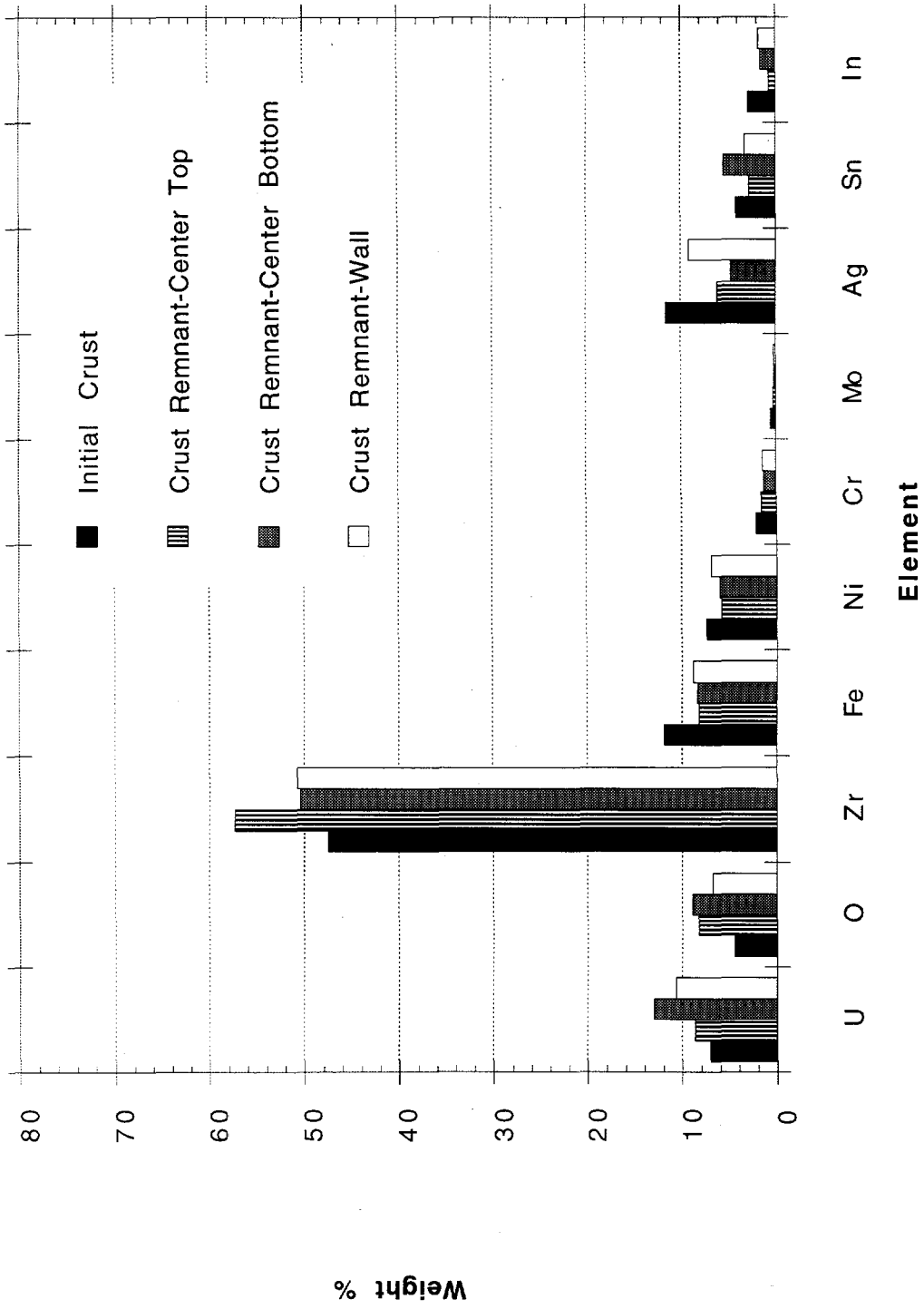

Figure 3.26 Elemental Bar Graphs Representing the Bulk Chemistry for Regions in the Crust Portion of the Test Capsule

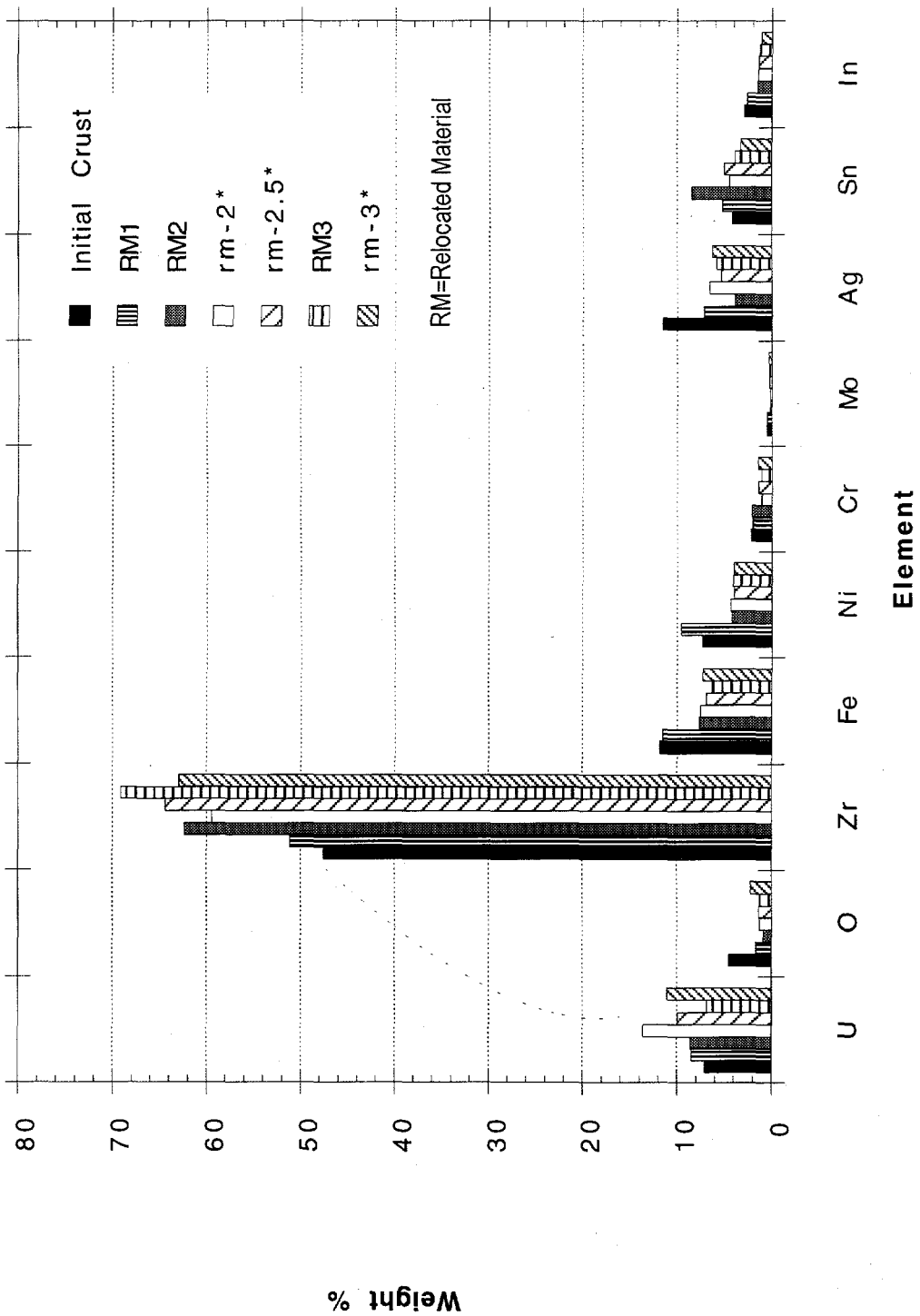

Figure 3.27 Elemental Bar Graphs Representing the Bulk Chemistry for Regions in the Lower Portion of the Test Capsule

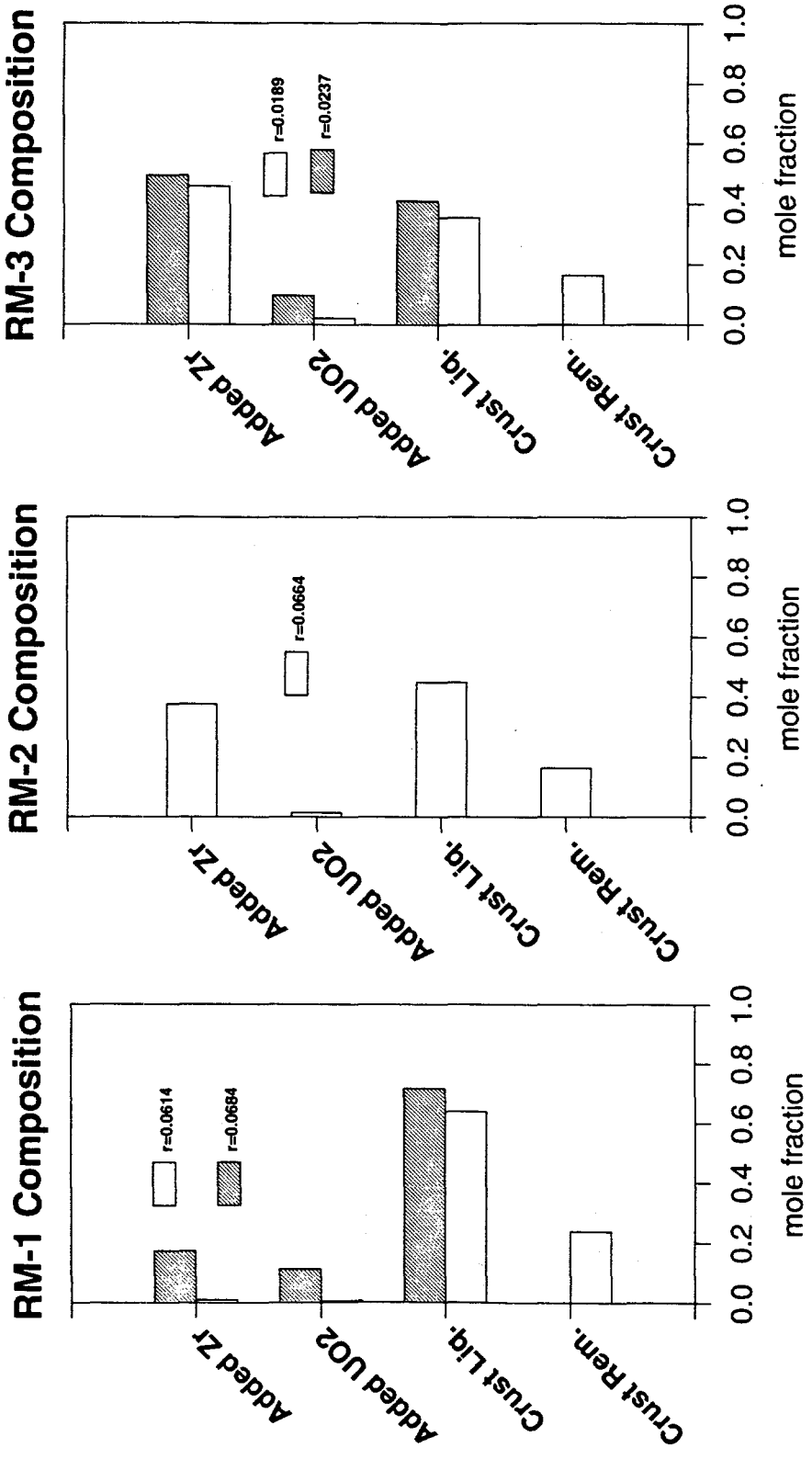

Figure 3.28 Mole Fractions of Four Simplified Material Classes Used to Approximate the Relocated Materials RM-1, RM-2, and RM-3

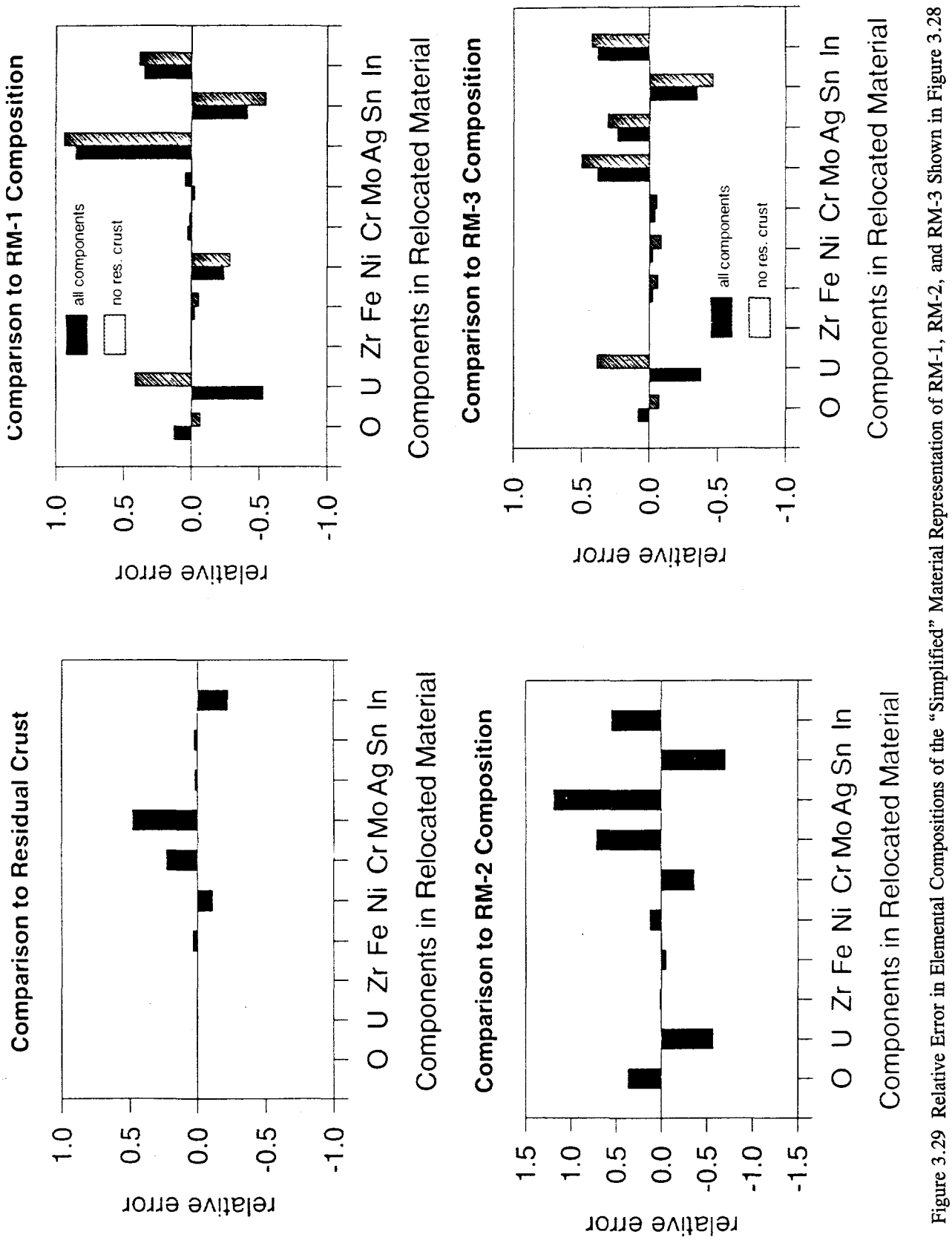

Figure 3.29 Relative Error in Elemental Compositions of the "Simplified" Material Representation of RM-1, RM-2, and RM-3 Shown in Figure 3.28

4.0 Results and Analyses

This section of the report provides a complete description of the analyses that were performed for the MP-2 experiment and presents the results of the measurements taken during conduct of the experiment. The approach, for the most part, is to directly compare the analytical results to the measured data to demonstrate both the degree to which the phenomena involved are understood and the accuracy with which the models describe the physics.

To facilitate comparison with the analytical results a summary of the key features of the measured data is provided first. Only those measured parameters that bear directly on the behavior of the debris bed, crust and rodded regions of the experiment are discussed in this section. A summary of the thermophysical properties used in the MP-2 analysis and a description of the methodology and results of the power coupling factor analysis are given in Appendix A. The formulation and solution of the cooling jacket heat transfer relationships is presented in Appendix B. A complete set of the measured data including temperatures, pressures, power history, and coolant flow rates for the entire experiment is given in Appendix D (Attached microfiche)

4.1 Measured Data

4.1.1 Measurement Uncertainties

For the MP-2 experiment, the primary source of information is obtained in the form of temperature measurements derived from thermocouple voltage outputs. Depending on the location of a thermocouple and the temperature range over which it is applied, thermocouple measurements may be subject to certain characteristic errors. In order to achieve accurate estimates of temperatures, it is often necessary to apply corrections to the raw thermocouple temperature data. The uncertainties arise from measurement errors that are essentially of two types. The first involves degradation of the thermocouple output due to increased electrical conductivity of the insulation separating the thermocouple wires. That phenomenon can occur at high temperatures. The second type of error has to do with the location and routing of thermocouple leads through the test section. This involves thermal shunting that perturbs the local temperature in the vicinity of the thermocouple installation due to the presence of a conductive heat transfer path provided by the thermocouple wires themselves and/or the thermocouple sheathing.

From direct measurements of W/Re type thermocouples at comparable temperatures it has been established that the error caused by electrical shunting may result in underestimating the temperature by amounts that can exceed 100 K for temperatures above ~2600 K. This appears to be a threshold phenomenon with the effect appearing rather abruptly at a specific temperature and thus not significantly affecting accuracy at lower temperatures. The phenomenon is well understood, and the onset of the degradation can be predicted.

At temperature in excess of ~2600 K, the electrical resistance of the hafnia insulation in the Type "C" W/Re thermocouples used in the debris bed begins to break down. Unlike most metals, ceramic materials are characterized by rapidly reduced resistivity at elevated temperatures. For example the resistivity of hafnia is reduced by 2 orders of magnitude (from 10^4 to 10^2 ohm-cm between 1500 and 2200 K). When the resistivity drops into the neighborhood of 10 ohm-cm, significant shunting current develops across the insulator and the voltage seen at the recording device is affected accordingly. The net result is that the voltages measured at the DAC are reduced such that they no longer accurately characterize the thermocouple. The trend is for an increasing underestimate of the temperature.

The magnitude of this type of error is difficult to estimate since the effective thermocouple junction is moved to an "unknown" location. The behavior of a particular W/Re thermocouple is therefore unpredictable in the temperature range from 2600 to 3000 K. As will be evident from the measured data, some of these thermocouples seem to survive and produce results that appear normal up to temperatures approaching 3000 K while others simple roll-over or flatten-out at temperatures about 2600 K. The latter behavior would suggest that the effective junction simply moves down the wire to an unknown location where the temperature is 2600 K. Probably the best approach is simply to discount the W/Re thermocouple measurements for temperatures above 2600 K. It is certain, however, that the temperature of the affected region is greater than 2600 K.

Standard practice for the routing of thermocouples provides that wherever possible thermocouple wires are routed along anticipated isotherms for the last few inches ahead of the thermocouple junction. This is done so that the thermocouple wires do not lie along a steep temperature gradient, which would result in the "shunting" of heat in the relatively high thermal conductivity pathway associated with the metallic wires and sheaths. However, cramped conditions within an experiment and other structural considerations sometimes make it necessary to route thermocouple wires in a less than optimal manner. In these situations corrections must be applied to the thermocouple data to account for the shunting effects.

In the thermal shunting phenomenon, the thermocouple wire and sheathing material act like a fin shunting heat away from the thermocouple junction and effectively perturbing the local temperature. The effect is that the junction temperature behaves like it is actually sensing the temperature in the cooler locations through which the thermocouple leads were routed.

Calculations were made for the MP-1 thermocouples located in the preformed crust region and the corrections ranged up to ~75 K at the highest temperatures observed in the crust region. These calculations are rather lengthy and a separate calculation must be made for each thermocouple since the effect depends strongly on the path through which the thermocouple was routed during assembly, the materials through which the wiring passes, and the thermal gradients along the wiring path. Therefore, these types of calculations were not undertaken for the MP-2 experiment. However, the crust in the MP-2 experiment, because of its higher metallic content,

had a higher effective thermal conductivity, and the effect would, therefore, be somewhat less pronounced in the MP-2 crust region. The presence of low melting temperature metals in the MP-2 crust appears to have caused early failure of the thermocouples located in this region. These metals may have reacted with the rhenium sheathing and perhaps with the thermocouple wires with the result that the crust thermocouples degraded sooner in the MP-2 experiment.

It is convenient and useful to present the ACRR power history before discussing the test section thermal response. Reference to the power history shown in Figure 4.1 will facilitate understanding of the measured temperature responses. Note in Figure 4.1 the alternating relatively short "bursts" of power followed by long periods at power levels about half of the previous peaks. As discussed earlier, each of the "bursts" was intended to raise the debris bed temperature by a prescribed amount and the longer duration, lower power periods were intended to return the system to steady-state before the next transient. At about 13,500 seconds the debris bed was deemed to be at a temperature just short of the melting point, and at this point, a steady power level of 0.4 MW was applied to take the debris bed into the melting process. Subsequent increases in power were required to continue the heatup process when the system attained steady-state conditions at the previous power level.

4.1.2 Summary of Temperature Measurements

The measured thermal responses in the debris bed region of the experiment are shown in Figures 4.2 through 4.4. These figures consist of the thermocouple traces for the nine instruments that were located in intimate contact with the rubblized material in the debris bed. Figure 4.2 shows the response in the lower regions of the debris bed, while Figures 4.3 and 4.4 show the response in the middle and upper regions of the bed. The most obvious characteristics of the temperature response, namely the stepped structure, was a result of the alternating high-and low-power levels. The experiment proceeded by alternate applications of ACRR power at levels that yielded a heatup rate in the debris bed of ~1 K/s, followed by reduced power levels designed to achieve thermal equilibrium at the given temperature before proceeding to the next heatup phase. The average debris bed heatup rate during the heatup phase of the experiment (from 0 to 13,500 seconds) was ~0.18 K/s. The steady-state phases were designed to provide the time to assess the condition of the assembly and estimate the power level needed to achieve the next targeted temperature plateau.

Referring back to Figure 2.5 will provide an idea of the relative positions within the debris bed that correspond to thermocouple measurements shown in Figures 4.2 to 4.4 as well as the remainder of the measured data shown in this section. The Six axial locations represented among the nine thermocouples in the debris bed correspond to distances above the crust of 0, 2, 4, 7, 11, and 16 centimeters (approximately 0, 1/8, 1/4, 1/2, 3/4, and 1) of the distance from the bottom to the top of the debris bed).

The general trends during the heatup phase show a temperature increase in the axial direction proceeding upward from the bottom of the bed to about the center and then dropping off from the center to the top.The highest temperature during the heatup phase is observed at the 21-cm location near the center (DBC2100). The peak temperature observed during the melt phase of the experiment was at the bottom of the debris bed (DBC1400 and DBC1401) and was observed to be somewhat in excess of 3200 K. This appears to be the location of the molten ceramic pool region late in the experiment as seen in the posttest axial cross sections (PIE). The effects of the formation and motion of molten ceramic can be observed from the crossover of the temperature traces for the thermocouples at the bottom of the debris bed (DBC1400 and DBC1401) and those just above (DBC1601 and DBC1801) as the molten ceramic moved closer to the former and contributed to the failure of the latter (Figure 4.2).

The radial temperature trend in the debris bed (Figure 4.3) shows a slight negative gradient with increasing distance from the centerline (~200 K difference between DBC2100 and DBC2103) during the heatup phase. This trend appears to be reversed during the melt phase when the centerline temperature (DBC2100) fell below the thermocouples radially outward (DBC2102 and DBC2103). However, the last is clearly in the degradation zone for these thermocouples (~2600 K).

The thermocouples that were located in the zone that first went through melting, those near the axial center of the debris bed, appear to become degraded at about 2600 K, particularly DBC1601 and DBC1801. The thermocouples near the bottom of the bed appear to remain viable up to about 2900 K. The thermocouple located at the top of the bed, DBC3000, does not seem to exhibit the typical failure characteristics and it recorded a peak temperature of about 2800 K. Although the Type "C" thermocouples are known to degrade above ~2600 K, there appears to be a difference in the responses between those that were exposed to molten ceramic and those that were not exposed or experienced limited exposure, the former seem to display a clearly delineated failure mode characterized by a sudden drop in temperature, an oscillating temperature trace, or a combination of both.

The thermal response of the solid crust region is depicted in Figure 4.5. The expected trend was not observed in the measured crust response. That is, the expected temperature increase moving from the bottom to the top of the crust was not apparent in the data. The peak temperature (2300 K) was recorded by CRC12-0, which was sited at about the 1/2-location (half way up from the bottom to the top of the crust) while the thermocouple at the 3/4-location (CRC13-1) and nearer the debris bed read nearly 300 K cooler. One of the thermocouples at the 1/4-location recorded higher temperatures than the one intact thermocouple at the 3/4-location. The thermocouples in the crust generally produced inconsistent results. It is suspected that interactions between the rhenium sheath and thermocouple wires with molten metallic phases that developed in the crust starting at the indium, tin, and silver melting temperatures (430 K, 505 K, and 1200 K) were responsible for the apparent inconsistencies. In addition, the temperature gradients along which the thermocouple wires were routed may have produced some thermal shunting. The crust thermocouples all suffered gross failure starting at about 17,300 seconds with the last one failing at about 18,300 seconds.

Although only two thermocouples were attached directly to fuel rods (FRK0514 and FRK0531), four other thermocouples were located at the boundaries of the rod stub region. The responses of these six thermocouples are shown in Figure 4.6. The expected trend in this region involved a large axial temperature gradient caused by the significant thermal mass associated with the lower grid spacer and the fact that it was in good thermal contact with the cooling jacket. And,

indeed, this is observed in the temperature history. The two thermocouples at the grid-spacer/rod-region interface (GSK0013 and GSK0018) recorded maximum temperatures of ~1000 K. The thermocouples attached to the rods (FRK0514 and FRK0531) near the axial center of the region "saw" peak temperatures of about 1600 K. And, of course, the thermocouples at the top of the rod region (bottom of the crust (FRS1000 and FRK1044) recorded higher temperatures, in the vicinity of 1700 K. These two thermocouples, however, were not high-temperature type "C" thermocouples and consequently failed at about 15,000 seconds. The actual temperatures at the bottom of the crust during the melt phase were much higher. The peak temperature gradient in the rod region was ~95 K/cm at the beginning of the melt phase just before the thermocouples at the bottom of the crust failed and clearly exceeded this value during the melt phase. Note the temperature "spikes" recorded on the two thermocouples at the bottom of the rod stub region (mounted to the top of the grid spacer). These temperature transients mark the arrival of molten material released from the crust onto the top of the grid spacer. There are at least five detectable events (three large and two small) between about 15,800 and 16,800 seconds in the melt phase. These events, which were not found to correspond to any clear cut signature in the interior crust thermocouples, can be associated with events that lead to the failure a few hundred seconds earlier of the two thermocouples at the bottom the crust (FRK1000 and FRK1044).

The rod-region-thermocouple data late in the experiment can be interpreted to indicate the relocation of a second and perhaps more massive relocation of molten material from the crust region. An increase in the heatup rate on all the rod-region thermocouples can be seen at 19,000 seconds when the reactor was taken to 0.6 MW. A second increase in heatup rate can be observed at about 19,500 seconds, and it this second sharp increase that may indicate the sudden relocation of molten ceramic into the preformed crust region and perhaps the release of additional crust material into the rod region. It cannot be ascertained with certainty that a second relocation event occurred at this time since there are no sharp temperature "spikes" of the type seen for the earlier relocation, but this fact does not preclude such an event. The thermocouples at the bottom of the rod region that detected the earlier events (GSK0013 and GSK0018) may have been embedded in a mass of resolidified material from the earlier relocation, which would have attenuated the thermal response.

The temperatures recorded by the thermocouples placed on the outside of the tantalum liner are depicted in Figure 4.7 (lower section of the liner opposite the rod and crust regions), Figure 4.8 (on the liner opposite the top of the crust and the lower portion of the debris bed), and Figure 4.9 (middle to upper section of liner opposite the lower to upper section of the debris bed). These temperatures were key inputs to running the experiment in the melt phase when the thermocouples in the debris bed became overranged, and served to provide a check on the estimated peak temperatures in the debris bed and molten pool. The highest observed temperatures (~2130 K) on the liner was recorded by ZRC1858 (Figure 4.9), which was located radially opposite the location of the molten ceramic pool. The temperature traces for the tantalum liner thermocouples also provide information regarding the motion of the molten pool as it moved into and attacked the metallic crust. The slight decline in temperature recorded by ZRC1858 at ~19,600 seconds may indicate the sudden movement of the ceramic pool down into the partially vacated crust region at this time. This same "turn over" in temperature is also observable on the two thermocouples (ZRC2158 and ZRC3058, Figure 4.9) above this location while no such trend is seen on the thermocouples below this location (Figure 4.7 and 4.8). The drop in temperature may reflect the movement of material axially downward as the ceramic pool descended into the crust region and away from the thermocouples that were located opposite the pool region. Thermocouples sited on the tantalum liner below the level of the molten ceramic pool consistently show an increase in heatup rate coincident with the temperature perturbation cited above (Figure 4.7), again suggesting that hot material moved downward in the test section.

A set of thermocouples were placed at various axial positions at about the radial center of the radial ZrO_2 fiber insulator tube. The responses of these instruments are given in Figure 4.10. Despite some obvious "spikes" in the data for one thermocouple (ZRC1463), the data appear consistent. From the difference between the measured temperatures on the liner and in the insulator radially opposite the bottom of the debris bed, it is estimated that the peak radial heat flux here was ~120 kW/m^2. The DEBRIS code predicted a radial heat flux at the boundary of the debris bed of ~140 kW/m^2 and about 70 kW/m^2 at the cooling jacket boundary opposite the debris bed. The flux in the intervening insulation obviously must lie between these two numbers and 120 kW/m^2 is, thus, consistent with code estimates. (See Section 4.2.2.4 for a discussion of the energy balance.)

The temperatures above the debris bed at the top of the thoria lid (TLC3200) and inside the ZrO_2 upper insulator (ZRS3400) are shown in Figure 4.11. Both these thermocouples failed during the melt phase, but the peak temperature 1/3 of the way up through the fiber insulator was about 1800 K, which would suggest temperatures significantly lower at the top of the insulator.

Temperatures at various locations on or near the boundaries of the experiment package are displayed in Figures 4.12 to 4.14. The aluminum spacer thermocouples showed a peak temperature of about 430 K opposite the middle of the debris bed (Figure 4.12) and this is confirmed by thermocouples on the outside of the primary containment (Figure 4.13), which are essentially identical. This would indicate that late in the melt phase nucleate boiling was occurring in the upper regions of the cooling jacket. However, the bulk coolant temperature at the outlet of the cooling jacket was well below boiling. Temperatures near the top and bottom of the primary system appear in Figure 4.14. The highest boundary temperature, 500 K, was recorded at the top of the upper insulator (CPK3800).

Some additional interpretation of the measured data will be discussed in the context of the code analysis results.

4.2 MP-2 Analyses

4.2.1 Analysis Uncertainties

The critical parameters that dominate the uncertainties in the analysis of the MP-2 experiment are essentially of two types. The first involves the energy deposition rate in the test section both with respect to the overall power deposition and

to the spatial distribution of the power. This parameter is estimated by determining the appropriate "figure of merit" or "coupling factor" that correlates the reactor operating power to the time and space dependent energy deposition rates within the experiment package. The second key consideration is the transport properties of the materials used in the experiment.

The postexperiment estimates of the coupling factors were achieved by two methods. The first method involved using the thermocouple responses to step changes in the reactor power level to estimate local coupling factors. The second method entailed the use of neutronics codes that model the entire system including the ACRR to calculate both the overall regional coupling factors and the geometrical shape factors.

The thermocouple response method essentially involves using the change in heatup rate as measured by each of the thermocouples in the fueled regions together with appropriate heat capacities and known reactor power levels to calculate the local power deposition rate. When this information is compared for all the available thermocouples an estimate of both spatial and regional average coupling factors can be obtained. A somewhat more detailed description of these methodologies is given in Appendix A.

The thermocouple response method achieved results for the coupling factors over a number of power changes that were repeatable to within ~5% (at the 90% confidence level). The two neutronics codes that were used agreed to within 10% in the debris bed, 5% in the crust, and 16% in the rods. These numbers represent biases between the two codes. On average the biases between the neutronics codes and the thermocouple response method were on the order of 5% in the bed, and 10% to 40% in the crust and rods. The thermocouple response method appeared to agree more closely with the TWODANT code analysis than with the MCNP code analysis (see Appendix A for a description of these analyses).

The MP-2 experiment took the test section into a thermal regime that involved temperatures in excess of 3000 K. Thermophysical properties for even common materials in this temperature range can be difficult to estimate. A further complication is the physical and mechanical configuration of the key structures. The fission heated sections of the package were composed of mixtures of materials in various mechanical configurations, i.e., debris bed, compressed composite materials, and nonhomogeneous distributions (fuel rods). The insulating layers were composed of highly porous materials in association with inert gas (helium). Although thermal conductivities are generally available for most of the pure materials, radiation effects at high temperature together with porosity and mixing considerations must be taken into account.

The best available estimates for thermophysical properties were employed in the analysis (see Appendix A for a summary of the properties used in the analysis and the appropriate references). In addition, an iterative process in which heat input and measured heat losses were balanced against heat absorption in the package as well as heatup rates at various locations in the test section was used to confirm the transport properties.

The DEBRIS models include all the significant heat sources and sinks in the system. The actual measured reactor power was input to the code. Power deposition, in addition to the fission heating in the fueled regions, also included gamma heating of all the system structures with account taken for attenuation. Thermocouple measurements taken at appropriate locations within the cooling system allowed direct measurement of the heat rejection rate from the assembly and, together with the extensive thermocouple network within the package, facilitated a good characterization of the overall heat balance throughout the experiment.

4.2.2 DEBRIS Code Analysis of MP-2

Only a brief description of the DEBRIS code models is given here. A detailed description of the models in the DEBRIS code may be found in References 11 through 14 while a somewhat more extensive overview is presented in the MP-1 final report[10].

4.2.2.1 DEBRIS Code Description

The DEBRIS models were developed in response to the need for a computational tool capable of treating the coupled heat and mass transport phenomena within a rubblized multicomponent medium that is undergoing melting and freezing with material interactions occurring between several species over a range of temperatures. In particular, the DEBRIS model was designed to analyze the "late phase" processes for a debris bed configuration in a disrupted LWR core. The module employs the two-dimensional (r,z) geometry that is characteristic of the cylindrical configuration in a nuclear reactor core. The module solves the energy, continuity, and momentum equations to describe the dynamics of melting and material relocation in a debris environment.

It is important to note here that the application of the DEBRIS code to the analysis of the MP experiments required "tailoring" of some models to adapt the code to the specific physics, geometry, configurations, and materials associated with the experiments. Because the DEBRIS models were specifically designed for a rubblized reactor core configuration, a number of features in the experiment were not obtainable from the set of options available in the unmodified version of the module. Thus some of the DEBRIS models documented elsewhere have been modified.

The DEBRIS modeling accounts for the melting of typical reactor core constituents and for interactions between these materials. Heat exchange within the debris medium and with the appropriate structures in the reactor environment are modeled by accounting for conduction, radiation, and convective processes associated with the movement of relocating materials. At the boundaries of the test package, the heat transfer calculations are linked to an ultimate heat sink through a convective heat transfer coefficient. The ultimate heat sink in the case of the MP experiments is an annular cooling jacket or heat exchanger, which carries off the excess heat from the package. The energy equation includes an internal heat source that is both temporally and spatially dependent and is an essential consideration for simulating the effects of the neutronic buckling (neutron flux curvature) and self-shielding effects associated with fission heating in the experiment environment. Reaction heats and heats of fusion for the various interactions and transitions are also modeled.

The motion of materials, both liquids and solids, is treated. Molten debris is allowed to move within the debris bed under the influence of gravitational, capillary, and drag forces by using a modified Darcy law formulation to balance these forces and calculate flow velocities at control volume interfaces. Empirical models are included, which determine the magnitude of the capillary forces based on the wetting properties of the various molten constituents (liquid-to-solid contact angle), as well as models for calculating the effective permeability of the debris bed based on particle size, bed saturation, and a number of other physical parameters. A simple model is in place that provides for the vertical movement of solids within the debris bed based on a critical porosity criterion. A more complete description of the various models only briefly touched on here can be found in Reference 16.

Mass conservation is satisfied by tracking the locations and quantities of each of the species present in both the liquid and solid phases. The DEBRIS model used for the MP-2 analysis currently tracks seven basic constituents: uranium oxide (UO_2), zirconium oxide (ZrO_2), zirconium metal (Zr), iron (Fe), silver (Ag), indium (In), and tin (Sn). These are the primary materials found in most LWR cores, the silver, tin, and indium being associated with control materials. The transition of materials between the solid and liquid phases is accomplished through the use of a simplified phase diagram for the UO_2-ZrO_2 system. The MP-2 debris bed contained only UO_2 and ZrO_2, but the crust region contained all the aforementioned constituents. No attempt was made to account for interactions between all of these materials, rather each material was assumed to melt at its own specific melt temperature and the molten composite materials were assumed to be completely miscible.

A two-dimensional (r,z) finite difference grid was employed for all calculations. The solution of the momentum equations uses an explicit scheme that is uncoupled during a time step from the heat transfer calculations. For the heat transfer calculations, the experiment-analysis version of the module uses an implicit ADI solver. The ADI solver links in one large grid the entire thermally involved structural constituents of the experiment package including the three fueled regions of the package and the other key heat structures (insulating layers, melt barriers, and grid, containment, and cooling system structures).

The modified version of the conduction model has been verified through the premelt phase of the experiment by direct comparison with the TAC2D (see Appendix A for reference) calculations. The results are essentially identical to those obtained from the TAC2D calculations. The unmodified version of DEBRIS employs an explicit solver for the heat transfer calculations and features only a single heated debris bed region.

Modeling of heat transfer between the experiment package and the heat removal system for MP-2 was complicated by several factors. Although the coolant flow rate in the heat exchanger was well down in the laminar flow regime, the available correlations for local heat transfer coefficients did not apply. The standard correlations are specifically developed for an isothermal heated wall or for a constant wall heat flux. The conditions at the heat exchanger interface cannot be described by either of these configurations. The actual wall temperature as a function of axial location along the coolant flow path is not only variable, it is nonlinear. The wall temperature is, in fact, time varying and a rather complicated function of axial position. As a consequence it was necessary to develop a heat transfer correlation starting from first principles using an approximate integral technique to solve the boundary layer equations in annular geometry for a step increase in wall temperature. Then Duhamel's method was used to estimate the heat transfer coefficients for a variable wall temperature (see Appendix B for the formulation).

The MP-2 analysis was performed with a version of the DEBRIS code that was somewhat modified from the one used in the MP-1 analysis. Of particular concern in the older version of the code was the constant heat capacity constraint. The assumption of constant heat capacity greatly simplified the coding and the solution algorithm, but for the temperature range over which calculation are performed, the heat capacity of several constituent materials, the foremost being UO_2, are highly temperature dependent. The result was that an average heat capacity had to be selected and the power coupling artificially modified in order to achieve an energy balance. In the current version of the DEBRIS code the constant heat capacity constraint has been removed through the addition of temperature dependent enthalpy functions for each material. The energy balance in the system is now exact and no modifications to the coupling factors are required.

4.2.2.2 Comparisons of DEBRIS Thermal Analysis With Measurements

The DEBRIS code was the primary tool applied to the MP-2 analysis for both phases of the experiment including the heatup phase. The TAC2D code, however, was used extensively to baseline the DEBRIS code and to do parametric calculations particularly with respect to the heat transfer correlations and thermophysical properties that were subsequently adapted to the DEBRIS analysis of MP-2.

To facilitate discussion, the course of the experiment is somewhat loosely divided into three phases: the heatup, meltdown, and cooldown phases. The heatup phase could be defined as the period that starts from first application of ACRR power until the end of the final "plateau" when the power level was applied that took the experiment through the meltdown phase. However, for the purpose of describing the analysis it is more convenient to define the end of the heatup phase as the time at which incipient melting occurred in the debris bed. The analysis indicated that this took place at ~13,900 seconds when melting first appeared at a location close to the center of the debris bed. The meltdown phase extended out to ~19,870 seconds when the ACRR was shut down. The cooldown phase then extended to ~21,950 seconds when data acquisition was terminated.

Post-irradiation examination of the MP-1 test section showed that the debris remaining at the top of the debris bed was depleted in ZrO_2. This fact tends to support the hypothesis that melting in the debris bed did not proceed along the UO_2/ZrO_2 pseudo-binary equilibrium phase diagram. Rather, it is postulated that melting first occurred at the ZrO_2 melting temperature and that when sufficient molten ZrO_2 had formed to allow movement of the melt and wetting of the surrounding UO_2 particulate, the diffusion-limited process for the dissolution of the urania was initiated. The composition of the mixture then gradually approached the pseudo-binary equilibrium phase compositions as a limit.

Therefore, as was done in the MP-1 analysis, the present analysis for MP-2 consists of two basic melting scenarios.

The code has available two options regarding the UO_2-ZrO_2 melting process: the first constrains the binary system to melt along the pseudo-binary phase diagram, while the second forces the UO_2 and ZrO_2 system to undergo phase transitions separately at their respective melting points. The second model further assumed that there is no subsequent reaction between UO_2 and ZrO_2. This treatment clearly represents the opposite limit from the equilibrium phase diagram assumption. The actual physics lies somewhere between the two limiting cases with the system approaching the binary phase diagram composition for long times while more closely following the second model near incipient melting. A potential improvement to the DEBRIS code could be achieved by the addition of a diffusion model to treat melting kinetics. For the present analysis, however, the approach has been to run the code using both options to test the effects of each assumption and determine which more closely reproduces the observed results. The results that are presented below will include both model configurations with the pseudo-binary melting case referred to as ***Case-'A'*** and the case that used separate melting temperatures referred to as ***Case-'B'***. Because the thermal responses between the two cases are only marginally different, especially during the heatup phase, only the results of the thermal analysis for ***Case-'A'*** are presented here. The chief differences between the two cases involve the ultimate disposition of material in the experiment, so comparisons between the two cases are treated in the section on material relocation (Section 4.2.2.5).

To provide a general picture regarding the relative accuracy of the calculated thermal response of the test package, a set of plots of DEBRIS module predictions compared to actual thermocouple measurements is shown in Figures 4.15 through 4.42. Figures 4.15 through 4.23 represent the temperature comparisons with thermocouples located in the debris bed region. Figures 4.24 through 4.27 show the measured versus calculated temperatures for thermocouples in the crust zone. Comparisons of calculated and measured temperatures in the rod region and on the tantalum liner are given in Figures 4.28 through 4.33 and Figures 4.34 through 4.42 respectively.

During the heatup phase (0 to 13,500 seconds) there was substantial agreement between the calculated and the measured temperatures in the debris bed. The thermocouples at the bottom of the debris bed (DBC1400 and DBC1401 - Figures 4.15 and 16), although showing a trend in which temperatures were slightly underpredicted at lower temperatures and slightly overpredicted at higher temperatures, indicated maximum deviations of ~100 K. Quite good agreement was also achieved in this location during the melt phase. Neither of these two thermocouples displayed the characteristic failure mode (oscillations in the trace) until they approached the debris bed melt temperature (~2900 K). At this temperature both thermocouple traces "flattened out" while the calculated temperatures continued to rise. At 19,000 seconds when the power was boosted to 0.6 MW, both thermocouples, and particularly DBC1400, showed signs of gross failure. The calculated peak temperature at the bottom of the debris bed was 3350 K at the end of the test, which is consistent with the measured temperature trends if they are extrapolated from the thermocouple failure points.

The maximum deviations between measurement and prediction occurred for the DBC1601 (Figure 4.17) thermocouple located about 2 centimeters above the bottom of the bed. Here the calculated results appear to be biased 100 to 200 K lower than measured. This thermocouple was routed down through the middle of the debris bed where the highest temperatures occurred. It is likely that the temperatures at the location of the thermocouple junction were perturbed by the "fin effect" wherein heat is transmitted along the metal sheathing of the thermocouple from the hot region to the junction. The nearer the location of the thermocouple junction to the center of the debris bed the better is the apparent agreement between measured and calculated results. DBC1801 (Figure 4.18), which was below the midplane but closer to the center than DBC1601, although slightly lower than measured, showed good agreement until it failed at ~14,000 seconds. The best comparison during the heatup phase was achieved for the thermocouple at the midplane (DBC2100, Figure 4.19).

The calculated temperatures for the DBC1601 and DBC1801 thermocouple locations continued to rise and responded sharply to increased reactor power levels. Peak temperatures in the region of 3300 to 3400 K were predicteded, indicating that the thermocouples in these locations remained in direct contact with molten debris during the melt phase. The early failure of both these thermocouples also supports the conclusion that these devises remained in extended contact with molten ceramic. This also indicates that the extended contact with molten ceramic may have precipitated or accelerated thermocouple failure, which occurred somewhat earlier and more conspicuously for these two thermocouples than for any of the other debris bed thermocouples.

For locations that were initially sources of molten ceramic but which were voided after melting occurred (central regions of the debris bed, DBC2100, DBC 2102, DBC2103 and DBC2501 - Figures 4.19, 20, 21, and 22), the temperatures did not appreciably exceed 3000 K. This region was depleted of a heat source by the melting and relocation of material out of the zone and subsequently was heated primarily by radiation.

Small quantities of material were left clinging to the upper thoria liner at the top of the bed so that some heat source remained there, but the temperatures rolled over at higher location in the bed with the peak temperature approaching 2900 K at the 3/4 location (Figure 4.22) and only about 2800 K at the upper thoria liner interface (Figure 4.23). Calculations at both these locations were in substantial agreement with measurements.

The experimentally measured temperatures in the crust region of the assembly compare well with those predicted by DEBRIS for most of the heatup phase of the test. See Figures 4.24 through 4.27 for the temperature response comparisons in the crust region. At about 12,000 seconds, the calculated results begin to diverge significantly, with the calculated temperatures becoming progressively higher than measurements. It has already been noted that the comparison between measured temperatures is inconsistent in the crust region. The reliability of the thermocouples in this area has been called into question due to possible phase interactions between the thermocouple sheathing and wires and low melting temperature metals in the crust. The divergence between calculation and measurement for all four of the thermocouples in the crust (there were originally five with one failing at the beginning of the test) took place at ~12,000 seconds. At that point the crust temperature was above the melting point of the silver that was present in sufficient concentration in the crust to have affected thermocouple integrity if, in fact, such reactions took place. The calculated

temperatures in the crust continued to diverge from the measured temperatures in the melt phase until the crust thermocouples one-by-one underwent gross failure between 17,000 and 18,000 seconds.

An increase in the heatup rate can be seen at about 16,000 seconds in the calculated crust temperatures due to a power boost from 400 to 450 kW. This seems to be associated with the sudden relocation of molten metallic constituents out of the crust. This removal of metals and the associated increase in porosity of the crust resulted in an effective decrease in the crust thermal conductivity. This event can be seen clearly in the thermocouples in the rod region but was not detected by the crust thermocouples that may have been severely degraded at this point for the reasons already posited.

Rod region thermocouple versus calculation comparisons can be seen in Figure 4.28 through 4.33. Most of the thermocouples in this zone were type "K" chromel/alumel instruments. These thermocouples are normally accurate up to somewhat over 1600 K. Again, there was reasonably good agreement with calculations through most of the heatup phase. Divergence began to occur about 14,000 seconds at the beginning of the melt phase for those rod region thermocouples that were sited near the bottom of the crust (FRK1044 and FRS1000 - Figures 4.31 and 4.32) and this is consistent with the behavior of the crust region thermocouples. Note that FRK0531 (Figure 4.29) was producing anomalous readings at the beginning of the experiment and seemed to recover at about 11,000 seconds when it began responding to the reactor power changes.

The calculated temperature shows transient events in the locations of the two midrod-region thermocouples (FRK0514 and FRK0531 - Figures 4.28 and 4.29) at about 16,500 seconds, corresponding to the calculated arrival there of materials that relocated out of the crust at this time. This event did not appear in the FRK0514 data but oscillations are visible in the FRK0531 thermocouple data at this time and there are clear indications on both thermocouples (GSK0013 and GSK0018 - Figure 4.32 and 4.33) at the bottom of the rod region of the arrival of material at the top of the lower grid spacer. The DEBRIS calculations show material arriving at the bottom of the rod region almost simultaneously with the thermocouple responses. Thus there is good evidence that the DEBRIS code accurately predicts the release of materials from the crust, at least in terms of the timing of this event.

The final set of plots showing direct comparisons of calculated and measured temperature histories are those for the thermocouples sited on the outside of the tantalum liner and are presented in Figures 4.34 through 4.42. Except for those in the lower section of the package, ZRK0058 and ZRK0558, these were Type "C", bare wire W/Rh thermocouples. The thermocouple junctions were place in slots cut into the inside surface of the zirconia insulator tube such as to be either in direct contact with or very near the outside surface of the tantalum liner, but not bonded directly to the liner.

The calculations for the two thermocouples at the bottom of the test section ZRK0058 (Figure 4.34) and ZRK0558 (Figure 4.35) are virtually identical to the measured data. There is, however, a rather pronounced rise in heatup rate at about 19,600 seconds recorded on these thermocouple and in fact on all the liner thermocouples at the level of or below the molten pool that do not seem to be reflected in the calculations. This increase in heatup rate is partly due to the boost at 19,000 seconds that took the reactor power to 600 kW. However, there is a second increase in heatup rate that shows up more clearly on the thermocouples opposite the crust and debris bed regions as seen in Figures 4.36, 4.37, and 4.38 at ~19,600 seconds. This can be interpreted as the sudden relocation of the ceramic pool into the partly voided crust region. This interpretation is supported by the measurements on thermocouples near the top of or above the molten ceramic pool, namely, ZRC1858 (Figure 4.40), ZRC2158 (Figure 4.41), and ZRC3058 (Figure 4.42) that show a simultaneous decrease in heatup rate. The latter mentioned thermocouples, in fact, show a drop in temperature correlated with this event. The sudden movement of the pool as it slumped into the crust region essentially moved the heat source downward resulting in increased temperatures on the thermocouples toward where the source moved and a drop in temperatures for thermocouples away from where the material moved. There is some suggestion from oscillations on the GSK0018 thermocouple at this time (Figure 4.33) that some material from this event also reached the bottom of the rod region. This may have been metallic components that had relocated out of the crust earlier, solidified on fuel rods partway down and then remelted and flowed to the bottom coincident with this event. It may also be interpreted as representing material that was displaced out of the crust region as a result of the intrusion of molten ceramic. The DEBRIS calculations do show some downward motion, mostly of zircaloy, in this period (see Section 4.2.2.5 on material relocation).

The calculated temperatures reflect the history of material motion as predicted by the DEBRIS code for this case, which implies a more gradual penetration of the ceramic pool into the crust region starting at about 17,000 seconds. Thus the predicted liner temperatures run somewhat higher in the period from 17,000 to 19,500 seconds for the lower liner locations (Figures 4.37, 4.38, and 4.39) while agreeing very well with thermocouple readings that would not have been strongly affected by pool motion (ZRC1858 and ZRC2158 - Figures 4.40 and 4.41).

Although the debris bed thermocouples in general are degraded in terms of reading accuracy, there is somewhat equivocal evidence in these thermocouple data of the pool relocation event. The thermocouples, for example, that were located above the pool (DBC2100, DBC2102, and DBC2103 - Figures 4.19 through 4.21) show a clear drop in temperature at 19,500 seconds as does the thermocouple DBC1801 (Figure 4.18) that was located very near the top of the pool before it slumped. This thermocouple, in fact, may have been directly perturbed as the pool slumped down and perhaps was affected by the movement of gas bubbles upward through the pool that were formed perhaps in the pool slumping event and that are clearly visible in the PIE photographs.

In the interest of complete documentation and in order to provide a more cohesive picture of the overall performance of the DEBRIS code in modeling the thermal response of the MP-2 experiment two additional sets of graphs are included in this section. The first set of graphs (Figure 4.43 through Figure 4.52) give the axial temperature profiles for two radial locations, one along the radial centerline of the test section (r=0) and the other along the tantalum liner (r=5.8 cm). The calculated temperature profiles are shown by solid and dashed lines and the symbols represent the temperatures measured by thermocouples at the appropriate locations. The second set of graphs (Figure 4.53 through Figure 4.62) show the radial temperature profiles in the test section along the

axial centerline of the debris bed (z=39 cm elevation; see Appendix A for a map of the grid elevations). For the radial plots the measured temperatures were supplied by thermocouples DBC2100, DBC2102, DBC2103, ZRC2158, ZRC2163, ZRC2167, ALK2176, and TSKPCS2 (see Figure 2.5 for the positions of these thermocouples). The profiles are shown at 10 time slices during the course of the test starting at 6,600 seconds and ending at 19,870 seconds when the reactor was scrammed.

For the axial profiles, in general, the graphs show excellent agreement at all locations through the heatup phase of the test (0 to 13,500 seconds) at both the centerline and the tantalum liner. At entry into the melt phase, the calculated temperatures in the crust and rod regions begin to diverge from the measured data primarily due to thermocouple degradation and possibly to some uncertainty in the modeling of heat transfer in the rod stub region when radiation becomes the prominent heat transfer mode at about 1500 K. Also the thermocouples in the molten region of the debris bed have degraded by 15,600 seconds (Figure 4.48) and have fallen below the calculated temperature profile.

By 19,000 seconds (Figure 4.50) the crust thermocouples have all failed, but three of the debris bed thermocouples (near the top and bottom of the bed) tend to conform to the calculations while those exposed to molten ceramic have clearly degraded. At this time the calculated temperatures still agree well with the measurements on the tantalum liner, indicating that the calculated debris bed temperatures are probably reasonably accurate.

At the end of the test all of the thermocouples in the heated regions of the test section have degraded or failed (see Figure 4.52) except the one (DBC3000) at the top of the debris bed and the one at the bottom of the rod region (GSK0013). Calculations agree well with these two thermocouples and with the measured temperatures on the tantalum liner along the entire instrumented length of the liner.

The calculated radial profiles also show substantial concurrence with measurements in the heatup phase and divergence in the debris bed as thermocouple degradation proceeds in the melt phase. There were no measured temperatures in the thoria liner, but there is good agreement on the tantalum liner and the thermocouple on the aluminum spacer and the primary containment. The thermocouple at the middle of the fiber insulator at this elevation demonstrates excellent agreement through the entire test (i.e., Figure 4.62). Thus the radial profile starting at the cooling jacket interface and moving inward to the tantalum liner were apparently very well characterized in the code calculations and lend support to the calculated debris bed temperatures in both the heatup phase (Figures 4.53 through 4.57) and the melt phase (Figures 4.58 through 4.62).

4.2.2.3 Overview of DEBRIS Thermal Analysis

An overall assessment of the thermal response of the MP-2 test section can be obtained from a final collection of graphs that demonstrate in a more pictorial form the heatup of the test assembly taken as a whole. These illustrations are presented in Figure 4.63 through Figure 4.72. They consist of temperature contour plots that show the isotherms in the test section at 100 to 200 K temperature increments and at 10 time slices through the experiment. The time slices presented are the same as those in the previous section and those presented in the sections on material motion so that these "snap-shots" in time of temperature and material disposition can be easily compared.

In these temperature maps, the x-axis represents the radial direction starting from the centerline of the test section at the left and extending out to the cooling jacket at the right. The y-axis represents the axial (vertical) direction with the zero elevation at the bottom corresponding to the bottom of the secondary containment, and, although all the structures are not identified in the map, the top of the primary system (the plunger plate; see Figure 2.2) is at the 57.4 cm location on this axis. The dashed lines identify key boundaries in the test package with the debris bed, crust, and rod stub regions specifically labeled. What is shown, then, is one-half of the experiment cross section through the center, the other half would be a mirror image extending to the left.

Note that all the time slices in these "snap-shots" are chosen to correspond to the end of a period at which the power has been maintained constant for an interval sufficient to bring the test section essentially to a condition of steady state. Thus, each "snap-shot" represents a fairly stable nontransient thermal state.

Figure 4.63 shows the system thermal configuration at 6600 seconds near the end of the 4th steady-state period (see Figure 4.1 for the power level settings). At 6600 seconds the temperature in the center of the debris bed is in excess of 1400 K and about 1000 K near the debris bed boundaries. By the end of the 5th equilibrium period at 7900 seconds (Figure 4.64), the debris bed boundary isotherm has reached 1200 K and a 1600 K isotherm extends out to within ~2 cm of the top and bottom of the debris bed. The crust lies mostly between the 900 and 1000 K isotherms so that the low melting temperature metals in the crust, tin and indium, have melted.

A 2000 K isotherm has developed near the center of the debris bed at 9500 seconds (Figure 4.65) and the top of the crust lies at the 1200 K isotherm indicating that silver is just beginning to melt at the crust upper surface. The parallel isotherms to the right of the debris bed are becoming denser indicating the increased temperature gradient in the radial insulator. At 12,000 seconds after a rather extended period at 200 kW, the center regions of the debris bed are somewhat over 2400 K as seen in Figure 4.66, and the preformed crust is between 1200 and 1400 K. At this temperature the metallic silver is completely melted. There is still insufficient molten metal, however, to form a continuous liquid phase; no melt has left the crust at this stage.

Figure 4.67 shows the time slice at 13,500 seconds, which represents the last of the heatup phase steady-state periods before the power was boosted to 400 kW and the test taken into the melt phase. Here the 2600 K isotherm in the debris bed indicates the temperature at the debris bed center is near 2800 K and only about 100 K below the melting temperature for the UO_2-ZrO_2 binary system (these plots are for the phase diagram melting scenario, Case-"A"). At this stage, the top of the crust lies between the 1400 and 1600 K isotherms, indicating that steel is nearing its melt temperature at the top of the crust (iron melts at ~1800 K).

After operating the reactor at 400 kW for about 2000 seconds (15,600 second time slice) the test section approached a steady-state condition in which melting had occurred in the central portions of the bed, a molten pool had formed inside

the 2800 K isotherm as seen in Figure 4.68, and a substantial voided region had been created above the pool. Half of the crust at this point was above 2000 K and the steel, therefore, was predicted by DEBRIS to be completely melted. The zircaloy melting temperature had not yet been achieved at this stage (the temperature at the upper surface of the crust was at 2200 K) and even with the steel completely molten, there was insufficient melt present to comprise a continuous liquid phase (assumed to occur at 30% liquid volume fraction). Therefore, the molten phase as predicted by DEBRIS, remained immobile within the crust at this time slice.

With no indication that temperatures were continuing to rise in the test section at 15,600 seconds, the power was again boosted to 450 kW and the reactor operated at this level for about 900 seconds. Figure 4.69 shows the contour map at the end of this period (16,500 seconds). The 2800 K isotherm had extended out to include most of the lower half of the debris bed with the molten ceramic pool approaching the top of the crust. Figure 4.69 shows a 2200 K isotherm extending down into the crust near the radial centerline. This is the melting temperature of zircaloy. With the presence of the previously melted constituents, only partial melting of zircaloy was necessary to raise the melt volume fraction up to 30% so that sometime between the 15,600 second and the 16,500 second time slices molten material was predicted to be released from the crust region into the underlying rod region.

The reactor power level was adjusted to 500 kW shortly after the 16,500 second time slice and maintained at this level until about 19,000 seconds. The temperature contour at 19,000 seconds is shown in Figure 4.70. At this time a new steady-state condition had been established with a well defined molten pool approximately coincident with the 3000 K isotherm and extending perhaps one third of the way down into the preformed crust at the radial centerline. Almost the entire debris bed region above the pool was at or above the 2800 K isotherm so that only at the upper boundary of the debris bed and particularly at the upper radial boundary did there remain unmelted debris.

The last two contour maps (Figures 4.71 and 4.72) show the results of the final power boost up to 600 kW. At 19,600 seconds (Figure 4.71) the pool temperature had increased to include a 3200 K isotherm and the pool had advanced downward to nearly the middle of the crust. When the reactor was shutdown and the test terminated at 19,870 seconds a thermal steady-state condition had probably not yet been achieved, and there were indications in the thermocouple data that some material motion was occurring. The calculations show the pool to be above 3300 K and to have reached the middle of the crust near the radial center and formed a retaining ceramic crust about half way down in the preformed crust region. Little if any additional melting had occurred in the region above the void.

The Case-"B" results produced a slightly different thermal profile. A comparison of the thermal profiles for Case-"A" and Case-"B" at the end of the test is provided in Figure 4.73. The chief differences involve higher temperatures in the debris bed region and slightly lower temperatures in the crust and rod regions for Case-"B". The higher debris bed temperature is due to the higher temperature required to achieve initial melting (the melting temperature of pure ZrO_2, 2973 K, rather than the binary melting range). The higher melting temperature indirectly favors lower temperatures in the crust region by inhibiting the penetration of the ceramic melt front into the crust region (the ceramic crust advanced downward slightly less in Case-"B"). The liner temperatures for the two cases are also compared to the measured temperature in this figure. Although the Case-"B" tantalum liner temperatures are slightly higher opposite the debris bed, the measured thermal data does not appear to favor one of the cases over the other.

4.2.2.4 Overall Energy Balance

Three key pieces of information, which include the test assembly heatup rate, heat loss rate, and overall estimated heat generation rate, comprise a closed and consistent set of elements for characterizing the overall energy balance of the system. If one of these pieces of information is significantly in error, the effect should be seen in at least one of the other factors. Thus the heat loss rate is a particularly important measurement and, in combination with the thermocouple data and the coupling factor analysis, provides confirmation of the overall system energy balance.

As described in Section 2.6, the heat rejection rate was determined experimentally in a rather straightforward manner by measuring the inlet and outlet coolant temperatures together with the coolant flow rate. Figure 4.74 compares the measured heat rejection rate to that calculated by the DEBRIS code for Case-"A". Case-"B" is essentially identical to Case-"A". The calculated heat loss rate is nearly identical to the measured rate during the heatup phase and appears to be slightly overpredicted during the melt phase. The integrated difference can be seen in Figure 4.75, which shows the total energy rejected from the test package into the coolant and the difference appears to be about 7% (104 MJ measured compared to 111 MJ calculated at the end of the test). The small discrepancy here may be due to changes in the effective coupling factors as material melted and began to move around in the test section.

The calculated energy input rates include fission heating ($Q_{fission}$) in the fueled regions and gamma heating (Q_γ) in the surrounding structures. The total calculated input power is then given by,

$$Q_{intot} = Q_{fission} + Q_\gamma \qquad (4.1)$$

A more detailed inventory of the energy distribution was obtained by integrating the various rate components shown and including the energy stored as sensible heat and heats of fusion in the fueled zones and in the surrounding structures. This information is graphically depicted in Figure 4.76. This graph represents the energy balance for the system and shows the total sources as compared to the energy lost from the system through the coolant and the energy stored as sensible heat and heat of fusion. Conservation of energy requires that the total energy input to the system be equal to the sum of the stored energy plus the energy rejected by the cooling system,

$$\Delta H_{fission} + \Delta H_\gamma = \Delta H_{fuel} + \Delta H_{struct} + \Delta H_{loss} \qquad (4.2)$$

In terms of the DEBRIS code internal heat balance, these two components are in quite good agreement. This can be seen by comparing the **Gamma + Fission** curve (labeled ***"TOTAL ENERGY INPUT"***) with the **Stored + Loss** curve (labeled ***"TOTAL ENERGY STORED AND LOST"***) in Figure 4.75. These curves are so nearly the same that they

can not be distinguished in the figure. Also seen in Figure 4.76 are the energy stored in the system and the heat lost to the coolant. In terms of the total energy input to the system during the test (132 MJ), only 16.7% (22 MJ) was actually stored in the system at the point of reactor shutdown. The remaining energy was rejected to the coolant (110 MJ)

Heat fluxes in the experiment package were quite high due to the large energy deposition in a relatively small volume. The heat fluxes at the debris bed, crust, and rod region radial boundaries at the end of the test were 140, 125, and 50 kW/m^2, respectively. The peak downward axial heat flux at the lower surface of the crust was ~190 kW/m^2 while the peak at the lower surface of the rod region was ~230 kW/m^2.

The heat transfer rate into the coolant at various elevations along the length of the cooling jacket as predicted by the DEBRIS code reveals the overall heat flow pattern in the package near the end of the test. The mean cooling jacket heat transfer rate as predicted by the code was established for five segments along the cooling jacket interface: (1) from the coolant inlet to a location opposite the bottom of the rod region, (2) the length opposite the rod region, (3) the length opposite the crust region, (4) the length opposite the debris bed, and (5) the length opposite the region from the top of the debris bed to the upper primary containment boundary. Table 4.1 shows the average heat transfer rates to these five segments of the cooling jacket at the end of the test in order of the zone number defined above. The highest heat transfer rate into the heat exchanger was, of course, opposite the debris bed with ~45% of the heat entering the coolant in that segment. It is interesting to note that, in total, 80% of the heat flowed radially outward to the cooling jacket and 20% flowed downward into the lower grid spacer (heat sink) and from there into the lower segment of the cooling jacket.

Several modifications in the DEBRIS code models have resulted in improvements in the overall accuracy of the thermal results compared to that obtained in the MP-1 analysis. The primary improvement involved removing the constant property constraint that was responsible for a systematic bias in the MP-1 analysis and which required artificially high coupling factors to achieve the correct thermal response. Improved thermal transport in the debris bed porous media model also resulted in improved code results.

The performance of the DEBRIS module with respect to the MP-2 thermal analysis as judged from the comparisons with measured data is assessed to be quite good. In terms of heat transport processes, the code is mechanistic and the predictions appear to be in substantial accord with both the temperatures measured during the experiment and with the overall heat balance including heat sources, stored energy, and heat loss rates.

4.2.2.5 DEBRIS Analysis of Material Motion

4.2.2.5.1 Uncertainties and Modeling Considerations

The MP experiments are by necessity contained within completely enclosed capsules with no visual diagnostics available during the course of the experiments. Therefore, information regarding the evolution from the original configuration to the final configuration must, in large measure, be interpolated from only two data points, the initial condition and the end condition. There are aspects of the actual processes that take the system from the initial state to the final state which are clearly stochastic in nature. That is, the final configuration can be achieved along a number of possible paths (through a series of intermediate states). Which path was the actual one is uncertain and subject to random variables. Temperature measurements at key locations in the experiment supply pertinent information that help to reduce the uncertainty, but do not supply completely unambiguous information about the movement of materials in the test section. Temperature measurements do not supply sufficient information to completely characterize the evolution of the intermediate configurations.

As an example, a relatively large agglomeration of solid debris may be held in place by a set of perhaps tenuous "connections" or bonds to a surface or a larger mass within the debris bed. Predicting the time and mode of failure of these "connections" is probably not possible, but the result of the collapse or movement of a consolidated "chunk" of material may be significant in terms of the resulting change in configuration of the system. Small variations or asymmetries in actual power distribution resulting from, for example, small nonuniformities in UO_2 particle concentration or distribution may have significant effects on the end condition. Such nonuniformities are clearly unavoidable. Nonuniformities are inherently present by virtue of the medium under consideration, a particulate medium with a distribution of particle sizes, and nonuniform shapes.

Another source of nonuniformity is the presence of thermocouple assemblies routed through the debris bed. The thermocouple assemblies not only provide a local perturbation in fission heating, but may provide cooler surfaces to which materials may attach.

The primary point to be made here is that it is unlikely that a deterministic model for the movement of a combination of fluids and debris in the form of particles and thermally fused or consolidated agglomerations of particles can be achieved. Perhaps the best that can be done is to employ an approximate model that moves solids in the debris bed in a punctuated fashion based on a set of "reasonable" criteria.

At least three parameters are particularly important in predicting the disposition of materials within the debris bed. These three key parameters are the spatial distribution of the power deposition in the debris bed, the criterion for moving solids within the melting debris matrix, and the assumptions regarding the melting process.

For experiment analysis the actual distribution of power deposition in the debris bed as UO_2 melts and begins to move is coupled to the geometric shape factors that are in turn also affected by the motion of the heat source. Although it is not difficult to track the location of UO_2, the effects on the power coupling geometric shape factors as the heat source moves is effectively impossible without directly coupling a neutronics code. The overall effect in MP-2 is exacerbated by the very pronounced radial shape factors but mitigated by the small size and effectively one-dimensional character of the experiment. In full scale reactor analysis, shape factors are unimportant and tracking the movement of fuel bearing materials and correctly applying their individual contribution to the local heat source is the chief requirement. Thus the elimination of shape factors in reactor analysis is a considerable simplification over the considerations necessary in experiment analysis.

Such parameters as liquid-to-solid contact angle and other parameters that affect the rate of fluid motion through the debris matrix appear to adequately model fluid transport. However, the movement of solid debris within a melting debris bed matrix is a daunting problem. The problems associated with modeling the motion of debris in a melting particulate environment are numerous. If the types of processes that result in the agglomeration of particles (such as sintering or the "gluing" of particles by resolidification of previously molten debris) were not operating (this is probably never the case in a medium that is undergoing phase changes), models based on empirical information could be utilized to achieve a reasonable "correlation." Such a model, for example, might take into account empirical data that relates particle size, density, saturation, and fluid motion to determine the "angle of repose" of a debris bed. This type of model could then account for radial motion of solid debris. Because the DEBRIS model for solid particulate relocation limits the movement of solids to vertical motion between control volumes, it prevents the lateral motion of solids that would be expected to occur due to gross particle concentration gradients (resulting, for example from preferential melting near the center of the debris bed). The result is that the calculations may not reflect the complete range of motion that is likely to occur in the debris bed environment.

On the other hand, when agglomeration processes are included, which depend on a number of conditions within the bed, the debris medium will no longer behave like a loose collection of particles. In this alternate configuration the debris may behave much more like a rigid structure or like a collection of much larger particles. Complicating the problem is the likelihood that these two configurations, and perhaps others, will be present at the same time in different parts of the debris bed. The "rigid structure" configuration would not require an "angle of repose model," but would require a model that could specify a critical porosity above which a rigid structure could not support itself from above through "necks" or "connections" with more structurally stable masses or surfaces.

The solid relocation model in DEBRIS for the MP-2 analysis assumes that an agglomeration process will be operating subsequent to incipient debris bed melting. Relocation of debris is then allowed to occur only in the vertical direction (downward under the influence of gravity - with no radial component). The criterion for which solid debris is allowed to move is based on a user specified "critical porosity." Thus debris motion from one control volume to the one below it can occur if two conditions are satisfied: (1) the porosity of the "donor cell" is at or above a critical porosity, and (2) the "receiver cell" is above a specified porosity. A third condition specifies that the movement of solid debris into a control volume cannot reduce its porosity below the second critical value, which is currently set to be the original porosity of the bed. That is, the porosity of a control volume cannot be reduced below its initial value through the mechanism of solid debris settling. Of course, resolidification of molten material can reduce the porosity in a control volume to zero.

In terms of the third key parameter that affects material motion, the melting process itself, the tack taken in the MP-2 analysis was to scope the limits of the process. The kinetics of the diffusion driven dissolution of UO_2 by molten ZrO_2 is a higher order process, and is currently not incorporated in the DEBRIS models. The scoping of this effect was achieved by exercising the code with melt models that probe the two limits of the process. The first limit involves the assumption that diffusion is ***instantaneous*** and the process effectively follows the equilibrium phase diagram for the UO_2/ZrO_2 system. This corresponds to the ***Case-"A"*** configuration. The second limit assumes that diffusion is ***infinitely slow*** and that the two components do not effectively interact so that each component melts at its respective melting temperature and is not effected by the presence of the other component. This configuration is modeled in ***Case-"B"***.

4.2.2.5.2 Results of Ceramic Melt Relocation Analysis

Before discussing the comparisons between the end-point conditions predicted by the DEBRIS code and those estimated from the PIE findings, it will be enlightening to first review the evolution of the debris bed configuration (time history of the debris bed material dispositions) as predicted by DEBRIS.

Calculated results that show the phase volume fractions for Cases-"A" and -"B" are shown in Figures 4.77 through 4.85 and 4.86 through 4.93 respectively. Six separate time slices are shown in these graphs, which encompass the meltdown phase of the experiment. These correspond to the same time slices during the melting phase at which the thermal profiles were presented. The calculated volume fractions are depicted at each of the centerline nodes within the heated section of the test section starting at the bottom of the rod region and ending at the upper thoria liner (top of the debris bed). For both Case -"A" and Case-"B," the first six graphs shown are for gross material disposition along the radial centerline of the test section at the respective time slices followed by three additional disposition profiles at three different radial locations taken at the end of the test. The gross disposition of material in the test section predicted by DEBRIS is described in the figures by showing the volume fractions of the solid and the liquid that occupy each control volume along the axial trajectory that is taken. The first set of plots, those along the radial centerline, therefore, represent the average disposition of material in control volumes that are the shape of disks with a diameter of ~2 cm and with an average height of ~0.6 cm (30.1 cm by 51 axial control volumes). The disposition profiles shown at the other radial locations obviously represent the material disposition in ring-shaped control volumes with the same thicknesses as the corresponding disks. The outer ring for, example, is about 0.15 cm thick in the radial direction with a radius of ~4.35 cm. Note that the radial nodalization in the DEBRIS code model is "equal area" in the debris region so that the control volume radial thicknesses decrease with radial location.

Figure 4.77 shows the Case-"A" disposition of material at the 13,500 second time slice just prior to entering the melt phase. Because this time slice is before incipient melting in the debris bed, and since nothing had moved out of the crust region at this time, the Case-"B" configuration is identical to Figure 4.77 and is, therefore, not shown. It will be recalled from the thermal analysis that the preformed crust at this time was above the silver melting point but below the iron melting point. This is reflected in the crust configuration in Figure 4.77, which indicates a liquid volume fraction of about 9% in the crust. Note that the debris bed had an initial solid fraction of ~51%, the rod region about 41%, and the crust about 91% (before In, Sn Ag melted --82% + 9%)

At the end of the first melt-phase period (first power setting in the melt phase) when the reactor power was set at 0.4

MW, 15,600 seconds (Figure 4.78), a molten pool was predicted to have formed with a depth of about 2 cm and with the top of the pool located ~4.7 cm above the top of the crust. At this time a ceramic crust is predicted to have formed with the top surface somewhat over 2 cm above the preformed crust and extending down to ~1/2 cm from the top of the preformed crust. A zone at the top of the bed with the initial bed configuration remained at this time and a mostly voided region nearly half the axial height of the debris bed at the radial centerline had appear above the molten pool. The temperature of the crust at this time was above the iron melting point and the top of the crust was at the zirconia melting point. This is reflected in the liquid disposition in the crust, which shows the melt fraction in the crust at ~19%. The remnant solid material seemingly suspended in space in the voided region is an artifact of the solid relocation model and is transient in nature.

By the end of the second melt phase (see Figure 4.79) at 16,500 seconds (0.45 MW power setting), the material in the upper section of the debris bed had been reduced by about a third from the previous time slice and the pool had extended downward another centimeter for a total depth of about 3.5 cm. The bottom of the ceramic crust at this point is shown to be approximately 1/2 cm above the top of the preformed crust but is significantly thinner. The molten metal that had occupied the crust region is shown to have relocated into the rod stub region and partly resolidified there.

Figure 4.80 gives the disposition at the end of the third melt phase (0.5 MW power setting ending at 19,000 seconds). Perhaps slightly over 1 cm of unmelted particulate remains at the top of the bed, the pool has extended about a third of the way down into the preformed crust region, and the pool is indicated to be somewhat in excess of 5 cm deep. The bottom of the ceramic crust lies ~1/2 of the way down from the top of the original preformed metallic crust. The configuration at this point looks very much like the actual end condition of the test section as seen in the PIE.

The following two graphs, Figures 4.81 and 4.82 show the Case-"A" configuration near the end of the test. At 19,600 seconds the ceramic crust at the center of the preformed metallic crust region was predicted to have thinned to less than 0.5 cm with a corresponding increase in pool depth. At the end of the test, the DEBRIS code predictions for Case-"A" indicate that the bottom of the ceramic crust had remained at the same location as in the 19,000-second time slice, and this end configuration corresponds very well with the actual end-of-test configuration with the maximum penetration extending to about halfway into the preformed crust zone.

Figures 4.83 to 4.85 show the Case-"A" end-of-test material disposition for three other radial locations. At the 2.09-cm radius (Figure 4.83), the ceramic crust had also moved down to the center of the preformed crust, and at the 3.27 cm and 4.28 cm locations the ceramic crust penetrated to the middle and slightly above the middle of the preformed crust, respectively. Thus the DEBRIS model for Case-"A" predicts penetration of the ceramic pool to about the central elevation of the blockage and extending out to the radial boundary of the blockage with little dependence of downward penetration on radial location and no deposition of debris bed material below the original position of the preformed crust. The PIE also did not show penetration of the molten ceramic more than about halfway down into the crust at any radial location in the crust.

Figure 4.86 details the material distribution for Case-"B" at 15,600 seconds. This figure should be compared to its counterpart for Case-"A" (Figure 4.78). The essential differences are a somewhat shallower molten pool that actually was still a slurry at this point, a less extensive voided region, and a thinner ceramic crust that did not extend downward as far as in Case-"A." These observations are due primarily to the fact that melting started a little later for Case-"B" since in the absence of interactions between UO_2 and ZrO_2 incipient melting occurred at the ZrO_2 melting temperature (2973 K) rather than at the solidus of the UO_2/ZrO_2 system (~2900 K or less).

At the 16,500-second time slice, Figure 4.87, the Case-"B" distribution profile (compare to Figure 4.79 for Case-"A") indicates a shallower molten pool and slightly thicker ceramic crust with the top of the molten pool slightly higher and the downward penetration of the ceramic crust ~1 cm less than for Case-"A". The 19,000-second profile shown in Figure 4.88 indicates the ceramic crust to be approximately coincident with the top of the preformed crust while the Case-"A" profile (Figure 4.80) shows the crust to have penetrated halfway into the preformed crust. Note that the release of the molten metallic components from the crust into the rod region occurred some time after the 16,500-second time slice in Case-"B" whereas this event occurred somewhat before this time in Case-"A".

The end-of-test distribution profiles shown in Figures 4.89 and 4.90 place the bottom of the ceramic crust very near the axial center of the original preformed crust at the radial centerline of the test section (Figure 4.90).The ceramic crust is thicker than the end condition for Case-"A", indicating that it had just reformed at this elevation and had not yet had time to remelt. This is apparent from the position and thickness of the ceramic crust at the previous time slice (Figure 4.89) Thus the movement of the pool into the underlying preformed crust appears to have occurred rather abruptly when the pool encountered this partly voided region. This conclusion is suggested by the relatively large incremental change in the position of the crust between 19,600 and 19,870 seconds (Figures 4.89 and 4.90).

Again, a comparison of the four graphs shown in Figures 4.90 through 4.93 provides a description of the way in which the axial distribution of material in the test section varies with radial location for Case-"B". These graphs should be compared to Figures 4.82 through 4.85 for the material dispositions at the same times and radial locations for Case-"A." The figures suggest a similar shape for the bottom surface of the ceramic crust for Case-"B," that is, very slight variation in the location of the bottom of the ceramic crust with radial location. The Case-"B" end configuration could probably not be differentiated from the Case-"A" configuration after resolidification of the molten pool since, although the molten pool extended down further in Case-"A", the crust was thinner and the bottom surface of the ceramic crust was located at nearly the same place for both cases.

Taken together the results of the thermal analysis and the coupled relocation analysis seem to imply that the Case-"B" model in which UO_2 and ZrO_2 are assumed not to interact in the melting process did not achieve better agreement with either the measured temperature profiles or with the end-of-test configuration of the test section. In terms of gross material disposition, it can be concluded from the foregoing that the overall dynamics of the molten ceramic pool as well as its interaction with a preformed crust is not particularly sen-

sitive to the assumptions regarding the details of the melting model.

4.2.2.5.3 Results of Metallic Melt Relocation Analysis

The relative distribution of the various component chemical species is a function of their affinities and of the dynamics of their interactions during the overall gross redistribution process. Although Case-"A" used an equilibrium interaction model for the UO_2/ZrO_2 interaction, because of the complexity involved in determining all the possible interactions between the eleven atomic species involved, both Case-"A" and Case-"B" modeling neglected all interaction between species other than UO_2-ZrO_2. Thus, the relative timing of the relocation of specific components within the test section was based on their melting points (and, of course, on the critical porosity discussed above). This simplified modeling leads to a sort of "liquefaction" whereby species are separated and stratified according to their melting points. This type process may occur in reality but with the difference that stratification would be expected to occur with layers of associated (interacted) species rather than layers of pure species. The degree to which species stratification occurred would be a measure of the utility of the species-specific relocation model, although a counter-indicator for the species specific model would not necessarily negate the utility of the gross relocation model.

The species-specific material dispositions as predicted by the DEBRIS code for Cases "A" and "B" are shown in Figures 4.94 through 4.97, respectively, for the five primary components UO_2, ZrO_2, Zr, steel, and Ag. It has been assumed that the components of steel remained associated but have a single melting point, the melting point of iron, rather than a melting range as would actually be the case. These distributions are shown in axial profile and correspond to the disposition along the radial centerline of the package. The profiles at other radial locations differ accordingly. The extended penetration of the ceramic pool in Case-"A" is clearly seen in the distribution of UO_2 and ZrO_2 (Figures 4.94 and 95). For Case-"A" the UO_2 and ZrO_2 penetration is coextensive having penetrated down to the middle of the preformed crust. Species stratification is observed between the UO_2 and ZrO_2 in Case-"B" where UO_2 has penetrated only about a third of the way into the preformed crust while the lower melting point ZrO_2 has penetrated slightly over halfway into the crust so that the ceramic crust is essentially pure ZrO_2. The retarded ceramic pool penetration rate seen in Case-"B," attributed primary to the higher effective melting temperature, may be magnified by the fact that the motion of UO_2 is retarded relative to that of ZrO_2. Since the heat source is specifically associated with the UO_2 (by neutronic heating), heating at the crust boundary is likewise retarded (there is no UO_2 in the ceramic crust near the lower boundary) in the Case-"B" scenario thus somewhat inhibiting the rate of downward pool penetration compared to Case-"A".

Figure 4.96, which shows the distribution of zircaloy, indicates that this component has been completely relocated out of the preformed crust with the center of mass being at essentially the same elevation for both Case-"A" and Case-"B" (24 cm). For the still lower melting temperature steel, Figure 4.97, both cases place the entire mass about 2 centimeters above the grid spacer. Again, recall that these profiles look somewhat different at the other radial locations with the center of mass being slightly higher with increasing radial distance from the radial centerline. The low melting point components, indium and tin, were predicted in both cases to have been relocated to the top of the grid spacer, the tin and indium having remained liquid while the silver (Figure 4.98) resolidified very near the top of the grid spacer (19 cm).

Rough estimates of the volume of material that was relocated out of the preformed crust were obtained from photographs of the axial cross-sectional cuts made in the test section during the PIE. These estimates indicate that somewhat more than 23 cm^3 of metallic looking material was relocated to the rod region. The total metallic inventory of the crust including the zircaloy in the rod stubs was about 104 cm^3 with about 60% of this volume consisting of zircaloy. These numbers seem to indicate that chemical interactions wherein oxygen was transferred from UO_2 to some of the metallic species (probably mostly zirconium) took place on a rather significant scale and that much of this material did not relocate. If the entire inventory of zirconium in the crust formed a high melting point α(UZr)O phase and remained in the lower half of the crust region, the remaining metals would occupy a volume of ~40 cm^3. This still represents a shortage of about 17 cm^3 and would seem to imply that either some of the other metals also were partly oxidized, were trapped in pore structure of the crust, or were incorporated into the ceramic pool.

A comparison of the disposition of material (in terms of the porosity) in the two calculated cases to a rough estimate obtained from the PIE photographs is shown in Figure 4.99. The overall disposition of mass for the end-of-test configuration as calculated by the code is in qualitative agreement with region-averaged disposition estimated from the PIE. The amount of material at the upper region of the debris bed is roughly the same. The top surface of the molten pool sits higher by somewhat over a centimeter in the PIE but this is primarily due to the significant amount of pore space that exists in the resolidified pool region (see Figure 3.7) caused by the large gas bubbles that were trapped at the time that the pool solidified. The code does not currently model the motion of gases in the system.

The code predicted an essentially complete exodus of all the metallic components of the preformed crust with the result that the lower half of the original crust region shows as being much more porous than is indicated by the PIE (the PIE results in Figure 4.99 are labeled "MEASURED"). The rod stub region can be divided into two roughly equal zones in terms of the PIE results. The upper zone is more porous (~0.5) than the lower zone (~0.25). The profiles given for the PIE results in Figure 4.99 do not show any of the detail of the porosity profile, but the net result compared to the calculations is that the code indicates an overall lower porosity (more material deposited) in the upper half of the rod region and higher porosity (less material deposited) in the lower half of the rod region. The implications from the two points stated above are that the code overpredicted the quantity of material that relocated out of the crust and underpredicted the downward penetration of that material into the rod region.

Because the species sampling performed in the PIE was done for specific selected sites in which weight fractions of the constituents were obtained mostly for interacted material and do not include the cladding and fuel pellet components, it is difficult to make numerical comparisons with the calculations. The code deals with a homogeneous composition, that is, the fuel rods, cladding and ingressive material in the rod region, for example, are completely mixed in each con-

trol volume. To adjust the mass fractions obtained from the local PIE measurements requires that the densities of these components be known. In fact only the mass fractions are known. A further complication is that the oxygen is distributed between the various components in uncertain proportions so that the molecular species and, therefore, the species individual densities are uncertain. Also, in the partly voided section of the crust region (lower half) the actual density of the remnant material is not known so that again the fuel rod components cannot be factored in to compare directly with the code results. However, there are several qualitative comparisons that can be made between the PIE and the code results.

A key observation from the PIE is that there was significant phase interactions between the components of the preformed crust. The PIE reveals at least 12 separate phases within the relocated metallic components, for example. The result was that lower melting components were associated with higher melting point components, which depressed the effective melting range and resulted in a greater degree of mixing of these components as well as enhanced penetration of the higher melting components downward into the rod region. The component most affected was zirconium, which seems to display no significant stratification in the rod region, and in fact, the lowest section of the rod region was considerably enriched in zirconium presumably from dissolution and incorporation of rod cladding as the melt flowed downward along the fuel rods. The code, because of its non-interaction modeling, resolidified the zirconium higher up in the rod region with no penetration of zirconium lower than ~3.5 cm from the bottom of the rod zone. A second and perhaps equally important contribution to the DEBRIS code treatment of the redistribution of materials is the assumption of local thermal equilibrium. This model does not account for the possibility that fast moving materials may not reach equilibrium in each control volume as they flow downward, and thus will penetrate somewhat farther than would be predicted by the thermal equilibrium model.

The crust remnant, although in most cases depleted significantly (in terms of mass fractions approximately a factor of two lower but even lower in terms of actual masses) in the low melting temperature components, still retained considerable amounts of these constituents including silver, tin, indium, iron, and particularly zirconium. The code retained only trace quantities in the lower preformed crust region. This behavior was unexpected and is not well understood. There are probably two effects that influence this behavior. The first involves the capacity of the unmelted matrix to retain molten components. This is affected mostly by the wetting characteristics of the melt. In terms of code modeling, although critical saturation parameters can be applied to restrict the motion of fluid in the Darcy law formulation, these cannot be set for separate components which, of course, may have entirely different wetting characteristics. The critical saturation parameters, however, can be adjusted in the code to retain overall a larger fraction of the metallic components in the remnant crust.

Probably a more significant consideration is the large quantity of zirconium metal that was retained in the lower crust region at temperatures that are clearly above its melting point. Fifty percent of the crust remnant (not including the UO_2 in the fuel rods) was composed of zirconium. This is a larger mass fraction of zirconium than was initially in the crust with the increase clearly caused by the incorporation of rod cladding. The retention of such a large quantity of zirconium can only be accounted for by the reaction of zirconium with oxygen that must have been acquired from the UO_2 to form a higher melting point α(UZr)O component that must have formed the primary constituent of the remnant matrix.

The PIE results also showed that certain components tended to associate. The Fe, Ni, and Cr components, for example, were associated to form essentially stainless steel. The code also assumed that these components remain associated but the current model melts the steel at the Fe melting point that is somewhat higher than that of steel. Steel, of course, actually melts over a temperature range depending on its composition. There are a number of other components that have a high degree of affinity and tend to move together.

The code predictions show a thin zone at the top of the debris bed region that did not completely melt or relocate downward. The PIE confirmed the presence of this material. The PIE sample that was analyzed from this location was restricted to the interacted phase and the measured composition does not reflect the primary phase in the zone, which is composed of noninteracted urania particles. The interacted phase served as the "glue" that resolidified and ultimately held this material in place. There are no data available to quantify the ratio of the mass of the interacted material to that of nonreacted material so that insufficient information is available to make a conclusive judgment regarding the facility of the Case-"A" model versus the Case-"B" model. The interacted material was enriched in UO_2 relative to the original bulk composition (14.8 wt% Zr) but that would be predicted for both models to a differing degree. Case-"B" modeling would tend to reduce the local zirconia fraction more rapidly than the Case-"A" model, but without a complete characterization of this material no definitive conclusion can be drawn. The Case-"A" composition for this zone at the end of the test was about 14.6% zirconium as apposed to 0.3% for Case-"B." The PIE indicated 9.9% zirconium in the interacted phase (these numbers exclude the oxygen content). If the volume of UO_2 particulate is similar to the interacted phase, the Zr to U ratio could be reduced by a factor of 2 or more. The PIE results, then, seem to fall between the extremes of the two cases.

In terms of the composition of the resolidified pool region, comparisons of the zirconium to uranium mass ratio are given in Table 4.2. In general, except at the top of the pool, the Case-"A" modeling appears to have produced results somewhat more in line with the compositions (ratio of Zr mass to U+Zr mass) measured in the PIE. The best agreement was achieved for the top of the pool where Case-"B" was quite close to the measured mass fraction, there being only a +1.5% difference between measurement and Case-"B" while a +20% difference was observed for Case-"A". The composition at the middle of the pool was calculated to be slightly lower than measured (-2.8%) for Case-"A" and underpredicted by -32% for Case-"B." At the bottom of the pool the PIE showed a Zr/(U+Zr) ratio of about 9.9% while Case-"A" indicated about 14.2% Zr and Case-"B" produced a mass ratio of 40.5%. The bottom of the pool contained some undissolved UO_2 pellets that were not included in the scan sample and would, if included reduce the overall ratio at this location for the PIE results. The large discrepancy for Case-"B" at the bottom of the pool can easily be understood in terms of Figures 4.94 and 4.95 where the UO_2 and ZrO_2 densities are shown. Here it is seen that the zirconia penetrates farther down into the crust because of its lower melting temperature effectively separating it from the UO_2 at the leading edge of the ceramic crust. This is an artifact of the noninteractive

model with the same effect having been discussed earlier with respect to the artificial stratification of components in the rod stub region.

4.2.3 Implication of MP-2 Analysis for DEBRIS Code Modeling

The heat transfer processes in a debris medium appear to be quite adequately treated in the DEBRIS code framework. The overall thermal response of the MP-2 experiment package was successfully characterized in the code predictions. Some obstacles exist, however, with respect to modeling heat transfer in full-scale reactor accident analysis using the models currently in place in the DEBRIS code. The first involves the heat transfer correlations used for effective thermal conductivities in a rodded region. Correlations for heat transfer parallel and perpendicular to the rods exist and are used in the DEBRIS model. However, no correction is currently applied to these heat transfer correlations subsequent to the ingress of molten material into the rodded geometry as occurred in the MP-2 experiment. The second problem concerns the application of a radiation enhanced effective thermal conductivity in a debris bed medium that has formed large voided or partly voided zones caused by the melting and relocation of material out of these zones. The radiation enhanced conduction heat transfer model assumes that each control volume transfers heat to or from only those control volumes that are directly adjacent. This assumption is not rigorous if the porosity of a control volume is increased to the extent that the radiative mean free path length becomes comparable in magnitude to the control volume dimensions. This certainly becomes the case in the upper part of the debris bed region subsequent to gross melting and voiding. The small size of the debris bed mitigates this problem in the analysis of MP-2, but the modeling will need improvement for application to full-scale reactor analysis. The third problem deals with the heat transfer in an internally heated molten pool. The model that was adapted for the MP-2 experiment was a very simple approximation wherein the thermal conductivity was enhanced in the upper part of the molten pool if the temperature gradient was negative and if the Rayleigh number exceeded the critical value for the onset of convection. This simple model is one-dimensional and does not treat convective motion in the sense that it does not circulate molten material. More sophisticated convection models are being developed that will treat the heat and mass transfer processes in the high Rayleigh number regimes (highly turbulent convection processes) that are anticipated for molten pools which are likely to develop in a full-scale reactor analysis.

Some general conclusions can be drawn from the DEBRIS module analysis of the MP-2 experiment with respect to material and species relocation. In general, the code qualitatively predicts the key features that are observed in the experiment. These features include (1) melting of debris and relocation of the melt under the influence of gravity, (2) relocation of melt primarily in the downward and radial directions under the influence of gravity and capillary forces, (3) formation of a voided region in the central portions of the debris bed that results from melting and relocation of the material out of that region, (4) downward slumping of solid debris due to gravity, (5) formation of a crust in the lower region of the bed resulting from refreezing of the relocated molten materials in a colder region, (6) the formation of a molten pool that is crucibilized both by a crust that forms underneath the molten pool and a crust that forms at the radial boundaries of the pool, (7) the accelerated relocation of the ceramic pool into a partly voided region at the lower boundary of the debris bed, (8) the degree of penetration of the debris bed into the preformed blockage region, and (9) the timing as well as the gross overall processes involved in the relocation of the metallic components out of the original blockage region and the redistribution of these material at lower, cooler locations in the rod region.

However, calculation of the relocation of materials out of the blockage region into and through the rodded region is apparently a much less tractable problem than is the melting and material redistribution processes in a two-component debris bed medium. Also, a third component in the debris bed, particularly if it is a reactive component, will challenge the capabilities of the code as it is currently constituted. For a two-component debris bed, it appears that an adequate estimate of pool location, pool penetration rate, and debris species distribution is feasible without the added complexity of a **nonequilibrium** model. Multiple component debris-bed (greater than two species) analysis presents a considerably more difficult challenge particularly with respect to the presence in the debris medium of a lower melting point material such as steel or zirconium. For this situation it is possible that the kinetic processes of diffusion and material interactions involved in the dissolution of a higher melting temperature component by a liquid component may be required.

The key observations derived from the PIE of the MP-2 test section contained several elements that are germane to modeling the remelting of the preformed blockage and the relocation of its components caused by the advancing thermal front from the growth of the molten ceramic pool. First, it is apparent that to accurately characterize the processes involved it is necessary to model the chemistry to some extent and at least some of the material interactions. The code predicted, based on the separate melting of each component and the assumption of no transfer of oxygen between components, that except for trace quantities remaining as a result of the wetting of solids, the entire inventory of metallic components was relocated out of the blockage region. From the PIE this is clearly not the case. Significant quantities of most of these components remained in the remnant crust. The fact that any of these components remained at the high temperatures existing in this location at the end of the test implies that chemical reactions occurred in which UO_2 and ZrO_2 from the original crust matrix were reduced and the oxygen transferred to one or more of the metallic components. It is likely that the zirconium was the primary oxygen beneficiary. What is also clear is that oxygen was efficiently diffused out of the original UO_2/ZrO_2 components into the metallic zirconium phase to form an α(UZr)O matrix with a sufficiently high melting temperature to allow it to resist melting despite the proximity of the molten ceramic pool. The lesson here is that the oxygen chemistry involved between urania/zirconia and metallic blockage components (mostly zirconium) may need to be treated if it is deemed to be important that the disposition of these metallic components be tracked at a higher level of accuracy.

A second observation derived from the PIE concerns the redistribution of the relocated metallic components. Clearly the separate melting of each component results in an artificial stratification of components along the temperature field in order of melting points. The PIE revealed, as expected, that most of the components interacted and formed preferential associations with other components. These interactions

effectively reduced the melting points, eliminated stratification, and increased the downward penetration of the relocated material. The result was a large number of distinct phases. It is probably not feasible, and perhaps not necessary, to attempt to model ternary and higher order phases even though phases existed in which nearly all the components were present. It is evident, however, that this behavior must be simulated in the models used for full-scale analysis, particularly with respect to situations in which the relocated materials form secondary, tertiary, etc. blockages at successively lower elevation and perhaps continue to affect the motion of the ceramic melt front. A recommended solution to avoid the added complexity involved in multiple phases having multiple components is to use the data available from the MP-2 PIE to select a small number of groups of components that are the most commonly observed such as the Fe-Cr-Ni group. This group can essentially be modeled as "stainless" steel. Making the additional assumption, then, that the groups do not interact would significantly reduce the complexity of the analysis while still enhancing the predictive capability of the code in terms of achieving a more finely graded redistribution pattern for relocated materials.

A final observation with regard to the material relocation models in DEBRIS is the effect of the "local thermal equilibrium" assumption. The assumption that a single temperature characterizes each control volume forces molten material that may be moving from one control volume to another to come to thermal equilibrium in each control volume. Clearly, if the flow is rapid, this will not be an accurate characterization of the actual physics. The tendency under these conditions is to underpredict the extent of downward penetration for rapidly moving molten material. Because a particulate medium effectively limits the flow rate of molten material, the local thermal equilibrium model is accurate in the debris bed medium. However, the model tends to underpredict the downward penetration of molten materials flowing through a more open geometry such as that in a rodded region, particularly if the flow is parallel to the direction of the rods.

Table 4.1 MP-2 End-of-Test Heat Transfer Rates

Zone	Heat Transfer Rate	Normalized Heat Transfer Rate	Heat Flux
	(kW)	%	(kW/m^2)
1	2.8	20.0	29
2	2.4	17.1	44
3	1.2	8.6	64
4	6.3	45.0	70
5	1.3	9.3	25

Table 4.2 Molten Pool Composition Zr/(Zr+U))

	Top (%)	Middle (%)	Bottom (%)
Case-"A"	15.3 (+20%)	14.2 (-2.8%)	14.8 (+50%)
Case-"B"	12.9 (+1.5%)	10.0 (-32%)	40.5 (+300%)
PIE	12.7	14.6	9.9

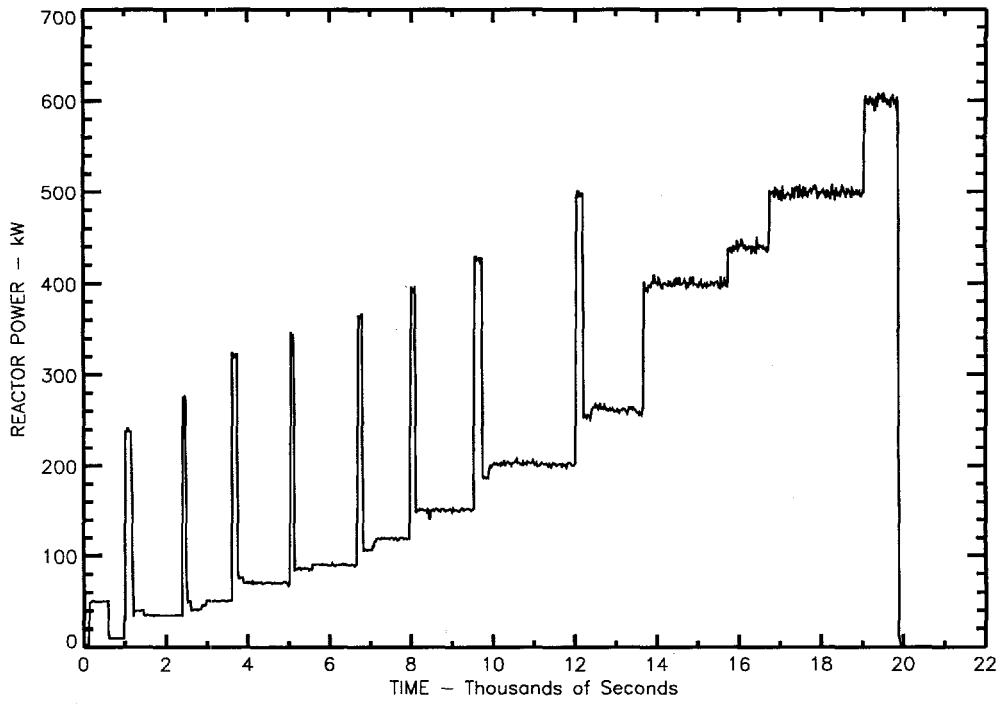

Figure 4.1 MP-2 Reactor Power Duty Cycle

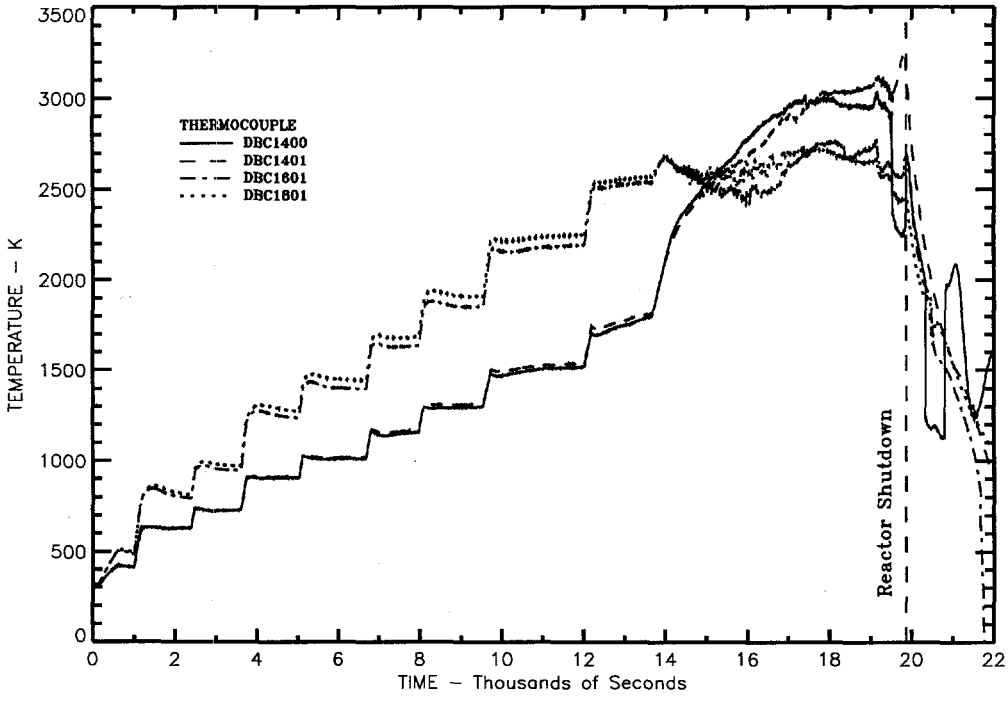

Figure 4.2 Measured Temperatures in the Lower Regions of the Debris Bed

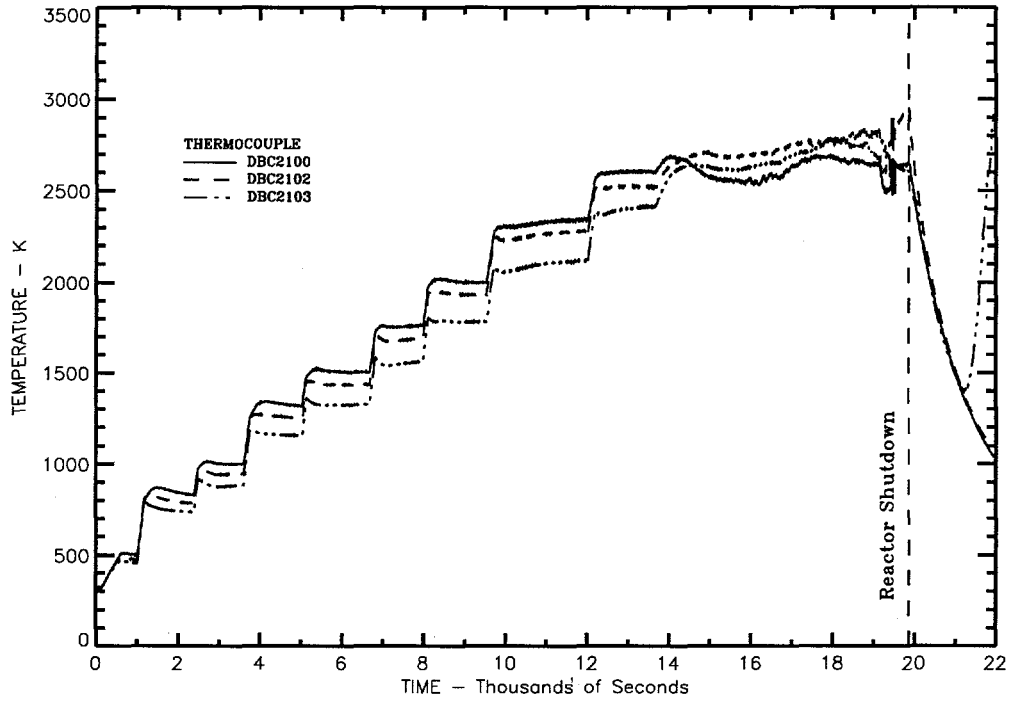

Figure 4.3 Measured Temperatures Near the Middle of the Debris Bed

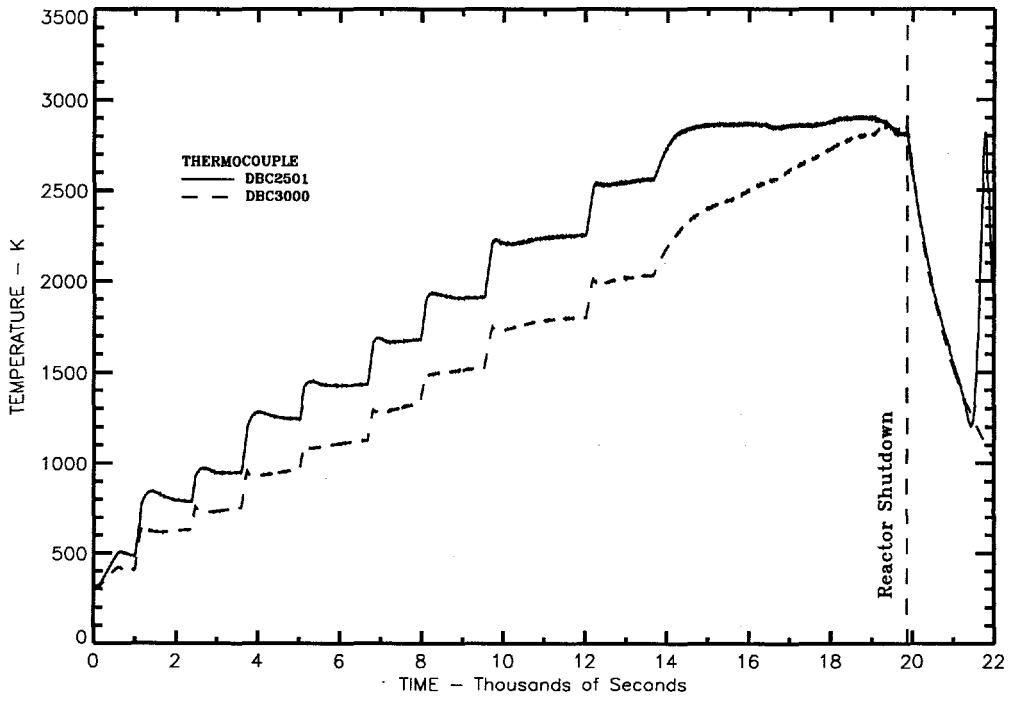

Figure 4.4 Measured Temperatures in the Upper Regions of the Debris Bed

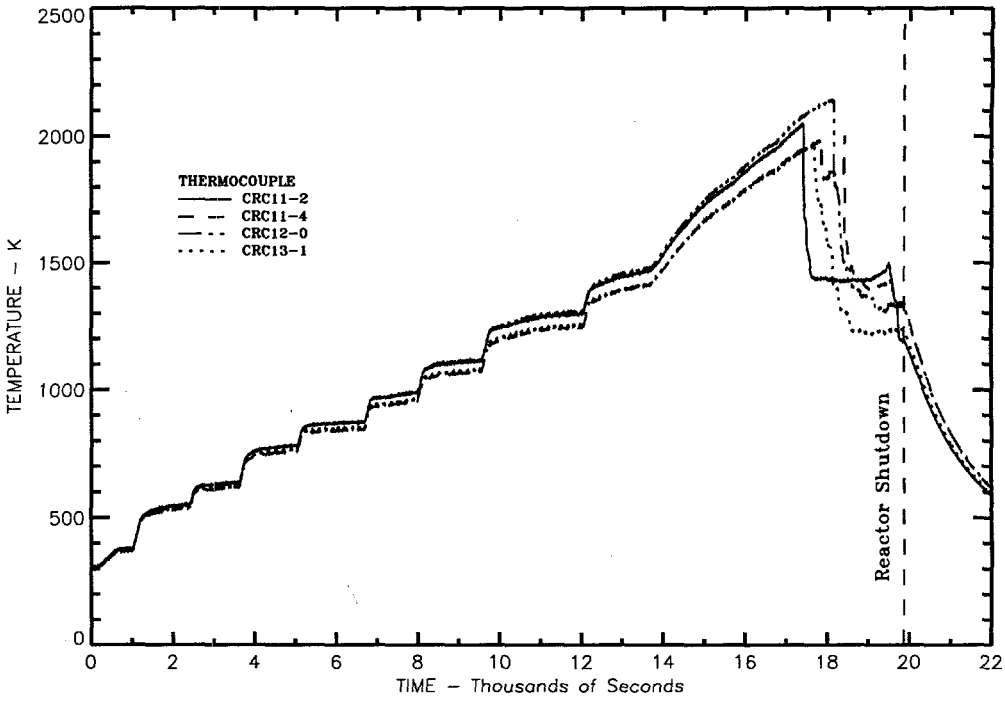

Figure 4.5 Measured Temperatures in the Preformed Crust

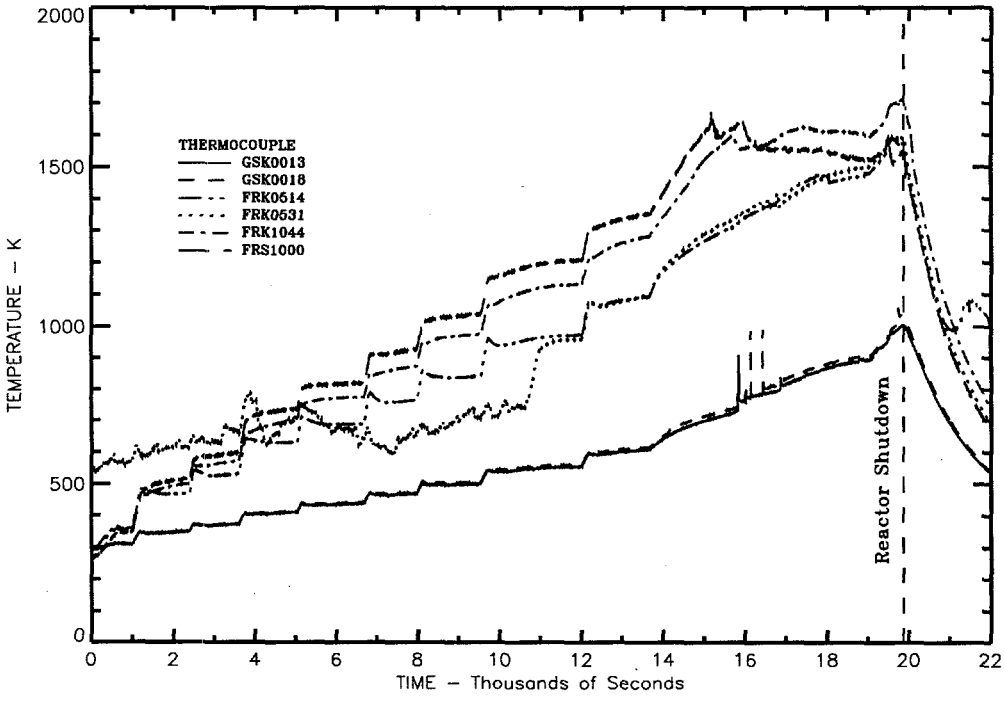

Figure 4.6 Measured Temperatures in the Rod Stub Region

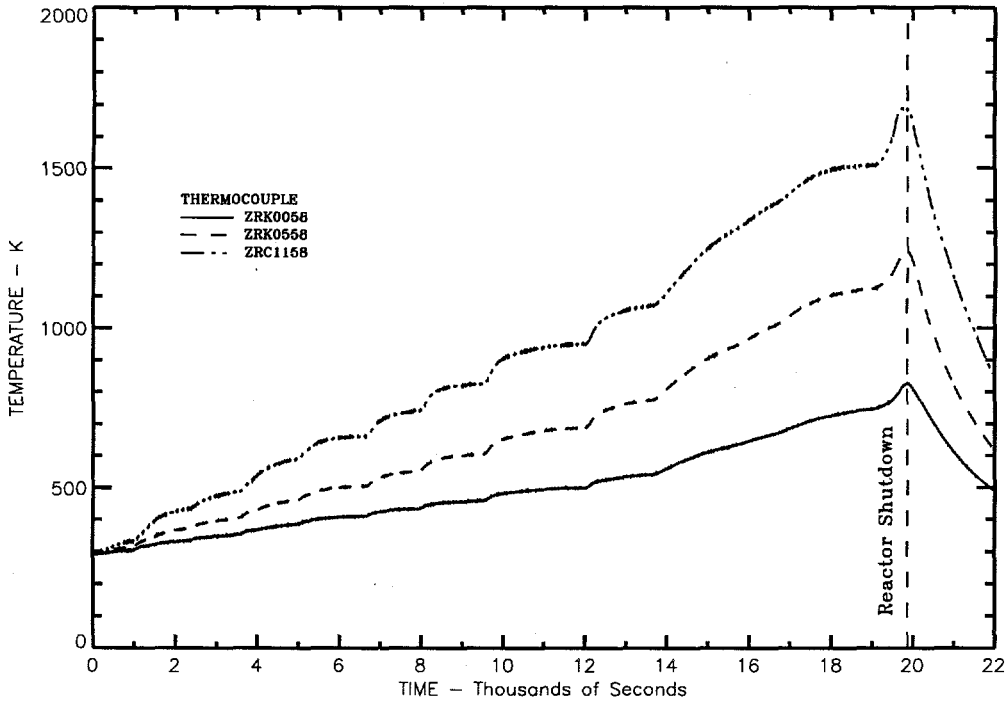

Figure 4.7 Measured Lower Tantalum Liner Temperatures

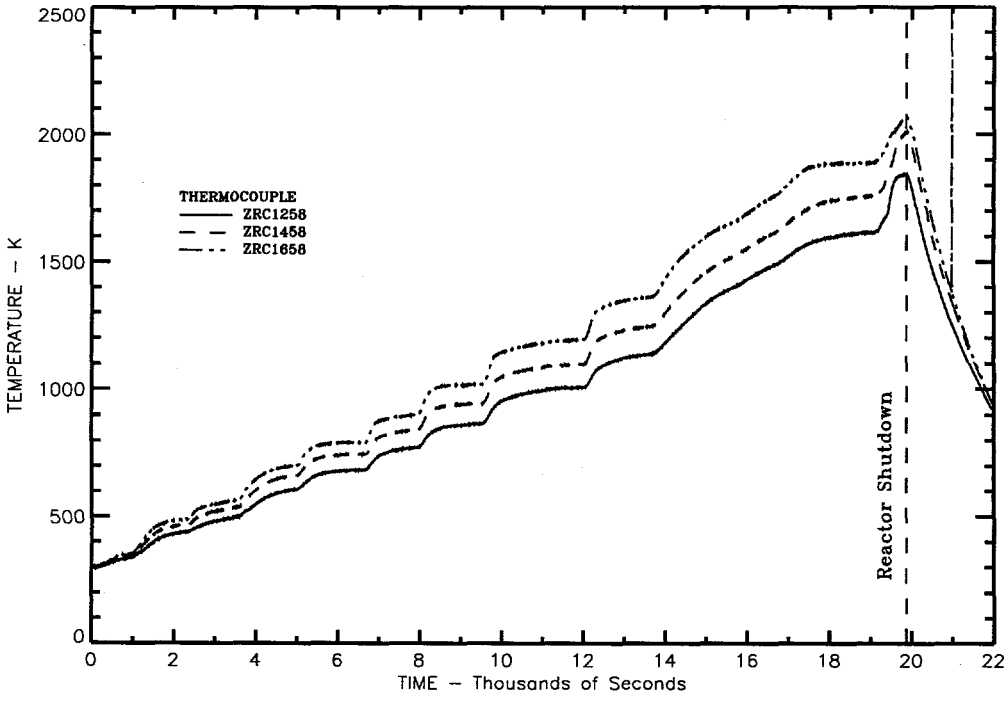

Figure 4.8 Measured Middle Tantalum Liner Temperatures

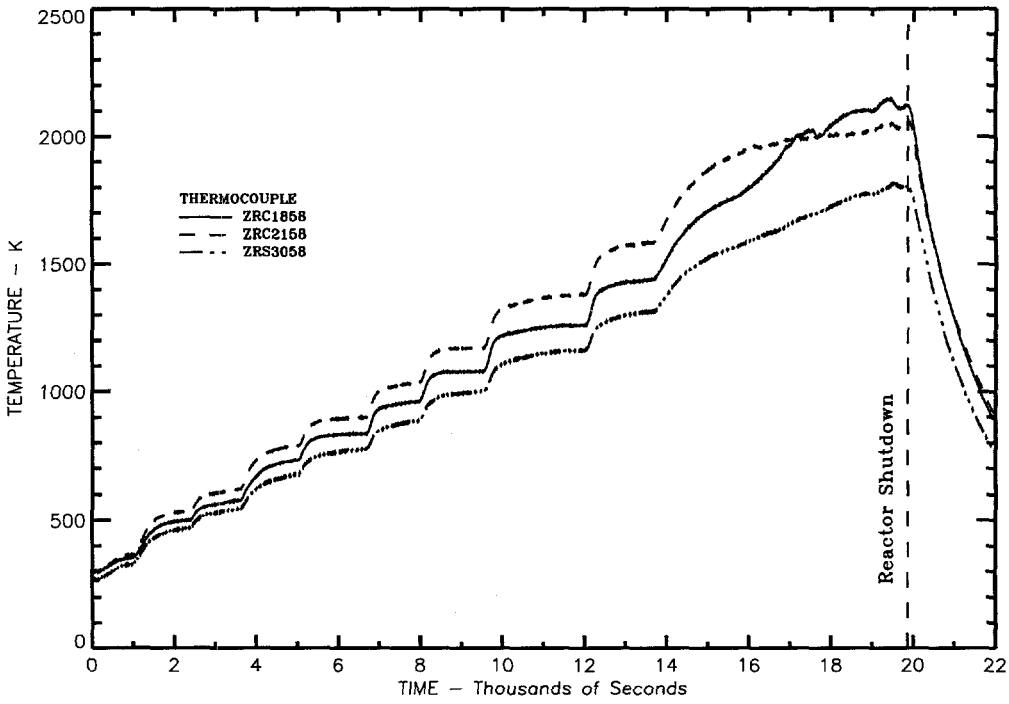

Figure 4.9 Measured Upper Tantalum Liner Temperatures

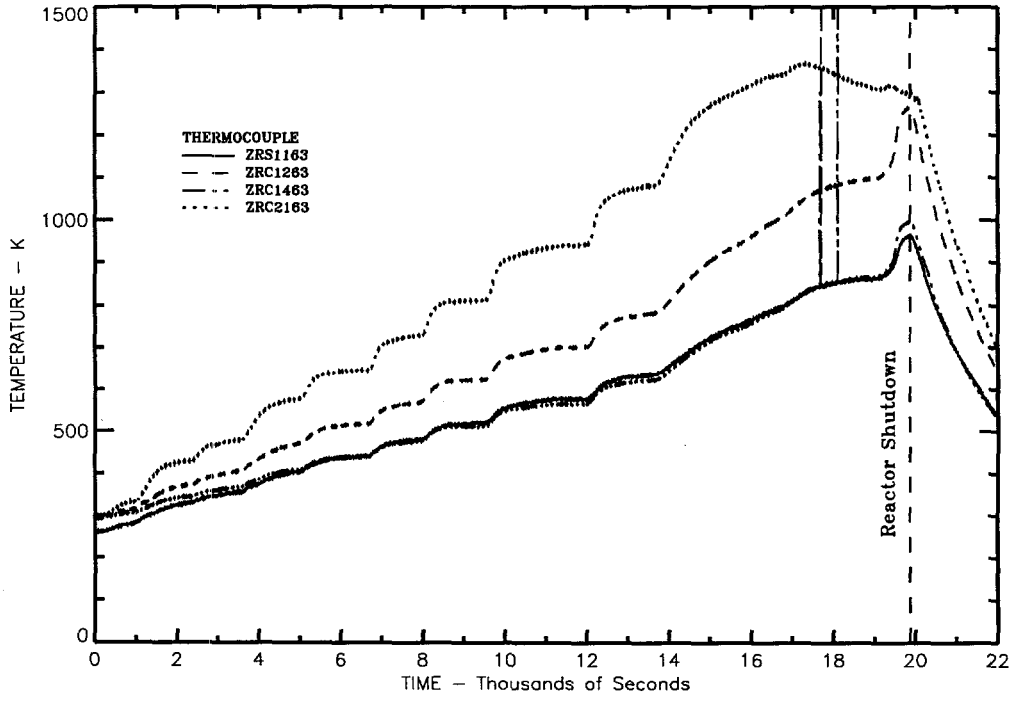

Figure 4.10 Measured Temperatures in the Radial Insulation

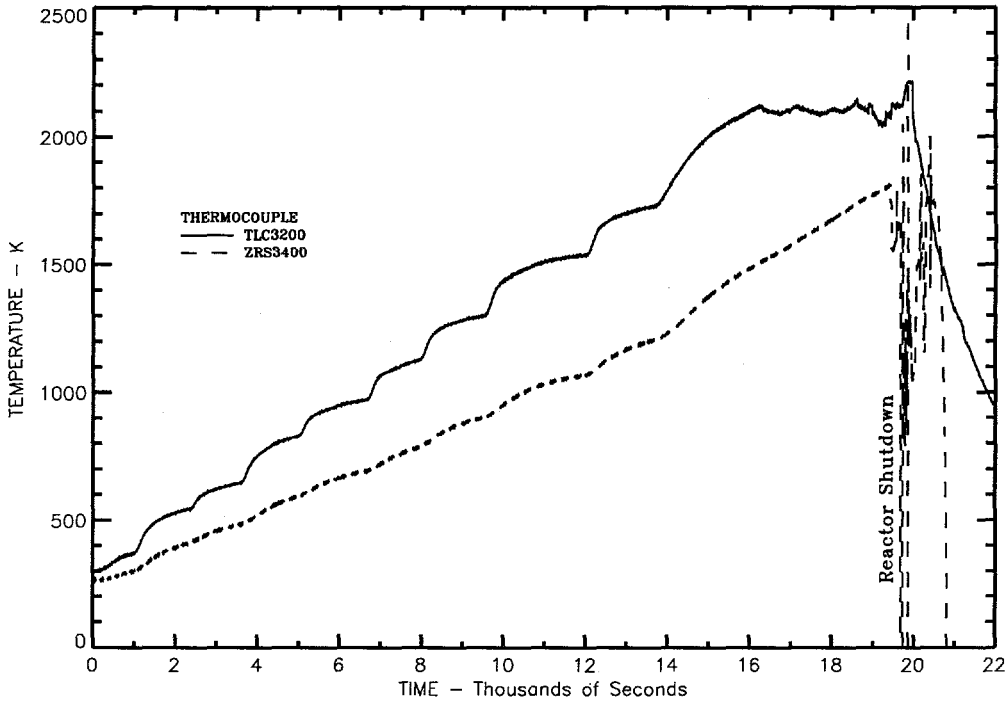

Figure 4.11 Measured Temperatures in the Upper Insulation

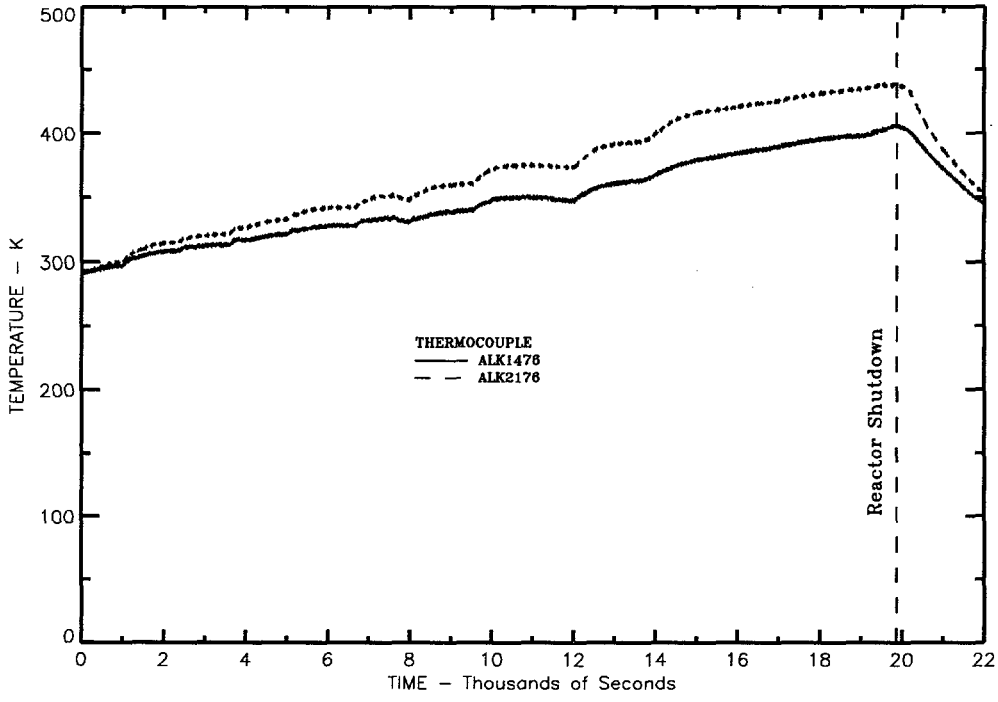

Figure 4.12 Measured Temperatures on the Aluminum Spacer

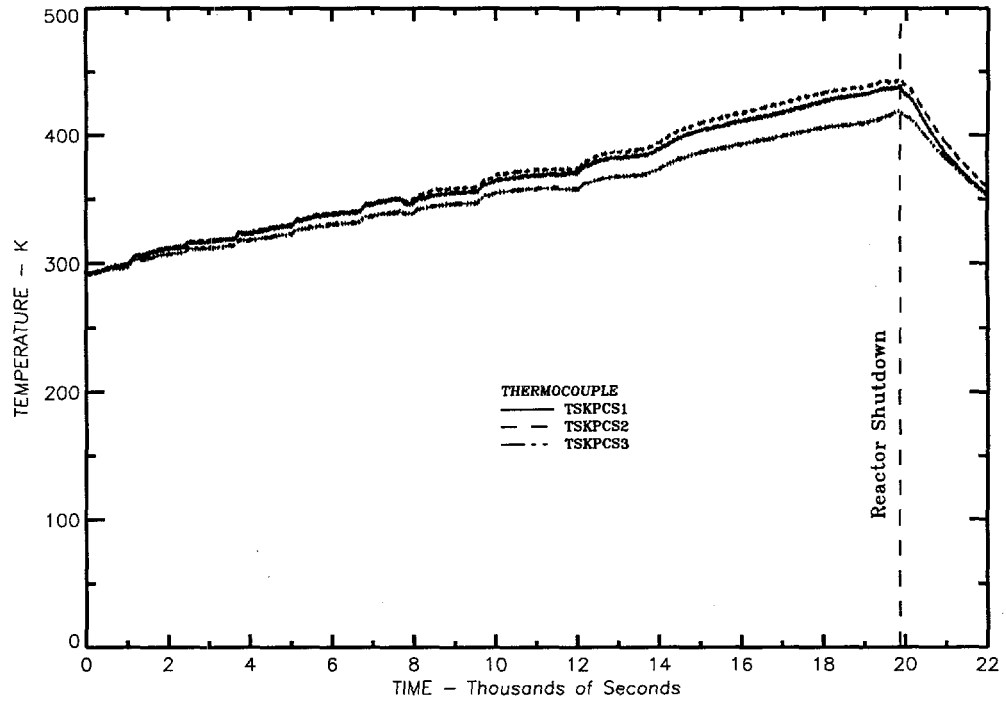

Figure 4.13 Measured Temperatures on the Radial Primary Containment

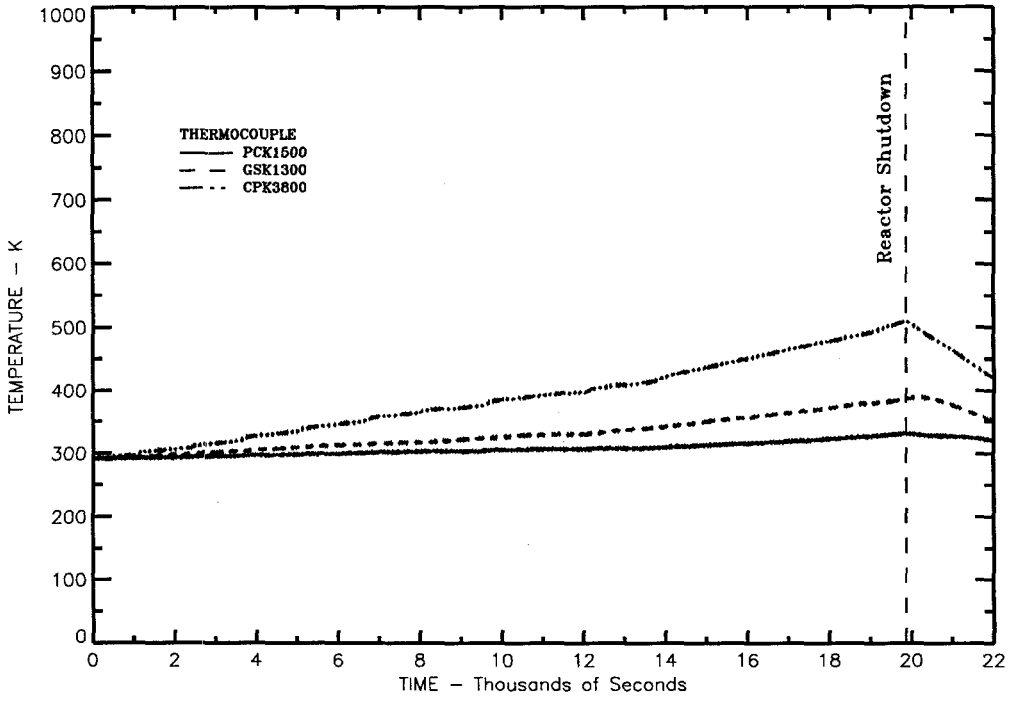

Figure 4.14 Measured Temperatures on Upper and Lower Test Section Boundaries

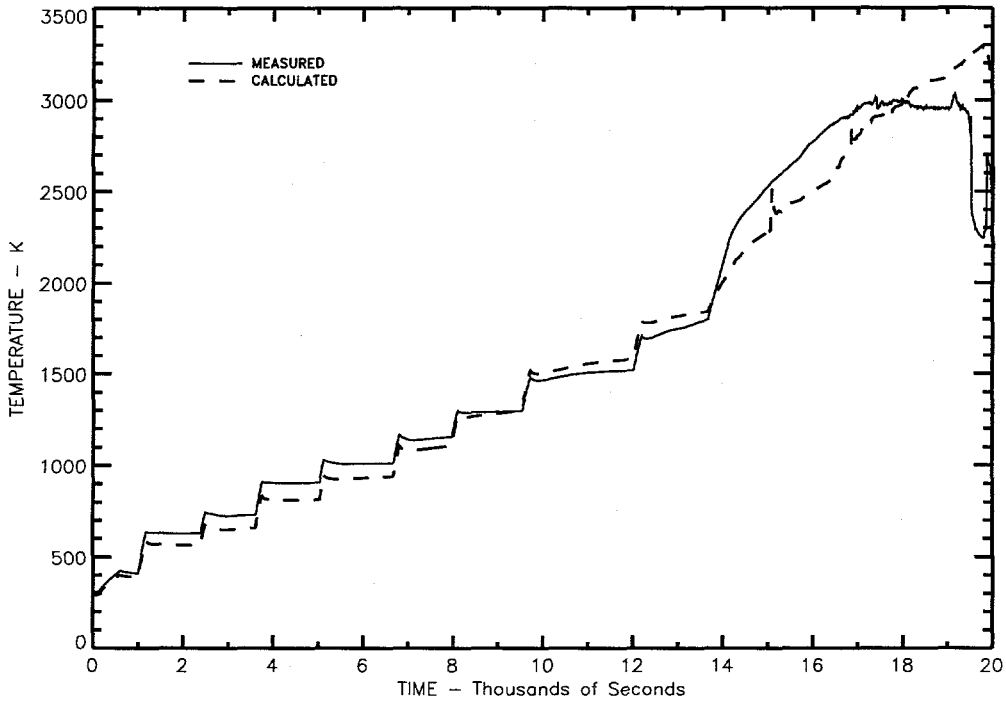

Figure 4.15 DEBRIS Code Results Compared With Debris Bed Thermocouple ***DBC1400***

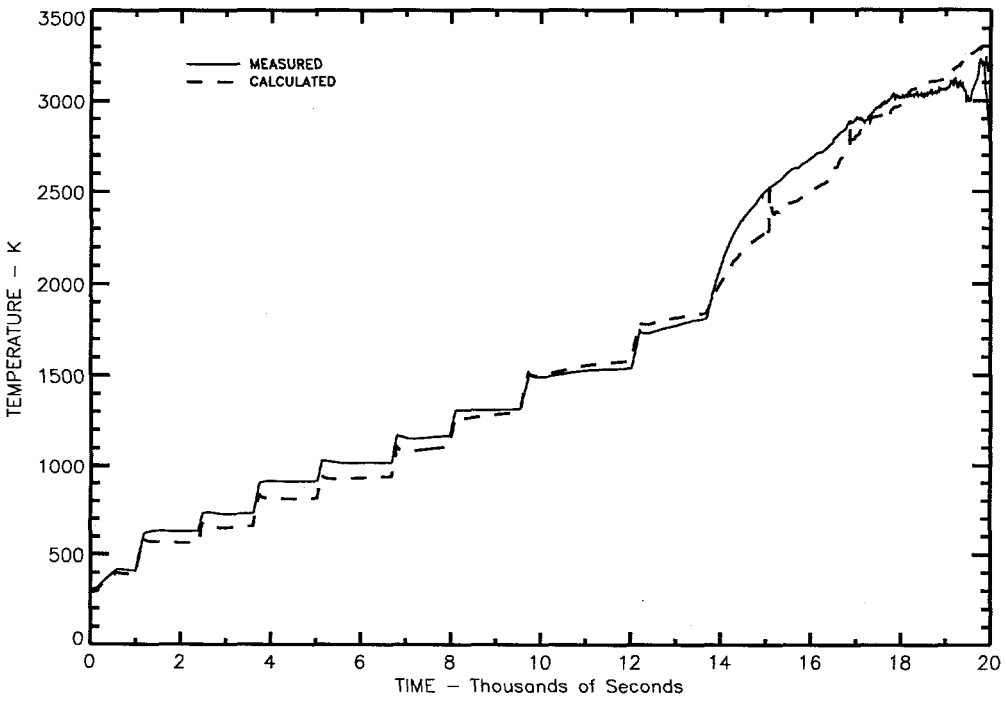

Figure 4.16 DEBRIS Code Results Compared With Debris Bed Thermocouple ***DBC1401***

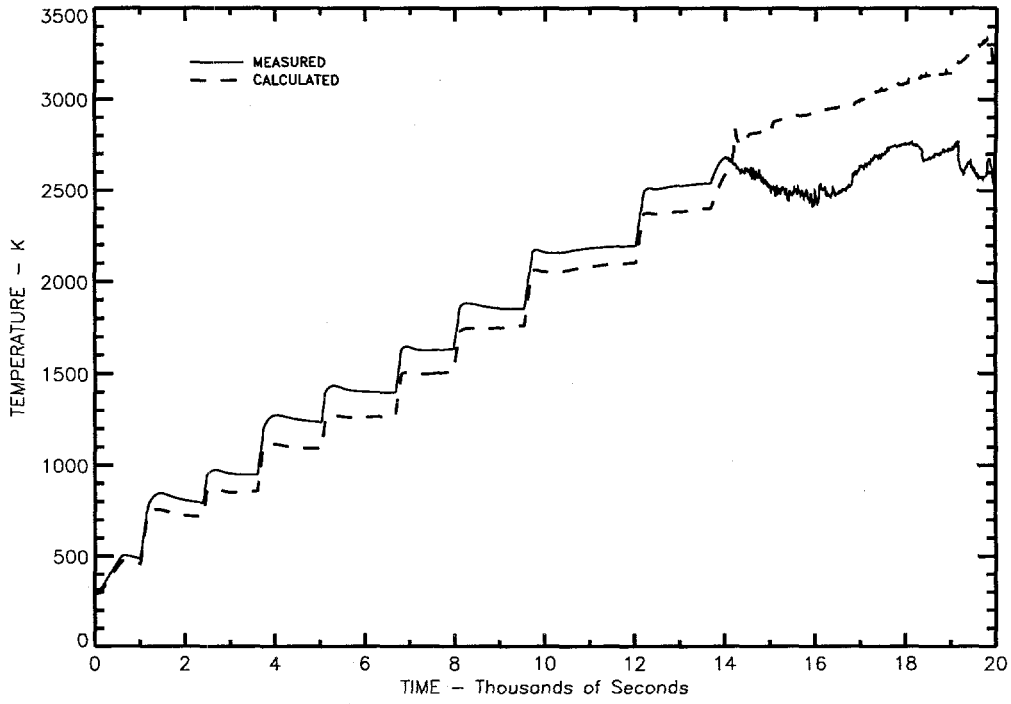

Figure 4.17 DEBRIS Code Results Compared With Debris Bed Thermocouple ***DBC1601***

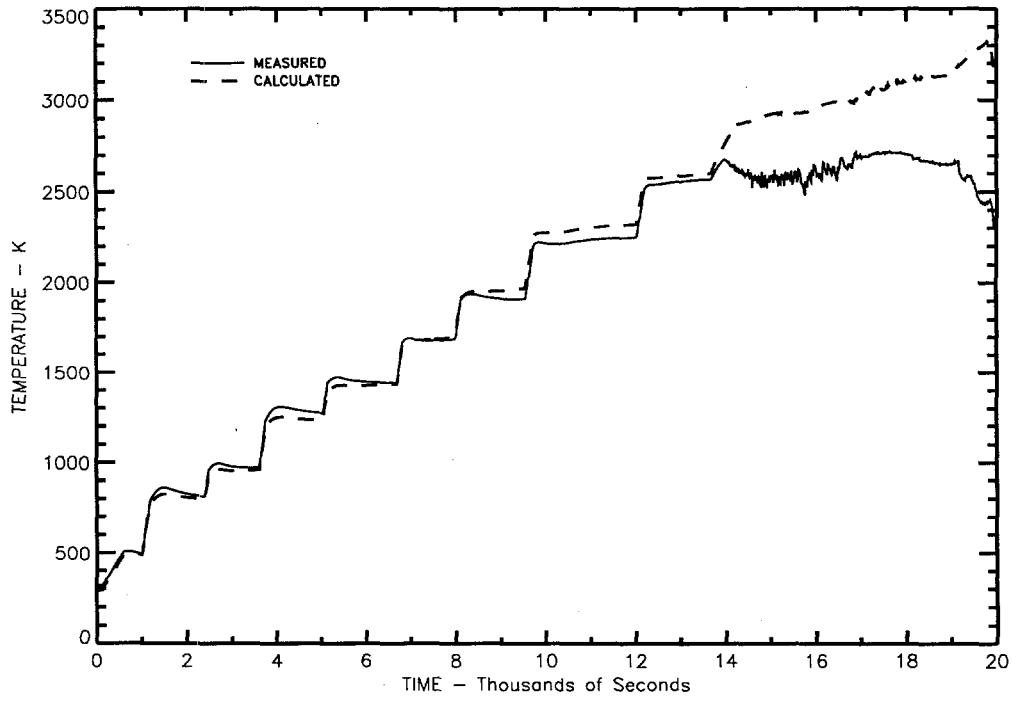

Figure 4.18 DEBRIS Code Results Compared With Debris Bed Thermocouple ***DBC1801***

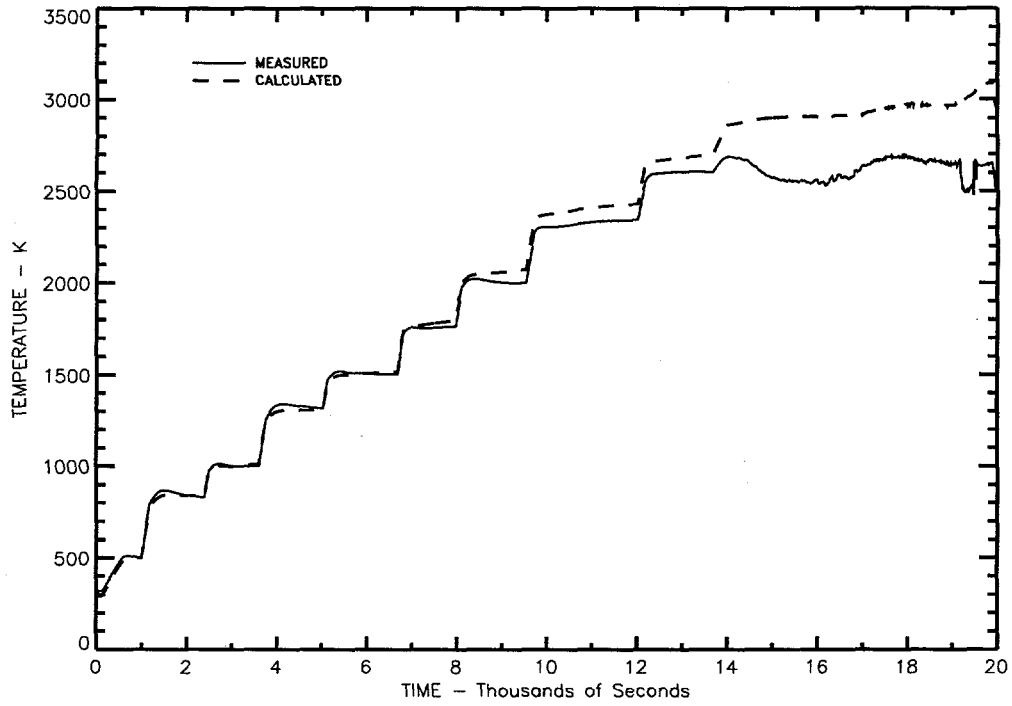

Figure 4.19 DEBRIS Code Results Compared With Debris Bed Thermocouple ***DBC2100***.

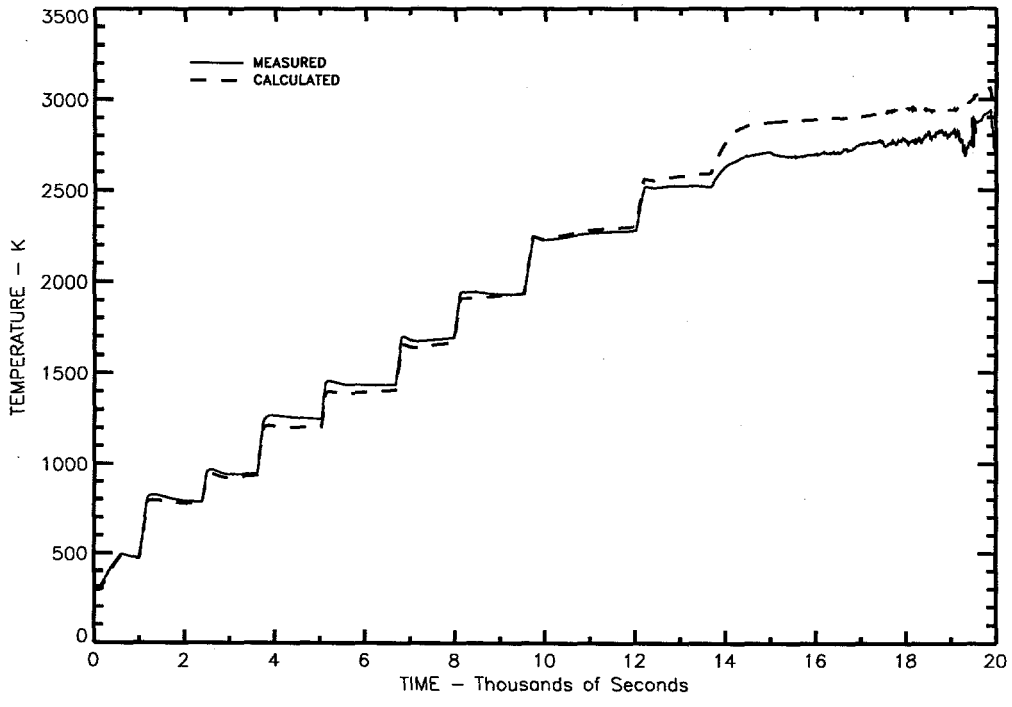

Figure 4.20 DEBRIS Code Results Compared With Debris Bed Thermocouple ***DBC2102***

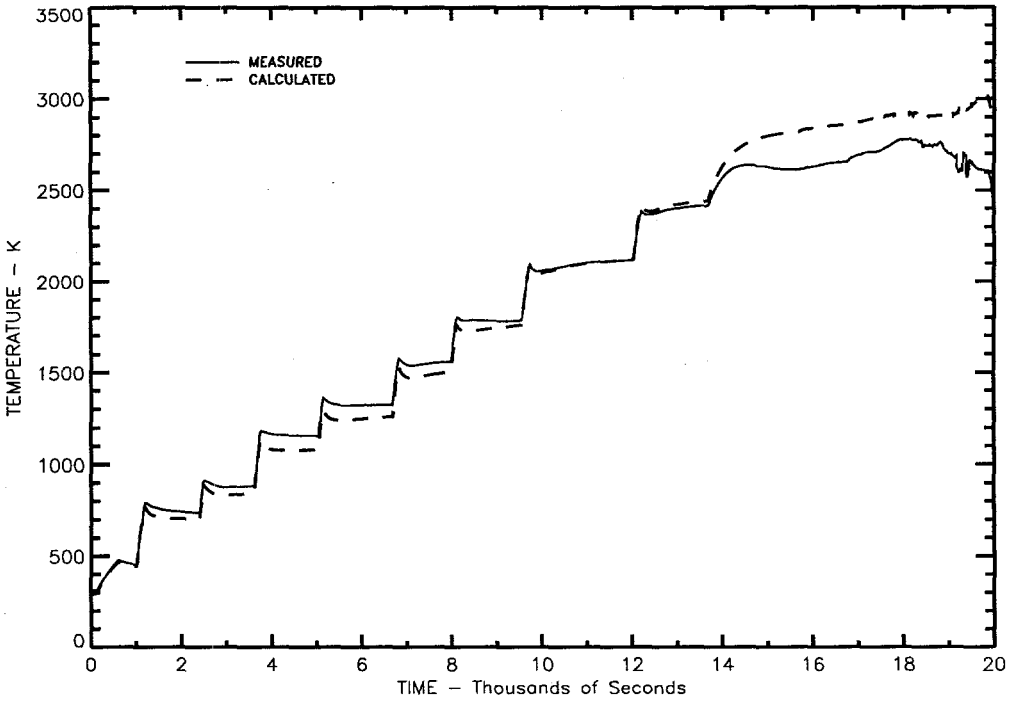

Figure 4.21 DEBRIS Code Results Compared With Debris Bed Thermocouple ***DBC2103***

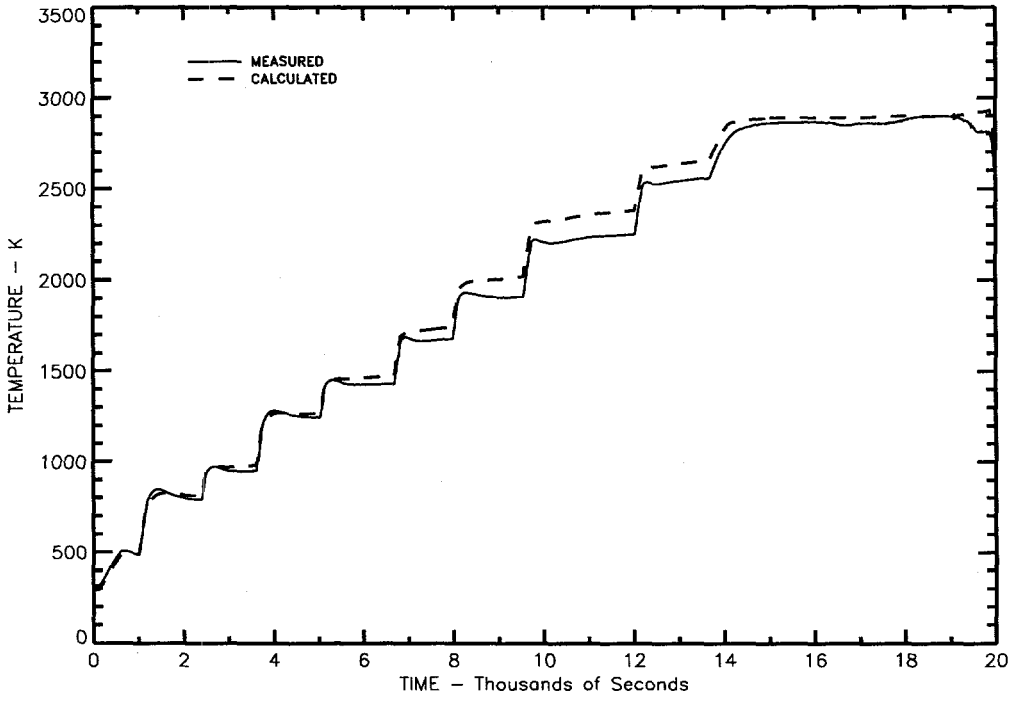

Figure 4.22 DEBRIS Code Results Compared With Debris Bed Thermocouple ***DBC2501***

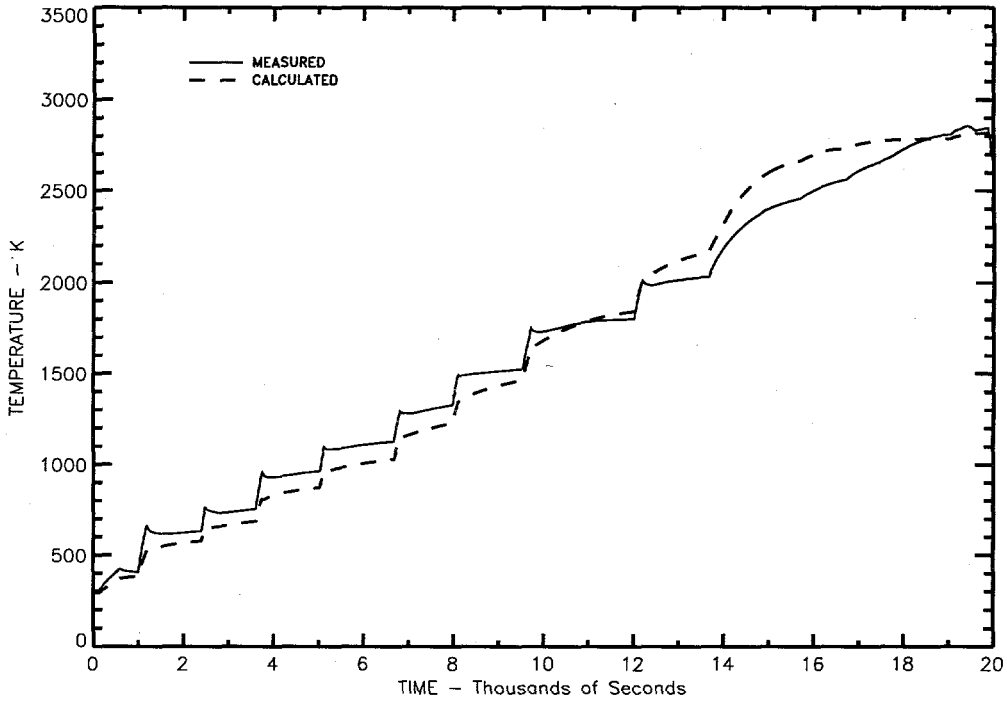

Figure 4.23 DEBRIS Code Results Compared With Debris Bed Thermocouple ***DBC3000***

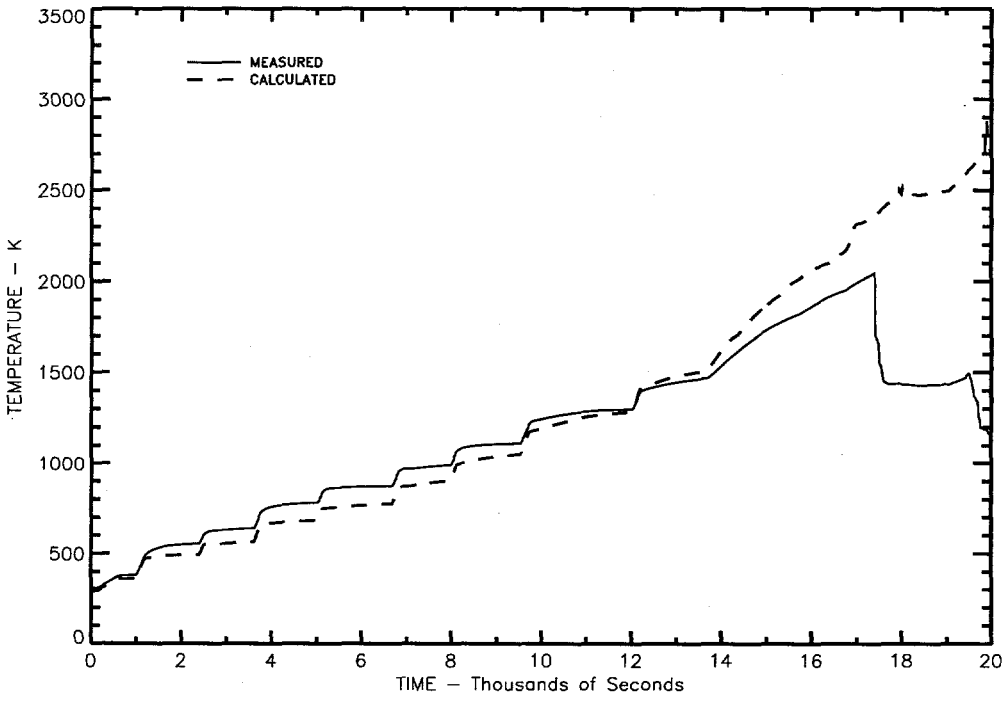

Figure 4.24 DEBRIS Code Results Compared With Crust Thermocouple ***CRC11-2***

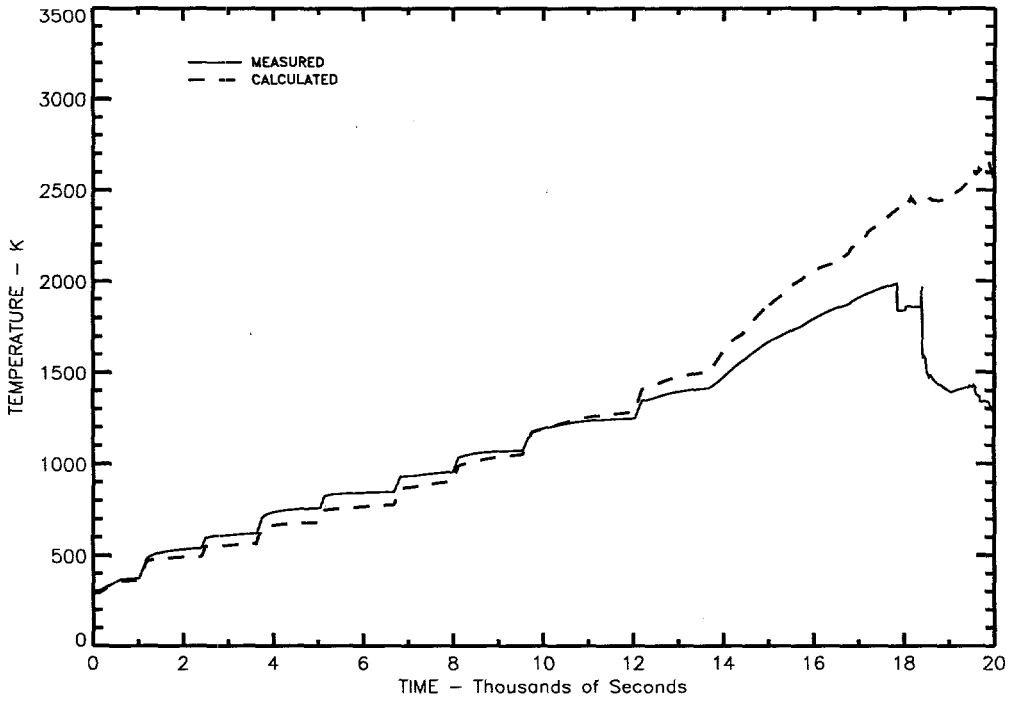

Figure 4.25 DEBRIS Code Results Compared With Crust Thermocouple ***CRC11-4***

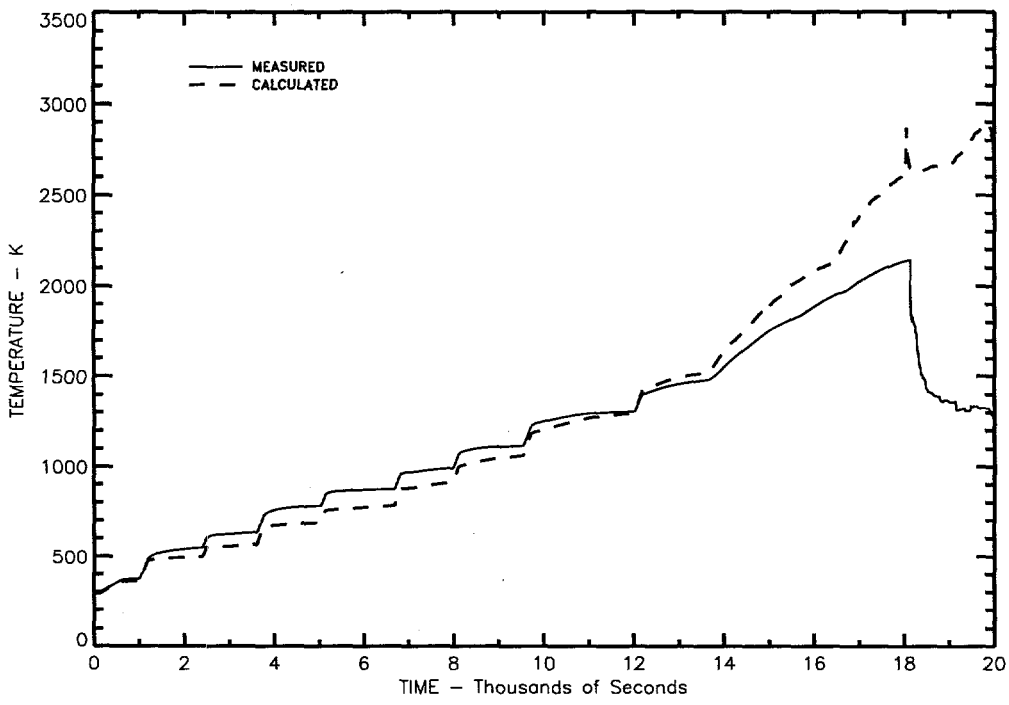

Figure 4.26 DEBRIS Code Results Compared With Crust Thermocouple ***CRC12-0***

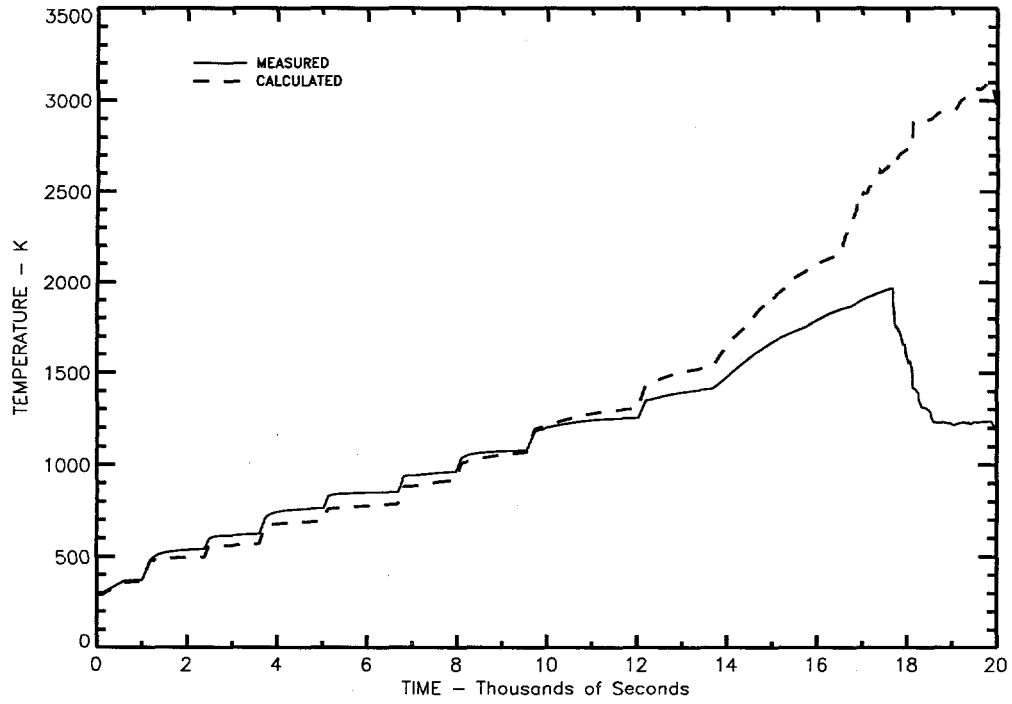

Figure 4.27 DEBRIS Code Results Compared With Crust Thermocouple ***CRC13-1***.

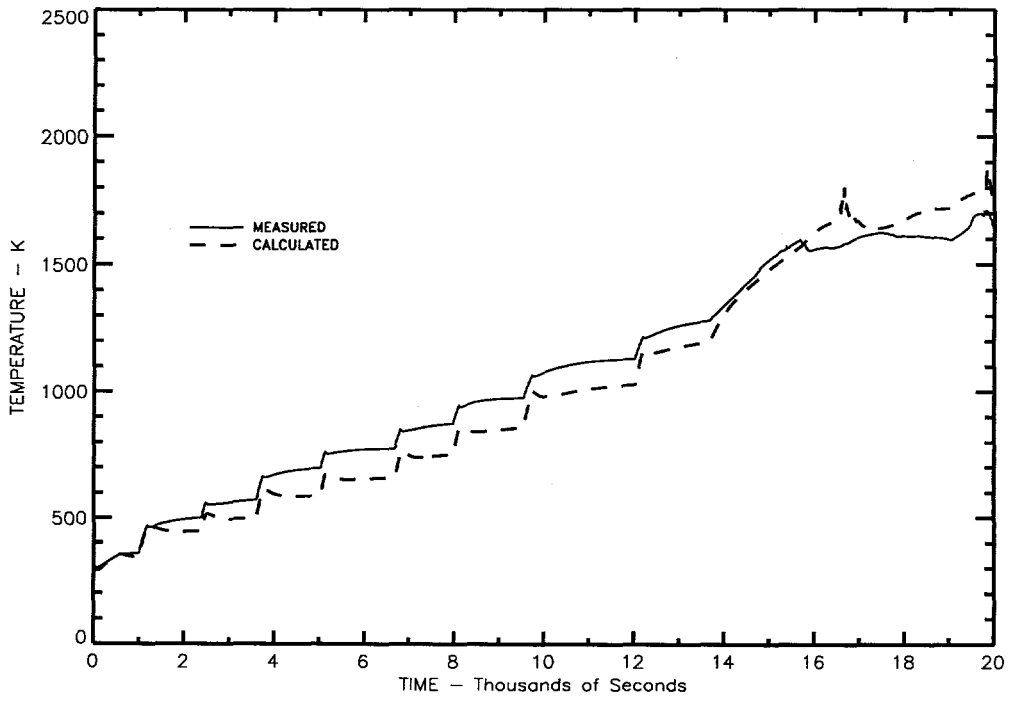

Figure 4.28 DEBRIS Code Results Compared With Rod Region Thermocouple ***FRK0514***

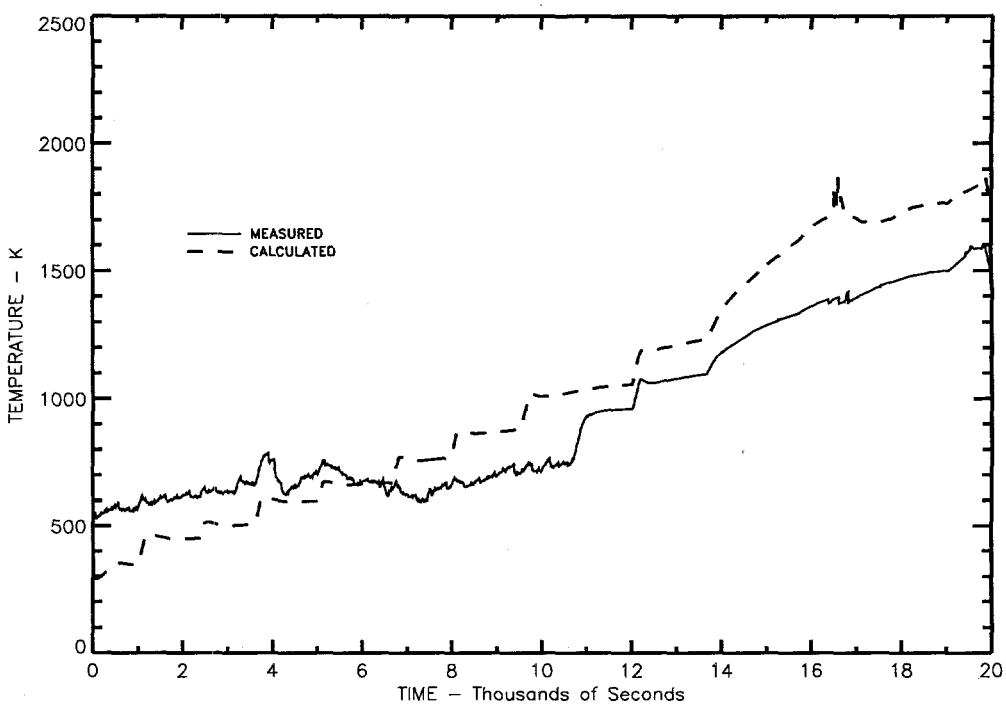

Figure 4.29 DEBRIS Code Results Compared With Rod Region Thermocouple ***FRK0531***

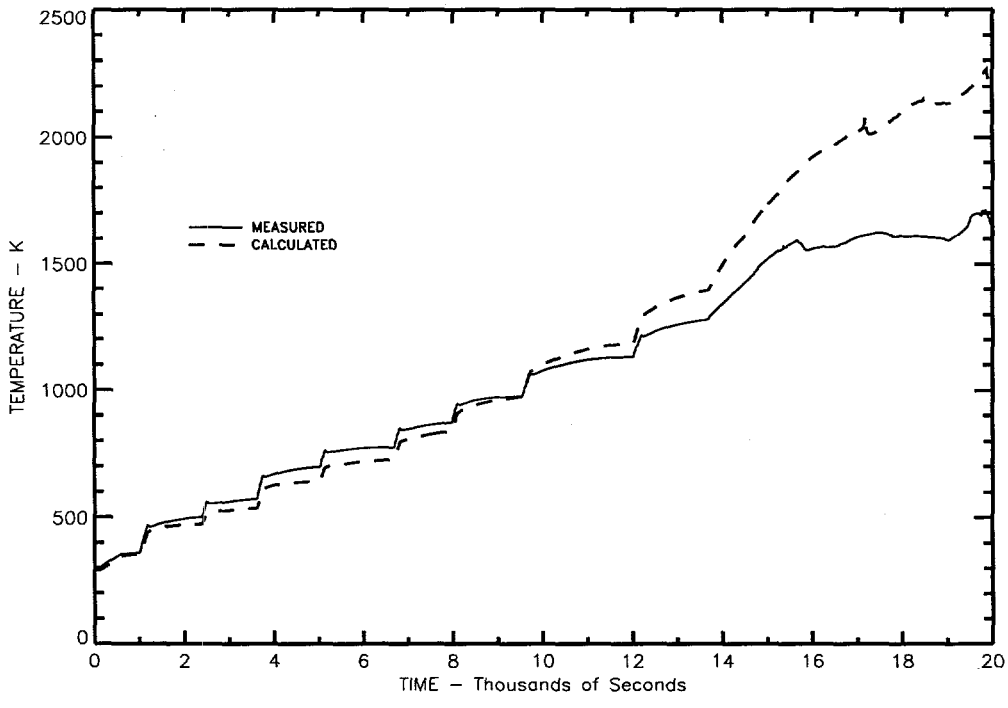

Figure 4.30 DEBRIS Code Results Compared With Rod Region Thermocouple ***FRK1044***

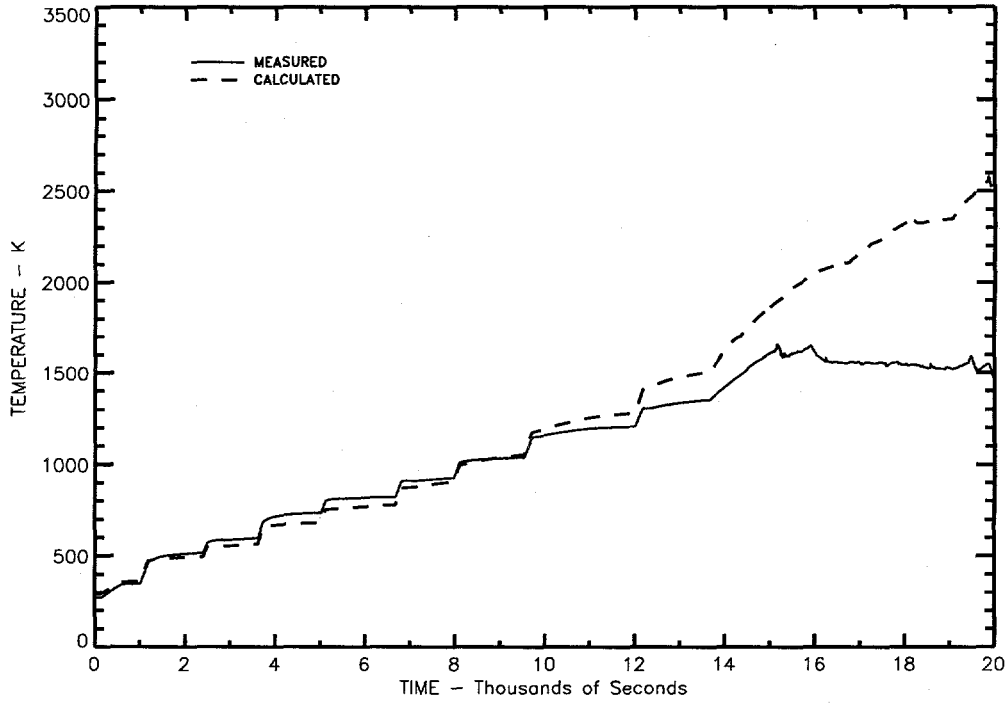

Figure 4.31 DEBRIS Code Results Compared With Rod Region Thermocouple ***FRS1000***

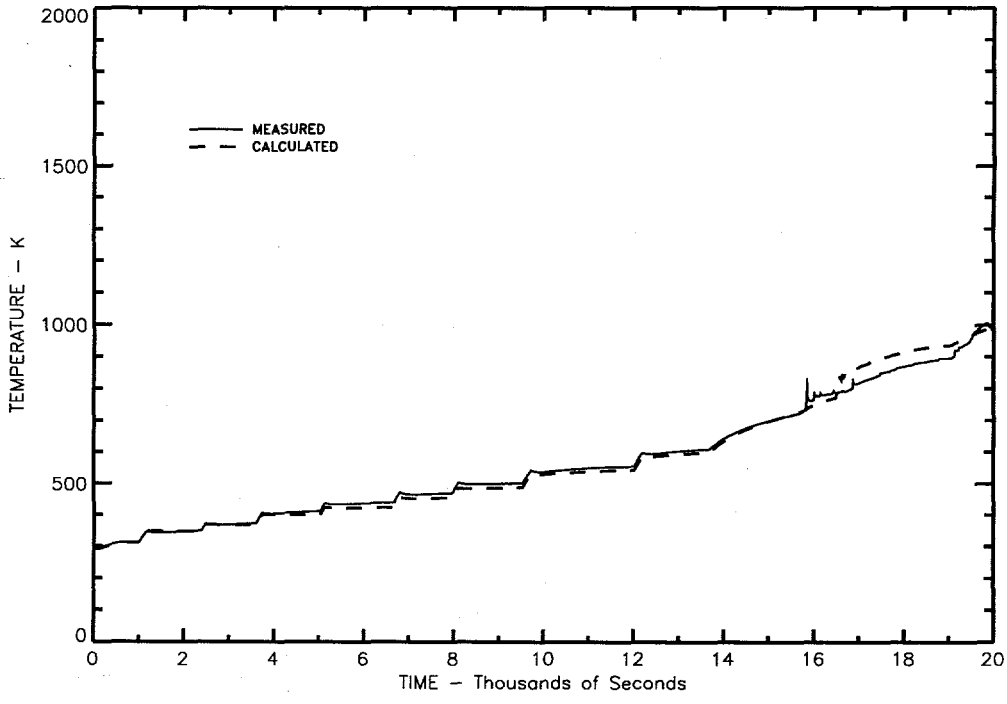

Figure 4.32 DEBRIS Code Results Compared With Rod Region Thermocouple ***GSK0013***

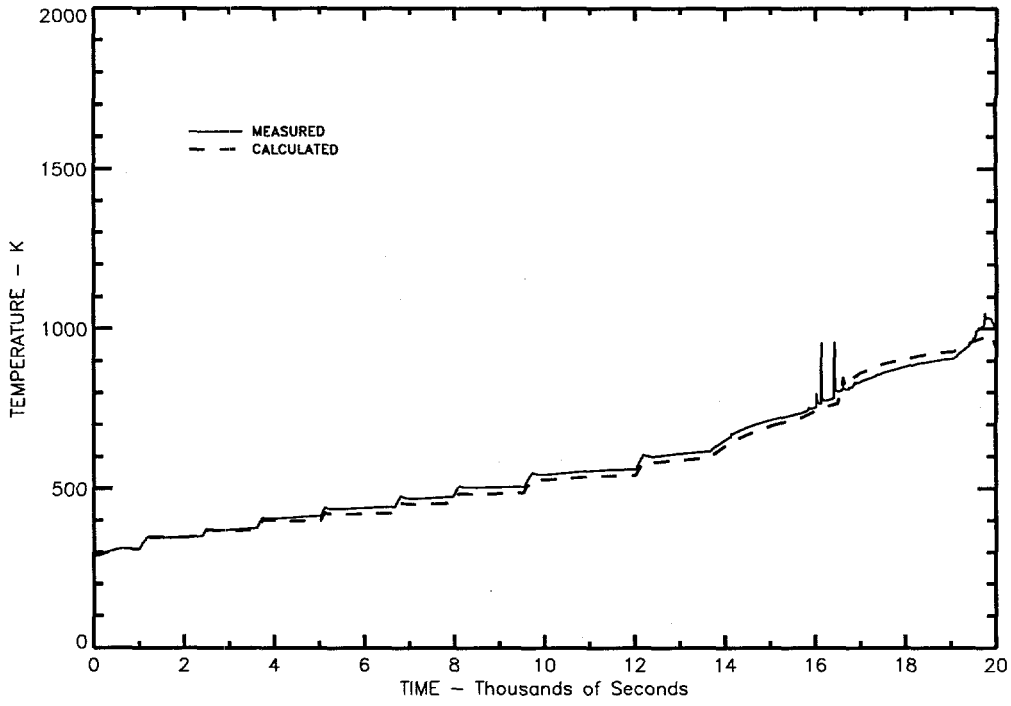

Figure 4.33 DEBRIS Code Results Compared With Rod Region Thermocouple ***GSK0018***

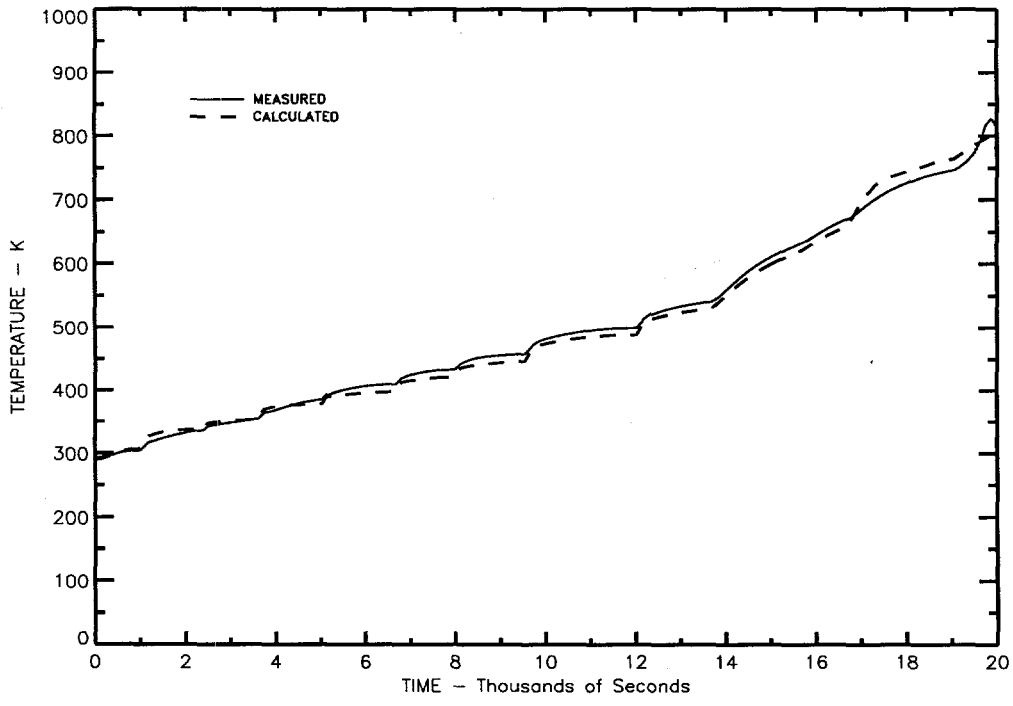

Figure 4.34 DEBRIS Code Results Compared With Tantalum Liner Thermocouple ***ZRK0058***

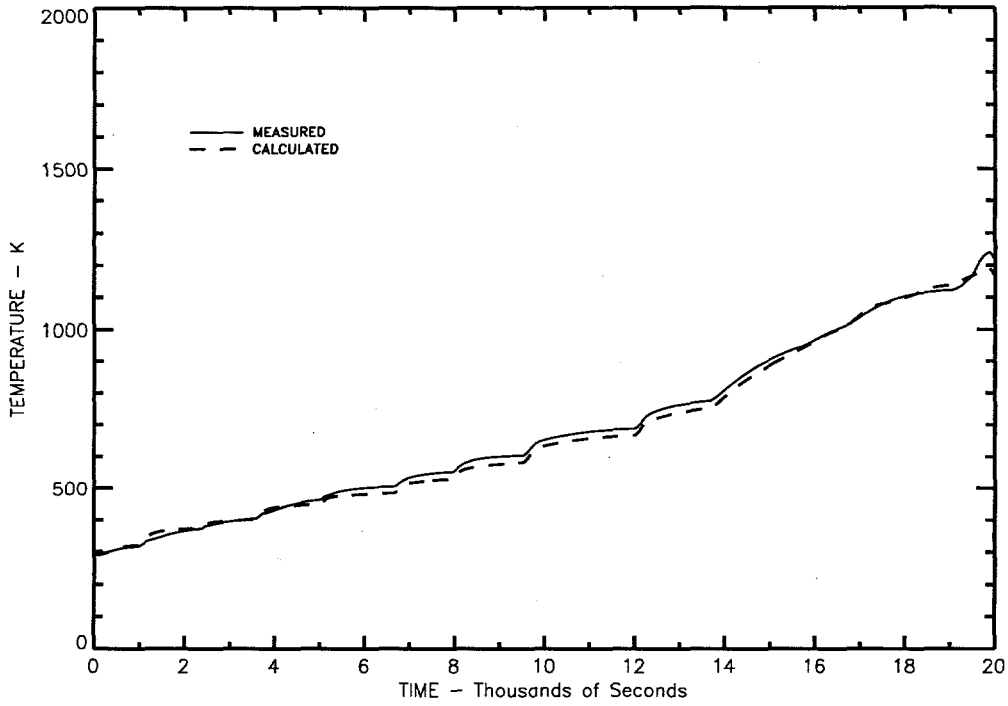

Figure 4.35 DEBRIS Code Results Compared With Tantalum Liner Thermocouple ***ZRK0558***.

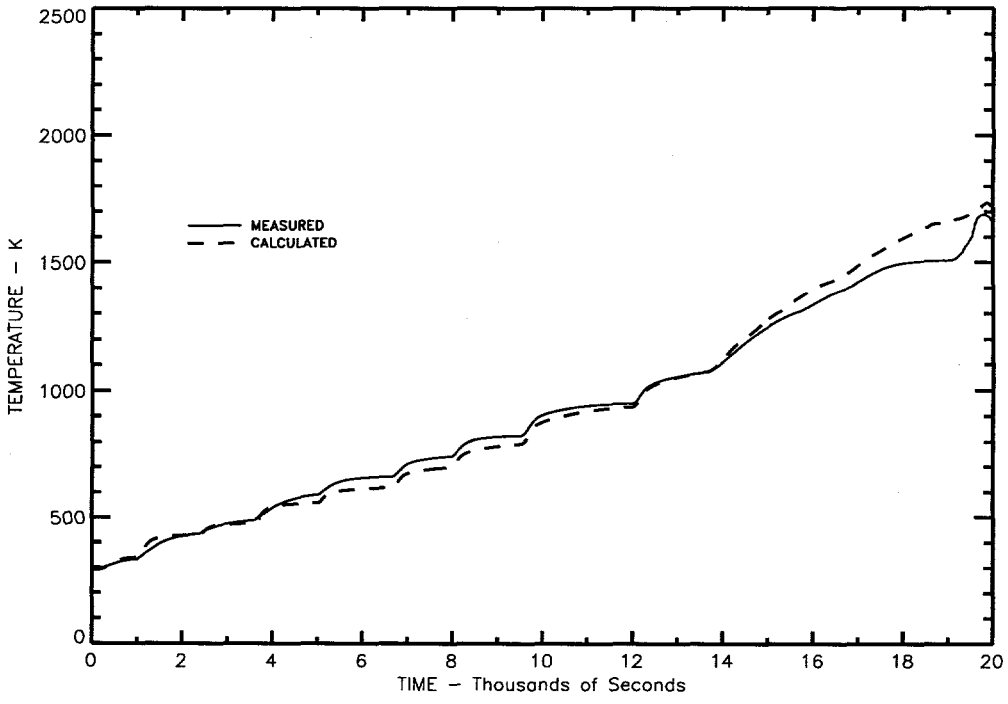

Figure 4.36 DEBRIS Code Results Compared With Tantalum Liner Thermocouple ***ZRC1158***

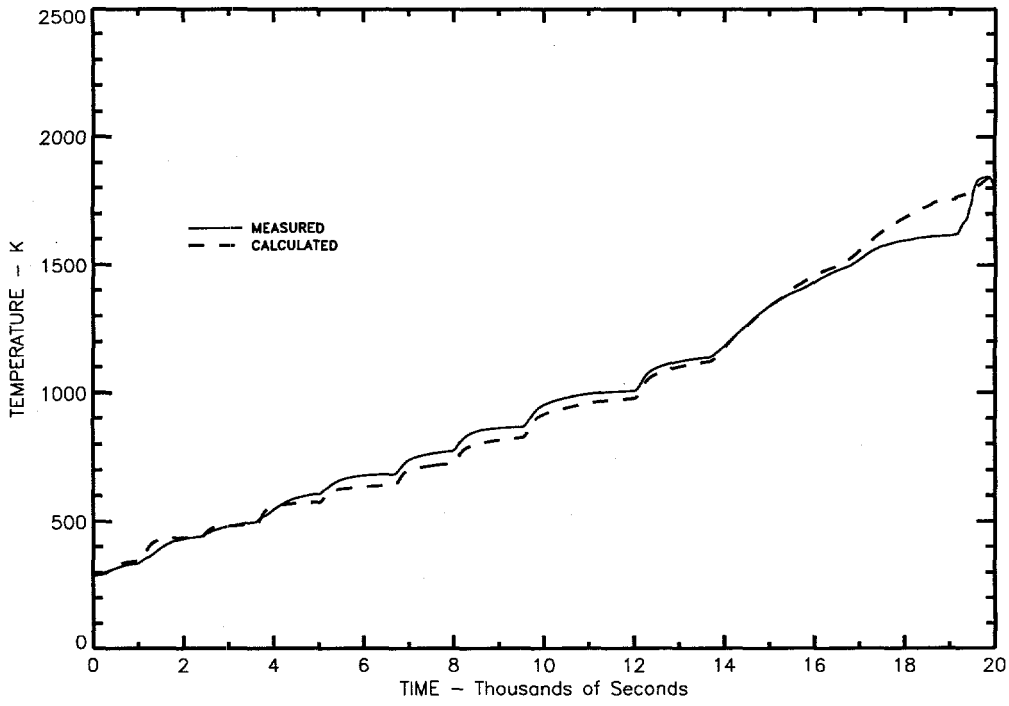

Figure 4.37 DEBRIS Code Results Compared With Tantalum Liner Thermocouple ***ZRC1258***

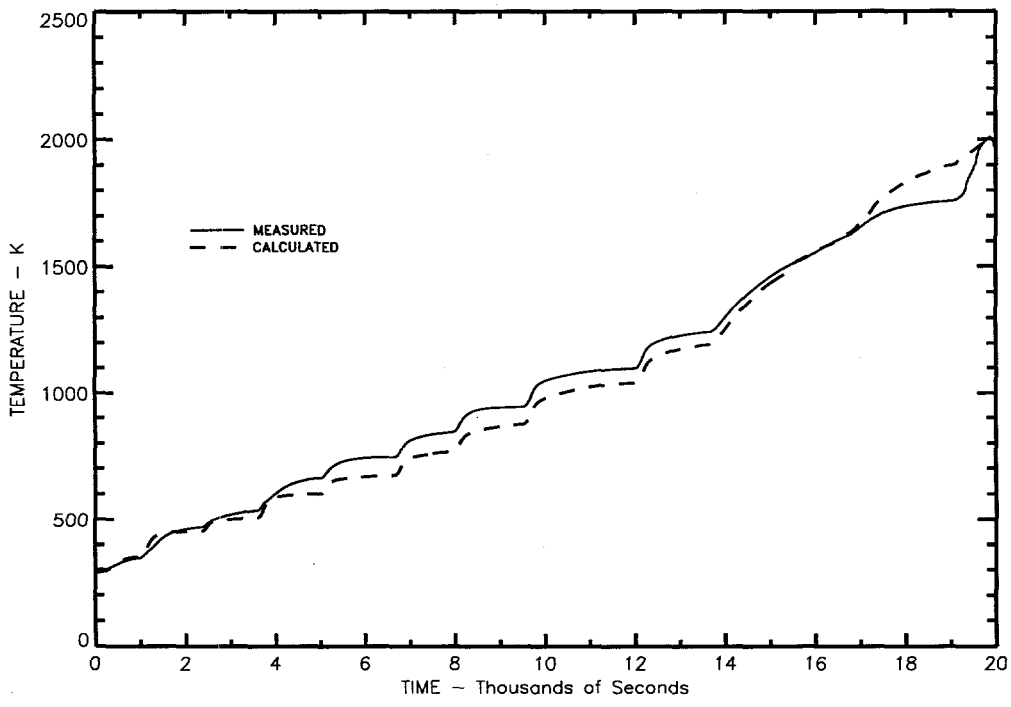

Figure 4.38 DEBRIS Code Results Compared With Tantalum Liner Thermocouple ***ZRC1458***

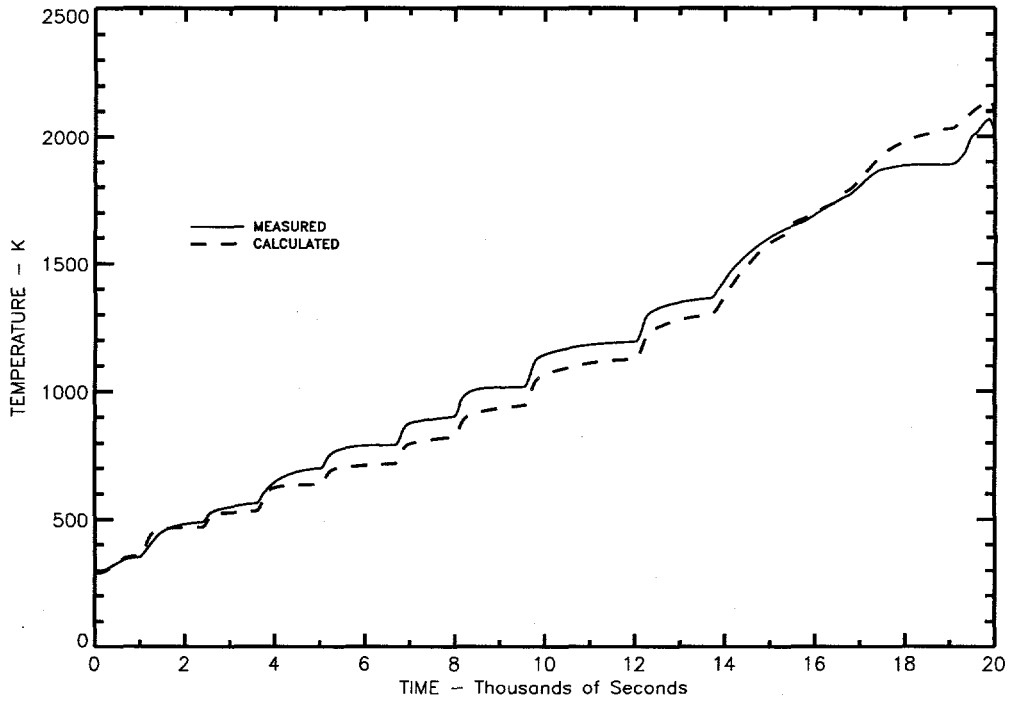

Figure 4.39 DEBRIS Code Results Compared With Tantalum Liner Thermocouple ***ZRC1658***

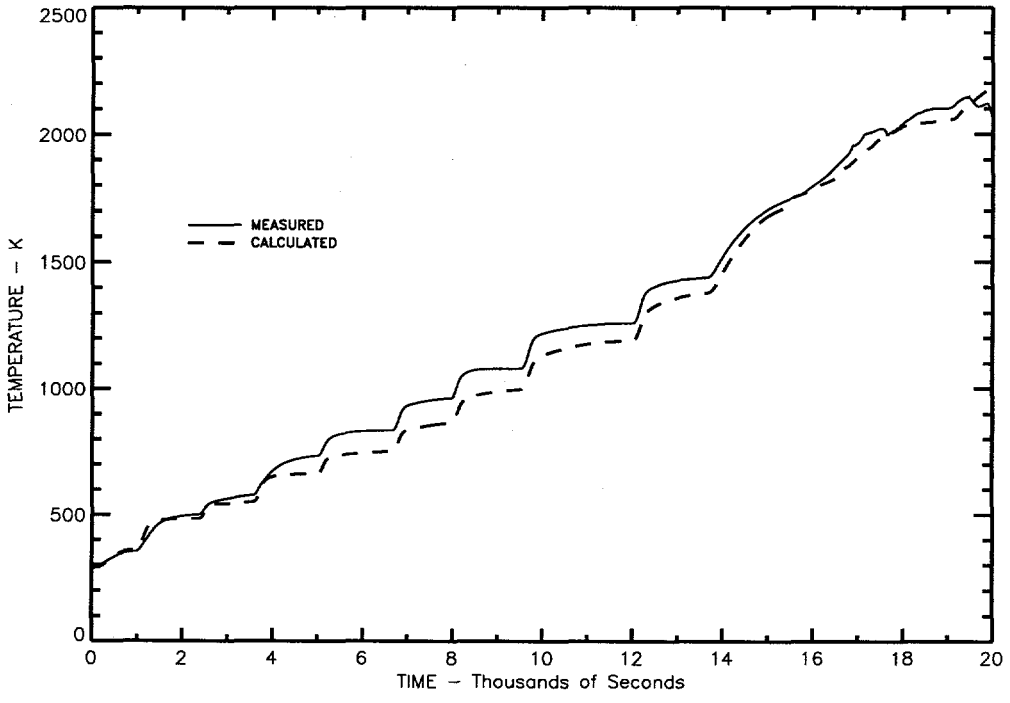

Figure 4.40 DEBRIS Code Results Compared With Tantalum Liner Thermocouple ***ZRC1858***

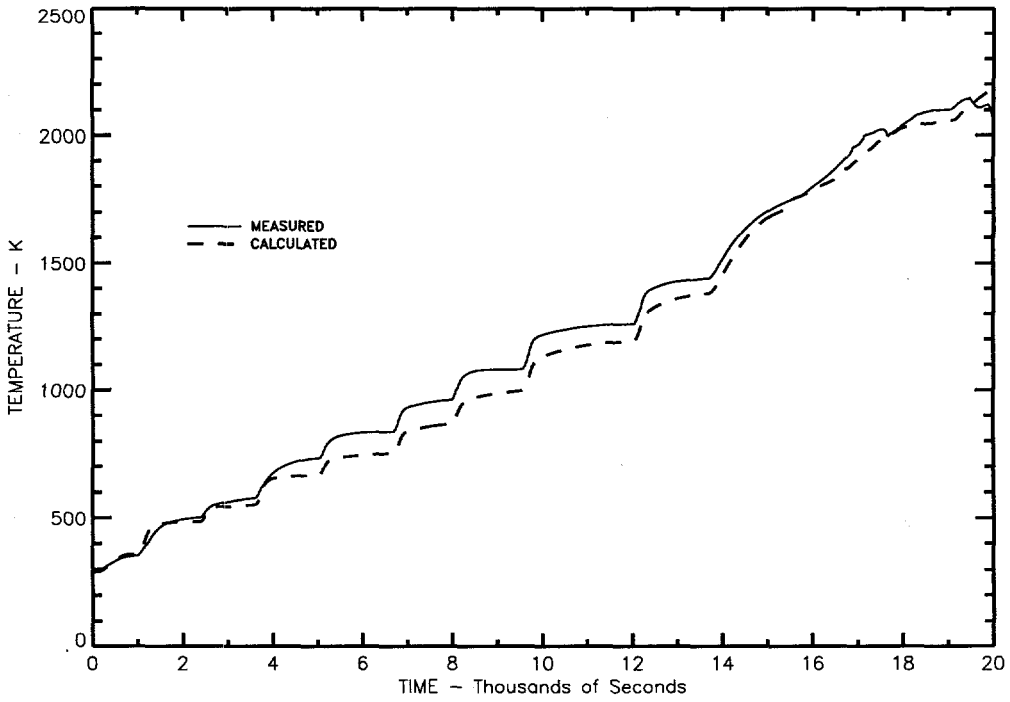

Figure 4.41 DEBRIS Code Results Compared With Tantalum Liner Thermocouple ***ZRC2158***

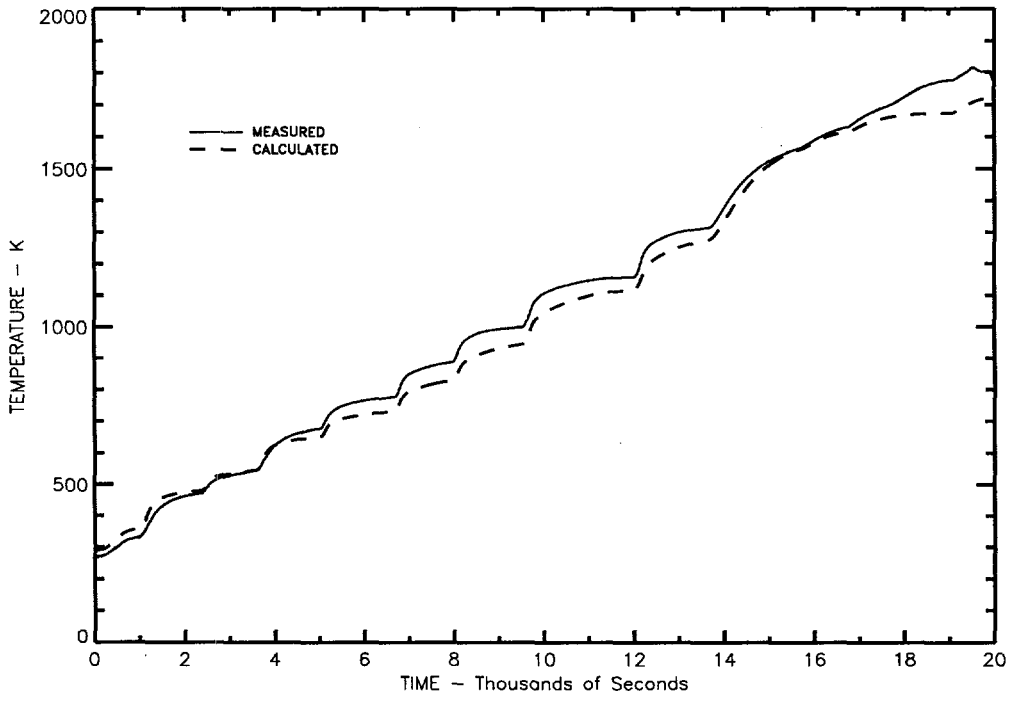

Figure 4.42 DEBRIS Code Results Compared With Tantalum Liner Thermocouple ***ZRC3058***

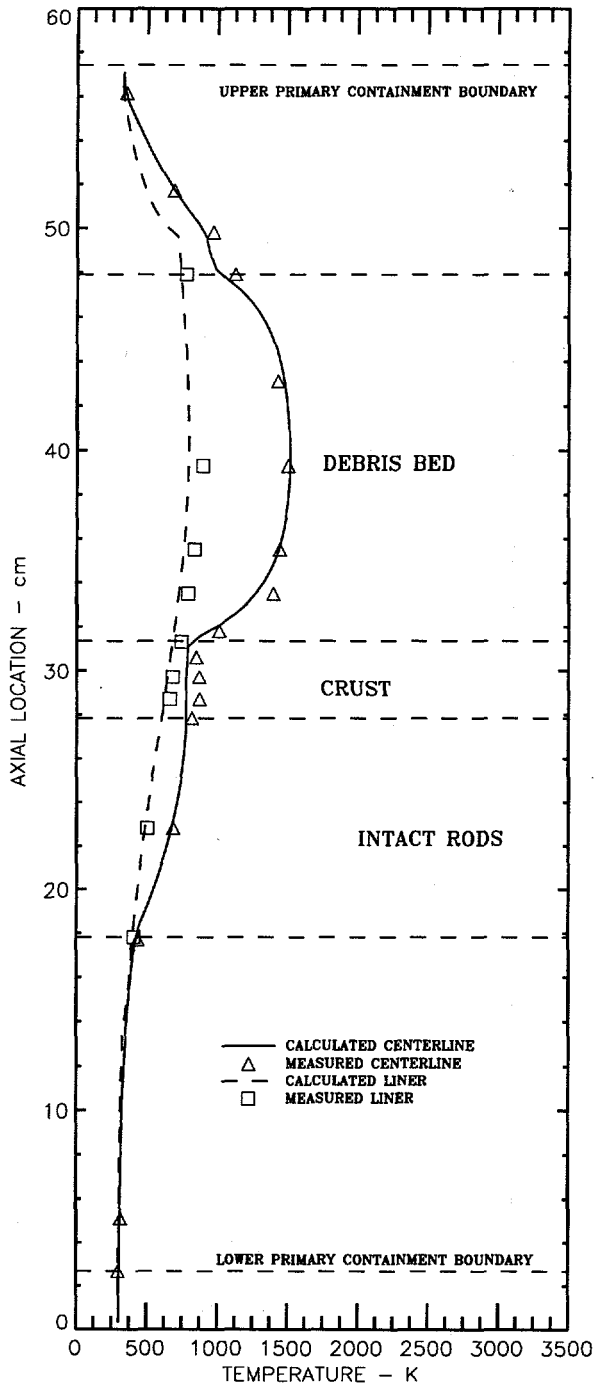

Figure 4.43 Calculated and Measured Axial Temperature Profiles at 6600 Seconds

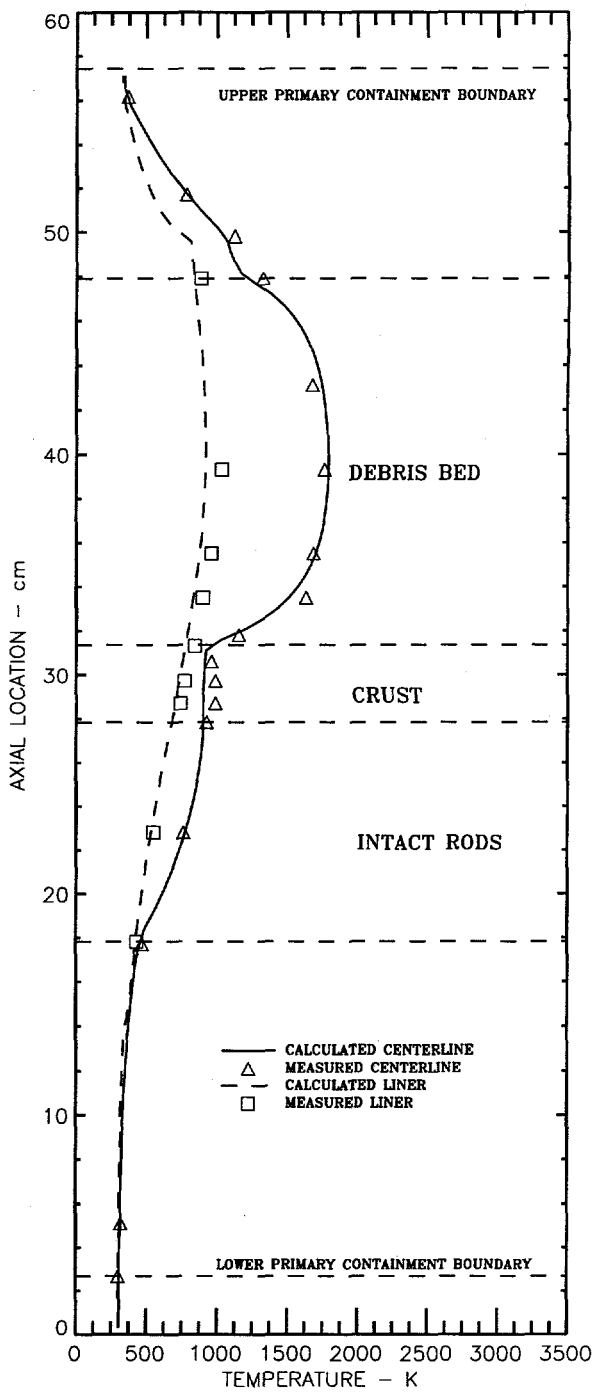

Figure 4.44 Calculated and Measured Axial Temperature Profiles at 7900 Seconds

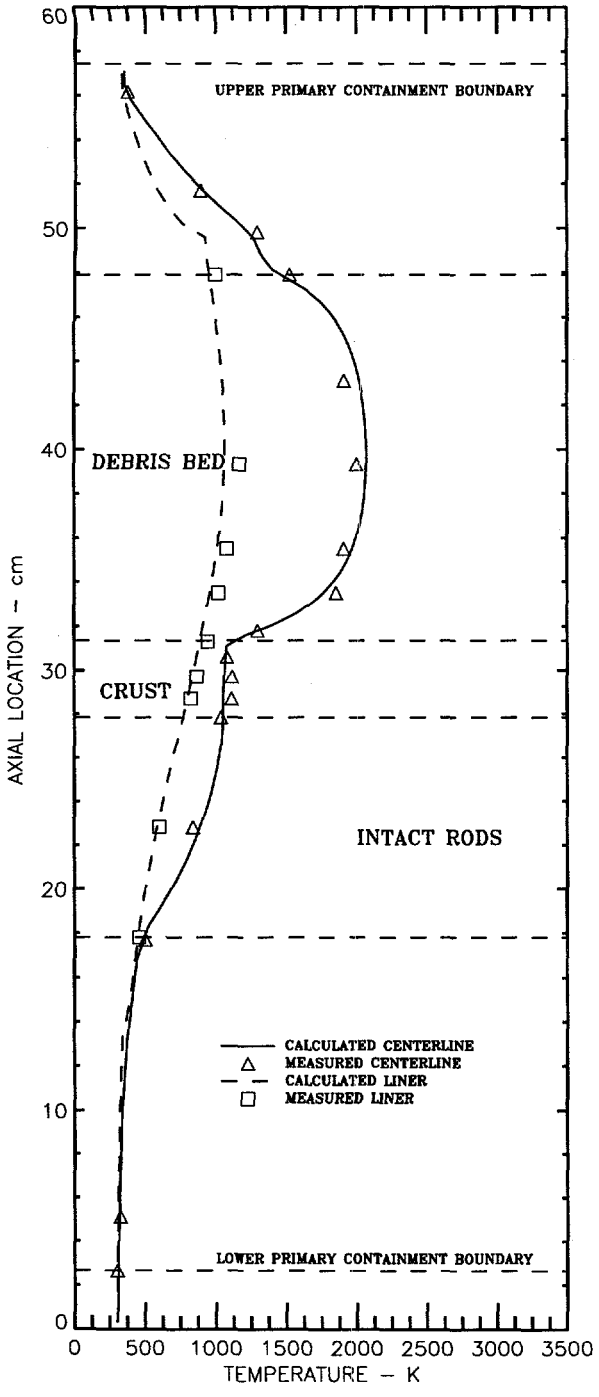

Figure 4.45 Calculated and Measured Axial Temperature Profiles at 9500 Seconds

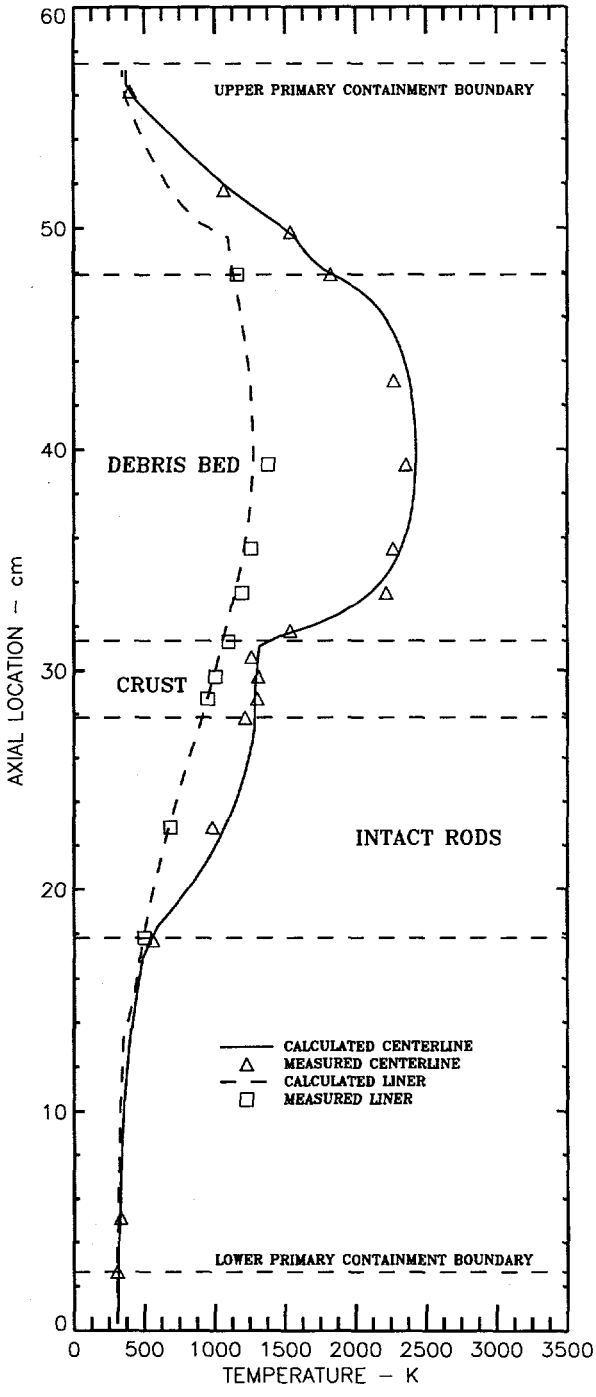

Figure 4.46 Calculated and Measured Axial Temperature Profiles at 12,000 Seconds

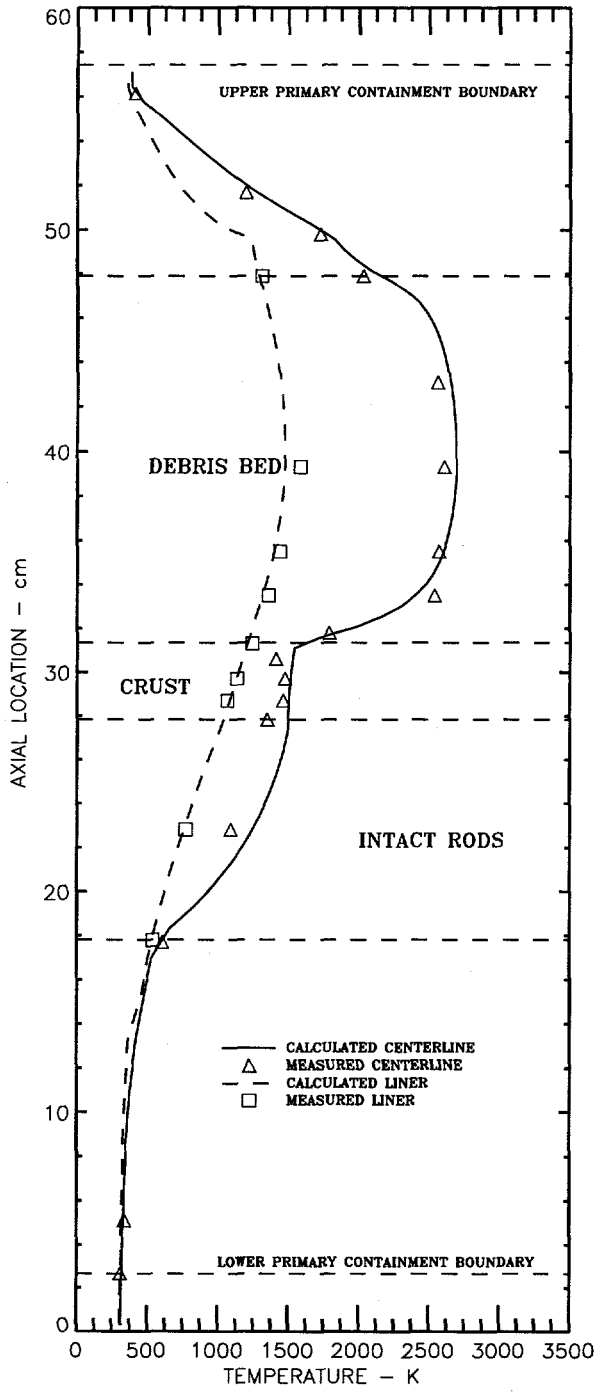

Figure 4.47 Calculated and Measured Axial Temperature Profiles at 13,500 Seconds

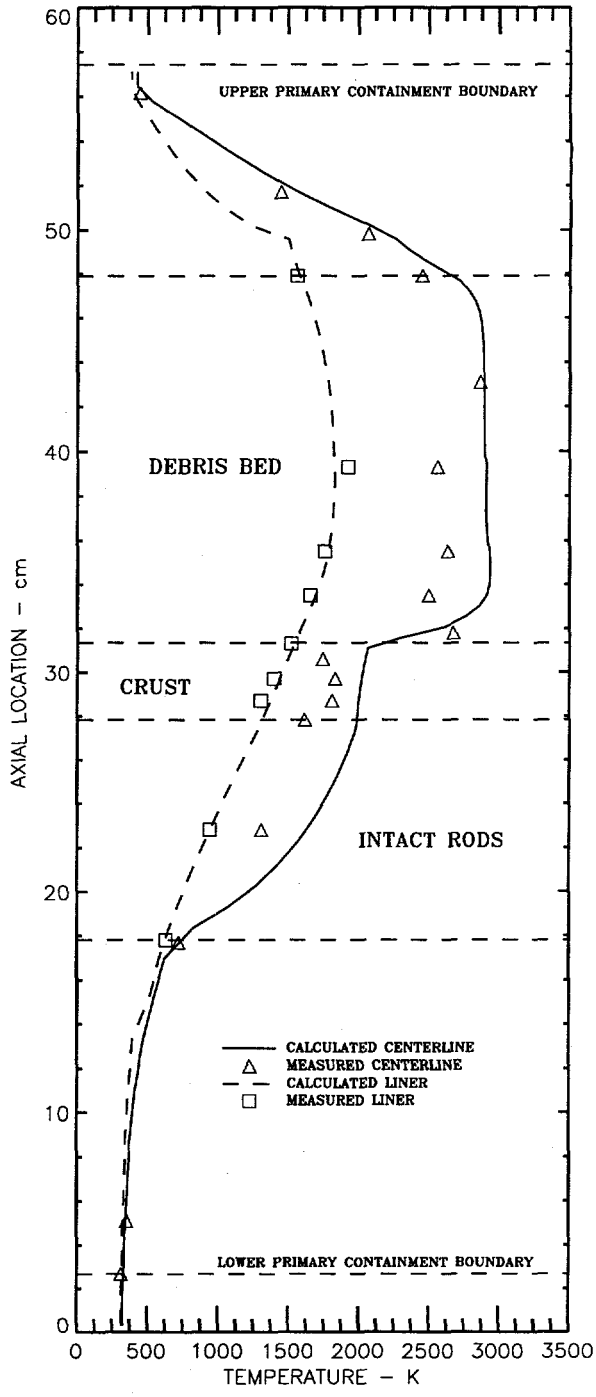

Figure 4.48 Calculated and Measured Axial Temperature Profiles at 15,600 Seconds

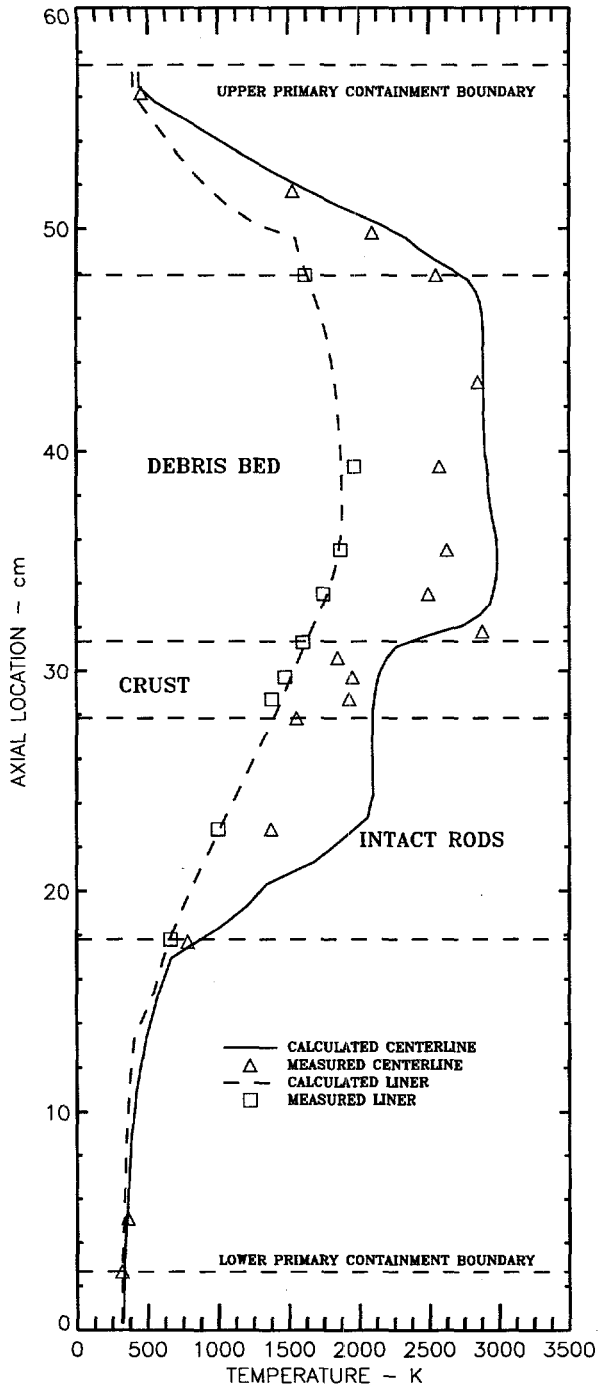

Figure 4.49 Calculated and Measured Axial Temperature Profiles at 16,500 Seconds

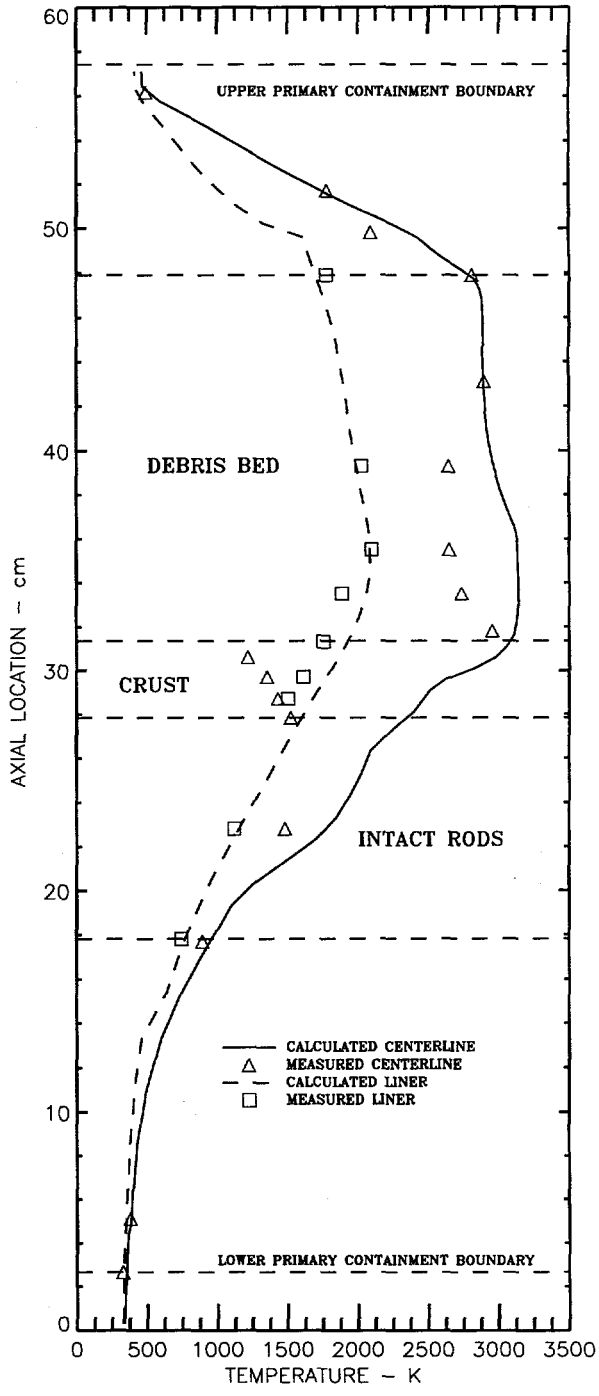

Figure 4.50 Calculated and Measured Axial Temperature Profiles at 19,000 Seconds

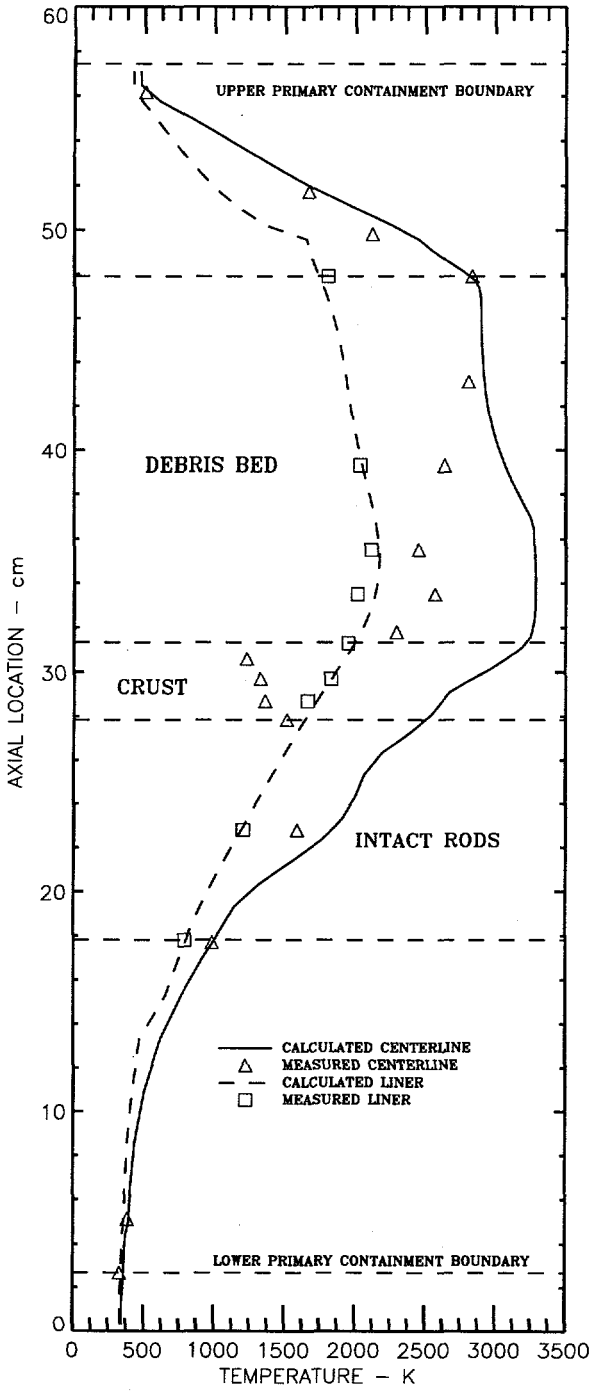

Figure 4.51 Calculated and Measured Axial Temperature Profiles at 19,600 Seconds

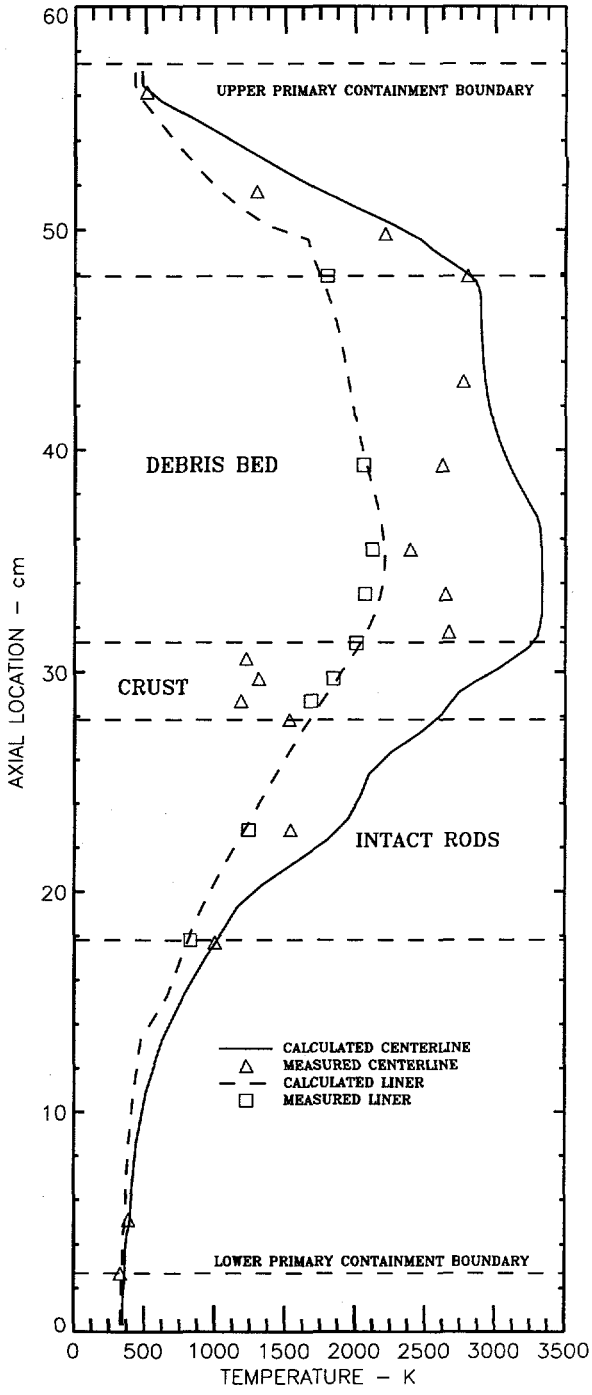

Figure 4.52 Calculated and Measured Axial Temperature Profiles at 19,870 Seconds

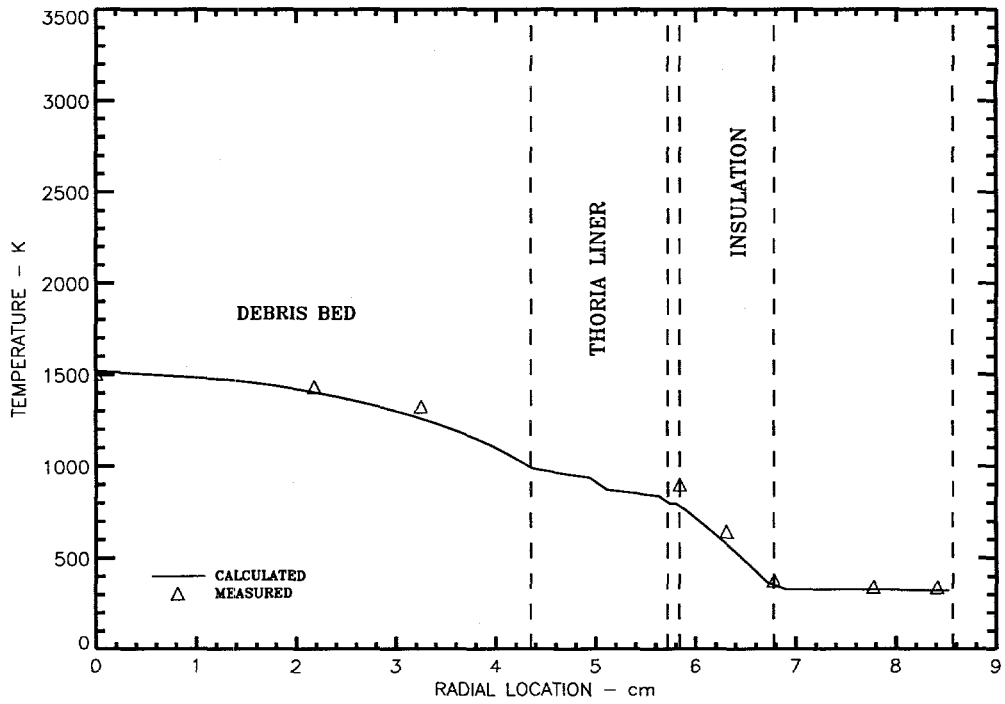

Figure 4.53 Calculated and Measured Radial Temperature Profiles at 6600 Seconds

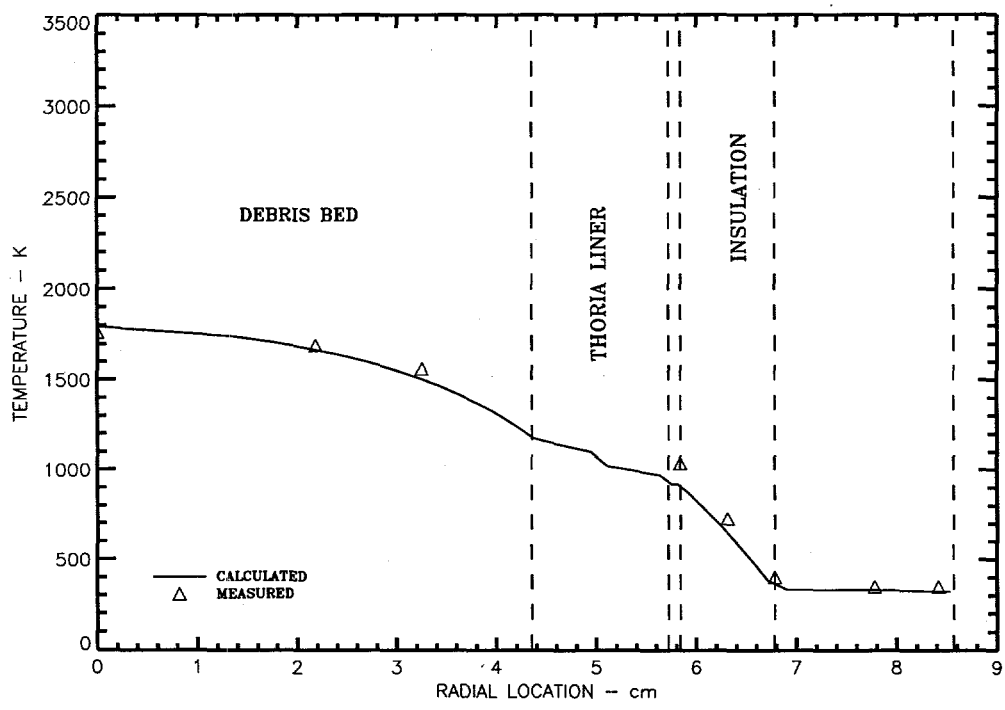

Figure 4.54 Calculated and Measured Radial Temperature Profiles at 7900 Seconds

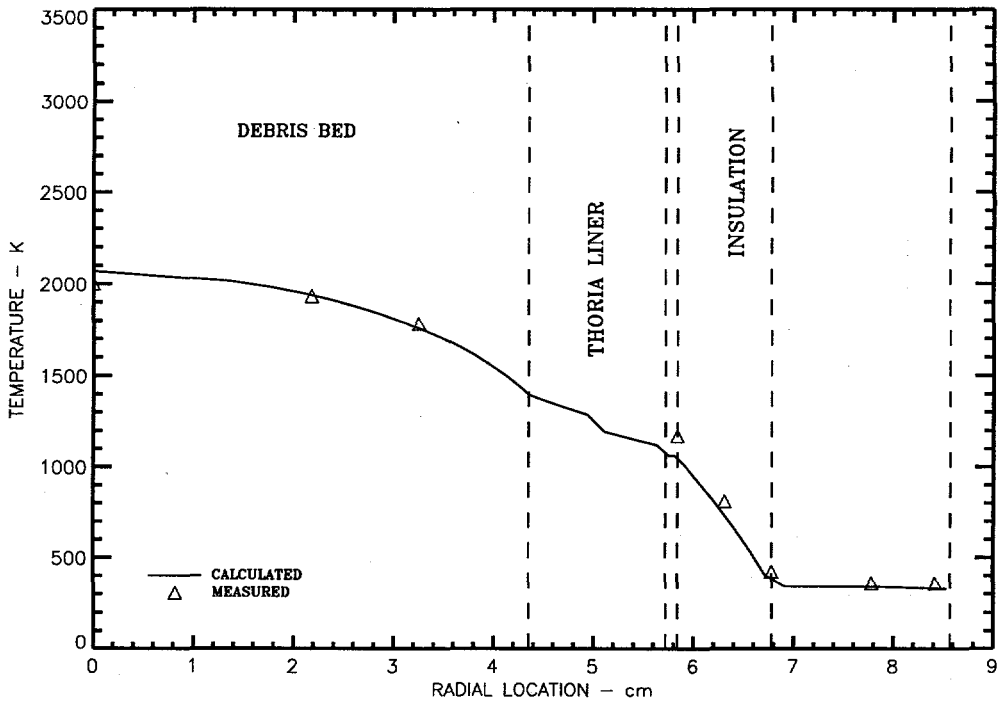

Figure 4.55 Calculated and Measured Radial Temperature Profiles at 9500 Seconds

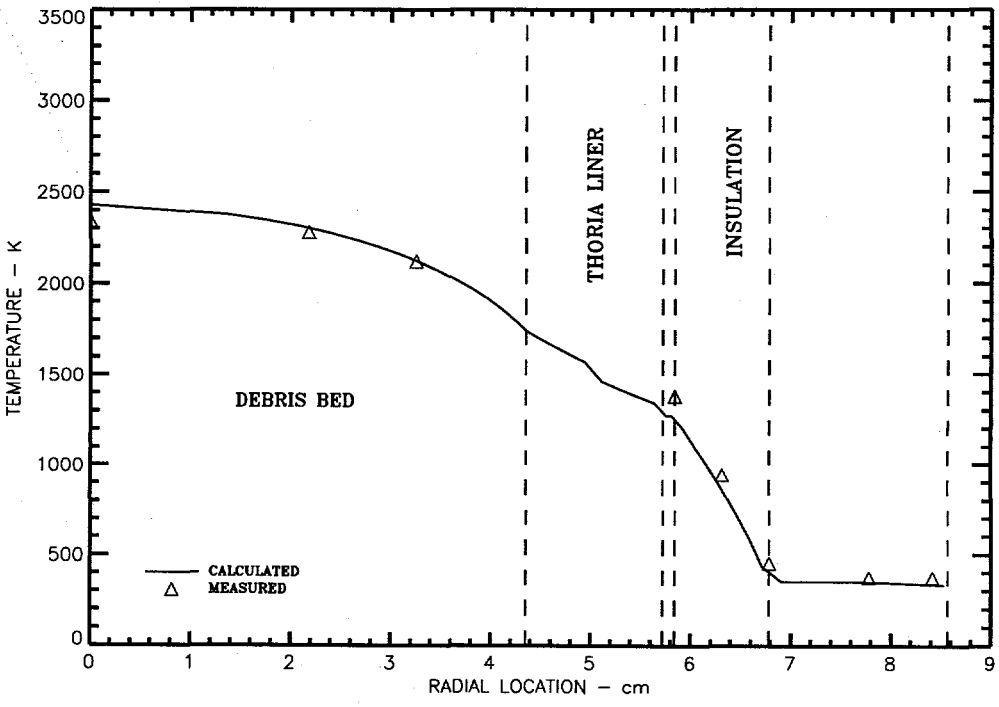

Figure 4.56 Calculated and Measured Radial Temperature Profiles at 12,000 Seconds

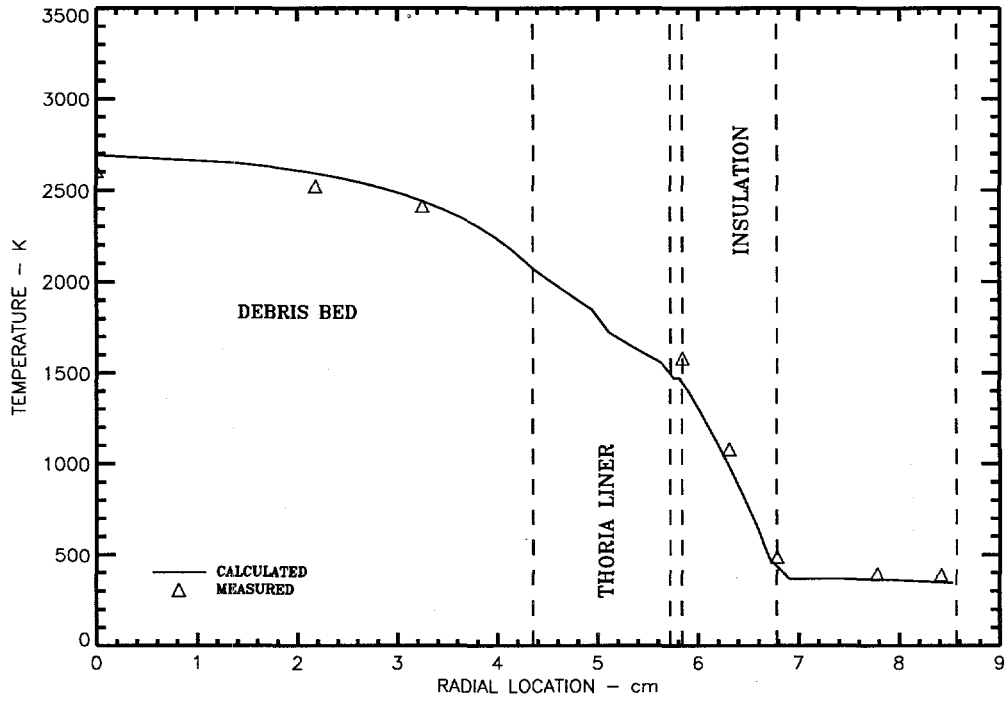

Figure 4.57 Calculated and Measured Radial Temperature Profiles at 13,500 Seconds

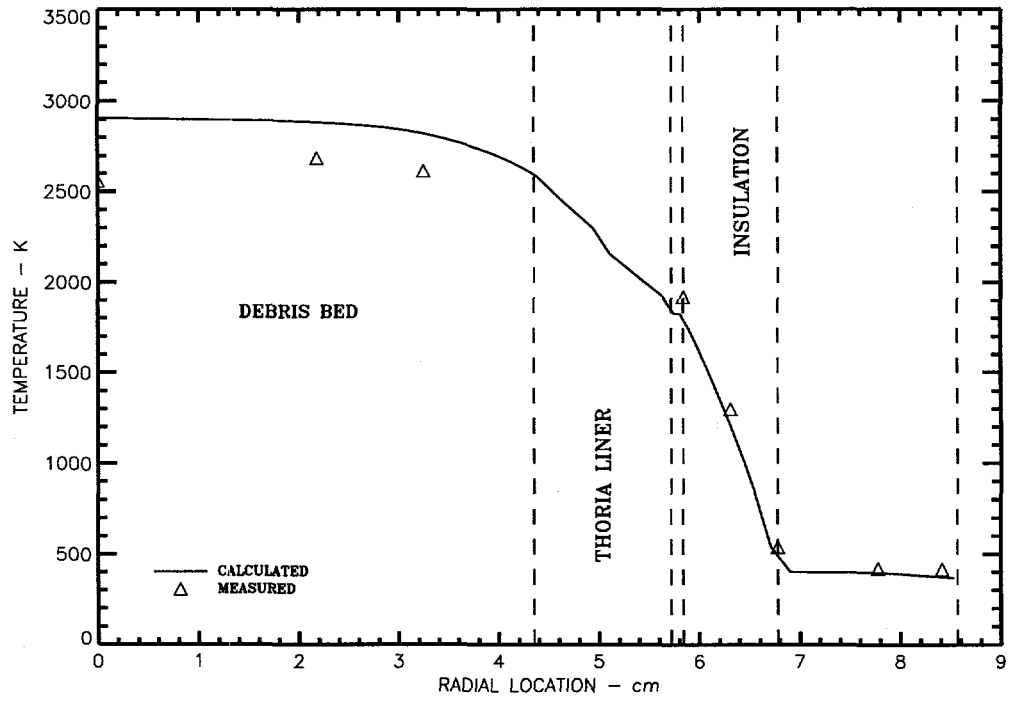

Figure 4.58 Calculated and Measured Radial Temperature Profiles at 15,600 Seconds

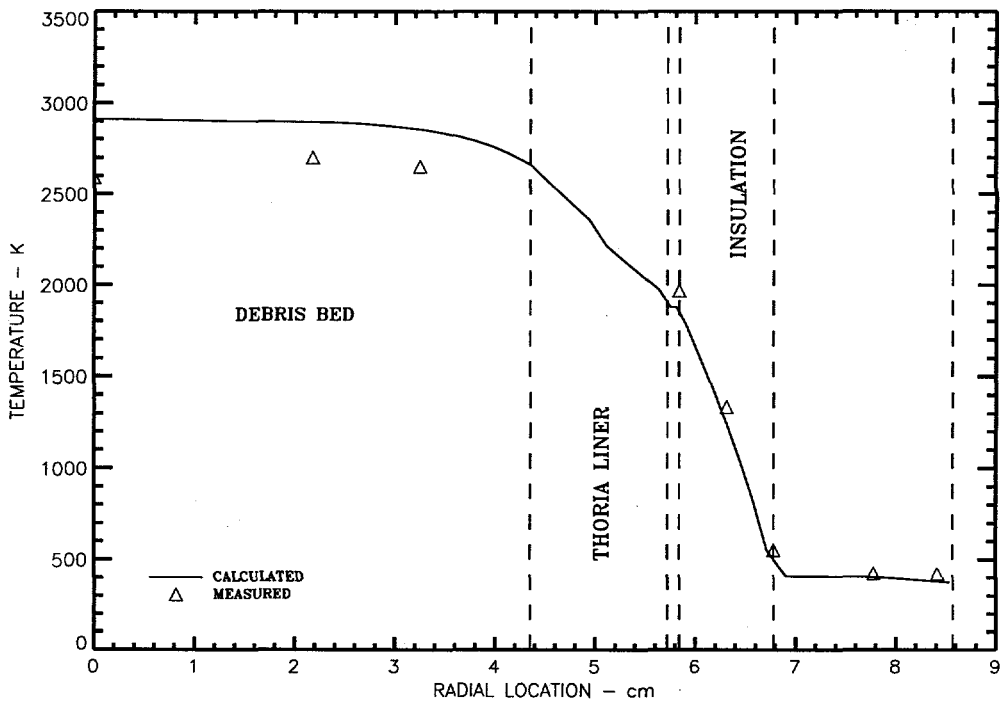

Figure 4.59 Calculated and Measured Radial Temperature Profiles at 16,500 Seconds

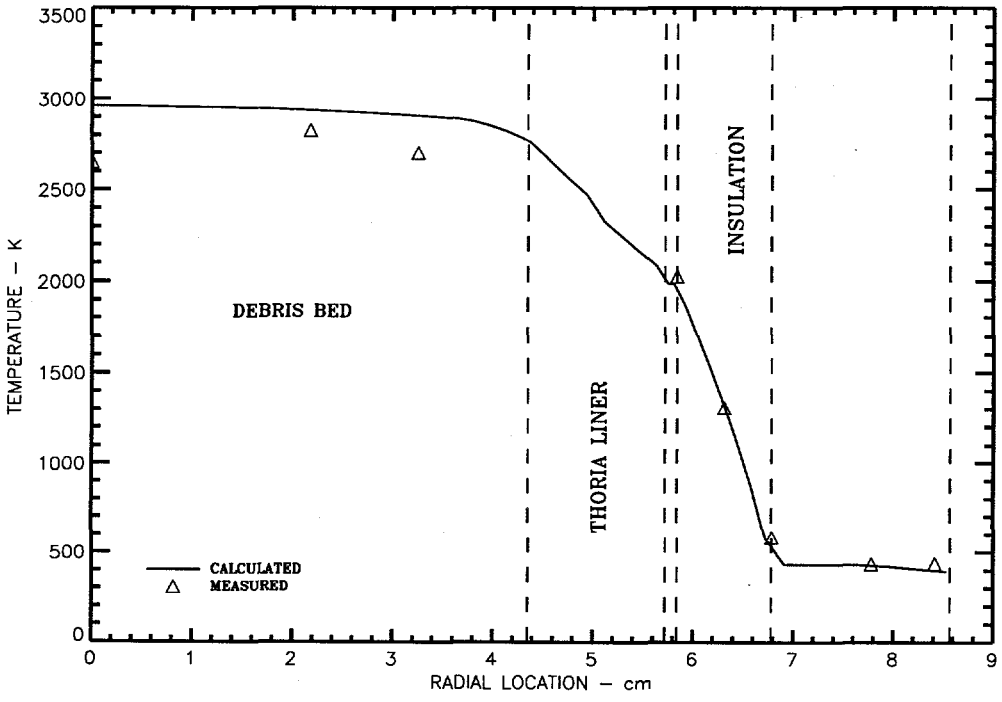

Figure 4.60 Calculated and Measured Radial Temperature Profiles at 19,000 Seconds

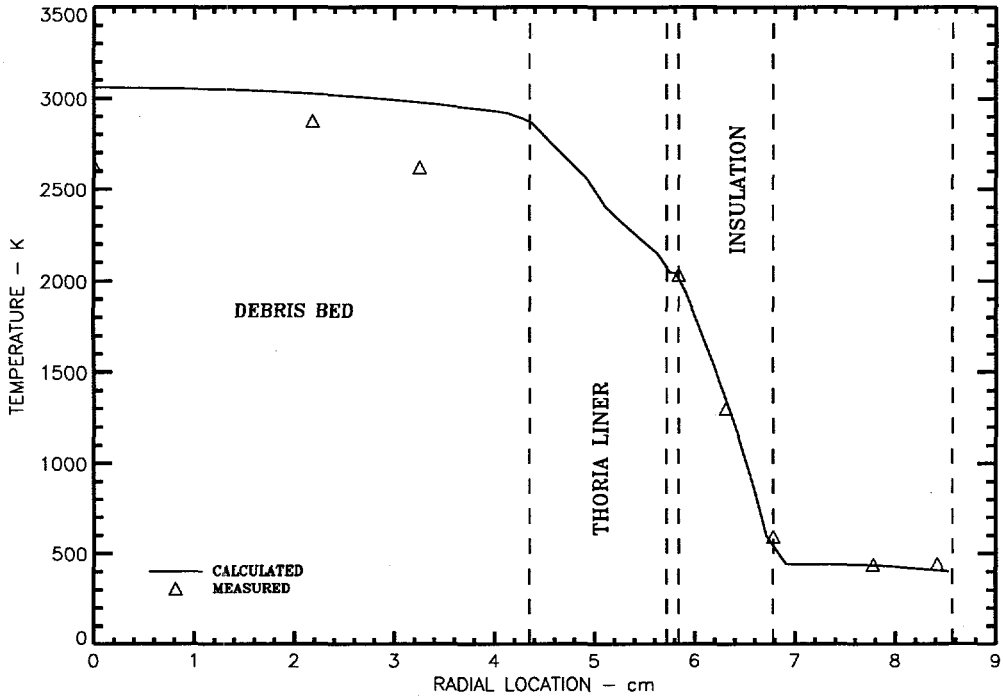

Figure 4.61 Calculated and Measured Radial Temperature Profiles at 19,600 Seconds

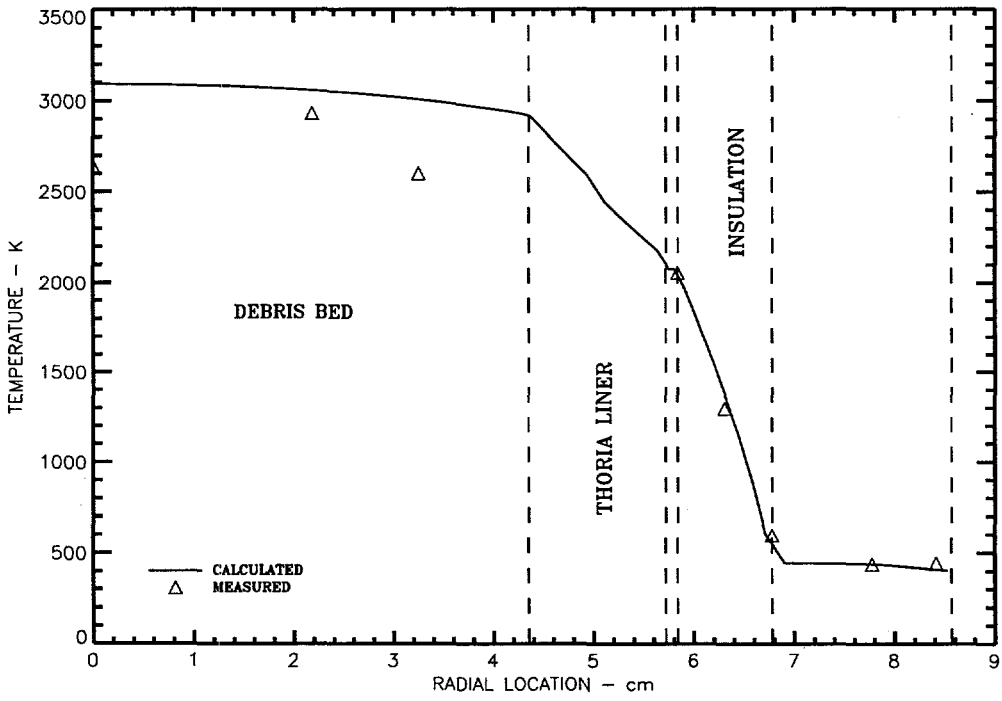

Figure 4.62 Calculated and Measured Radial Temperature Profiles at 19,870 Seconds

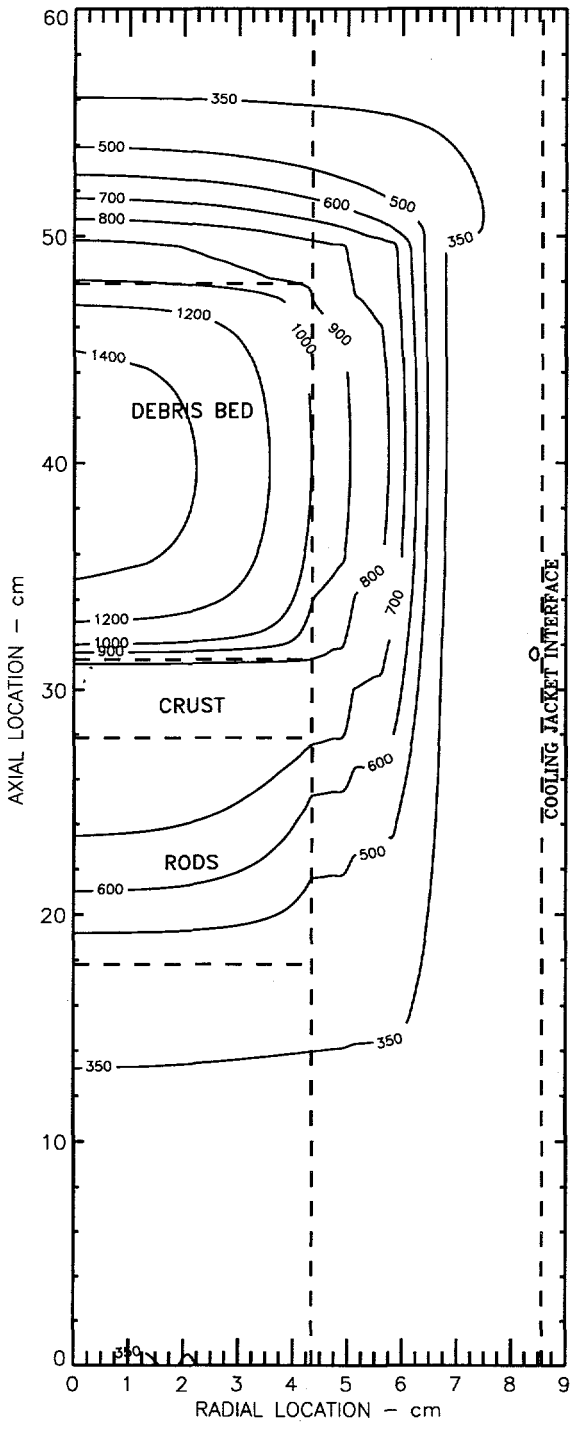

Figure 4.63 MP-2 Calculated Temperature Profile at 6600 Seconds in Heatup Phase

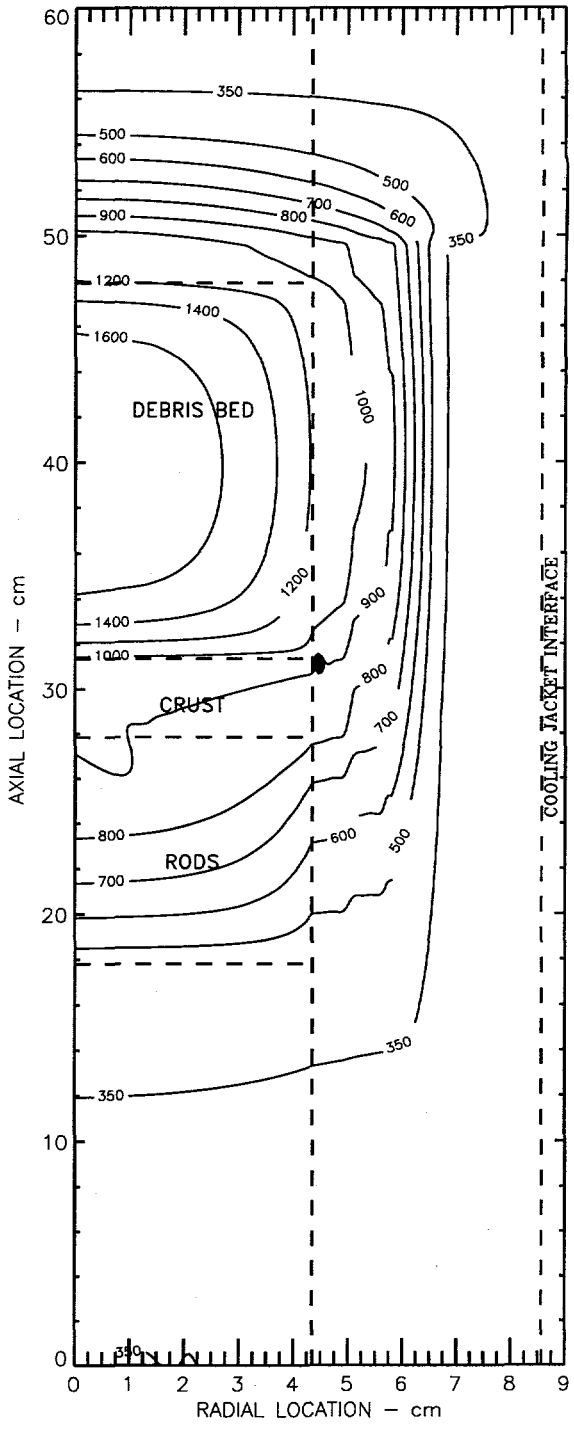

Figure 4.64 MP-2 Calculated Temperature Profile at 7900 Seconds in Heatup Phase

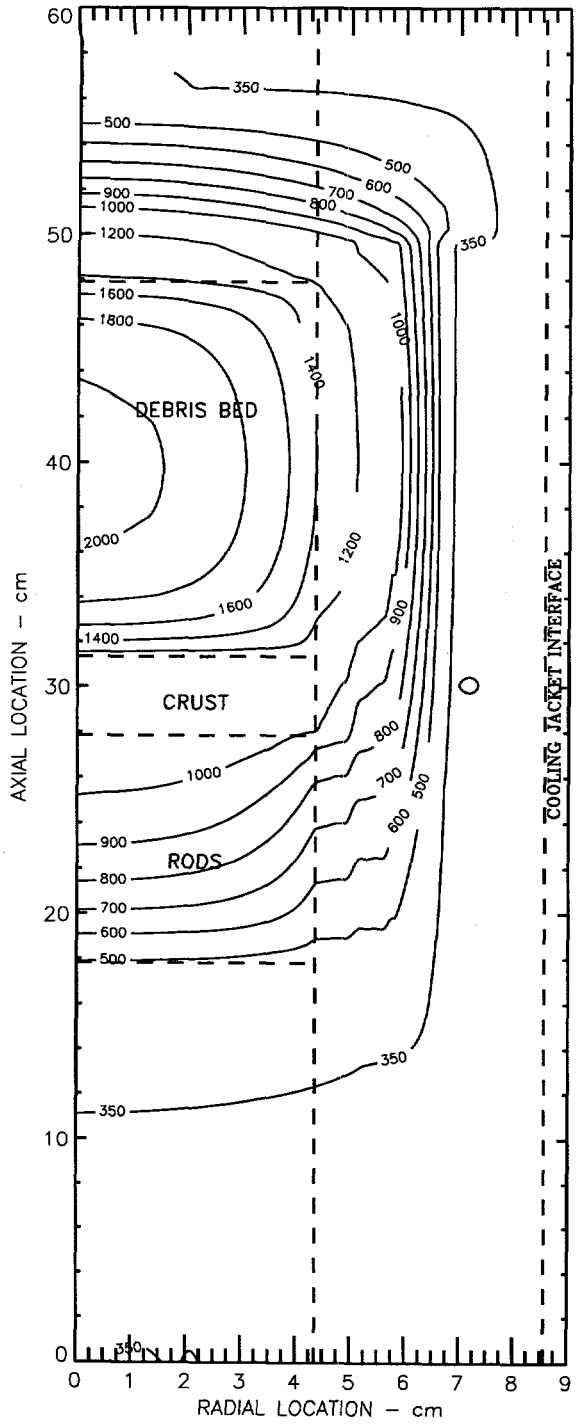

Figure 4.65 MP-2 Calculated Temperature Profile at 9500 Seconds in Heatup Phase

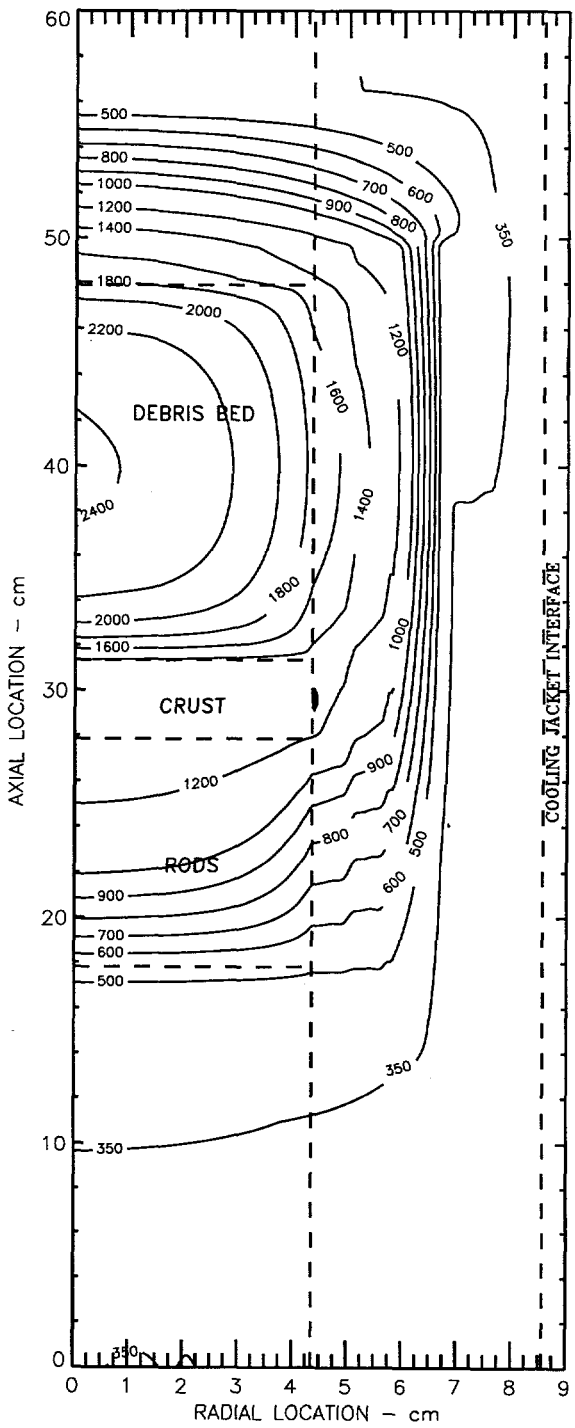

Figure 4.66 MP-2 Calculated Temperature Profile at 12,000 Seconds in Heatup Phase

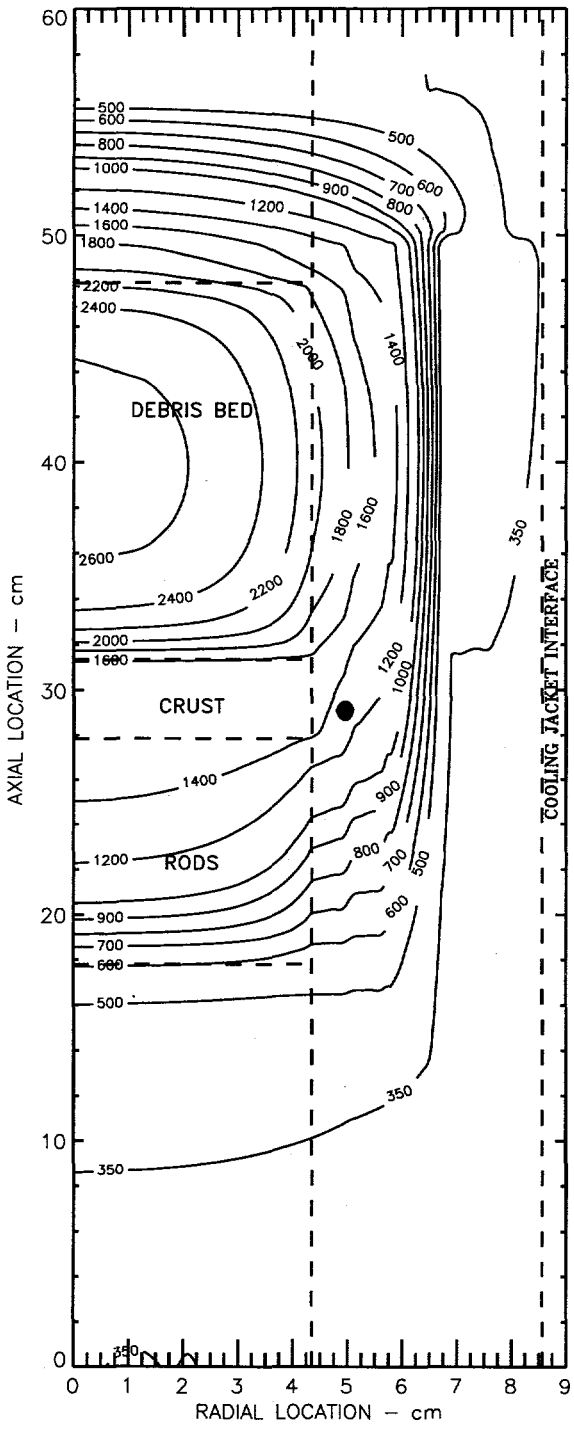

Figure 4.67 MP-2 Calculated Temperature Profile at 13,500 Seconds in Heatup Phase

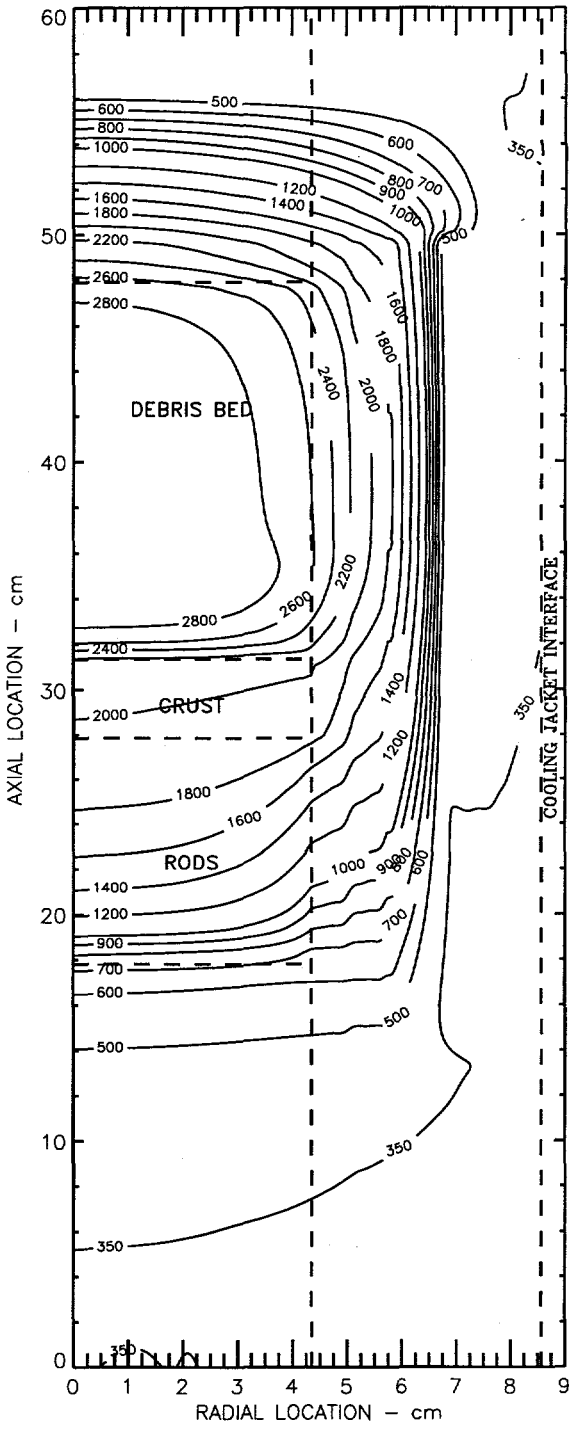

Figure 4.68 MP-2 Calculated Temperature Profile at 15,600 Seconds in Melt Phase

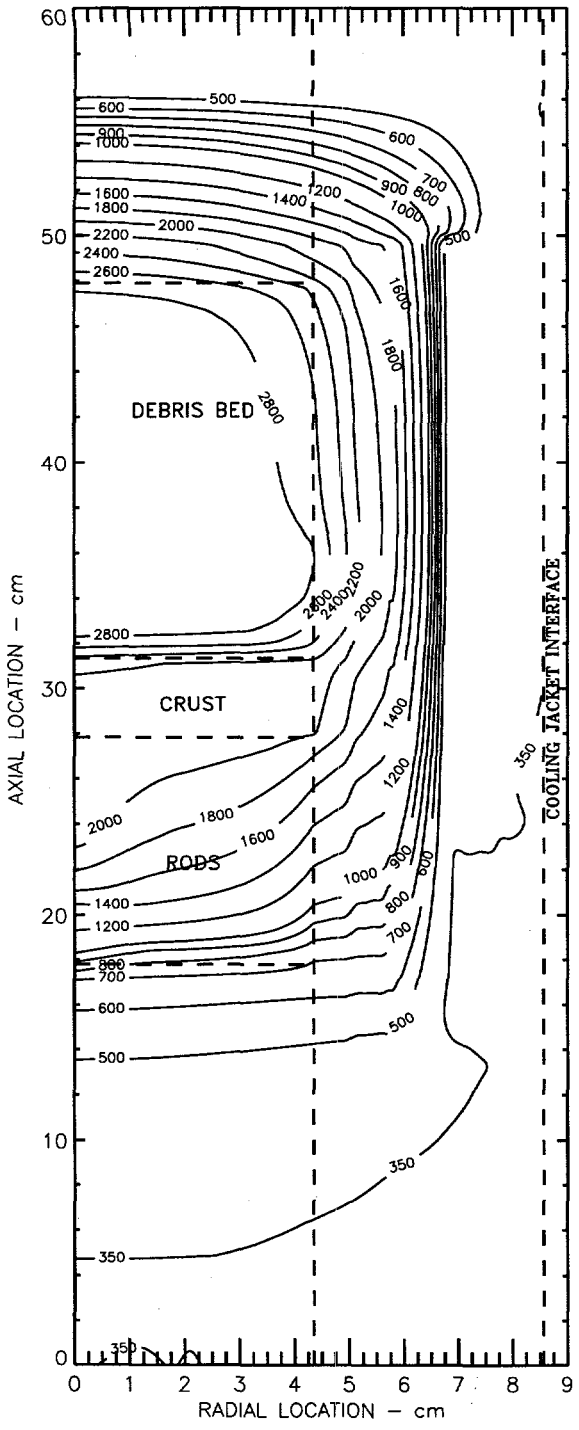

Figure 4.69 MP-2 Calculated Temperature Profile at 16,500 Seconds in Melt Phase

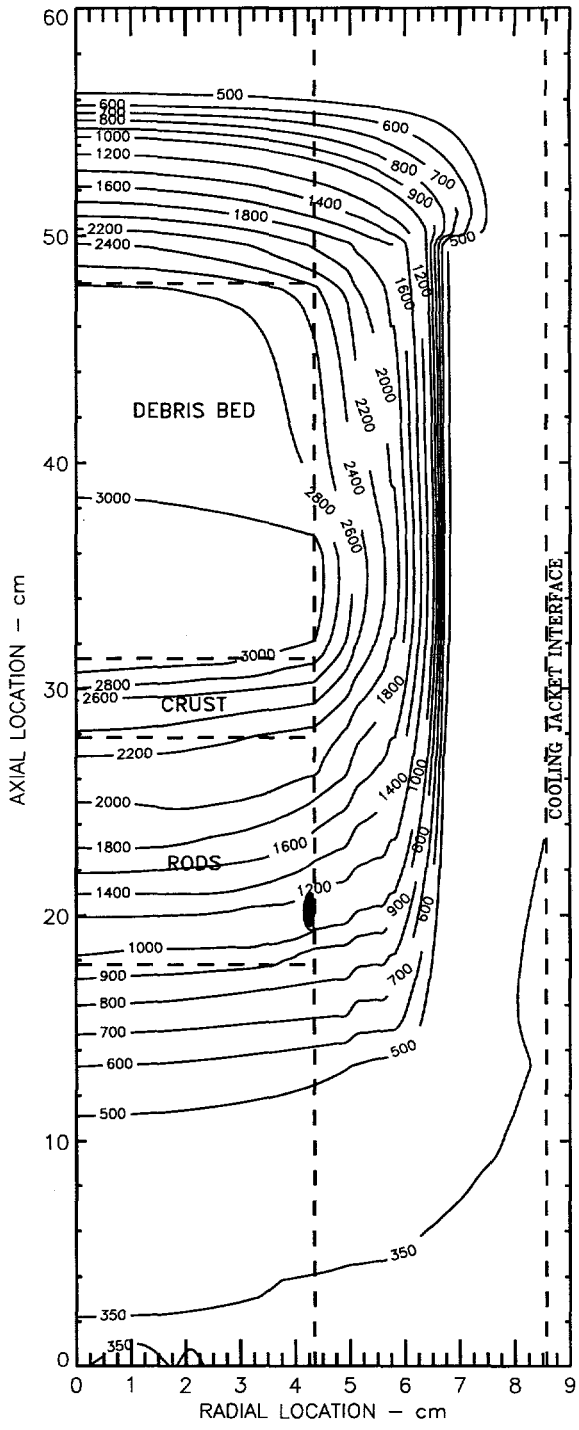

Figure 4.70 MP-2 Calculated Temperature Profile at 19,000 Seconds in Melt Phase

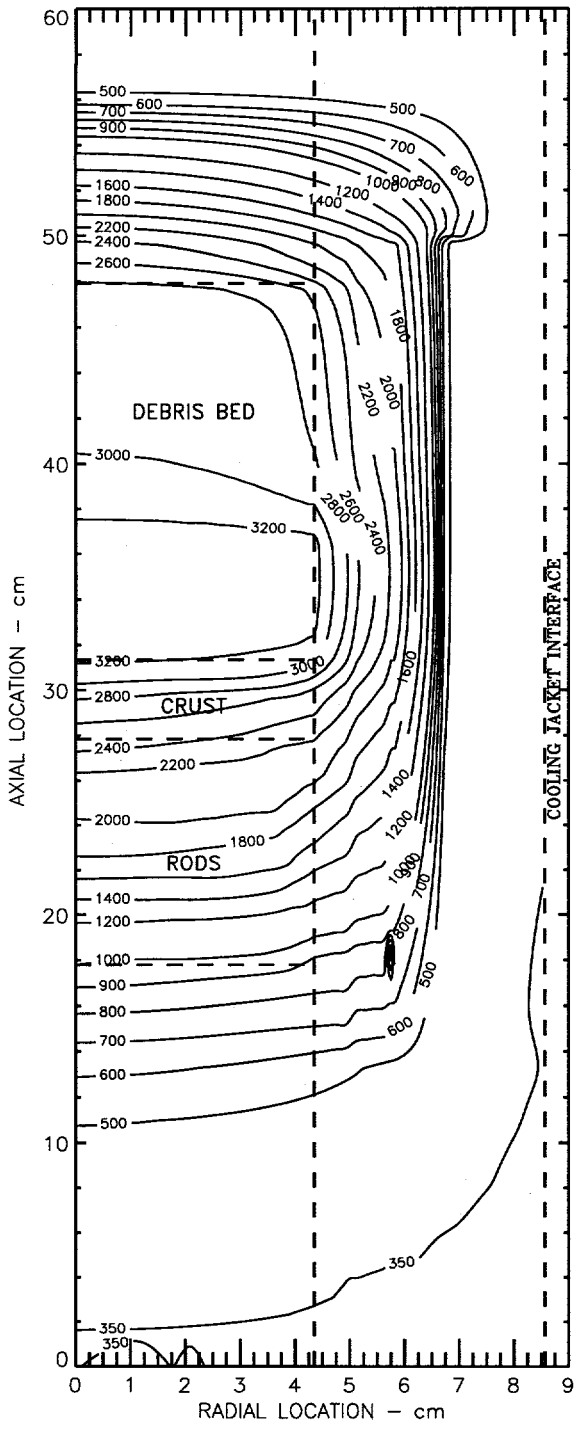

Figure 4.71 MP-2 Calculated Temperature Profile at 19,600 Seconds in Melt Phase

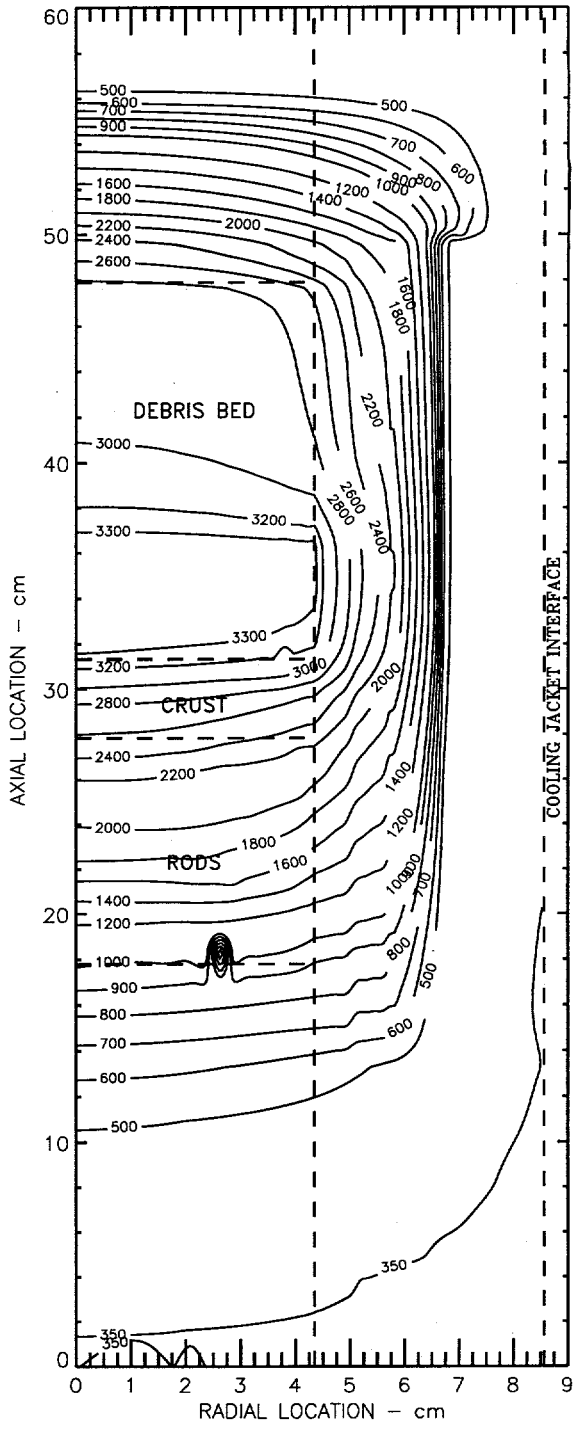

Figure 4.72 MP-2 Calculated Temperature Profile at 19,870 Seconds at End of Test

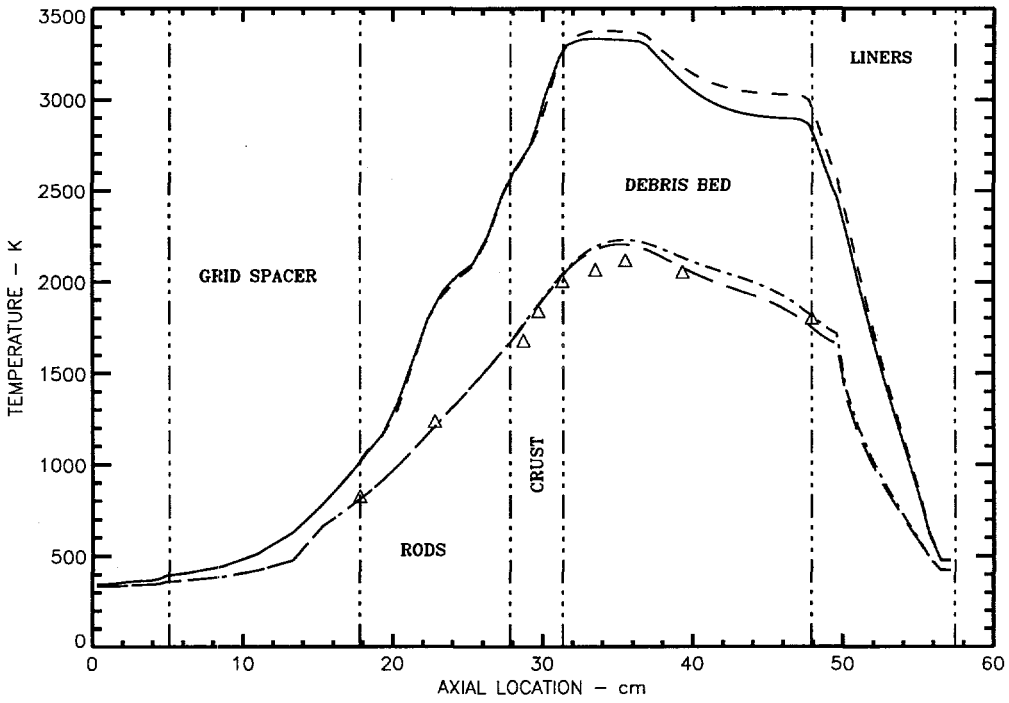

Figure 4.73 Comparison of Cases "A" and "B" End-of-Test Axial Temperature Profiles

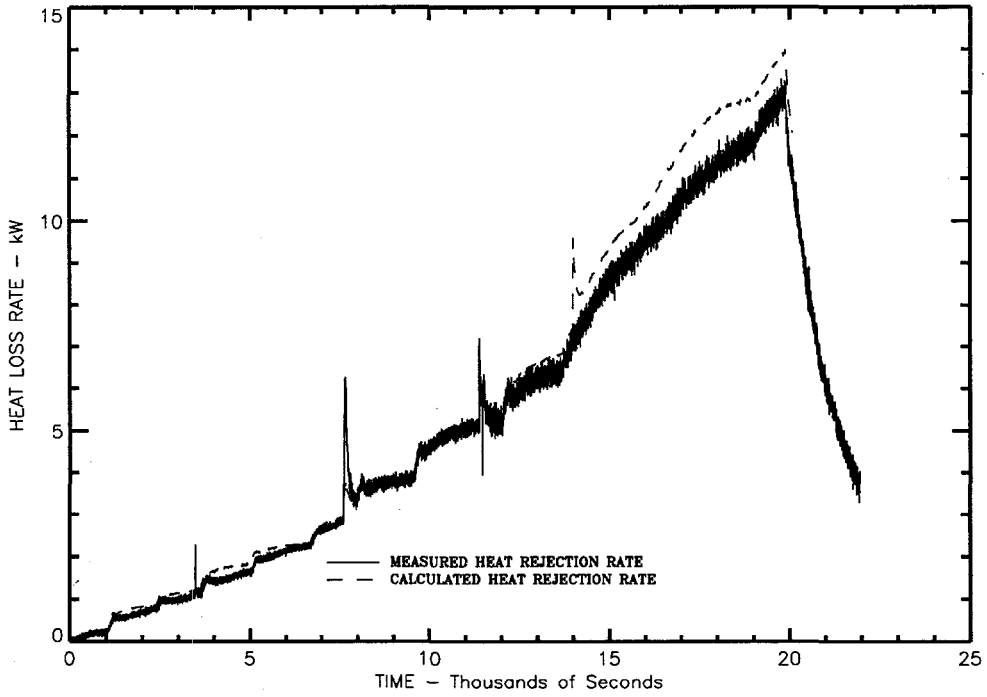

Figure 4.74 MP-2 Calculated Versus Measured Coolant Heat Rejection Rate

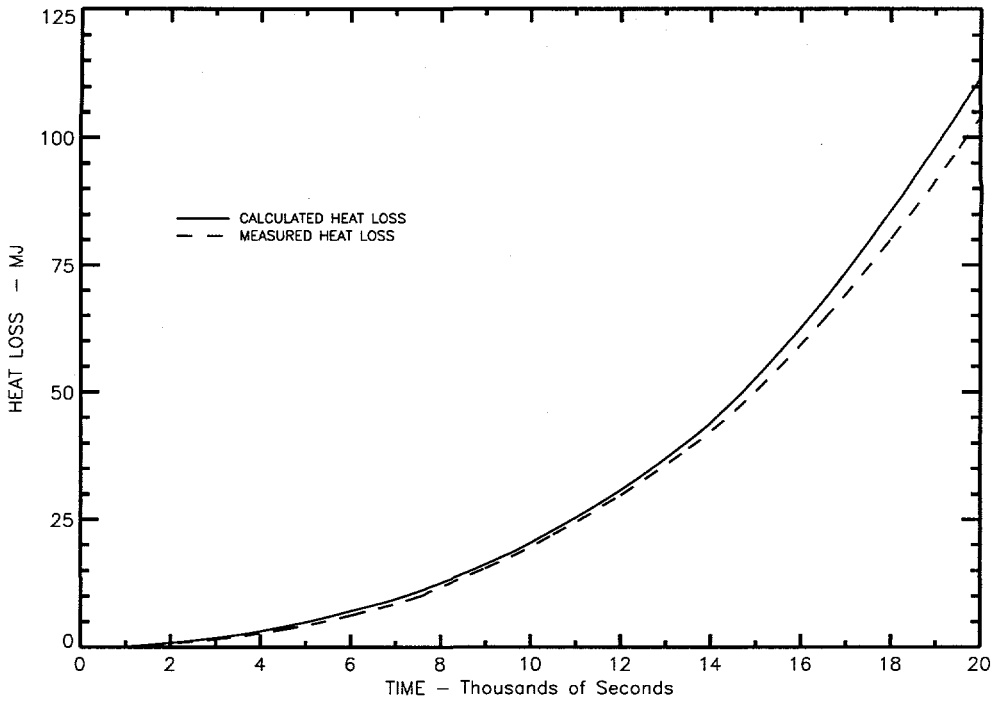

Figure 4.75 MP-2 Calculated Versus Measured Total Heat Losses

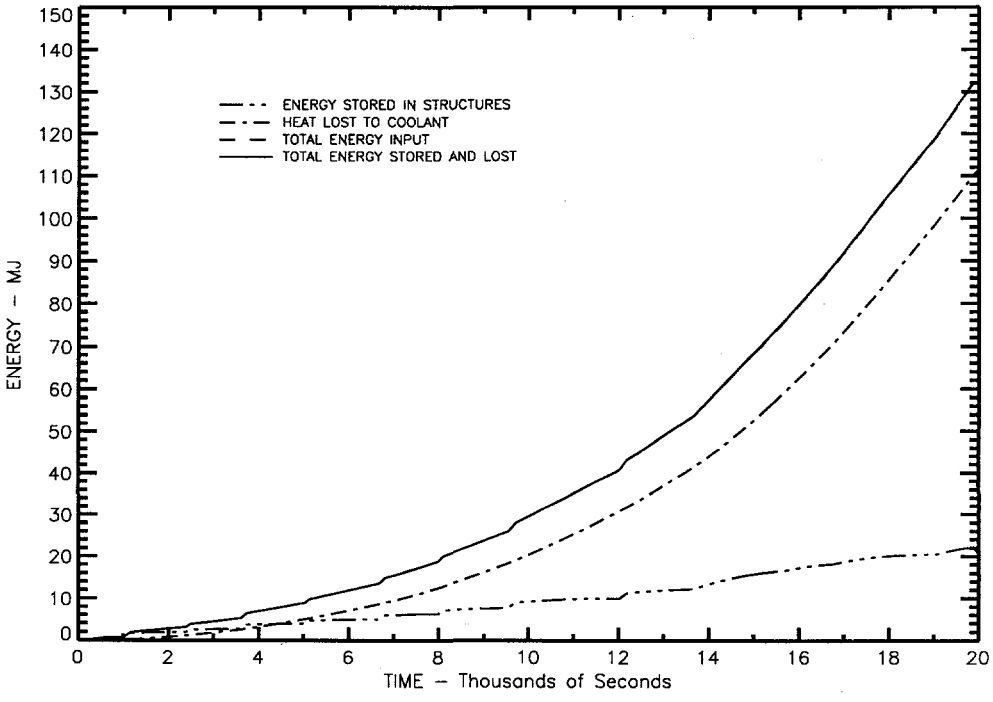

Figure 4.76 MP-2 DEBRIS Code Calculated Energy Balance

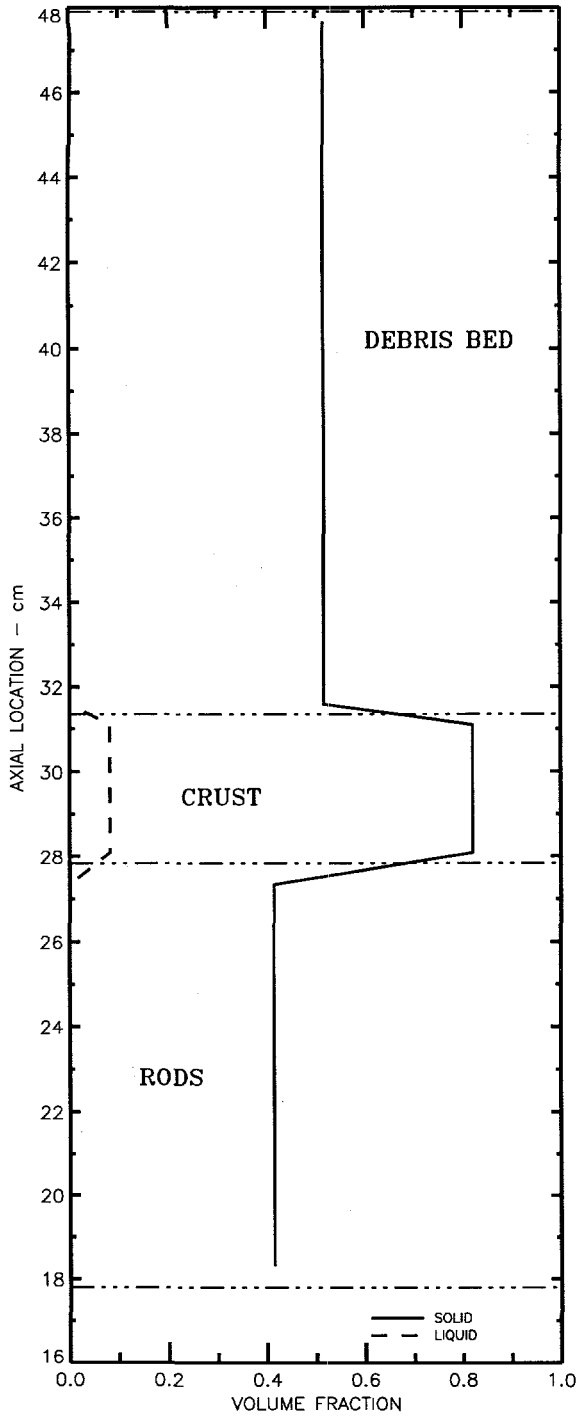

Figure 4.77 "*Case-A*" Gross Material Disposition Along Axial Centerline at 13,500 Seconds

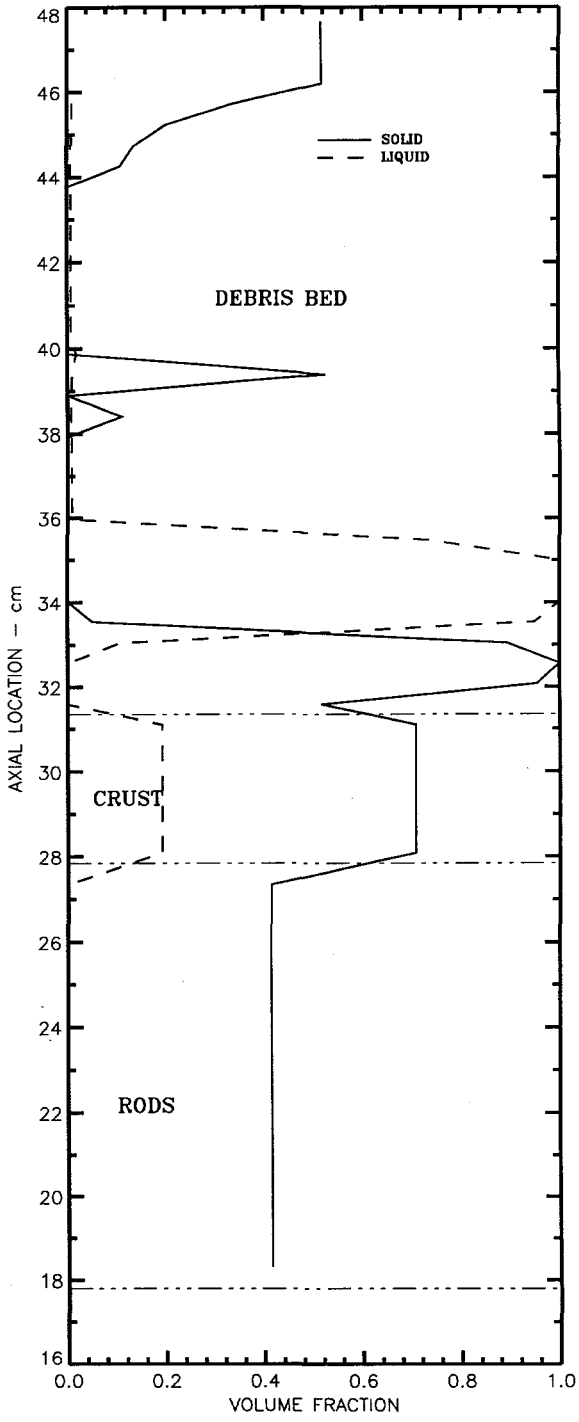

Figure 4.78 "*Case-A*" Gross Material Disposition Along Axial Centerline at 15,600 Seconds

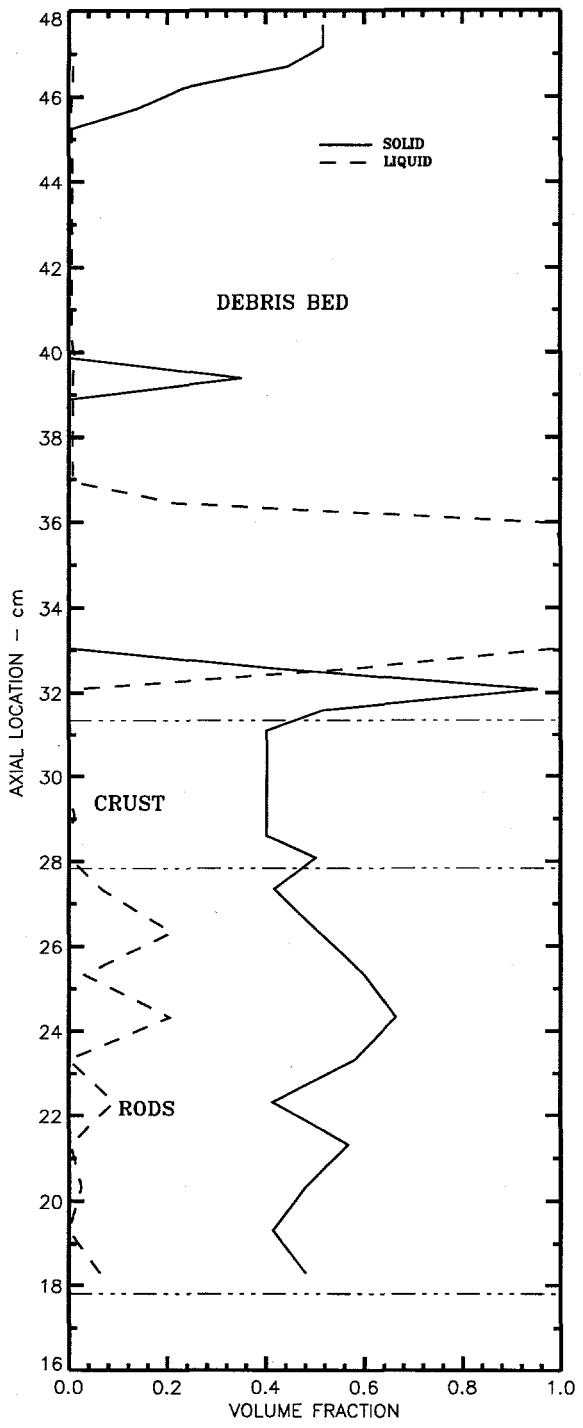

Figure 4.79 "*Case-A*" Gross Material Disposition Along Axial Centerline at 16,500 Seconds

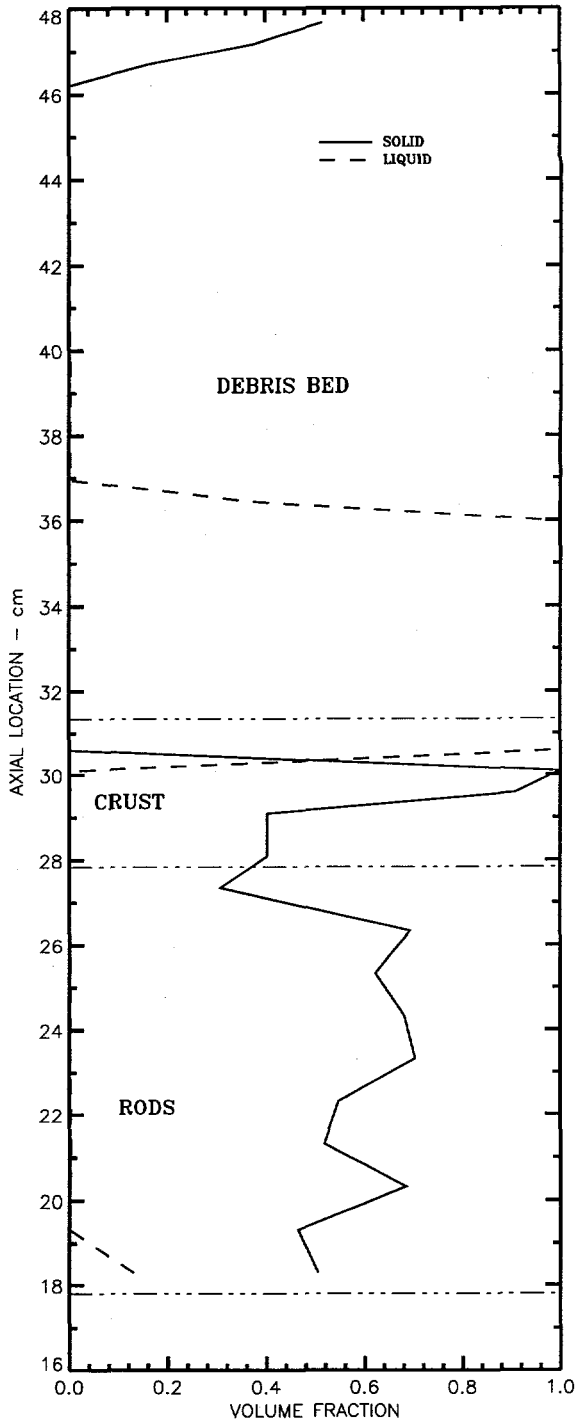

Figure 4.80 "*Case-A*" Gross Material Disposition Along Axial Centerline at 19,000 Seconds

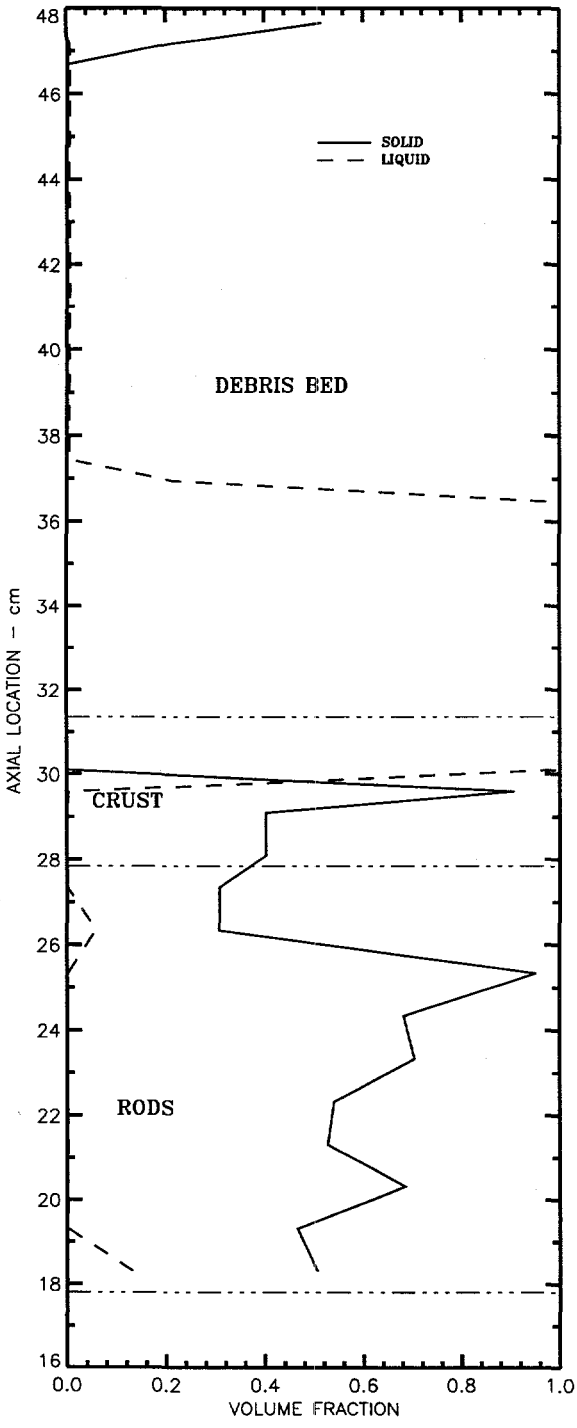

Figure 4.81 "Case-A" Gross Material Disposition Along Axial Centerline at 19,600 Seconds

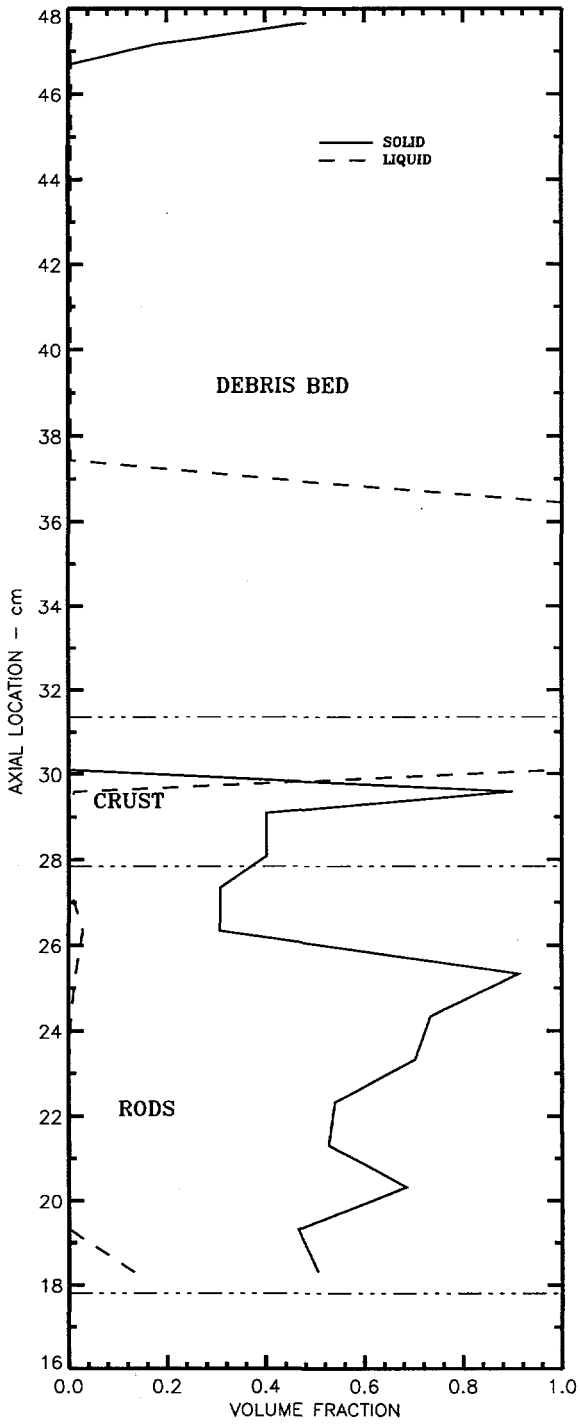

Figure 4.82 "Case-A" Gross Material Disposition Along Axial Centerline at 19,870 Seconds (End of Test)

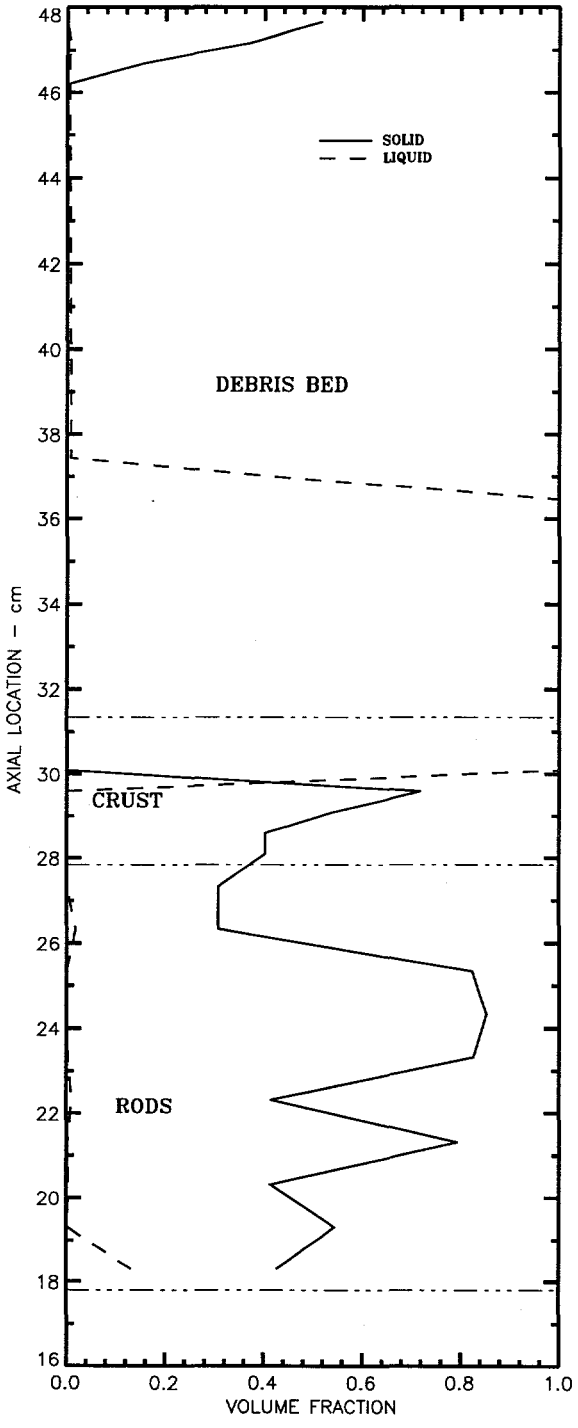

Figure 4.83 "*Case-A*" Gross Material Disposition at Radius = 2.09 cm at 19,870 Seconds (End of Test)

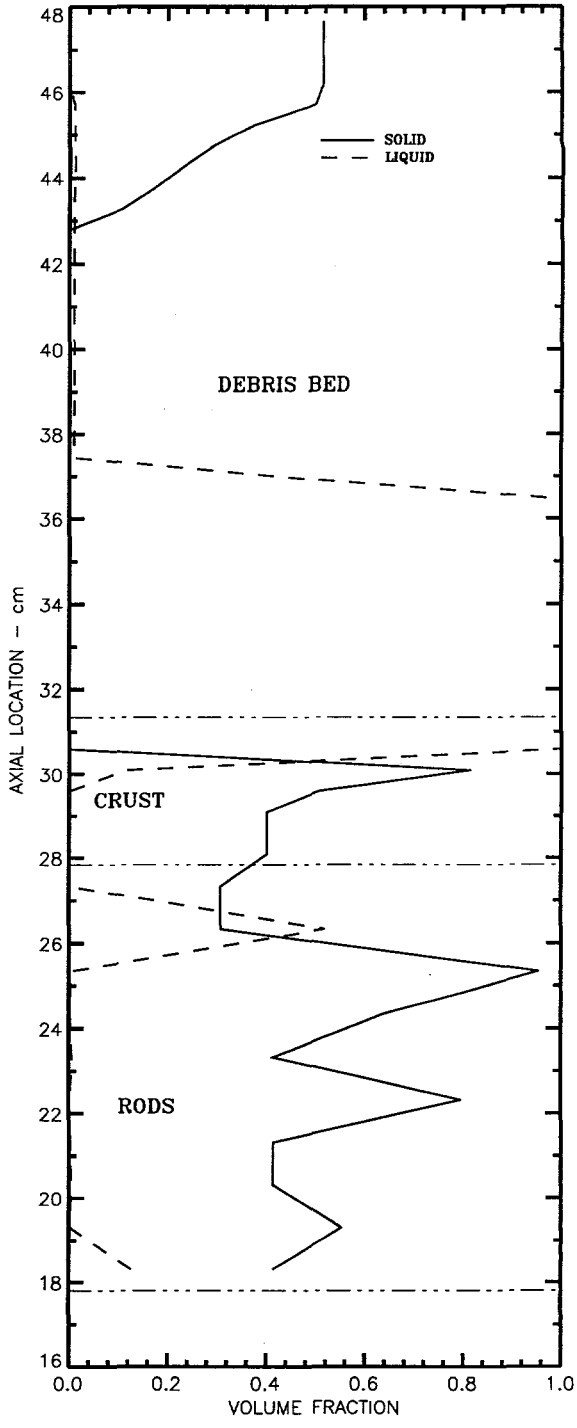

Figure 4.84 "*Case-A*" Gross Material Disposition at Radius = 3.27 cm at 19,870 Seconds (End of Test)

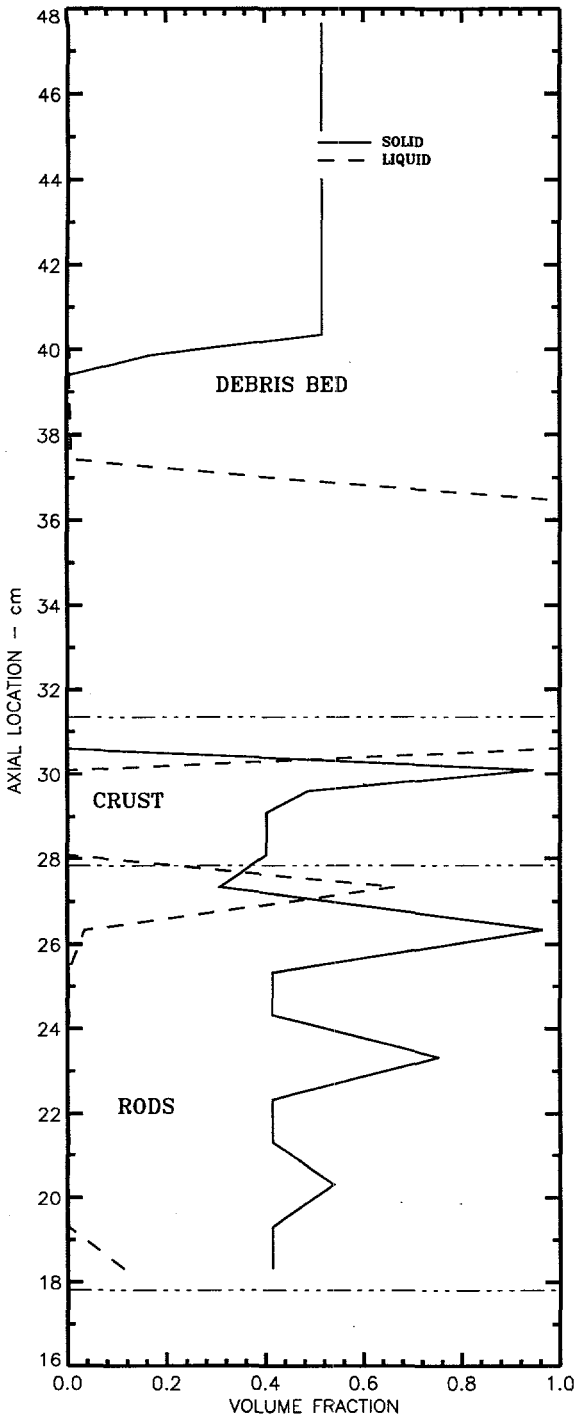

Figure 4.85 "*Case-A*" Gross Material Disposition at Radius = 4.28 cm at 19,870 Seconds (End of Test)

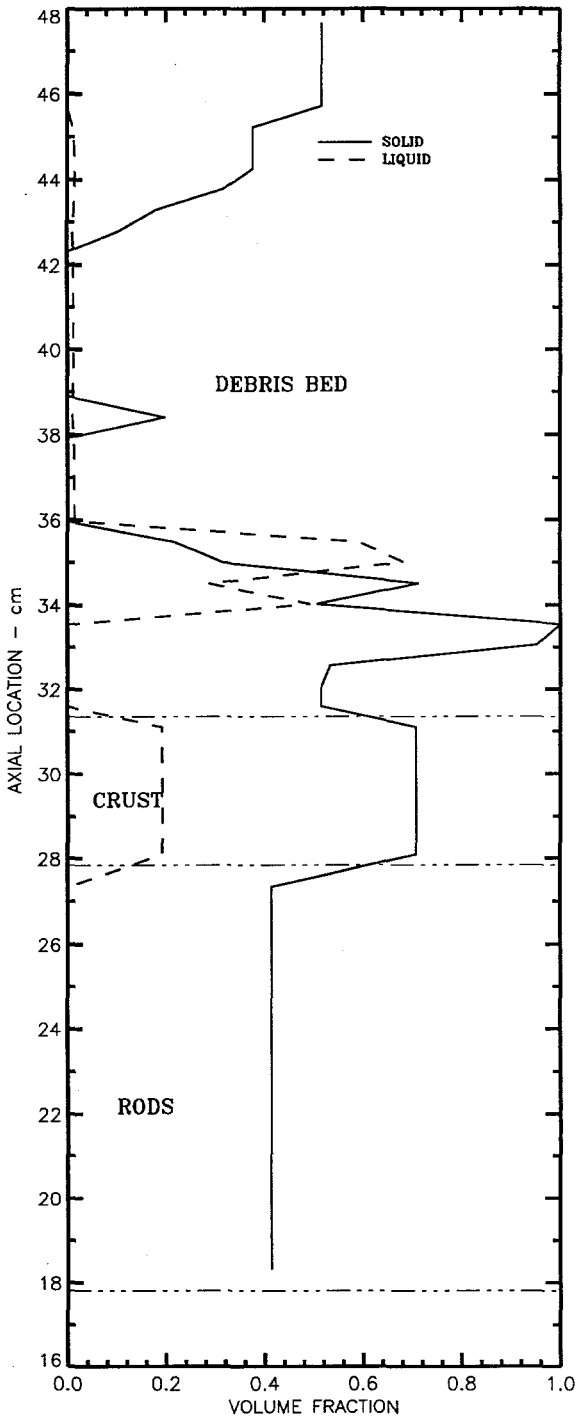

Figure 4.86 "*Case-B*" Gross Material Disposition Along Axial Centerline at 15,600 Seconds

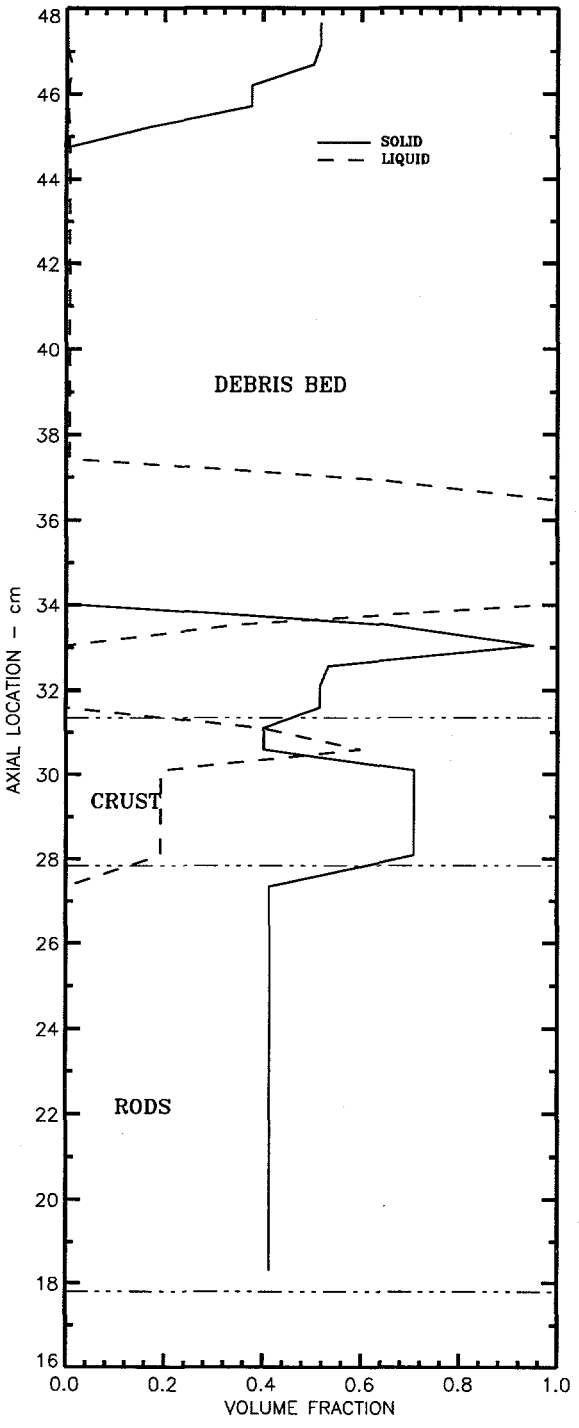

Figure 4.87 "*Case-B*" Gross Material Disposition Along Axial Centerline at 16,500 Seconds

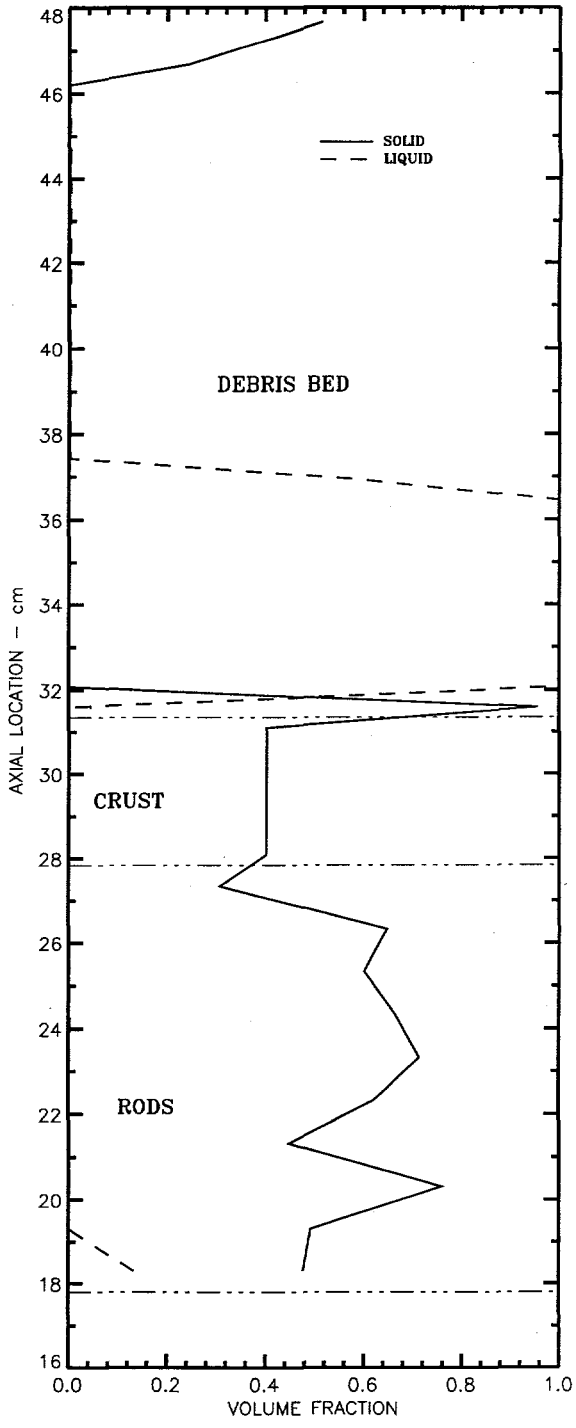

Figure 4.88 "*Case B*" Gross Material Disposition Along Axial Centerline at 19,000 Seconds

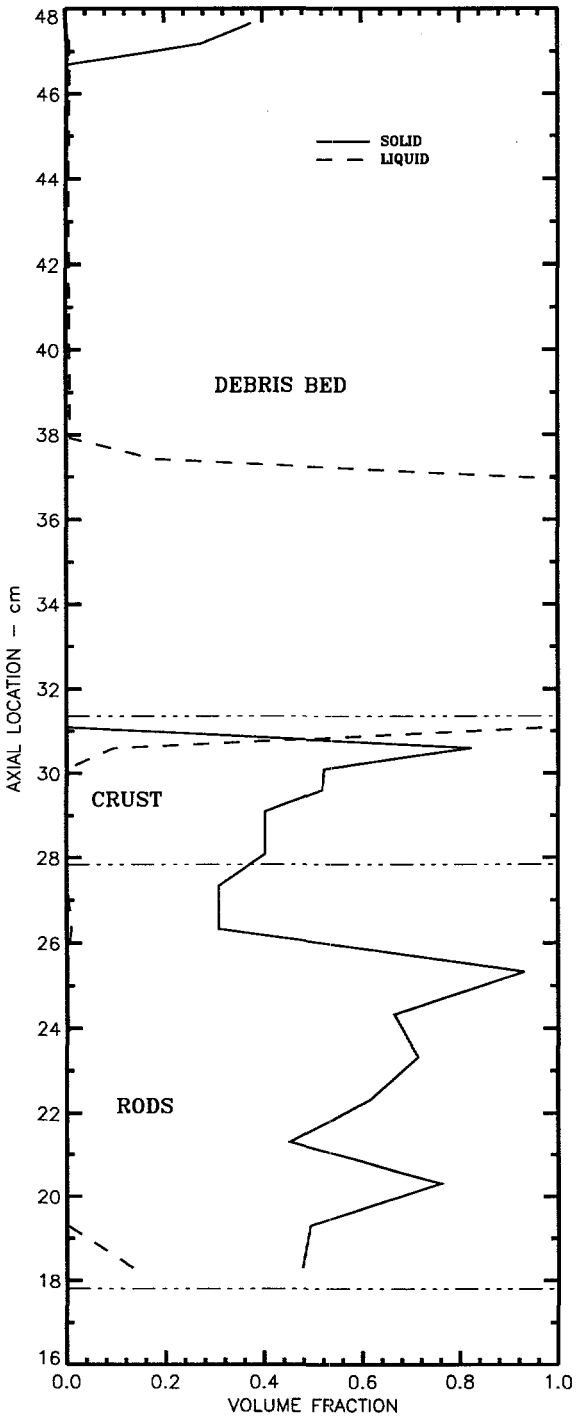

Figure 4.89 "*Case-B*" Gross Material Disposition Along Axial Centerline at 19,600 Seconds

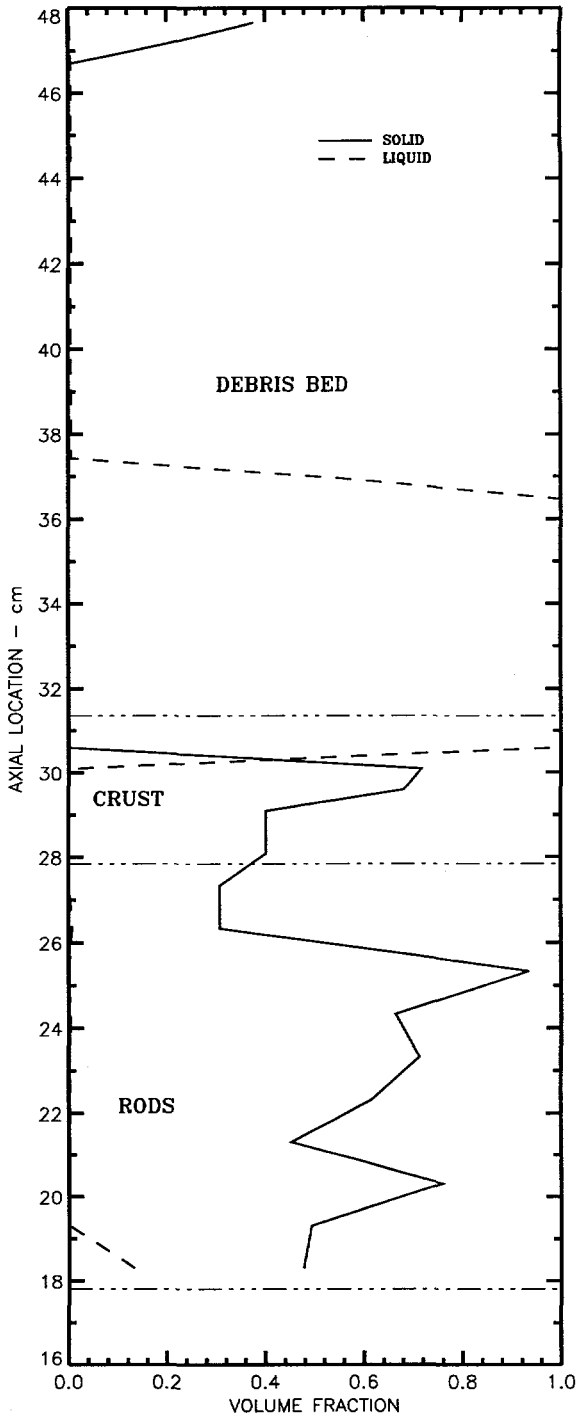

Figure 4.90 "*Case B*" Gross Material Disposition Along Axial Centerline at 19,870 Seconds (End of Test)

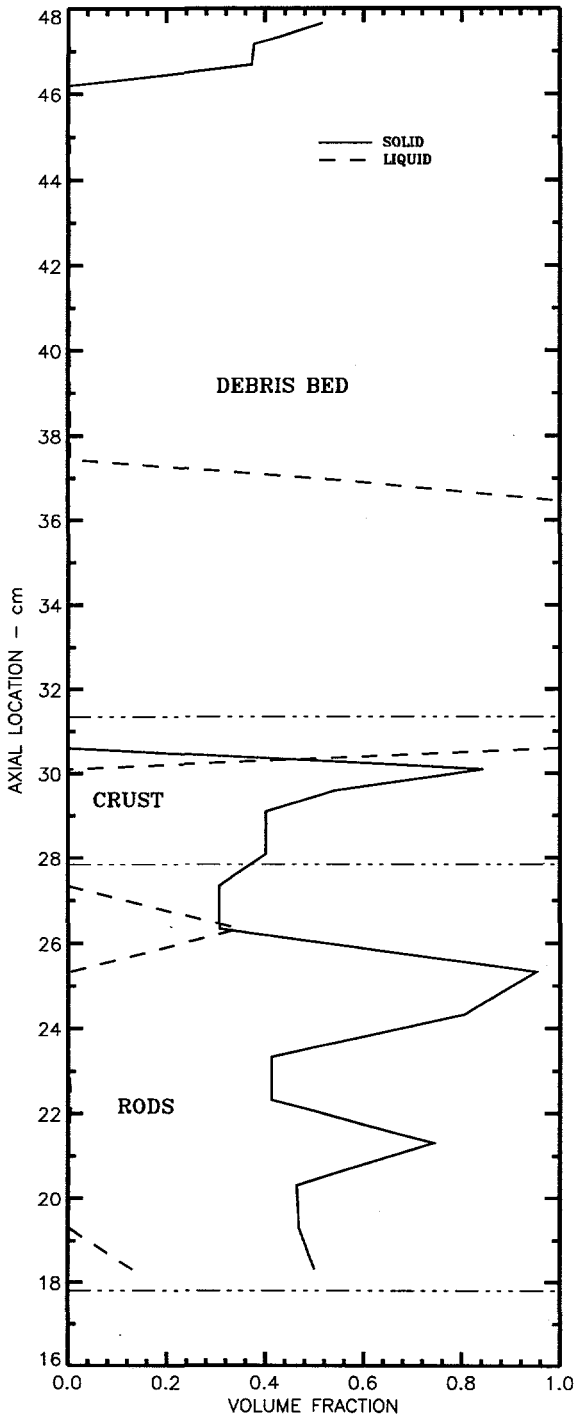

Figure 4.91 "*Case-B*" Gross Material Disposition at Radius = 2.09 cm at 19,870 Seconds (End of Test)

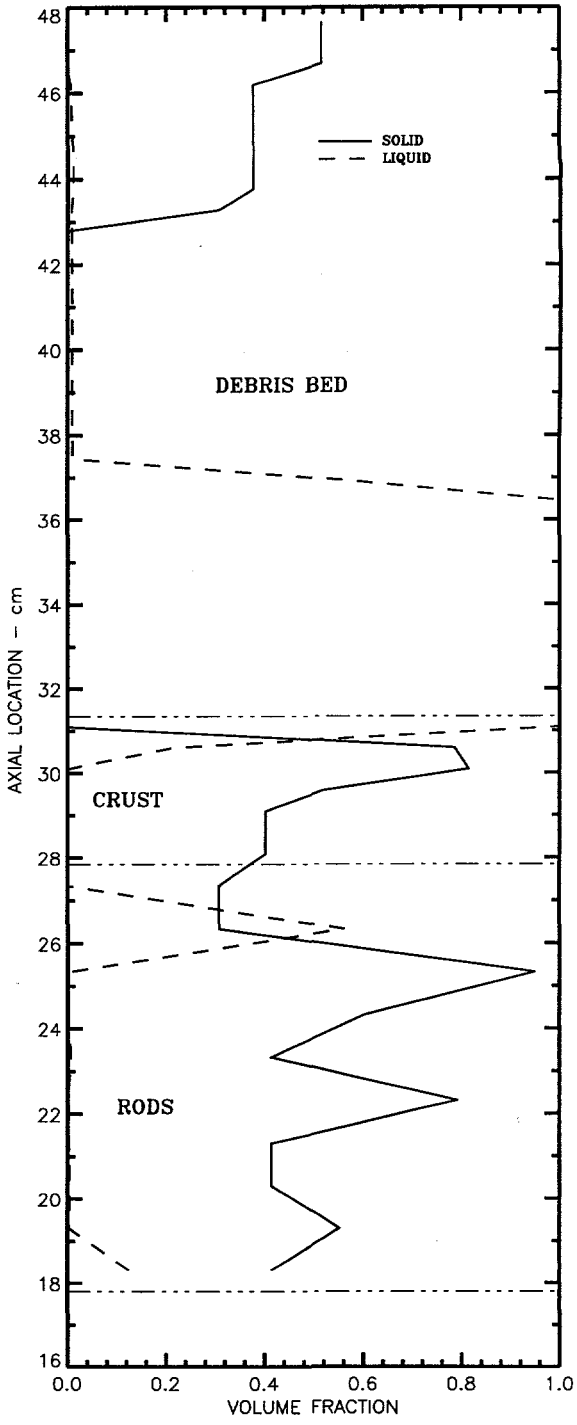

Figure 4.92 "*Case-B*" Gross Material Disposition at Radius = 3.27 cm at 19,870 Seconds (End of Test)

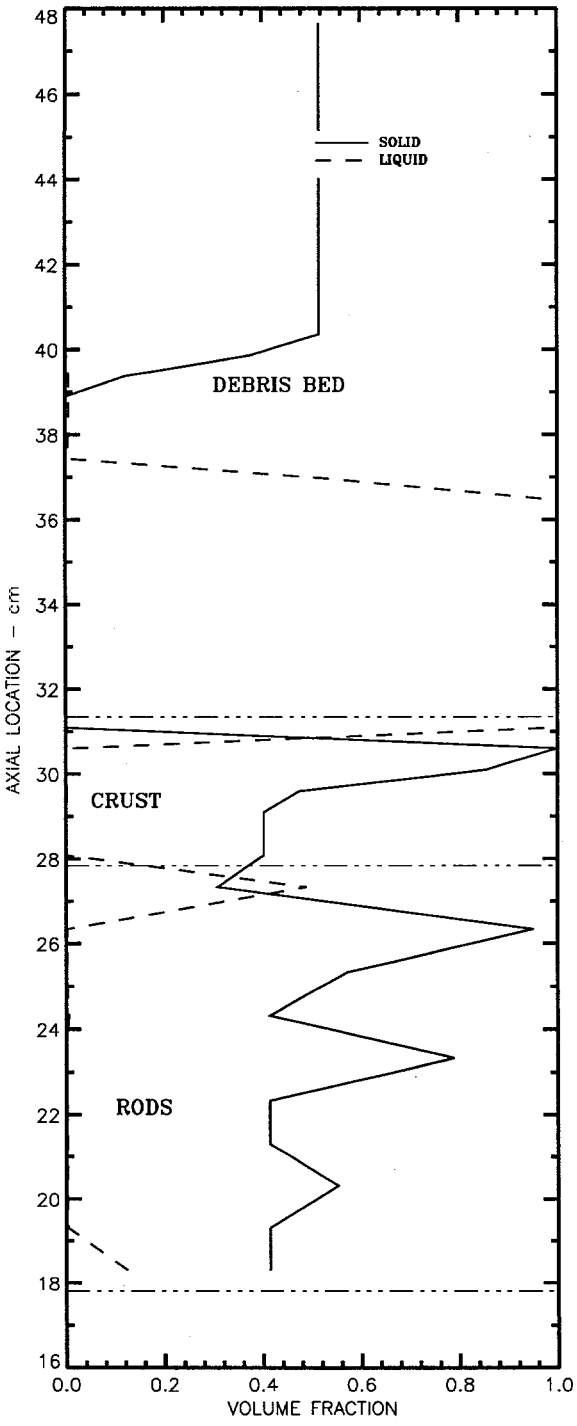

Figure 4.93 "*Case-B*" Gross Material Disposition at Radius = 4.28 cm at 19,870 Seconds (End of Test)

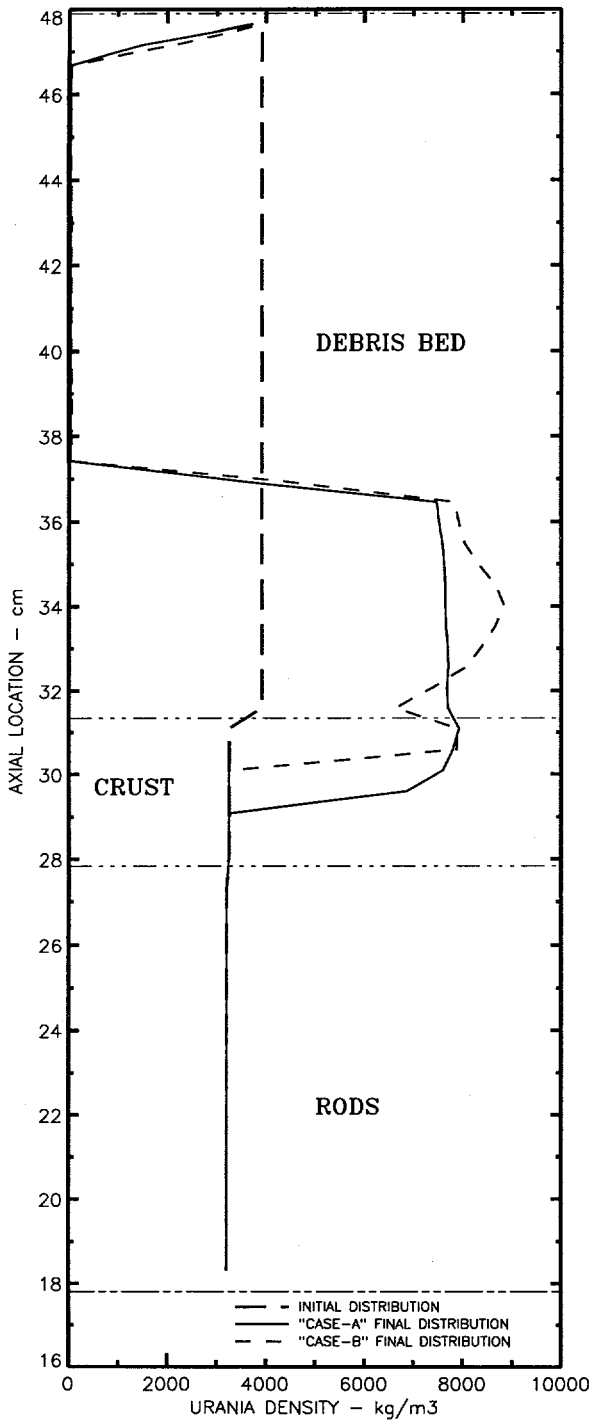

Figure 4.94 Comparison of Cases"*A*" and "*B*" UO_2 Disposition Along Axial Centerline at End of Test

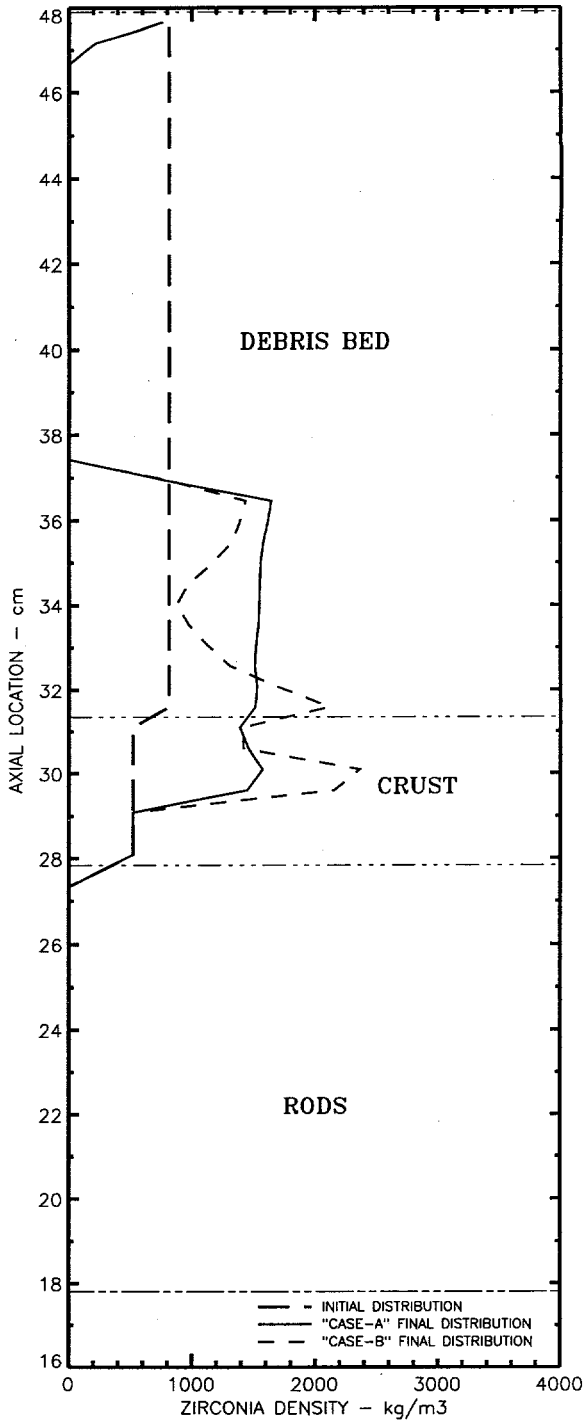

Figure 4.95 Comparision of Cases "*A*" and "*B*" ZrO_2 Disposition Along Axial Centerline at End of Test

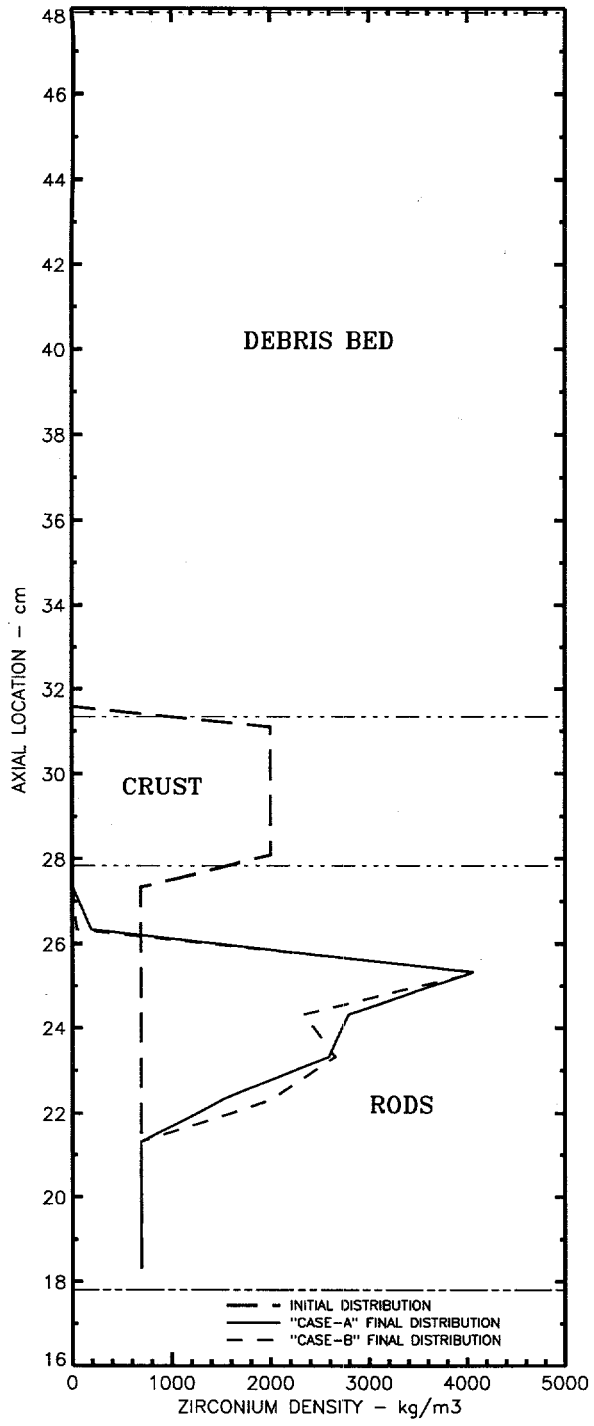

Figure 4.96 Comparison of Cases '*A*" and "*B*" Zr Disposition Along Axial Centerline at End of Test

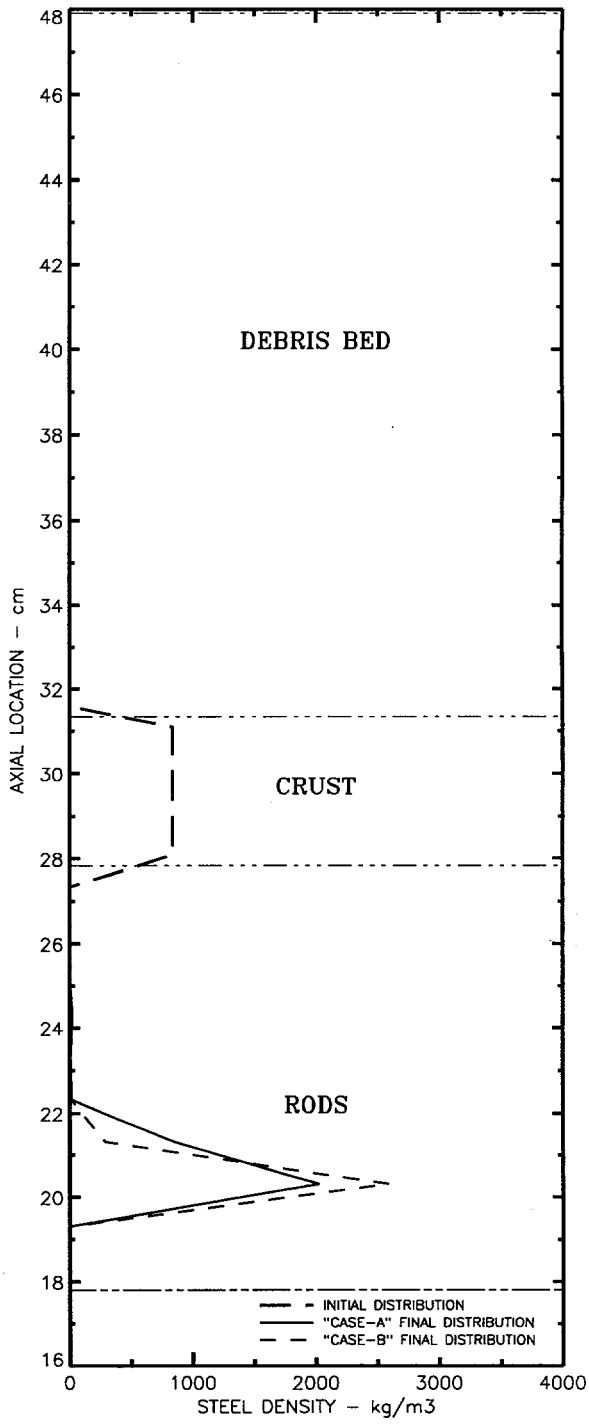

Figure 4.97 Comparison of Cases "A" and "B" Steel Disposition Along Axial Centerline at End of Test

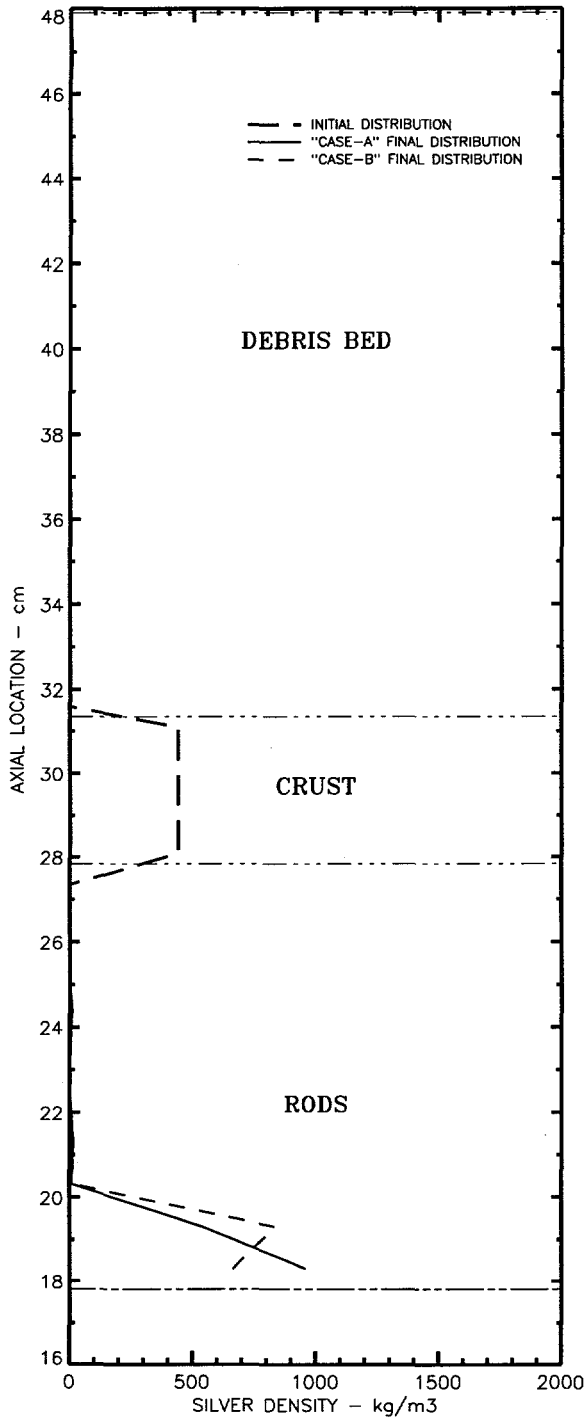

Figure 4.98 Comparison of Cases "A" and "B" Silver Disposition Along Axial Centerline at End of Test

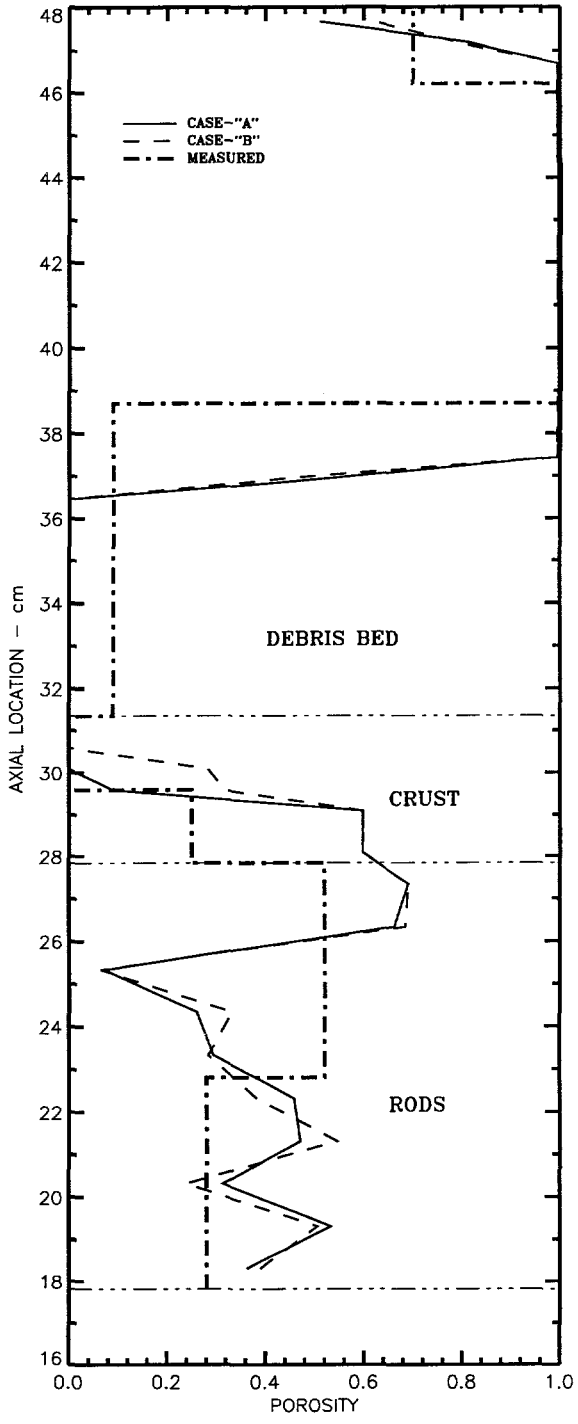

Figure 4.99 Comparison of Estimated Actual End Condition Gross Material Disposition with DEBRIS Code Estimates

5. Conclusions

A number of conclusions can be established from the measured data together with the Post-Irradiation Examination and the analytical results that were obtained from the MP-2 experiment. These conclusions are discussed in this section with the results of the MP-1 experiment juxtaposed to the MP-2 results to map out the information that has been obtained from the MP Late Phase experiments to date. The performance of the DEBRIS code models used in the analysis are discussed both with respect to their treatment of the experiment analysis and to their applicability to full scale reactor accident analysis. Finally, some assessments are made of the current state of knowledge regarding "Late Phase" processes particularly with respect to those areas that still require some clarification.

5.1 Experiment Results

The MP-1 experiment was terminated at an earlier phase, prior to the point at which molten ceramic from the debris bed had interacted with the prefabricated metallic crust. Thus, the MP-1 experiment provided a useful set of information regarding the intermediate phase prior to the interaction of the molten pool with the blockage. This information included data relevant to the dynamics of the debris bed melting process, the motion of materials within the melting debris bed environment, the formation of a ceramic crust, the formation of a molten pool, and the interactions between debris bed components.

The MP-2 experiment took the experiment package through the debris bed melting phase and well into the phase in which the ceramic melt pool generated in the debris bed melt phase interacted with the preformed blockage. Thus the MP-2 experiment added another key set of information associated with the interaction of a molten pool with a preexisting metallic blockage. The information obtained from the MP-2 experiment included the timing of the pool/blockage interaction, the timing and extent of relocation of metallic constituents out of the blockage region, the mutual interactions of the blockage constituents and the interaction of the blockage components with the fuel rods in the blockage zone and in the rod stub zone, the degree of penetration of relocated metallic blockage materials into the underlying standing fuel rods, and the mechanism for the relocation process.

5.1.1 Conclusions from Temperature Measurements and Analysis

A general summary of the key features, events and observations associated with the MP-2 experiment as derived from a combination of measured and calculated results are as follows:

1. The heatup phase of the test was initiated at about 1000 seconds when the first transient phase power pulse was applied to the test package.

2. The lowest melting temperature component (Indium) of the preformed crust began to melt at about 1095 seconds followed immediately by the melting of tin in the crust.

3. The interaction of these two components with higher melting temperature components in the preformed crust may have begun to dissolve some of these components.

4. A series of alternating transient and steady-state reactor power settings steadily increased the temperature of the test section until the crust region achieved a temperature of 1200 K at ~9500 seconds. At this time silver began to melt in the blockage region. A liquid phase that occupies roughly 30% of the total volume is required to achieve a continuous liquid phase necessary for the onset of fluid motion. This volume fraction had not yet been attained at this point and the liquid phase remained immobile within the solid crust matrix. The peak debris bed temperature at this time was approximately 2100 K.

5. The melt phase of the experiment was initiated at ~13,700 seconds when the ACRR power was increased to 0.4 MW and left at that setting for about 2000 seconds. The peak debris bed temperature at the beginning of the melt phase power boost was ~2600 K.

6. Incipient melting in the debris bed was attained at ~14,000 seconds. The melt front in the debris bed expanded rapidly in the radial direction accelerated by the downward relocation of molten ceramic, which formed a ceramic crust as it encountered cooler regions at lower elevation. Molten ceramic arriving at this crust was then subsequently directed radially outward toward the radial boundary of the debris bed, thus contributing to the rapid expansion of the melt zone in the radial direction and the general one-dimensional character of the melting and relocation process. The top of the initial ceramic crust formed about 2 centimeters above the preformed blockage.

7. The melting point of steel was achieved in the crust at 14,700 seconds, but insufficient melt was present to form a continuous liquid phase and the molten material remained immobile within the solid matrix.

8. The melting point of zirconium was achieved at the top of the preformed crust at about 15,600 seconds, but interactions with lower melting point metals by this time had probably already dissolved some of the cladding and the zircaloy contained in the crust matrix.

9. The reactor power was boosted to 0.45 MW at 15,700 seconds.

10. The first indications of molten material leaving the prefabricated crust and arriving in the rod stub region occurred soon after the power boost at ~16,000 seconds when perturbations appeared on thermocouples in the rod region and on the top of the lower grid spacer. This indicated that molten metallic components not only relocated out of the blockage region but penetrated quickly to the bottom of the rod region. At this time the bottom of the ceramic crust was still about 0.6 centimeters above the blockage region. It appears that the timing of the first relocation of material out of the blockage zone preceded the direct interaction of molten ceramic with the blockage.

11. The first material to relocate to the bottom of the rod region was not significantly different in composition from material that arrived later except that it was somewhat more enriched in zirconium, which implies at least 2 relocation events and, perhaps, two modes of relocation. It is postulated that the first relocation event was associated with the initial dissolution of the rod cladding adjacent to the fuel rod pellets at the bottom of the crust. This would have opened a channel between the preformed crust and the fuel pellets and provided a path for the molten cladding and other interacted components adjacent to the rods to relocate into the rod region below the crust. A second mechanism for relocation may then have been a more widespread gross failure of the preformed crust matrix later in the test.

12. The reactor power was boosted to 0.5 MW at 16,700 seconds. The first direct interaction of the ceramic material from the debris bed with the blockage probably occurred soon afterward at about ~17,000 seconds when the code analysis indicated that the bottom of the ceramic crust crossed the boundary into the blockage region.

13. The code calculations indicate that the ceramic pool subsequently moved rather steadily downward in the preformed blockage region and came to rest about 1/4th of the way down into the blockage zone by 19,000 seconds. The thermocouple measurements on the tantalum liner, however, show some evidence that the movement of ceramic material into the blockage region occurred rather abruptly after the power boost at 19,000 seconds that took the reactor power level to 0.6 MW. This evidence is not unequivocal and the thermocouple record may, in fact, be registering a second and perhaps more substantial movement of material out of the lower part of the crust region.

14. A steep increase in tantalum liner temperatures at ~19,600 seconds led to the shutdown of the ACRR and termination of the MP-2 experiment at about 19,870 seconds. The sudden increase in heatup rate on the liner occurred primarily for thermocouples in the lower half of the assembly with a decrease in heatup rate and even a decrease in temperature on liner thermocouples in the upper half of the assembly (above the molten ceramic pool). This can be interpreted as either the sudden relocation of molten ceramic into the blockage region, the sudden relocation of blockage constituents out of the preformed blockage region, or both of these.

15. The code analysis indicated that the molten ceramic pool, preceded by its self-containing ceramic crust, moved from its location approximately 1/4 of the way down into the crust at 19,000 seconds to a maximum downward penetration 1/2 of the way down into the blockage at the end of the test. The final motion was due to the increase of power to the final power setting of 0.6 MW. Had the test proceeded to the steady-state condition at this power level, the DEBRIS code indicates that the ceramic pool would have penetrated nearly to the bottom of the pre-fabricated blockage region.

16. The end configuration of the test section as predicted by the DEBRIS analysis consisted of the following: (A) A shallow region at the top of the debris bed composed of remnant unmelted particulate, (B) a completely voided region in the upper half of the debris bed slightly over one-half the volume of the original debris bed, (C) a molten ceramic pool slightly less than one-half of the original volume of the debris bed with its lower surface lying almost exactly at the middle of the original prefabricated crust region, (D) the original preformed crust nearly devoid of the initial metallic components including the zircaloy rod cladding leaving in place the UO_2 from the rod pellets and the original quantity of ZrO_2 that was present in the crust matrix, and (E) the metallic components originally resident in the preformed crust distributed in a stratified configuration at distinct locations in the rod stub region with the lower melting point metals at the bottom and the higher melting point metals at successively higher locations in the rod region.

5.1.2 Conclusions from Post-Irradiation Examination

Post-test examination of the assembly revealed the following information.

1. Nearly the entire debris bed inventory of particulate UO_2 and ZrO_2 had been melted during the experiment.

2. A thin zone of highly porous and unmelted UO_2 particulate remained intact clinging to the upper surface (thoria lid) of the debris bed. This layer was completely depleted of ZrO_2 particles and the unmelted urania particles were "cemented" together to form a rigid structure by a previously molten reacted phase that was somewhat enriched in UO_2 compared to the original bulk composition of the debris bed. This "glue" was the material that wetted the remnant UO_2 particulate and subsequently resolidified and held the resulting structure in place. There were probably two mechanisms that caused the resolidification of this reacted phase. The first resulted from the melting and relocation of large quantities of debris down-

ward from the upper half of the debris bed leaving a small quantity of material above it that contained insufficient internal heating to maintain its temperature at the melting point of the reacted phase. The second mechanism was the incorporation of UO_2 into the reacted phase driving its composition toward the left side of the equilibrium phase diagram effectively increasing its melting point and ultimately contributing to its resolidification.

3. Evidence from this test and from MP-1 is fairly conclusive that the debris bed began to melt at the zirconia melting point. Initially, only zirconia was melted until sufficient molten zirconia was available to wet the surface of the urania particles. At this point interactions began to take place between the molten zirconia and the solid urania in which dissolution of the urania occurred. When critical saturation was achieved, this molten phase, at first enriched in ZrO_2, flowed downward out of this zone. As the bulk of the molten material flowed away, the remaining molten phase that wetted the urania particulate continued to react with urania and at the time it resolidified was enriched in urania.

4. A large voided region nearly half the volume of the original debris bed zone was formed in the upper half of the debris bed. This zone was completely devoid of material and represents the material that formed the molten ceramic pool.

5. A molten ceramic pool with a volume of roughly one-half of the original debris bed zone formed in the lower half of the debris bed and extended downward about halfway into the original prefabricated crust region. While the pool was still molten, it was held in place by a ceramic crust that formed at the lower boundary of the pool. This crust was fairly flat at the lower surface curving upward slightly as it contacted the radial bed boundary (radial thoria liner).

6. The resolidified molten pool was composed of a UO_2/ZrO_2 solid phase with some large voided regions that were believed to have been formed when the pool "slumped" into the blockage zone and entrapped gases, which were rising toward the top of the pool at the time that the experiment was terminated. The resolidified molten ceramic pool was enriched in UO_2 near the bottom from dissolution of fuel rods in the upper half of the original crust region. The pool also contained, in the middle and upper sections, small inclusions of metallic constituents from the prefabricated crust region. This indicates that some remnants of these constituents remained in the upper half of the crust at the time that the ceramic pool flooded this region. The fact that they appeared at the top of the pool also suggested that convection driven heat and mass transfer was occurring in the molten pool. This implies that there was probably a negative temperature gradient at least in the upper part of the pool sufficient to drive a convective process. Density differences between components could also account for the convective process that redistributed some of the metallic components upward in the molten pool. In fact, density differences would probably be the primary mixing mechanism in the lower regions of the ceramic pool.

7. The lower half of the original blockage zone was not invaded by ceramic from the molten debris bed. It had suffered considerable depletion of its original metallic components, but it was not entirely devoid of material. The remnant left in the non-invaded crust zone was enriched in zirconium from the cladding that was present on the fuel rods in this zone and was enriched by nearly a factor of 2 in oxygen. In addition, the remnant contained no ZrO_2 or Zr and was composed primarily of UO_2 particles in a larger matrix consisting of a (UZr)O phase. The latter observation suggests that the remnant metallic zirconium reacted with the urania and zirconia in the original crust matrix, forming an α(UZr)O phase. The formation of this higher melting point phase probably accounts for the presence of the metallic components in the lower crust region when the extreme high temperatures at the end of the test would seem to preclude their presence in the quantities observed.

8. Estimates of the composition of the relocated metallic components found in the rod stub region show it to be only slightly enriched in most of the metallic components compared to the original crust composition, but significantly enriched in zirconium. This is interpreted to be due to the interaction and melting of the fuel rod cladding both in the crust region and in the rod region. The rods in the crust region were essentially devoid of cladding and considerable cladding was stripped from the fuel rods in the rod stub region as well, probably by dissolution into the flowing molten material. From the degree of cladding erosion, it can be surmised that the downward flowing molten material likely flowed in rivulet form or as a film primarily down along the surface of the fuel rods as apposed to "free falling" down between the rods.

9. A gradient in the zirconium composition was evident between the bottom and the top of the relocated metallic component with the highest zirconium content occurring at the bottom of the rod stub region. This may suggest that two or more relocation events occurred. The earlier event may have been characterized by the relocation of melted and reacted cladding from the fuel rods in the crust region. This material was augmented with metallic components of the crust matrix that were in close enough proximity to the cladding to be carried along when the cladding near the bottom of the crust melted and opened a path for this early relocation event (~16,000 seconds as discussed above). This early event appears to have resulted in droplets of material that collected on the grid spacer. A later event (~19,600 seconds) apparently deposited molten material on the top of the earlier material and this material possessed a more consolidated structure. This later event is thought to represent the bulk of the metallic melt relocated to the lower fuel rod region. This final relocation event appears to be associated with the migration of the ceramic melt into the preformed crust region. It is likely, therefore, that the late metallic re-

location event was associated with the penetration of the ceramic into the blockage region.

5.2 DEBRIS Code Performance

The overall assessment of the DEBRIS code performance in application to the MP-1 and MP-2 analyses is favorable. Code limitations that were present in the MP-1 analysis have been subsequently removed with the result that the predictive capabilities of the code have been markedly improved. The most severe limitation of the code in the MP-1 analysis was the "constant properties" modeling, which did not adequately handle the highly temperature dependent heat capacities. The assumption of a constant heat capacity produced gross errors in the total energy balance when applied over the large temperature ranges characteristic of experiment or accident analysis regimes. This limitation has been removed in the current version of the DEBRIS code, and the energy balance is essentially exact. Improvements to the radiative heat transfer models in the debris bed and rodded geometry have also enhanced the accuracy of the code.

The comparisons of measured temperatures as obtained from MP-2 instrumentation with temperatures predicted by the code are well within expected tolerances. The DEBRIS code heat conduction solver appears to be robust, and when applied to problems for which exact solutions can be obtained, the code produces results that are essentially identical to the exact solutions.

The formulation for fluid transport in a porous medium appears to accurately predict the motion of molten material through the debris bed medium. Molten material is transported by the code to cooler regions of the bed (primarily downward) where it resolidifies at the leading edge of the flow field to form a self-crucibilizing boundary, which inhibits further movement and leads to the formation of a molten pool. The extent and location of the molten pool are accurately simulated by the code. The end-of-test configuration of the MP-2 experiment in terms of debris bed, molten pool, and ceramic crust locations relative to the debris bed boundaries and the prefabricated crust were essentially exact as compared with the PIE assessment.

The relative motion of debris bed constituents (i.e., stratification, etc.) depends largely on the models used to simulate melting in the multicomponent debris bed environment. The relative disposition of UO_2 and ZrO_2 is strongly influenced by the assumption of equilibrium melt thermodynamics. For the urania-zirconia system (particularly for the hyper-stoichiometric system in which the melting temperature of UO_{2+} is lower), the melting temperature is not the key issue, but rather, the relative motion of species. The current version of DEBRIS calculates the liquid/solid composition of the melt using two options. In the first option concentrations are determined from the equilibrium pseudo-binary isomorphous phase diagram for the UO_2/ZrO_2 system. In the second option it is assumed that there is no interaction between UO_2 and ZrO_2, and that each melts at a separate melt temperature (noninteraction model). These two models represent the two extremes that bracket the measured results and produce quite good results for the MP-2 experiment. This is primarily attributable to the simple two-component system and to a fortuitous zirconia/urania mole fraction that happens to produce similar quantitative results for both models. For analysis of debris beds with residual low melting temperature constituents that react with urania/zirconia, the equilibrium model is clearly not appropriate. For these configurations, and for somewhat better accuracy in application to the current configuration, addition of a diffusion driven kinetics model for material phase interactions is probably appropriate.

It should be noted that, although the model employed by the DEBRIS code for the motion of solid debris within the melting debris environment is parametric and rather simple, the stochastic character of the complex processes involved may not warrant a more sophisticated model.

The main features of the MP-2 experiment that were not present in MP-1 were the interaction of the ceramic pool with the prefabricated metallic crust and the motion of molten metallic components out of this preformed blockage region into the underlying fuel rod stub region. The interaction of the various components of the preformed crust, the interaction of these metallic components with the fuel rod cladding, and the fuel pellets in both the original blockage region and in the rod stub region are also features of the MP-2 experiment that were not encountered in MP-1. With regard to the treatment of these processes in the DEBRIS code analysis of MP-2 the following observations are noted:

1. The code successfully predicted the timing of the initial event in which molten metallic components were relocated out of the preformed crust into the rod region.

2. The quantity of relocated metallic components was somewhat overpredicted in the DEBRIS code analysis. Thus the code predicted that the crust was nearly depleted of metallic components, which except for trace quantities were all relocated to the rod region. This was primarily caused by the lack of a model in DEBRIS for the treatment of chemical reactions. The PIE showed that a significant quantity of these components (mostly zirconium) remained in the crust region despite the fact that the temperature was well above the point at which these components would be molten and mostly relocated downward into the rod zone. This was true even though the crust region was significantly depleted in the metallic components and the rod stub region enriched in these components. The key point here is that the remnant material in the crust region was primarily composed of an α(UZr)O phase with a higher melting point than the zirconium, which was the primary remnant in the crust. This allowed the remnant to remain in place at the high temperatures that existed in this region at the end of the test. The positive temperature gradient in the crust allowed the molten metals to be held in place for a considerable length of time. This enabled the zirconia and the metallic zirconium of the crust matrix to react with the UO_2 in the crust matrix and form an α(UZr)O phase in the crust that remained solid at the temperatures involved.

3. Clearly, in order to improve the accuracy of the DEBRIS models with regard to the relocation of a highly metallic blockage that contains zirconium and urania debris, it will be necessary to model the interaction of zirconium with urania/zir-

conia.

4. The DEBRIS code results show a significant stratification of the resolidified relocated metallic components in the rod region. This distribution was not observed in the PIE analysis. Because of the complexity of modeling the numerous phases that are possible for the 11 components of the preformed crust, the current model simply assumes that none of these components interact except the components associated with stainless steel. The steel components were modeled as a single material that was assumed to have a fixed melting point. Each of the components, including the steel, was assumed to melt at a fixed melting temperature and, therefore, to resolidify at a specific location as it moved downward along the negative temperature gradient. Thus each species resolidified at a location with a temperature that corresponded to its melting point. This effect was exacerbated by the "local thermal equilibrium" model which brings liquid and solid components of each control volume to a single temperature at each time step.

5. The observed composition of the relocated metallic material was one in which the highest melting temperature component, zirconium, actually had a higher concentration at the bottom of the rod region. The zirconium enrichment was apparently caused by the dissolution and incorporation of rod cladding into the melt. However, the zirconium concentration gradient seems to indicate that either it was associated with other metallic components in one or more low melting point phases or the relocation process was so rapid that the molten material did not have time to come to thermal equilibrium with its immediate environment as it flowed downward. At least a dozen different phases were observed in the relocated material. It is not feasible to determine the melting range of these phases. Zirconium was clearly the primary component in many of the phases and Fe, Cr, and Ni were strongly associated to form basically "stainless steel."

6. It is not apparent that modeling the details of the distribution of components in the relocated metallic blockage is important to the overall ceramic molten pool relocation process in a full-scale accident analysis. However, it cannot be demonstrated in the context of the MP-2 experiment that it is, in fact, not important. It is clearly not feasible to model all the phase interactions in terms of binary, ternary, and higher order processes; it may, however, be possible to achieve a better distribution of species by attempting to model the most prevalent phases as single materials with melting ranges rather than fixed melting points.

7. The basic assumption involving a single control volume temperature (local thermal equilibrium) would have to be relaxed and a heat transfer mechanism between phases supplied in order to achieve a completely accurate predictive tool for situations in which molten material is moving rapidly between control volumes.

5.3 Conclusions Regarding Generic Late Phase Processes

The MP experiments have produced some general observations with respect to the generic processes involved in melting and relocation in a debris bed environment.

1. Sufficient internal heating of the debris medium ultimately progresses to a point at which melting occurs near the center of the medium. A liquid phase accumulates until a critical saturation is reached at which time the liquid phase begins to move primarily downward under the influence of gravity.

2. For a debris bed consisting of separate particles of UO_2 and ZrO_2, the melting process proceeds by first melting the ZrO_2 until a sufficient quantity of molten ZrO_2 is available to wet the surrounding UO_2 particles. Diffusion processes enhanced by any bulk fluid motion that ensues results in the dissolution of the UO_2 particulate.

3. Continued heating of the debris bed expands the zone in which melting is occurring and the downward flux of molten liquid increases. The molten phase moves downward until it encounters a region that is sufficiently subcooled to resolidify a major fraction of the molten phase. A ceramic crust begins to form at this location.

4. The ceramic crust that forms tends to impede the downward flow of liquid resulting in an accumulation of molten ceramic above the crust, which is then driven by the static head to flow radially outward. The outward flowing ceramic then moves to a radial location in which temperatures are cool enough to begin resolidifying the molten phases and a crust begins to build in the radial direction. This process results in the creation of a "receptacle," which inhibits the motion of the molten pool through the particulate medium.

5. There is evidence, particularly from MP-1, that as long as the ceramic crust is completely surrounded by a particulate medium and the surrounding particulate continues to heat up, the ceramic crust, although consisting of a rigid structure, may be porous. Such a porous structure may allow molten material to move through it in a continuous "creep flow" motion. The surface of the crust that formed in the MP-1 experiment and also, although no longer in a particulate medium, in MP-2, was axisymmetric with a relatively smooth bottom surface. This would probably not be the case if the motion of the crust was governed by a process in which the ceramic crust completely remelted and allowed a sudden incremental movement of the molten pool to a new location where a new crust would form. The latter, however, might be the case in the event that the pool encountered a more open region such as a standing rod array, for example. The dynamics of the ceramic crust may be envisioned as a process wherein a porous structure forms that is self regulating by freezing just the right amount of material to regulate the

flow of liquid through the resulting matrix and balance the internal heat against the loss of heat to the surrounding medium. Thus the crust in a non-steady-state configuration may be a porous structure with molten ceramic flowing (or more accurately "oozing") through it with continuous solidification occurring at the surface in the downsteam direct of the flow. Balancing this is a continual melting processes at the upstream surface of the crust resulting in a net continuous downward motion of the crust and the molten pool behind it.

6. The region from which molten material flows becomes voided, and overlying solid material internal to the debris bed, which is not too close to the upper surface of the bed, slumps into the voided region until no further source of loose overlying material remains to "feed" the voided region. At this point the region remains voided and the voided zone grows in volume until it encompasses the available space.

7. The melting and relocation of material away from the center and upper portion of the debris medium removes the bulk of the heat source away from the upper portions of the debris bed. Any material that did not slump downward begins to cool as the heat source retreats, with the result that the molten phase that wets the remaining particulate resolidifies and essentially "glues" the particulate into a highly porous rigid structure. This type of structure was observed at the top of the debris bed region in both MP-1 and MP-2.

8. With sufficient heat source the molten pool continues to grow toward the debris bed boundaries. Depending on the debris bed thermal boundary conditions, the ceramic crust that encloses the pool will eventually reach either the lower or the radial boundary of the debris medium. This boundary may consist of a blockage formed by the early phase melting and relocation of mostly metallic core components such as cladding and structural components, which resolidified in cooler locations.

9. The MP-2 test showed that the molten ceramic pool as it approaches the metallic blockage first thermally attacks the blockage with the result that some fraction of the metals melt and relocate downward out of the blockage. The remaining metallic components (probably most zirconium), if associated with intact fuel rod pellets or fuel debris, will react with the urania in the fuel. This will result in the formation an α(UZr)O phase that remains as the primary component of the remnant crust matrix and provides a porous structure in which other metallic components may remain trapped. This high melting point crust with some remnant metallic components included is present when the molten ceramic pool melts into and absorbs the crust remnant.

10. As the molten ceramic pool continues to expand out of the original debris bed boundaries, growth will be governed by processes that are associated with the motion of a crust region in a more open geometry. This open geometry could be a standing rod or a coarser debris (perhaps collapsed fuel pellets) medium. The MP-2 experiment "took" the molten pool into the somewhat more voided region associated with a partly voided metallic crust, but was not carried out to the point where the pool directly contacted the more open geometry of a rodded structure. The MP-2 test demonstrated that the molten-pool/ceramic-crust configuration survives in a somewhat more porous medium and may survive in the fuel rod medium over a range of conditions.

11. In the event that the molten-pool/ceramic-crust configuration survives as the molten pool expands into a rodded region, a process may be envisioned in which the pool/crust continues to move outward and downward with the metallic components that comprised the original blockage moving somewhat ahead of the ceramic crust. When the pool encounters an open geometry either at the lower core support structure or the radial boundary of the reactor core, it will be free to move rapidly into the lower vessel head region.

References

1. K. O. Reil and R. O. Gauntt, "Results of the ACRR-DFR Experiments," Proc. International ANS/ENS Topical Meeting on Thermal Reactor Safety, San Diego, CA. (Feb 1986).

2. R. O. Gauntt and R. D. Gasser, "Results of the DF-4 BWR Control Blade-Channel BoxTest," Proc. 18th NRC Water Reactor Safety Information Mtg., Rockville, MD (Oct 1990).

3. R. D. Gasser, C. P. Fryer, R. O. Gauntt, A. C. Marchall, K. O. Reil and K. T. Stalker, Damaged Fuel Experiment DF-1: Results and Analysis, NUREG/CR-4668, SAND86-1030, Sandia National Laboratories, Albuquerque, NM (Jan 1990).

4. R. D. Gasser, C. P. Fryer, R. O. Gauntt, A. C. Marchall, K. O. Reil and K. T. Stalker, A. W. Cronenberg, Damaged Fuel Experiment DF-2: Results and Analysis, NUREG/CR-4669, SAND86-1441, Sandia National Laboratories, Albuquerque,NM (Sept 1992)

5. C. P. Fryer, R. O. Gauntt and A. W. Cronenberg, Damaged Fuel Experiment DF-3: Test Results, NUREG/CR-6006, SAND87-1212, Sandia National Laboratories, Albuquerque, NM (Nov 1989).

6. R. O. Gauntt, R. D. Gasser and L. J. Ott, The DF-4 Fuel Damage Experiment in ACRR with a BWR Control Blade and Channel Box, NUREG/CR-4671, SAND86-1443, Sandia National Laboratories, Albuquerque, NM (Nov 1989).

7. M. D. Allen, H. W. Stackman, K. O. Reil and A. J. Grimley, "Fission Product Release and Fuel Behavior of Irradiated Fuel Under Severe Accident Conditions: The ST-1 Experiment," Nuc. Tech (92), 214-228 (Nov 1990).

8. P Hofmann, et al., "Reactor Core Materials at Very High Temperatures," Nuclear Technology (87) (Aug 1989).

9. D. A. Petti, et al., Power Burst Facility (PBF) Severe Fuel Damage Test 1-4, Test Results Report, NUREG/CR-5163, EG&G Idaho, Ins., Idaho Falls, Idaho 83415 (April 1989).

10. R. D. Gasser, R. O. Gauntt and S. Bourcier, Late Phase Melt Progression Experiment: MP-1 Results and Analysis, SAND92-0804, Sandia National Laboratories, Albuquerque, NM (a draft copy can be obtained from Sandia National Laboratories).

11. S. S. Dosanjh, "Melt Progression in Dry Core Debris," Nucl Tech, (88), 30-46, (1989).

12. S. S. Dosanjh, Melt Progression in Severely Damaged Reactor Cores, NUREG/CR-5029, SAND87-2384, Sandia National Laboratories , Albuquerque, NM (Dec 1987).

13. S. S. Dosanjh, Relocation of Metallic Constituents in Core Debris Beds, NUREG/CR-5109, SAND88-0535, Sandia National Laboratories, Albuquerque, NM, (Sept 1988).

14. S. S. Dosanjh, Melt Progression, Oxidation, and Natural Convection in a Severely Damaged Reactor Core, NUREG/CR-5316, SAND88-3476, Sandia National Laboratories, Albuquerque, NM (Feb 1990).

15. D. W. Akers, et. al, TMI-2 Core Debris Grab Samples--Examination and Analysis, Part 1, GEND-INF-075, EG&G Inc. Idaho Falls, Idaho, (Sept 1986).

16. R. C. Schmidt, R. D. Gasser, "Models and Correlations of the DEBRIS Late-Phase Melt Progression Model", SAND93-3922, Sandia National Laboratories, Albuquerque N.M., (Dec 1993).

Appendix A. DEBRIS Model Description

A.1 MP-2 DEBRIS Code Parameters

This section of Appendix A contains the graphical or tabular record of the important parameters that were used in the MP-2 analysis. These parameters are necessary in order to reproduce the calculations. The parameters include thermophysical properties such as thermal conductivity, specific heat and density. For the most part the thermophysical properties were obtained from either Touloukian[1] or MATPRO[2].

In addition, since the power coupling factors, and the power geometrical shape factors are key to the energy deposition that drives the experiment, this section also includes a detailed description of how these parameters were obtained as well as the actual numerical values used in the analysis.

The dimensions of the experiment assembly and its key components are also shown with respect to the DEBRIS Code nodalization scheme.

A.1.1 Thermophysical Properties

Thermal Conductivity (W/m/K)

UO_2:

$$K = \frac{A}{\frac{1}{B + CT} + DT^3} \qquad \text{(A.1)}$$

A = 100.0, B = 4.0, C = 2.57 x 10^{-2},
D = 7.3 x 10^{-13} {T < 3023 K}
A = 11.5, B = 1.0,
C = D = 0.0 {T > 3023 K}

ZrO_2:

$$K = A + BT \qquad \text{(A.2)}$$

A = 0.835, B = 3.62 x 10^{-4} {T < 2973 K}

A = 1.4, B = 0.0 {T > 2973 K}.

Zircaloy:

$$K = A + BT + CT^2 + DT^3 \qquad \text{(A.3)}$$

A = 7.51, B = 2.09 x 10^{-2},
C = -1.45 x 10^{-5},
D = 7.67 x 10^{-9} {T < 2098}
A = 36.0, B = C = D = 0.0 {T > 2098}

Stainless Steel:

$$K = A + BT \qquad \text{(A.4)}$$

A = 7.581, B = 1.89 x 10^{-2} {T < 1671 K}
A = 610.9393,
B = -0.342176 {1671 < T < 1727 K}
A = 20.0, B = 0.0 {T > 1727 K}

ZrO_2 Fiber Insulation:

$$K = A + BT + CT^2 + DT^3 \qquad \text{(A.5)}$$

A = 1.84 x 10^{-1}, B = 3.9828 x 10^{-4},
C = -5.6108 x 10^{-8}, D = 6.24578 x 10^{-12}

ThO_2 (Melt Barrier):

$$K = \eta\left(A + BT + CT^2 + DT^3 + ET^4 \right) \qquad \text{(A.6)}$$

A = 27.88269, B = -6.720693 x 10^{-2},
C = 7.1066831 x 10^{-5},
D = -3.429394 x 10^{-8},
E = 6.2224843 x 10^{-12}, η = 0.9 {T < 1900 K}

A=0.25, B = C = D = E = 0.0 {T > 1900 K}

Helium:

$$K = AT^B \qquad \text{(A.7)}$$

A = 2.639, B = 0.7085.

Tantalum (Liner):

$$K = A + BT \qquad \text{(A.8)}$$

A = 75.438,
B = -1.4226 x 10^{-2} {T < 600 K}
A = 72.718,
B = -9.6232 x 10^{-3} {600 < T < 1000 K}
A = 65.521,
B = -2.5104 x 10^{-3} {1000 < T < 1800 K}
A = 59.699, B = 6.9733 x 10^{-3} {T > 1800 K}

Silver:

$$K = A + BT + CT^2 \qquad \text{(A.9)}$$

A = 445.06, B = -0.044052, C = -2.1635 x 10^{-5}

Indium:

$$K = A \qquad \text{(A.10)}$$

A = 25.0

Tin:

$$K = A + BT + CT^2 \quad \text{(A.11)}$$

A = 101.33, B = -0.1825, C = 2.166 x 10^{-4}

Densities (kg/m^3)

UO_2: ρ = 10,400.

ZrO_2: ρ = 5840.

Zircaloy: ρ = 6560.

Steel: ρ = 7500.

ZrO_2 Fiber: ρ = 1440.

ThO_2: ρ = 9860.

Ta: ρ = 16,600.

Ag: ρ = 10,500

In: ρ = 7300

Sn: ρ = 6500

Heat Capacities (J/kg/K)

UO_2:

$$C_p = \frac{Ae^{\frac{B}{T}}}{\left[T\left(e^{\frac{B}{T}} - 1\right)\right]^2} + CT + D\frac{e^{\frac{E}{T}}}{T^2} \quad \text{(A.12)}$$

A = 8.501346 x 10^7, B = 535.285,
C = 2.43 x 10^{-2},
D = 1.658692 x 10^{12}, E = 1.896732 x 10^4.

ZrO_2:

$$C_p = A + BT + CT^2 \quad \text{(A.13)}$$

A = -121.14, B = 3.3651,
C = -4.797 x 10^{-3} {T < 300 K}

$$C_p = A + BT + \frac{C}{T^2} \quad \text{(A.14)}$$

A = 565.0, B = 6.11 x 10^{-2},
C = -1.14 x 10^7 {T < 1478 K}

$$C_p = A \quad \text{(A.15)}$$

A = 604.5 {T < 2000 K}

$$C_p = A + BT \quad \text{(A.16)}$$

A = 171.7, B = 0.2164 {T > 2000 K}

Zircaloy:

$$C_p = A \quad \text{(A.17)}$$

A = 339.77 {T < 1113 K}
A = 676.6 {T < 1233 K}
A = 356.98 {T > 1233}

Stainless Steel:

$$C_p = A + BX + CX^2 \quad \text{(A.18)}$$

A = 326.0, B = 0.298, C = -9.56 x 10^{-5}
where,
X = min(T,1558)

ZrO_2 Fiber:

Same as Zirconia above.

ThO_2 (Melt Barrier):

$$C_p = A + B + \frac{C}{T^2} \quad \text{(A.19)}$$

A = 260.0, B = 3.328 x 10^{-2},
C = -3.5 x 10^6

Tantalum:

$$C_p = A + BT \quad \text{(A.20)}$$

A = 139.76, B = 1.339 x 10^{-2}.

Helium:

$$C_p = A \quad \text{(A.21)}$$

A = 5204

Silver:

$$C_p = A + BT \quad \text{(A.22)}$$

A = 219.766, B = 0.05232 {T < 1200 K}
A = 282.55, B = 0.0 {T > 1200 K}

Indium:

$$K = A + BT \quad \text{(A.23)}$$

A = 196.0, B = 0.14 {T < 430 K}
A = 252.0, B = 0.0 {T > 430 K}

Tin:

$$K = A + BT \quad \text{(A.24)}$$

A = 178.667, B = 0.166667 {T < 505 K}
A = 257.0, B = 0.0 {T > 505 K}

Heats of Fusion (J/kg)	Melt Temperature (K)
UO2: $h_{sl} = 2.78 \times 10^5$.	3023
ZrO2: $h_{sl} = 7.06 \times 10^5$.	2973
Zircaloy: $h_{sl} = 2.51 \times 10^5$.	2125
Steel: $h_{sl} = 2.80 \times 105$.	1700
Silver: $h_{sl} = 1.0465 \times 105$.	1200
Indium: $h_{sl} = 2.8465 \times 104$.	430
Tin: $h_{sl} = 6.0278 \times 104$.	505

Phase Diagrams

Becasue of the number of components and the vast number of phases possible from the various combinations of these materials, it was not feasible to incorporate the models to describe the interations. Thus, except for the UO_2/ZrO_2 components, all other constituents were assumed not to interact. These materials were assumed to melt at their respective melting temperatures.

The UO_2/ZrO_2 system was modeled in two ways. The first method involved the use of an approximate pseudo-isomorphous phase diagram. This diagram is shown in Figure A.1. The approximation associated with the use of this phase diagram implies that thermodynamic equilibrium exists at each time step, that each control volume is at one temperature and that, therefore, the kinetics of the interaction are extremely fast. The second method simply assumes that UO_2 and ZrO_2 do not interact and therefore melt at their respective melting temperatures. The assumption here is that the kinetics of the interactions are extremely slow.

The equations that were used to describe the phase diagram shown in Figure A.1 were selected to fit the measured data where data exists, namely near the 50% mole fraction and at the pure material melting points. The four functions, liquidus and solidus to the left and right of the 50% composition, also intersect at the same point and with the slopes all equal to zero at that point. The functions are:

$$T_{sl} = 3023 + 740f(f-1), \quad \textbf{(A.25)}$$

$$T_{ll} = 2930.5 + 92.5\cos(2\pi f), \quad \textbf{(A.26)}$$

$$T_{sr} = 2973 + 540f(f-1), \quad \textbf{(A.27)}$$

$$T_{lr} = 2905.5 + 67.5\cos(2\pi f), \quad \textbf{(A.28)}$$

where T_{sl}, T_{sr}, T_{ll}, T_{lr} are the solidus temperatures and liquidus temperatures left and right of the 50% composition, and f is the ZrO_2 mole fraction.

A.1.2 Effective Regional Thermal Transport Properties

Since the three fueled regions that are modeled in DEBRIS can be significantly different in configuration and composition, each of these zones requires a different heat transport model. The debris bed, for example, is a particulate medium, while the crust region is a composite, essentially solid region, and the rod region is a multicomponent medium with anisotropic transport properties. The purpose of this section is to describe the models used for these three zones.

Debris Bed

The effective thermal conductivity, K_{eff}, in the debris bed is calculated using the method suggested by Imura-Takeqoshi[3]. Radiation in the bed is incorporated using the Vortmeyer model (parallel conduction/radiation). In this model the effective thermal conductivity is given by:

$$K_{eff} = K_{cond} + K_{rad} \quad \textbf{(A.29)}$$

where

$$K_{rad} = 4\varepsilon\sigma d_p T^3 \eta \quad \textbf{(A.30)}$$

and

ε = emissivity of the solid,
σ = Stefan-Boltzmann constant,
d_p = mean particle diameter,
η = a parameter (0.25 best fits the observed bed thermal response).

The solid and the liquid are treated as a single component with a volume-averaged thermal conductivity, K_σ, and K_{cond} is then given by

$$K_{cond} = \Psi K_g + \frac{1-\Psi}{K_\sigma \omega + K_g(1-\omega)} K_\sigma K_g \quad \textbf{(A.31)}$$

where

$$\omega = 0.3\alpha_g^{1.6}\left[\frac{K_\sigma}{K_g}\right]^{-0.044}, \quad \textbf{(A.32)}$$

and

$$\Psi = \frac{\alpha_g - \omega}{1-\omega} \quad \textbf{(A.33)}$$

In these equations $\alpha_g = \varepsilon(1-S)$, which is the volume fraction of the gas given the porosity, ε, and the saturation, S.

In the limit of a gas volume fraction of zero, both ω and ψ go to zero, and consequently, $K_{cond} = K_\sigma$. For the other limit in which the gas volume fraction goes to 1.0, ψ approaches 1 and $K_{cond} = k_g$.

Crust Region:

In the crust region there is very little pore space and the region is effectively a composite solid. The effective thermal conductivity is, therefore, taken to be the volume average of the conductivities of the various components:

$$K_{eff} = \sum_i K_i Y_i, \qquad \textbf{(A.34)}$$

where K_i and Y_i are the thermal conductivity and the volume fraction of the i-th component.

Rod Stub Region:

Because of the parallel orientation of the fuel rods in this zone, the thermal conductivity is anisotropic. In the axial direction (parallel to the rods), the following parallel heat flow model was used:

$$K_z = K_\sigma (1-\varepsilon) + K_g \varepsilon + K_{z,\,rad}. \qquad \textbf{(A.35)}$$

Here K_z is the effective thermal conductivity in the axial, z, direction, K_σ is the volume averaged thermal conductivity, while K_g is the thermal conductivity of the gas and $K_{z,rad}$ is the axial radiation component given by:

$$K_{z,\,rad} = 4\varepsilon\sigma\eta\lambda T^3 \ , \qquad \textbf{(A.36)}$$

where η is a parameter (0.8 in the MP-2 analysis), ε is the emissivity (taken as 0.3 in MP-2), and λ is a characteristic length in the z direction (taken to be 0.02 m in MP-2).

The effective thermal conductivity across the rods (K_r - in the r-direction) is handled somewhat differently[4] and is given by:

$$K_r = K_g \Phi_1 + \frac{K_\sigma}{1 + \dfrac{K_\sigma \Phi_1}{K_g \Phi_2}} + K_{r,\,rad} \ , \qquad \textbf{(A.37)}$$

where the radiation component in the radial direction is,

$$K_{r,\,rad} = 4\varepsilon\sigma\eta\lambda T^3 \ , \qquad \textbf{(A.38)}$$

and

$$\Phi_1 = 1 - \sqrt{1-\varepsilon} \ , \qquad \textbf{(A.39)}$$

$$\Phi_2 = \sqrt{1-\varepsilon} \ . \qquad \textbf{(A.40)}$$

In Equation (A.38) the emissivity, ε, as before is taken as 0.3, the parameter, η, is 0.8, and the characteristic length, λ, is 0.005 m. Note that ε, the thermal emissivity, should be distinquished from ε, the overall porosity of the region.

A.2 Coupling Factors

Two methods were employed to estimate the reactor-to-experiment power coupling. The first method used the neutronic codes that have been used extensively for the performance of reactor core calculations to determine the reactivity of experiments inserted into the reactor. These neutronic calculations normally address experiment design and safety considerations but the code output can be augmented to yield information regarding power coupling between the reactor and the experimental assembly. The second method entails the reduction of thermocouple response data to determine local heatup rates during step changes in reactor power. This is a postexperiment procedure that involves some approximating assumptions and, therefore, serves primarily as a confirmation of the large neutronic code calculations.

A.2.1 Neutronic Code Coupling Factor Estimates

The MP-2 experiment was modeled with two fundamentally different neutronic codes, TWODANT[5] and MCNP[6]. TWODANT is a two-dimensional discrete-ordinates (S_n) solution to the steady state, multigroup form of the Boltzmann transport equation. MCNP, however, is a nondeterministic, Monte Carlo solution using a continuous rather than a multigroup energy format. Consequently, the TWODANT code imposes two limitations on the neutronic model not encountered with the MCNP code, i.e., highly three-dimensional problems must be approximated by two-dimensional geometries and the energy dependence is treated by a multigroup approximation. Early comparisons between pre-test calculations and posttest results showed that errors in the power coupling factor as high as 30% may result if the energy structure is not selected judiciously. These errors could result from resonance absorption in structural materials physically located between the ACRR and fueled regions of the MP-2 package. The errors can be overcome by selecting narrow energy groups that isolate ^{235}U resonance energies from resonance energies of other materials.

The MCNP code has certain limitations as well. Because the Monte Carlo technique is a nondeterministic approach, prohibitively large numbers of particle simulations may be required to obtain results within a desired range of accuracy. This is particularly true when calculating the worths of small reactivity perturbations or in calculating detailed power shape functions. These two calculations are more readily handled by deterministic codes such as TWODANT.

However, since these two codes complement each other, both were used in the neutronic analysis and the results of both are discussed below.

TWODANT Model:

The TWODANT calculation used an S_8 order of quadrature. Multigroup cross sections were collapsed from a 218 group cross-section library using XSDRNPM and the AMPX II modular code system. A 36-group energy structure was selected with the intention of isolating ^{235}U resonances from other material resonances as discussed above. The final working cross-section library contains the first four terms of the Legendre polynomial expansion for anisotropic scattering, i.e., P_3 for each isotope.

The nodalization scheme used in the TWODANT model featured 50 nodes horizontally and 69 nodes vertically. This nodalization was chosen to maximize the number of nodes in the fueled regions of the package and where possible, to match the nodalization of the Debris code. The crust region, the intact fuel region, and the ACRR have been homogenized in order to accommodate the 2-dimensional requirement.

MCNP Model:

The MCNP code permits a detailed 3-dimensional description of the MP-2 experiment package. Individual fuel rods in the package as well as individual fuel and control rods in the ACRR core are modeled explicitly.

One thousand cycles were performed, each cycle containing 1500 particles, giving 1,500,000 source particles. The only variance reduction technique used in the calculation was to set the importance of regions in the experimental package to twice that of the ACRR core. This allowed particle splitting for neutrons traveling from the ACRR to the package and Russian roulette for neutrons returning from the package to the ACRR. Such a calculation requires 32 CPU hours on an IBM RISC System/6000.

A tally of the track length estimate of fission heating (Mev/g) was kept throughout the calculation for the purpose of extracting the power coupling factor. If a tally, t_i, is kept for each of the three fueled regions in the experiment package and also for the ACRR core, t_a, the average region power coupling factor, CF_i can be obtained from:

$$CF_{i=1,3} = \frac{t_i}{t_a} \frac{1}{M_{UO_2}(gm)} \times 10^6 \left(\frac{W}{MW}\right) . \quad \textbf{(A.41)}$$

Since the coupling factor is calculated from a ratio of two statistically estimated tallies, its error must be calculated from the estimated relative errors of the two tallies. Gauss's law of propagation of errors states that if a function, $y=f(x_i,x_a)$, of two quantities, x_i and x_a, is to be calculated, and if only estimated values, t_i and t_a, with standard deviations, σ_i and σ_a, are available for x_i and x_a, then the standard deviation, σ_y of y, is given by

$$\sigma_y = \sqrt{\left(\frac{\partial f}{\partial x_a}\right)^2 \sigma_a^2 + \left(\frac{\partial f}{\partial x_i}\right)^2 \sigma_i^2} . \quad \textbf{(A.42)}$$

The standard deviation for the coupling factor is therefore

$$\frac{\sigma_{CF_i}}{CF_i} = \sqrt{\frac{\sigma_a^2}{t_a^2} + \frac{\sigma_i^2}{t_i^2}} . \quad \textbf{(A.43)}$$

Neutronic Results:

The overall region power coupling factors calculated from both TWODANT and MCNP are presented in Table A.1. Since the MCNP code is nondeterministic, the 2σ statistical uncertainty range is presented alongside those results. Note that results from the two codes do not agree within the statistical uncertainty of the Monte Carlo calculations, though they are not far off. It is believed that at least part of this systematic error can be attributed to the difference in how the tungsten liner was described in the two models. The cross section for ^{183}W was not available in the TWODANT cross-section library and was therefore neglected in that calculation. This would account for the fact that the coupling factor predicted by TWODANT is greater than that predicted by MCNP. Other factors that could give rise to these discrepancies are the differences in the way the ACRR and the rod stubs were modeled. In particular, since fuel material was uniformly distributed throughout the rod stub and crust regions in the TWODANT model, there would be less self-shielding and a corresponding higher coupling factor predicted for both these regions using the TWODANT model.

The debris bed region is essentially black, i.e., the thermal neutron flux is almost entirely depleted at the debris axial centerline. In fact, most of the thermal neutrons are absorbed in the outer centimeter of the debris region. The enrichment is high enough in the debris that with the depletion of thermal neutrons at the center, fission from fast and epithermal neutrons also become significant. Overall, 57% of all fission in the debris region are from thermal neutrons, 16% from epithermal, and 27% from fast neutrons. This underlies the need to carefully select epithermal energy groups so as to accurately account for neutron losses to resonances in the tantalum and thoria liners.

The coupling factors above have been averaged over an entire material region. Locally, the power factor can be quite different from these average values. For example, the power density is much greater near the outer surfaces of the debris than it is in the self-shielded interior. TWODANT

was used to calculate the local power coupling factor at each node in the model and shape factor functions for each of the three fueled regions were fit to these data. These shape factor functions are calculated from the definition of an average coupling factor, i.e.,

$$\langle CF\rangle P(MW)\,\bar{\rho}V = \langle CF\rangle P(MW)\int_V f(\vec{R})\,\rho d\vec{R} \qquad \textbf{(A.44)}$$

where

$$\bar{\rho}V = 2\pi\int_{z_1}^{z_1 R}\int f(r,z)\,\rho r dr dz \ , \qquad \textbf{(A.45)}$$

and f(r,z) is the local shape factor calculated by TWODANT. When separability is assumed, i.e., the local shape factor can be adequately expressed as a product of an axial and a radial shape factor function, then the following equations for the axial and radial shape functions result:

$$f_r(r) = \frac{\int_{z_1}^{z_2} f(r,z)\,dz}{(z_2 - z_1)} \ , \qquad \textbf{(A.46)}$$

and

$$f_z(z) = \frac{\int_0^R rf(r,z)\,dr}{\int_0^R rdr} \ , \qquad \textbf{(A.47)}$$

where it has also been assumed that the density is uniform throughout the region. The shape factors obtained in the manner described above are presented in Figures A.2 and A.3 for the radial and axial directions, respectively. These plots show the geometric shape factors for the three fueled regions of the experiment (debris bed, preformed crust, and rod stub regions).

Since there is energy deposited in the surrounding nonfueled regions primarily by gamma heating, coupling and shape factors must also be applied to these regions. The coupling factors were obtained for a wide variety of materials by placing small samples of each material in the ACRR central cavity and pulsing the reactor while recording the temperature response of the samples to the gamma and neutron energy deposition. Shape factors were obtained by using the standard shielding equations to estimate gamma attenuation. Table A.2 records the effective coupling factors for the appropriate materials utilized in MP-2 and Figures A.4 and A.5 shows the shape factors for the eight zone configurations involving nonfueled structures. In this figure the zones correspond to the following axial nodes (refer to Figure A.6 which shows the nodalization scheme used in the MP-2 DEBRIS code calculations):

Zone #1 (Steel) = axial nodes 1,2,5,6,9-12,78,79

Zone #2 (Helium) = axial nodes 3,4

Zone #3 (Steel, Helium) = axial nodes 7,8

Zone #4 (Steel,Al,ZrO_2,Ta,ThO_2) = axial nodes 13,14

Zone #5 (Steel,Al,ZrO_2,Ta,ThO2) = axial nodes 66-69

Zone #6 (Steel,ZrO_2) = axial nodes 70,77

Zone #7 (Steel,Al,ZrO_2,Ta,ThO_2) = axial nodes 15-31

Zone #8 (Steel,Al,ZrO_2,Ta,ThO_2,W) = axial nodes 32-65.

A.2.2 Thermocouple Response Coupling Factor Estimates

The thermocouple data collected from the MP-2 experiment can be used to estimate the observed power coupling between the ACRR and the MP-2 package. The local coupling factor can be estimated by assuming that the net heat transport into a small control volume containing the thermocouple junction is constant over a small time interval centered around a step change in the ACRR power. We can write energy balances for this control volume surrounding a particular thermocouple immediately before and after a step change in reactor power:

$$MC_p\frac{dT_1}{dt} = P_1 M_{UO_2} f - L_1 \ , \qquad \textbf{(A.48)}$$

$$MC_p\frac{dT_2}{dt} = P_2 M_{UO_2} f - L_2 \ , \qquad \textbf{(A.49)}$$

where f is the local coupling factor, P_1 and P_2 are the reactor power levels before and after the step change, and L_1 and L_2 are the net heat loss rates before and after the step change in power, respectively. From the above discussion on shape factors it follows that this local coupling factor can be expressed as the product of the shape factor and the average coupling factor for that region. If it can be assumed that the net heat transfer through the surface of the control volume does not change rapidly following an abrupt step change in reactor power, then $L_1 \approx L_2$, and Equations (A.48) and (A-49) can be used to estimate the local coupling factor from:

$$f = \frac{\left(\frac{dT_1}{dt} - \frac{dT_2}{dt}\right)\sum_i \rho_i C_{p_i}}{(P_1 - P_2)} \frac{}{\rho_{UO_2}} + \varepsilon \ , \qquad \text{(A.50)}$$

$$\varepsilon = \frac{(L_1 - L_2)}{M_{UO_2}(P_1 - P_2)} \ , \qquad \text{(A.51)}$$

where ε is the error associated with this assumption.

Sixteen separate step power adjustments (eight increases and eight decreases) were used to make independent estimates of the local power coupling factor. These power adjustments can be seen in Figure 4.1 as the eight narrow power "spikes" that take place between 1000 and 12,000 seconds. The independent estimates are statistically analyzed to determine agreement with the coupling factors predicted from the neutronic codes.

The assumption on which Equation (A.50) is based should be discussed before assessing the results of this analysis. It was assumed that the rate of heat loss does not change rapidly following a step change in power. This assumption is probably most accurate in the center of the debris bed where the heat loss from the assumed control volume is a function of the local thermal diffusivity, which is small in the debris, and the local temperature gradient, which is also small near the center of the debris. Near the boundaries of the debris bed, the heat loss becomes more strongly influenced by the thermal properties of materials in the adjacent regions. Also, since it is likely that the net flow of heat out of a control volume near the debris boundary increases after a boost in reactor power, Equation (A.50) will tend to underestimate (ε is positive) the local coupling factor there.

The use of Equation (A.50) in determining the local coupling factor requires both the specific heat and the density of constituent materials in the three fueled zones. The correlations given in Section A.1.1 for C_p were used in this analysis.

There is a certain amount of statistical error associated with estimating the rate of temperature change before and after a step change in the ACRR power. There is some variance associated with the temperature data, i.e., the points do not all lie on a smooth curve due to noise in the thermocouple data channels. Also several seconds are actually required to change the reactor power level. These effects, together with the time lag associated with the heat capacity of the thermocouple are responsible for the curvature in the temperature traces just after the power level is changed. Data points just before and after the power change were used to determine the slope of the temperature/time curve. These points must be selected judiciously to assure that the data is not within the transient response period yet not delayed long enough so that changes in the heat loss rate negate the constant heat loss assumption. There are generally about 8 to 14 data points on either side of the power change that are usable with this criteria in mind. These points may be used in various combinations to estimate the heatup rate. The excellent correlation of the data with a straight line seems to indicate that much of the discrepancy may simply be statistical in nature. To remove some of the statistical uncertainty six such slopes were estimated for each power change and then averaged to obtain a mean rate of temperature change following a step change in ACRR power. This average slope is then used in Equation (A.50) to calculate the local power coupling factor. The same strategy is used to estimate the slope of a linear fit to the data points just prior to the power boost. The error in the estimated coupling factor associated with this estimated slope for thermocouple i and power step j can then be derived from:

$$\varepsilon_{i,j} = \frac{\sqrt{\frac{\sigma_{1,i,j}}{5} + \frac{\sigma_{2,i,j}}{5}}\, t}{\left|\mu_{1,i,j} - \mu_{2,i,j}\right|} \ , \qquad \text{(A.52)}$$

where $\sigma_{1,i,j}$ and $s_{2,i,j}$ and $\mu_{1,i,j}$ and $\mu_{2,i,j}$ are the sample variance and mean for the six estimates, m_i, of the slope before and after the power change and t is the student t-parameter for a 90% confidence limit. For five degrees of freedom, t=2.01505. This average slope is then used in Equation (A.50) to calculate the local power coupling factor. The same strategy is used to estimate the slope of a linear fit to the data points for both the power-boost and the power-decrease phases of each of the transient phases of the heatup cycle.

The mean and variance of the coupling factor estimates can be calculated in at least two ways. First, one can accept the variance calculated above for each data point based on the six separate estimates of the slope and weight each estimate of the coupling factor by the inverse of the square of the variance associated with the estimate, i.e.,

$$\mu_{wt} = \sum_j F_j \frac{\sigma_{wt}^2}{\sigma_k^2} \ , \qquad \text{(A.53)}$$

where

$$\sigma_{wt}^2 = \left(\sum_k \frac{1}{\sigma_k^2}\right)^{-1} \ . \qquad \text{(A.54)}$$

Alternatively, one can simply assume that each estimate is equally important and ignore the previous estimate of uncertainty in the estimate of the heatup rate (the slope) to arrive at a sample mean and variance. This was the method used to calculate the mean and variance shown in Figures A.7 through A.10. The 90% confidence range surrounding the mean is then obtained from:

$$\delta = \frac{ts}{\sqrt{n}} , \qquad \text{(A.55)}$$

where s is the sample variance and n in the degree of freedom. For 16 samples n=15, and the student t parameter for 90% confidence is t=1.753.

Figures A.7 through A.10 show estimates for the local power coupling factor for the four thermocouples located within the debris bed including the 16 step changes in reactor power (either power increase or decrease). The mean coupling factor is shown for each data set together with the 90% confidence range. For temperatures less than ~2000 K, the coupling factor estimates appear randomly distributed about the mean and uncorrelated to the temperature. Above 2000 K the coupling factor begins to show a correlation with the temperature. The MCNP calculations show that temperature effects (doppler and other temperature effects on reactivity) can not account for the temperature dependence. These results may be explained by uncertainty in the specific heat functions at higher temperatures or by the effects of radiation on the effective thermal conductivity resulting in an increased error associated with the assumed constant heat loss rate.

Table A.3 gives the comparison of coupling factors as estimated using the neutronic code calculations and the thermal response calculations. The first two columns of Table A.3 present the estimated local coupling factor calculated from both a simple average of the 16 estimates and the weighted average calculated from Equation (A.53). The numbers in parentheses indicate the 90% confidence range discussed above. The thermocouples presented in Table A.3 were all accepted as having performed adequately during the test. Also shown in the table are the values predicted by both TWODANT and MCNP along with the relative difference between this value and that predicted from the thermocouple analysis. The agreement along the centerline of the debris bed region, away from the boundaries, is well within the error of the thermocouple analysis. For thermocouples placed close to the outer edge of the debris bed, where the shape factor is steepest, heat losses are relatively large, and the control volume may intersect the neighboring region, the error becomes more significant. Thermocouples DBC1400, DBC1401 and DBC2103 all give results that indicate coupling factors that exceed those predicted by the neutronic calculations. Since these thermocouples were located in a region of high heat loss near a region of high heat capacity and much lower heat generation, it is consistent that an estimate based on an assumed constant heat loss rate would underpredict the local coupling factor.

The analysis for thermocouple DBC3000 was modified slightly in an attempt to correct for the boundary effect. It was assumed that the thermocouple was located exactly on the debris bed/thoria lid interface and that the control volume surrounding this thermocouple intersects the debris bed and the thoria lid equally, i.e., the specific heat function is an average of the thoria and debris bed specific heat functions. It was also assumed that the heat generated in the thoria is negligible compared to the heat generated in the debris. With these assumptions, the estimated coupling factor agrees with the TWODANT predictions within 6%.

The DBC2102 thermocouple gave results that were 11% higher than the neutronic calculations. This thermocouple appears to be located far enough from the bed boundary that its response would not be significantly influenced by heat losses to the adjacent thoria liner. However, thermocouple DBC2102 was located in a region where the gradient of the shape factor was quite steep.

The coupling factors predicted by both TWODANT and MCNP lie outside the 90% confidence range for the thermocouple analysis performed in both the crust and rod stub regions. In the crust region, this systematic error is greater at the top near the debris/crust interface and is probably attributed to the importance of the heat transfer from the debris region into the crust and its impact on the error of Equation (A.50). It should be noted that for all thermocouples in the crust region, this analysis predicts coupling factors that are higher than the neutronic calculations predicted. Since these are all regions of high heat gain from the debris region above, this trend is consistent with the error associated with the approximation of Equation (A.50), i.e., ε is negative.

Conclusions:

The thermocouple analysis, which is inherently approximate in nature, cannot directly confirm the results of the neutronic analysis, but it does seem to support those results. As discusses previously, the two methods agree only near the center of the debris bed. However, for most thermocouples it can be argued that the magnitude and direction of the error can be explained by the assumption upon which the approximation of Equation (A.50) is based. Even so, this discrepancy may also be attributed to errors in the calculated shape factors as well as errors in the equations for the specific heat, or errors due to the nonhomogeneous nature of the crust and rod arrays. Confirmation of the neutronic analysis requires detailed calculations of heat transfer throughout the experiment package.

Appendix A. - References

1. Y. S. TOULOUKIAN, Thermophysical Properties of High Temperature Materials, Thermophysical Properties Research Center, Purdue Univ., Lafayette, IN, Vols 1-6, 1967.

2. J. K. Hohorst, editor, SCDAP/RELAP5/MOD2 Code Manual, Volume 4: MATRPRO-A Library of Material Properties for Light Water Reactor Accident Analysis, NUREG/CR-5273, T190 008333, EG&G Idaho, Feb 1990.

3. S. Imura, E. Takegoshi, Effect of Gas Pressure on the Effective Thermal Conductivity of Packed Beds, Heat Transfer Japanese Research, Vol. 3, No. 4, p. 13 (1974).

4. R. Viscanta, S. Chellaiah, M. M. Moallemi, Thermal Analysis of Core Barrel Heating and Coolant Recirculation During Core Uncovery in PWR Accidents, EPRI Report NP-5586, Project 1760-3, Final Report, p 3-7, Nov. 1987.

5. User's Guide for TWODANT: A Code Package for Two-Dimensional, Diffusion-Accelerated, Neutron-Particle Transport, Los Alamos National Laboratories, Los Alamos , NM, LA-10049-M, Rev. 1.

6. W. L. Thompson, MCNP - A General Monte Carlo Code for Neutron and Photon Transport A Summary, LA-8176-MS, UC-20, UC-34c. and UC-80, Los Alamos National Laboratories, Los Alamos, NM, Dec 1979.

Table A.1 Calculated MP-2 Coupling Factors (W/g(UO_2)/MW(ACRR))

Region	Calculated (TWODANT)	Calculated (MCNP)	Difference (%)	MCNP Statistical Uncertainty
Debris Bed	4.59	4.15 ± 0.053	10.1	1.27
Preformed Crust	1.5	1.44 ± 0.058	5.40	3.6
Rods Stubs	1.55	1.32 ± 0.035	16.0	2.5

Table A.2 Gamma Heating Coupling Factors for Nonfueled Regions

Material Number	Material	Coupling Factor (W/MW/kg)
4	Steel	0.1072
5	ZrO_2	0.1072
6	ThO_2	0.1658
7	Tantalum	0.1486
8	Helium	0.1130
9	Aluminum	0.1092
10	Tungsten	0.1419

Table A.3 Comparison of Local Coupling Factors (W/g/MW) Predicted by Heatup Rate and Neutronic Code Estimates

Thermocouple	Simple Average[a]	Equation A.50[b]	TWODANT[c]	MCNP[d]
DBC3000	7.45 (±5.1%)	7.51 (<±1%)	7.00 (-6.2%)	6.33 (-19%)
DBC2501[e]	2.87 (±4.6%)	2.75 (<±1%)	2.75 (4.3%,<1%)	2.48 (-14%)
DBC2103	3.72 (±2.6%)	3.67 (<±1%)	3.85 (3.4%)	3.49 (-6.4%)
DBC2102	3.40 (±2.2%)	3.46 (<±1%)	3.08 (-10%)	2.78 (-20%)
DBC2100[e]	2.79 (±2.4%)	2.80 (<±1%)	2.85(2.1%,1.8%)	2.57 (-8%)
DBC1801[e]	2.95 (±3.3%)	2.89 (<±1%)	2.90(-1.7%,<1%)	2.61 (-12%)
DBC1601[e]	3.09 (±6.4%)	2.97 (<±1%)	2.92(-5.6%,1.7%)	2.64 (-16%)
DBC1401	2.11 (±8.2%)		3.17 (40%)	2.86 (30%)
DBC1400	2.43 (±3.9%)	2.44 (<±1%)	3.17 (26%)	2.86 (16%)
CRC13-1	1.57 (±3.0%)		1.05 (-40%)	1.01 (-43%)
CRC12-0	1.41 (±5.4%)		1.05 (-30%)	1.01 (-33%)
CRC11-2	1.26 (±6.4%)		1.19 (-6%)	1.14 (-10%)
CRC11-4	1.68 (±3.0%)		1.35 (-21%)	1.30 (-25%)
FRK0514	1.13 (±2.6%)		1.25 (10%)	1.06 (-6%)

(a) Number in parenthesis is the relative error associated with the simple mean.
(b) Number in parenthesis is the relative error associated with Equation A.53.
(c) First Number in parenthesis is the relative error between TWODANT and the simple mean. The second number is the relative error between TWODANT and Equation A.53.
(d) Number in parenthesis is the relative error between MCNP and the simple mean.
(e) Internal thermocouples along debris bed centerline where agreement is best.

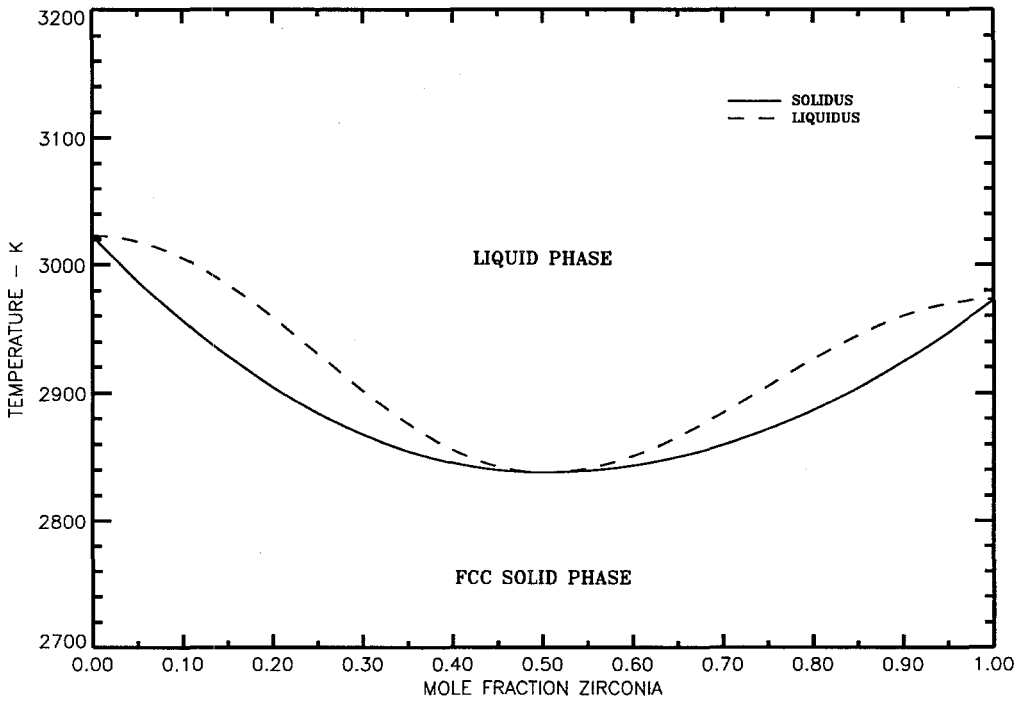

Figure A.1 Simplified Phase Diagram for the Hyper-Stoichiometric UO2-ZrO2 Pseudo-Binary System

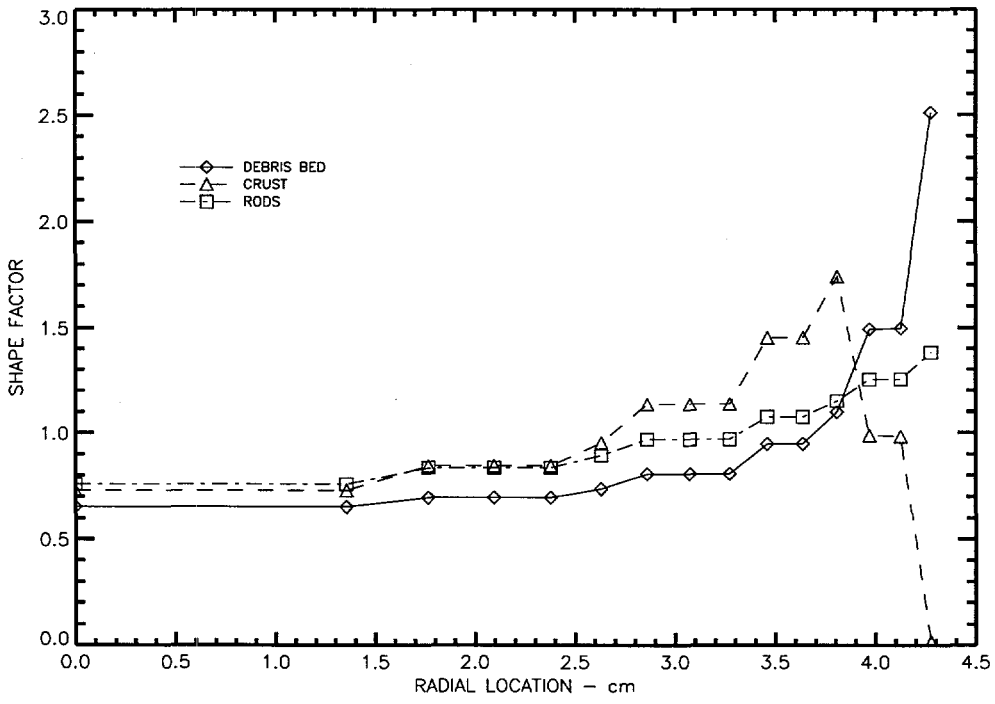

Figure A.2 MP-2 Radial Power Shape Factors in the Fission Zones

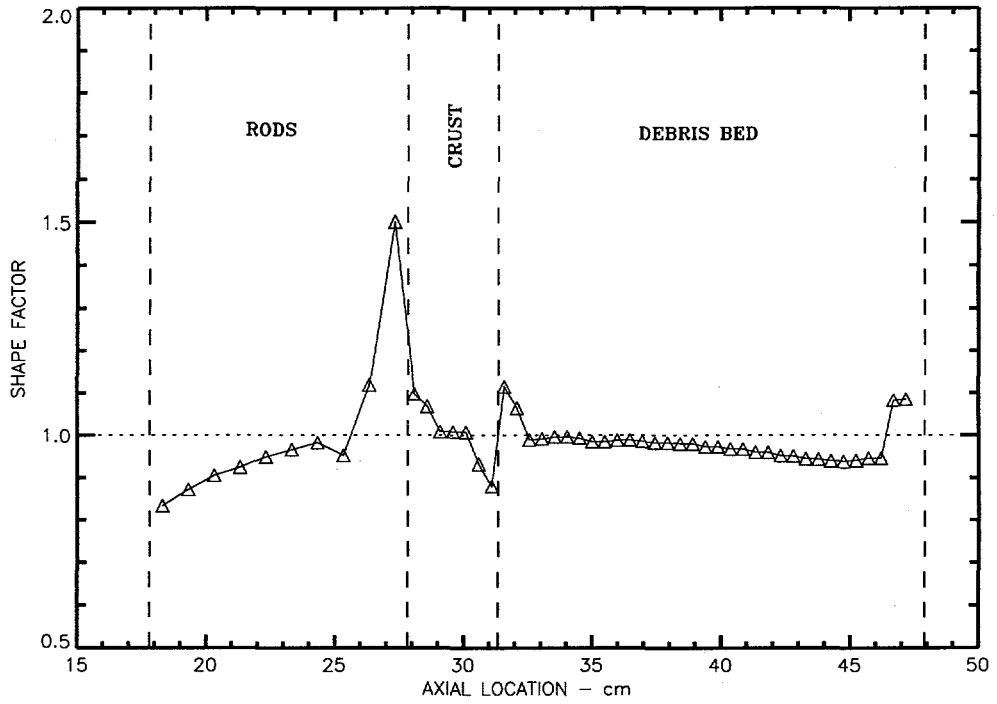

Figure A.3 MP-2 Axial Power Shape Factors in the Fission Zones

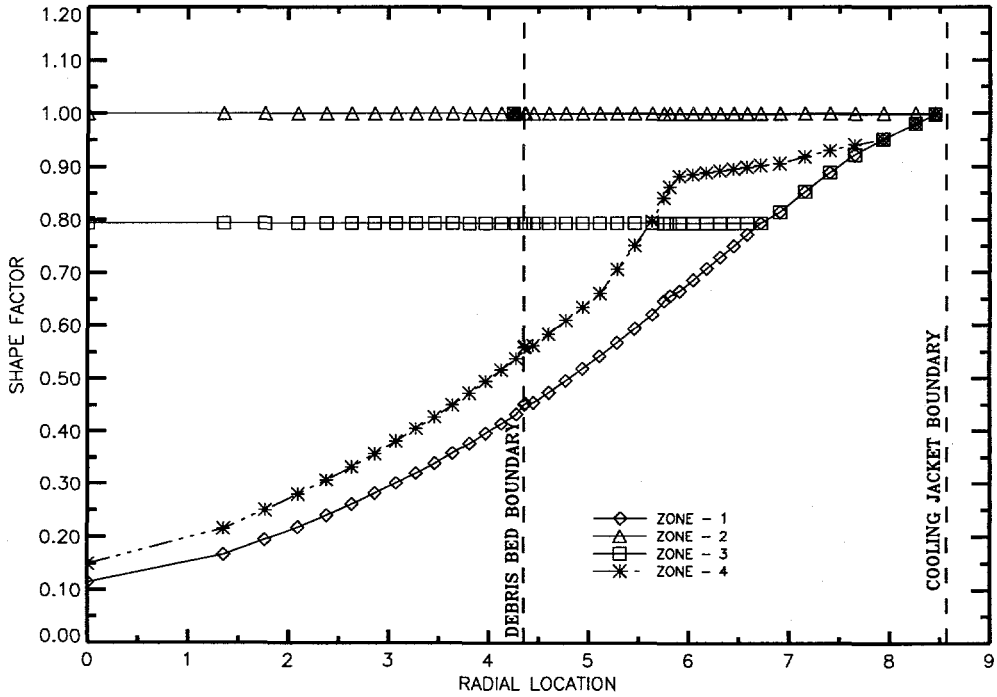

Figure A.4 MP-2 Radial Gamma-Heating Shape Factors in Axial Zones 1 to 4

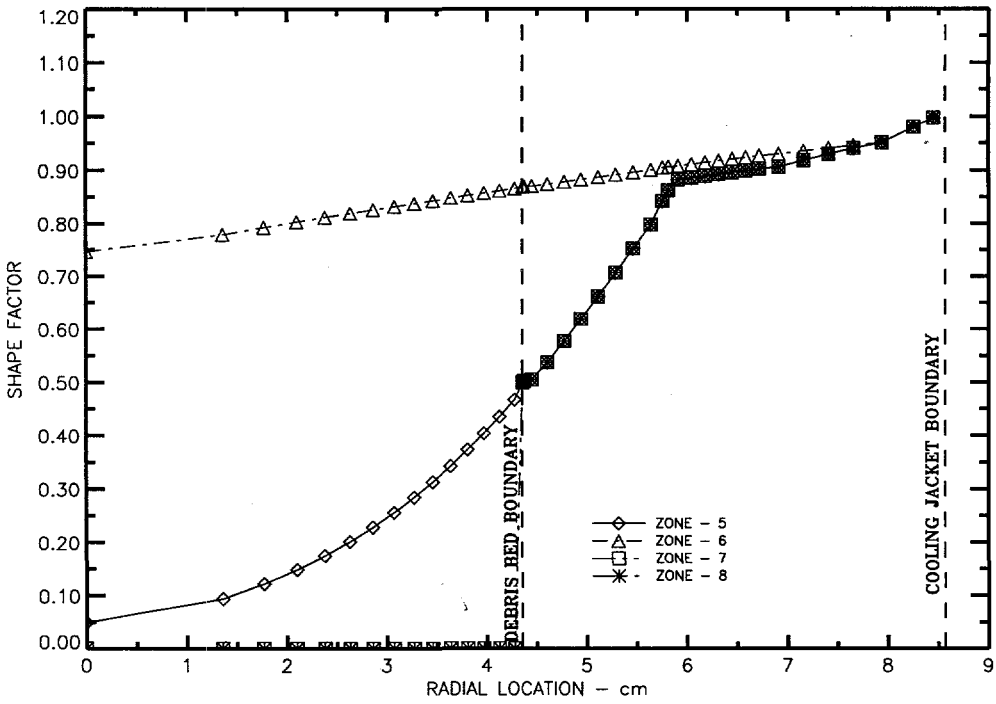

Figure A.5 MP-2 Radial Gamma-Heating Shape Factors in Axial Zones 5 to 8

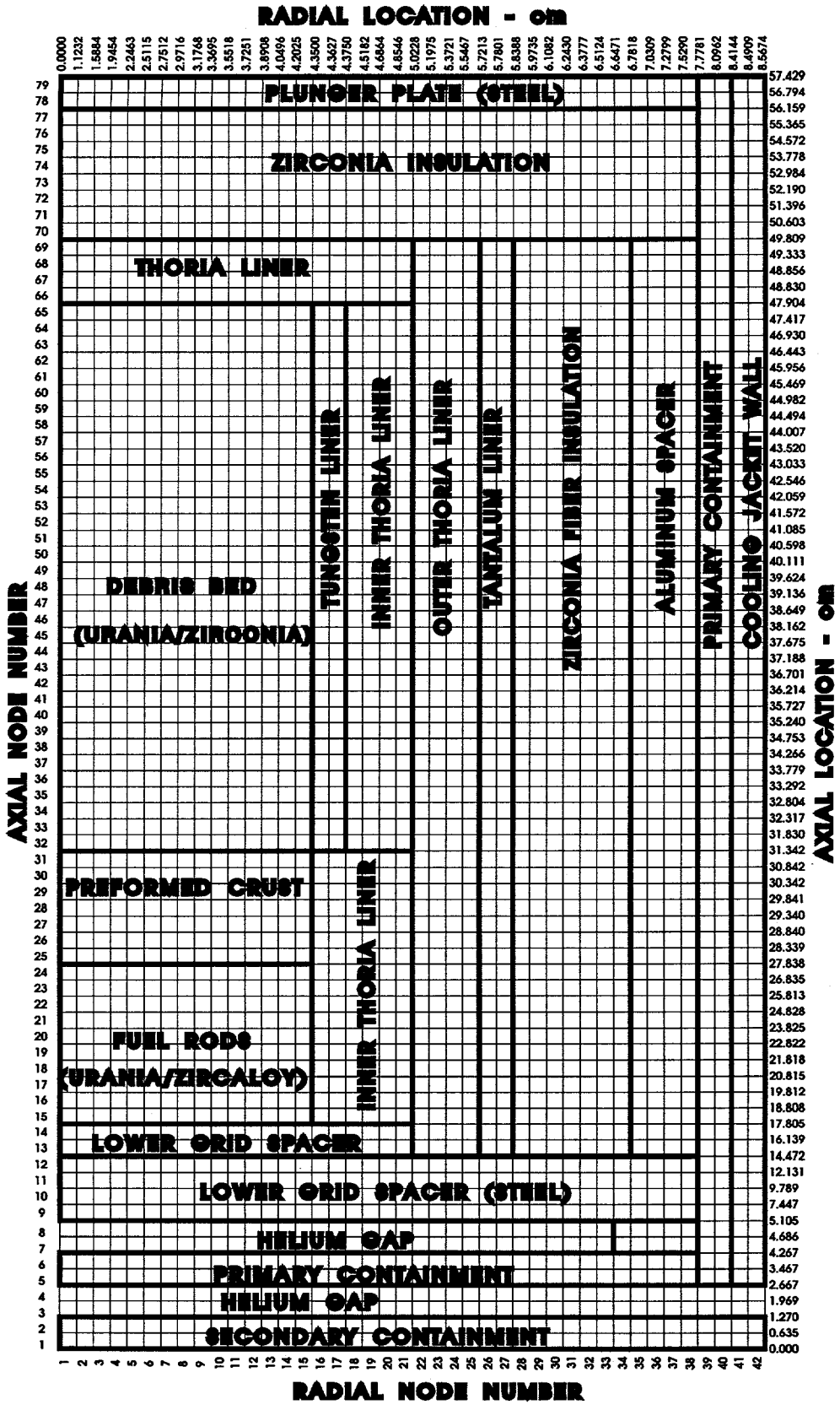

Figure A.6 MP-2 DEBRIS Code Nodalization Scheme Showing System Dimensions

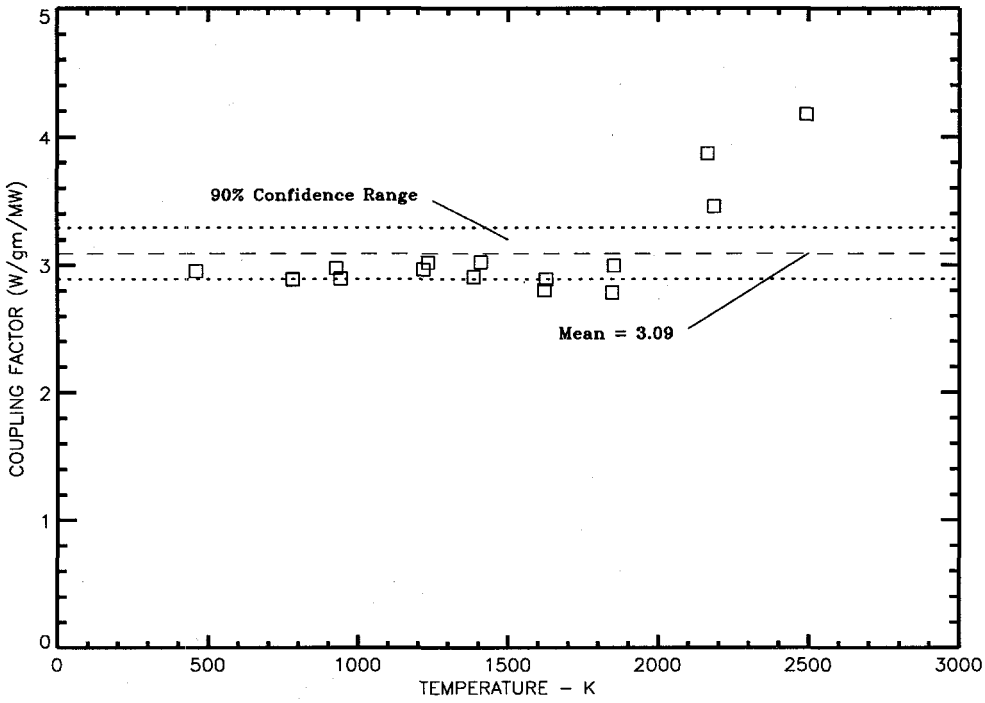

Figure A.7 Coupling Factor Estimates from Thermocouple DBC1601 Responses

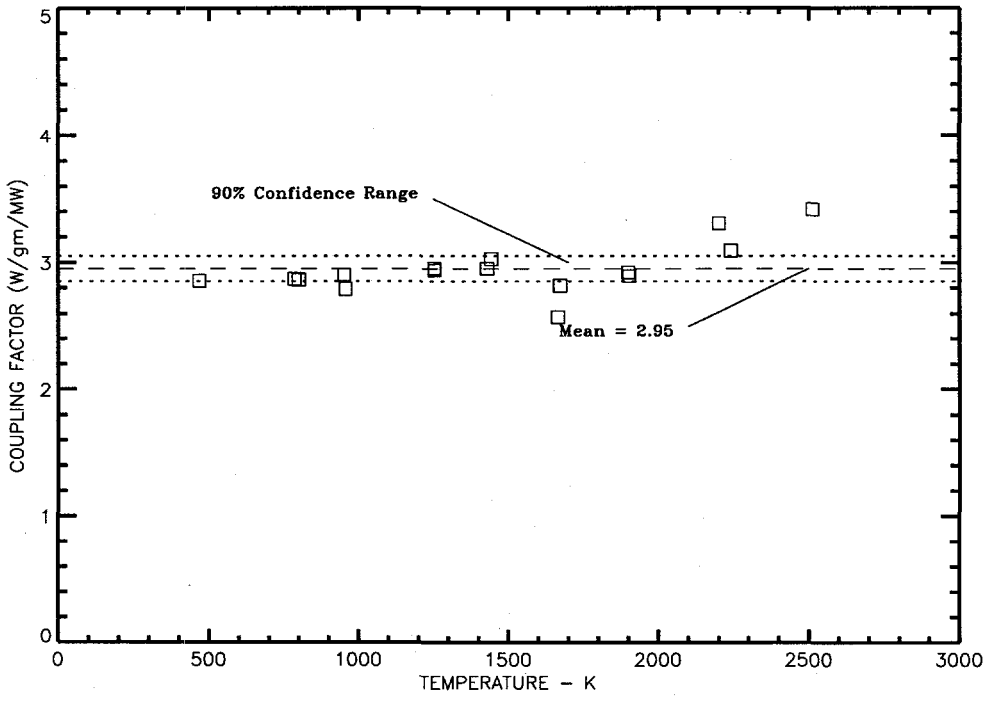

Figure A.8 Coupling Factor Estimates from Thermocouple DBC1801 Responses

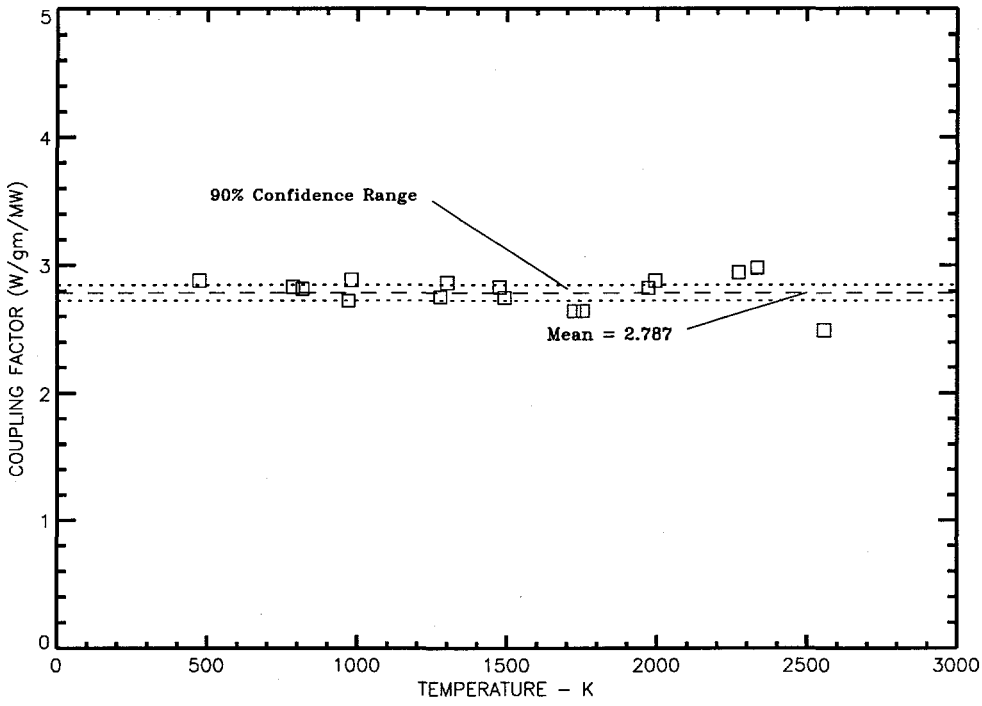

Figure A.9 Coupling Factor Estimates from Thermocouple DBC2100 Responses

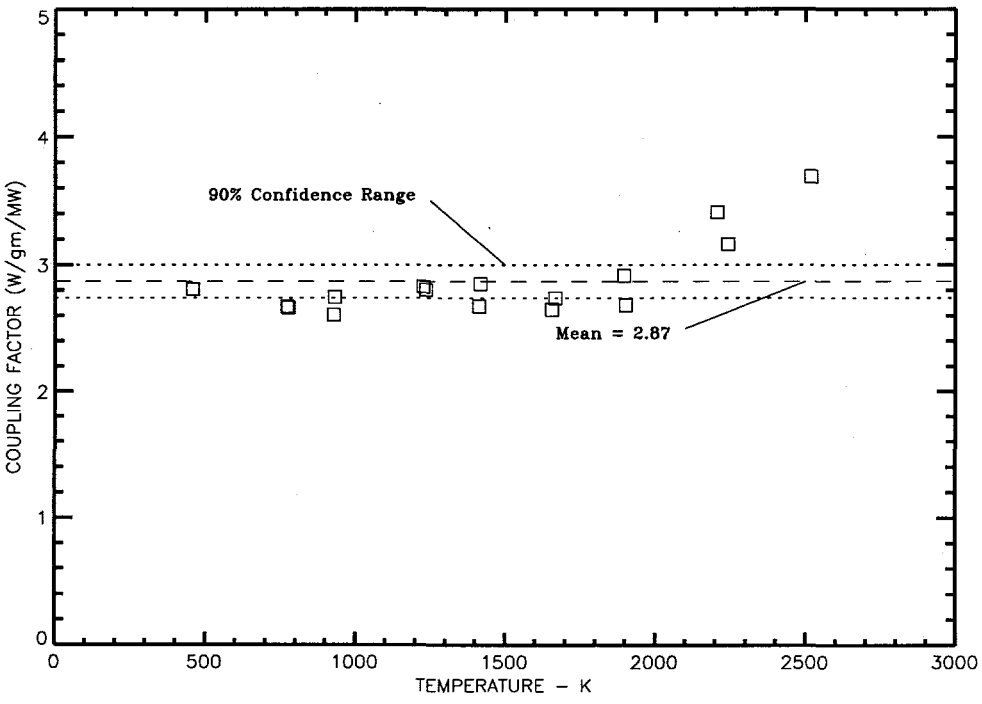

Figure A.10 Coupling Factor Estimates from Thermocouple DBC2501 Responses

Appendix B. Heat Transfer in the MP-2 Cooling Jacket

Several aspects of the design of the MP-2 heat removal system and the demands placed upon it during the course of the experiment required that special methods be used to effectively predict the heat transfer rates from the test package to the heat rejection system. At the peak coolant flow rate during the experiment, the Reynolds number based on the cooling jacket lateral dimension (r_2-r_1) did not exceed 150 which is well inside the laminar flow regime. A schematic diagram of the heat removal system is shown in Figure B.1. The relative positions of the primary heat sources in the package together with the distribution of insulating and melt barrier materials resulted in a heat flux distribution that varied both in time and in location along the axial extent of the cooling jacket surface. Thus the cooling jacket could not be modeled using either standard correlations for isothermal walls or constant heat flux walls to determine the wall-to-coolant heat transfer coefficients. Late in the experiment, natural convection began to play a role and at late times for certain locations in the cooling jacket the wall temperature exceeded 400 K and nucleate boiling in this limited zone also occurred.

The geometry of the MP-2 cooling jacket was cylindrical with the coolant flowing upward in a single-pass through the cooling jacket in an annular shaped passage (See Figure B.1). The cooling jacket was fabricated in two half-annular sections with the two halves bolted together to form a tight fit with the outer surface of the primary containment wall. The coordinate system adopted for the present model is given in Figure B.1 along with some of the nomenclature used in the following formulation. Coolant was supplied to the input manifold at the bottom of each half-annual section through four 1/4-inch diameter feeder lines (eight in all) and flowed out of the upper outlet manifold through a single 1/2-inch diameter tube (two in all). The coolant entered the annulus of the cooling jacket from the inlet manifold through 11 0.22-inch (0.5588-cm) diameter orifices in the top of the inlet manifold and exited through an identical set of orifices at the bottom of the outlet manifold. Although the flow higher up in the cooling jacket was clearly laminar, this arrangement of inlet orifices produced 22 separate jets at the inlet and rendered characterization of the flow near the bottom and the top of the cooling jacket quite difficult. The assumption is made in the analysis that the flow is everywhere laminar. The Prandtl number for water (the coolant) in the temperature range associated with the experiment is about 5.0. Therefore, the assumption has been made in this formulation that the velocity profile develops much more rapidly than the temperature profile and is fully developed over the entire heated section of the cooling jacket.

The momentum and energy equations that apply follow:

$$\frac{\nu}{r}\frac{\partial}{\partial r}\left(r\frac{\partial u}{\partial r}\right) = \frac{1}{\rho}\frac{\partial P}{\partial z} \quad , \tag{B.1}$$

$$u\frac{\partial T}{\partial z} = \frac{\alpha}{r}\frac{\partial}{\partial r}\left(r\frac{\partial T}{\partial r}\right) \quad . \tag{B.2}$$

These equations are not mutually coupled since Equation (B.1) can be solved directly to obtain:

$$u = -2u_m \frac{\left[(1-R_s)^2R^2 + 2R_s(1-R_s)R\right]ln(R_s) + \left(1-R_s^2\right)ln\left[\frac{(1-R_s)}{R_s}+1\right]}{\left[\left(1-R_s^2\right)+\left(1+R_s^2\right)ln(R_s)\right]} \tag{B.3}$$

where u_m is the mean flow velocity and the parameters R and R_s are defined as:

$$R = \frac{(r-r_1)}{(r_2-r_1)} \quad , \tag{B.4}$$

$$R_s = \frac{r_1}{r_2} \quad . \tag{B.5}$$

Since the present application is to cases in which R_s is close to 1.0, and since use of the ln profile does not lead to finite series

functions in the integral method, a good approximation consists in assuming a parabolic velocity profile in the annulus which leads to;

$$u = 6u_m R(1-R) \quad . \tag{B.6}$$

We may also non-dimensionalize the temperature in the following manner:

$$\theta = \frac{(T-T_w)}{(T_0-T_w)} \quad . \tag{B.7}$$

Using an approximate integral technique we will integrate Equation (B.2) across the boundary layer. Multiplying Equation (B.2) by *rdr and* integrating from $r = r_1$ to $r = r_1 + \delta$ we have, where δ is the boundary layer thickness:

$$\int_{r_1}^{(r_1+\delta)} ru\frac{dT}{dz}dr = \int_{r_1}^{(r_1+\delta)} \alpha\frac{\partial}{\partial r}\left(r\frac{\partial T}{\partial r}\right)dr \quad . \tag{B.8}$$

Since we are assuming that the flow is fully developed, the velocity, u, is not a function of z, and we can rewrite Equation (B.8) as:

$$\int_{r_1}^{(r_1+\delta)} \frac{\partial}{\partial z}(ruT) = \alpha\left[r\frac{\partial T}{\partial r}\right]\Bigg|_{r_1}^{r_1+\delta} = \alpha(r_1+\delta)\frac{\partial T}{\partial r}\Bigg|_{(r_1+\delta)} - \alpha r_1\frac{\partial T}{\partial r}\Bigg|_{r_1} \tag{B.9}$$

By the definition of the thermal boundary layer, the heat flux at the edge of the boundary layer is zero, so the first term on the right is identically zero. If we apply the Leibnitz rule to the left side of Equation (B.9), we arrive at the final form of the integral equation for the temperature in the boundary layer,

$$\frac{d}{dz}\int_{r_1}^{(r_1+\delta)} (ruT)\,dr - \left[(r_1+\delta)\,u_\delta T_0\frac{d}{dz}(r_1+\delta)\right] = -\alpha r_1\frac{\partial T}{\partial r}\Bigg|_{r_1} \quad . \tag{B.10}$$

At this point it is necessary to chose an appropriate approximation for the temperature profile across the boundary layer. A polynomial profile (quadratic or cubic) could be used, but experience has shown that the choice of a sine profile achieves the best results. In order to derive an expression for the heat flux at the wall for a nonisothermal wall, it is first necessary to find a solution for an isothermal wall. From this solution Duhamel's theorem can be applied to derive the solution for a nonisothermal wall condition. We proceed by assuming a temperature profile,

$$\theta = \sin(a + bR) \quad , \tag{B.11}$$

subject to:

$$\theta|_{r=r_1} = \theta|_{R=0} = 0 \quad , \tag{B.12}$$

$$\theta|_{r=(r_1+\delta)} = \theta|_{R=R_\delta} = 1 \quad , \tag{B.13}$$

$$\frac{\partial\theta}{\partial r}\Bigg|_{r_\delta} = \frac{\partial\theta}{\partial R}\Bigg|_{R_\delta} = 0 \quad , \tag{B.14}$$

and from the original differential equation:

$$\frac{\partial^2 T}{\partial r^2}\Bigg|_{r=(r_1+\delta)} = \frac{\partial^2\theta}{\partial R^2}\Bigg|_{R=R_\delta} = 0 \quad . \tag{B.15}$$

These boundary conditions are satisfied by,

$$\theta(R) = \sin\left[\frac{\pi R}{2R_\delta}\right] . \tag{B.16}$$

The second term on the left of Equation (B.10) can be included inside the integral with no loss of generality and the expression for the velocity, u, can be replaced by Equation (B.6). We also need to transform the remaining r-dependent terms in the equation to the appropriate R-dependency. From Equation (B.4) we get,

$$r = r_m R + r_1 , \tag{B.17}$$

where $r_m = r_2 - r_1$, which represents the flow channel width. Note that $R_\delta = \delta / r_m$. Using the assumed temperature profile in Equation (B.16) we can rewrite the right side of Equation (B.10),

$$\left.\frac{\partial T}{\partial r}\right|_{R=0} = \frac{\partial\theta\, dT dR}{\partial R d\theta dr} = \frac{\pi}{2R_\delta r_m}(T_0 - T_w)\cos\left[\frac{\pi R}{2R_\delta}\right]\Bigg|_{R=0} = \frac{\pi}{2R_\delta r_m}(T_0 - T_w) . \tag{B.18}$$

The integral form of the thermal boundary layer equation then takes on the form:

$$\frac{d}{dz}\int_0^{R_\delta} [r_m R + r_1]\,[6u_m R(1-R)]\,[T_0 - T_w]\left[\sin\left[\frac{\pi R}{2R_\delta}\right] - 1\right] r_m dr = \left(-\frac{\pi\alpha r_1}{2R_\delta r_m}\right)(T_0 - T_w) . \tag{B.19}$$

When the constants are gathered on the right side and the polynomials in R are multiplied out, the final form before integration becomes,

$$\frac{d}{dz}\int_0^{R_\delta}\left[-r_m R^3 + (r_m - r_1)R^2 + r_1 R\right]\left[\sin\left(\frac{\pi R}{2R_\delta}\right) - 1\right] dR = -\frac{\alpha r_1 \pi}{12 u_m r_m^2 R_\delta} . \tag{B.20}$$

After doing the integration on the left and multiplying by $12/\pi$ the result is:

$$\frac{d}{dz}\{r_1\psi_1 R_\delta^2 + (r_m - r_1)\psi_2 R_\delta^3 + r_m\psi_3 R_\delta^4\} = \frac{-\alpha r_1}{u_m r_m^2 R_\delta} , \tag{B.21}$$

where Ψ_1, Ψ_2, and Ψ_3 are determined to be:

$$\Psi_1 = \frac{48}{\pi^3} - \frac{4}{\pi} , \tag{B.22}$$

$$\psi_2 = 96\left[\frac{1}{\pi^3} - \frac{2}{\pi^4}\right] - \frac{4}{\pi} , \tag{B.23}$$

$$\psi_3 = \frac{3}{\pi} - 144\left[\frac{1}{\pi^3} - \frac{8}{\pi^5}\right] . \tag{B.24}$$

By defining a Reynolds number based on r_m, the annular flow channel radial width, as:

$$Re = \frac{u_m r_m}{\nu} , \tag{B.25}$$

we can rewrite the right side of Equation (B.21),

$$-\frac{\alpha r_1}{u_m r_m^2 R_\delta} = -\frac{r_1}{r_m} Pr^{-1} Re^{-1} \quad . \tag{B.26}$$

Performing the differentiation on the left side of Equation (B.21) and multiplying both sides by R_δ, we get the final form of the differential equation,

$$\left[2r_1\psi_1 R_\delta^2 + 3(r_m - r_1)\psi_2 R_\delta^3 + 4r_m\psi_3 R_\delta^4\right]\frac{dR_\delta}{dz} = -\frac{r_1}{r_m} Pr^{-1} Re^{-1} \quad . \tag{B.27}$$

This equation can now be integrated directly with the boundary conditions given that the dimensionless thermal boundary layer thickness, R_δ, is equal to zero at the axial location, z_0, where the wall temperature steps from the inlet temperature, T_0 to the constant wall temperature, T_w. Upon integration, Equation (B.27) yields the dimensionless thermal boundary layer thickness as a function of the axial (downstream) location,

$$\frac{2}{3} r_1\psi_1 R_\delta^3 + \frac{3}{4}(r_m - r_1)\psi_2 R_\delta^4 + \frac{4}{5} r_m\psi_3 R_\delta^5 = -\frac{r_1}{r_m} Pr^{-1} Re^{-1} [z - z_0] \quad . \tag{B.28}$$

If we define a parameter R_s as the ratio of the inside radius to the outer radius of the annular flow channel,

$$R_s = \frac{r_1}{r_2} \quad , \tag{B.29}$$

and define a dimensionless downstream location as:

$$\zeta = \frac{(z - z_0)}{r_m} \quad , \tag{B.30}$$

we may then divide Equation (B.28) by r_2 and arrive at the final form:

$$\frac{2}{3} R_s\psi_1 R_\delta^3 + \frac{3}{4}(1 - 2R_s)\psi_2 R_\delta^4 + \frac{4}{5}(1 - R_s)\psi_3 R_\delta^5 = -R_s Pr^{-1} Re^{-1}\zeta \quad . \tag{B.31}$$

The thermal boundary layer can be considered to be fully developed when it has impinged on the outer flow channel wall. This occurs when R_δ is equal to 1.0. Inserting this value into Equation (B.31) and solving for the axial location at which the boundary layer reaches the outside wall, we get,

$$\zeta_1 = -\left[\frac{2}{3}\psi_1 + \frac{3}{4}\psi_2\frac{\{1 - 2R_s\}}{R_s} + \frac{4}{5}\psi_3\frac{\{1 - R_s\}}{R_s}\right] PrRe \quad . \tag{B.32}$$

This concludes the thermal penetration depth part of the solution. For locations downstream of ζ_1 the problem is one of "volumetric rise." To deal with this problem, we assume a similarity type of solution in which the temperature profile retains the sine shape, and require that the solution in this regime match the penetration depth solution at $\zeta = \zeta_1$. The temperature is assumed to take the form,

$$\theta = \sin\left[\frac{\pi R}{2}\right]\Lambda(\zeta) \quad , \tag{B.33}$$

with the boundary condition:

$$\Lambda(\zeta_1) = 1 \quad . \tag{B.34}$$

As before we use the approximate integral method and integrate this time across the entire flow channel. The integral formulation looks exactly like Equation (B.10) except that the limits on the integral are different and the second term on the left side is zero since the velocity at the wall is zero, i.e.,

$$\frac{d}{dz}\int_{r_1}^{r_2}(ruT)\,dr = -r_1\alpha\left.\frac{\partial T}{\partial r}\right|_{r=r_1} \quad . \tag{B.35}$$

Because the derivative with respect to z of the integral of ruT_0 over the width of the channel is zero for the developed case, we can add this term under the integral in Equation (B.35) to get

$$\frac{d}{dz}\int_{r_1}^{r_2} ru\,(T-T_0)\,dr = -r_1\alpha\left.\frac{\partial T}{\partial r}\right|_{r=r_1} \quad . \tag{B.36}$$

Since the surface at r_2 is adiabatic in this problem, the boundary conditions for the radial temperature profile are the same in this domain as in the penetration depth problem including the condition specified by Equation (B.13) which sets the upper wall temperature to T_0. The increase in upper wall temperature above T_0 is inherent in the $\Lambda(\zeta)$ term and the function in Equation (B.33) meets all the boundary conditions when it is required to equal 1.0 at ζ_1. We proceed by making the substitution for ($T-T_0$) as follows:

$$T-T_0 = (T-T_w) - (T_0-T_w) = (T_0-T_w)\,(\theta-1) = (T_0-T_w)\left[\sin\left(\frac{\pi R}{2}\right)\Lambda-1\right] . \tag{B.37}$$

The velocity profile remains the same and the right side of Equation (B.36) is determined as before so that Equation (B.36) reduces to:

$$\frac{d}{dz}\int_0^1\left(r_1R+(r_m-r_1)R^2-r_mR^3\right)\left[\sin\left(\frac{\pi R}{2}\right)\Lambda-1\right]dR = -\frac{r_1\alpha\pi\Lambda}{12u_m r_m^2} \quad . \tag{B.38}$$

When the integrals on the left are performed, both side of Equation (B.38) are multiplied by $12/\pi$, the Prandtl and Reynolds numbers are substituted and the definition of ζ is used to chain rule the derivative with respect to z, the result is:

$$\frac{1}{r_m}\frac{d\Lambda}{d\zeta}([r_1\Phi_1+(r_m-r_1)\Phi_2-r_m\Phi_3]) = -\frac{r_1}{r_m}Pr^{-1}Re^{-1}\Lambda(\zeta) \quad , \tag{B.39}$$

where Φ_1, Φ_2 and Φ_3 are given by:

$$\Phi_1 = \frac{48}{\pi^3} \quad , \tag{B.40}$$

$$\Phi_2 = \frac{96}{\pi^3}\left[1-\frac{2}{\pi}\right] , \tag{B.41}$$

$$\Phi_3 = \frac{144}{\pi^3}\left[1-\frac{8}{\pi^2}\right] . \tag{B.42}$$

Multiplying both sides by r_m/r_2 and using Equations (B.29),

$$\frac{d\Lambda}{\Lambda} = -\frac{R_s Pr^{-1} Re^{-1}}{[R_s\Phi_1 + (1-2R_s)\Phi_2 - (1-R_s)\Phi_3]} d\zeta . \tag{B.43}$$

Upon integration we find the functional form of $\Lambda(\zeta)$ to be:

$$\Lambda(\zeta) = e^{-R_s Pr^{-1} Re^{-1} \Phi_s (\zeta - \zeta_1)} , \tag{B.44}$$

where

$$\Phi_s = \frac{1}{(R_s\Phi_1 + (1-2R_s)\Phi_2 - (1-R_s)\Phi_3)} . \tag{B.45}$$

We have thus far determined the temperature profiles in the developing thermal boundary layer region from Equation (B.16) where θ is a function of R, the dimensionless radial coordinate, and ζ the dimensionless axial coordinate (through R_δ, which is by Equation (B.31) a function of ζ), and the temperature in the fully developed region beyond ζ_1 through Equations (B.33) and (B.44). These represent the solution for the thermal response of a fluid flowing through an annular channel in which the temperature takes a single step from the inlet temperature, T_0, to a constant wall temperature, T_w. The next step is to determine the thermal response at any location resulting from an arbitrarily varying wall temperature. The final step will be to integrate the result over the flow channel to find the "bulk" or mean fluid temperature as a function of axial location from which we can obtain the heat transfer rate and the local Nusselt number correlation for each regime.

The incremental change in temperature from the uniform inlet temperature at a downstream location r and z (dimensionless R and ζ) caused by a step change in wall temperature at z_0 is:

$$T(R,\zeta) - T_0 = (T - T_w) - (T_0 - T_w) = (T_0 - T_w)(\theta - 1) . \tag{B.46}$$

Now we can approximate the wall temperature profile by dividing the axial length of the flow channel into N nodes and defining the node wall temperature as a mean temperature of the node and locate it at the center of the node. Then, because the energy equation is linear, we can sum the incremental temperature changes at the Kth node, resulting from the change in wall temperature at each upstream node, as:

$$T_K - T_0 = \sum_{k=1}^{K} (1-\theta_k)(T_{w,k} - T_{w,k-1}) . \tag{B.47}$$

Then the temperature difference between the fluid and the wall becomes:

$$T_K - T_{w,K} = (T_K - T_0) - (T_{w,K} - T_0) = \sum_{k=1}^{K} (1-\theta_k)\Delta T_{w,k} - \sum_{k=1}^{K} \Delta T_{w,k} , \tag{B.48}$$

and

$$T_K - T_{w,K} = -\sum_{k=1}^{K} \theta_k \Delta T_{w,k} \ , \tag{B.49}$$

where for k not equal to 1

$$\Delta T_{w,k} = T_{w,k} - T_{w,k-1} \ , \tag{B.50}$$

and for k equal to 1

$$\Delta T_{w,1} = T_{w,1} - T_0 \ , \tag{B.51}$$

where T_0 is, of course, the inlet fluid temperature. Now, if for a node, K, there corresponds a node, κ, which is the nearest upstream node for which the boundary layer has not reached the outer wall at the location of the Kth node, we may rewrite Equation (B.49) as:

$$T_K - T_{w,K} = -\sum_{k=1}^{\kappa-1} \sin\left(\frac{\pi R}{2}\right) e^{-\beta(\zeta-\zeta_{1,k})} \Delta T_{w,k} - \sum_{k=\kappa}^{K} \sin\left(\frac{\pi R}{2R_{\delta_{K,k}}}\right) \Delta T_{w,k} \ , \tag{B.52}$$

where $R_{\delta_{k,K}}$ is the dimensionless boundary layer thickness at the center of the Kth node that is generated by the increase in wall temperature at the kth node, and the parameter β is defined as:

$$\beta = \frac{R_s \Phi_s}{PrRe} \ . \tag{B.53}$$

Equation (B.52) specifies the wall-to-fluid temperature difference at any location in the flow stream. However, to calculate an effective heat transfer coefficient we must know the bulk or mean fluid temperature. Defining a Nusselt number based on the flow channel width, r_m, we have,

$$Nu = -\frac{r_m \left.\frac{\partial T}{\partial r}\right|_{r=r_1}}{T_B - T_w} \ . \tag{B.54}$$

There are two regimes that must be considered in determining the bulk fluid temperature. One regime involves axial locations for which none of the upstream boundary layers have reached the outer wall at the location of interest. The other regime is for locations in which at least one upstream boundary layer has impinged on the outer wall at the Kth axial location. For the first regime the bulk fluid temperature may be defined as:

$$u_m A_c (T_{B,K} - T_{w,K}) = \int_{r_1}^{(r_1+\delta_1)} u (T_K - T_{w,K}) \, dA + \int_{(r_1+\delta_1)}^{r_2} u (T_0 - T_{w,K}) \, dA \ . \tag{B.55}$$

Here the first integral on the right contains the sum of the individual responses and the summation is in front of the integral. For the second regime the second integral is not present but the first integral involves components from both thermally devel-

oped and thermalty developing responses. We will first develop the bulk-to-wall formulation for the first regime. If we call the first integral on the right I_1, and the 2nd, I_2, they can be expanded as follows:

$$I_1 = -2\pi \sum_{k=1}^{K} \int_0^{R_{\delta_k}} (r_m R + r_1)\, 6u_m R(1-R)\, r_m \Delta T_{w,k} \sin\left[\frac{\pi R}{2R_{\delta_k}}\right] dR \ , \tag{B.56}$$

and

$$I_2 = -2\pi \int_{R_{\delta_1}}^{1} (r_m R + r_1)\, 6u_m R(1-R))\, r_m (T_0 - T_{w,K})\, dR \ . \tag{B.57}$$

When the integral I_1 and I_2 are evaluated we get,

$$I_1 = -12\pi u_m r_m \sum_{k=1}^{K} \{r_1 \xi_1 R^2_{\delta_{k,K}} + (r_m - r_1)\, \xi_2 R^3_{\delta_{k,K}} - r_m \xi_3 R^4_{\delta_{k,K}}\}\, \Delta T_{w,K} \ , \tag{B.58}$$

$$I_2 = -2\pi r_m u_m (T_0 - T_{w,K}) \left\{\frac{r_1\left(1 - R^2_{\delta_1}\right)}{2} + \frac{(r_m - r_1)\left(1 - R^3_{\delta_1}\right)}{3} - \frac{r_m\left(1 - R^4_{\delta_1}\right)}{4}\right\} \ , \tag{B.59}$$

with ξ_1, ξ_2, and ξ_3 determined to be:

$$\xi_1 = \frac{4}{\pi^2} \ , \tag{B.60}$$

$$\xi_2 = \frac{8}{\pi^2}\left[1 - \frac{2}{\pi}\right] \ , \tag{B.61}$$

$$\xi_3 = \frac{12}{\pi^2}\left[1 - \frac{8}{\pi^2}\right] \ . \tag{B.62}$$

Defining a new parameter, $r_p = (r_2 + r_1)$, the left side of Equation (B.55) is simply:

$$\pi\left(r_2^2 - r_1^2\right) u_m (T_{B,K} - T_{w,K}) = \pi r_m r_p u_m (T_{B,K} - T_{w,K}) = \pi r_m r_p u_m \Delta T_{Bw} \ . \tag{B.63}$$

Then the temperature differential between the bulk and the wall at the Kth axial node reduces to:

$$\Delta T_{Bw} = -\frac{12}{(1+R_s)} \sum_{k=1}^{K} \left[R_s \xi_1 R^2_{\delta_{k,K}} + (1 - 2R_s)\, \xi_2 R^3_{\delta_{k,K}} - (1 - R_s)\, \xi_3 R^4_{\delta_{k,K}}\right] \Delta T_{w,k} + \Xi \ , \tag{B.64}$$

where

$$\Xi = -\frac{12}{(1+R_s)} (T_{w,K} - T_0) \left\{\frac{R_s}{2}\left(1 - R^2_{\delta_{1,K}}\right) + \frac{(1-2R_s)}{3}\left(1 - R^3_{\delta_{1,K}}\right) - \frac{(1-R_s)}{4}\left(1 - R^4_{\delta_{1,K}}\right)\right\} \ . \tag{B.65}$$

The bulk temperature equation for the second regime in which at least one boundary layer has reached the outer wall and the nearest upstream boundary layer that has not reached the outer wall is the Kth node, takes the form:

$$\pi u_m r_m r_p \Delta T_{Bw} = I_3 + I_4 \ , \tag{B.66}$$

where I_3 and I_4 are formulated in the following way:

$$I_3 = -12\pi u_m r_m \sum_{k=1}^{\kappa-1} e^{-\beta(\zeta_K - \zeta_{1k})} \Delta T_{w,k} \int_0^1 [r_m R + r_1] R(1-R) \sin\left(\frac{\pi}{2}R\right) dR \ , \tag{B.67}$$

$$I_4 = -12\pi u_m r_m \sum_{k=\kappa}^{K} \int_0^{R_{\delta_{k,K}}} [r_m R + r_1] R(1-R) \sin\{\frac{\pi R}{2R_{\delta_{k,K}}}\} \Delta T_{w,k} dR \ . \tag{B.68}$$

These integrals yield:

$$I_3 = -12\pi r_m u_m \{r_1\xi_1 + (r_m - r_1)\xi_2 - r_m\xi_3\} \sum_{k=1}^{\kappa-1} e^{-\beta(\zeta_K - \zeta_{1,k})} \Delta T_{w,k} \ , \tag{B.69}$$

$$I_4 = -12\pi r_m u_m \sum_{k=\kappa}^{K} \left[r_1\xi_1 R^2_{\delta_{k,K}} + (r_m - r_1)\xi_2 R^3_{\delta_{k,K}} - r_m\xi_3 R^4_{\delta_{k,K}}\right] \Delta T_{w,k} \ . \tag{B.70}$$

Combining Equations (B.66), (B.69) and (B.70), solving for ΔT_{Bw}, and dividing the result by r_2 to convert to the R_s parameter, we have,

$$\Delta T_{Bw} = -\frac{12}{(1+R_s)}(S_1 + S_2) \ , \tag{B.71}$$

and

$$S_1 = [R_s\xi_1 + (1-2R_s)\xi_2 - (1-R_s)\xi_3] \sum_{k=1}^{\kappa-1} e^{-\beta(\zeta_K - \zeta_{1k})} \Delta T_{w,k} \ , \tag{B.72}$$

$$S_2 = \sum_{k=\kappa}^{K} \left[R_s\xi_1 R^2_{\delta_{k,K}} + (1-2R_s)\xi_2 R^3_{\delta_{k,K}} - (1-R_s)\xi_3 R^4_{\delta_{k,K}}\right] \Delta T_{w,k} \ . \tag{B.73}$$

We now have the expressions for the wall to bulk temperature differences and we merely need to insert these into Equation (B.54) together with the derivative of the temperature at the wall. For the thermally developing region we obtain:

$$Nu_K = -\frac{\frac{\pi}{2}\sum_{k=1}^{K} \frac{\Delta T_{w,k}}{R_{\delta_{k,K}}}}{(T_{B,K} - T_{w,K})} \ . \tag{B.74}$$

Here the bulk-to-wall temperature difference is obtained from Equation (B.64). For the regime in which at least one boundary layer has impinged on the outer wall, the Nusselt number takes the form:

$$Nu_K = \frac{-\frac{\pi}{2}\left[\sum_{k=1}^{\kappa-1} e^{-\beta(\zeta_K - \zeta_{1,k})}\Delta T_{w,k} + \sum_{k=\kappa}^{K} \frac{\Delta T_{w,k}}{R_{\delta_{k,K}}}\right]}{(T_{B,K} - T_{w,K})} \quad . \tag{B.75}$$

In this regime the temperature difference is obtained from Equation (B.71).

It is of interest before looking at some of the solutions obtained for nonisothermal walls to show the solution obtained from this method for isothermal walls. The Nusselt number in the thermally developing regime is found to be:

$$Nu = \frac{\frac{(1+R_s)}{2}}{\frac{(1+R_s)R_\delta}{\pi} + \Psi_1 R_s R_\delta^3 + \Psi_2 (1-2R_s) R_\delta^4 + \Psi_3 (1-R_s) R_\delta^5} \quad . \tag{B.76}$$

In the thermally developed regime, the Nusselt number is, as expected, a constant:

$$Nu = \frac{(1+R_s)}{2\left[R_s\Phi_1 + (1-2R_s)\Phi_2 - (1-R_s)\Phi_3\right]} \quad . \tag{B.77}$$

Here, clearly, the Nusselt number is a constant that depends only on the geometric factor, R_s.

In the limit as R_s goes to 1.0, which corresponds to the parallel plate configuration, we get:

$$Nu = \frac{1}{(\Phi_1 - \Phi_2)} \quad . \tag{B.78}$$

The Nusselt number for the fully developed regime calculated from Equation (B.78) is 2.364 which exactly matches a similar analysis done for the parallel plate also using a sine temperature profile. Using a cubic temperature profile in flat plate geometry, a Nusselt number of 2.3077 was obtained.

Figure B.2 shows a graph of the Nusselt number as a function of the of the reciprocal Graetz number for several geometric factors for the constant wall temperature solution. The Graetz number is defined as:

$$Gr_z = \frac{z}{Pe} = \frac{z}{RePr} \quad , \tag{B.79}$$

where, Pe, is the Peclet number. The heat exchanger in the MP-2 experiment had a geometric factor of 0.915, which places the fully developed Nusselt number in Figure B.2 at about 2.346.

To demonstrate the effect of the wall temperature profile, three cases were calculated using the model developed here and using a constant wall temperature, a linearly increasing wall temperature, and a parabolic wall temperature (a quadratic function of the axial position). The radial dimensions of the MP-2 cooling jacket (and an axial dimension of 1.0 meter) were used in the calculations with an assumed inlet coolant temperature of 300 K. A constant wall temperature of 500 K was used for the first case. For the linear wall temperature (the 2nd case), a wall temperature was used that increased linearly from 400 K at the entrance to 600 K at the exit with a mean wall temperature of 500 K. The parabolic wall temperature profile in the third case was selected such that the inlet temperature was 400 K, the outlet temperature was 800 K, and the mean temperature was also 500 K. The comparisons of wall temperature with bulk coolant temperature for these three configurations are shown in Figures B.3 through B.5. The key piece of information that comes out of these three cases is that, although the mean wall temperature is the same for all three cases, the fluid temperature at the outlet of the heat exchanger is significantly different for the three cases. The outlet temperature for the isothermal wall was ~380 K while it was ~425 K for the linearly increasing wall temperature case and ~550 K for the parabolic wall temperature case. Clearly, the heat transfer processes are more efficient for

nonisothermal walls. The reason for this is that as long as the wall temperature is changing with position along the direction of flow, the coolant does not become thermally developed and the heat transfer coefficient retains the characteristics of the developing regime. Note that the wall temperatures were selected here to exaggerate the thermal response of the fluid for purposes of comparison. Clearly the coolant, which is water, cannot attain these high temperature.

The thermal boundary layer for a step inlet-to-wall temperature change for the cooling jacket configuration is shown in Figure B.6. This boundary layer profile is the one that develops in the cooling jacket when the coolant flow rate is set such that the mean flow velocity is 2.5 cm/s. This velocity corresponds to a Reynolds number (based on hydraulic diameter) of ~300, well down in the laminar flow regime. There were three flow rate settings used during the experiment. The 2.5 cm/s velocity was derived from the maximum flow rate (set for the melt phase of the experiment). The boundary layer profiles for the earlier flow settings (lower flow rates) developed more rapidly, that is, the boundary layers impinged on the outer wall nearer the inlet than for the one shown here. The dimensionless axial location used on the x-axis in the four previous figures is ζ as defined in Equation (B.30). The heated length of the MP-2 test package was ~0.574 m, which in terms of the ζ dimension is at ~71.8. Thus, since ζ_1 was ~97 (see Figure B.6), for the melt phase flow rate, the boundary layer generated at the inlet did not impinge on the outer cooling jacket wall within the heated length and the flow was, therefore, nowhere fully thermally developed.

A final graph (Figure B.7) shows the Nusselt number correlations generated for the three wall temperature profiles shown earlier (Figures B.3 through B.5). This figure clearly demonstrates the more effective convective heat transfer rates associated with a nonisothermal wall temperature. The thermally developed regime that develops for the isothermal wall approaches a Nusselt number of ~2.35 while the linear wall profile for this case appears to approach ~3.5. The parabolic profile actually yields a Nusselt number that dips below even the isothermal case, because the wall temperature initially drops relative to the wall temperature at the inlet. However, it subsequently rises rapidly and for downstream locations produces Nusselt numbers considerably exceeding those for the isothermal and linear wall temperature profiles reaching a downstream peak of about 6.0.

Although the present formulation requires calculating an n by n triangular matrix of boundary layer thicknesses (where n is 79 in the MP-2 analysis nodalization), this matrix has to be recalculated only when the coolant flow velocity in the experiment is changed (this occurred only three times during the experiment). The alternative approaches using the Graetz functions or the functions derived for the exact solution to this problem[1] is much more cumbersome especially since these functions must be derived from their corresponding power series solutions, which converge very slowly and have a number of associated problems. The methodology developed here seems to work well in nearly all cases. Situations may arise, however, that will lead to numerical problems. The only such problem that has been identified to date occurs when the bulk coolant temperature profile crosses the wall temperature profile. In this situation the Nusselt number as defined in Equation (B.54) will approach infinity (as T_B-T_w approaches zero) at the node where the crossover occurs. This normally will not occur, but a numerical filter should be put in place to trap this eventuality.

Nomenclature

A_c - Cross Sectional Flow Area
Gr_z - Graetz Number
P - Pressure
Pe - Peclet Number
Pr - Prandtl Number
Nu - Nusselt Number
r - Radial dimension
r_1 - Radial location of inside coolant channel wall
r_2 - Radial location of outside coolant channel wall
r_m - (r_2-r_1)= 1/2 hydraulic diameter
r_p - (r_2+r_1)
R - Dimensionless radial location
Re - Reynolds Number
R_s - Annulus Ratio = r_1/r_2
R_δ - Dimensionless boundary layer thickness
T - Temperature
T_B - Bulk fluid temperature
Tw - Wall temperature
T_0 - Inlet coolant temperature
T_K - Fluid temperature at axial node K
$T_{w,k}$ - Wall temperature at k-th node
u - Coolant flow velocity
u_m - Mean coolant flow velocity
α - Thermal diffusivity
β - Parameter grouping
δ - Boundary layer thickness
ΔT_{Bw} - Wall-to-coolant temperature difference
ζ - Dimensionless axial location
ζ_1 - Dimensionless axial location where boundary layer impinges on outer channel wall
θ - Dimensionless coolant temperature
Λ - Axial temperature function
ν - kinematic viscosity
ξ_1, ξ_2, ξ_3 - Constants
π - Pi
ρ - Density
Φ_1, Φ_2, Φ_3 - Parameter groupings
Ξ - Parameter grouping
Ψ_1, Ψ_2, Ψ_3 - Parameter Groupings

References

1. R. E. Lundberg and W. C. Reynolds, "Heat Transfer with Laminar Flow in Concentric Annuli with Constant and Variable Wall Temperature with Heat Flux", NASA TN D1972, NASA Washington, Aug 1963.

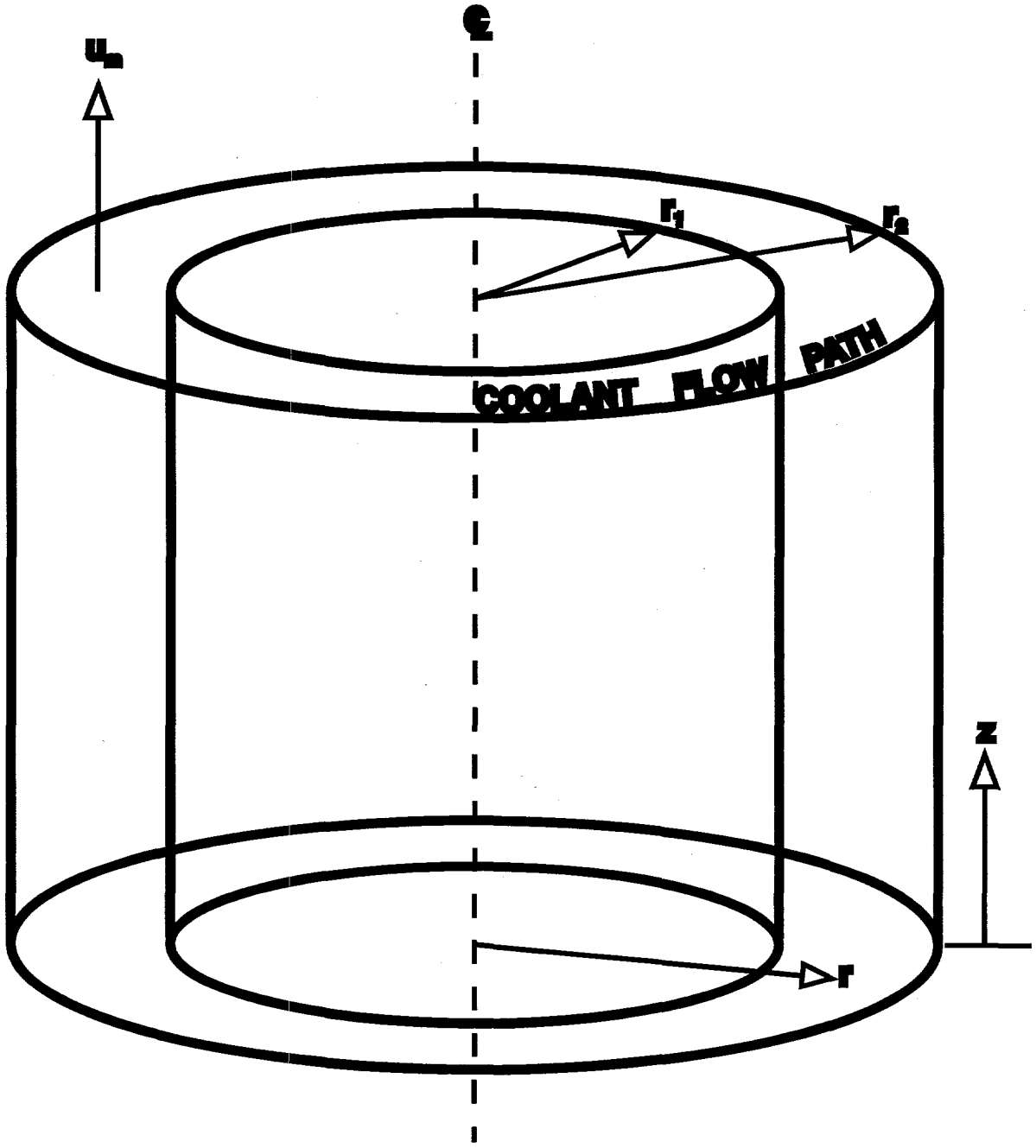

Figure B.1 Diagram of the MP-2 Cooling Jacket Showing the Coordinate System Used in the Cooling Jacket Heat Transfer Analysis

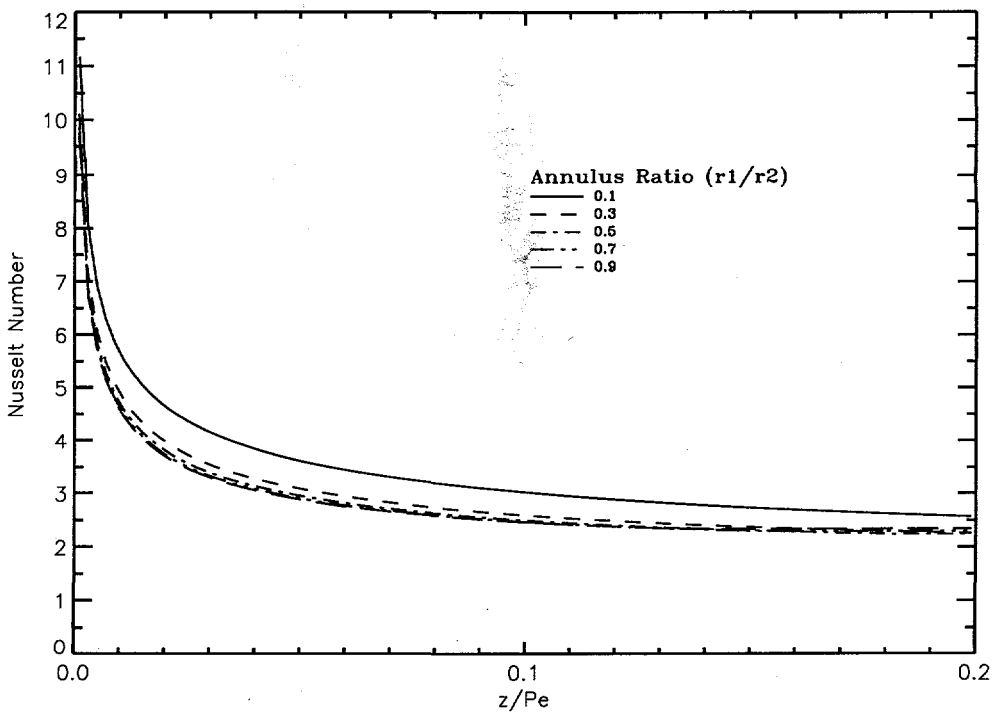

Figure B.2 Nusselt Number for Constant Inner Wall Temperature with Annular Flow and an Adiabatic Outer Wall. Correlation Shown for Various Annular Ratios, $R_s=r_1/r_2$

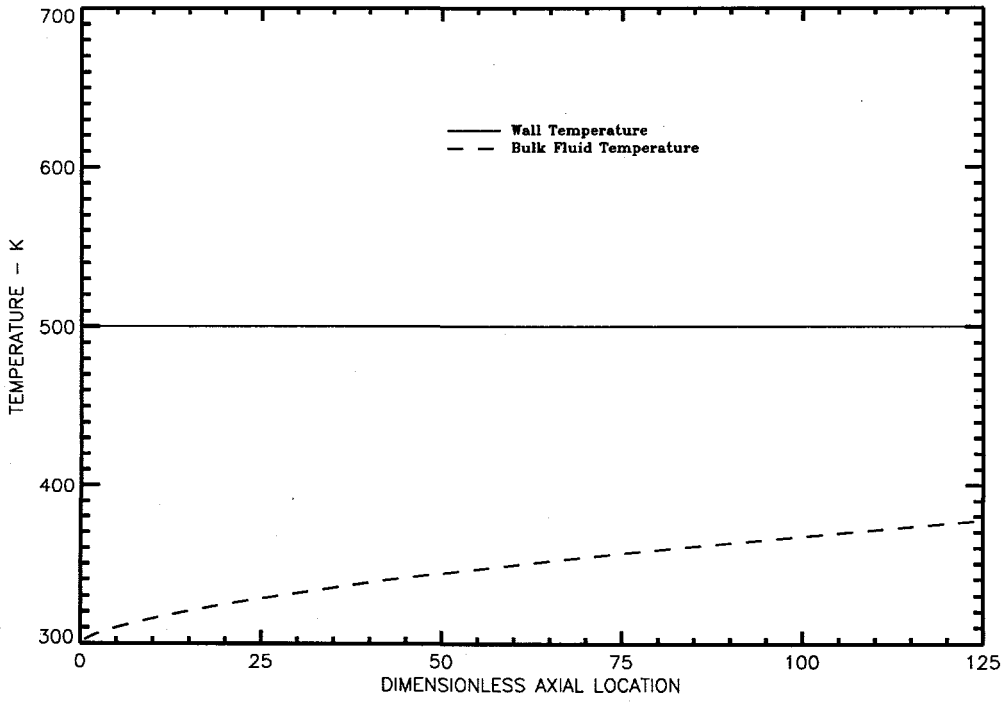

Figure B.3 Coolant Temperature Response to a Constant Wall Temperature (u_m = 2.5 cm/s) Using Dimensions of MP-2 Cooling Jacket

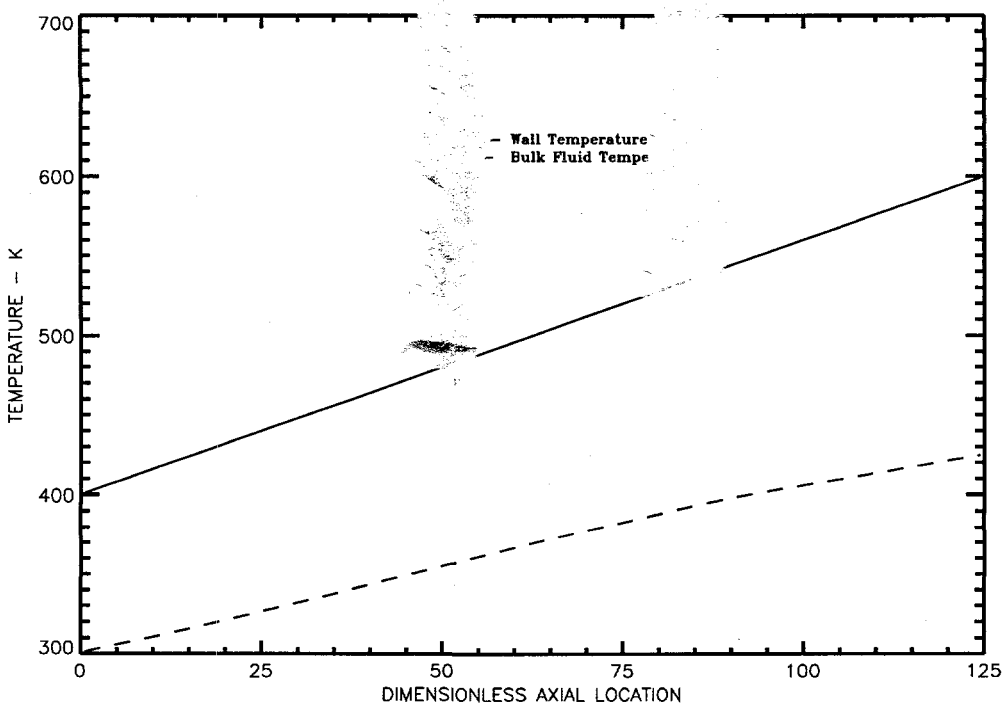

Figure B.4 Coolant Temperature Response to a Linear Wall Temperature (u_m = 2.5 cm/s) Using Dimension of MP-2 Cooling Jacket

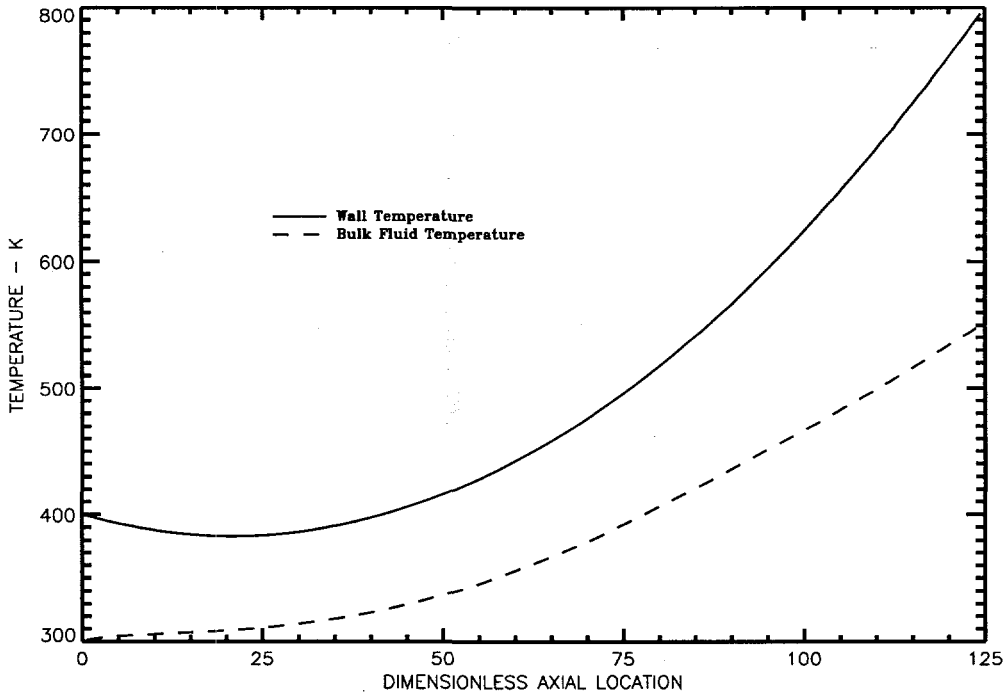

Figure B.5 Coolant Temperature Response to a Parabolic Wall Temperature (u_m = 2.5 cm/s) Using Dimensions of MP-2 Cooling Jacket

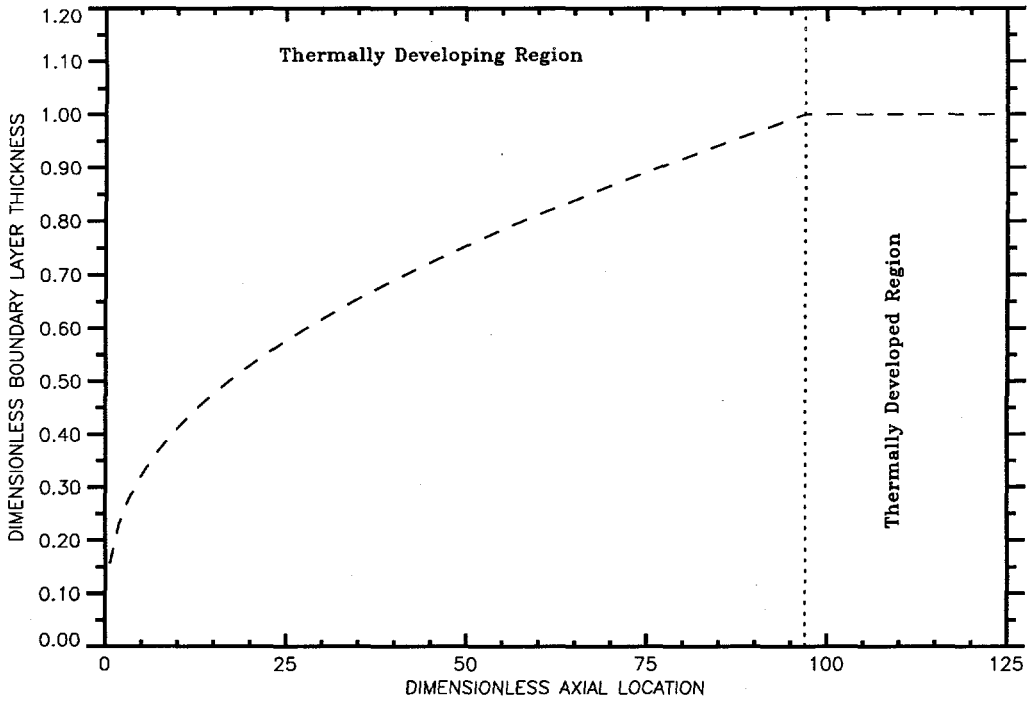

Figure B.6 Boundary Layer Thickness for Constant Wall Temperature (u_m = 2.5 cm/s) Using Dimensions of MP-2 Cooling Jacket

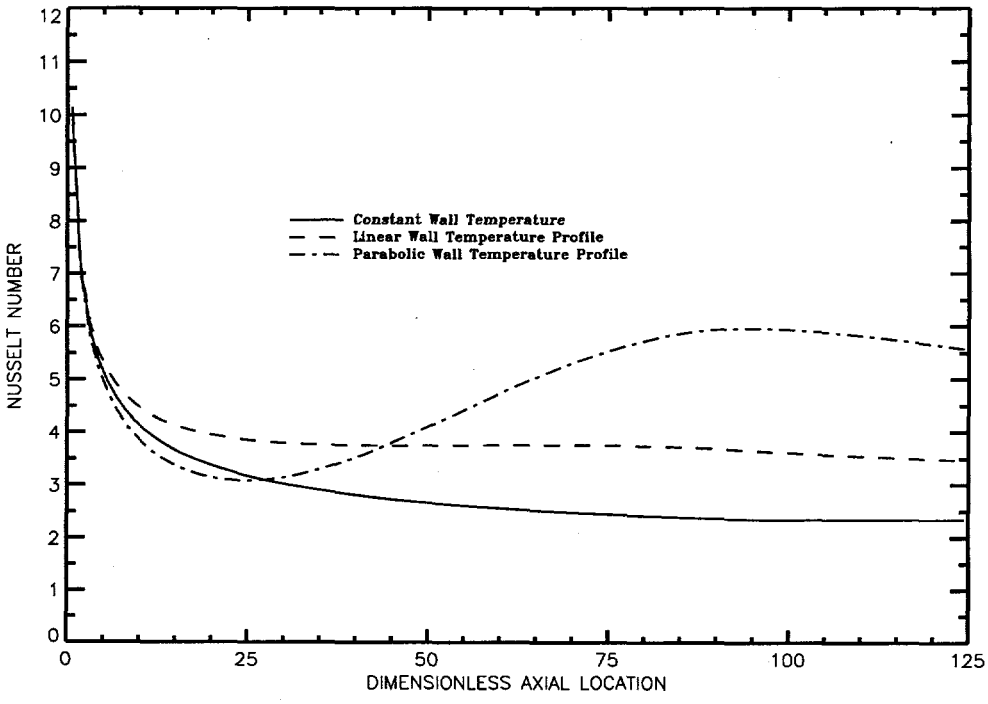

Figure B.7 Nusselt Number Correlations for Three Wall Temperature Profiles (u_m = 2.5 cm/s) Using Dimensions of MP-2 Cooling Jacket

Appendix C-1. MP-2 Preexperiment Analysis of the Preformed Crust

Appendix C-1 consists of two Sandia Laboratories' internal memoranda which document the results of analyses of pre-experiment tests and measurements that were conducted on the pre-fabricated metallic/ceramic crust. These tests were intended to characterize the strength and composition of this crust under high temperature conditions in an effort to predict its behavior during the MP-2 experiment.

The first memorandum, from W. F. Hammetter, details the results of DTA (Differential Thermal Analysis) measurements on small samples of the crust material. This analysis found evidence for the melting of certain constituents in specific temperature ranges, but found no indication of sample deformation under no-load conditions.

The second memorandum, from K. G. Ewsuk, presents the results of further tests performed at high temperature using a Gleeble high temperature mechanical testing apparatus. This equipment was used to test the strength of somewhat larger samples under various mechanical loads. These tests were able to characterize the degree of deformation of the crust material under specified temperature and mechanical loading. Results of SEM/EDS (scanning electron microscopy/electron dispersive spectroscopy) tests are also detailed in this memorandum. These results were used to characterize the crust in terms of its constituents and the various phases that were formed during its fabrication process.

Sandia National Laboratories

Albuquerque, New Mexico 87185

date: August 27, 1991

to: R. D. Gasser, 6423

Bill Hammetter

from: W. F. Hammetter, 1842

subject: Thermal analysis results

I finally got a chance to review the thermal analysis results on your depleted uranium samples. The purpose of this memo is to document what I see in the Differential Thermal Analysis (DTA) traces.

We made three separate runs; two on small chunks which you provided and one on a powdered sample made by crushing a few of the chunks. Each run was made at a heating/cooling rate of $10°C \cdot min^{-1}$ in an atmospheres of 5% H_2 in Ar flowing at 100 sccm. We heated to the upper temperature limit of the instrument, 1600°C, but in each case the actual maximum temperature achieved was on the order of 1550-1570°C. The samples were held in magnesia crucibles.

The resulting DTA traces are attached. If I were under oath in front of a jury of my peers, I would have to state that these traces show no features which I can (without reasonable doubt) attribute to a melting event. However, if I am allowed the licence of gross speculation, I could point to several features that I **think** may be associated with a partial melting of some constituent of the samples. In Figure 1, the endotherm on heating at about 1100°C and the (really) small exotherm on cooling at about 1000°C may be consistent with a melting event. That is, a **small** portion of the sample melted at about 1100°C on heating and solidified on cooling at about 1000°C. The 1100°C endotherm on heating can be seen (it helps if you squint a lot) in Figure 2, which is the DTA trace for a much smaller sample. But, even I cannot claim to see the expected exotherm on cooling. There is, however, an exotherm between 1100 and 1200°C which might be due to solidification of an even higher temperature melting event. In order to increase the sensitivity of the high-temperature region we used a powdered sample. The results of that run are shown in Figure 3. The 1100°C events are now somewhat obscure but there is something at about 1500°C that may be melting. There is a small exotherm at 1400°C which may be the solidification of that melt composition.

In summary, I **think** some of the constituents of the sample may be melting. I can't identify what those constituents might be and I can't quantify how much of the sample may be melting. One common observation was that after cooling to room temperature the 'chunk' samples retained their sharply faceted shape and the powder sample was still powder. No evidence of gross melting was observed nor was there any evidence of crucible interaction.

It may be best to do some sort of microscopic analysis of these samples to determine what constituents are present. From such an identification we may be able to guess more intelligently at the reason for the DTA features consistent with what, I think, are melting events.

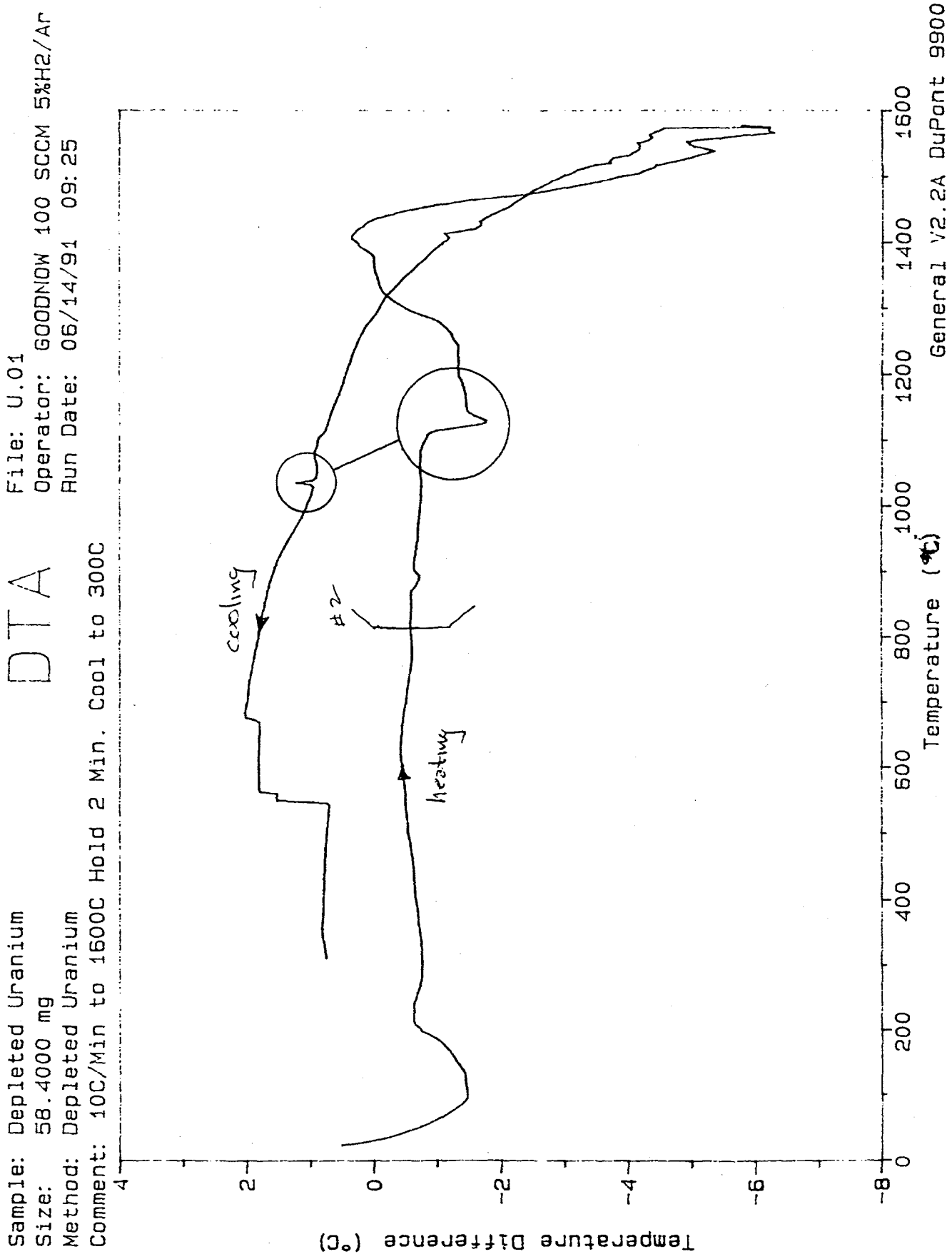
#1
DTA
File: U.01
Operator: GOODNOW 100 SCCM 5%H2/Ar
Run Date: 06/14/91 09:25
Sample: Depleted Uranium
Size: 58.4000 mg
Method: Depleted Uranium
Comment: 10C/Min to 1600C Hold 2 Min. Cool to 300C
cooling
#2
heating
Temperature Difference (°C)
Temperature (°C)
General V2.2A DuPont 9900
4
2
0
-2
-4
-6
-8
0
200
400
600
800
1000
1200
1400
1600

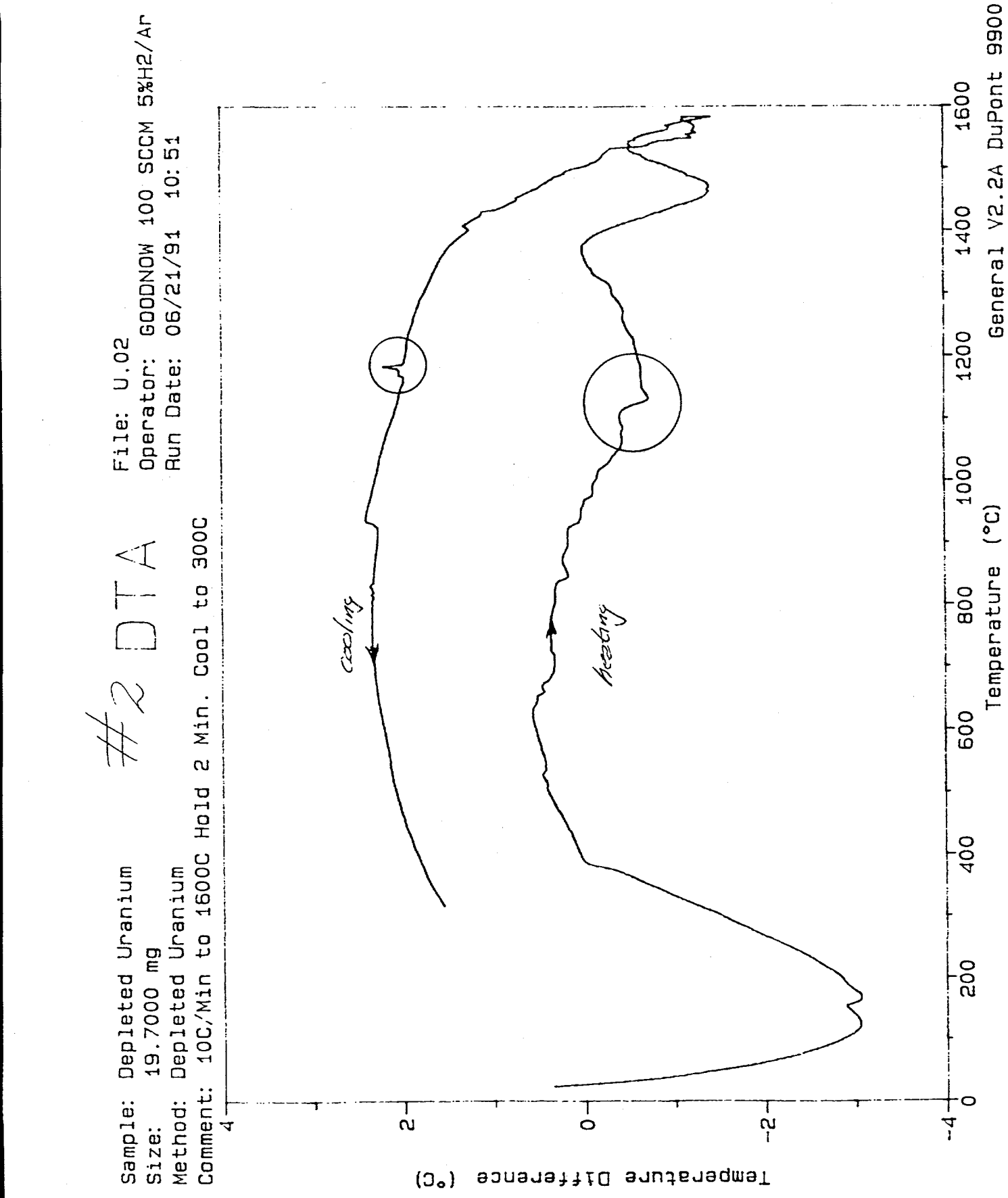
#2 DTA
Sample: Depleted Uranium
Size: 19.7000 mg
Method: Depleted Uranium
Comment: 10C/Min to 1600C Hold 2 Min. Cool to 300C
File: U.02
Operator: GOODNOW 100 SCCM 5%H2/Ar
Run Date: 06/21/91 10:51
cooling
heating
Temperature Difference (°C)
Temperature (°C)
General V2.2A DuPont 9900
4
2
0
-2
-4
0
200
400
600
800
1000
1200
1400
1600

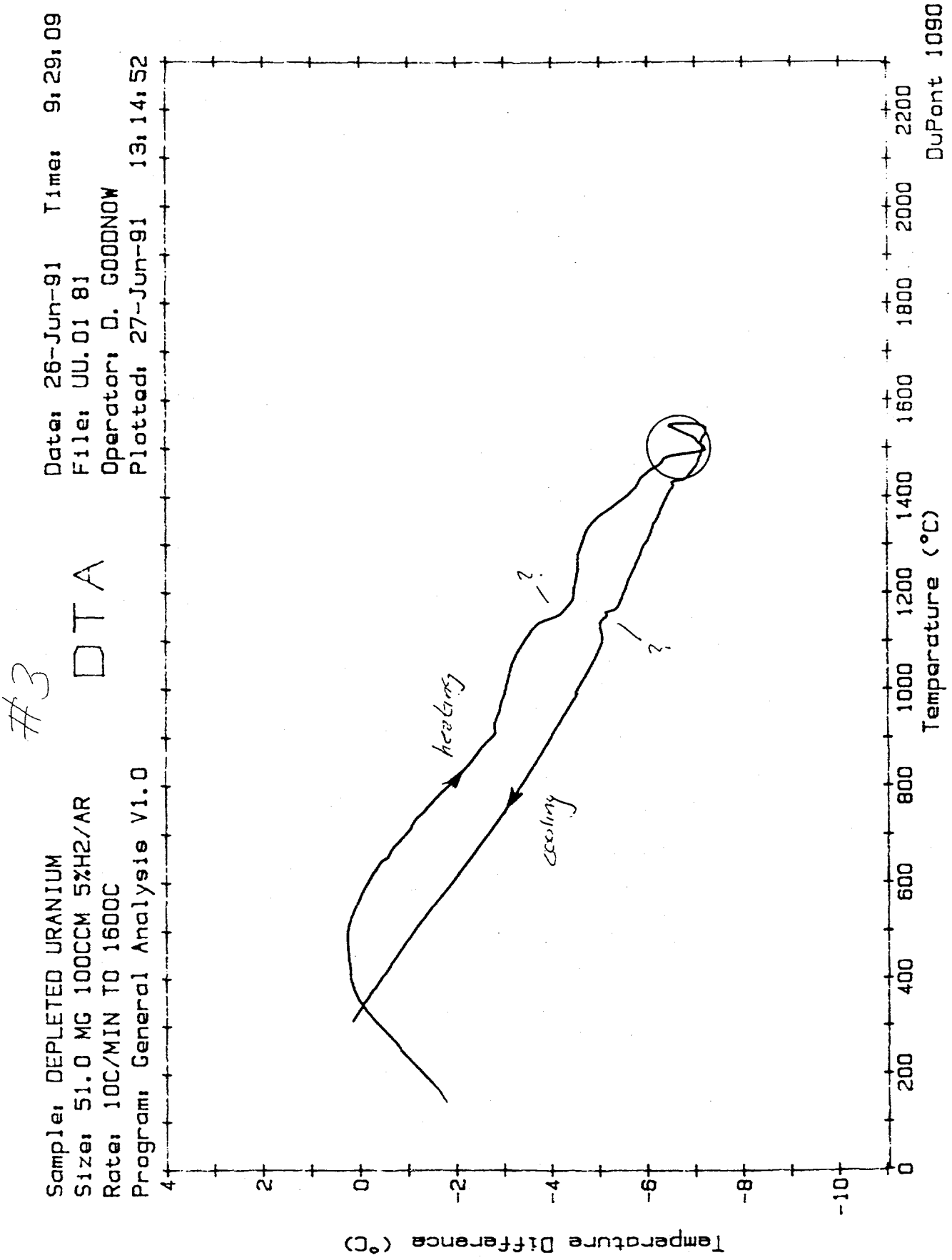
Sample: DEPLETED URANIUM
Size: 51.0 MG 100CCM 5%H2/AR
Rate: 10C/MIN TO 1600C
Program: General Analysis V1.0
Data: 26-Jun-91 Time: 9:29:09
File: UU.01 81
Operator: D. GOODNOW
Plotted: 27-Jun-91 13:14:52
#3
DTA
heating
cooling
Temperature Difference (°C)
Temperature (°C)
DuPont 1090
4
2
0
-2
-4
-6
-8
-10
0
200
400
600
800
1000
1200
1400
1600
1800
2000
2200

June 19, 1992

K. O. Reil, 6423

copy to: R. O. Gauntt, 6423
R. D. Gasser, 6423
S. C. Bourcier, 6454
J. Van den Avyle, 1831
A. J. Hurd, 1841
J. Bingert, LANL MS G770

K. G. Ewsuk, 1841

DRAFT - **SNL/LANL MP-2 Deformation Studies** - DRAFT

Executive Summary

This memorandum summarizes preliminary conclusions of the research work conducted at SNL and contracted to John Bingert of Los Alamos National Laboratories (PR# AB-4589) to characterize simulated crust material in the TMI-2 end-state core configuration for MP-2.

The primary objective of the work was to determine the deformation temperature of the crust material to at least within 100°C to design future reactor experiments. We were interested in the temperature at which the crust material will no longer support its own weight and would flow or slump down into a lower layer of supporting rods in the test configuration during a reactor experiment. Calculations by S. Bourcier determined the self supporting pressure in the test configuration to be ~3.5 psi .

The results of the deformation experiments coupled with the SEM/EDS and phase equilibria information indicate that, at low temperatures, the structural integrity of the crust material is primarily controlled by a rigid, refractory metal and oxide skeleton. On heating the crust material, liquids of In, Sn, Ag, Ni, and Fe melts (and mixtures thereof) progressively form within the rigid skeletal structure. Although there is evidence of some melt formation at temperatures ≤900°C, under no load conditions (i.e., under the samples own weight), there is insufficient liquid phase present in the system to break down the rigid skeletal structure until >1650°C. Under a compressive pressure of ~150 psi, the skeletal structure breaks down at an appreciably lower temperature (~1180°C). In the later case, Ni-Zr eutectic melting appears to be responsible for the liquid formation that degrades the structural integrity of the crust. Break-down of the skeletal structure at 1850°C appears to be related to the formation of liquid in the Fe-Zr system. The critical temperature for deformation of the crust material under no load conditions is between 1650 and 1800°C, and may be at the 1675 peritectic melting temperature in the Fe-Zr system.

Experimental

Test Materials

Ten nominally 0.30" diameter by 0.40" tall cylindrical samples of the crust material were sent from Susan Bourcier, 6454 to John Bingert, LANL, for analysis. These samples were

machined from larger, bulk samples originally fabricated at Los Alamos National Laboratory having the nominal composition noted in Table 1.

Table 1. Composition of Simulated Crust Material used in MP-2 Studies

8.2 (wt)% UO_2 (depleted)
13.76% ZrO_2
37.35% Zr
4.14% Sn
11.61% Ag
2.93% In,
11.88% Fe
2.17% Cr
7.39% Ni
0.57% Mo

Thermal Analysis

Preliminary evaluations of the melting behavior of the crust material were conducted at SNL by D. Goodnow, 1845, and reported by W. Hammeter, 1845 in August 1991. These experiments involved heating 20 - 60 mg of crushed crust material at 10°C/minute to ~1600°C in 100 sccm flowing 5% H_2:95% Ar in a differential thermal analyzer (DTA) to monitor thermal events such as melting and recrystallization.

Deformation Tests

Preliminary experiments at LANL were conducted under a compressive load on a Gleeble high temperature mechanical testing apparatus. Gleeble tests were conducted by compressing a cylindrical samples between two water-cooled rams, and measuring the linear deformation and change in applied (hydraulic) pressure as a function of time and/or temperature. Direct joule heating of the sample was accomplished by passing a current through the sample during the test. Temperature was measured using a W/Re thermocouple bonded directly to the mid section of the sample (where the temperature was most uniform and highest during the test). Experiments were discontinued once ~10% total linear deformation occurred.

Subsequent experiments were conducted under a no-load condition using standard, high-temperature furnaces. Standard furnace tests were conducted in controlled atmosphere, resistance element heated furnaces in which the samples were heated by conduction and convection. Uniform sample heating was assumed. During these experiments the sample temperature was measured by a thermocouple in the hot zone of the furnace near the sample. The samples were supported on or by an alumina crucible or setter during the tests.

To prevent oxidation of the crust material during testing, the experiments were conducted in an inert, argon atmosphere. A heating rate of ~60°C/min from room temperature to the desired soak or hold temperature was used to duplicate the heating conditions to be used in subsequent reactor experiments to be conducted at SNL. A summary of the experiments conducted at LANL and the preliminary results are presented in Table 2.

Table 2. A Summary the Deformation Experiments Conducted at LANL

Sample	Dimensions (in.) Dia.	Height	Experimental Procedure	Comments
1	0.307	0.394	Gleeble Test (GT) ~600 psi RT-1300°C @ 1°C/min	deformation starts at ~1000°C ~8% linear def. by ~1160°C
2	0.304	0.395	GT ~150 psi, RT-1300°C @ 1°C/min, 0 min soak	deformation starts at ~1000°C ~9% linear def. by ~1160°C
4	0.306	0.400	GT ~150 psi, RT-1000°C @ 1°C/min, 40 min soak	deformation starts ~1000°C ~0.25% lin. def. after 40 min.
*5	0.305	0.401	GT ~150 psi, RT-1100°C @ 1°C/min, 40 min soak	*thermocouple failed, no soak deformation starts ~960°C ~9% linear def. by ~1100°C
6	0.304	0.395	Standard (no-load) furnace test (FT), 1000°C, 60 min.	no visible deformation
7	0.308	0.406	FT, 1200°C, 60 min. soak	no visible deformation
8	0.306	0.398	FT, 1100°C, 60 min. soak	no visible deformation
9	-.----	-.----	FT, 1800°C, 60 min. soak	extensive deformation reacted with alumina crucible
10	-.----	-.----	FT, 1650°C, 60 min. soak	little or no shape deformation, some reaction with alumina

Results

Thermal Analysis

DTA results reveal endothermic events indicative of melting at ~900°C, ~1100°C, and ~1500°C. Exothermic peaks indicative of recrystallization are noted at 1000°C and 1400°C. The results from DTA experiments indicated that little or no melting occurs at <1600°C

Deformation

Initial results from Gleeble tests conducted at LANL revealed that, under a compressive load, measurable deformation occurs at temperatures as low as 960°C. Appreciable (~10% linear) deformation occurs by 1160°C on heating to 1300°C at 1°C/min when the sample is under 600 or 150 psi compressive pressure. Under 150 psi compressive pressure, only 0.25% linear deformation is noted after holding for 40 min at 1000°C. (Results from the similar experiment conducted at 1100°C are inconclusive as the thermocouple became detached during the experiment, and the exact temperature of the experiment is suspect.)

In contrast to the Gleeble results, samples from experiments conducted under no load at 1100°C, 1200°C, and 1650°C for 60 minutes in standard furnace tests showed no visible deformation. Additionally, the results from DTA experiments indicated that little or no melting occurred at ≤1600°C (However, these experiments were conducted on crushed, 20-50 milligram samples that may not have been representative of the bulk.). Appreciable deformation and reaction with the supporting alumina crucible or setter is observed after heat treating a sample of the crust material for 1H at 1800°C.

Microstructure/Composition

Samples of the MP-2 crust material as-received and after the various heat treatments at LANL have been analyzed by D. Huskisson, 6454, using scanning electron microscopy coupled with electron dispersive spectroscopy SEM/EDS. The SEM/EDS analysis was used to evaluate microstructure, chemical homogeneity, and any association between the different elements that comprise the crust material.

Elemental density maps obtained from SEM/EDS analysis of the as-received material revealed that;

- In and Sn are associated,
- Ni, Ag, and Zr are associated,
- Fe remains distinct,
- Cr remains distinct,
- Mo remains distinct, and
- U is associated with O,but UO_2 remains distinct,

SEM/EDS analysis also reveals the presence of gross, 10-100 μm regions of physical and chemical heterogeneities within the bulk crust material.

Elemental density maps obtained from SEM/EDS analysis of sample #6 of the crust material heat treated at 1000°C for 60 minutes in an Ar atmosphere in a standard furnace test reveal that;

- In and Sn are associated,
- In and Ni are associated,
- In and Ag are associated,
- Ni, Ag, and Zr are associated,
- Ni and Fe are associated,
- Fe and Cr are associated,
- Fe and Mo are apparently moderately associated, and
- U is associated with O,but UO_2 remains distinct,

Gross, 10-100 μm regions of physical and chemical heterogeneities are present within the bulk crust material after the heat treatment, and SEM micrographs reveal visible evidence of melting.

Elemental density maps obtained from SEM/EDS analysis of sample #2 of the crust material heat treated to 1160°C at 1°C/minute under 150 psi compressive pressure in a Gleeble test reveal that;

- In and Ni are associated,
- Ag remains distinct,
- Ni and Zr are associated,
- Fe, Cr, Mo, and Zr are associated, and
- U is associated with O,but UO_2 remains distinct.

A visual inspection of the sample after the Gleeble test revealed that the geometry had changed from the original cylindrical shape to a cylinder with a bulge in the middle in the direction perpendicular to the pressing direction (where the sample temperature was highest). An analysis of the material in the bulge in comparison to the bulk revealed that there are no

major compositional differences between the two. Within the bulk, large aspect ratio (>10:1) UO_2 particles are aligned perpendicular to the pressing direction and are surrounded by a layer of material rich in Ni and Zr. Stria of material rich in Ni and Zr are also present perpendicular to the pressing direction.

Gross, 10-100 μm regions of physical and chemical heterogeneities are present within the bulk crust material after the heat treatment, and SEM micrographs reveal visible evidence of melting.

Elemental density maps obtained from SEM/EDS analysis of sample #7 of the crust material heat treated at 1200°C for 60 minutes in an Ar atmosphere in a standard furnace test reveal that;

- Sn is distinct or possible associated with Zr,
- In and Ni are associated,
- In and Ag are associated,
- Ni, Ag, and Zr are associated,
- Fe is associated with Cr (crystals),
- Fe,Cr, Mo, Ni, and Zr are associated, and
- U is associated with O, but UO_2 remains distinct, and

There is a visible morphological difference in the microstructure of the samples treated at 1200°C as compared to those treated at 1160 and 1000°C (which are similar). In the samples treated at 1200°C, there is strong evidence of recrystallization as lath-like crystals comprised of Fe and Cr are present throughout the microstructure. Gross, 10-100 μm regions of physical and chemical heterogeneities are present within the bulk crust material after the heat treatment, and SEM micrographs reveal visible evidence of melting.

Visible evidence of melting is revealed in the SEM micrographs.

Discussion

Phase Equilibria/Melting

Indium and tin are the two lowest melting metals in the crust material. Pure indium (In) melts at 152.6°C, while pure tin (Sn) melts at 231.9°C. Because only minor concentrations of both are present in the bulk material, there influence on the structural integrity of the crust material at <800°C can be expected to be minimal. The DTA results, which revealed no thermal events at <800°C, are consistent with this hypothesis. The results from the Gleeble tests also support this hypothesis. At higher temperatures, In and Sn may have a more pronounced effect on the structural integrity of the crust material as both are good fluxes, and may promote lower temperature melting of the higher melting temperature metals and alloys.

Pure silver (Ag) melts at 960.8°C. The DTA results of an endothermic event at ~900°C could possible reflect the melting of impure silver. Although present in a greater concentration than In and Sn, the results form the Gleeble tests indicate that the <12 wt% Ag present in the bulk crust material has no significant effect on the structural integrity of the crust material at <1000°C.

For iron and chrome (Fe-Cr), the appropriate phase diagram may be the one (including oxygen) for the $FeO\text{-}Cr_2O_3$ system. Spinel ($FeCr_2O_4$) plus liquid crystallizes to form

Wurstite (FeO) plus spinel at ~1400°C, which may be responsible for the exothermic event (crystallization) at ~1400° in the DTA results.

A summary of significant compositions, thermal events, and temperatures for the nickel and zirconium (Ni-Zr) system appear in Table 3.

Table 3. Significant thermal events and compositions in the Ni-Zr system

Composition (wt%)	Event	Temperature (°C)
100% Ni	melt	1455
13% Zr	eutectic melt	1170
31% Zr	peritectic melt	1440
47 % Zr	eutectic melt	1070
61% Zr	peritectic melt	1260
73% Zr	eutectic melt	1010
83% Zr	eutectic melt	960
100% Zr	melt	1855

The eutectic melt temperatures of 960°C, 1010°C and 1170°C in the Ni-Zr system all fall in the temperature range where measurable and appreciable deformation of the crust material occurred in the Gleeble tests. Additionally, Ni and Zr are always associated with each other in the heat treated samples. Chemical interactions in the nickel and zirconium system appear to be of significant importance with regard to the integrity of the crust at temperatures >900°C up to ~1500°C.

A summary of significant compositions, thermal events, and temperatures for the iron and zirconium (Fe-Zr) system appear in Table 4.

Table 4. Significant thermal events and compositions in the Fe-Zr system

Composition (wt%)	Event	Temperature (°C)
100% Fe	melt	1538
14% Zr	eutectic melt	1304
44% Zr	peritectic melt	1675
84% Zr	eutectic melt	947
100% Zr	melt	1855

Pure iron melts at 1538°C. DTA results showing an endothermic event at ~1500°C are consistent with the formation of liquid Fe on heating the crust material. Reactions between the crust and the alumina setter at 1650°C and 1800°C are also indicative of the presence of Fe liquid. Chemical interactions in the iron and zirconium system appear to be of significant importance with regard to the integrity of the crust at temperatures >1650°C. The critical temperature with regard to structural integrity of the crust may be 1675°C, which is the peritectic melting temperature in the Fe-Zr system.

Uranium (U) melts at 1132°C; however, most of the uranium in the crust is in the form of uranium dioxide (UO_2), which melts at ~2878°. It is expected that UO_2 melting or decomposition is not a factor at the temperatures examined

Zirconia (ZrO_2) melts at ~2700°C, and is also not expected to be of concern at the temperatures examined.

Deformation

The results of the deformation experiments coupled with the SEM/EDS and phase equilibria information indicate that, at low temperatures, the structural integrity of the crust material is primarily controlled by a rigid, refractory metal and oxide skeleton. On heating the crust material, liquids of In, Sn, Ag, Ni, and Fe melts (and mixtures thereof) progressively form within the rigid skeletal structure. Although there is evidence of some melt formation at temperatures ≤900°C, under no load conditions (i.e., under the samples own weight), there is insufficient liquid phase present in the system to break down the rigid skeletal structure until >1650°C. Under a compressive pressure of ~150 psi, the skeletal structure breaks down at an appreciably lower temperature (~1180°C). In the later case, Ni-Zr eutectic melting appears to be responsible for the liquid formation that degrades the structural integrity of the crust. Break-down of the skeletal structure at 1850°C appears to be related to the formation of liquid in the Fe-Zr system. The critical temperature for deformation of the crust material under no load conditions is between 1650 and 1800°C, and may be at the 1675 peritectic melting temperature.

Due to their insignificant concentrations in the crust material, In, Sn, and Ag ar not considered to be critical to the structural integrity of the crust material. Thermal (melting) events in the Ni-Zr system are critical at 1000-1200°C under a compressive pressure of ≥150 psi. Under its own weight, thermal (melting) events in the Fe-Zr system become critical to the structural integrity of the crust material at 1650-1800°C.

Appendix C-2

Discussion of Scanning Electron Microscopy of Selected Areas

C-2.1 Metallic Crust Remnant (Center Top)

Scanning electron micromaps and the corresponding elemental maps are given in Figure C-2.1 for the metallic crust remnant at the center line near the upper portion of the crust. The secondary and backscattered electron images revealed a multiphase mixture. Large spherical porosity varying between 60 - 100 μm in size were present. The elemental dot maps revealed the microstructure present consisted of six distinct phases. Chart C-2.1 is an element by element indicator of where a particular element segregated. Primary indicates that for all the phases in which an element was present, the dot map showed that element to be most strongly associated with that phase. For example, Fe was present in three phases, but was most dominant in Phase 2, as seen in the Fe dot map. Secondary indicates that a particular element was present in that phase, but was not a dominant element with respect to only that element. In other words, Fe was a secondary element in Phase 3 when compared to the amount of Fe in Phase 2. However, from the elemental map intensity information, which is provided in the chart, the secondary phase intensity cannot be ranked. For example, more Fe than Ag may or may not exist in Phase 1 by wt %.

Chart C-2.1 Element Indicator - Center Top

Element	Primary Phase	Secondary Phase	Constant	Trace
U	5	2, 4, 6		
Zr	4		1, 2, 3, 6	
O			4, 5	
Fe	2	3, 6		
Ni	3	1, 2, 6		
Cr	2			
Sn	1	3, 6		
In	3	1, 6		
Ag	6	1		
Mo	2			

The following trends are observed for the phases present in the crust remnant at the top, center line location:

Fe/Ni/Ag/Zr/In/Sn/U are associated

Fe/Ni/Cr/Mo/Zr are associated

Ni/In/Fe/Sn/Zr are associated

U/Zr/O are associated

U/O are associated

Sn/In/Ni/Zr/Ag are associated

C-2.2 Metallic Crust Remnant (Middle)

Scanning electron micrographs and the corresponding elemental maps are given in Figure C-2.2 for the metallic crust remnant. The secondary and backscattered electron images revealed a multiple phase mixture.

Large spherical porosity varying between 60 - 90 μm in size was present. The elemental dot maps revealed the microstructure present consisted of six distinct phases. Chart C-2.2 is an element by element indicator of where a particular element segregated.

Chart C-2.2 Element Indicator - Middle

Element	Primary Phase	Secondary Phase	Constant	Trace
U	5	3, 4		
Zr	4		1, 2, 3, 6	
O			4, 5	
Fe	2	1, 3		
Ni	3	1, 6		
Cr	2			
Sn	6	3		
In	3	6		
Ag	1	3		
Mo				2

The following trends are observed for the phases present in the crust remnant:

Fe/Ni/Ag/Zr are associated

Fe/Cr/Zr are associated

Ni/In/Fe/Sn/U/Zr/Ag are associated

U/Zr/O are associated

U/O are associated

Sn/In/Ni/Zr are associated

C-2.3 As-Fabricated Crust

Scanning electron micrographs and the corresponding elemental maps are given in Figure C-2.3 for the as-fabricated metallic crust. The secondary and backscattered electron images revealed a multiple phase mixture. Large spherical porosity varying between 40 - 70 μm in size was present. The elemental dot maps revealed the microstructure present consisted of eight distinct phases. Chart C-2.3 is an element by element indicator of where a particular element segregated.

Chart C-2.3 Element Indicator - Crust

Element	Primary Phase	Secondary Phase	Constant	Trace
U	5			
Zr	4		1, 3, 6, 7	
O			4, 5	
Fe	6			1
Ni	7	1, 3		
Cr	2			
Sn	3			
In	3			
Ag	1			
Mo				8

The following trends are observed for the phases present in the as-fabricated crust:

Fe/Ni/Ag/Zr are associated

Cr was distinct

In/Sn/Zr/Ni are associated
ZrO2 was distinct

UO2 was distinct

Fe was distinct

Ni/Zr are associated

In comparing the evolved microstructure of the crust remnant to that of the as-fabricated condition, the following observations can be made. First and foremost, urania particles that remained were retained in the crust remnant, which indicated that the crust was not at a temperature high enough or at temperature long enough to dissolve the initial amount of urania in the crust. Second, Fe/Ni/Zr/Ag and In/Sn/Zr/Ni still maintained their association despite liquefaction and resolidification. Finally, the ZrO_2 that was present initially, had dissolved and upon solidification was associated with every phase that had once been liquid (i.e., every phase except undissolved UO_2).

C-2.4 Relocated Metallic Material

Six regions of relocated material were examined using scanning electron microscopy in conjunction with wave length dispersive analysis. Chart C-2.4 provides the name/location of each of the six regions, the sample number, the table number that gives the chemical analysis of each sample, and the figure number that shows the scanning electron micrographs and corresponding elemental maps. In addition to the data provided in the cited tables, a detailed description of the morphology of the phases RM-1, RM-2, and RM-3 are given in the following sections.

Chart C-2.4 Relocated Material Regions

Name/Location	Sample	Table	Figure
Relocated Material/Top (RM-1)	5.2.3	C-2.1	C-2.4
Relocated Material/Middle (RM-2)	6.4.3A	C-2.2	C-2.5
Relocated Material/Middle (RM-2*)	6.4.3	C-2.3	C-2.6
Relocated Material/Bottom (RM-2.5*)	6.4.7	C-2.4	C-2.7
Relocated Material/Bottom (RM-3*)	6.4.12	C-2.5	C-2.8[a]
Relocated Material/Bottom (RM-3)	6.4.10	C-2.6	C-2.9
[a]Even though some of the photos are labeled 6-2-12, all photos are of Sample 6-4-12.			

Figure C-2.4 shows the scanning electron micrographs and the corresponding elemental maps for the relocated material that was just below the crust remnant (RM-1). The secondary and backscattered electron images revealed a multiple phase mixture. The elemental dot maps revealed the microstructure present consisted of six distinct phases. Chart C-2.5 is an element by element indicator of where a particular element segregated.

Chart C-2.5 Element Indicator - Crust Remnant

Element	Primary Phase	Secondary Phase	Constant	Trace
U	5	3, 4		
Zr	4		1, 2, 3, 5	
O				
Fe	2	2, 3, 4, 5		4
Ni	3	4, 5		
Cr	2	4		
Sn	6	3		
In	3	6		
Ag	1	3		
Mo		2		

The following trends are observed for the phases present in the relocated material located just below the crust remnant (RM-1):

Ag/Zr are associated

Fe/Cr/Zr are associated

Ni/In/Fe/Sn/U/Zr/Ag are associated

Fe/Ni/Cr/Zr are associated

U/Zr/Ni/Fe are associated

Sn/In/Zr are associated

The **bold** items indicate similarities to the crust remnant.

Figure C-2.5 shows the scanning electron micrographs and the corresponding elemental maps for the relocated material that was located in the middle section of the fuel rod array (RM-2). The secondary and backscattered electron images revealed a multiple phase mixture. The elemental dot maps revealed the microstructure present consisted of six distinct phases. Chart C-2.6 is an element by element indicator of where a particular element segregated.

Chart C-2.6 Element Indicator - Fuel Rod Array

Element	Primary Phase	Secondary Phase	Constant	Trace
U			1, 4, 5	
Zr			1, 2, 3, 4, 5	
O				x
Fe	2	1, 3, 4, 5		
Ni	4	1, 3, 5		
Cr	2	5		
Sn	6	3		
In	3			
Ag	1			
Mo	2			

The following trends are observed for the phases present in the relocated material located in the middle of the fuel array:

Fe/Ni/U/Ag/Zr are associated

Fe/Cr/Zr are associated

In/Fe/Ni/Sn/Zr are associated

Fe/Ni/U/Zr are associated

Fe/Ni/Cr/U/Zr are associated

Sn/Zr are associated

The **bold** items indicate similarities to RM-1.

Figure C-2.9 shows the scanning electron micrographs and the corresponding elemental maps for the relocated material that was located at the bottom of the test capsule (RM-3). The secondary and backscattered electron images revealed a multiple phase mixture. The elemental dot maps revealed the microstructure present consisted of three distinct phases. Chart C-2.7 is an element by element indicator of where a particular element segregated.

Chart C-2.7 Element Indicator - Test Capsule

Element	Primary Phase	Secondary Phase	Constant	Trace
U	1	2		
Zr			1, 2, 3	
O				x
Fe	2	1		
Ni	2	1		
Cr	2	1		
Sn	3			
In	3	1		
Ag	1	2		
Mo	1			

The following trends are observed for the phases present in the relocated material located at the bottom of the test capsule:

In/Sn/Zr are associated

Fe/Ni/Cr/U/Ag/Zr are associated

Ag/Fe/Ni/Cr/U/Zr/In/Mo/Sn are associated

The **bold** items indicate similarities to RM-1.

Table C-2.1 Relocated Material - Top (RM-1)
ANALYSIS: 5-2-3 (1000x) Relocated material at center

Sample	Element	Normalized Wt %	Normalized At %	Count Err (s wt %)
5-2-3	U	8.58	2.95	0.0334
	O	1.14	5.51	0.0221
	Zr	51.14	45.86	0.0537
	Fe	11.78	17.26	0.0156
	Ni	9.62	13.4	0.0151
	Cr	2.08	3.27	0.0079
	Mo	0.571	0.487	0.0067
	Ag	6.99	5.3	0.0168
	Sn	5.46	3.76	0.0184
	In	2.65	1.89	0.0093
5-2-3a	U	8.38	2.81	0.0333
	O	1.67	8.36	0.0252
	Zr	51.3	45.03	543
	Fe	11.36	16.29	0.0155
	Ni	9.88	13.47	0.0155
	Cr	1.85	2.85	0.0077
	Mo	0.506	0.423	0.0069
	Ag	7.92	5.88	0.018
	Sn	4.69	3.16	0.0178
	In	2.48	1.73	0.0093
5-2-3b	U	8.45	2.82	0.0333
	O	1.93	9.58	0.0274
	Zr	51.1	44.42	0.0543
	Fe	11.56	16.41	0.0157
	Ni	9.43	12.75	0.0152
	Cr	2	3.05	0.0079
	Mo	0.536	0.443	0.0069
	Ag	6.8	5	0.017
	Sn	5.53	3.7	0.0188
	In	2.66	1.84	0.0095
average	**U**	**8.5 (.08)**	**2.9 (.06)**	
(SD)	**O**	**1.6 (.3)**	**7.9 (1.6)**	
	Zr	**51.2 (.09)**	**45.10 (.6)**	
	Fe	**11.6 (.2)**	**16.7 (.4)**	
	Ni	**9.6 (.2)**	**13.2 (.3)**	
	Cr	**2.0 (.1)**	**3.1 (.2)**	
	Mo	**.5 (.03)**	**.5 (.03)**	
	Ag	**7.2 (.5)**	**5.4 (.4)**	
	Sn	**5.2 (.4)**	**3.5 (.37)**	
	In	**2.60 (.08)**	**1.8 (.07)**	

Table C-2.2 Relocated Material - Middle (RM-2)
ANALYSIS: 6-4-3A (1000x) Relocated material-around left pin

Sample	Element	Normalized Wt %	Normalized at %	Count Err (s wt %)
6-4-3aq	U	8.77	3.23	0.0331
	O	0.823	4.5	0.02
	Zr	62.75	60.18	0.0618
	Fe	7.6	11.91	0.0125
	Ni	4.19	6.24	0.011
	Cr	1.99	3.35	0.0077
	Mo	0.21	0.192	0.0061
	Ag	3.98	3.23	0.0133
	Sn	8.26	6.09	0.0211
	In	1.42	1.08	0.0076
6-4-3a1	U	8.35	3.04	0.0323
	O	1.01	5.45	0.0193
	Zr	62.13	58.91	0.0601
	Fe	7.69	11.91	0.0122
	Ni	4.23	6.24	0.0108
	Cr	2.15	3.58	0.0077
	Mo	0.18	0.163	0.0062
	Ag	3.89	3.12	0.0129
	Sn	8.81	6.42	0.0212
	In	1.56	1.18	0.0078
average	**U**	**8.6 (.2)**	**3.1 (.1)**	
(SD)	**O**	**0.9 (.09)**	**5.0 (.5)**	
	Zr	**62.4 (.3)**	**59.6 (.6)**	
	Fe	**7.7 (.05)**	**11.9 (0)**	
	Ni	**4.2 (.02)**	**6.2 (0)**	
	Cr	**2.1 (.08)**	**3.5 (.2)**	
	Mo	**0.2 (.02)**	**0.2 (.02)**	
	Ag	**3.9 (.05)**	**3.2 (.06)**	
	Sn	**8.5 (.3)**	**6.3 (.2)**	
	In	**1.5 (.07)**	**1.1 (.05)**	

Table C-2.3 Chemical Analysis of the Relocated Material (RM-2*)

LOCATION: 6-4-3

ANALYSIS: 6-4-3 (1000x) Relocated Material

Sample	Element	Normalized Wt %	Normalized At %	Count Err (s wt %)
6-4-3ay	U	13.72	5.18	0.0399
	O	0.94	5.28	0.0219
	Zr	59.66	58.73	0.0622
	Fe	7.51	12.07	0.0143
	Ni	4.35	6.66	0.0127
	Cr	1.08	1.87	0.0071
	Mo	0.21	0.2	0.0065
	Ag	6.6	5.5	0.0194
	Sn	4.49	3.4	0.017
	In	1.44	1.13	0.0092
6-4-3az	U	13.54	4.94	0.0397
	O	1.67	9.05	0.0269
	Zr	59.22	56.34	0.0622
	Fe	7.55	11.73	0.0143
	Ni	4.31	6.37	0.0127
	Cr	1.06	1.77	0.0072
	Mo	0.22	0.2	0.0066
	Ag	6.5	5.22	0.0193
	Sn	4.49	3.28	0.171
	In	1.44	1.09	0.0092
average	**U**	**13.63 (.09)**	**5.06 (.12)**	
(SD)	**O**	**1.31 (.37)**	**7.17 (1.9)**	
	Zr	**59.44 (.22)**	**57.54 (1.2)**	
	Fe	**7.53 (.02)**	**11.9 (.34)**	
	Ni	**4.33 (.02)**	**6.52 (.15)**	
	Cr	**1.07 (.01**	**1.82 (.05)**	
	Mo	**.22 (.02)**	**.2 (0)**	
	Ag	**6.6 (.01)**	**5.36 (.14)**	
	Sn	**4.49 (0)**	**3.34 (.06)**	
	In	**1.44 (0)**	**1.11 (.02)**	

Table C-2.4 Chemical Analysis of the Relocated Material (RM-2.5*)

LOCATION: 6-4-7

ANALYSIS: 6-4-7 (1000x) Relocated Material

Sample	Element	Normalized Wt %	Normalized At %	Count Err (s wt %)
6-4-7y	U	9.97	3.6	0.0351
	O	1.43	7.67	0.0218
	Zr	64.11	60.5	0.0641
	Fe	7.02	10.82	0.0133
	Ni	3.99	5.85	0.0119
	Cr	1.42	2.34	0.0074
	Mo	0.24	0.21	0.0063
	Ag	5.37	4.29	0.0172
	Sn	5.07	3.67	0.0171
	In	1.39	1.04	0.0084
6-4-7z	U	9.97	3.64	0.0352
	O	1.24	6.71	0.0213
	Zr	64.75	61.66	0.0646
	Fe	6.94	10.79	0.0132
	Ni	3.9	5.77	0.0118
	Cr	1.39	2.32	0.0073
	Mo	0.24	0.21	0.0063
	Ag	5.28	4.25	0.0172
	Sn	4.96	3.63	0.017
	In	1.36	1.03	0.0084
average	**U**	**9.97 (0)**	**3.62 (.02)**	
(SD)	**O**	**1.34 (.10)**	**7.19 (.48)**	
	Zr	**64.43 (.32)**	**61.08 (.58)**	
	Fe	**6.98 (.04)**	**10.81 (.15)**	
	Ni	**3.95 (.05)**	**5.81 (.04)**	
	Cr	**1.41 (.02)**	**2.33 (.01)**	
	Mo	**.24 (0)**	**.21 (0)**	
	Ag	**5.33 (.09)**	**4.27 (.02)**	
	Sn	**5.02 (.06)**	**3.65 (.02)**	
	In	**1.38 (.02)**	**1.04 (.01)**	

Table C-2.5 Chemical analysis of the relocated material (RM 3.0 *)

LOCATION: 6-4-12

ANALYSIS: 6-4-12 (1000x) Relocated Material

Sample	Element	Normalized Wt %	Normalized at %	Count Err (s wt %)
6-4-12.1	U	11.13	3.9	0.0368
	O	2.16	11.29	0.0257
	Zr	63	57.62	0.0644
	Fe	7.25	10.83	0.0138
	Ni	3.97	5.65	0.0121
	Cr	1.51	2.42	0.0076
	Mo	0.33	0.29	0.0066
	Ag	6.27	4.86	0.0186
	Sn	3.28	2.3	0.0151
	In	1.15	0.84	0.0086
6-4-12.2	U	11	3.83	0.0366
	O	2.3	11.93	0.0241
	Zr	62.89	57.1	0.0645
	Fe	7.41	10.99	0.014
	Ni	4.02	5.68	0.0122
	Cr	1.48	2.36	0.0076
	Mo	0.32	0.28	0.0065
	Ag	6.19	4.75	0.0185
	Sn	3.25	2.27	0.0152
	In	1.13	0.82	0.0085
average	**U**	**11.07 (.07)**	**3.87 (.04)**	
(SD)	**O**	**2.23 (.07)**	**11.61 (.32)**	
	Zr	**62.95 (.06)**	**57.36 (1.26)**	
	Fe	**7.33 (.08)**	**10.91 (.08)**	
	Ni	**4 (.03)**	**5.67 (.02)**	
	Cr	**1.5 (.02)**	**2.39 (.03)**	
	Mo	**.33 (.02)**	**.29 (.01)**	
	Ag	**6.23 (.04)**	**4.81 (.06)**	
	Sn	**3.27 (.02**	**2.29 (.02)**	
	In	**1.14 (.01)**	**.83 (.01)**	

Table C-2.6 Relocated material - bottom (RM-3)

ANALYSIS: 6-4-10 (1000x) Relocated material-at bottom

Sample	Element	Normalized Wt %	Normalized At %	Count Err (s wt %)
6-4-10	U	6.85	2.44	0.0314
	O	1.44	7.62	0.0229
	Zr	69	64.14	0.071
	Fe	6.29	9.55	0.0124
	Ni	4.08	5.89	0.0115
	Cr	1.15	1.88	0.0069
	Mo	0.246	0.217	0.0062
	Ag	5.8	4.56	0.0158
	Sn	3.85	2.75	0.0165
	In	1.31	0.966	0.0081
6-4-10a	U	6.88	2.48	0.0316
	O	1.19	6.35	0.0215
	Zr	69.19	65.06	0.0713
	Fe	6.24	9.59	0.0123
	Ni	4.1	5.99	0.0115
	Cr	1.15	1.9	0.007
	Mo	0.228	0.203	0.0062
	Ag	5.88	4.67	0.0159
	Sn	3.82	2.76	0.0165
	In	1.32	0.986	0.0082
average	**U**	**6.9 (.02)**	**2.5 (.02)**	
(SD)	**O**	**1.3 (.13)**	**6.9 (.6)**	
	Zr	**69.10 (.1)**	**64.6 (.5)**	
	Fe	**6.3 (.03)**	**9.6 (.02)**	
	Ni	**4.1 (.01)**	**5.9 (.05)**	
	Cr	**1.2 (0)**	**1.9 (.01)**	
	Mo	**.2 (.009)**	**.2 (.007)**	
	Ag	**5.8 (.04**	**4.6 (.06)**	
	Sn	**3.8 (.02)**	**2.8 (.005)**	
	In	**1.3 (.005)**	**1.0 (.01)**	

SEM

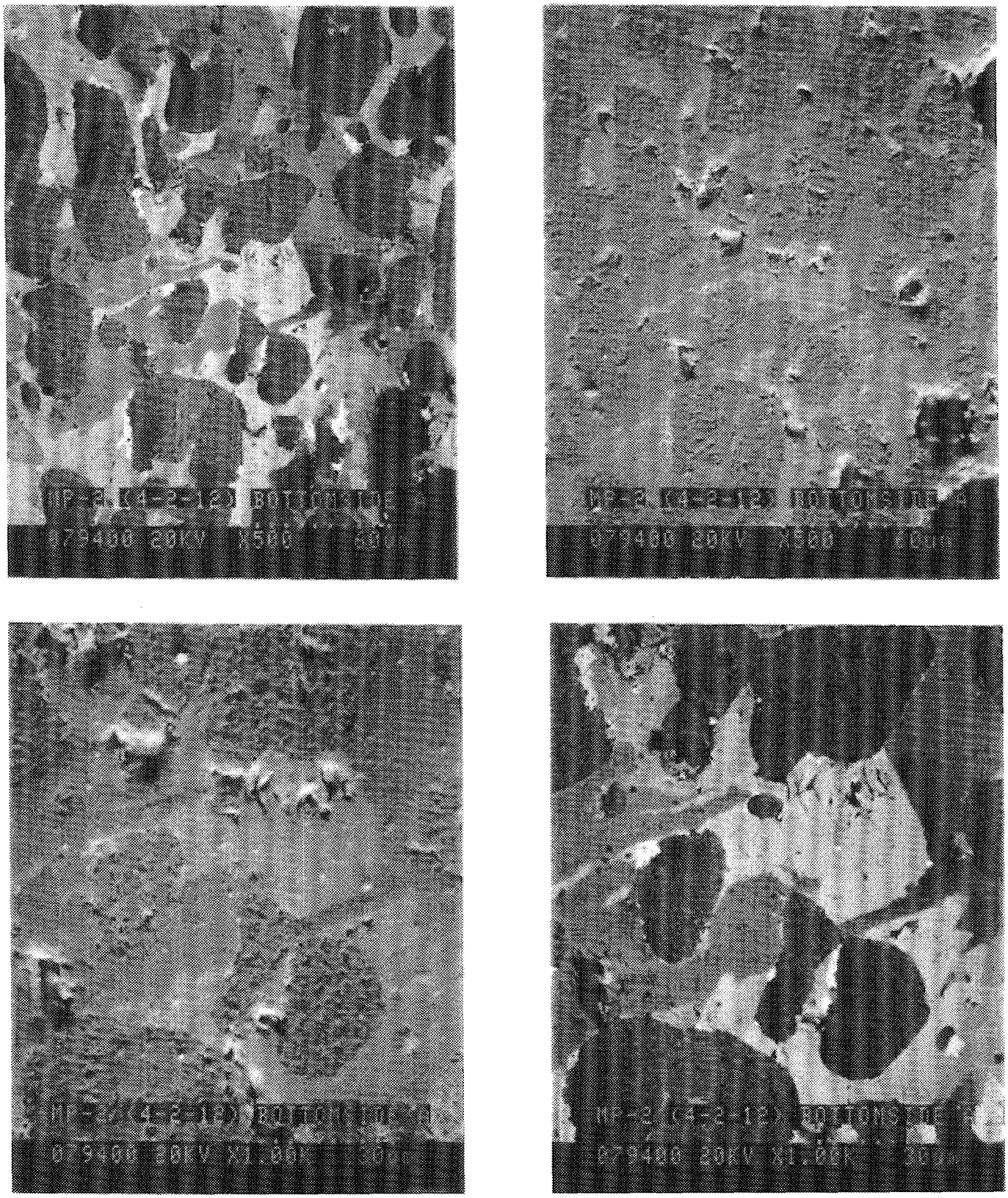

Figure C-2.1a Scanning Electron Micrographs and Corresponding Elemental Maps for the Metallic Crust Remnant

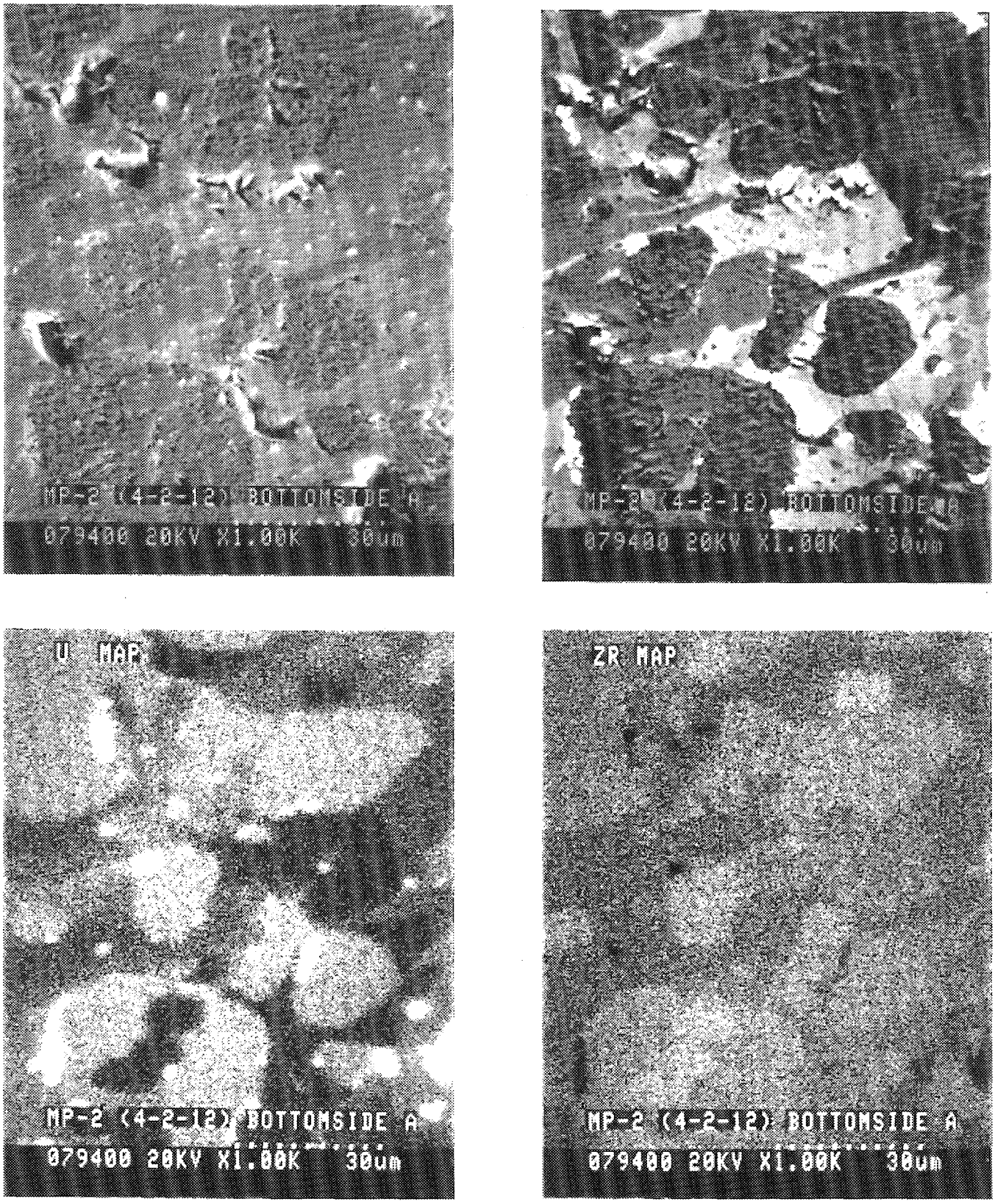

Figure C-2.1b Scanning Electron Micrographs and Corresponding Elemental Maps for the Metallic Crust Remnant

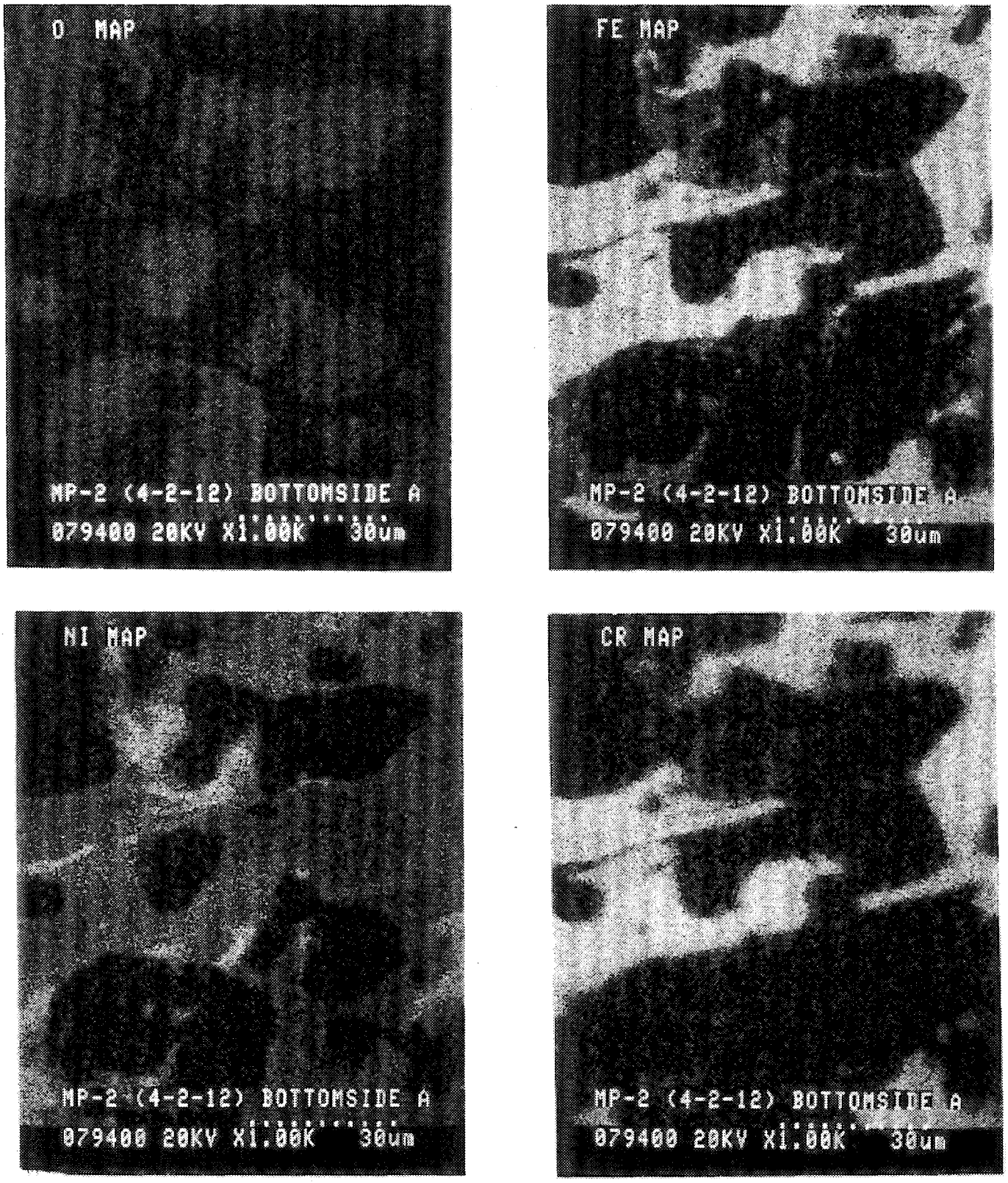

Figure C-2.1c Scanning Electron Micrographs and Corresponding Elemental Maps for the Metallic Crust Remnant

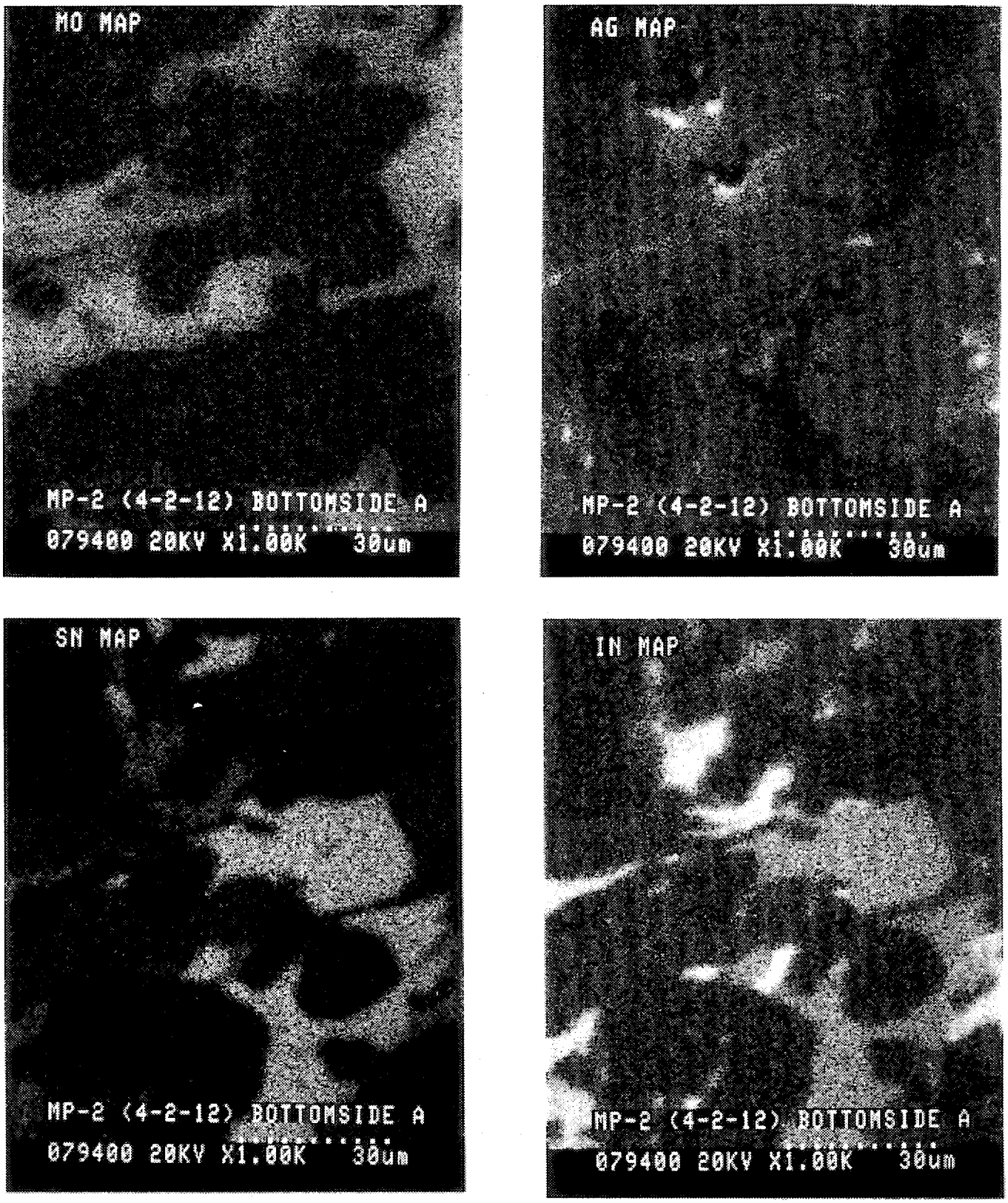

Figure C-2.1d Scanning Electron Micrographs and Corresponding Elemental Maps for the Metallic Crust Remnant

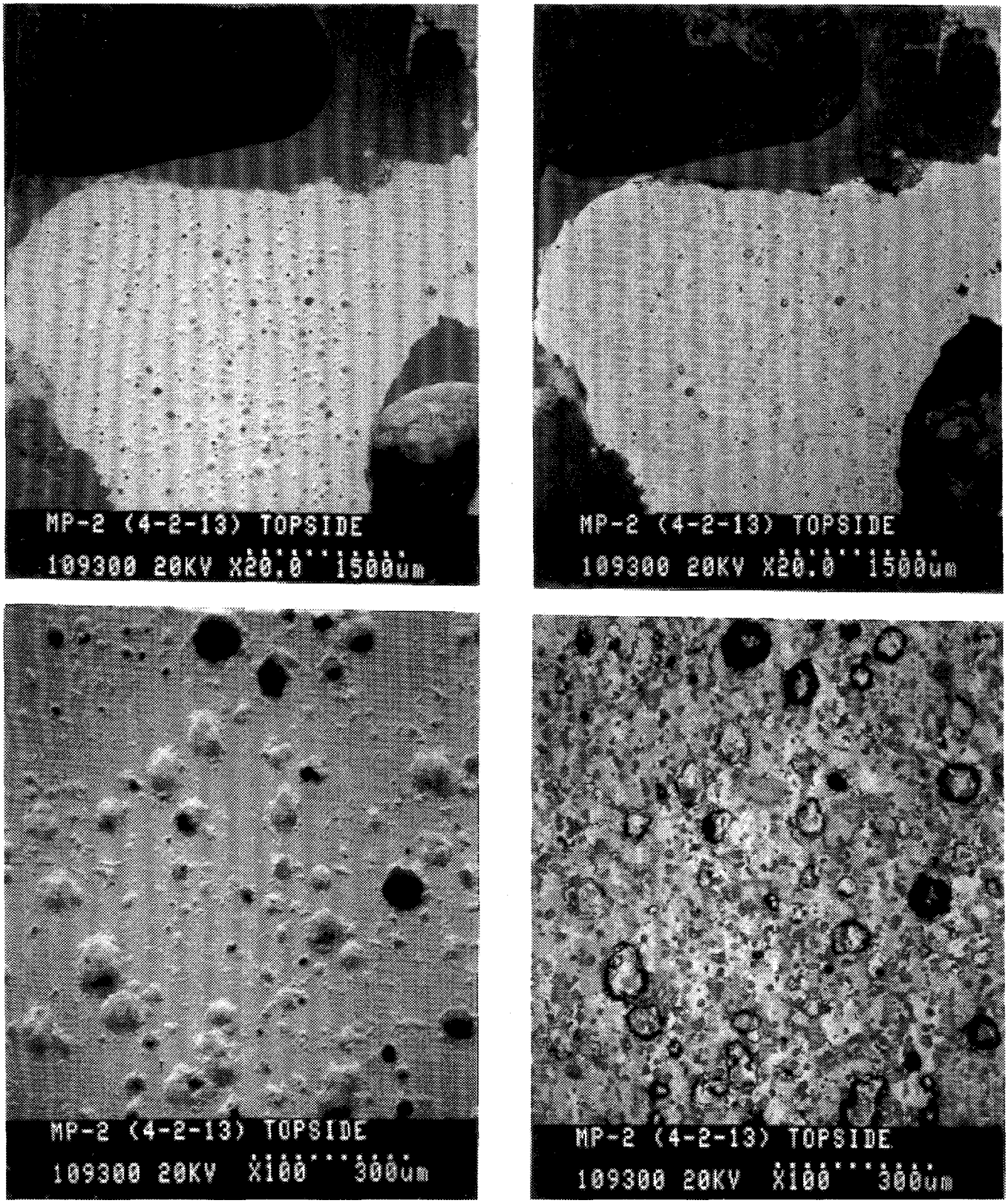

Figure C-2.2a Scanning Electron Micrographs and Corresponding Elemental Maps for the Metallic Crust Remnant

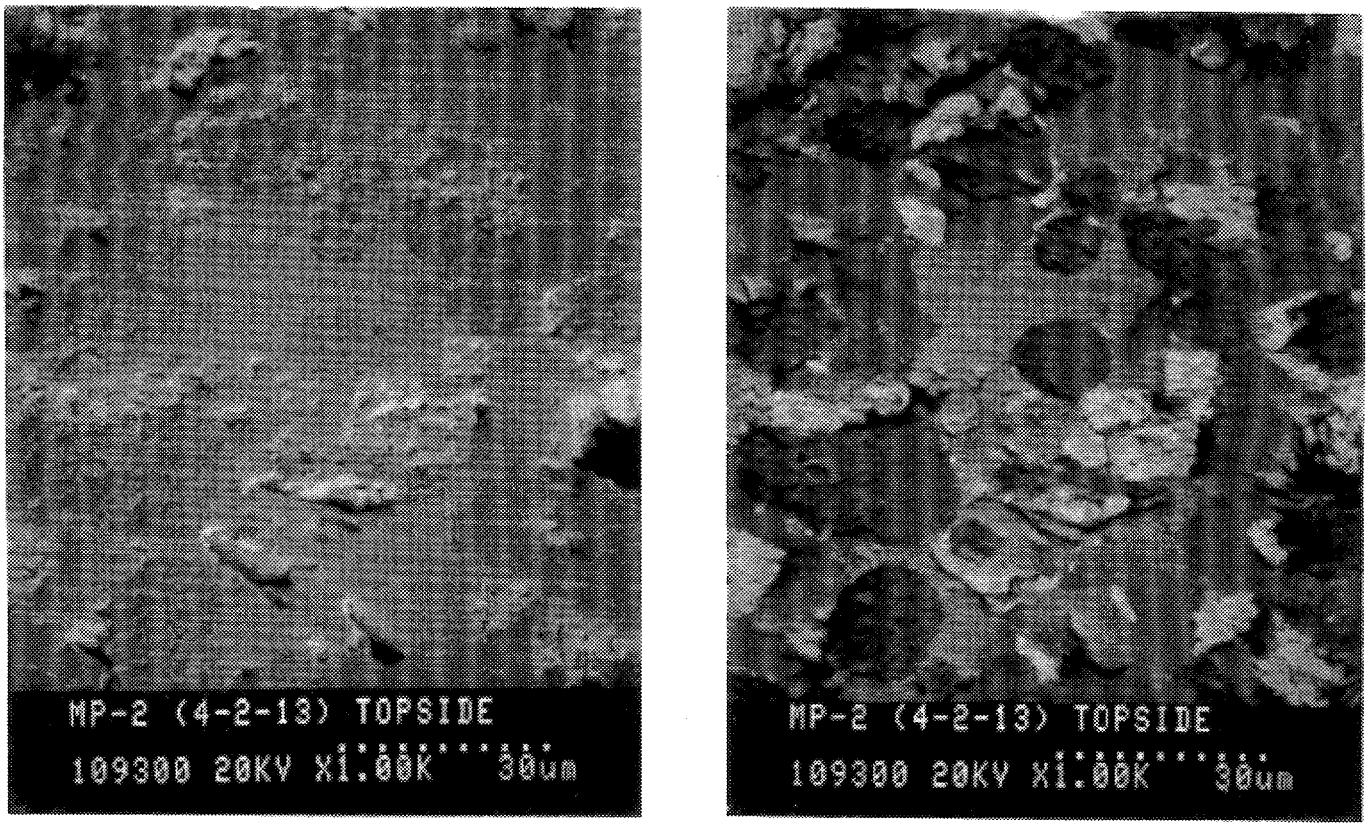

Figure C-2.2b Scanning Electron Micrographs and Corresponding Elemental Maps for the Metallic Crust Remnant

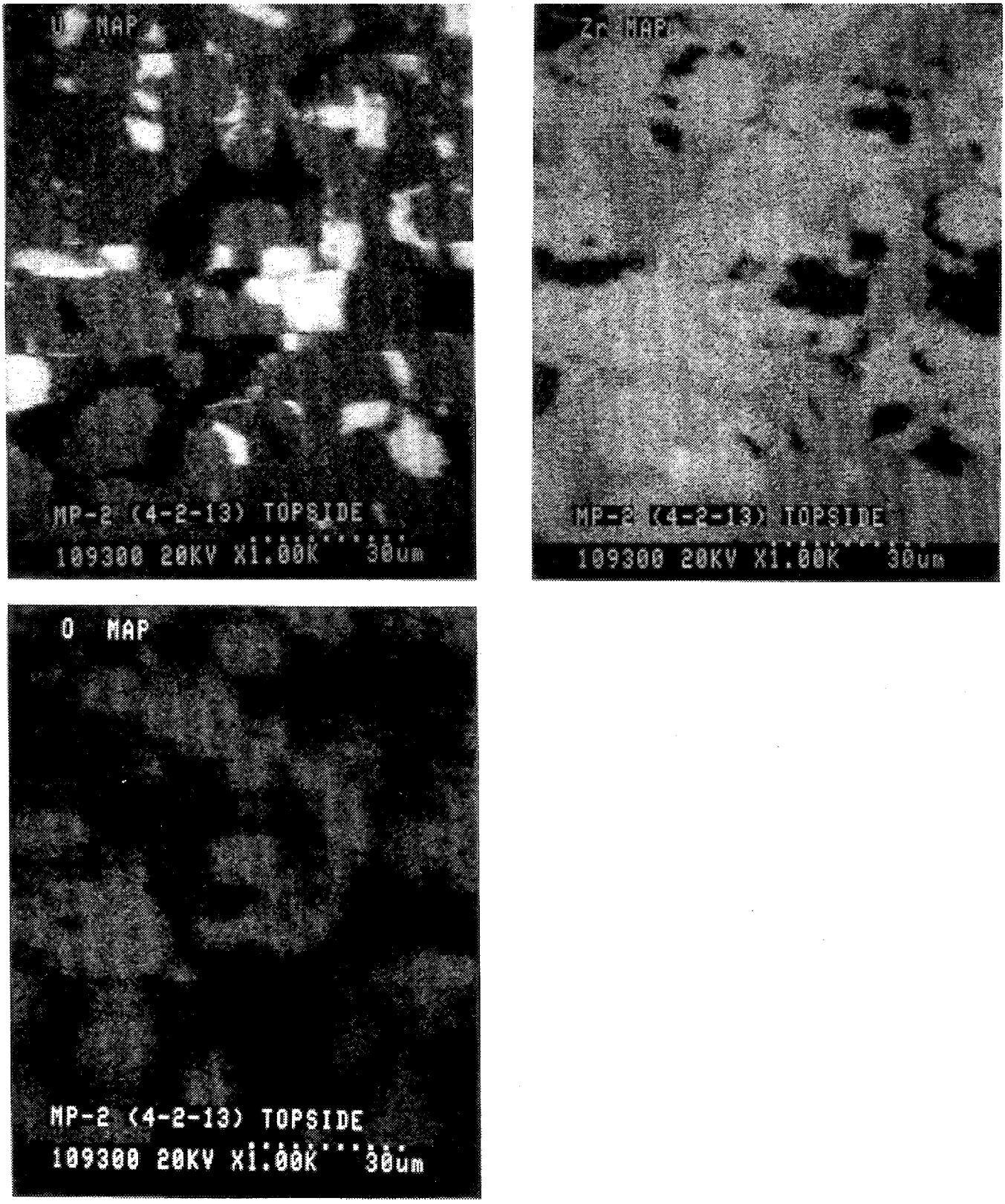

Figure C-2.2c Scanning Electron Micrographs and Corresponding Elemental Maps for the Metallic Crust Remnant

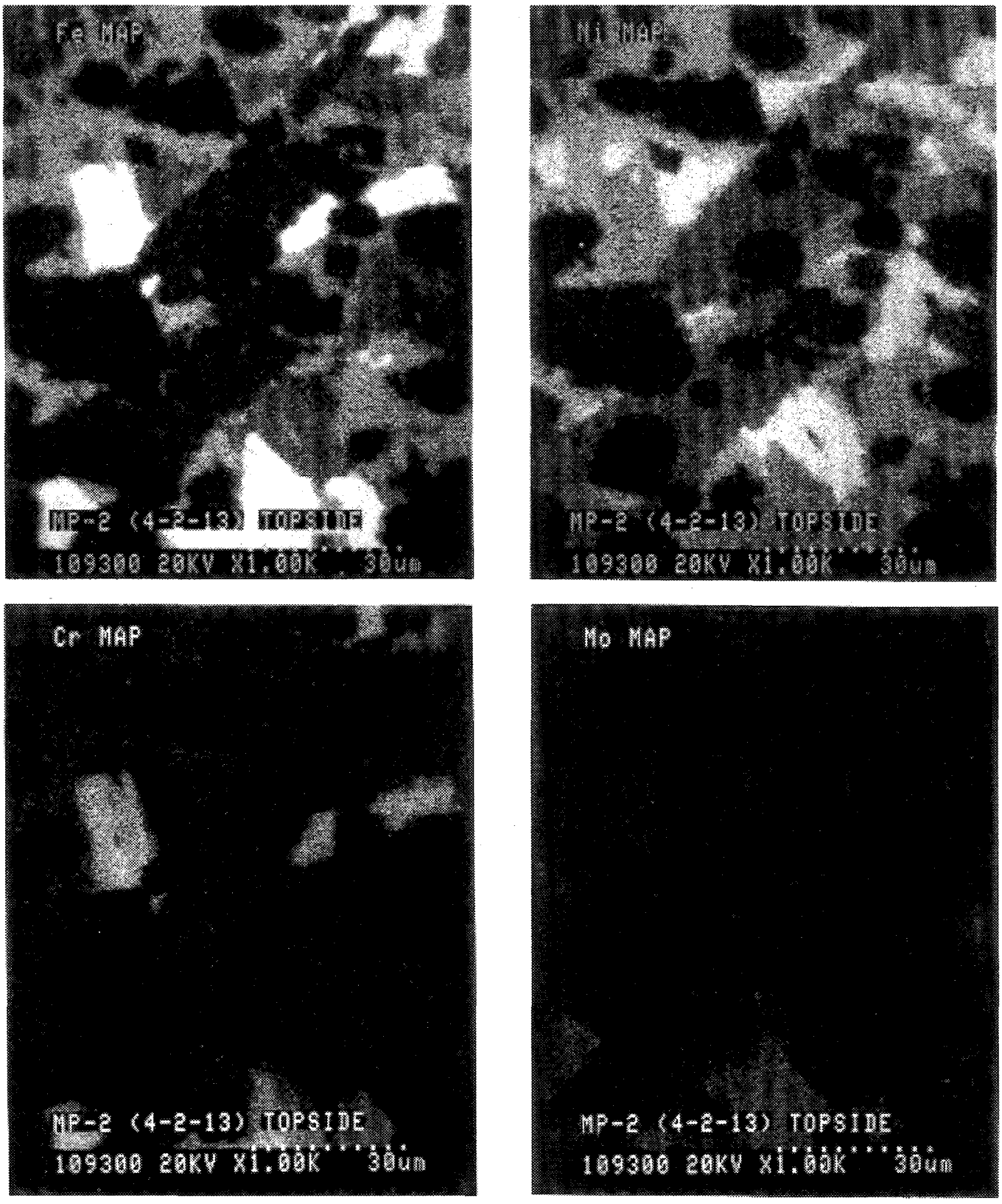

Figure C-2.2d Scanning Electron Micrographs and Corresponding Elemental Maps for the Metallic Crust Remnant

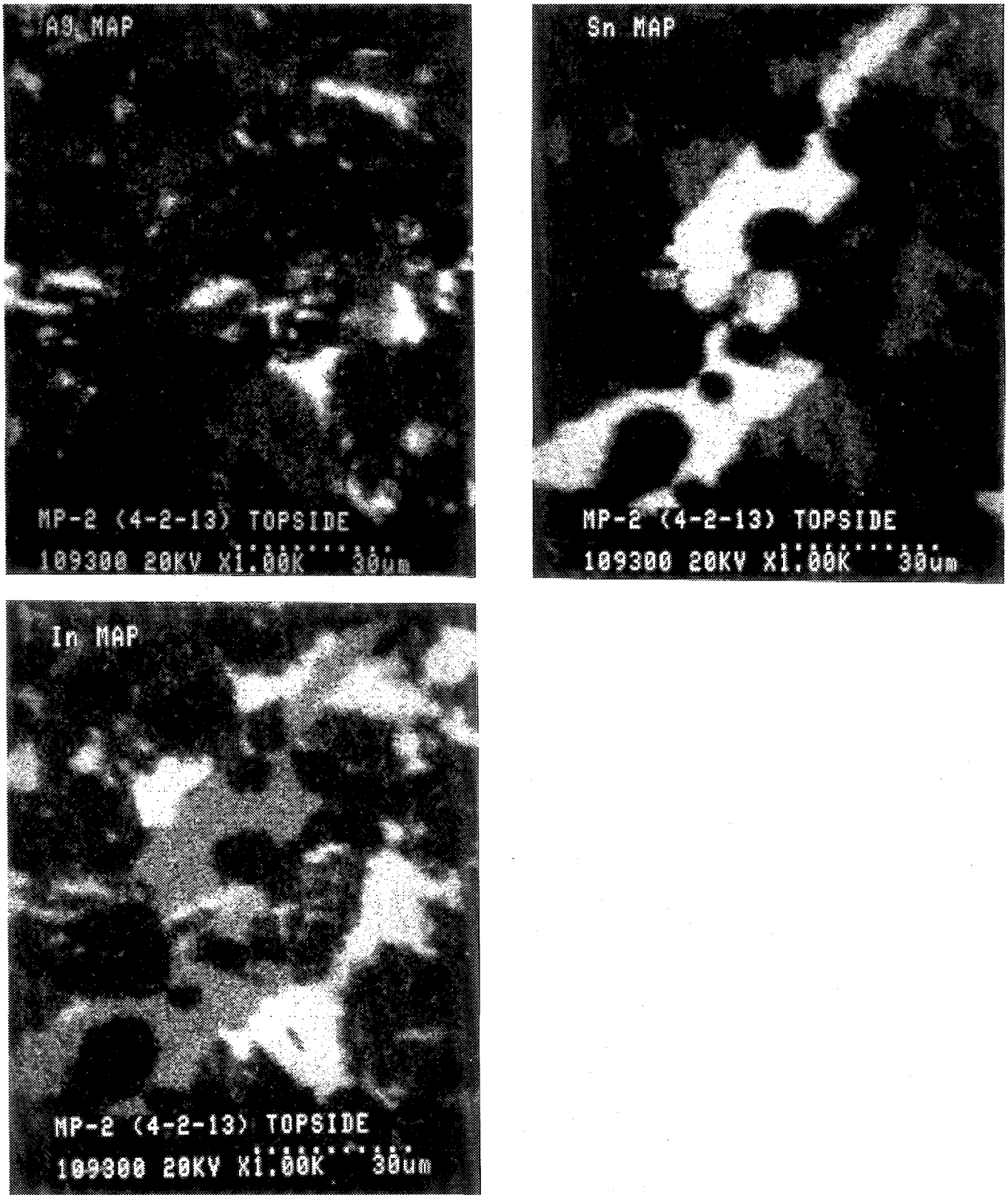

Figure C-2.2e Scanning Electron Micrographs and Corresponding Elemental Maps for the Metallic Crust Remnant

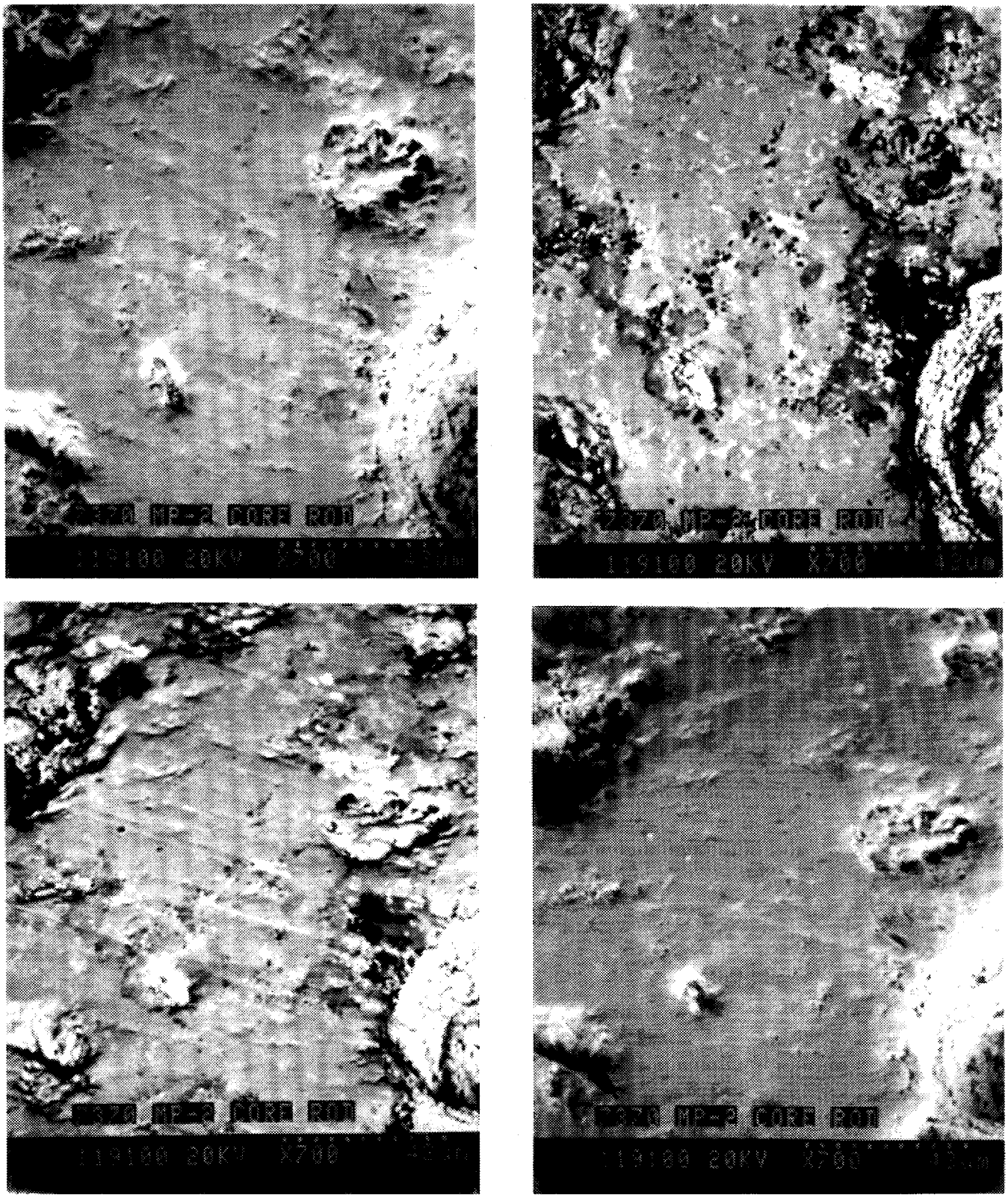

Figure C-2.3a Scanning Electron Micrographs and Corresponding Elemental Maps for the As-Fabricated Metallic Crust

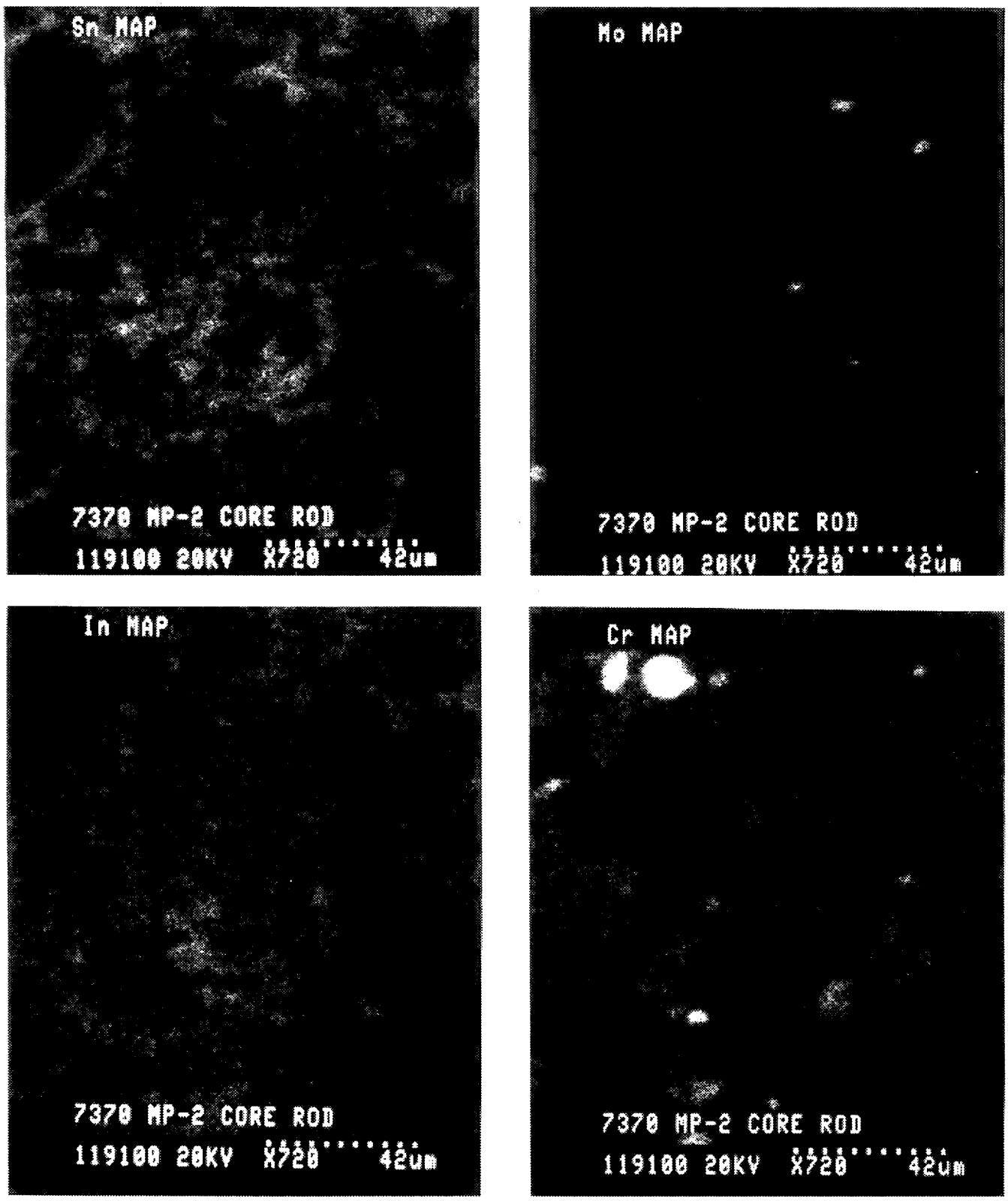

Figure C-2.3b Scanning Electron Micrographs and Corresponding Elemental Maps for the As-Fabricated Metallic Crust

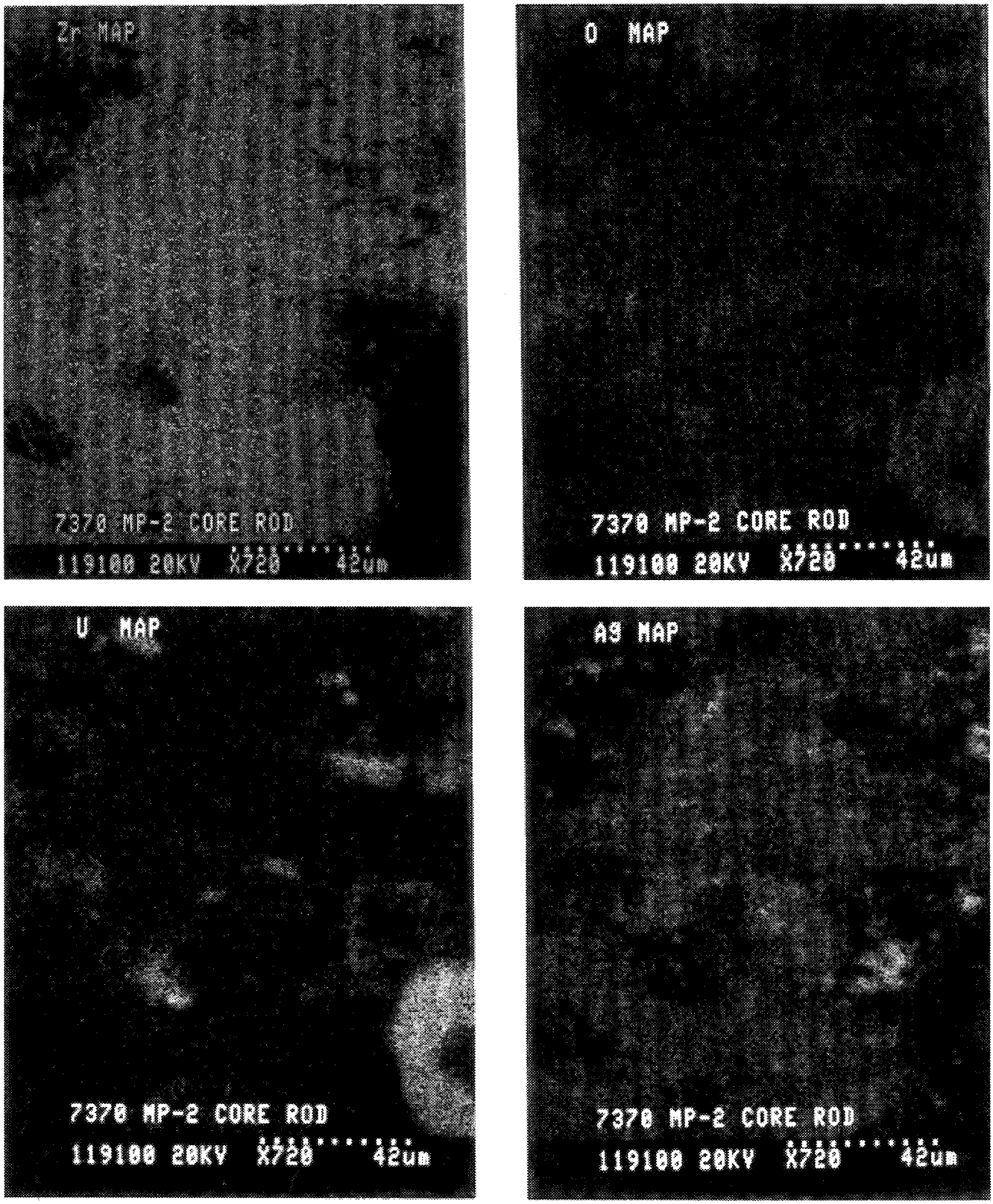

Figure C-2.3c Scanning Electron Micrographs and Corresponding Elemental Maps for the As-Fabricated Metallic Crust

SEM

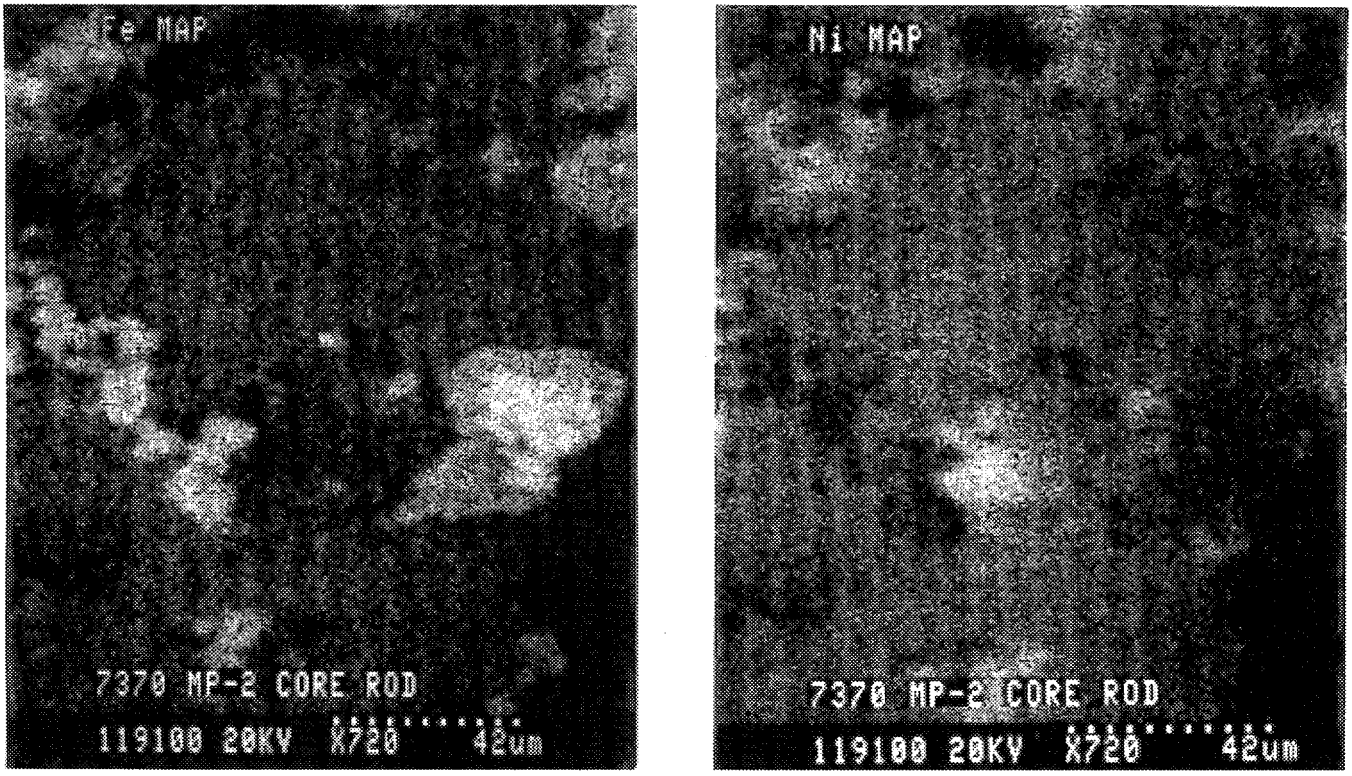

Figure C-2.3d Scanning Electron Micrographs and Corresponding Elemental Maps for the As-Fabricated Metallic Crust

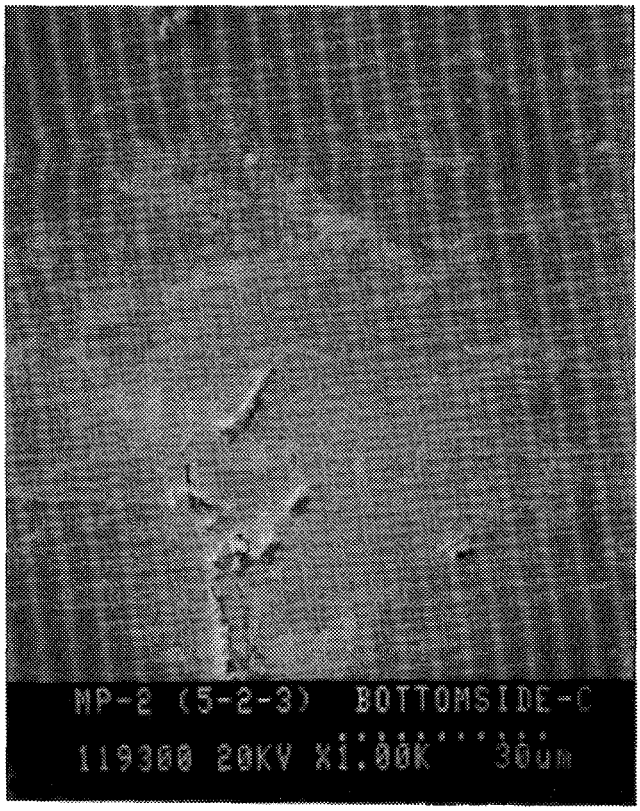

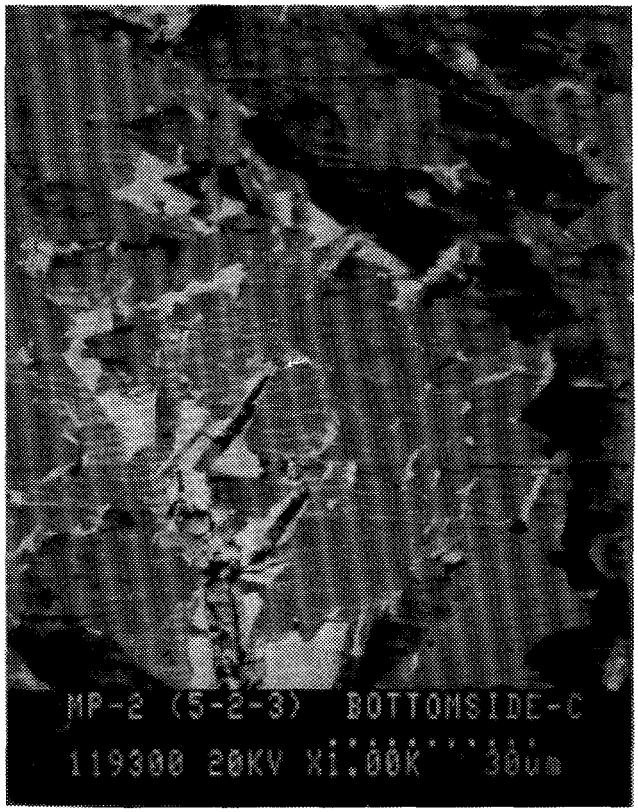

Figure C-2.4a Scanning Electron Micrographs and Corresponding Elemental Maps for the Relocated Material Just Under Metallic Crust Remnant (RM-1)

SEM

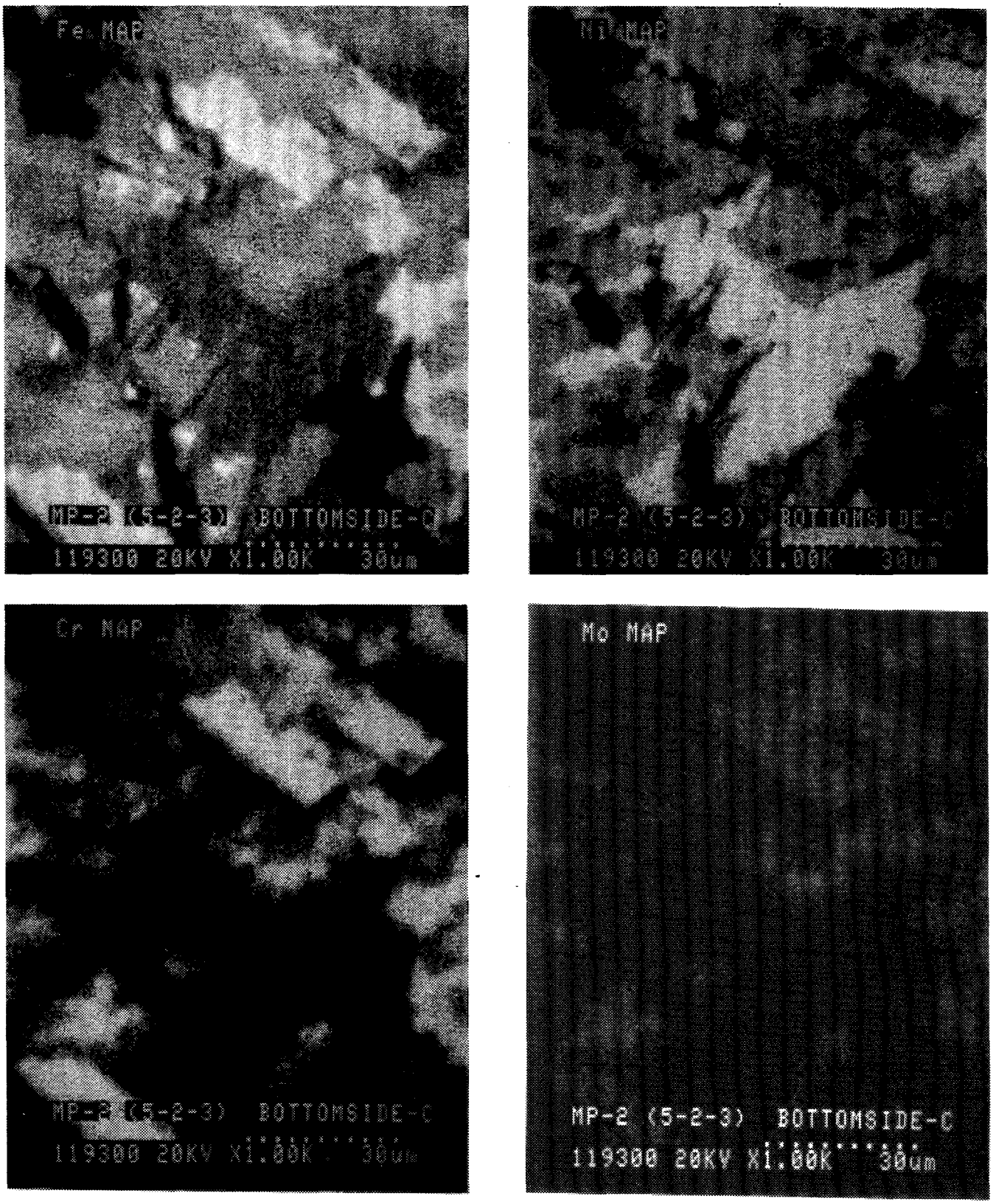

Figure C-2.4b Scanning Electron Micrographs and Corresponding Elemental Maps for the Relocated Material Just Under Metallic Crust Remnant (RM-1)

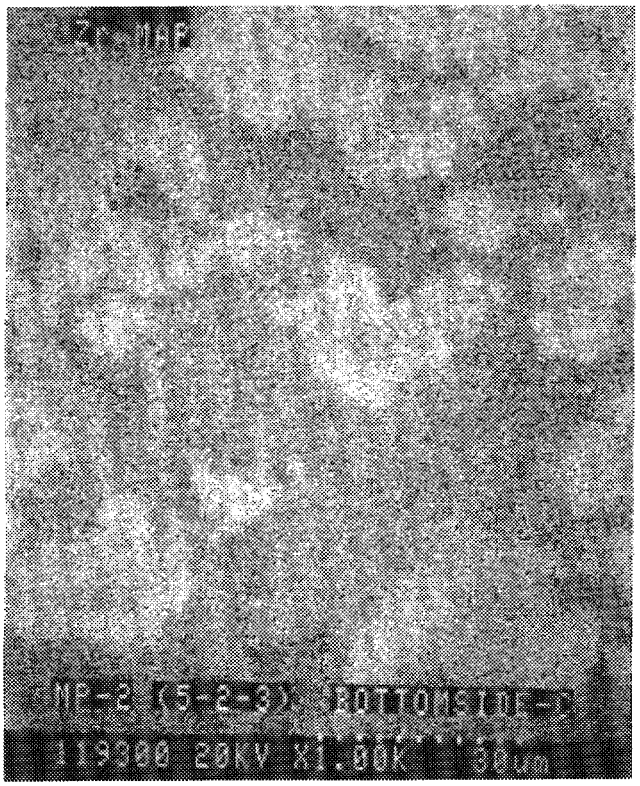

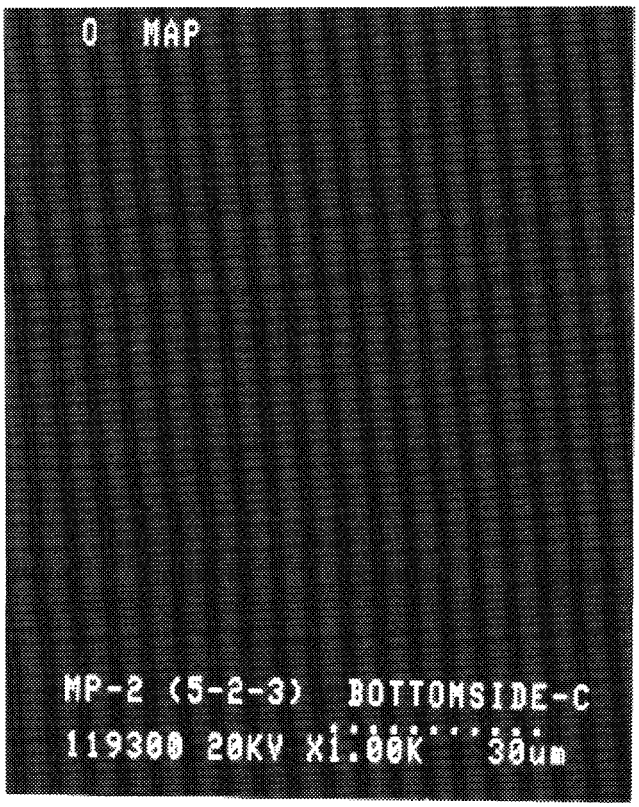

Figure C-2.4c Scanning Electron Micrographs and Corresponding Elemental Maps for the Relocated Material Just Under Metallic Crust Remnant (RM-1)

SEM

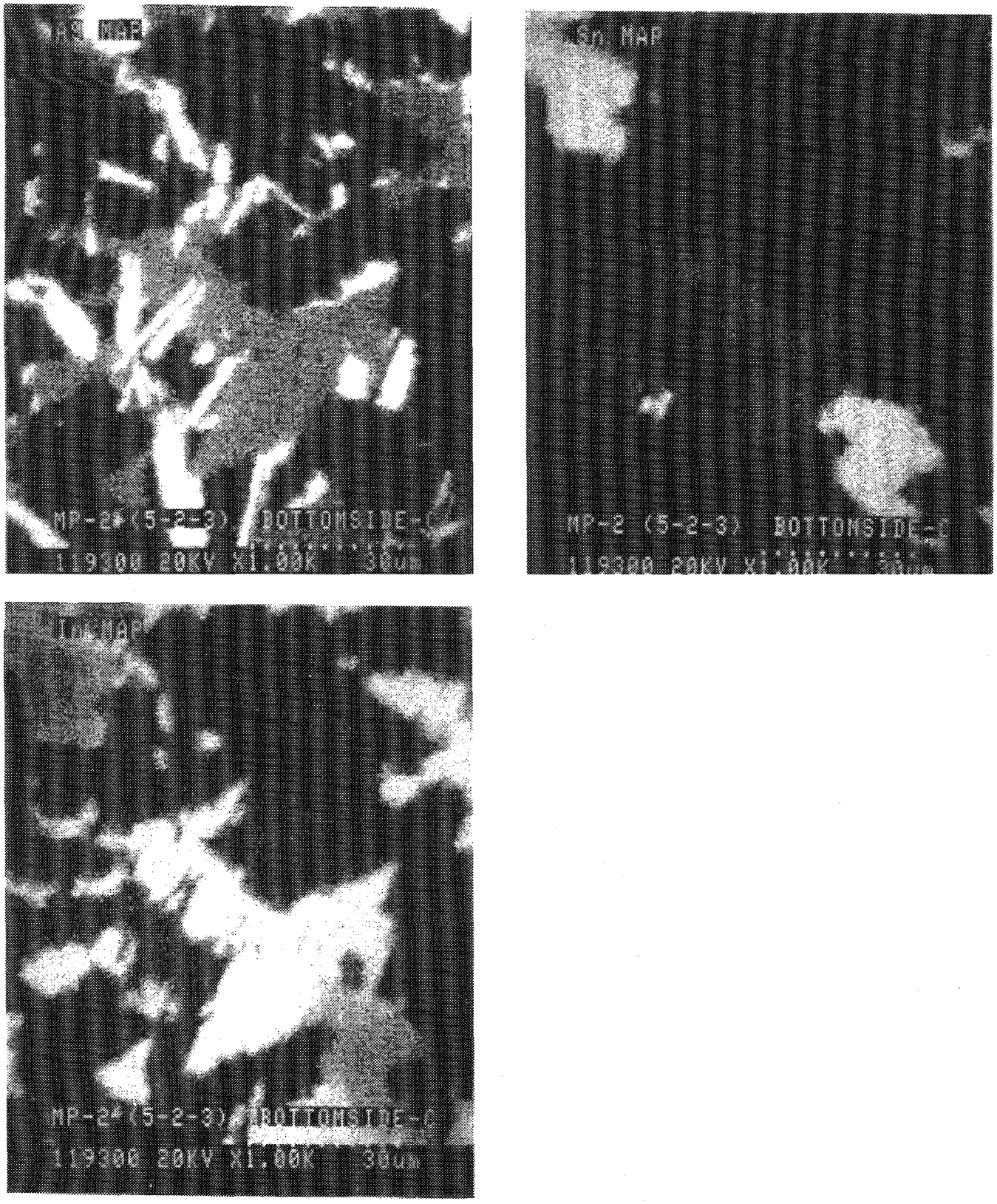

Figure C-2.4d Scanning Electron Micrographs and Corresponding Elemental Maps for the Relocated Material Just Under Metallic Crust Remnant (RM-1)

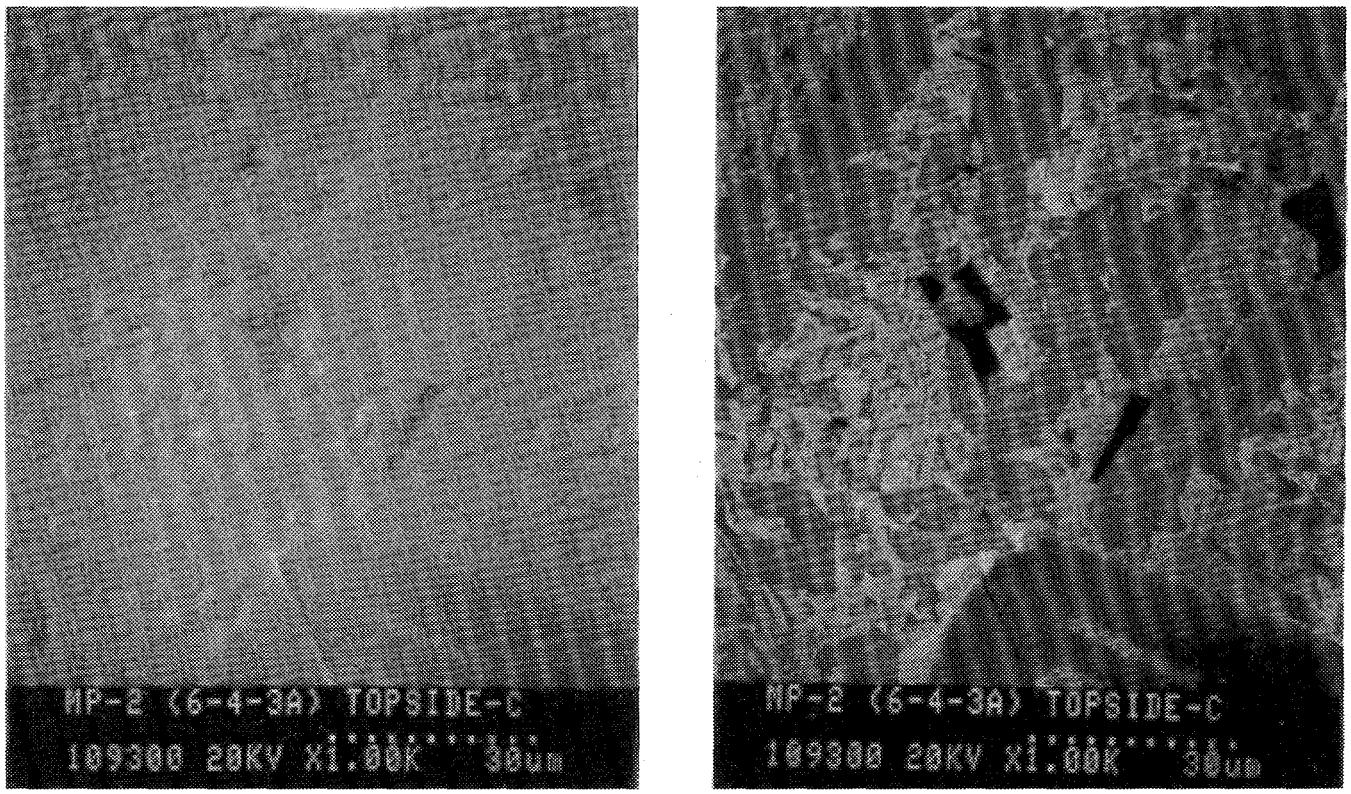

Figure C-2.5a Scanning Electron Micrographs and Corresponding Elemental Maps for the Relocated Material in the Mid-Section of Fuel Array (RM-2)

SEM

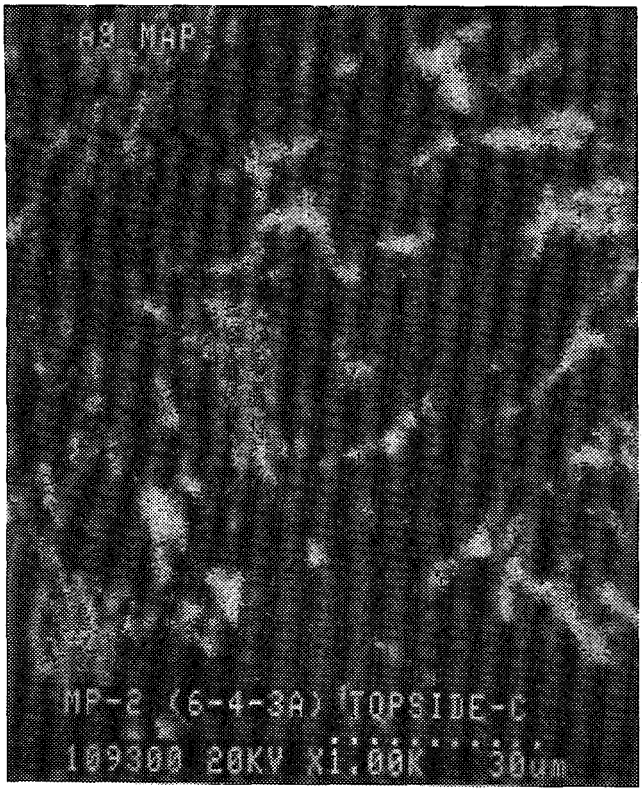

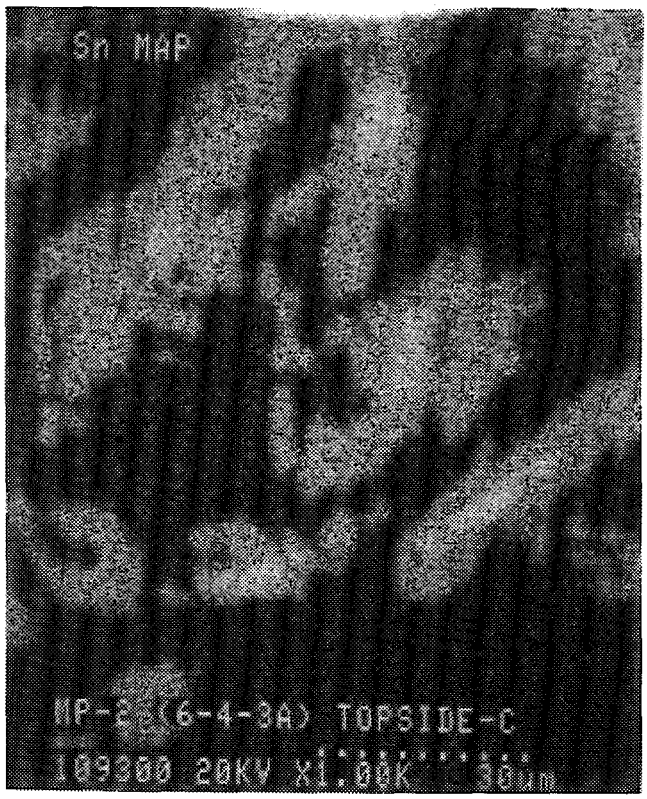

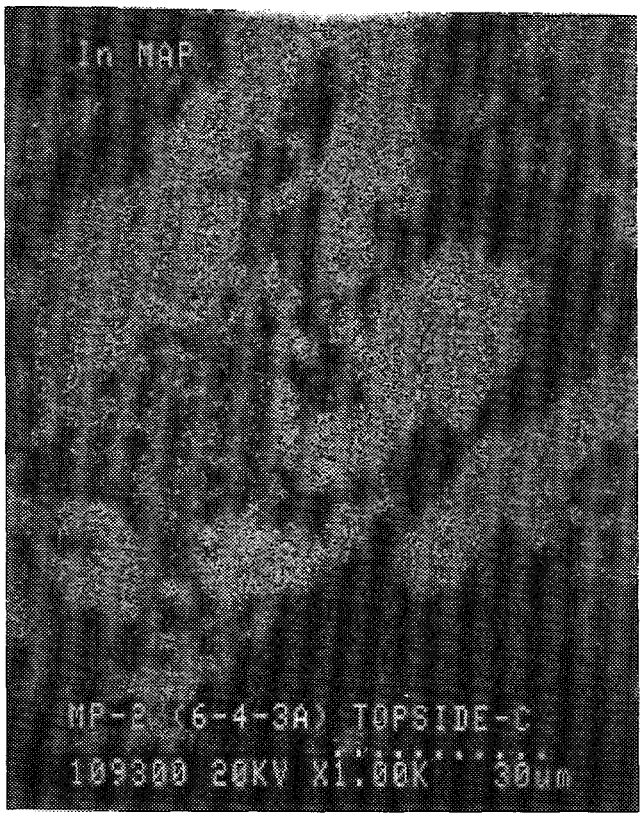

Figure C-2.5b Scanning Electron Micrographs and Corresponding Elemental Maps for the Relocated Material in the Mid-Section of Fuel Array (RM-2)

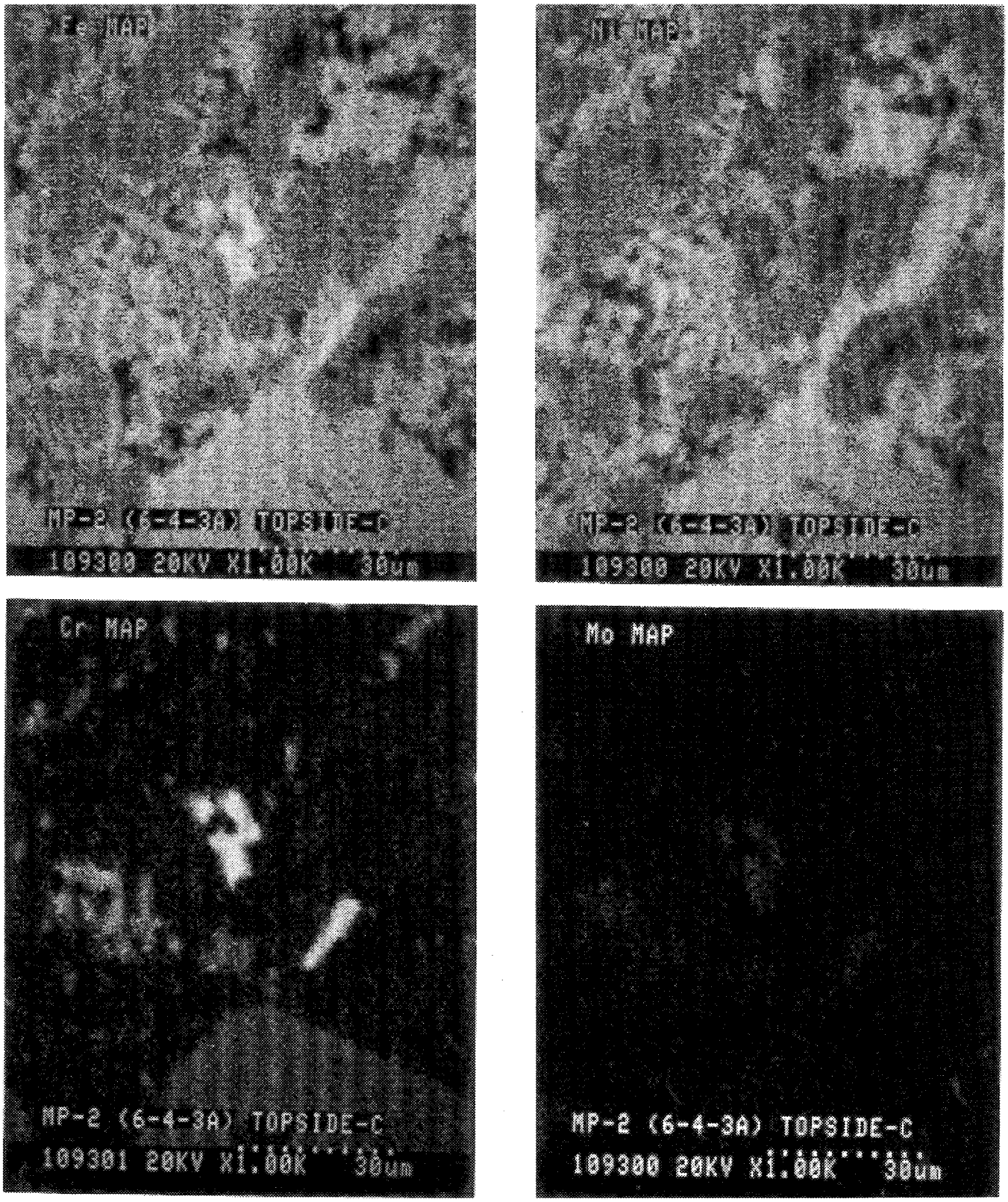

Figure C-2.5c Scanning Electron Micrographs and Corresponding Elemental Maps for the Relocated Material in the Mid-Section of Fuel Array (RM-2)

SEM

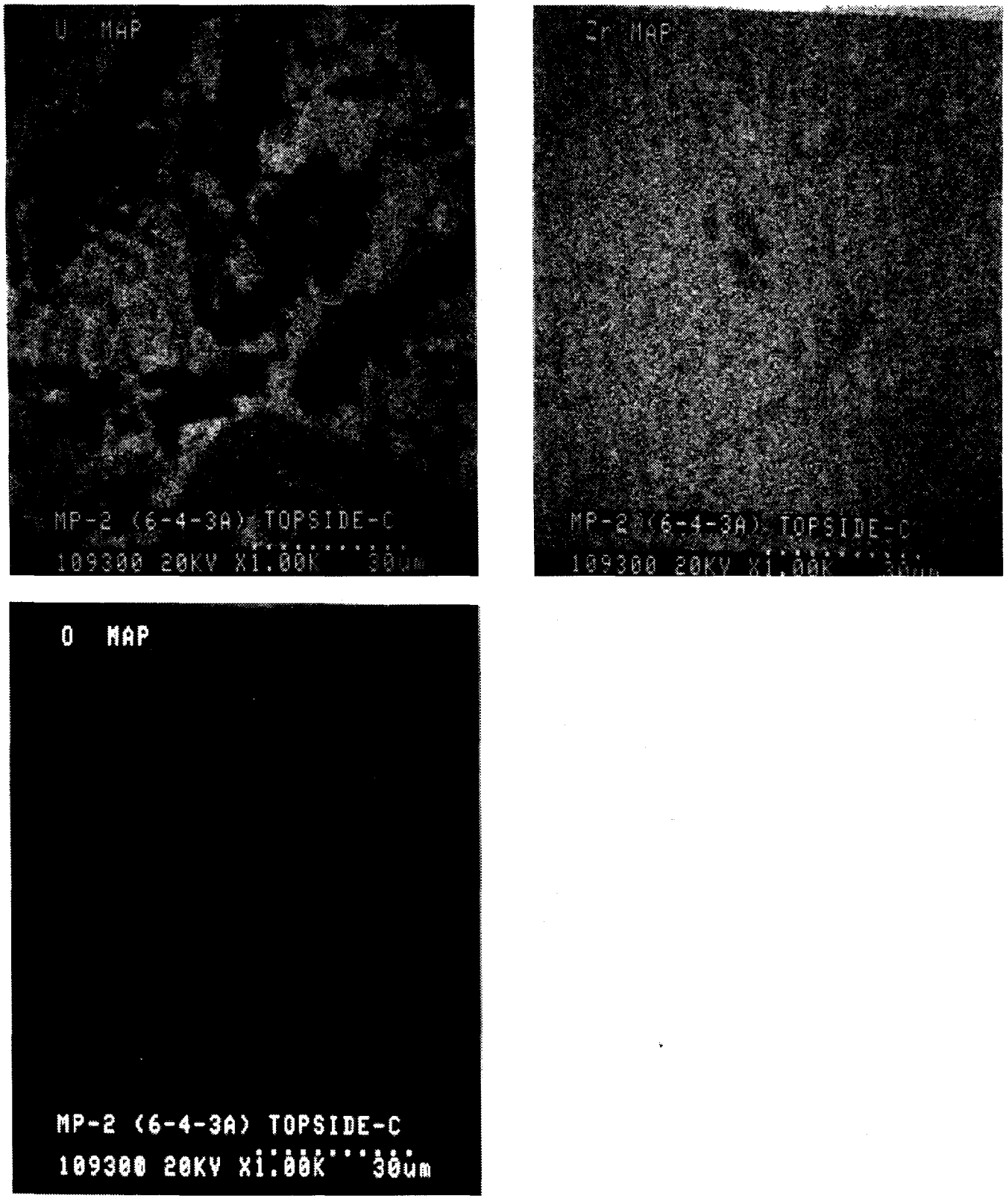

Figure C-2.5d Scanning Electron Micrographs and Corresponding Elemental Maps for the Relocated Material in the Mid-Section of Fuel Array (RM-2)

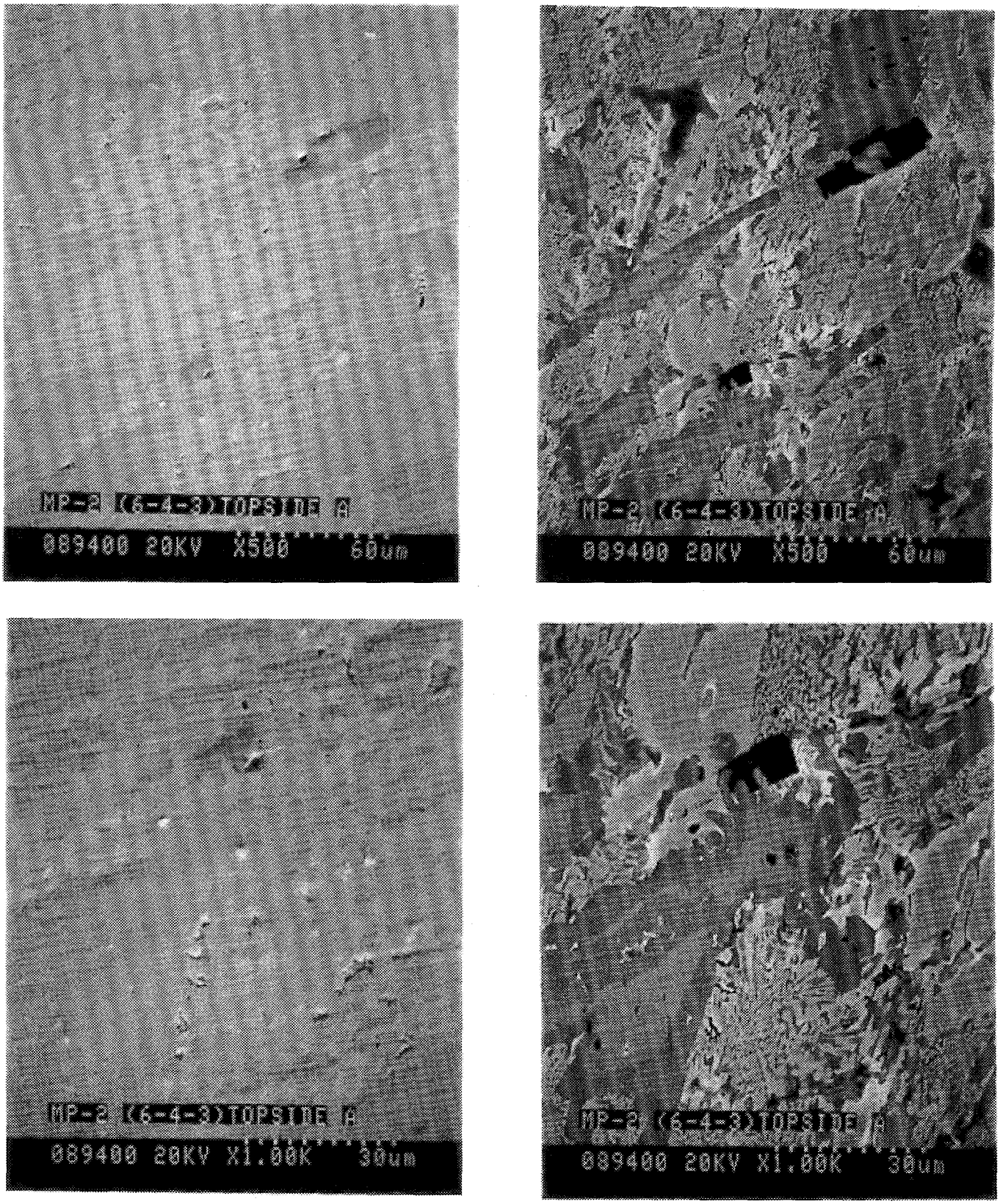

Figure C-2.6a Scanning Electron Micrographs and Corresponding Elemental Maps for the Relocated Material in the Mid-Section of Fuel Array (RM-2*)

SEM

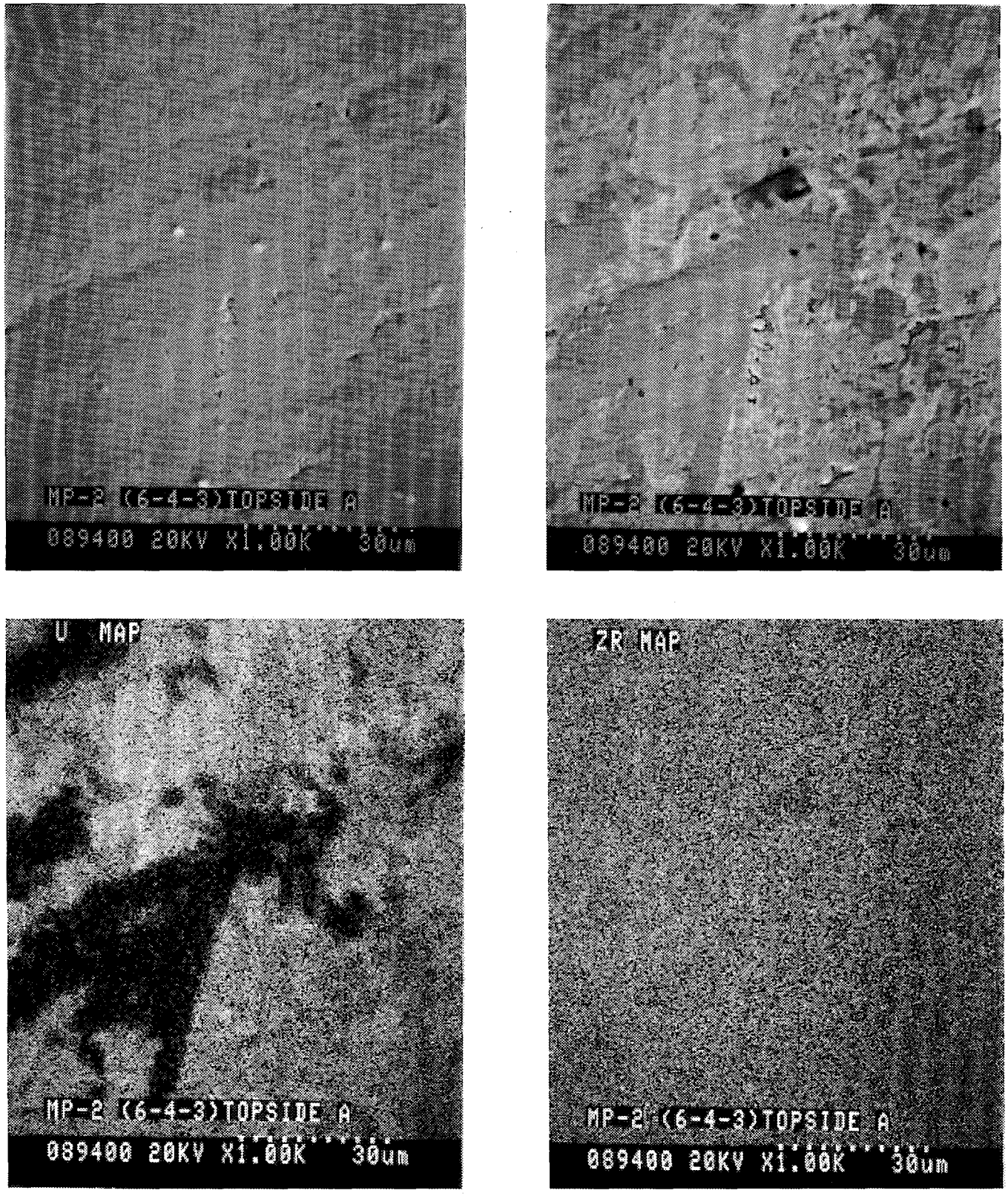

Figure C-2.6b Scanning Electron Micrographs and Corresponding Elemental Maps for the Relocated Material in the Mid-Section of Fuel Array (RM-2*)

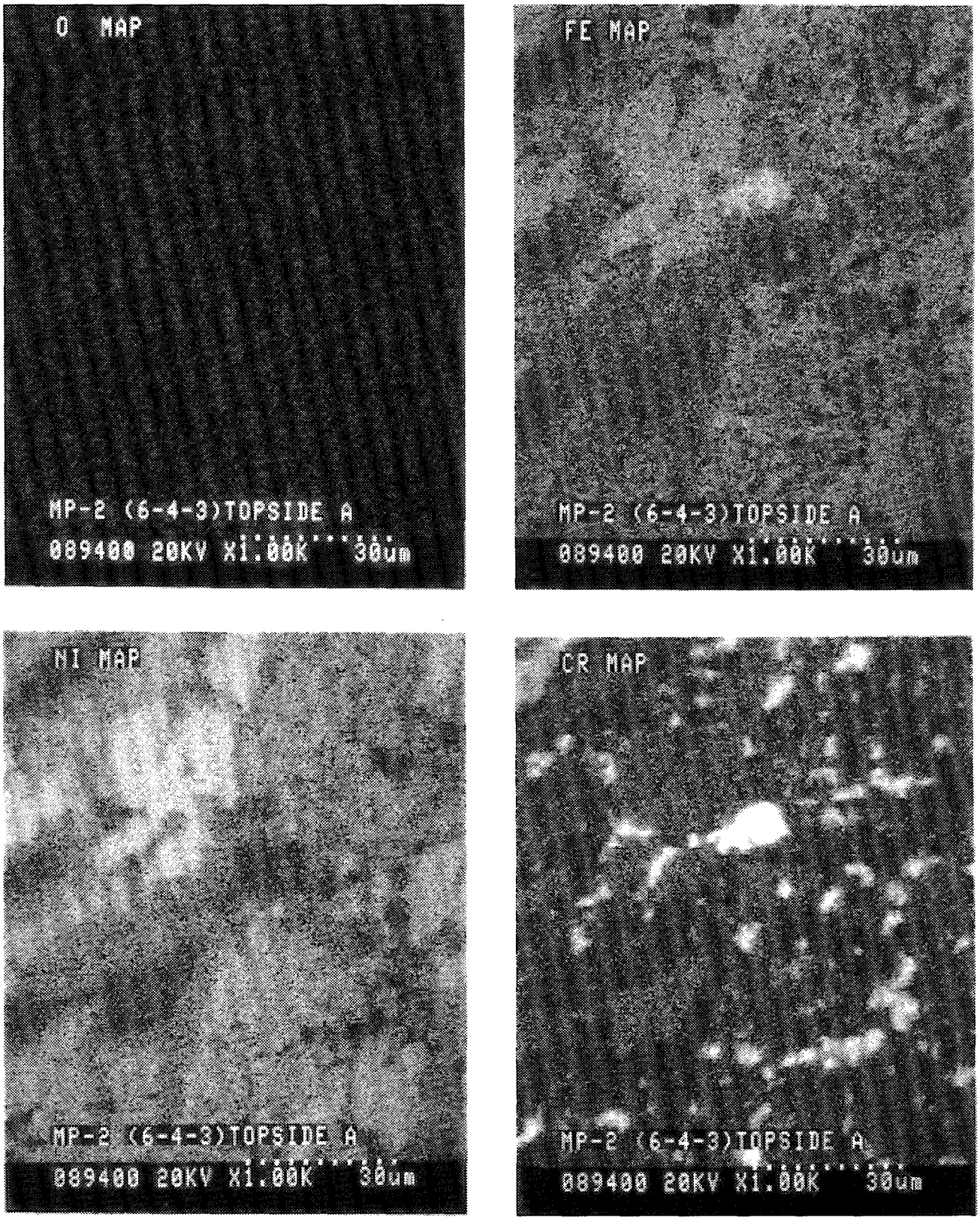

Figure C-2.6c Scanning Electron Micrographs and Corresponding Elemental Maps for the Relocated Material in the Mid-Section of Fuel Array (RM-2*)

SEM

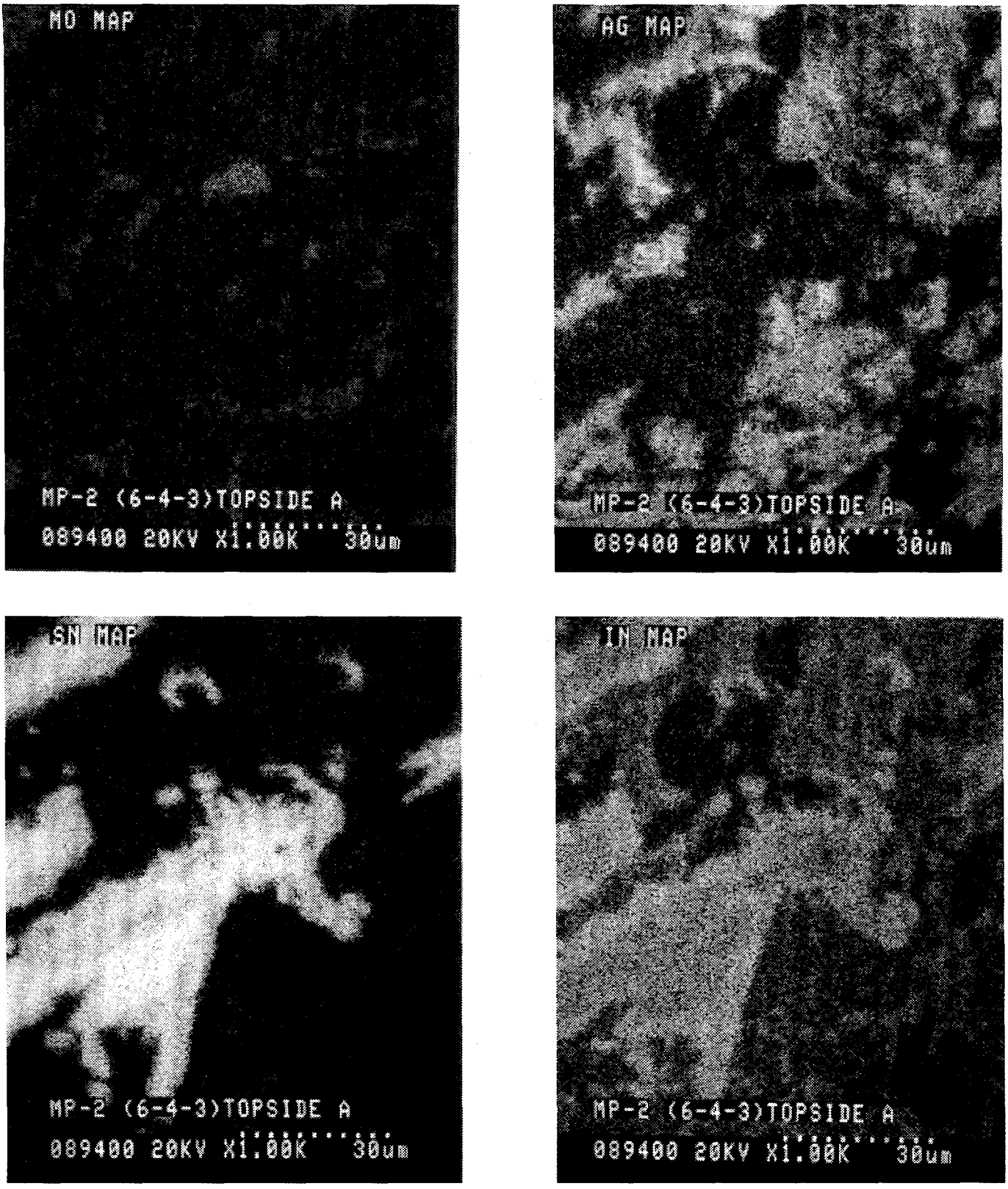

Figure C-2.6d Scanning Electron Micrographs and Corresponding Elemental Maps for the Relocated Material in the Mid-Section of Fuel Array (RM-2*)

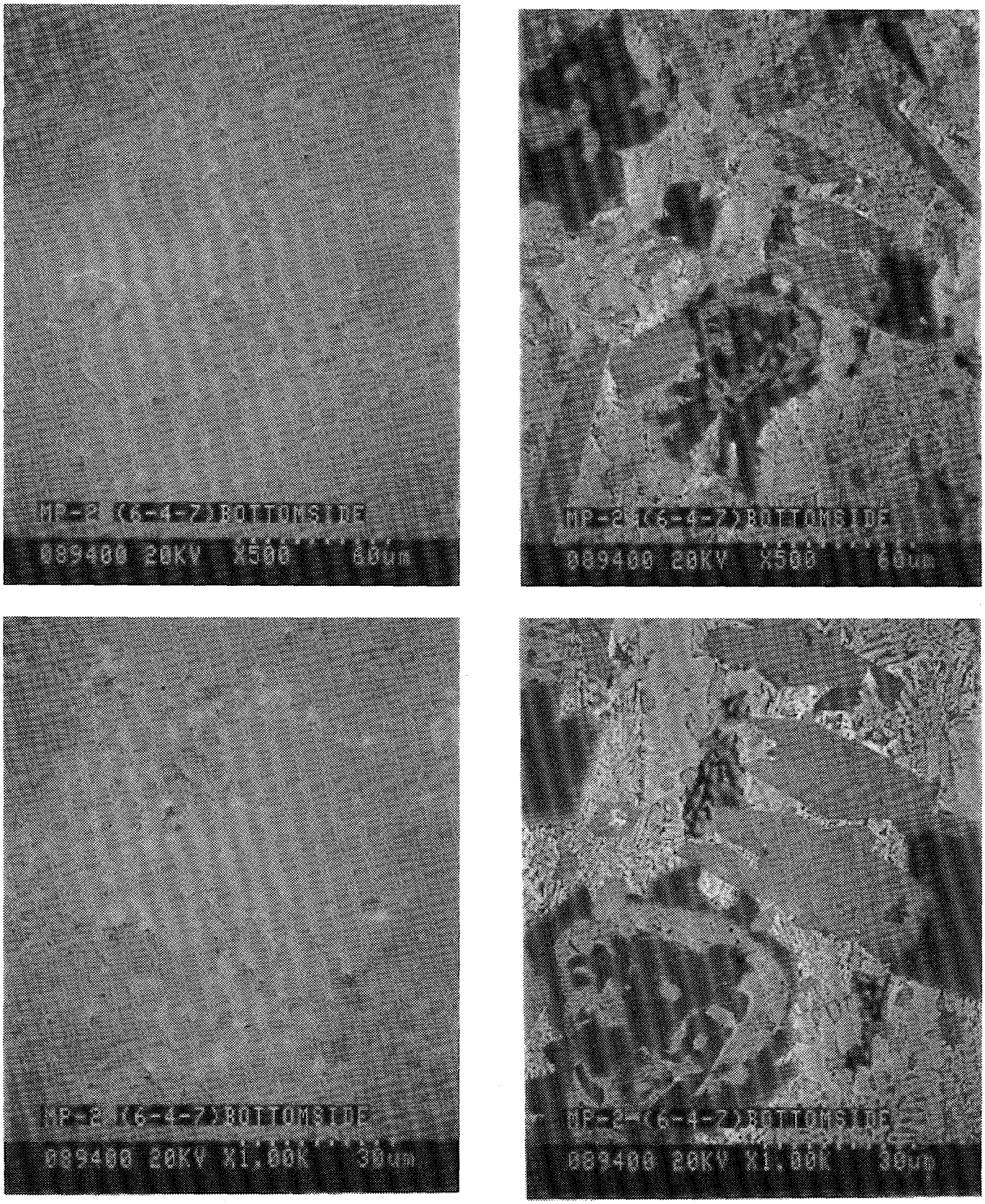

Figure C-2.7a Scanning Electron Micrographs and Corresponding Elemental Maps for the Relocated Material in the Bottom of the Test Capsule (RM-2.5)

SEM

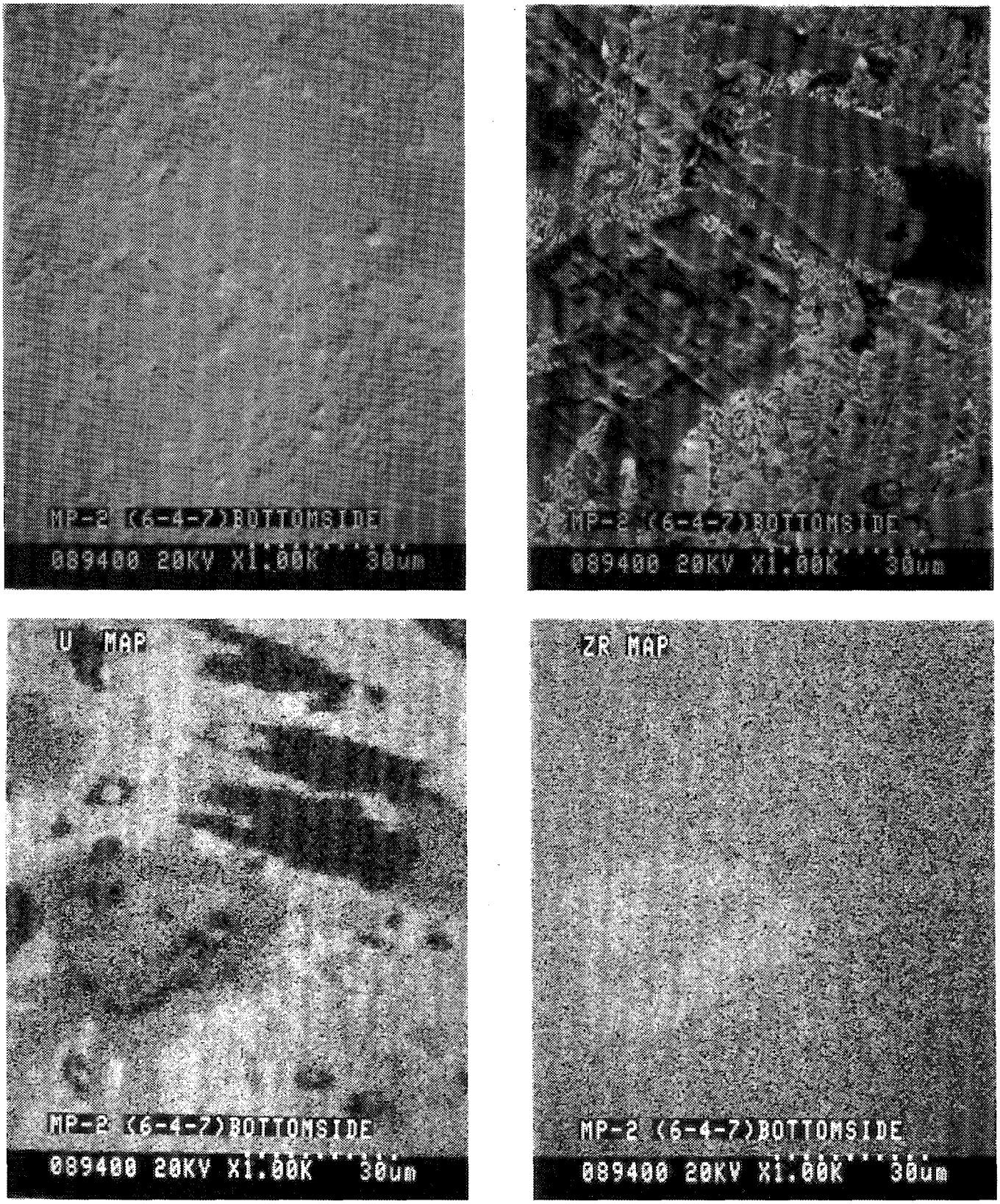

Figure C-2.7b Scanning Electron Micrographs and Corresponding Elemental Maps for the Relocated Material in the Bottom of the Test Capsule (RM-2.5)

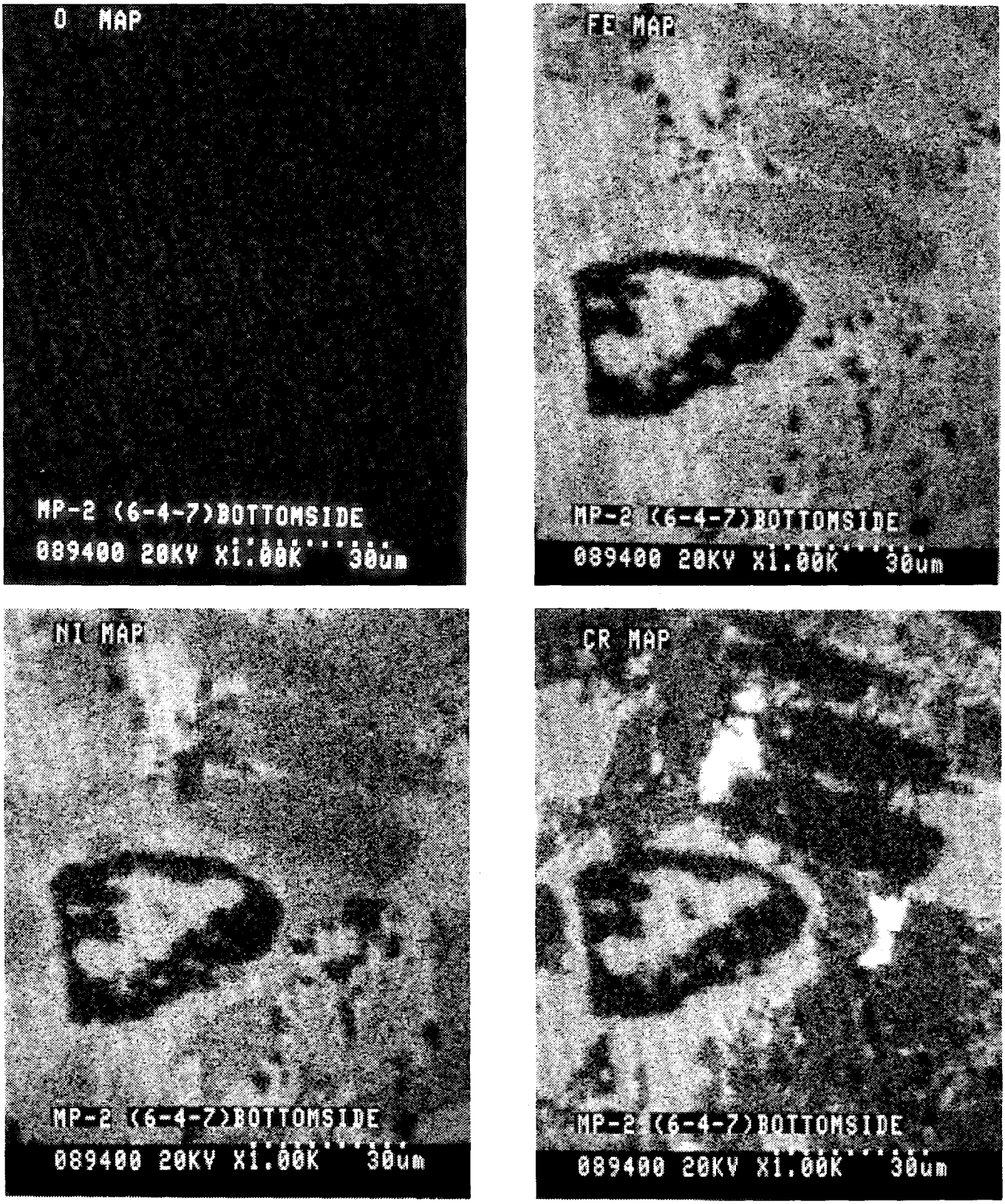

Figure C-2.7c Scanning Electron Micrographs and Corresponding Elemental Maps for the Relocated Material in the Bottom of the Test Capsule (RM-2.5)

SEM

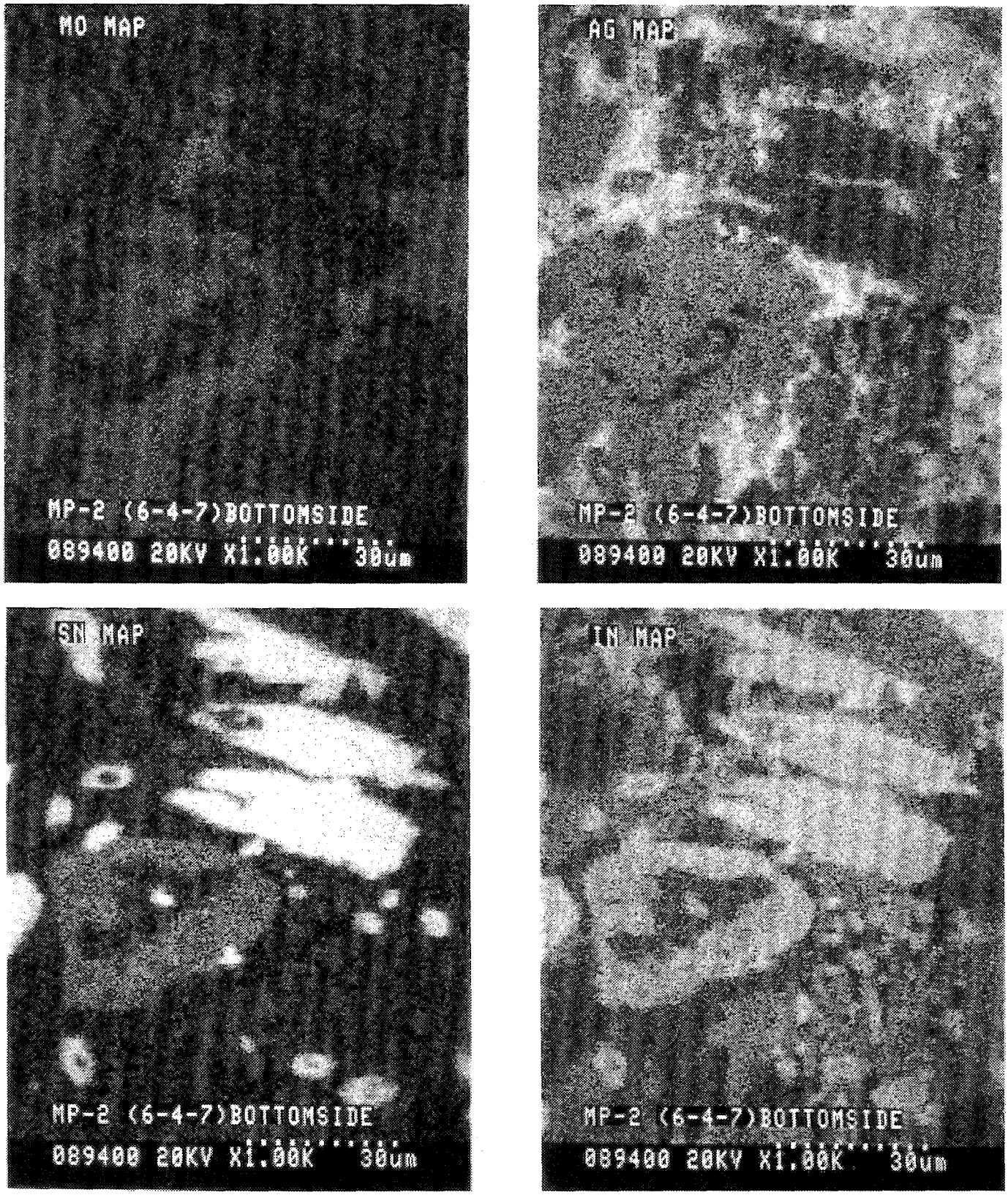

Figure C-2.7d Scanning Electron Micrographs and Corresponding Elemental Maps for the Relocated Material in the Bottom of the Test Capsule (RM-2.5)

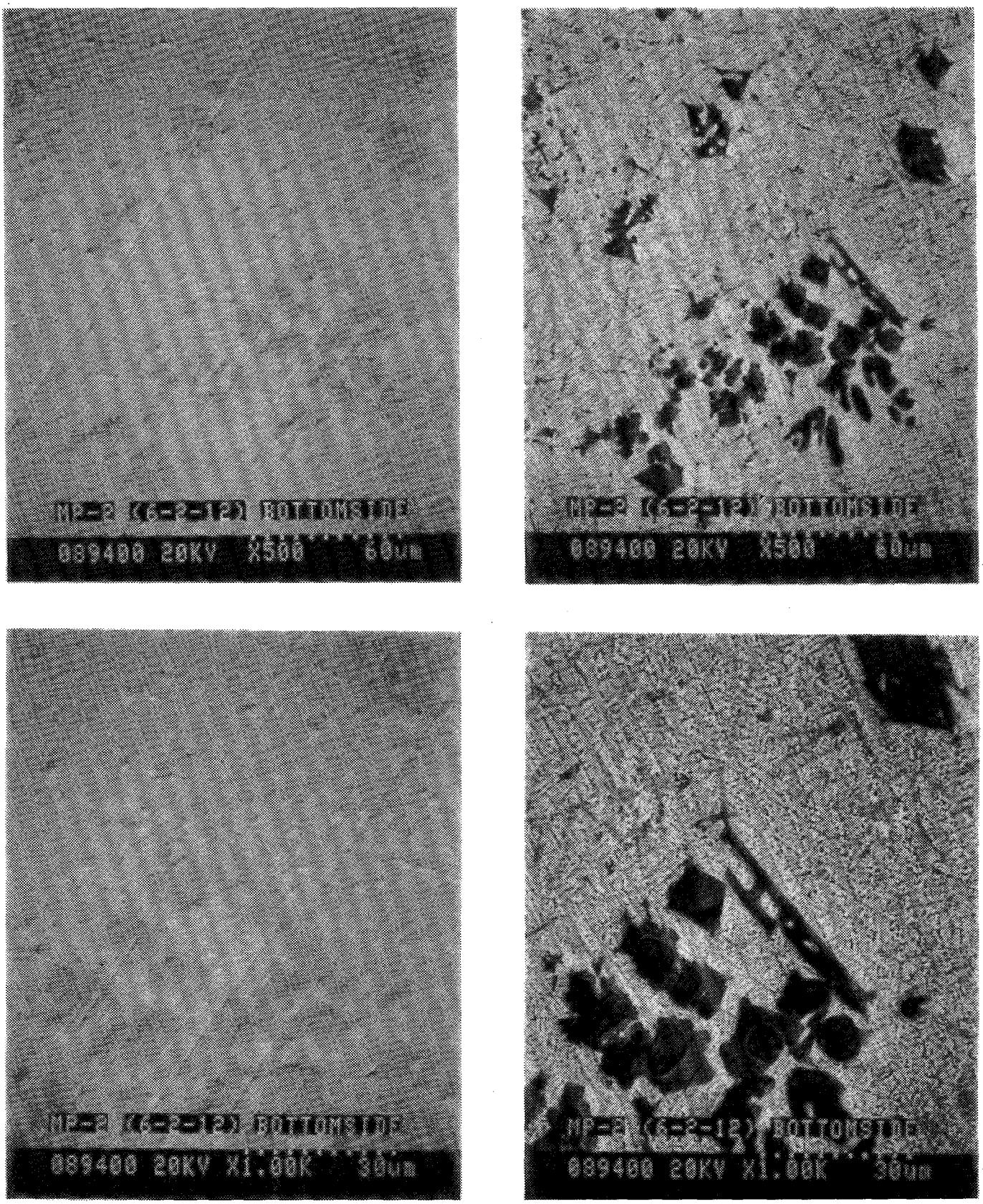

Figure C-2.8a Scanning Electron Micrographs and Corresponding Elemental Maps for the Relocated Material in the Bottom of the Test Capsule (RM-3*)

SEM

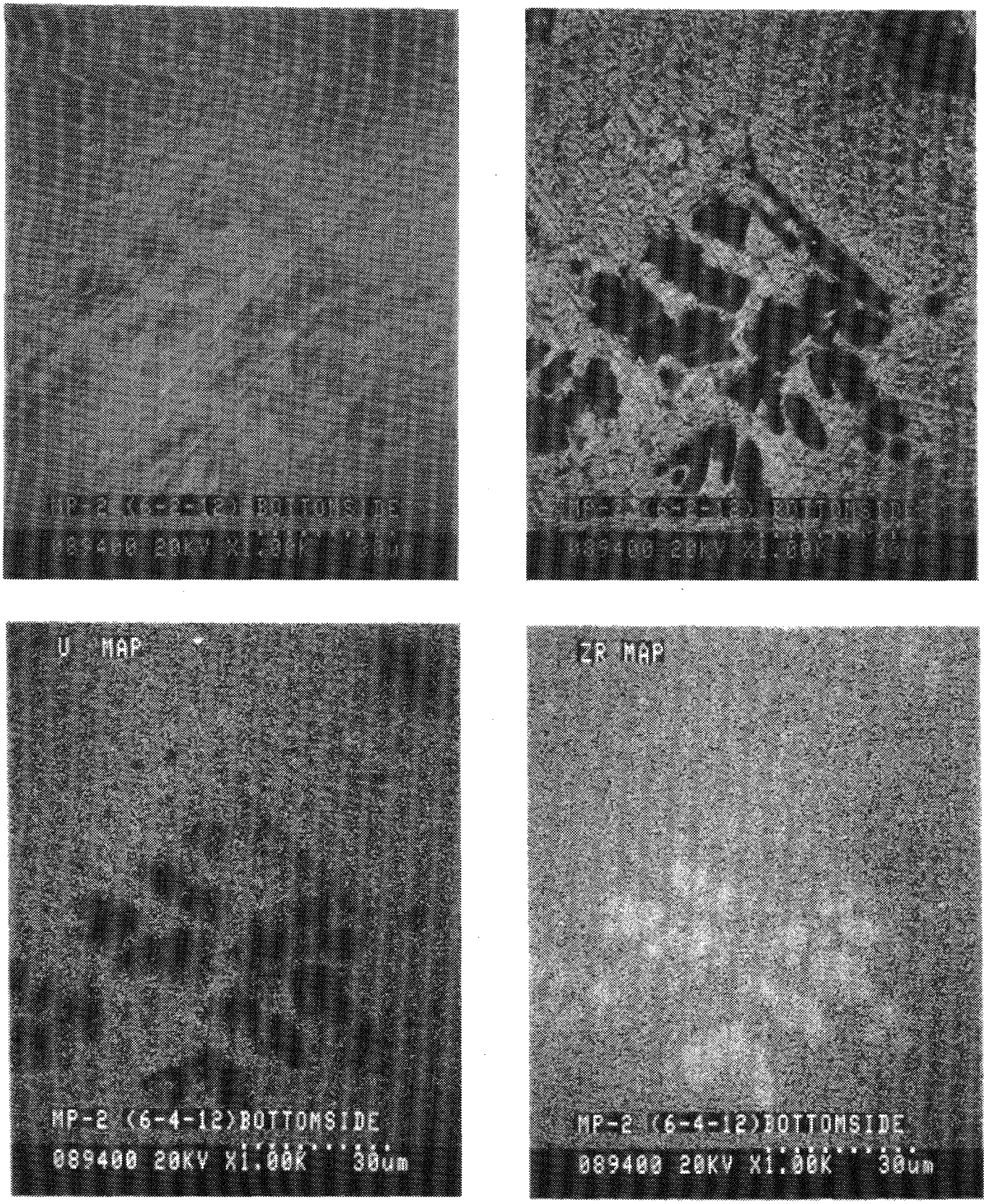

Figure C-2.8b Scanning Electron Micrographs and Corresponding Elemental Maps for the Relocated Material in the Bottom of the Test Capsule (RM-3*)

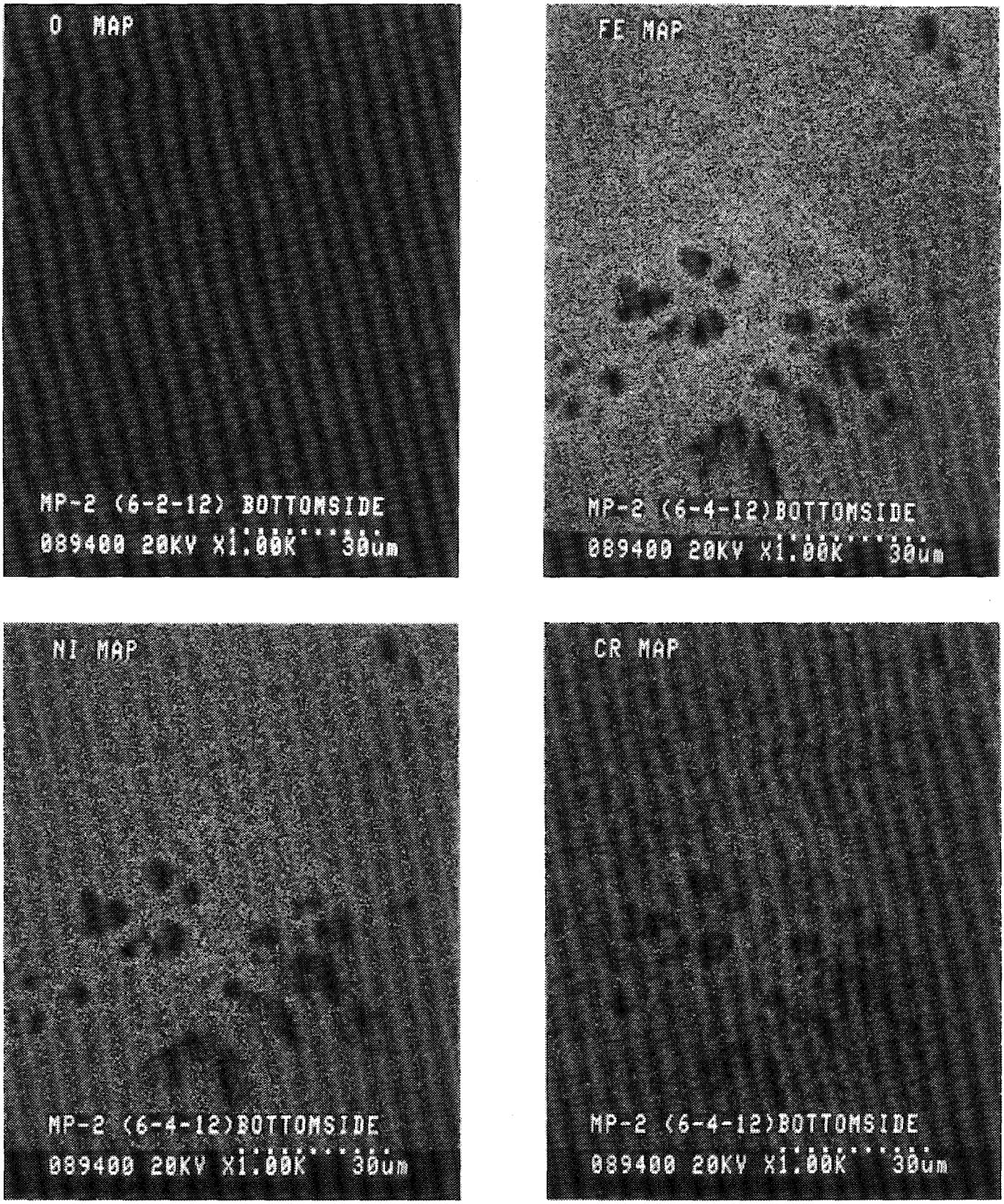

Figure C-2.8c Scanning Electron Micrographs and Corresponding Elemental Maps for the Relocated Material in the Bottom of the Test Capsule (RM-3*)

SEM

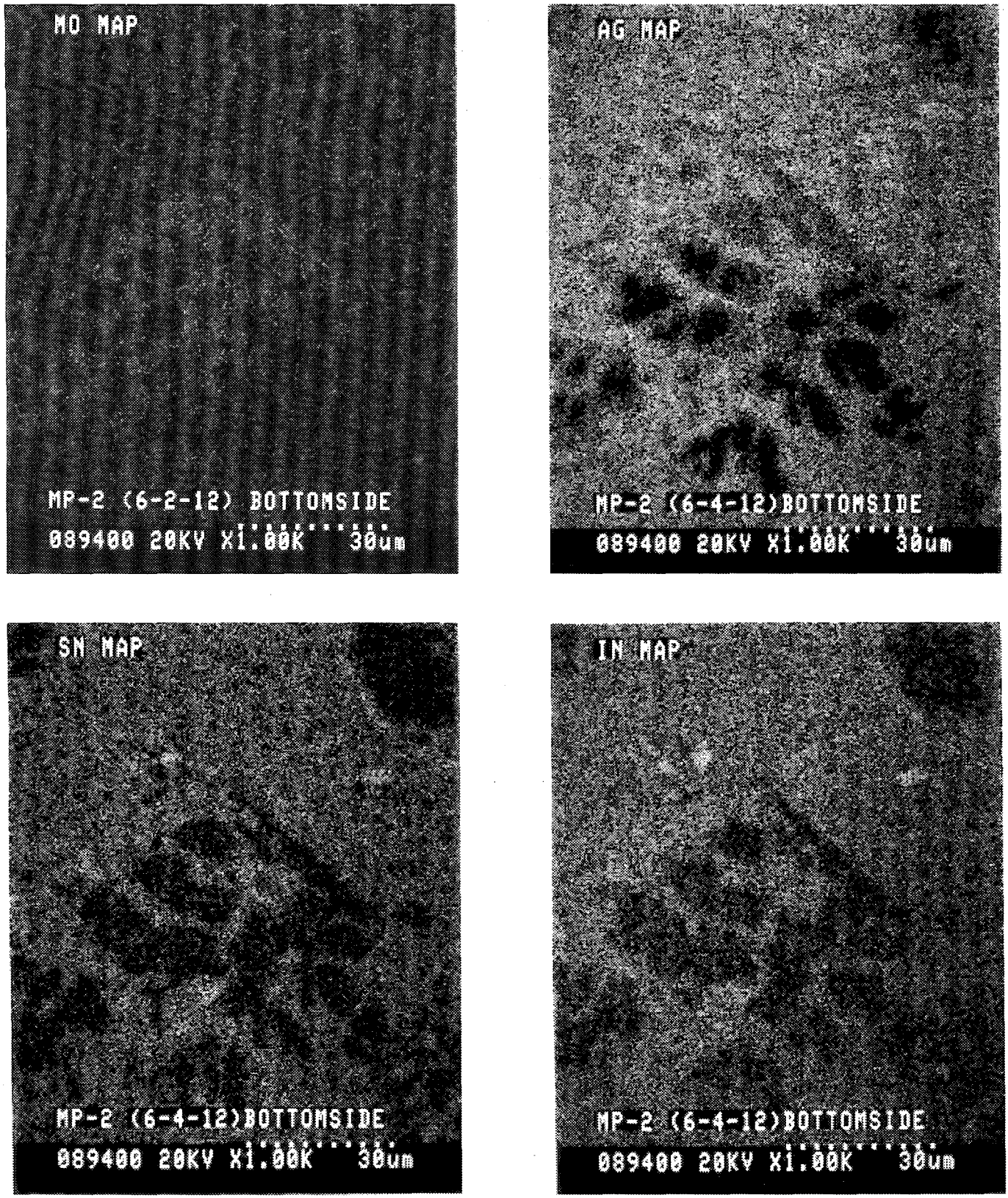

Figure C-2.8d Scanning Electron Micrographs and Corresponding Elemental Maps for the Relocated Material in the Bottom of the Test Capsule (RM-3*)

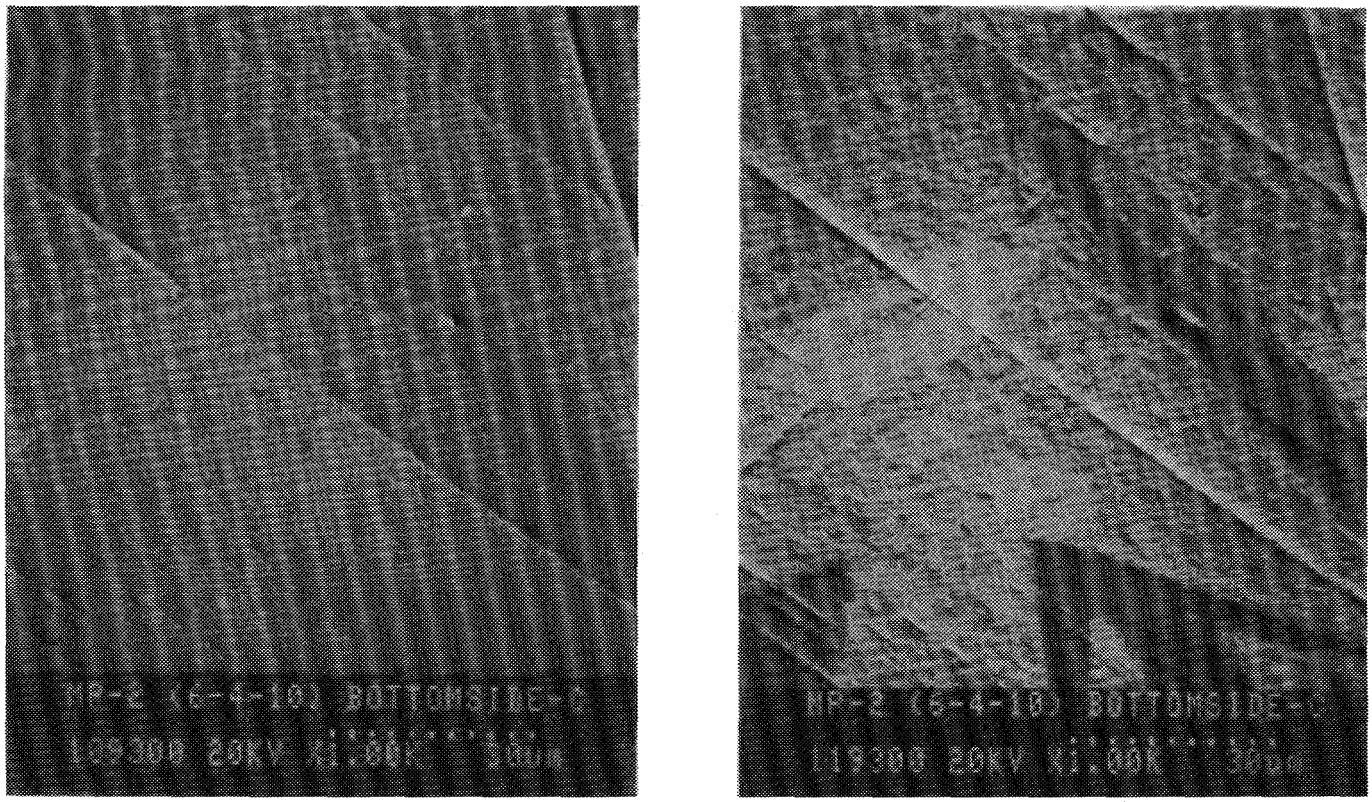

Figure C-2.9a Scanning Electron Micrographs and Corresponding Elemental Maps for the Relocated Material in the Bottom of the Test Capsule (RM-3)

SEM

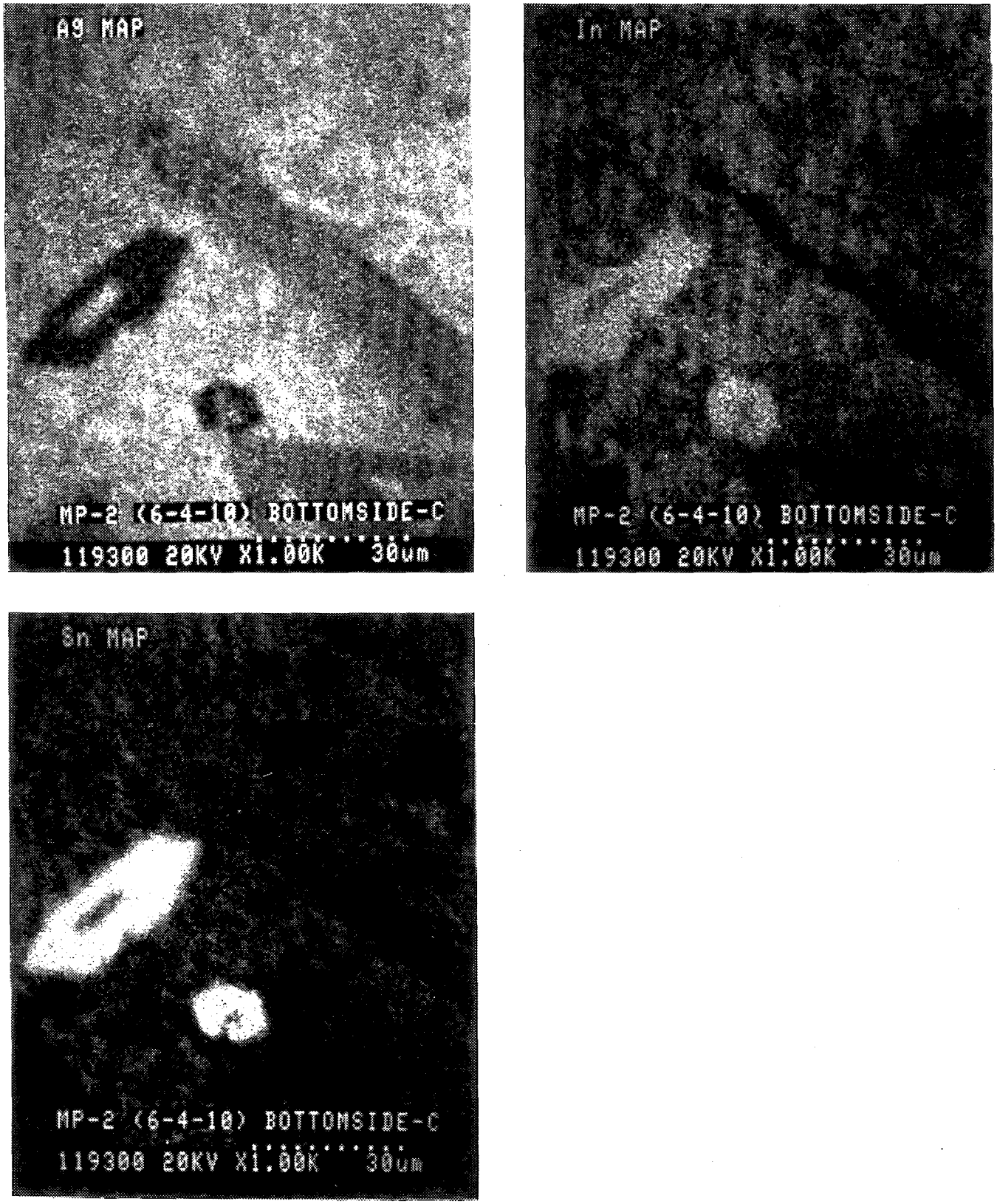

Figure C-2.9b Scanning Electron Micrographs and Corresponding Elemental Maps for the Relocated Material in the Bottom of the Test Capsule (RM-3)

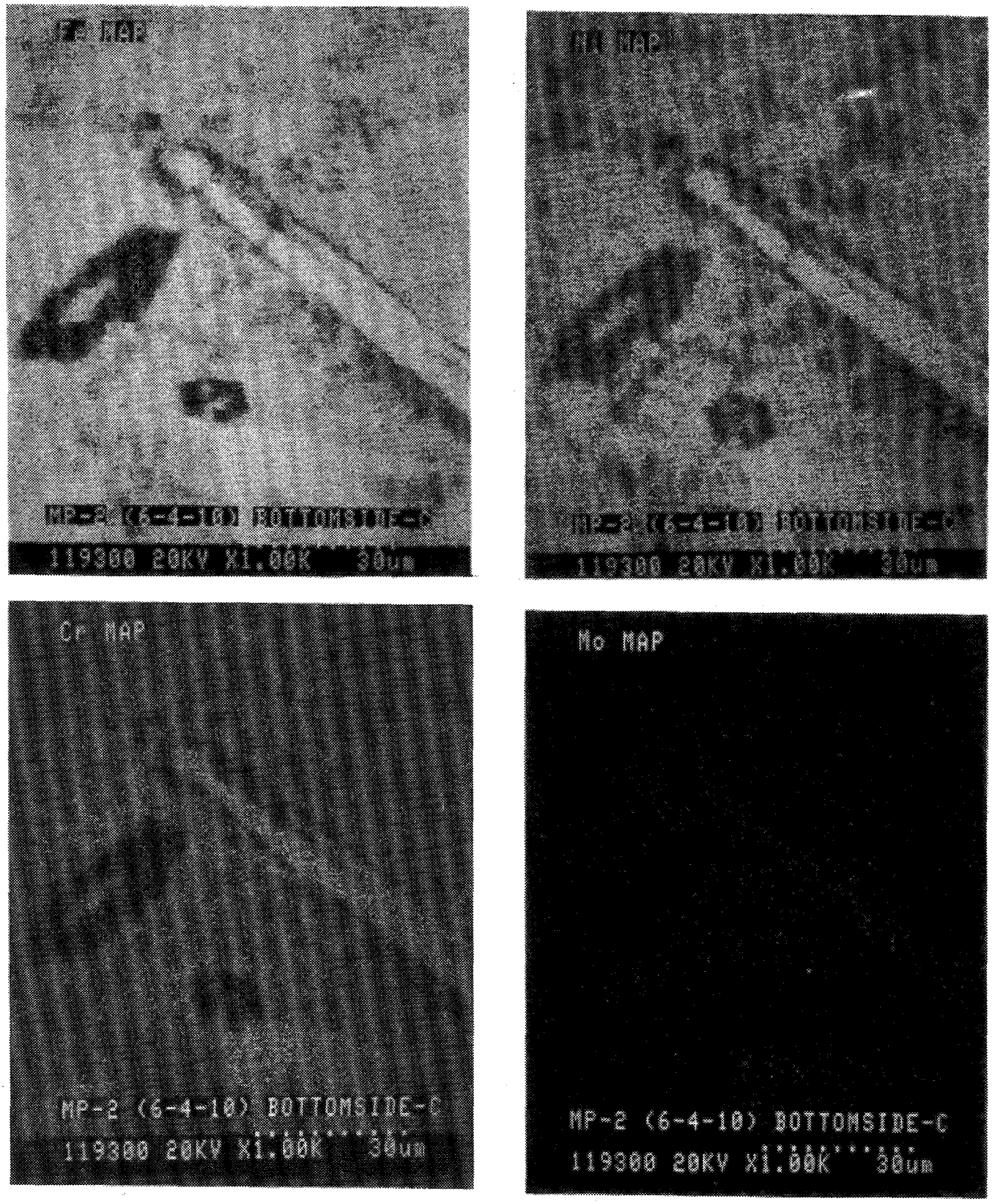

Figure C-2.9c Scanning Electron Micrographs and Corresponding Elemental Maps for the Relocated Material in the Bottom of the Test Capsule (RM-3)

SEM

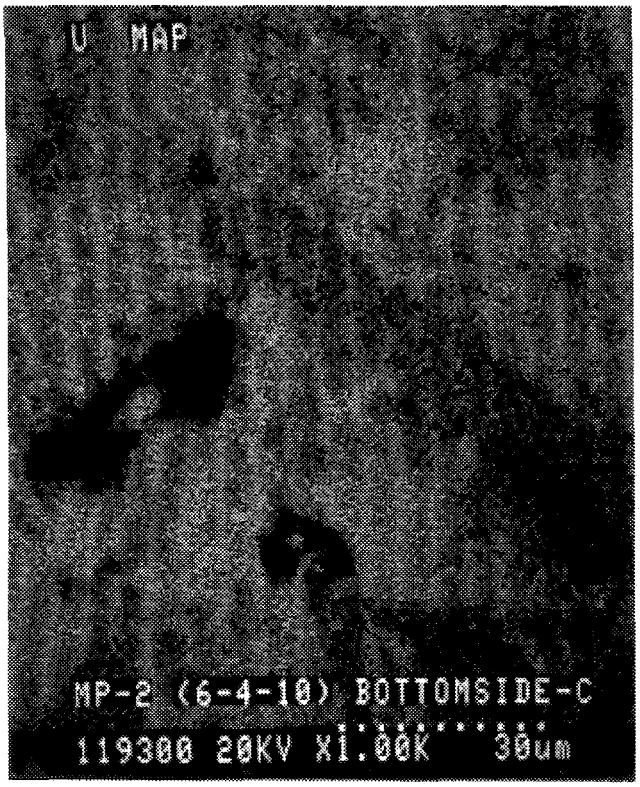

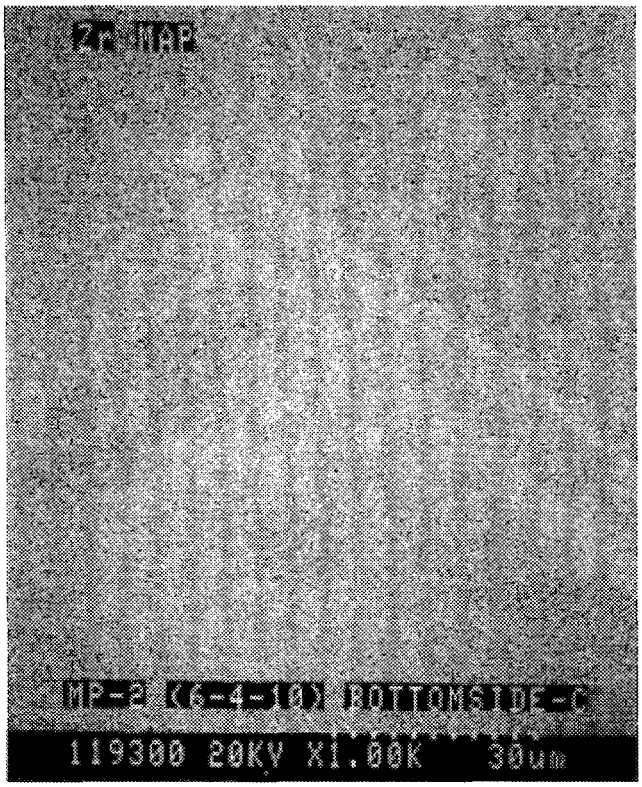

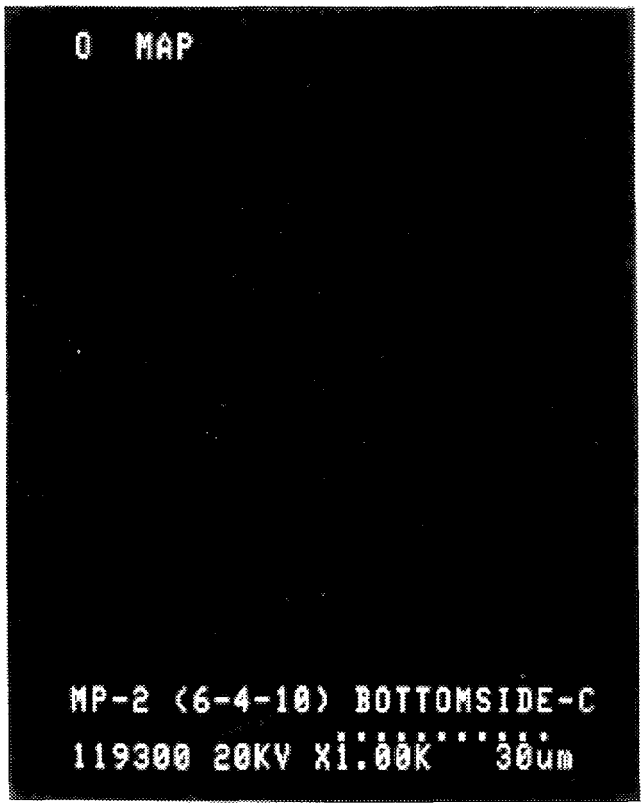

Figure C-2.9d Scanning Electron Micrographs and Corresponding Elemental Maps for the Relocated Material in the Bottom of the Test Capsule (RM-3)

Appendix D. MP-2 Measured Data

Appendix D is on one card of microfiche in pocket on inside of back cover.

NRC FORM 335 (2-89) NRCM 1102, 3201, 3202

U.S. NUCLEAR REGULATORY COMMISSION

BIBLIOGRAPHIC DATA SHEET

(See instructions on the reverse)

1. REPORT NUMBER (Assigned by NRC, Add Vol., Supp., Rev., and Addendum Numbers, if any.)

NUREG/CR-6167
SAND93-3931

2. TITLE AND SUBTITLE

Late Phase Melt Progressioin Experiment MP-2: Results and Analysis

3. DATE REPORT PUBLISHED

MONTH	YEAR
May	1997

4. FIN OR GRANT NUMBER

A1335, L2452

5. AUTHOR(S)

R.D. Gasser, R.O. Gauntt, S.C. Bourcier, R.C. Schmidt, L.L. Humphries,* K.O. Reil

6. TYPE OF REPORT

Technical

7. PERIOD COVERED *(Inclusive Dates)*

1988 - 1995

8. PERFORMING ORGANIZATION - NAME AND ADDRESS *(If NRC, provide Division, Office or Region, U.S. Nuclear Regulatory Commission, and mailing address; if contractor, provide name and mailing address.)*

Sandia National Laboratories
Albuquerque, NM 87185-1139

*Science Applications International Corporation
2109 Park Road SE
Albuquerque, NM 87106

9. SPONSORING ORGANIZATION - NAME AND ADDRESS *(If NRC, type "Same as above"; if contractor, provide NRC Division, Office or Region, U.S. Nuclear Regulatory Commission, and mailing address.)*

Division of Systems Technology
Office of Nuclear Regulatory Research
U.S. Nuclear Regulatory Commission
Washington, DC 20555-0001

10. SUPPLEMENTARY NOTES

A.C. Malliakos, NRC Project Manager

11. ABSTRACT *(200 words or less)*

A series of in-pile experiments addressing the phenomenology associated with Late-Phase processes in Light Water Reactors (LWRs) has been performed in the Annular Core Research Reactor (ACRR) at Sandia National Laboratories. The Melt Progression (MP) experiments were designed to provide information as part of the effort to develop and verify computer models for the LWR core damage during severe accidents. The MP-2 experiment is the second experiment in this series. The MP-2 experiment examine the formation and movement of ceramic molten pools that form in the disrupted regions of a reactor core. The MP-2 experiment assembly consisted of three regions of three regions: (1) a rubble bed composed of enriched UO_2 and ZrO_2 that simulated the severely disrupted regions of the reactor core, (2) a composite ceramic/metallic crust which represented the blockage formed by the early phase melting, relocation, and refreezing of mostly metallic core components, and (3) an intact rod stub region that remained in place below the blockage region. The test assembly was fission heated in the central cavity of the ACRR at an average rate of ~0.2 K/s ultimately achieving a peak temperature in the molten pool of ~3400 K. As ACRR power levels were increased over time, the crust gradually remelted and reformed, penetrating into and attacking the ceramic/metallic blockage. the metallic components of the blockage region melted and relocated downward to the bottom of the intact rod stub region. The ceramic pool penetrated halfway into the blockage region at the end of the experiment. Postexperiment examination of the assembly with the associated material interactions and metallurgy are discussed in detail together with the analyses and interpretation of the results.

12. KEY WORDS/DESCRIPTORS *(List words or phrases that will assist researchers in locating the report.)*

late phase melt progression
debris bed heat transfer
molten pool propagation
molten pool/blockage interaction
core melt progression
severe reactor accident
in-vessel core meltdown
relocation phenomenology

13. AVAILABILITY STATEMENT

unlimited

14. SECURITY CLASSIFICATION

(This Page) unclassified

(This Report) unclassified

15. NUMBER OF PAGES

16. PRICE